

# Wind Farm as Power Plant

# Dynamic modelling studies

J.T.G. Pierik (ECN Wind Energy)

Y. Zhou

P. Bauer

(TUD Electrical Power Processing)





### **Abstract**

In the Wind farm as Power plant project (WaP) a library of four offshore wind farm dynamic models is extended with nine new models. The models can be used to investigate dynamic behaviour of wind farms, develop wind farm control strategies and determine the dynamic effects of wind farms on the grid. This report describes the nine new wind farm models and three new wind turbine and wind farm controllers. One of the new farm models is connected to shore by a thyristor bridge. Six models for the thyristor bridge have been developed and are described. The new wind farm models are demonstrated in a case study on flicker, voltage and frequency dip. For one particular case, the DFIG-ac system, control during an asymmetrical dip is developed and described. The project is completed by an aggregate wind farm model and a model for the wind speed deficit and turbulence in the farm.

**Keywords:** offshore wind farm electrical systems, offshore wind farm control, offshore wind farm models, offshore wind farm dynamics.

## Acknowledgement

The Wind Farm as Power Plant project (WaP) has been financially supported by the BSIK Program, executed by the we@sea consortium and by the ECN Programmafinanciering of the Ministry of Economic Affairs of the Netherlands.

This project is a continuation of the Erao projects, in which steady state (load flow), economic and dynamic models of offshore wind farms have been developed and validated.

The rotor effective wind, mechanical and pitch control models of the wind turbines models used in this project have been developed by Tim van Engelen and Eric van der Hooft (ECN). The description of the rotor effective wind model in appendix A is based on comments in the *vwroteff.m* routine by Tim van Engelen. The GCL model used in appendix A was developed by Gunnar Larson (Risoe National Laboratory). The description of GCL model is partly reproduced from [6] and partly based on a fax from Gunnar Larson. Gerard Schepers' help with the interpretation and programming of the GCL model is kindly acknowledged.

We@sea project number: 2004-009

Project title: Windfarm as Powerplant (WaP)

Project coordinator: ECN

Project partners: TUD-EPP, Nuon, Kema

Period: 1 september 2004 - 31 december 2007

ECN project number: 7.4392

# Contents

1	Intro	oduction	11
	1.1	Wind farm models developed in WaP	12
2	Cont	trol of variable speed electrical systems	17
	2.1	IGBT inverter control	17
	2.2	IGBT rectifier control	18
3	Thyr	ristor Bridge Models for Balanced and Unbalanced Conditions	21
	3.1	Introduction	21
	3.2	Specification of the thyristor bridge model	21
	3.3	Park transformation	23
		3.3.1 Park transformation for an unbalanced system	23
		3.3.2 RMS values and phase angles	24
	3.4	Quasi-steady state thyristor bridge models	25
		3.4.1 Average quasi steady-state model for balanced conditions (Model Thy1)	
		3.4.2 Average quasi steady-state model, unbalanced, Fourier (Model Thy2) .	31
		3.4.3 Av. quasi-steady state, unbalanced, partially symmetrical (Model Thy3)	
	3.5	Instantaneous thyristor bridge models	44
		3.5.1 Instantaneous diode bridge without commutation inductance (Model Thy	4a) 44
		3.5.2 Instantaneous thyristor bridge without commutation inductance (Model 7	
		3.5.3 Instantaneous thyristor bridge with commutation inductance (Model Thy	
	3.6	Thyristor bridge models summary	
	3.7	Verification of the thyristor bridge models	
		3.7.1 Verification for balanced conditions	
		3.7.2 Verifications for unbalanced conditions	
	3.8	Conclusion and recommendation	65
4	N	late of mind for any mids and any death and in a (CCC)	67
4		lels of wind farms with constant speed stall turbines (CSS)	67
	4.1	Wind farm with a CSS-IG-dc electric system (# 1)	
		4.1.1 CSS-IG-dc layout and control	
	4.0	4.1.2 CSS-IG-dc wind farm normal operation	
	4.2	Wind farm with a CSS-CCIG-dc electric system (# 2)	
		4.2.1 CSS-CCIG-dc layout and control	72
		4.2.2 CSS-CCIG-dc wind farm normal operation	74
5	Mod	els of wind farms with variable speed pitch turbines (VSP)	77
	5.1	Wind farm with a VSP-CCIG-ac electric system (# 3)	77
		5.1.1 VSP-CCIG-ac layout and control	77
		5.1.2 VSP-CCIG-ac wind farm normal operation	79
	5.2	Wind farm with a VSP-CCIG-dc electric system (# 4)	82
		5.2.1 VSP-CCIG-dc layout and control	82
		5.2.2 VSP-CCIG-dc wind farm normal operation	83
	5.3	Wind farm with a VSP-DFIG-dc electric system (# 5)	86
		5.3.1 VSP-DFIG-dc layout and control	86

		5.3.2 VSP-DFIG-dc wind farm normal operation
	5.4	Wind farm with a VSP-FCIG-ac electric system (# 6) 90
		5.4.1 VSP-FCIG-ac layout and control
		5.4.2 VSP-FCIG-ac wind farm normal operation
	5.5	Wind farm with a VSP-FCSM-ac electric system (# 7)
		5.5.1 VSP-FCSM-ac layout and control
		5.5.2 VSP-FCSM-ac wind farm normal operation
	5.6	Wind farm with a VSP-FCSM-dc electric system (# 8)
		5.6.1 VSP-FCSM-dc layout and control
		5.6.2 VSP-FCSM-dc wind farm normal operation
6	Wind	farm with a VSP-DFIG-thy electric system (# 9) 107
	6.1	Objective
	6.2	DFIG-thy Steady State
		6.2.1 System layout
		6.2.2 Steady State Calculation
	6.3	Control of DFIG-thy
		6.3.1 Traditional $P$ , $Q$ control in high voltage transmission power system 112
		6.3.2 Traditional Grid-Flux Oriented Control of DFIG
		6.3.3 Terminal Voltage Control of DFIG-thy
		6.3.4 Stator-Flux Oriented Control of DFIG-thy
	6.4	Simulink Models of Terminal Voltage Control and Stator-Flux Oriented Control 122
		6.4.1 DFIG-thy with terminal voltage control
		6.4.2 DFIG-thy with Stator-Flux Oriented Control
	6.5	VSP-DFIG-thy normal operation
	6.6	Conclusions and future work
7	Case	studies 129
	7.1	Introduction
	7.2	Flicker evaluation
	7.3	Response to a balanced voltage dip
	7.4	Response to a frequency dip
	7.5	Case study conclusions
8	Cont	rol of the DFIG-ac system for an unbalanced short circuit 161
	8.1	Introduction
		8.1.1 Symmetrical and unsymmetrical voltage dip
		8.1.2 Instantaneous active and reactive power with positive and negative sequence components 163
	8.2	Real time determination of positive and negative sequence components 164
	8.3	Positive and negative sequence control of DFIG
		8.3.1 Positive and negative sequence control of the rotor VSC 165
		8.3.2 Positive and negative sequence control of the grid VSC 166
	8.4	Modeling and simulation
		8.4.1 Simulink model of the control of the DFIG system for an asymmetrical dip 167
		8.4.2 Rotor VSC asymmetrical control results

	8.5 Rotor and grid VSC asymmetrical control result	. 170
	8.6 Conclusions and recommendations	. 172
9	Aggregate wind farm models	173
	9.1 Aggregate model for a CSS wind farm	173
	9.2 Implementation of CSS-AWFM in Simulink	
	•	
	9.2.1 Model layout	
	9.3 Aggregate model for a VSP wind farm	
	9.4 Conclusions and recommendations	. 181
10	Conclusions	183
A	A simple model for local wind conditions inside a wind farm	187
	A.1 Turbine wind model: rotor effective wind	. 187
	A.1.1 Stochastic wind model	. 187
	A.1.2 Rotor effective wind	
	A.2 GCL wind farm wake model	
	A.2.1 GCL model	
	A.2.2 GCL model in Matlab	
	A.3 Conclusion	
В	Simulation initialization procedure	201
C	New Variable Speed Pitch turbine model	205
_	The second secon	
D	Induction machine flux oriented control	209
Е	Three phase AC systems, time and space vector	213
F	Synchronous machine parameters from manufacturers' data sheet	215
1	F.1 Introduction	
	F.2 Models and model parameters	
	•	
	F.3 Data sheet parameters	
	F.4 Conversion example	
	F.5 Comparison of estimated results with measured parameter values	
	F.6 Conclusion	
	F.7 Appendix A. Matlab file of Steady State Calculation DFIG-thy	. 223
G	Conference contributions and journal paper of the WaP project	227
Н	Executive summary of the Erao-2 project	273

### **EXECUTIVE SUMMARY**

### INTRODUCTION

Integrating an increasing amount of wind power in the electric power system will require the utilisation of the full potential of wind farms. Wind farms will be required to operate as much as possible in the same way as conventional power plants, equiped with controllable power source and synchronous generator. Wind power is an inherently stochastic power source, but it still can be controlled to a large extent to exhibit the same or similar dynamic behaviour as conventional power plants. Especially wind farms equiped with power electronic converters can make a contribution to grid control at the local and the global grid level. This requires the development of dynamic models of wind farms as a tool to design new wind farm control strategies. If wind turbines are controlled individually, specific grid related control aspects can be implemented for the whole farm. Different types of wind farms will require different control strategies, dictated by the hardware present in the farm.

#### **OBJECTIVE**

The main objective of the *Wind Farm as Power Plant* project is to develop dynamic models for offshore wind farms with different electrical systems and to demonstrate these models. The models can be used to develop wind farm control strategies that satisfy grid requirements and to investigate the interaction between the offshore wind farm and the electric grid.

#### METHOD

For grid integration and control instantaneous dynamic models are needed. The emphasis will be on models which describe each turbine individually. Since wind farm models are large, i.e. consist of many differential and algebraic equations, a method has to be chosen which limits computer time. For control of electrical drives the Park transformation is used (instantaneous space phasors). This method can be extended to passive electrical components in a grid and has been used to model all electrical components in this project. Different reference frames can be chosen, to suit the needs of a specific component. All models have been developed from scratch using Simulink, which is widely used for dynamic simulation.

### OFFSHORE WIND FARM MODEL DEVELOPMENT RESULTS

All wind farm concepts in WaP include power electronic converters and the control of these converters determines to a large extent the behaviour of the farm during normal as well as fault conditions. The emphasis in the WaP project is on development of new component models required in some of the concepts and on the control strategies for the new electrical concepts. Nine new offshore wind farm concepts have been developed:

- (i) Constant Speed Stall-Induction Generator-dc link to shore (CSS-IG-dc)
- (ii) Constant Speed Stall-Cluster Controlled Induction Generator-ac connection to shore (CSS-CCIG-dc);
- (iii) Variable Speed Pitch-Cluster Controlled Induction Generator-ac connection to shore (VSP-CCIG-ac);
- (iv) Variable Speed Pitch-Cluster Controlled Induction Generator-dc connection to shore (VSP-CCIG-dc);
- (v) Variable Speed Pitch-Doubly Fed Induction Generator-dc connection to shore (VSP-DFIG-dc).
- (vi) Variable Speed Pitch-Full Converter Induction Generator-ac connection to shore (VSP-FCIG-ac);
- (vii) Variable Speed Pitch-Full Converter Synchronous Machine-ac connection to shore (VSP-FCSM-ac);
- (viii) Variable Speed Pitch-Full Converter Synchronous Machine-dc connection to shore (VSP-FCSM-dc);
- (ix) Variable Speed Pitch-Doubly Fed Induction Generator-thyristor based dc connection to shore (VSP-DFIG-thy).

The electrical part of these model are based on the Park transformation which calculates instantaneous dq-values of voltages and currents in all nodes of the electrical system. The converter models calculate average values, the switching of the IGBT's or thyristors is not included. These models have been developed primarily for symmetrical conditions (equal voltage and current in all three phases) but can, under certain conditions, also be used for asymmetrical conditions.

### OFFSHORE WIND FARM CONTROL STRATEGY RESULTS

Three of the new offshore wind farm concepts required a new controller design: the VSP-FCIG-ac, VSP-FCSM-ac and the VSP-DFIG-thy system. The control of the VSP-DFIG-thy was by far the most difficult to realise. This is caused by the limited control capability of the thyristor converter, so the rotor and grid side converters of the DFIGs have to take care of wind farm grid stabilisation. Two controllers have been developed, the control of the VSP-DFIG-thy system still can be improved, however.

#### WIND FARM COMPONENT MODEL RESULTS

The main new component model developed in WaP is the model of the thyristor bridge converter. Although the thyristor bridge already exists for many years, modelling it is still an issue of much debate. Six models have been made, each for a specific application. In order of complexity:

- (i) average symmetrical;
- (ii) average unsymmetrical Fourier;
- (iii) average partially unsymmetrical;
- (iv) instantaneous diode without commutation;
- (v) instantaneous thyristor without commutation;
- (vi) instantaneous thyristor with commutation.

The models have been verified by comparison with the thyristor bridge model in the commercial Power System Blockset. The models satisfy the requirements, deviations can be explained by the modeling method.

### CASE STUDY RESULTS

The dynamic behaviour of four representative systems (CSS-IG-dc, VSP-CCIG-ac, VSP-FCIG-ac and VSP-DFIG-thy) has been investigated in a case study. The wind farm flicker, response to a voltage and a frequency dip have been determined.

### ASYMMETRICAL RESULTS

The WaP project includes the development of a controller for a wind farm electrical system during an asymmetrical fault. The system chosen is the commercially often used DFIG-ac system. This work particularly focussed on modification of component models for asymmetrical phenomena, the method to separate the asymmetrical variables in instantaneous positive and negative sequence components and the design of the controller. The controller was able to reduce the electric torque pulsation and the ripple in the DC voltage during an asymmetrical voltage dip.

### MISCELLANEOUS RESULTS

The WaP also includes the implementation of the existing VSP turbine model in Simulink and the implementation of the existing GCL model for wind speed deficit and turbulence in a wind farm in Matlab. An aggregate model, that does not model each turbine in a farm individually, was developed for a constant speed wind farm.

## CONCLUSIONS

A versatile library of offshore wind farm models is now fully operational. The approach to develop the necessary component models from scratch, as opposed to using existing commercial electrical modelling software, has been gratifying and successful. Now full control can be exerted over all modeling aspects: nothing is hidden behind a user interface. The models have proven their use in developing wind farm controllers and investigating wind farm dynamic behaviour.

### RECOMMENDATIONS

Optimising offshore wind farm behaviour with respect to local and global grid control, during normal as well as fault conditions is the logical next step in making wind farm replace and emulate traditional power plants. New offshore wind farm control strategies need to be developed that meet certain grid requirements (e.g. steady state voltage support, stability improvement during faults, damping of angle oscillations, delta control and power curtailment, frequency droop control, limitation of short circuit contribution). These new control strategies can be demonstrated in a dynamic grid model with a high percentage of wind power.

Wind farm dynamic model validation is still an issue of concern. A start was made in the Erao-3 project, but this validation was seriously hampered by the unavailability of the wind turbine parameters and control. Additional validation exercises are recommended.

# LIST OF DELIVERABLES

- (i) Nine new offshore wind farm dynamic models (Simulink);
- (ii) New controllers for the VSP-FCIG-ac, VSP-FCSM-ac and the VSP-DFIG-thy system (Simulink);
- (iii) A new implementation of the variable speed pitch turbine dynamic model (Simulink);
- (iv) New dynamic thyristor converter models with different levels of complexity (Simulink);
- (v) An aggregate model for the constant speed wind farm (Simulink);
- (vi) The implementation of the GLC model for wind speed deficit and turbulence in a wind farm (Matlab);
- (vii) Journal papers and conference contributions (7);
- (viii) A detailed report describing the dynamic models.

# COMPARING PROJECT RESULTS TO PROJECT OBJECTIVES:

The central, most important, project objectives have all been met. On some aspects, more has been achieved than anticipated in the project plan:

- thyristor bridge modelling has been more complete than planned: average and instantaneous models for different purposes (symmetrical and asymmetrical conditions) have been developed;
- control of the DFIG-thy system proved to be more complicated than assumed at the start of the project but was completed to a sufficient level;
- control of the DFIG system during an asymmetrical fault was not part of the proposal but
  was included because of its interest for turbine manufacturers and becaused it is seldom
  addressed in literature.

In the WaP project we hoped to take measurements of voltage dips on a variable speed turbine for model validation. Due to unsufficient collaboration by the turbine manufacturer no measurements could be taken. The opportunity occured to receive voltage dip measurements perfomed by a different manufacturer on a similar turbine. These measurements have been received recently.

The following objectives have not been fully met:

- Updating the Erao-1 database. This is only a minor activity. This task will be included in a separate project, EeFarm-II, starting 2008, in collaboration with Vattenfall.
- The development of control strategies that support the grid has been not been pursued in this project since it needs much more attention and depth than can be given in WaP. It will be the objective of a new project, WaP-II, to be executed in collaboration with TUD-EPS (Electrical Power Systems) and TUD-EPP.

• The aggregate model of the constant speed wind farm has been developed but the aggregate model of the variable speed wind farm has been postponed to a next project.

# CONTEXT OF THE PROJECT

This project is a continuation of the model development of the Erao-projects. In the Erao-project steady state (load flow) models have been developed and used in combination with a component price database to estimate the contribution of the electrical system to the cost of electricity. In the Erao-2 project dynamic models for four different ITWF have been developed and demonstrated [33, 34]. A partial verification of the developed wind farm models has been executed in the Erao-3 project [31, 30, 32].

# 1 Introduction

The objective of the we@sea project Wind Farm as Power Plant (WaP) is to develop and demonstrate dynamic models of offshore wind farms. These models can than be used to:

- simulate the dynamic interaction between individual turbines in an offshore wind farm;
- develop wind turbine and wind farm control strategies;
- optimize wind farms;
- investigate the effects of a short circuit in a wind farm;
- investigate the effects of a short circuit in the grid on a wind farm;
- determine the dynamic effects of a wind farm on the local electrical grid;
- adapt grid control to large scale wind power.

The WaP project is a continuation of the Erao-2 project (see appendix H for the executive summary). The Erao-2 project was limited to wind farms based on:

- constant speed turbines with directly connected induction generators (CSS-IG-ac);
- groups of induction generators connected to a single IGBT converter (cluster controlled constant speed turbines in variable speed mode: CSS-CCIG-ac)
- variable speed pitch turbines with doubly fed induction generators (VSP-DFIG-ac);
- variable speed pitch turbines with permanent magnet generators and full converters (VSP-FCPM-ac).

In the Erao-2 project a number of important component and system models were still missing and have been developed in WaP:

- (i) models of the conventional thyristor bridge converter (for instance in the HVDC Classic system);
- (ii) models for more complex electrical concepts, combining two sets of converters;
- (iii) models for the evaluation of asymmetrical short circuits <sup>1</sup>:
- (iv) a model for the wind conditions in the wind farm (deficit and turbulence intensity);
- (v) an Aggregate Wind Farm Model (AWFM), which treats the wind farm as a black box, without discriminating between individual turbines.

In the Individual Turbine Wind Farm Models (ITWFM) each turbine in the farm is modelled in detail. A detailed turbine model includes an aerodynamic and mechanical model (wind, blades, tower, mechanical drive train, pitch control and torque setpoint algorithm) and an electrical system model (generator, AC-DC converters, transformer, cable and the electromagnetic torque and other control).

The emphasis in the project WaP is on the development of Individual Turbine Wind Farm Models (ITWFM), especially the electrical component models and their control. The aerodynamic models of the two generic types of turbines, the constant speed stall (CSS) and the variable speed pitch (VSP) turbine have been developed in a previous ECN-Windenergy project, which focused on wind turbine control [12]. In the WaP project, the VSP model has been reprogrammed in Simulink, to make it more compatible: the models of the electrical components have also been developed in Simulink. This report describes the development of nine new ITWF models (see section 1.1 for an overview) and demonstrates a representative subset of these models in a case study. New wind farm electrical system models and the new controllers required for these systems.

<sup>&</sup>lt;sup>1</sup>if the zero is not connected, asymmetrical short circuits can be simulated by the dq models of Erao-2

This results in the following division of this report:

- Since the control of the investigated electrical systems is a crucial aspect, chapter 2 summarises the inverter and rectifier controllers developed in Erao-2.
- Chapter 3 describes the development of the new thyristor bridge models.
- For each new wind farm electrical system the layout and control are described followed by the model overview and the simulation of normal operation (Chapters 4, 5 and 6).
- This is followed by a demonstation of a representative selection of the new wind farm models in a case study (Chapter 7).
- The control of the DFIG-ac system for an unbalanced short circuit is described in chapter 8.
- Chapter 9 describes the development of the aggregate wind farm model based on constant speed turbines.
- Appendix A describes the implementation of a simple model for the local wind conditions inside a wind fram.
- Based on the results in the previous chapters, conclusions and recommendations on the operation and applicability of the new models and wind farm concepts are summarized in Chapter 10.

# 1.1 Wind farm models developed in WaP

Table 1 lists the nine new wind farm electrical concepts. The concepts are identified by:

- the type of turbine: Constant Speed Stall (CSS) or Variable Speed Pitch (VSP);
- the electrical system in the turbine: generator and converter (CCIG, DFIG, FCIG, FCSM);
- the connection to shore: alternating current or direct current (ac, dc, thy).

New electrical component models in the WaP project are:

- the thyristor converter model;
- the model DC connection to shore;
- three converter control models:
  - field oriented control for the induction machine with full converter without stator frequency knowledge;
  - control of a DFIG in combination with a thyristor bridge;
  - control of a synchronous machine with full converter.

For the most complicated concept, the VSP-DFIG-thy system, the modelling and control for normal operation has been developed. Control of an asymmetrical voltage dip has been developed for the DFIG-ac.

Table 1: Electrical configurations developed in Erao-2 and WaP

Turbine	CSS		VSP				
WF El. confi g.	IG	CCIG	CCIG	FCIG	DFIG	FCSM	FCPM
AC transmission	Erao-2	Erao-2	# 3	# 6	Erao-2	#7	Erao-2
DC transmission (DFIG)	# 1	# 2	# 4		# 5	# 8	
DC transmission (Thy)					# 9		

# 1	CSS-IG-dc	Constant speed stall, Induction generator, DC to shore (IGBT)		
# 2	CSS-CCIG-dc	Constant speed stall, Induction generator, cluster controlled, DC to shore (IGBT)		
# 3	VSP-CCIG-ac	Variable speed pitch, Induction generator, cluster controlled, AC to shore		
# 4	VSP-CCIG-dc	Variable speed pitch, Induction generator, cluster controlled, DC to shore (IGBT)		
# 5	VSP-DFIG-dc	Variable speed pitch, Induction generator, doubly fed, DC to shore (IGBT)		
# 6	VSP-FCIG-ac	Variable speed pitch, Induction generator, full converter, AC to shore		
#7	VSP-FCSM-ac	Variable speed pitch, Synchronous machine, full converter, AC to shore		
# 8	VSP-FCSM-dc	Variable speed pitch, Synchronous machine, full converter, DC to shore (IGBT)		
# 9	VSP-DFIG-thy	Variable speed pitch, Induction generator, doubly fed, DC to shore (thyristor)		

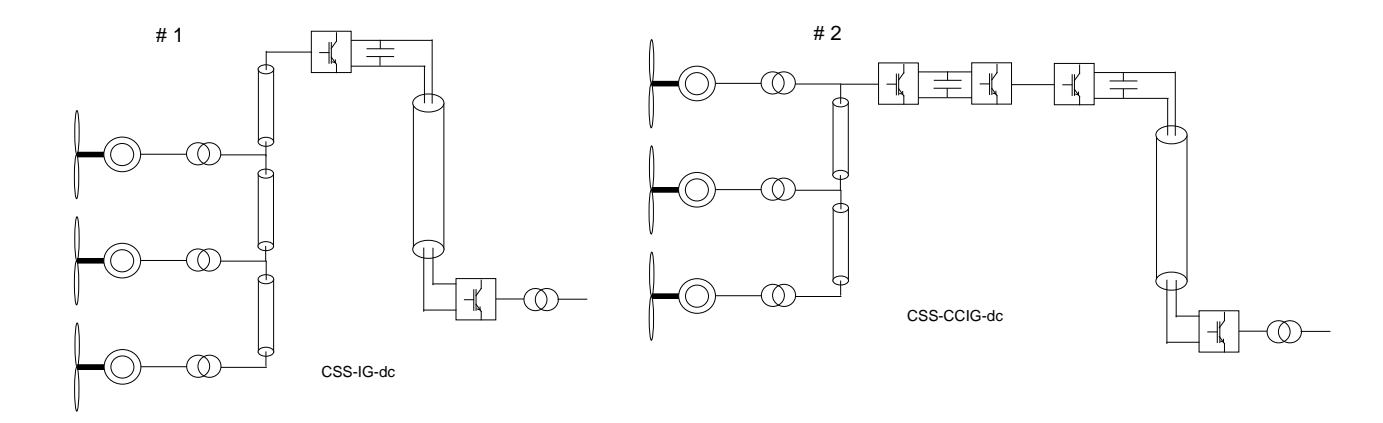


Figure 1: Layout of concepts based on constant speed stall turbine

Figure 1 shows the layout of the systems with stall controlled turbine and squirrel cage induction generator. The CSS-IG-dc concept (System # 1) uses a dc connection to shore and the turbines are operated in constant speed mode. The CSS-CCIG-dc concept (System # 2) includes clusters of turbines on a single back-to-back converter system. The turbines in a cluster are operated at variable speed. In the CSS-CCIG-dc system the individual clusters connect to a dc link to shore.

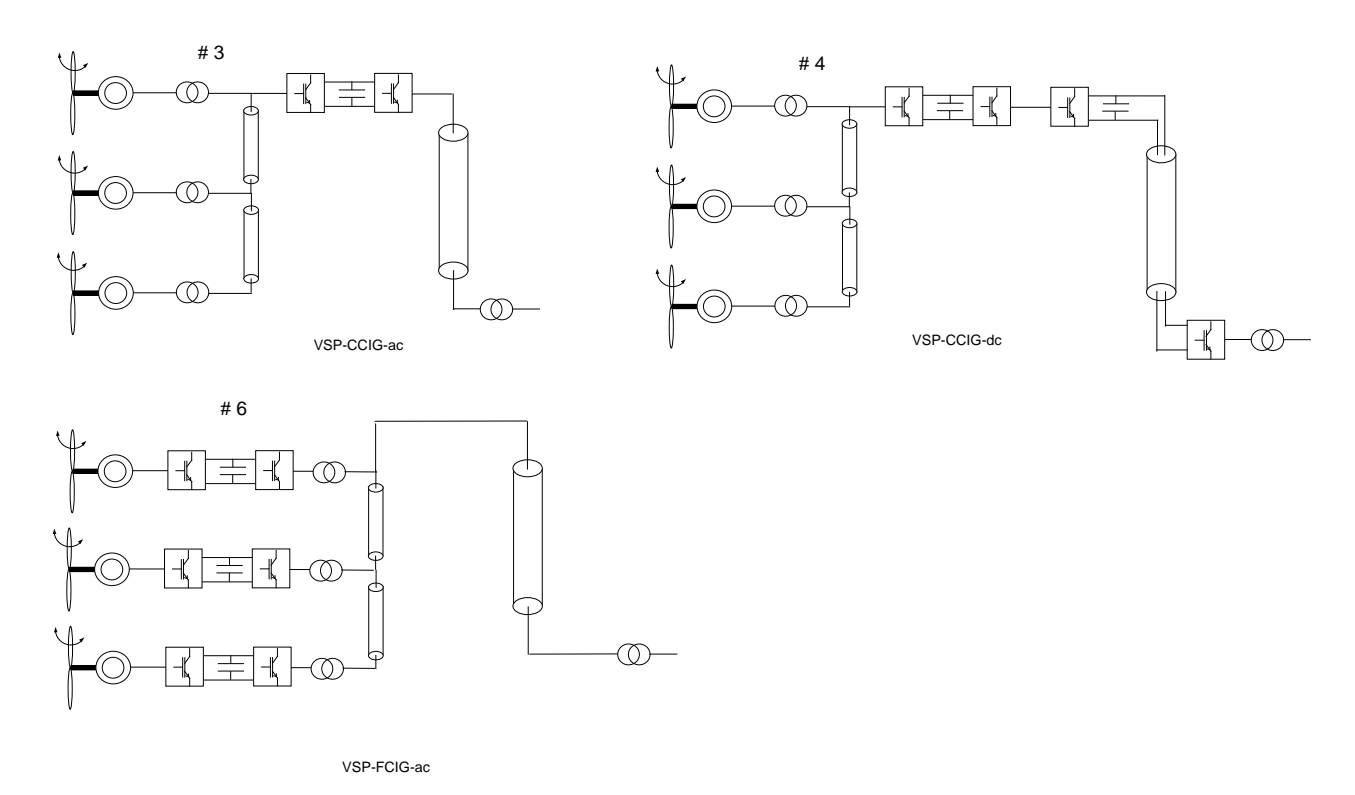


Figure 2: Layout of concepts based on variable speed speed stall turbine and induction generator

Figure 2 shows the concepts with variable speed pitch controlled turbines and induction generator. The VSP-CCIG-ac (System # 3) system is cluster controlled with an ac connection to shore. In the VSP-CCIG-dc system (System # 4) the connection to shore is a dc cable. The VSP-FCIG-ac concept (System # 6) combines a converter controlled induction generator with an ac connection to shore.

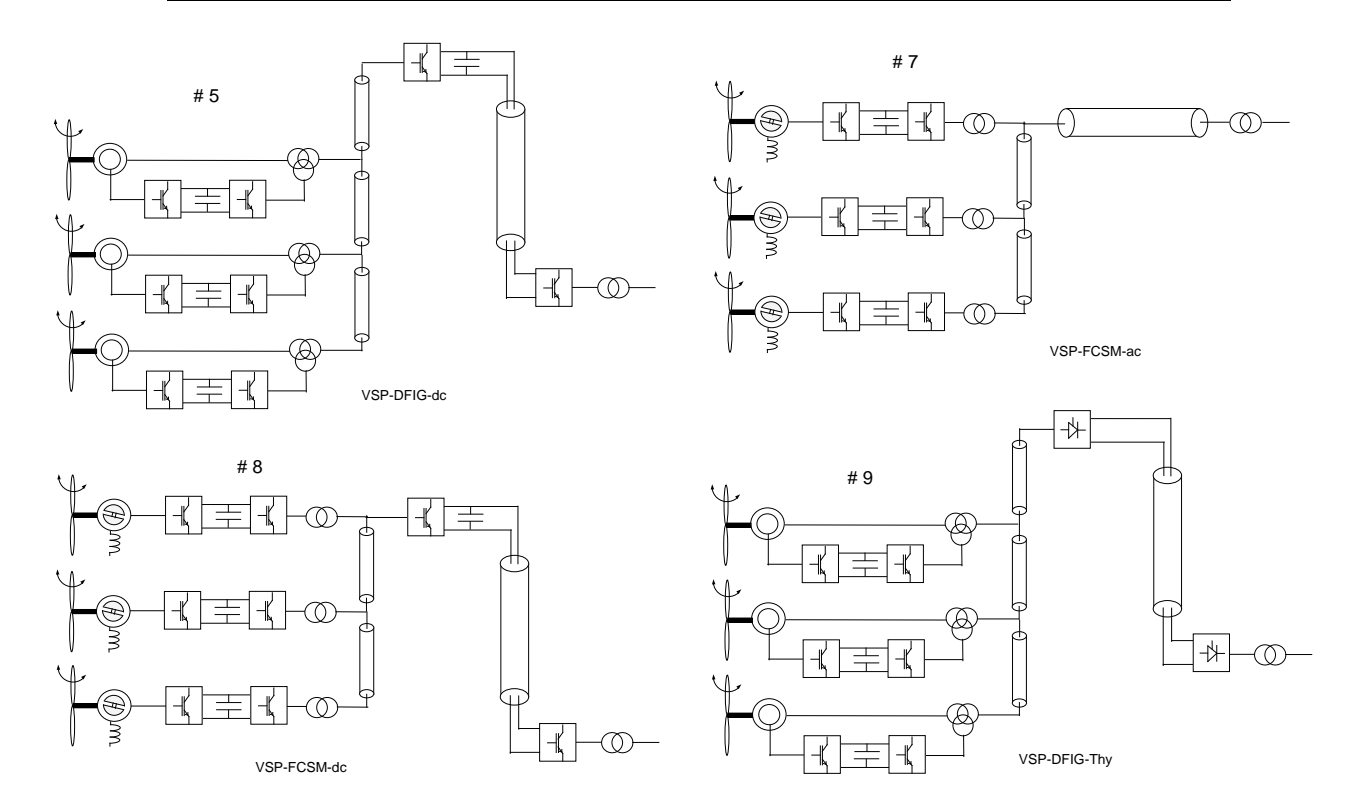


Figure 3: Layout of concepts based on variable speed speed stall turbine and DFIG or SM in the turbine

Figure 3 displays the remaining concepts modelled in WaP and based on variable speed speed turbines. Two concepts are based on synchronous generators: VSP-FCSM-ac and VSP-FCSM-dc (Systems # 7 and # 8) with either an ac or a dc connection to shore. The two remaining concepts use a VSP-DFIG with either an IGBT or a thyristor converter dc connection to shore (Systems # 5 and # 9).

In the Erao-2 project Simulink has been chosen as programming language, since the emphasis is on dynamic behaviour and control of wind farms. Simulink is a simulation platform based on Matlab, a language especially usefull in the development of control systems. The advantages of Simulink are:

- it includes solvers for stiff systems (systems with a wide range of time constants);
- it includes many useful features for the simulation of dynamic systems in general (for instance zero crossing detection and algabraic loop handling);
- it is based on a graphical user interface, which greatly facilitates changing the system to be simulated;
- orderly, structured signal flow;
- easy extension of system models with existing subsystem models.

Simulink is constantly being extended and improved and it is the current standard tool for the simulation of dynamic systems.

All models of electrical components make use of the Park tranformation (dq0 models). In the Erao-2 report [33] the dq0-model is described. A description of the four wind farm models developed in Erao-2 can also be found in that report.

This project is a continuation of the model development of the Erao-projects. In the Erao-project steady state (load flow) models have been developed and used in combination with a

component price database to estimate the contribution of the electrical system to the cost of electricity. In the Erao-2 project dynamic models for four different ITWF have been developed and demonstrated [33, 34]. A partial verification of the developed wind farm models has been executed in the Erao-3 project [31, 30, 32].

# 2 Control of variable speed electrical systems

All new concepts developed in the WaP project include converters, in the turbine or in the connection to shore or both. The control of these converters is an important aspect in the design of the wind farm. The converters are either based on thyristors (system #9) or IGBTs (all other systems). IGBT power electronic switches can be switched on and off by a control signal, which makes them well suited for control purposes. IGBT converters are operated at a high switching frequency, for instance 5 kHz. This enables fast control as well as accurate tracking, which is useful if generation of a sinusoidal wave form is required or if currents are impressed on the rotor or stator of an electrical machine. Thyristor converters have the advantage of availability in high voltage and power rating. The disadvantage is the limited controllability and the sensitivity to voltage dips. The converters applied in wind turbines, wind farms and DC connections to shore are connected back to back to each other, with either a capacitor or an inductor or a DC cable in between.

The control of the converter is determined by the type of generator (i.e. squirrel cage induction generator, doubly fed induction generator, synchronous generator and permanent magnet generator) and the location of the converter (rectifier or inverter).

# 2.1 IGBT inverter control

In all concepts, the grid side converter (inverter) is controlled in the same way: the amplitude and the phase of the output AC current is controlled by means of the d- and q-components of the AC voltage. The d- and q-components of the current are determined by the desired power and reactive power to the grid. The setpoint for the power to the grid is determined by a master control loop on the DC link voltage. The reactive power setpoint can be chosen freely.

Figure 4 illustrates the control of the grid converter. The main components are two PI-controllers and two cross-voltage compensators. The cross-voltage compensators result from the fact that the electrical components are described in dq-coordinates instead of the abc values of the individual phases [33] and compensate for the cross coupling in the dq voltage equations (the d-current influences the q-voltage and vice versa). The d- and q-currents currents result from the voltage difference over a small inductance at the grid side of the converter. The d- and q-current setpoints are calculated from the power and reactive power setpoints. The PI-controllers generate the converter output dq-voltages.

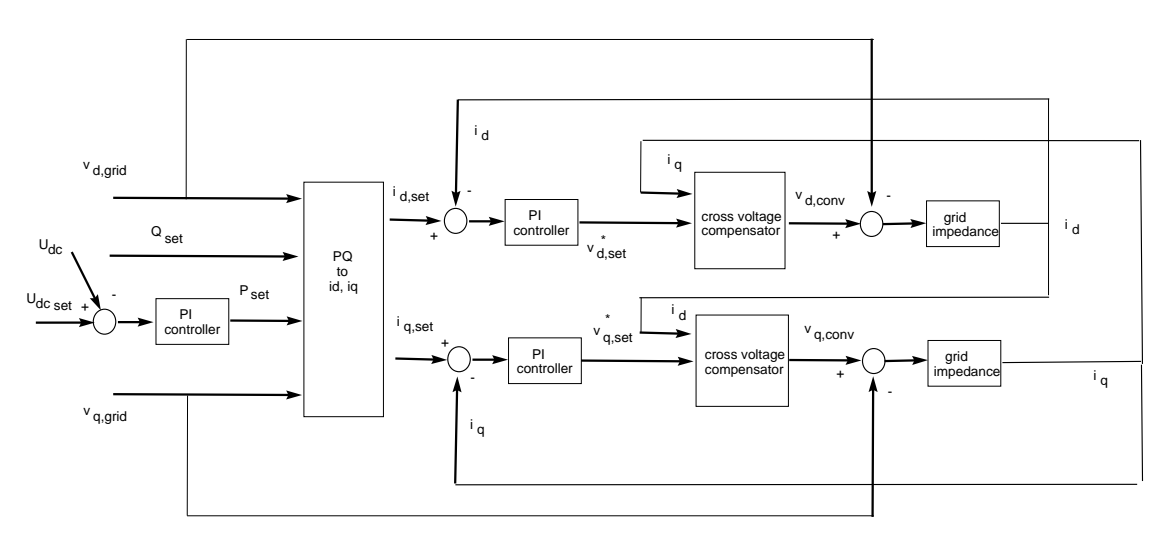


Figure 4: Control of the grid side converter

# 2.2 IGBT rectifier control

The control of the machine side converter depends on the system concept:

- the type of electrical machine to be controlled: squirrel cage induction generator, doubly fed induction generator, synchronous or permanent magnet generator;
- the location of the converter (on the stator or on the rotor).

The three types of controllers of the machine side converters in the Erao-2 project will first be summarized, since this is a good starting point for the description of the new electrical system concepts developed in WaP. These controllers are:

- CCIG: cluster control of a set of squirrel cage induction generators;
- DFIG: rotor converter control of the doubly fed induction generator;
- FCPM: full converter control of the permanent magnet generator.

### **CCIG**

In the CCIG system the cluster side converter is connected the stators of the squirel cage induction machines in the cluster and it controls the frequency and the d- and q-voltage (see figure 5). The control concept is simple: frequency and voltages are impressed on the stator instantaneously, a feedback control loop is not required (the voltage is an input variable for the generator models).

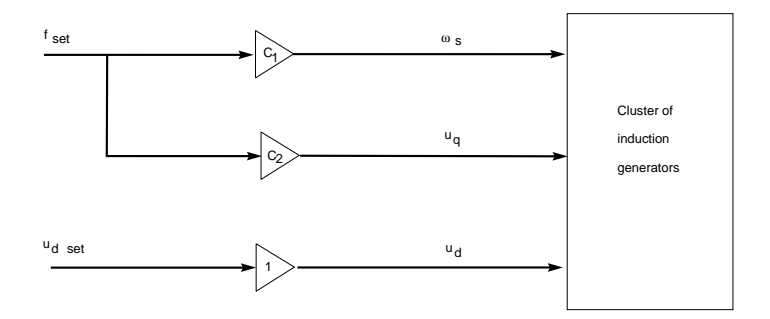


Figure 5: Control of the cluster side converter of the CCIG system

### **DFIG**

In the DFIG system the machine side converter is connected to the wound rotor of an induction machine and it controls the electromagnetic torque and the reactive power of the stator of the machine (see figure 6). The control is realised by two master-slave control loops on the rotor currents  $i_{rd}$  and  $i_{rq}$ . The output of the slave loops are the d- and q-voltage on the rotor. The control concept is similar to the control of the grid side converter, including the performance improvement by cross-voltage compensation.

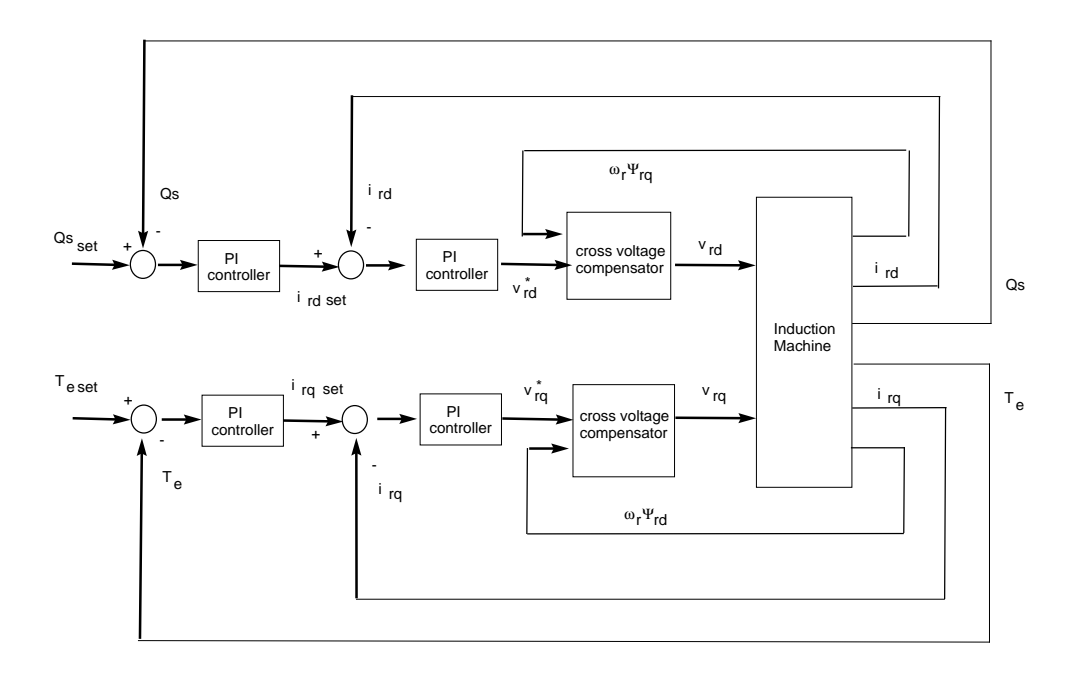


Figure 6: Control of the machine side converter of the DFIG system

# **FCPM**

In the FCPM system the machine side converter is connected to the stator of a permanent magnet machine and controls the electromagnetic torque and the reactive power of the stator (see figure 7). Since the rotor field is in the direction of the d-axis, the stator q-current corresponds to the power and the reactive power is zero, if the current in the d-axis is zero.

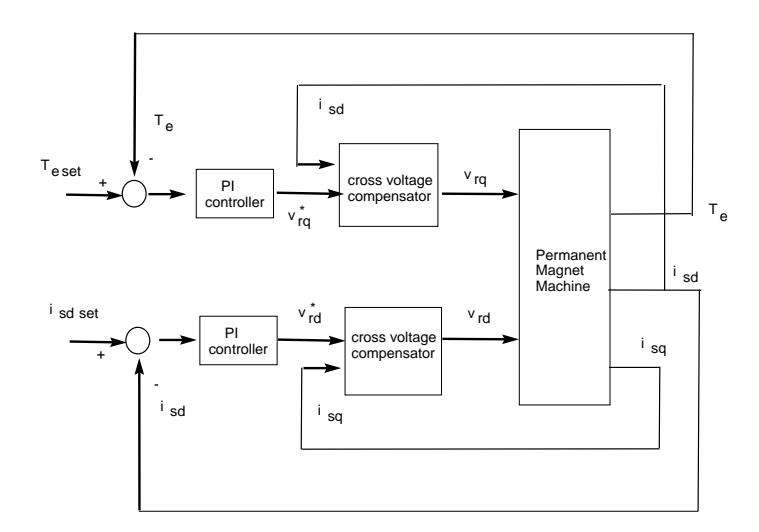


Figure 7: Control of the machine side converter of the FCPM system

# 3 Thyristor Bridge Models for Balanced and Unbalanced Conditions

# 3.1 Introduction

Most current offshore wind power projects are close to shore and use HVAC connections. HVDC links are superior for large power capacity and long transmission distances. The HVDC system can be based on current source converters using thyristor bridges or they can be based on voltage source converters using IGBTs. Voltage source converters using IGBTs have better controllability and dynamic behavior than thyristor bridges, but they are expensive and the power losses are higher. HVDC connections for offshore wind farms are compared in [4], [14], [22], [20] and [10]. A general conclusion is that HVAC can be used for small wind farms, 200 MW for example, and short transmission distance, 100 km for example. For large power capacities and long transmission distances, HVDC transmissions are more favorable. Considering the cost and efficiency, HVDC using thyristors can be used for an extremely large wind farm, 600 MW for example, which is connected with strong AC grid. HVDC using IGBTs can be integrated with a relatively weak grid for its good controllability and voltage ride through capability. The choice of connection type can be based on the following table [4, 10]:

	HVAC	HVDC-thyristor	HVDC-VSC
Maximum power	200MW at 150kV	1200MW	350MW
	350MW at 245kV		(500MW announced)
Maximum voltage	245kV	500kV	150kV
Maximum distance	200km		

Table 2: Offshore wind farm connection options

Simulation is a valuable research method, because it makes it possible to investigate the integration problems without the necessary of a full or reduced scale test, which is often expensive, time consuming or even impossible to be carried out. In [33, 25] dynamic models using the Park transformation have been developed in Matlab/Simulink. The advantage of using the Park transformation is that voltages and currents for balanced three phase system are dc values in steady state condition. Therefore, large simulation time steps can be used during steady state, and thus the simulation speed is greatly improved. The models developed in [33, 25] include generator, transformer, cable, transmission line and voltage source converter models. A thyristor bridge model was not available yet. Since the HVDC thyristor bridge can be a choice for connection of large offshore wind farm, the thyristor bridge model is developed in this project.

# 3.2 Specification of the thyristor bridge model

The thyristor bridge is a current source converter. Unlike the voltage source inverter which can be fully controlled, the thyristor bridge is controllable in ignition, but uncontrollable in extinction. Therefore, the model is more complex than the model of the voltage source inverter. Although the thyristor converter is in use for many decades, building an appropriate model, which suits the purpose of simulation with acceptable simulation time, still draws a lot of attention.

Thyristor bridge models can be divided into three categories:

- Quasi stead-state models which are suitable for electromechanical transients studies;
- Small signal dynamic models which are suitable for small signal stability studies;
- Detailed instantaneous models which are suitable for electromagnetic transients studies.

The time frame of electromechanical transient study stays between 0.01s to several tens of seconds, while the time frame of power electronics is below several tens of milliseconds. In

other words, the electromechanical transients are much slower than the transients of power electronics. The application of the three types of models can be characterized as follows:

- The quasi-steady state model of the thyristor bridge can be used in electromechanical transient studies, for example, the voltage dip. Under unbalanced conditions, the quasi steady-state thyristor bridge model has problems to represent the instantaneous AC voltages in dq0-coordinates;
- The small signal model linearises the thyristor bridge equations near the operating point. It is suitable for small signal stability studies such as response to a small step change of voltage, but it is not suitable for faults analysis. Because during and after the faults, the system does not stay at the same operation point, it will transfer to another operation point. The linearized equations are not suitable for the new operation point;
- The detailed instantaneous model, which represents the switching of the thyristors, is suitable for electromagnetic studies, but is not the best choice for the electromechanical studies. For unbalanced conditions it is necessary to use this model.

In most studies of wind power integration as in table 3, the detailed transients or switching of power converters are not required. Most of the wind power integration problems can be studied with electromechanical simulations using dq0-calculations:

Wind pov	ver integration study	Required simulation
Steady state	Power control	Electromechanical
Power quality	er quality Flicker	
	Frequency deviation	Electromechanical
	Harmonic	Electromagnetic
Dynamic stability	Transient voltage stability	Electromechanical
Long term stability	Sub synchronous oscillations	Electromechanical

Table 3: Type and application of dynamic models in wind power integration studies

The objective in this project is to develop a thyristor bridge model which can be used with the other dynamic models of the ERAO II project. This gives the following requirements:

- inputs and outputs are instantaneous values in dq0-coordinates;
- the switching transients in the converter need not be included in the model, only the fundamental frequency components are necessary, higher order harmonics can be omitted;

An additional requirement, which did not have much attention in the ERAO II project, is that unbalanced conditions will also be considered. This may result in including a model for the switching of the thyristors. The thyristor bridge models developed in the WaP project can be divided into two groups:

- quasi stead-state models which only have fundamental frequency components;
- instantaneous models which simulate the switching of the thyristors, i.e. the commutation process and include higher order harmonics.

Five models have been developed. They represent compromises between accuracy of simulation result and model simplicity. The models are compared with the thyristor bridge model of the Power System BlockSet in Matlab/Simulink in back to back configuration (rectifier-inverter). The models are summarized in table 4.

Model type Name Properties Symmetrical quasi-steady model Quasi-steady state models Thy1 Unsymmetrical quasi-steady model using Fourier analysis Thy2 Thy3 Unsymmetrical quasi-steady partially symmetrical model Thy4 Instantaneous model without commutation inductance Instantaneous models Thy5 Instantaneous model with commutation inductance Instantaneous models PSB Power System BlockSet Reference

Table 4: List of thyristor models developed in this project

In the next section the Park transformation will be analyzed first, with focus on unbalanced conditions. This is followed by a description of the five thyristor bridge models. Then the thyristor bridge models are compared to the Power System BlockSet model. The final section of this chapter draws conclusions and gives recommendations for future work.

### 3.3 Park transformation

The electrical component models developed in the Erao-II project are based on the Park transformation which results in dq0-coordinates. Under balanced three phase conditions, voltages and currents in dq-coordinates are DC values, i.e. constant in steady state. For an unbalanced three phase system, voltages and currents in dq0-coordinates vary, i.e. are not constant in steady state. Then, the d- and q-values have a two times fundamental frequency component and the zero values have a fundamental frequency component. A zero component may not be present under unbalanced conditions due to the presence or absence of a physical zero or neutral [33].

## 3.3.1 Park transformation for an unbalanced system

The following section discusses the situation that the Park transformation is applied to an unbalanced three phase system. The voltage equations are taken as an example and only the RMS values of the phases are considered to be unbalanced. The unbalanced three voltage equations are:

$$V_a(t) = \sqrt{2}V_a \sin(\omega t + \phi_a)$$

$$V_b(t) = \sqrt{2}V_b \sin(\omega t - \frac{2}{3}\pi + \phi_a)$$

$$V_c(t) = \sqrt{2}V_c \sin(\omega t + \frac{2}{3}\pi + \phi_a)$$
(1)

The Park transformation is:

$$T_{dq0} = \sqrt{\frac{2}{3}} \begin{bmatrix} \cos(\theta_d) & \cos(\theta_d - \frac{2}{3}\pi) & \cos(\theta_d + \frac{2}{3}\pi) \\ -\sin(\theta_d) & -\sin(\theta_d - \frac{2}{3}\pi) & -\sin(\theta_d + \frac{2}{3}\pi) \\ \frac{1}{\sqrt{2}} & \frac{1}{\sqrt{2}} & \frac{1}{\sqrt{2}} \end{bmatrix}$$
(2)

The inverse Park transformation is:

$$T_{dq0}^{-1} = \sqrt{\frac{2}{3}} \begin{bmatrix} \cos(\theta_d) & -\sin(\theta_d) & \frac{1}{\sqrt{2}} \\ \cos(\theta_d - \frac{2}{3}\pi) & -\sin(\theta_d - \frac{2}{3}\pi) & \frac{1}{\sqrt{2}} \\ \cos(\theta_d + \frac{2}{3}\pi) & -\sin(\theta_d + \frac{2}{3}\pi) & \frac{1}{\sqrt{2}} \end{bmatrix}$$
(3)

Applying equation 2 to equation 1, we get the expression for unbalanced three phase voltages in dq0-coordinates:

$$\begin{bmatrix} V_d(t) \\ V_q(t) \\ V_0(t) \end{bmatrix} = T_{dq0} \begin{bmatrix} V_a(t) \\ V_b(t) \\ V_c(t) \end{bmatrix} = \frac{1}{\sqrt{3}} \begin{bmatrix} (V_a + V_b + V_c) \sin(\omega t + \phi_a - \theta_d) \\ -(V_a + V_b + V_c) \cos(\omega t + \phi_a - \theta_d) \\ 0 \end{bmatrix} +$$

$$+\frac{1}{\sqrt{3}} \begin{bmatrix} +V_{a}\sin(\omega t + \phi_{a} + \theta_{d}) + V_{b}\sin(\omega t + \phi_{a} + \theta_{d} - \frac{4}{3}\pi) + V_{c}\sin(\omega t + \phi_{a} + \theta_{d} + \frac{4}{3}\pi) \\ -V_{a}\cos(\omega t + \phi_{a} + \theta_{d}) + V_{b}\cos(\omega t + \phi_{a} + \theta_{d} - \frac{4}{3}\pi) + V_{c}\cos(\omega t + \phi_{a} + \theta_{d} + \frac{4}{3}\pi) \\ V_{a}\sin(\omega t + \phi_{a}) + V_{b}\sin(\omega t + \phi_{a} - \frac{2}{3}\pi) + V_{c}\sin(\omega t + \phi_{a} + \frac{2}{3}\pi) \end{bmatrix}$$
(4)

If initially the d-coordinate is aligned with phase a, then  $\theta_d = \omega t$ , the above equations can be simplified to

$$\begin{bmatrix} V_d(t) \\ V_q(t) \\ V_0(t) \end{bmatrix} = \frac{1}{\sqrt{3}} \begin{bmatrix} (V_a + V_b + V_c)\sin(\phi_a) \\ -(V_a + V_b + V_c)\cos(\phi_a) \\ 0 \end{bmatrix} +$$

$$+\frac{1}{\sqrt{3}} \begin{bmatrix} V_a \sin(2\omega t + \phi_a) + V_b \sin(2\omega t + \phi_a - \frac{4}{3}\pi) + V_c \sin(2\omega t + \phi_a + \frac{4}{3}\pi) \\ -V_a \cos(2\omega t + \phi_a) + V_b \cos(2\omega t + \phi_a - \frac{4}{3}\pi) + V_c \cos(2\omega t + \phi_a + \frac{4}{3}\pi) \\ V_a \sin(\omega t + \phi_a) + V_b \sin(\omega t + \phi_a - \frac{2}{3}\pi) + V_c \sin(\omega t + \phi_a + \frac{2}{3}\pi) \end{bmatrix}$$
(5)

From 5, it can be seen that only when the RMS values of the a, b, and c phase are equal, the second terms of  $V_d$  and  $V_q$  are zero. Then  $V_d$  and  $V_q$  are constant and  $V_0$  is zero. Under unbalanced conditions,  $V_a \neq V_b \neq V_c$  and one of the advantages of the Park transformation is lost. The calculation speed will be similar to the speed using abc-coordinates.

# 3.3.2 RMS values and phase angles

The quasi steady state model of the thyristor bridge requires RMS values and phase angles of the line to line voltages. But under unbalanced conditions, the RMS values and phase angles cannot be calculated from the instantaneous values in dq0-coordinates. This can be seen as follows. In order to calculate the RMS values and phase angles, the invers Park transformation of equation 3 is applied on the instantaneous values in dq0-coordinates:

$$\begin{bmatrix} V_{a}(t) \\ V_{b}(t) \\ V_{c}(t) \end{bmatrix} = T_{dq0}^{-1} \begin{bmatrix} V_{d} \\ V_{g} \\ V_{0} \end{bmatrix} = \sqrt{\frac{2}{3}} \begin{bmatrix} V_{d}\cos(\theta_{d}) - V_{q}\sin(\theta_{d}) + \frac{1}{\sqrt{2}}V_{0} \\ V_{d}\cos(\theta_{d} - \frac{2}{3}\pi) - V_{q}\sin(\theta_{d} - \frac{2}{3}\pi) + \frac{1}{\sqrt{2}}V_{0} \\ V_{d}\cos(\theta_{d} + \frac{2}{3}\pi) - V_{q}\sin(\theta_{d} + \frac{2}{3}\pi) + \frac{1}{\sqrt{2}}V_{0} \end{bmatrix}$$
(6)

Under balanced system,  $V_0$  equals zero,  $V_d$  and  $V_q$  are constants and orthogonal. Then the phase voltages can be written as:

$$\begin{bmatrix} V_{a}(t) \\ V_{b}(t) \\ V_{c}(t) \end{bmatrix} = \sqrt{\frac{1}{3}} \begin{bmatrix} \sqrt{V_{d}^{2} + V_{q}^{2}} \cos(\omega t + \phi_{a}) \\ \sqrt{V_{d}^{2} + V_{q}^{2}} \cos(\omega t + \phi_{a} - \frac{2}{3}\pi) \\ \sqrt{V_{d}^{2} + V_{q}^{2}} \cos(\omega t + \phi_{a} + \frac{2}{3}\pi) \end{bmatrix} = \begin{bmatrix} \sqrt{2}V_{rms}\cos(\omega t + \phi_{a}) \\ \sqrt{2}V_{rms}\cos(\omega t + \phi_{a} - \frac{2}{3}\pi) \\ \sqrt{2}V_{rms}\cos(\omega t + \phi_{a} + \frac{2}{3}\pi) \end{bmatrix}$$
(7)

Where the RMS value of phase voltage is

$$V_{rms} = \frac{\sqrt{V_d^2 + V_q^2}}{\sqrt{2}\sqrt{3}} \tag{8}$$

And phase angle of phase voltage is

$$\phi_a = \arctan(\frac{V_q}{V_d}) \tag{9}$$

But for the unbalanced three phase system equations 8 and 9 are not true. The reason can be understood by the fact that for the unbalanced three phase system, there are six unknowns: three unknown RMS values and three unknown phase angles; and there are only three independent equations in dq0-coordinates. It is not possible to determine the six unknowns from solving three independent equations. In section 3.4 this problem will be solved by reducing the number of unknown variables from six to three using two methods: Fourier analysis and partial symmetric conditions. Figure 8 shows the results of equation 8 and 9 for the balanced and unbalanced condition.

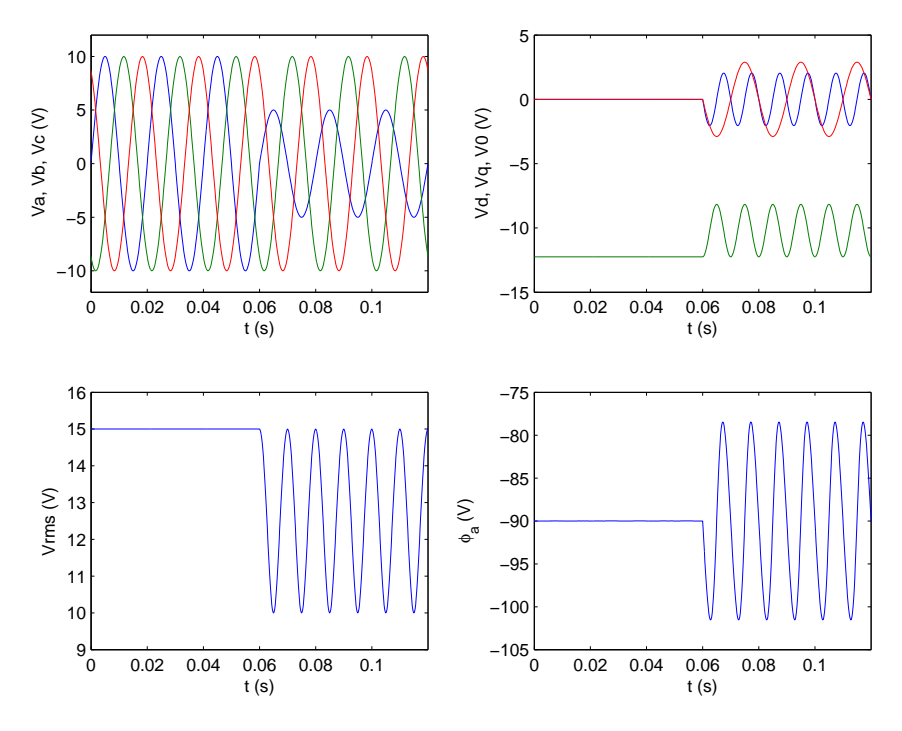


Figure 8: Phase voltages, dq0 voltages, RMS value and angle of voltage phasor in balanced and unbalanced condition (RMS value and angle are not correct for unsymmetrical conditions, see discussion in section 3.3.2)

# 3.4 Quasi-steady state thyristor bridge models

For an electromechanical transient study, the response time of electrical machines and tap change transformers are slow compared to the fast switching of the thyristor bridge. Therefore, the switching of the thyristor bridge can be considered to be instantaneous. The main characteristics of the resulting quasi steady-state model are:

- a change of firing angle is instantaneous;
- the transformer tap position remains unchanged during a change of firing angle;

- the DC side voltage is considered to be smooth and is actually equal to the average value per cycle;
- the DC side current is considered to be smooth due to a large smoothing inductance;
- the AC side voltage and current are assumed to be purely sinusoidal at fundamental frequency, all high order harmonics are filtered out.

# 3.4.1 Average quasi steady-state model for balanced conditions (Model Thy1)

The averaged DC side voltage  $V_{dc}$  is expressed in  $V_d$ ,  $V_q$ , DC current  $I_{dc}$ , firing angle and commutation reactance  $X_c$ :

$$V_{dc} = \frac{3\sqrt{2}}{\pi} V_{LL} \cos \alpha - \frac{3}{\pi} X_c I_{dc}$$

$$\tag{10}$$

with  $V_{LL}$  the RMS value of line to line voltage:

$$V_{LL} = \sqrt{V_d^2 + V_q^2} (11)$$

The AC phase current lags the AC phase voltage by an angle  $\phi_{vi}$ . This angle can be expressed in the firing angle  $\alpha$  and the commutation angle  $\mu$ :

$$\phi_{vi} = \alpha + \frac{\mu}{2} \tag{12}$$

with commutation angle  $\mu$ :

$$\mu = \frac{2X_c \cdot I_{dc}}{\sqrt{2}U_{LL}\sin\alpha} = \frac{2X_c \cdot I_{dc}}{\sqrt{2}\sqrt{V_d^2 + V_q^2}\sin\alpha}$$
(13)

To calculate the commutation angle, the initial values of line to line voltage must be set to nonzero values. The phase angle  $\phi_{va}$  of the phase a voltage is:

$$\phi_{va} = \arctan(\frac{V_q}{V_d}) \tag{14}$$

Then the phase angle  $\phi_{ia}$  of the current of phase a is:

$$\phi_{ia} = \phi_{va} - \phi_{vi} \tag{15}$$

The RMS value of fundamental component of the AC side current can be calculated by Fourier analysis and expressed in the DC side current  $I_{dc}$ , firing angle, and commutation angle  $\mu$ :

$$I_a = k \frac{\sqrt{6}}{\pi} I_{dc} \tag{16}$$

with k equal to:

$$k = \frac{\sqrt{\left[\cos 2\alpha - \cos(2\alpha + 2\mu)\right]^2 + \left[2\mu + \sin 2\alpha - \sin(2\alpha + 2\mu)\right]^2}}{4\left[\left(\cos \alpha - \cos(\alpha + \mu)\right]} \approx 1 \tag{17}$$

Finally, the instantaneous values of  $I_d$  and  $I_q$  can be calculated as:

$$I_d = \sqrt{3} I_{a,rms} \sin \phi_{ia}$$

$$I_q = -\sqrt{3} I_{a,rms} \cos \phi_{ia}$$
(18)

# Implementation in Simulink

The symmetrical quasi steady-state back-to-back thyristor bridge model is built as a hierarchical Simulink model:

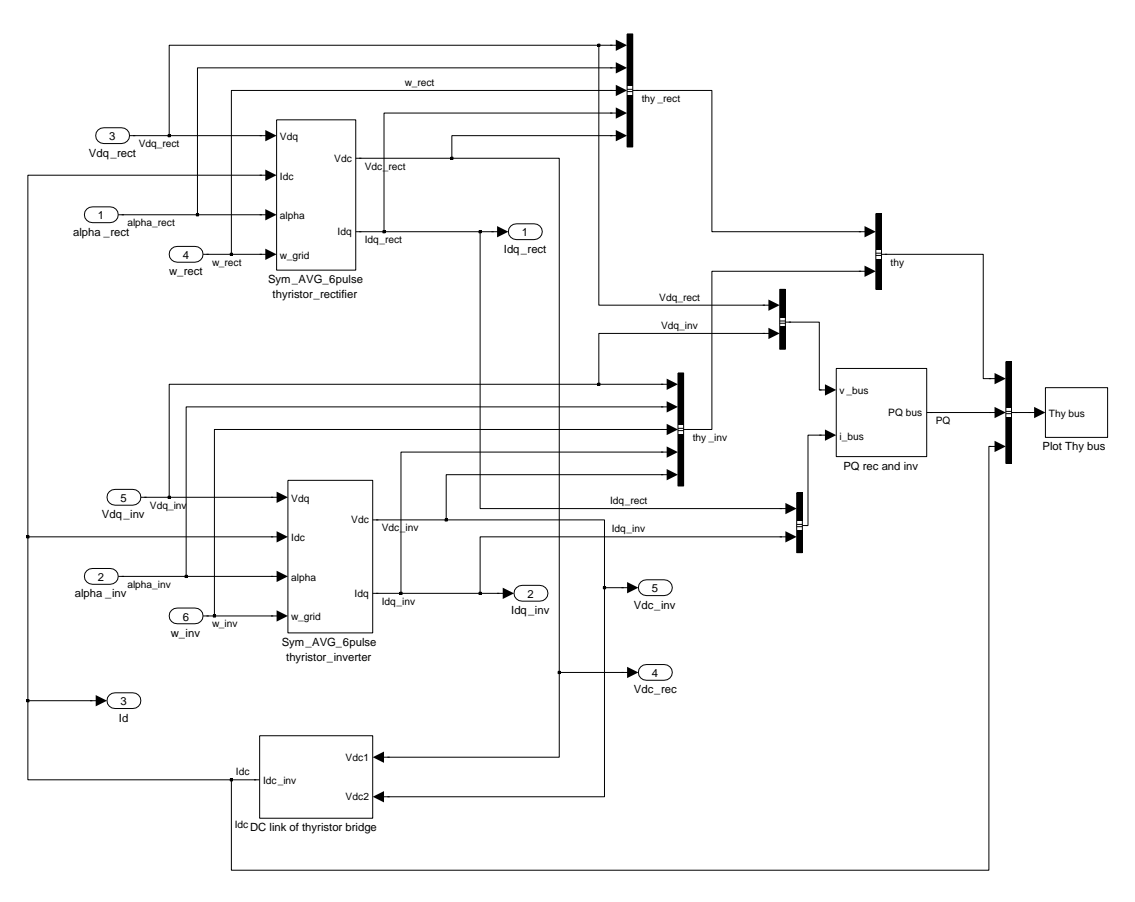


Figure 9: The symmetrical quasi steady-state thyristor bridge model in Simulink

The model consists of two almost identical thyristor converters, one operating as rectifier and one as an inverter. These connect at the DC side to a DC link. The symmetrical quasi steady-state thyristor inverter model in Simulink is:

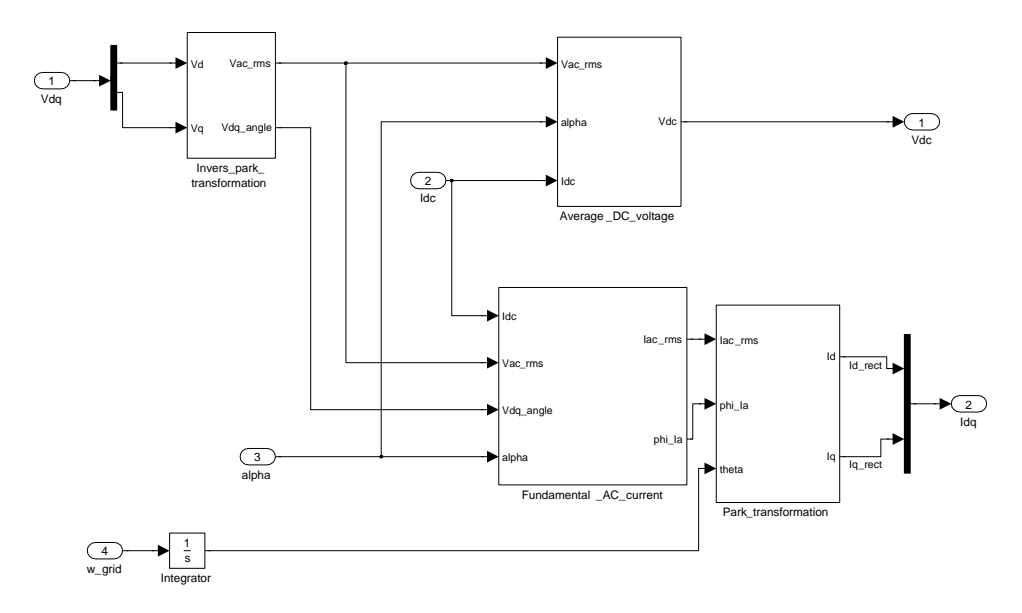


Figure 10: Symmetrical quasi steady-state thyristor inverter model in Simulink

The symmetrical quasi steady-state thyristor inverter model first calculates the AC voltage amplitude and the voltage dq angle:

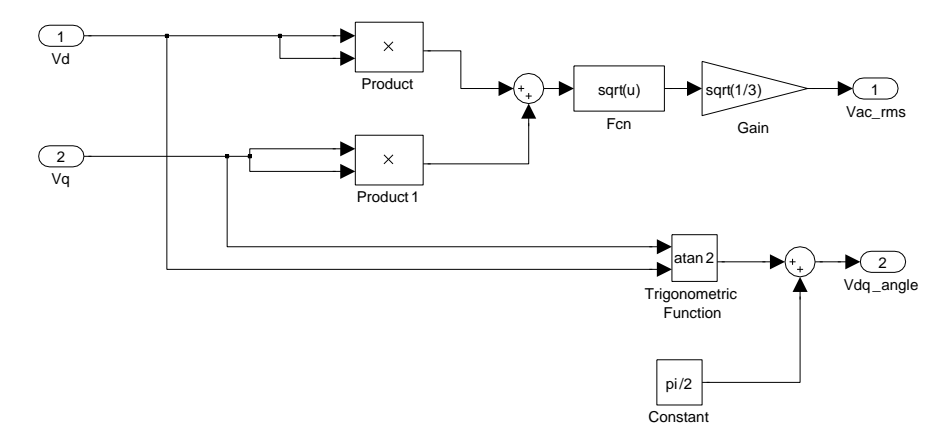


Figure 11: Calculation of RMS value and dq angle

The average DC voltage is calculated from the AC voltage amplitude, the firing angle and the DC current:

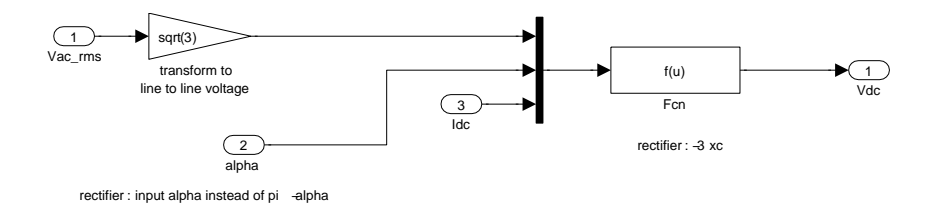


Figure 12: Average DC voltage

The fundamental AC current is calculated:

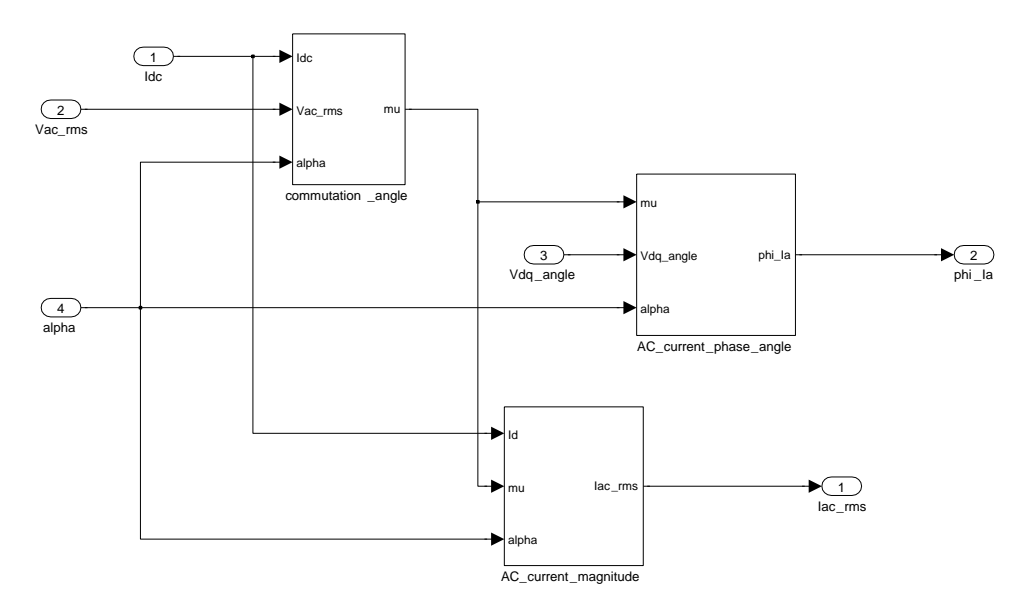


Figure 13: Fundamental AC current

Finally, a new value of the DC link voltage is calculated:

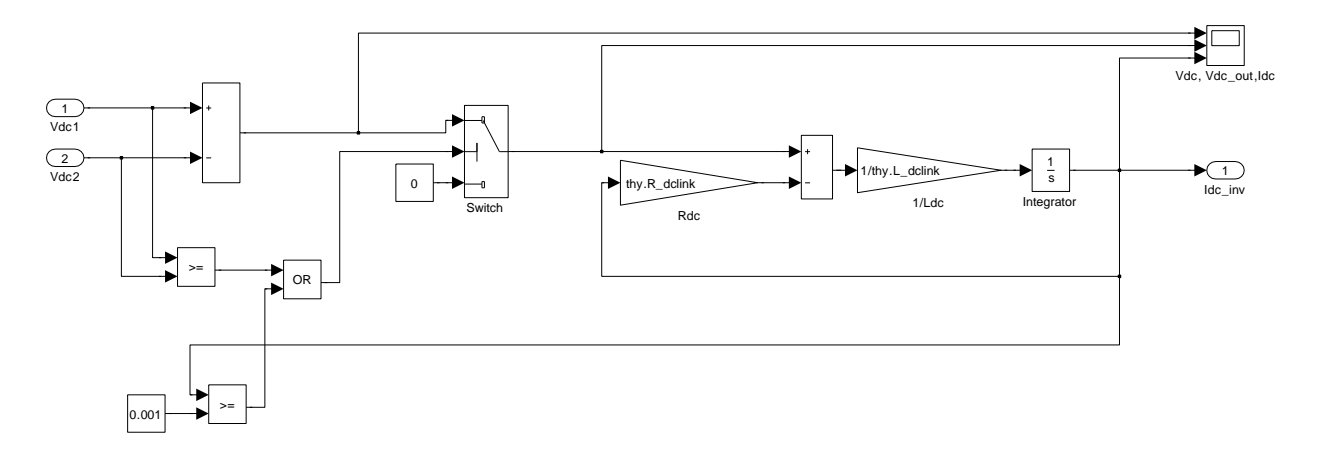


Figure 14: DC link

### **Simulation example**

The symmetrical quasi stead-state model is tested in a simple simulation. A three phase symmetrical AC voltage source is connected to an AC voltage  $V_{ac}$  generated by the invers Park transformation. The DC current and grid frequency are set as constants. A firing angle step from 30 degree to 45 degrees (0.52-0.78 rad) is used. Figure 15 shows the results for the back-to-back model (rectifier, DClink and inverter).

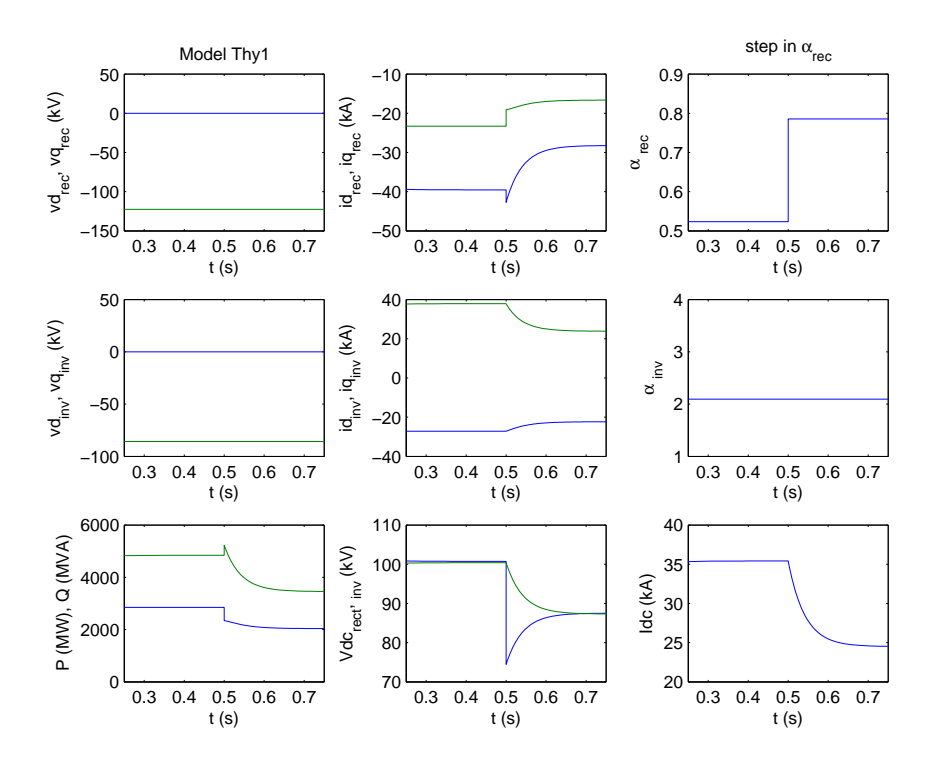


Figure 15: A step in rectifier firing angle in the average symmetrical thyristor model (Thy1)

# Connection with other dynamic models

Connecting the quasi-steady state thyristor bridge model to the other dynamic models can lead to conflicts. The thyristor bridge model inputs are the AC voltages and the outputs are the AC currents. In most cases, the thyristor bridge model is at the AC side connected to a transformer or a cable and both have the secondary voltage and primary current as inputs and the primary voltage and secondary current as outputs. If we want to connect the thyristor bridge model with the secondary side of the transformer or cable model, we have a conflict. Both models require an AC voltage as input and an AC current as output. To solve this problem, a model which has two AC currents as inputs and two AC voltages as outputs has to be inserted between the transformer and the thyristor model. This actually is a shunt capacitor model. The next figure illustrates the connection.

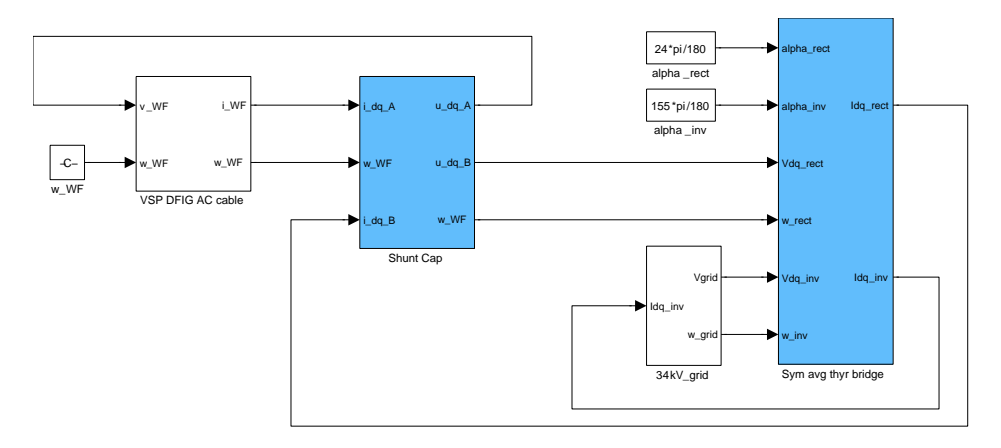


Figure 16: Connection of the thyristor bridge model to a wind farm and grid model

# 3.4.2 Average quasi steady-state model, unbalanced, Fourier (Model Thy2)

In this section an average quasi steady-state model for unbalanced conditions using Fourier analysis will be derived. For unbalanced conditions the average DC voltage equation is more complex:

$$U_{dc} = \frac{\sqrt{2}}{\pi} U_{ba} [\cos(C_1 + \alpha - C_3 + \pi) - \cos(C_2 + \alpha - C_1 + \pi)]$$

$$+ \frac{\sqrt{2}}{\pi} U_{ac} [\cos(C_2 + \alpha - C_1) - \cos(C_3 + \alpha - C_1)]$$

$$+ \frac{\sqrt{2}}{\pi} U_{bc} [\cos(C_3 + \alpha - C_2) - \cos(C_1 + \alpha + \pi - C_2)]$$

$$- \frac{I_{dc}(X_{c1} + X_{c2} + X_{c3})}{\pi}$$

$$(19)$$

 $U_{ba}, U_{bc}, U_{ac}$  are the RMS values of line to line voltages,  $C_1, C_2, C_3$  are the corresponding phase angles of the line to line voltages.  $I_{dc}$  is the DC current.  $X_{c1}, X_{c2}, X_{c3}$  are the commutation inductances on the AC side,  $\alpha$  is the firing angle. The meanings of the angles can be seen in the following graph.

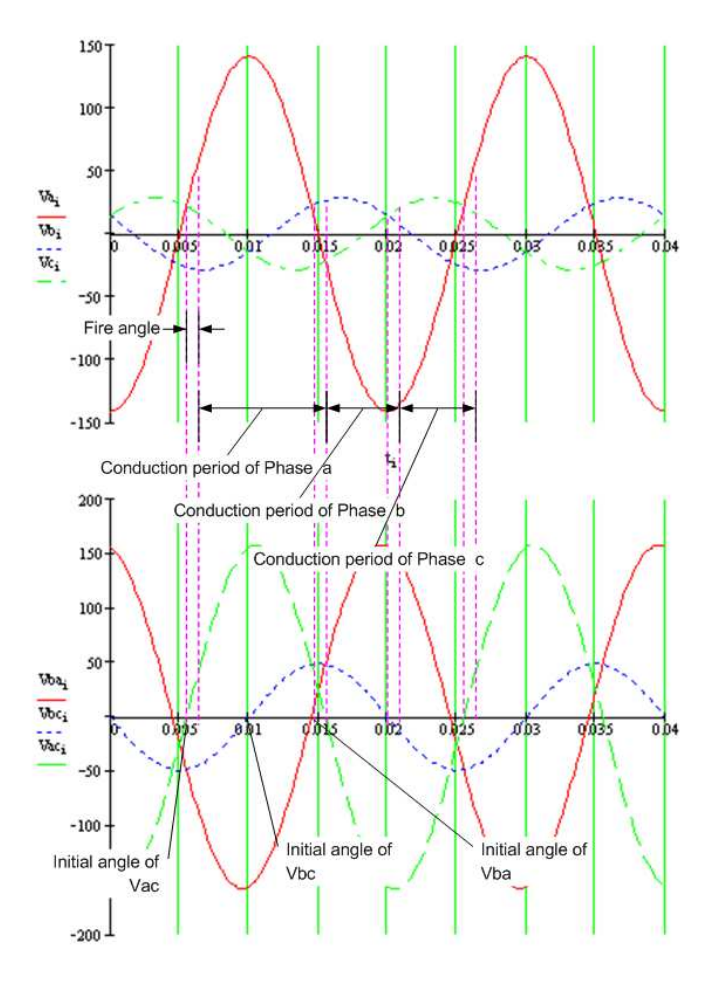


Figure 17: Wave forms of unbalanced voltages

Fourier analysis is used to calculate the RMS values and phase angles of the line to line voltages from the instantaneous voltages in dq0-coordinates:

$$U_{ba}(t) = \sqrt{2}\left[V_d \sin(\omega t - \frac{\pi}{3}) + V_q \cos(\omega t - \frac{\pi}{3})\right]$$
 (20)

$$U_{ac}(t) = \sqrt{2}\left[V_d \sin(\omega t + \frac{\pi}{3}) + V_q \cos(\omega t + \frac{\pi}{3})\right]$$
 (21)

$$U_{bc}(t) = \sqrt{2}[V_d \sin(\omega t) + V_q \cos(\omega t)]$$
 (22)

The commutation angles  $\mu_i$  are:

$$\mu_1 = \arccos\left(\cos\alpha - \frac{X_{c1} + X_{c3}}{\sqrt{2}V_{ac}} \cdot I_{dc}\right) - \alpha$$
 (23)

$$\mu_2 = \arccos\left(\cos\alpha - \frac{X_{c2} + X_{c1}}{\sqrt{2}V_{ba}} \cdot I_{dc}\right) - \alpha$$
 (24)

$$\mu_3 = \arccos\left(\cos\alpha - \frac{X_{c2} + X_{c3}}{\sqrt{2}V_{bc}} \cdot I_{dc}\right) - \alpha$$
 (25)

The RMS values of the AC phase currents are:

$$I_{i,rms} = \frac{4}{\pi} \frac{I_{dc}}{\sqrt{2}} \sin(\frac{T_i}{2}) \tag{26}$$

 $T_i$  is the conduction time of each phase. From the figure 17 with the unsymmetrical voltage waveforms we get:

$$T_a = \phi_{ba} + \alpha - (\phi_{ac} + \alpha) = \phi_{ba} - \phi_{ac} \tag{27}$$

$$T_b = \phi_{bc} + \pi + \alpha - (\phi_{ba} + \alpha) = \phi_{bc} - \phi_{ba} + \pi$$
 (28)

$$T_c = \phi_{ac} + 2\pi + \alpha - (\phi_{bc} + \pi + \alpha) = \phi_{ac} - \phi_{bc} + \pi$$
 (29)

The phase angles of the AC phase currents are:

$$\phi_{vi} = \alpha + \frac{\mu_i}{2} \tag{30}$$

$$\phi_i = \phi_v - \overline{\phi_{vi}} \tag{31}$$

The AC currents in phase a, b and c are:

$$i_a(t) = \sqrt{2}I_a\sin(\omega t + \phi_{Ia}) \tag{32}$$

$$i_b(t) = \sqrt{2}I_b\sin(\omega t + \phi_{Ib}) \tag{33}$$

$$i_c(t) = \sqrt{2}I_c\sin(\omega t + \phi_{Ic}) \tag{34}$$

The AC currents in dq0-coordinates are:

$$\begin{bmatrix} I_d(t) \\ I_q(t) \\ I_0(t) \end{bmatrix} = T_{dq0} \begin{bmatrix} i_a(t) \\ i_b(t) \\ i_c(t) \end{bmatrix} = \frac{1}{\sqrt{3}} \begin{bmatrix} I_a \sin(\phi_{ia}) + I_b \sin(\phi_{ib} + \frac{2}{3}\pi) + I_c \sin(\phi_{ic} - \frac{2}{3}\pi) \\ - \left[ I_a \cos(\phi_{ia}) + I_b \cos(\phi_{ib} + \frac{2}{3}\pi) + I_c \cos(\phi_{ic} - \frac{2}{3}\pi) \right] \\ 0 \end{bmatrix}$$

$$+\frac{1}{\sqrt{3}} \begin{bmatrix} I_{a} \sin(2\omega t + \phi_{ia}) + I_{b} \sin(2\omega t + \phi_{ib} - \frac{2}{3}\pi) + I_{c} \sin(2\omega t + \phi_{ic} + \frac{2}{3}\pi) \\ -[I_{a} \cos(2\omega t + \phi_{a} + \theta_{d}) + I_{b} \cos(2\omega t + \phi_{b} - \frac{2}{3}\pi) + I_{c} \cos(2\omega t + \phi_{c} + \frac{2}{3}\pi)] \\ I_{a} \sin(\omega t + \phi_{ia}) + I_{b} \sin(\omega t + \phi_{ib}) + I_{c} \sin(\omega t + \phi_{ic}) \end{bmatrix}$$
(35)

# Implementation in Matlab/Simulink

The implementation of the average unsymmetrical quasi-state thyristor bridge model using Fourier coefficients in Simulink is:

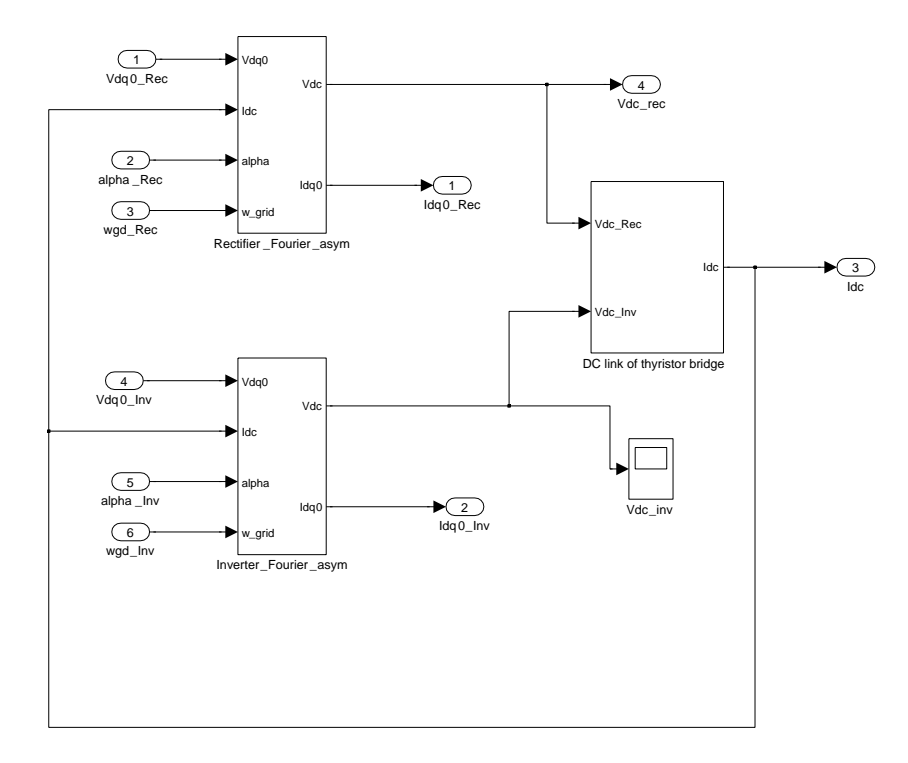


Figure 18: Thyristor bridge model using Fourier coefficients in Simulink (Model Thy2)

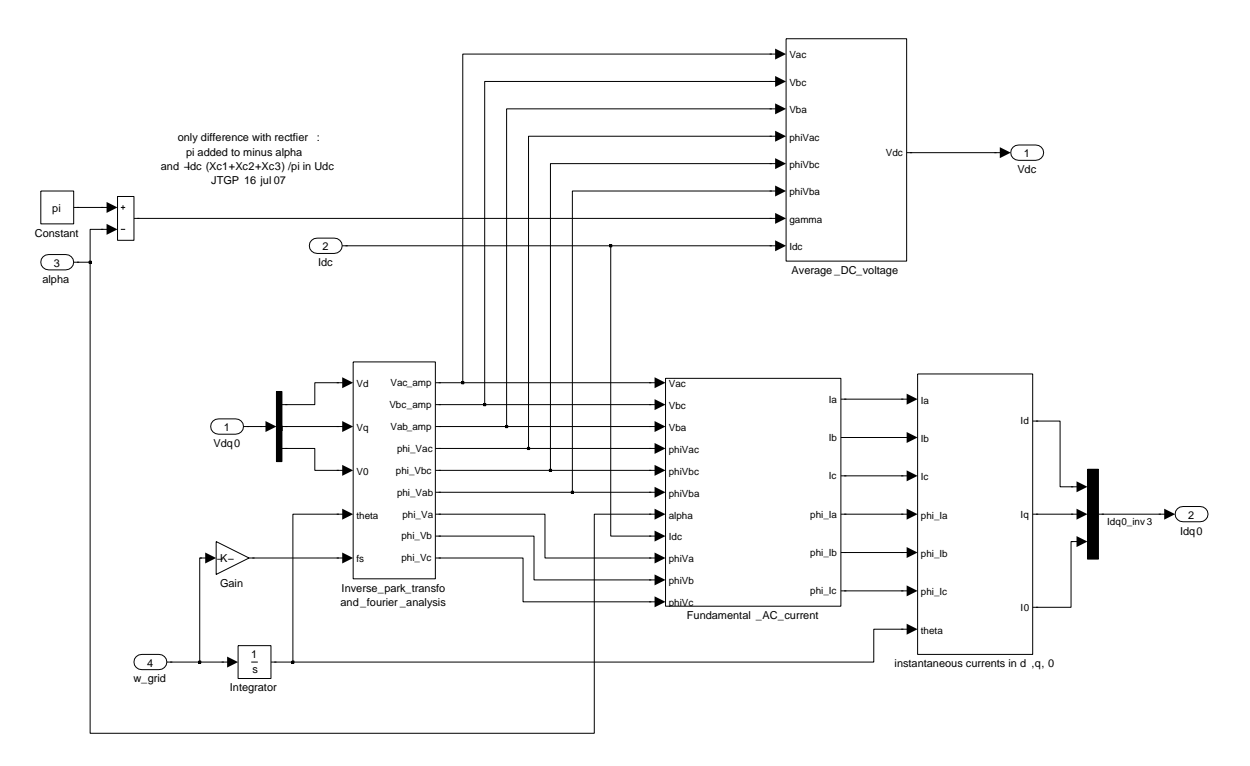


Figure 19: Inverter model using Fourier coefficients in Simulink (Model Thy2)

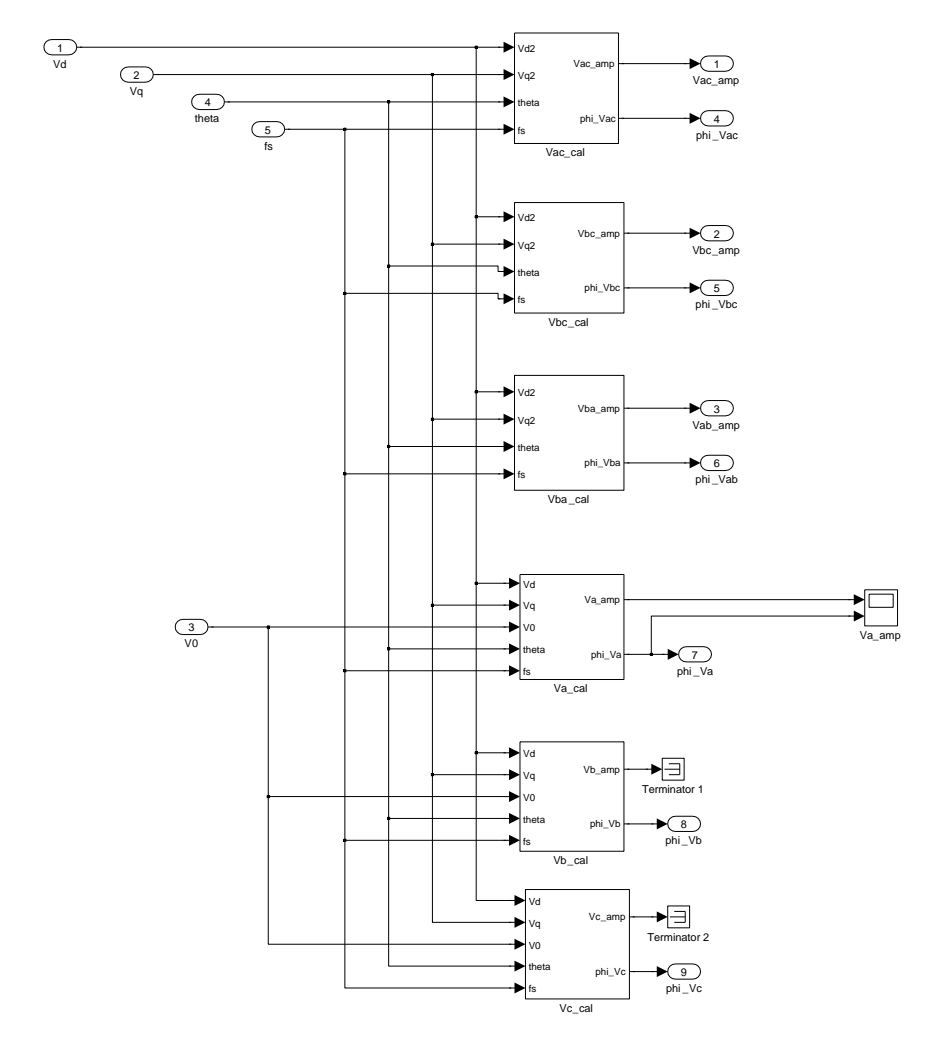


Figure 20: Fundamental voltages in Simulink (Model Thy2)

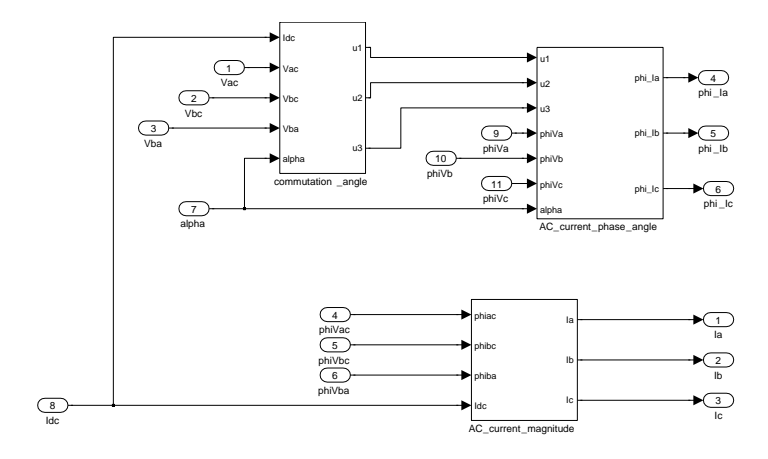


Figure 21: Fundamental currents in Simulink (Model Thy2)

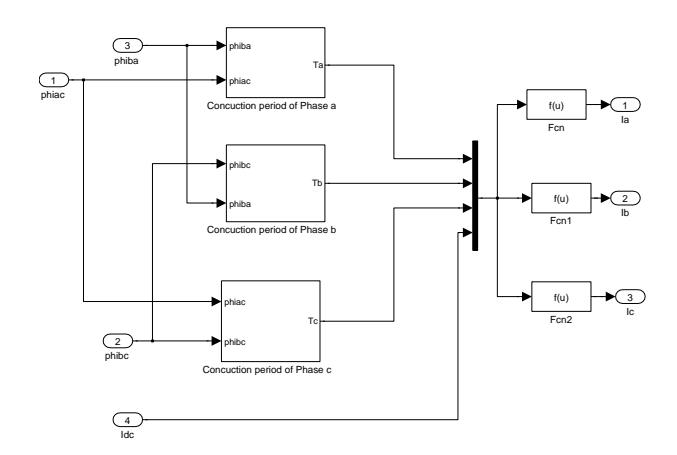


Figure 22: Current magnitudes in Simulink (Model Thy2)

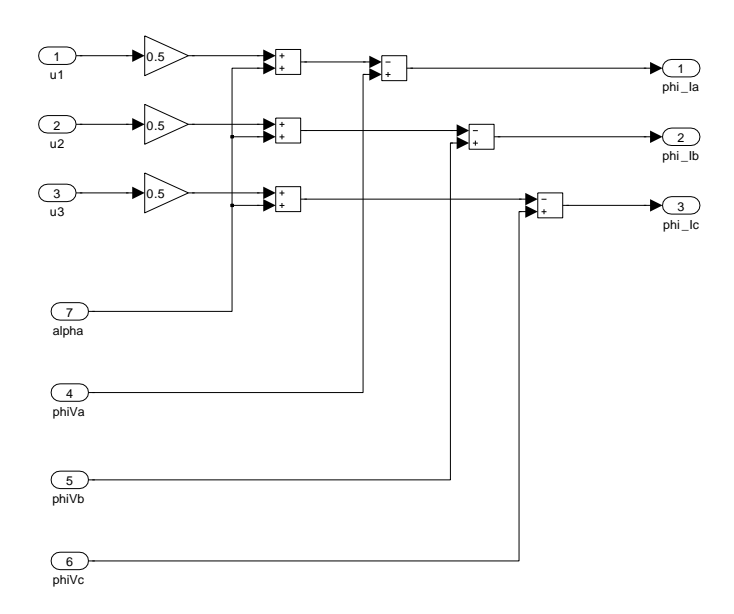


Figure 23: Current phase angles in Simulink (Model Thy2)

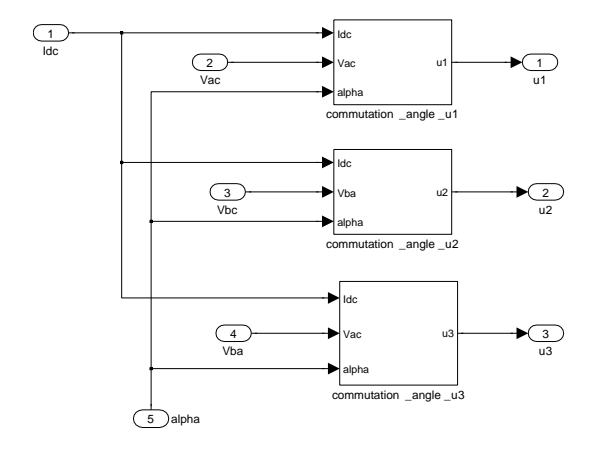


Figure 24: Commutation in Simulink (Model Thy2)

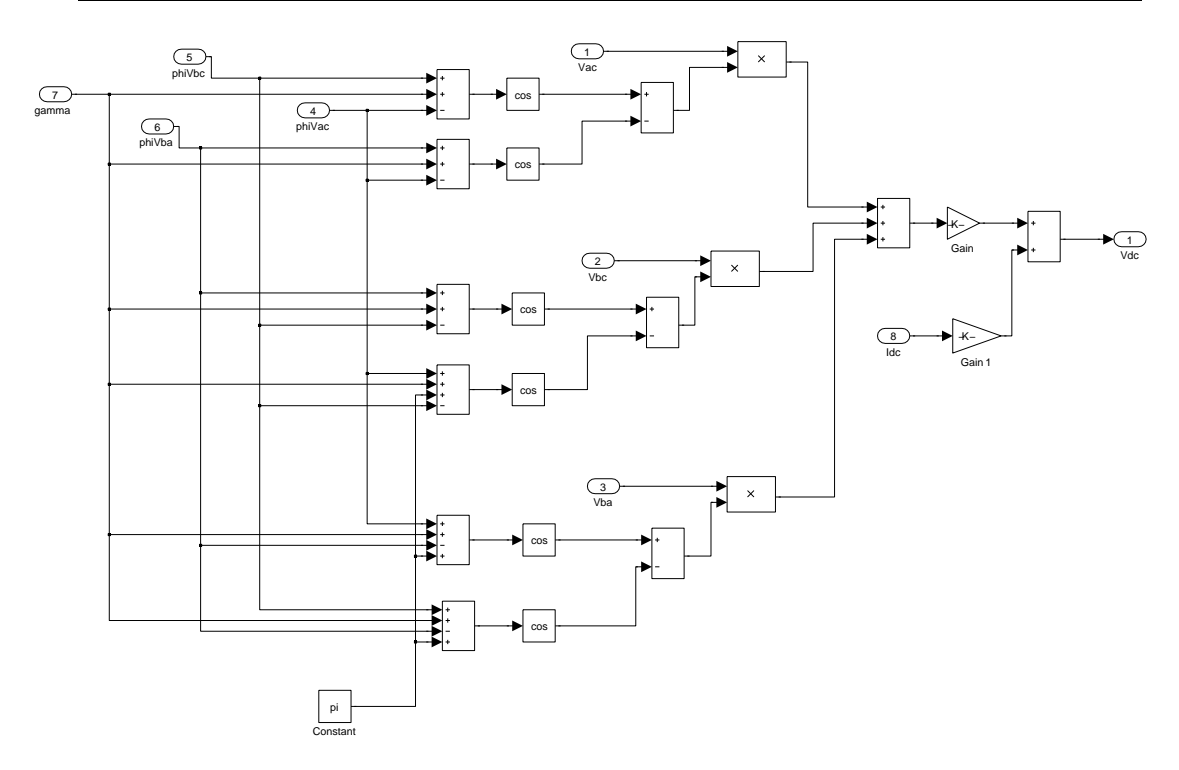


Figure 25: DC voltage in Simulink (Model Thy2)

# Simulation example

Figure 26 shows the results of a dip in the RMS voltage of phase a for the inverter model using Fourier (Model Thy2). The Fourier analysis method introduces a time delay in the result of about 0.01 s, which can be seen in the figure. Because of this disadvantage, a second quasi steady state model will be developed, assuming partially symmetrical unbalanced conditions.

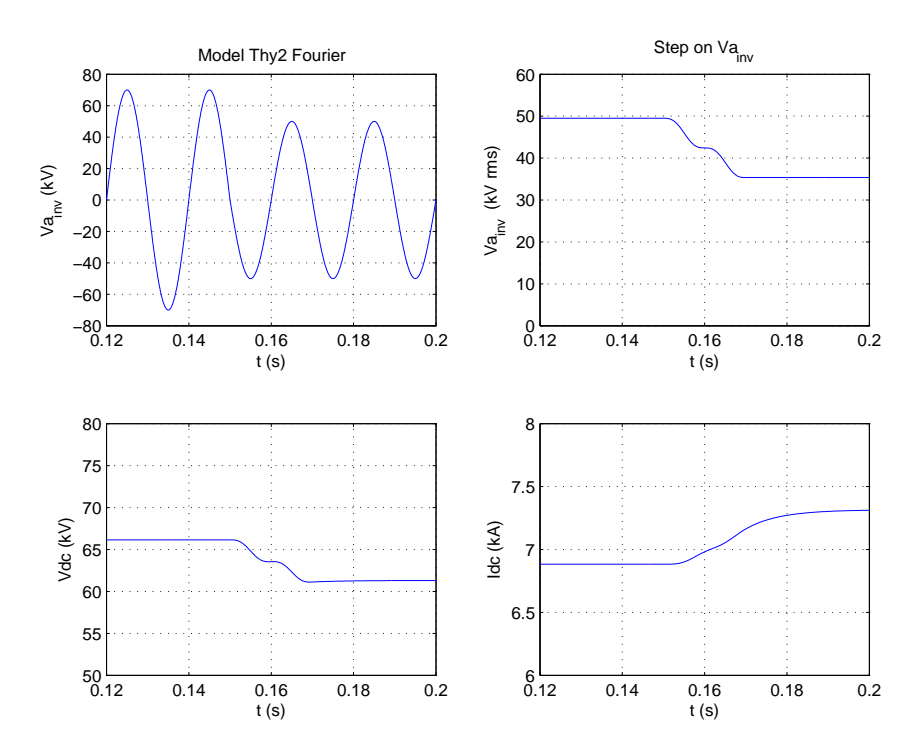


Figure 26: A dip in the RMS voltage of phase a of the inverter in the model using Fourier analysis (Thy2)

# 3.4.3 Av. quasi-steady state, unbalanced, partially symmetrical (Model Thy3)

For an unbalanced three phase system, the three phase voltages may still be considered to be partially symmetrical. For example, for a double phases to ground fault, the two faulted phase voltages have the same RMS value. For a single phase to ground fault, the unfaulted two phase voltages also have the same RMS value. This partially symmetrical condition can be used to calculate the RMS values and phase angles of the voltages from the instantaneous values in dq0-coordinates because it can help to reduce the number of unknown variables to three, which can be determined by the three independent equations in dq0-coordinates. The following assumptions have been made:

- two phase voltage RMS values are always the same;
- the phase voltages are displaced by 120 degrees.

Now there are two different RMS values and the initial angle of one phase. Using the inverse park transformation, we get:

$$\sqrt{2}V_a\sin(\omega t + \phi_a) = \sqrt{\frac{2}{3}}\left[V_d\cos(\theta_d) - V_q\sin(\theta_d) + \frac{1}{\sqrt{2}}V_0\right]$$
(36)

$$\sqrt{2}V_b \sin(\omega t + \phi_b) = \sqrt{\frac{2}{3}} \left[ V_d \cos(\theta_d - \frac{2}{3}\pi) - V_q \sin(\theta_d - \frac{2}{3}\pi) + \frac{1}{\sqrt{2}}V_0 \right]$$
(37)

$$\sqrt{2}V_c \sin(\omega t + \phi_c) = \sqrt{\frac{2}{3}} \left[ V_d \cos(\theta_d + \frac{2}{3}\pi) - V_q \sin(\theta_d + \frac{2}{3}\pi) + \frac{1}{\sqrt{2}}V_0 \right]$$
(38)

From the two assumptions, we get:

$$V_b = V_c \tag{39}$$

$$\phi_b = \phi_a - \frac{2}{3}\pi \tag{40}$$

$$\phi_c = \phi_a + \frac{2}{3}\pi \tag{41}$$

If the d-axis is aligned with phase a initially, then:

$$\theta_d = \omega t \tag{42}$$

The phase voltage equations can be simplified to:

$$\sqrt{2}V_a\sin(\omega t + \phi_a) = \sqrt{\frac{2}{3}}\left[V_d\cos(\theta_d) - V_q\sin(\theta_d) + \frac{1}{\sqrt{2}}V_0\right]$$
(43)

$$\sqrt{2}V_b \sin(\omega t + \phi_a - \frac{2}{3}\pi) = \sqrt{\frac{2}{3}} \left[ V_d \cos(\theta_d - \frac{2}{3}\pi) - V_q \sin(\theta_d - \frac{2}{3}\pi) + \frac{1}{\sqrt{2}}V_0 \right] (44)$$

$$\sqrt{2}V_b \sin(\omega t + \phi_a + \frac{2}{3}\pi) = \sqrt{\frac{2}{3}} \left[ V_d \cos(\theta_d + \frac{2}{3}\pi) - V_q \sin(\theta_d + \frac{2}{3}\pi) + \frac{1}{\sqrt{2}}V_0 \right]$$
(45)

The three independent equations are used to solve three unknowns:  $V_a, V_b, \phi_a$ . The solution is:

$$V_b = V_c = \frac{\sqrt{V_d^2 + V_q^2 + 2V_0^2 - 2\sqrt{2}V_dV_0\cos(\omega t) + 2\sqrt{2}V_qV_0\sin(\omega t)}}{\sqrt{3}}$$
(46)

$$V_a = \frac{V_d \cos(\omega t) - V_q \sin(\omega t) + \frac{1}{\sqrt{2}} V_0}{V_d \cos(\omega t) - V_q \sin(\omega t) - \sqrt{2} V_0} \cdot V_b$$

$$(47)$$

$$\phi_a = \arctan\left(-\frac{\frac{V_d \cos(\omega t) - V_q \sin(\omega t) - \sqrt{2}V_0}{V_d \sin(\omega t) + V_q \cos(\omega t)} - \tan(\omega t)}{1 - \frac{V_d \cos(\omega t) - V_q \sin(\omega t) - \sqrt{2}V_0}{V_d \sin(\omega t) + V_q \cos(\omega t)} \cdot \tan(\omega t)}\right)$$
(48)

The RMS values of phase to phase voltages are:

$$V_{ab} = V_{ac} = \sqrt{V_a^2 + V_b^2 - 2V_a V_b \cos(\frac{2}{3}\pi)}$$
 (49)

$$V_{bc} = \sqrt{V_b^2 + V_c^2 - 2V_b V_c \cos(\frac{2}{3}\pi)}$$
 (50)

Phase angles of phase to phase voltages are:

$$\phi_{ac} = \arctan\left(\frac{V_a \sin(\phi_a) - V_c \sin(\phi_a + \frac{2}{3}\pi)}{V_a \cos(\phi_a) - V_c \cos(\phi_a + \frac{2}{3}\pi)}\right)$$
(51)

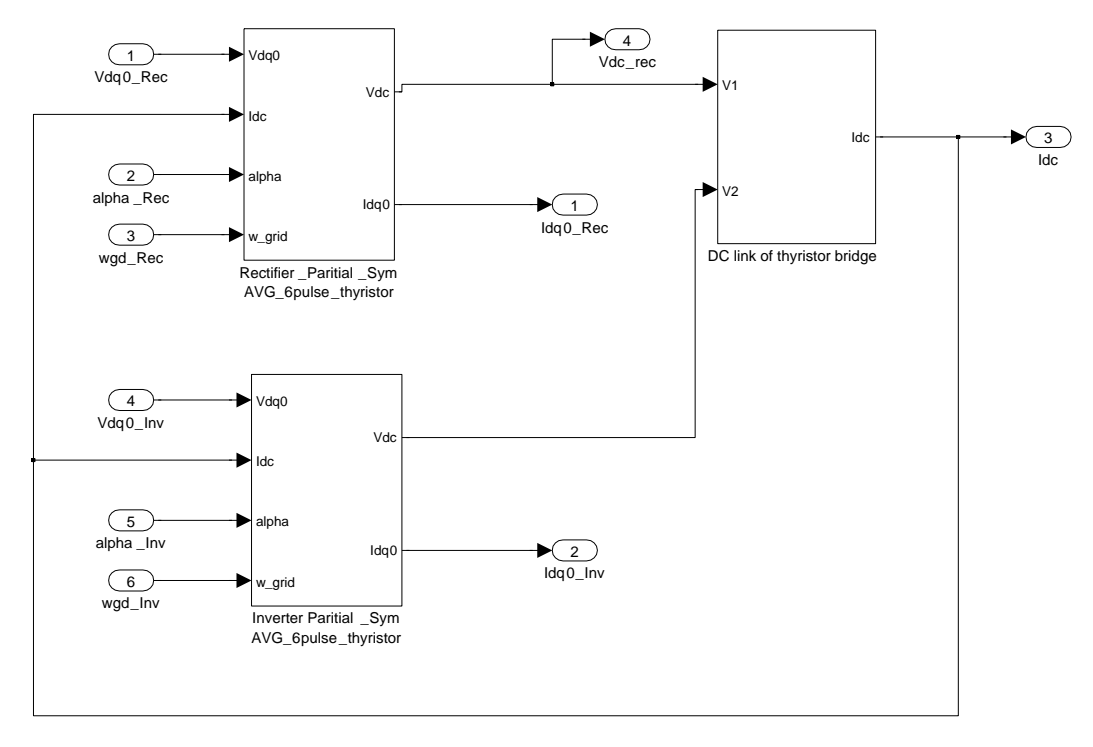
$$\phi_{bc} = \arctan\left(\frac{V_b \sin(\phi_a - \frac{2}{3}\pi) - V_c \sin(\phi_a + \frac{2}{3}\pi)}{V_b \cos(\phi_a - \frac{2}{3}\pi) - V_c \cos(\phi_a + \frac{2}{3}\pi)}\right)$$
(52)

$$\phi_{ba} = \arctan\left(\frac{V_b \sin(\phi_a - \frac{2}{3}\pi) - V_a \sin(\phi_a)}{V_b \cos(\phi_a - \frac{2}{3}\pi) - V_a \cos(\phi_a)}\right)$$
(53)

The equations of the thyristor bridge are the same as for the average quasi-steady state model using Fourier analysis, see section 3.4.2.

## Implementation Model Thy3 in Matlab/Simulink

Figures 27 to 33 give the main component blocks in the Simulink average quasi-steady state thyristor bridge model assuming partially symmetrical conditions.



 $\label{thm:condition} Figure~27:~Simulink~average~quasi-steady~state~thyristor~bridge~model~assuming~partially~symmetrical~conditions~(Model~Thy3)$ 

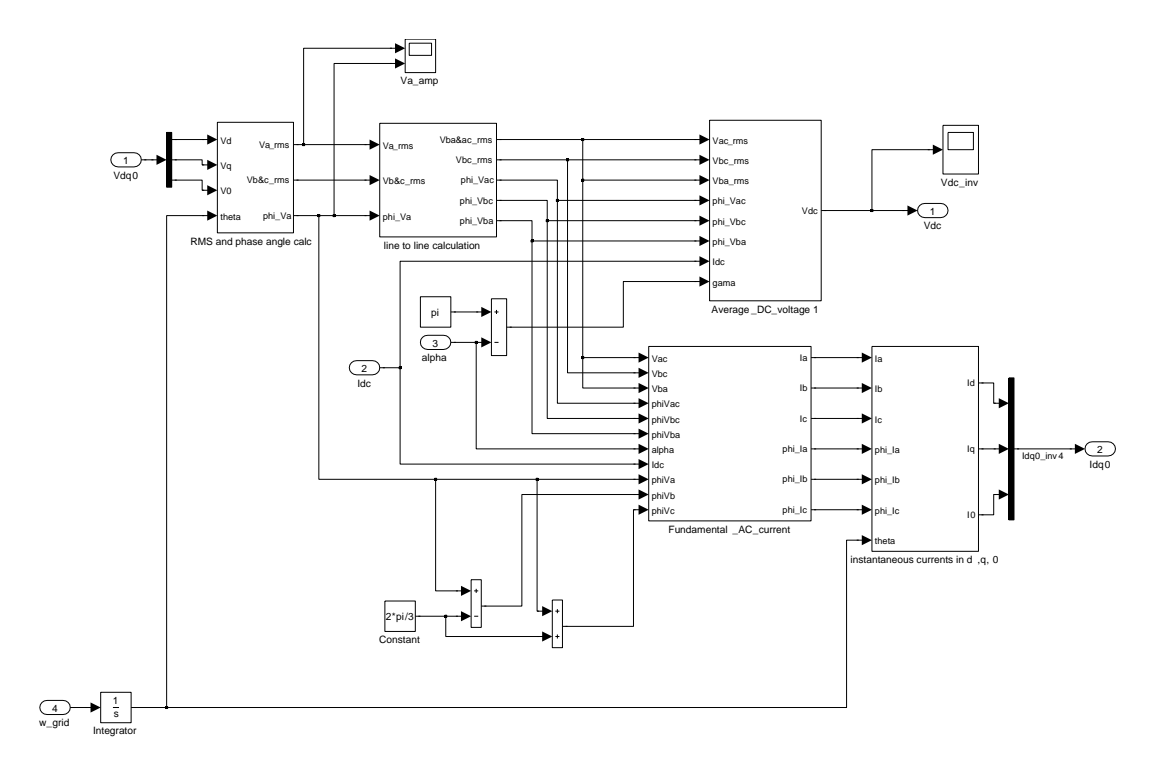


Figure 28: Inverter model assuming partially symmetrical conditions (Model Thy3)

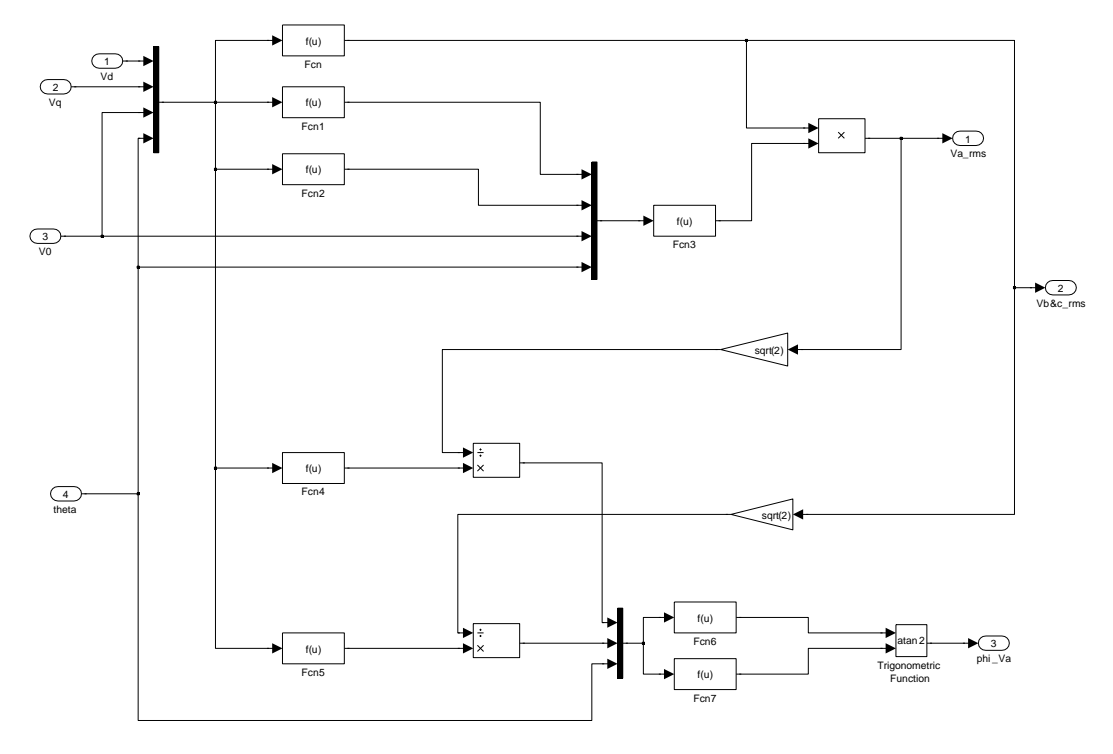


Figure 29: RMS and phase angle calculation (Model Thy3)

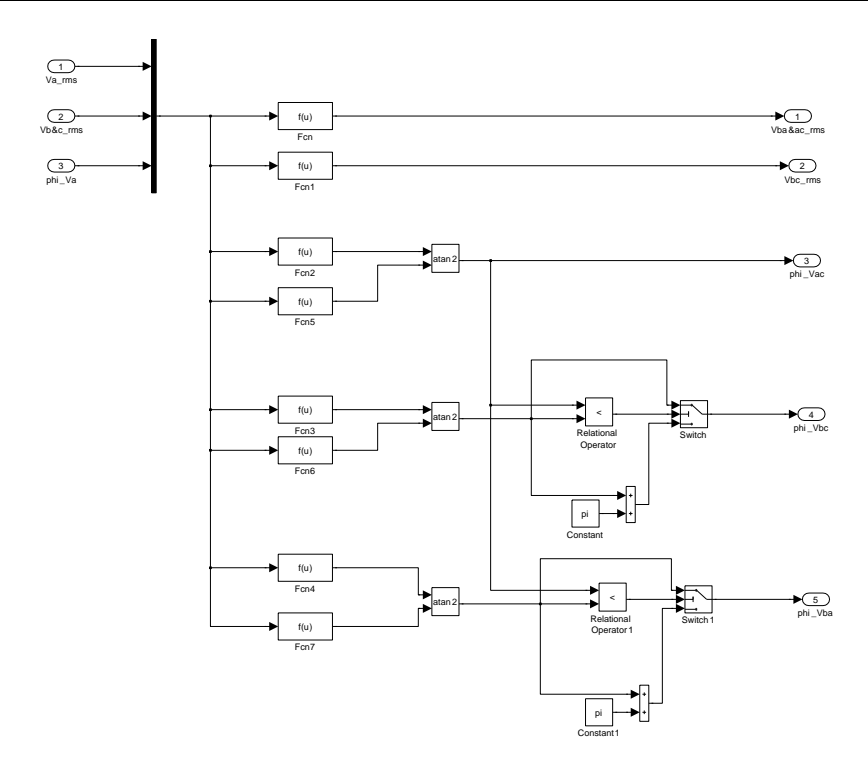


Figure 30: Line to line calculation (Model Thy3)

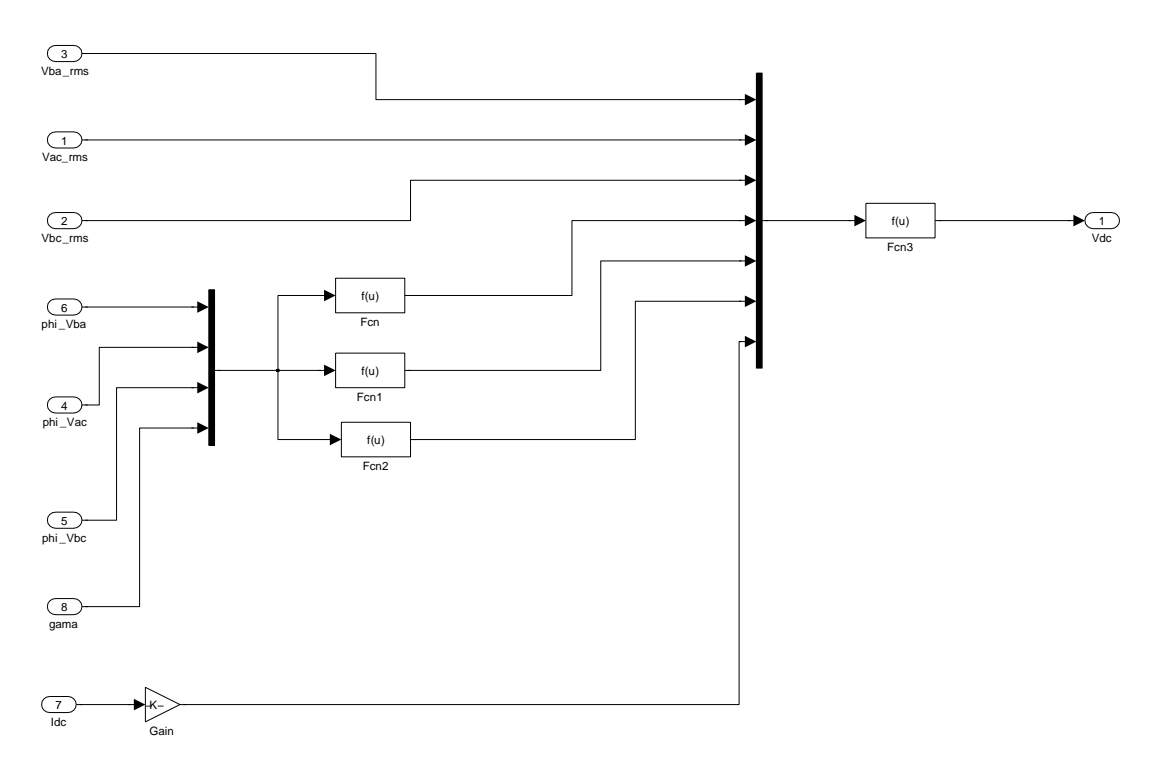


Figure 31: Average DC voltage calculation (Model Thy3)

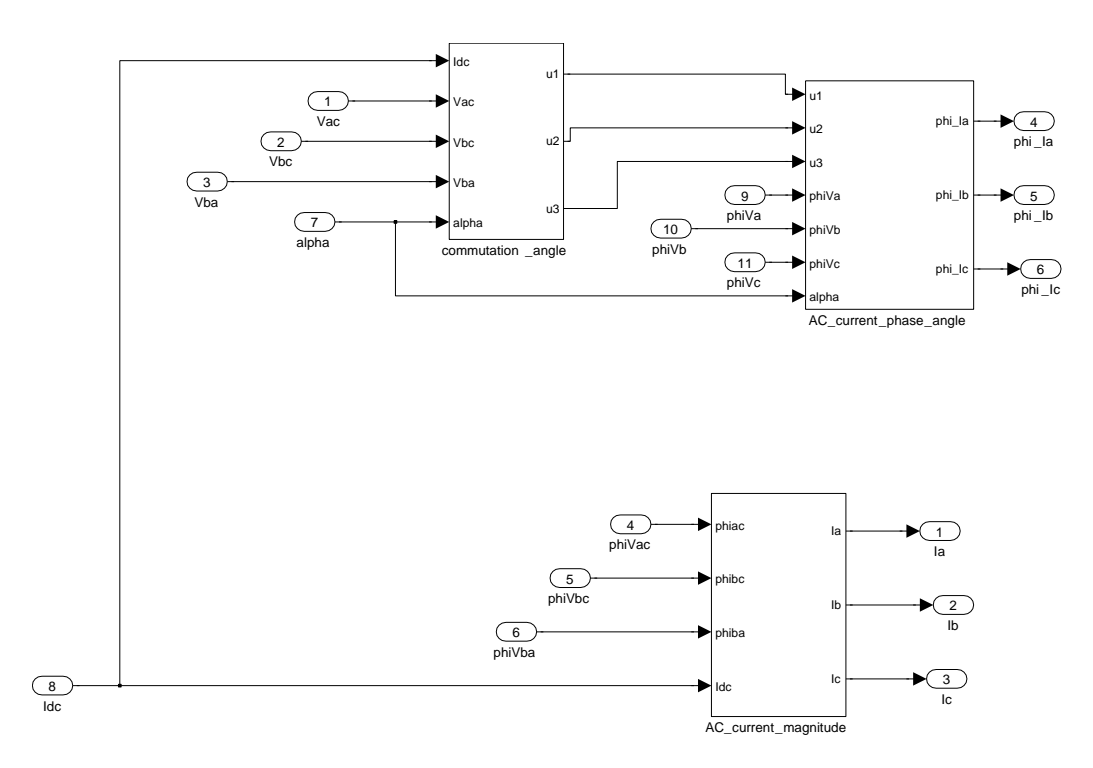


Figure 32: Fundamental AC current calculation (Model Thy3)

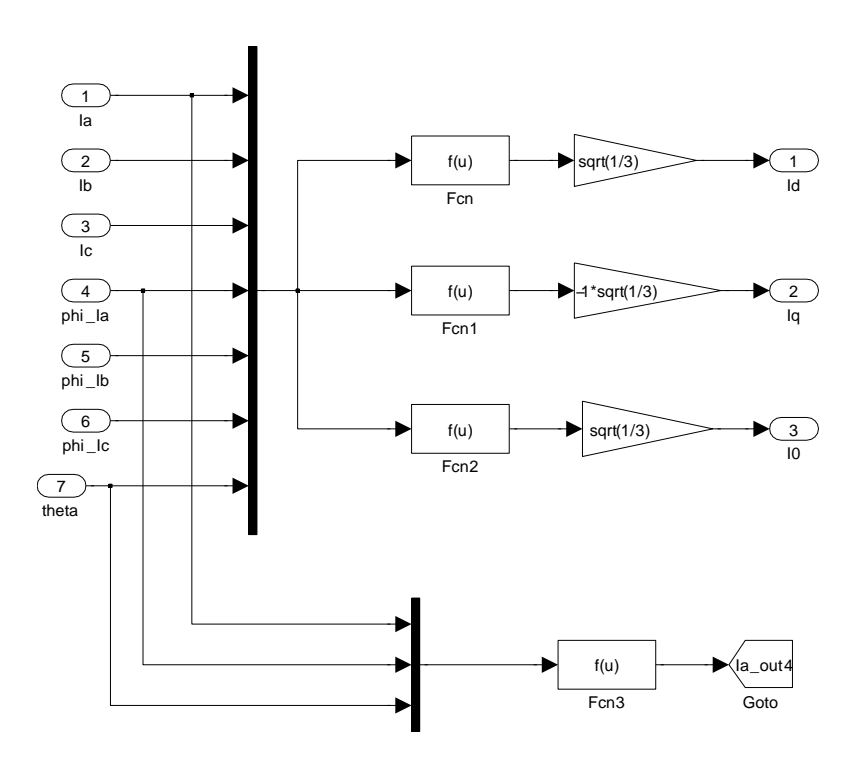


Figure 33: DQ0 current calculation (Model Thy3)

#### Simulation example Model Thy3

The quasi-steady state model assuming partially symmetrical conditions is tested in a simple simulation. A voltage dip in the AC voltage of the inverter occurs in phase a at 0.15 s, see figure 34. The partially symmetrical model does not have a 0.01s time delay.

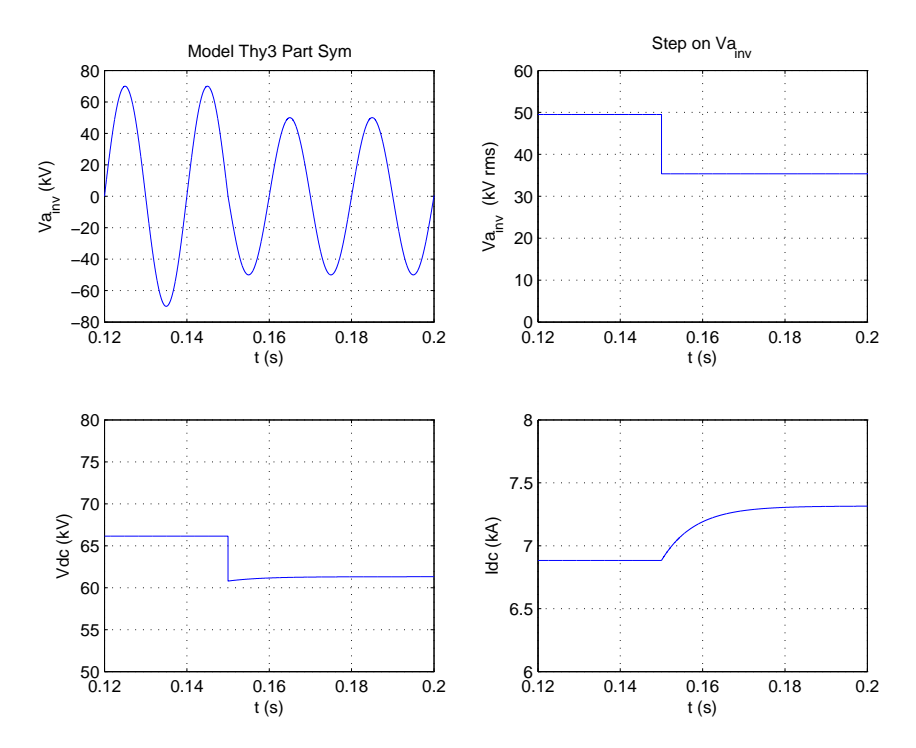


Figure 34: A dip in the RMS voltage of phase a of the inverter in the model assuming partially symmetrical conditions (Thy3)

# 3.5 Instantaneous thyristor bridge models

# 3.5.1 Instantaneous diode bridge without commutation inductance (Model Thy4a)

The instantaneous model calculates the instantaneous DC voltage instead of the average value over one period of the voltage/current (0.02s) in the quasi steady state model. Unlike the voltage source converter, which can use a relatively simple transfer function to describe the relation between DC voltage and AC voltage or DC current and AC current, the instantaneous model of the thyristor bridge is much more complex due to the uncontrollable extinction of the thyristors. The Matlab/Simulink Power System Blockset and DIgSILENT include instantaneous models of thyristor bridge, but these are masked and not accessible to the users. The development of the instantaneous model starts with a three phase diode bridge model. This is easier than the thyristor bridge model because the firing angle is not considered. The switching scheme of the diode bridge is shown in the figure 35.

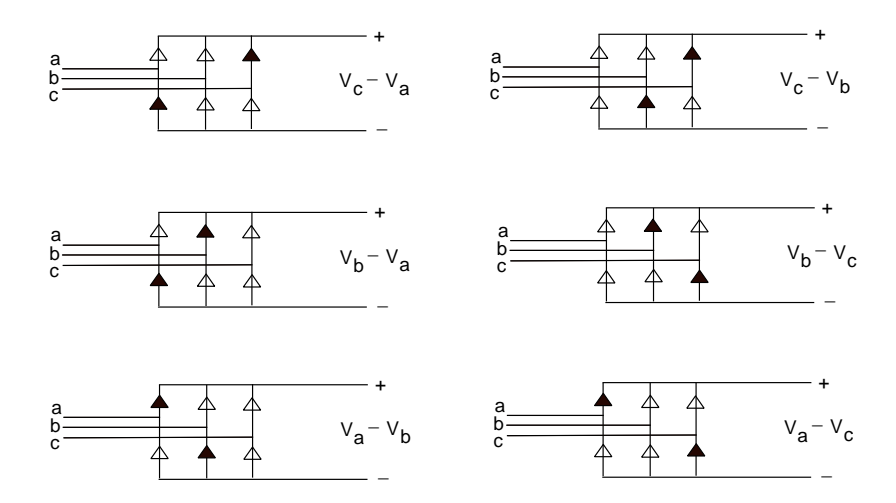


Figure 35: Switching scheme of the diode bridge

The diode positive branch conducts when its phase voltage is the most positive, while the negative branch conducts when its phase voltage is the most negative. The phase current only flows when one of the diodes is conducting. In order to implement the diode bridge in Simulink, the states of the diodes are defined:

	Conducting	Blocked
D1, D3, D5	1	0
D4, D6, D2	-1	0

The commutation inductance only causes a small drop in the DC side voltage at normal operating points and is omitted at this moment because of the difficulty of implementation. The six states of three phase diode bridge during one cycle of the AC voltage are:

Conducting Diodes	Positive DC voltage	Negative DC voltage	Total DC voltage
D1, D2	Va	Vc	Va-Vc
D3, D2	Vb	Vc	Vb-Vc
D3, D4	Vb	Va	Vb-Va
D5, D4	Vc	Va	Vc-Va
D5, D6	Vc	Vb	Vc-Vb
D1, D6	Va	Vb	Va-Vb

So if the states in the time domain are determined correctly, the instantaneous DC voltage and AC current can be calculated. If we define the matrix of states K, then the instantaneous DC voltage and AC current can be expressed as:

$$V_{dc} = K \cdot \begin{bmatrix} V_a \\ V_b \\ V_c \end{bmatrix}, \begin{bmatrix} I_a \\ I_b \\ I_c \end{bmatrix} = K \cdot I_{dc}$$
 (54)

$$K = \begin{bmatrix} D1 + D4 \\ D3 + D6 \\ D5 + D2 \end{bmatrix}$$
 (55)

Since the model assumes instantaneous commutation of the current from one diode to the next, there is only one diode conducting in the upper branch (1-3-5) and only one diode conducting

in the lower branch (4-6-2) at any given moment. This means that K always contains a 1, a -1 and a 0 element. The states of the diodes are calculated by comparing the instantaneous phase voltages of Va, Vb, Vc.

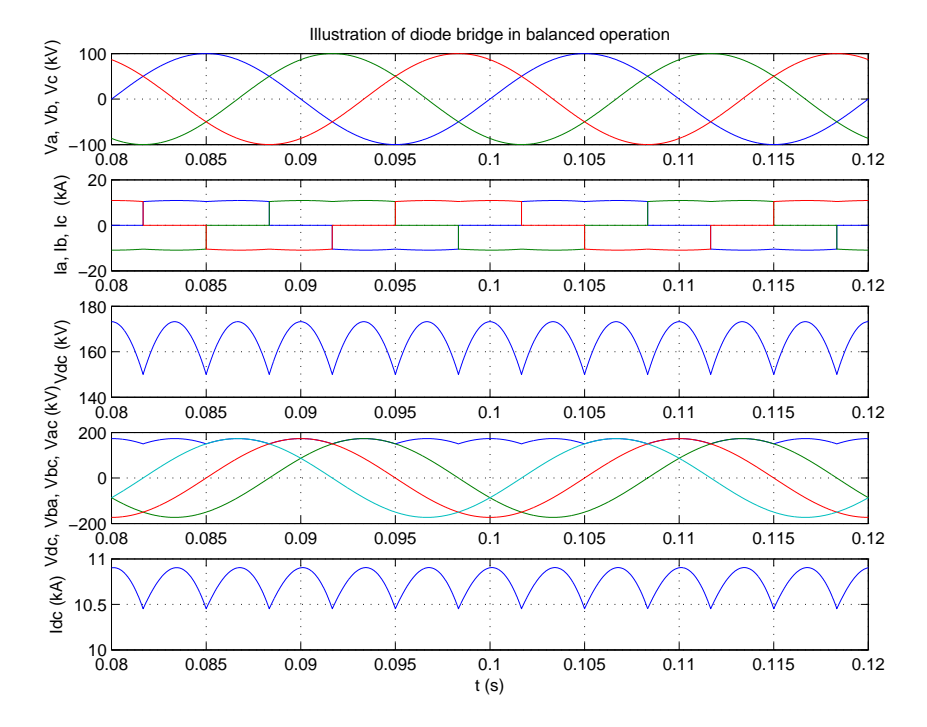


Figure 36: Diode bridge operation in balanced condition (Model Thy4a)

Figure 36 illustrates the operation of the diode bridge under balanced conditions. At any moment one diode in the upper branche conducts, resulting in a positive current in that phase (current into the DC link), and one diode in the lower branche conducts, resulting in a negative current in that phase (current out of the DC link). The DC voltage is always positive and follows the peaks in the line voltages (or minus their negative value). The AC currents are block shaped, with a small ripple superimposed. The DC current shows the same ripple, with six periods per period of the AC voltage, since it is a six-pulse model.

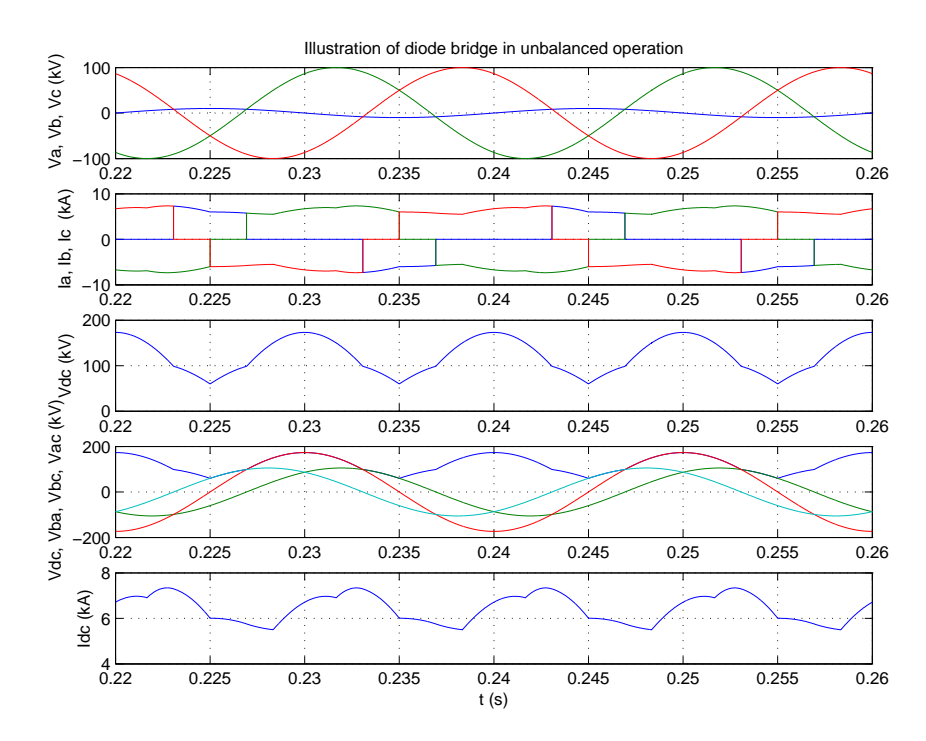


Figure 37: Diode bridge operation in unbalanced condition (Model Thy4a)

Figure 37 illustrates the operation of the diode bridge under unbalanced conditions. The voltage amplitude of phase a is 0.1 times the amplitude of the other two phases. This decreases the conduction period of phase a and results in a larger variation in the DC voltage. The DC current is smaller compared to the balanced case.

#### Implementation of Model Thy4a in Matlab/Simulink

The following figures illustrate the implementation of instantaneous diode bridge model in Matlab/Simulink.

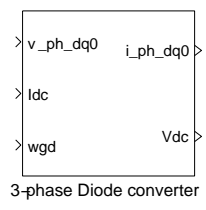


Figure 38: Top level of model of instantaneous diode bridge without commutation inductance (Model Thy4a)

At the top level of the diode bridge model, the inputs are the phase voltage in dq0-coordinates, the DC current  $I_{dc}$  and grid frequency  $\omega_{gd}$ . Outputs are phase currents in dq0-coordinates and the DC voltage  $V_{dc}$ . The input  $V_d$ ,  $V_q$ ,  $V_0$  are transformed to  $V_a$ ,  $V_b$ ,  $V_c$  using the inverse Park transformation and are then compared to each other to calculate the state matrix K:

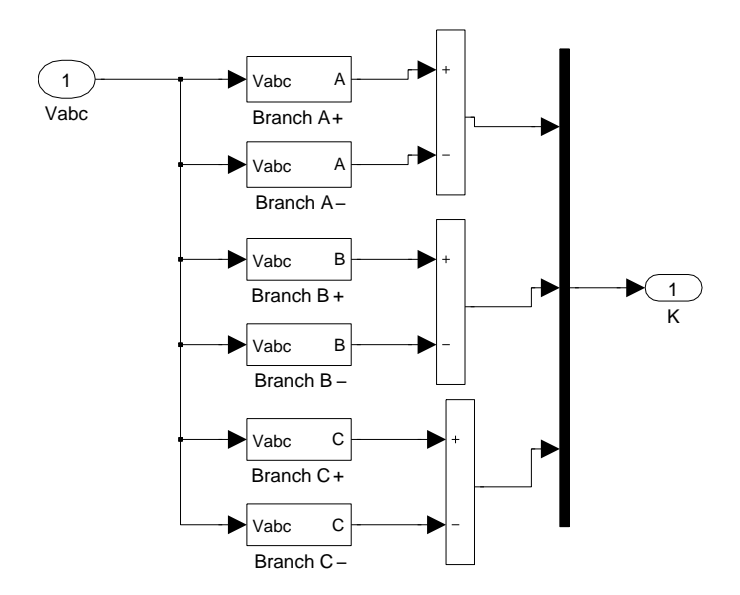


Figure 39: Model to calculate the state matrix K (Model Thy4a)

The diode logic of "Branch A+" (D1) is:

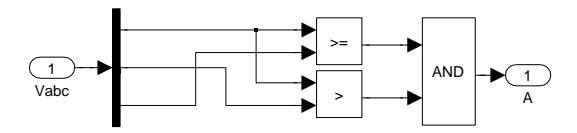


Figure 40: Model to calculate the state of a single diode (Model Thy4a)

After state matrix K is calculated, the DC Voltage  $V_{dc}$  and phase current  $I_a, I_b, I_c$  and  $I_d, I_q, I_0$  can be calculated:

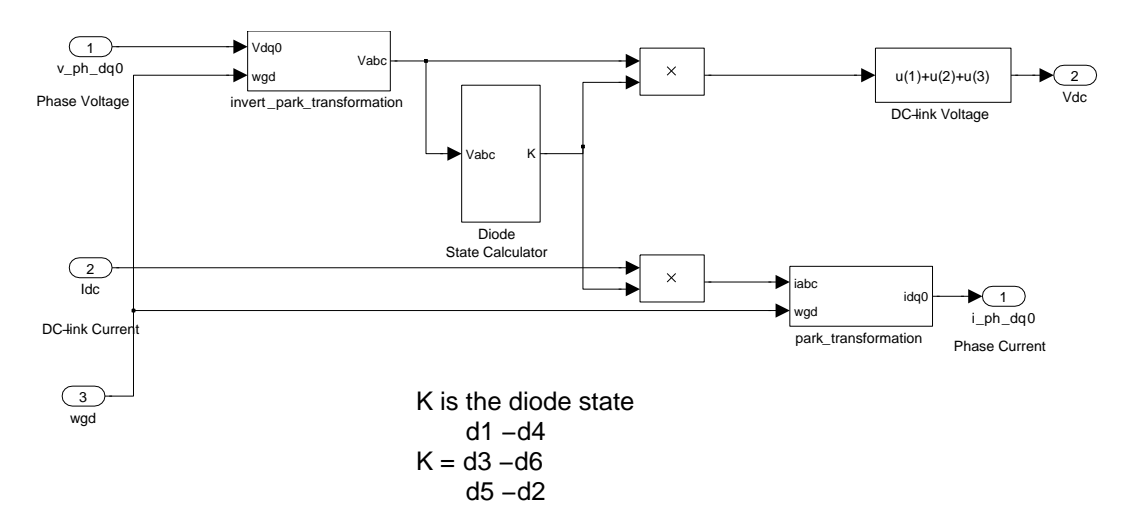


Figure 41: Overview of the diode bridge model (Model Thy4a)

Note that when calculating the state matrix, the "sum" block must be set that the type of output value is "double". The default setup of Simulink is "same as input". Because the input values

are "Boolean", it will not give "-1" when negative branch diodes (D4, D6, D2) are conducting, but will give "0" instead. This will generate an error in the state matrix K.

#### Simulation example (Model Thy4a)

The Simulink model of the diode bridge is tested by applying a voltage dip to the AC voltage of the diode bridge phase a at 0.15 s, see figure 42. The AC voltages, AC currents, DC voltage and DC current are shown.

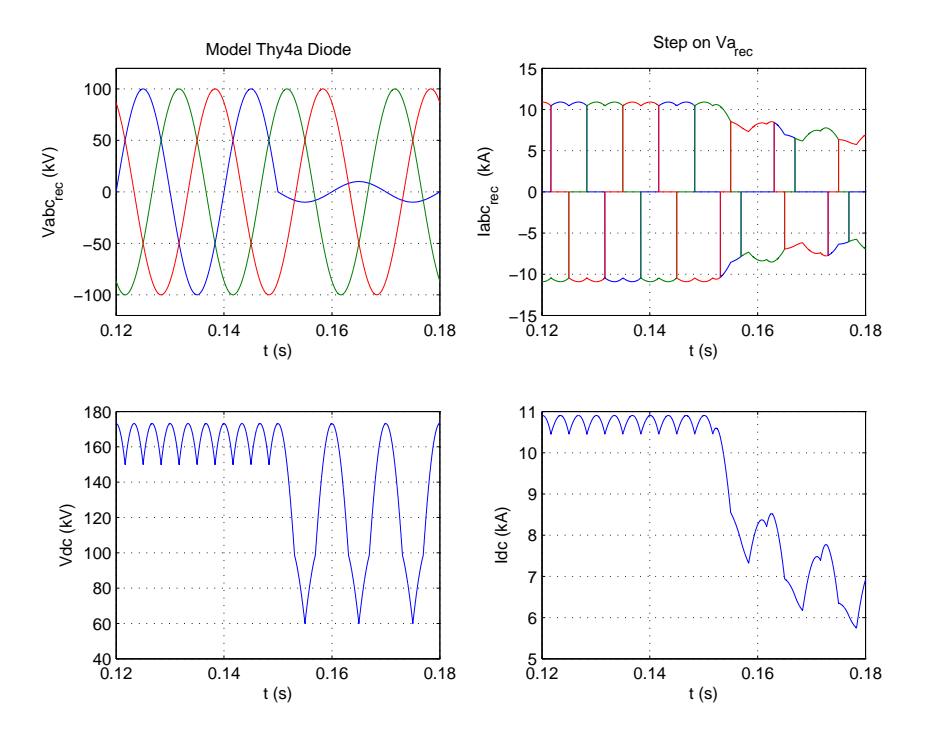


Figure 42: AC voltages, AC currents, DC voltage and DC current in diode model with step on voltage amplitude phase a (Model Thy4a)

# 3.5.2 Instantaneous thyristor bridge without commutation inductance (Model Thy4b)

The difference between the thyristor bridge and the diode bridge is the firing angle  $\alpha$  which controls the ignition of the thyristor. The thyristor stays blocked until it receives a firing pulse, then it compares the three phase voltages to see if the positive branch (T1, T3, T5) or the negative branch (T4, T6, T2) commutates. The method of using a state matrix K to calculate the DC voltage and the AC current is the same as in the diode bridge model, but the way to calculate the state matrix K is more complex. The instantaneous phase voltages  $V_a$ ,  $V_b$ ,  $V_c$  are compared and the integration of grid frequency over time  $\int \omega dt$  is compared to the firing angle  $\alpha$ .

#### Implementation of Model Thy4b in Matlab/Simulink

The inputs of the instantaneous thyristor bridge model without commutation inductance are the phase voltage in dq0-coordinates, the DC current Idc, the grid frequency  $\omega_{gd}$ , and firing angle  $\alpha$ . Outputs are DC voltage  $V_{dc}$  and phase currents in dq0-coordinates. The state matrix K is calculated first and then the DC voltage  $V_{dc}$  and phase current  $I_d$ ,  $I_q$ ,  $I_0$  are calculated using the state matrix.

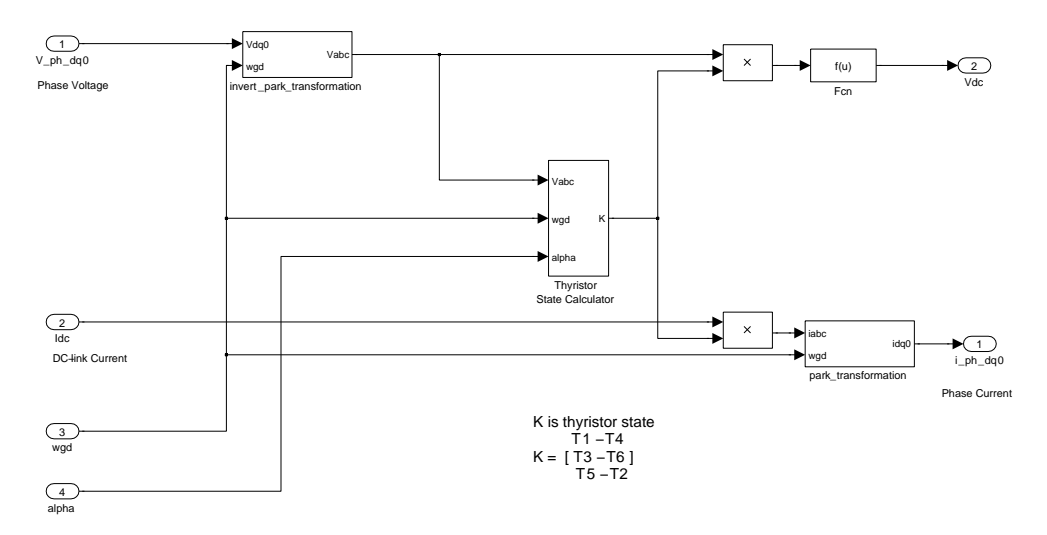


Figure 43: Model of the instantaneous thyristor bridge without commutation inductance  $(Model\ Thy4b)$ 

The thyristor state calculator is shown in the following figure:

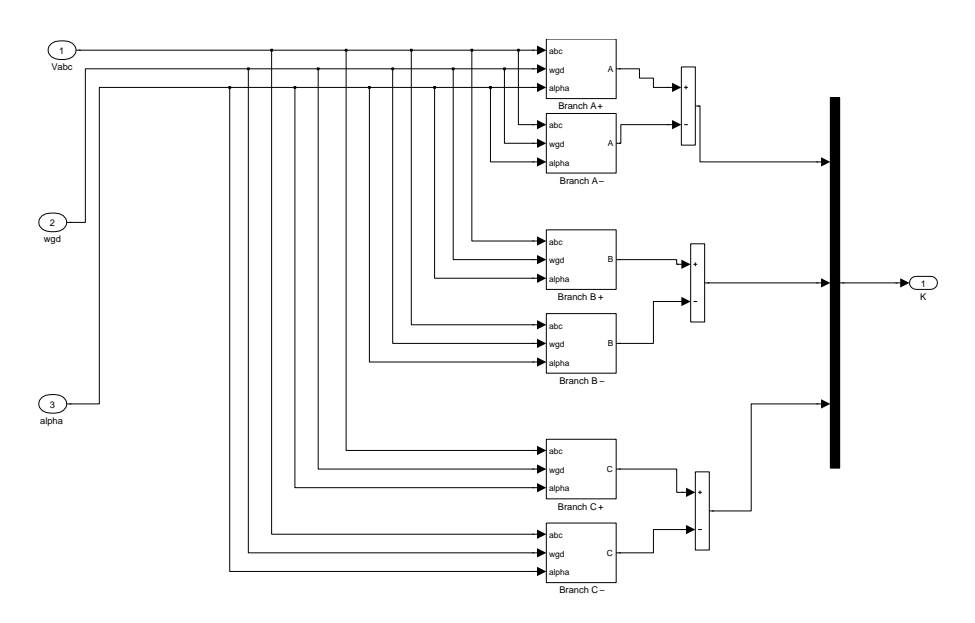


Figure 44: Model to calculate the state matrix (Model Thy4b)

The calculation of the state of branch A+ (thyristor T1):

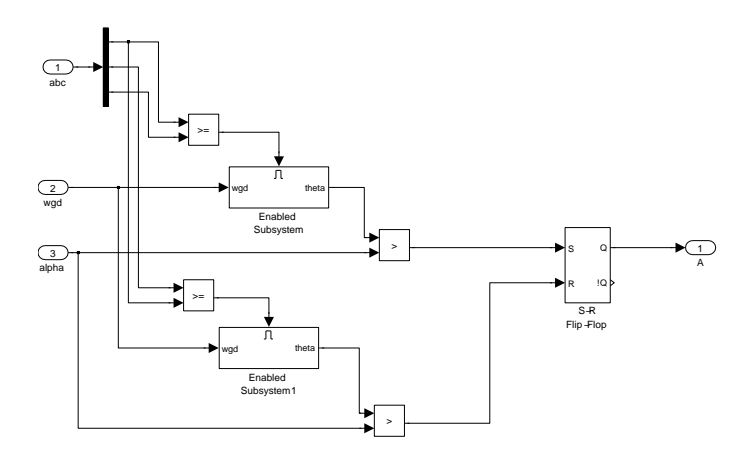


Figure 45: *Calculation of the state of thyristor 1 (branch A+) (Model Thy4b)* 

When  $V_a \geq V_c$ , a subsystem is enabled to integrate the grid frequency  $\omega$  from that time on. This value is then compared to the firing angle  $\alpha$ . If the integration result is larger than  $\alpha$ , thyristor T1 begins to conduct. T1 will stop conducting when T3 begins to conduct. A setreset flip-flop is used to calculate the correct conduction period of thyristor T1. Without the flip-flop, the logic is only correct in rectifier mode, the firing angle  $\alpha$  cannot be larger than 90 degree because the enabled subsystem will reset  $\int \omega \ dt$  to 0 when  $V_a > V_c$ . With the flip-flop, the thyristor logic is also correct in inverter mode. The model can also be used as a diode bridge if the firing angle is set to 0.

#### Simulation example (Model Thy4b)

The Simulink model of the instantaneous thyristor bridge without commutation inductance is tested in two simulations. First a voltage dip is applied to the AC voltage of rectifier phase a at 0.15 s, see figure 46. The AC voltages, AC currents, DC voltage and DC current are shown.

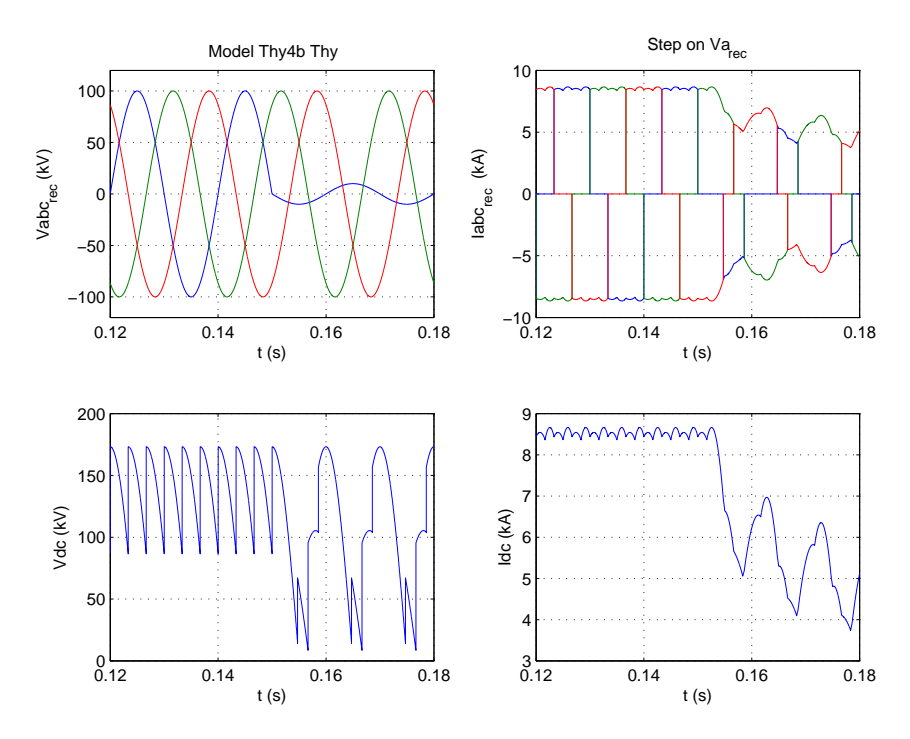


Figure 46: AC voltages, AC currents, DC voltage and DC current in the instantaneous rectifier model without commutation inductance for step on voltage amplitude phase a ( $\alpha_{rect}=30^{\circ}$ )

In the second simulation, the same voltage dip is applied to the AC voltage of inverter phase a at 0.15 s, see figure 47.

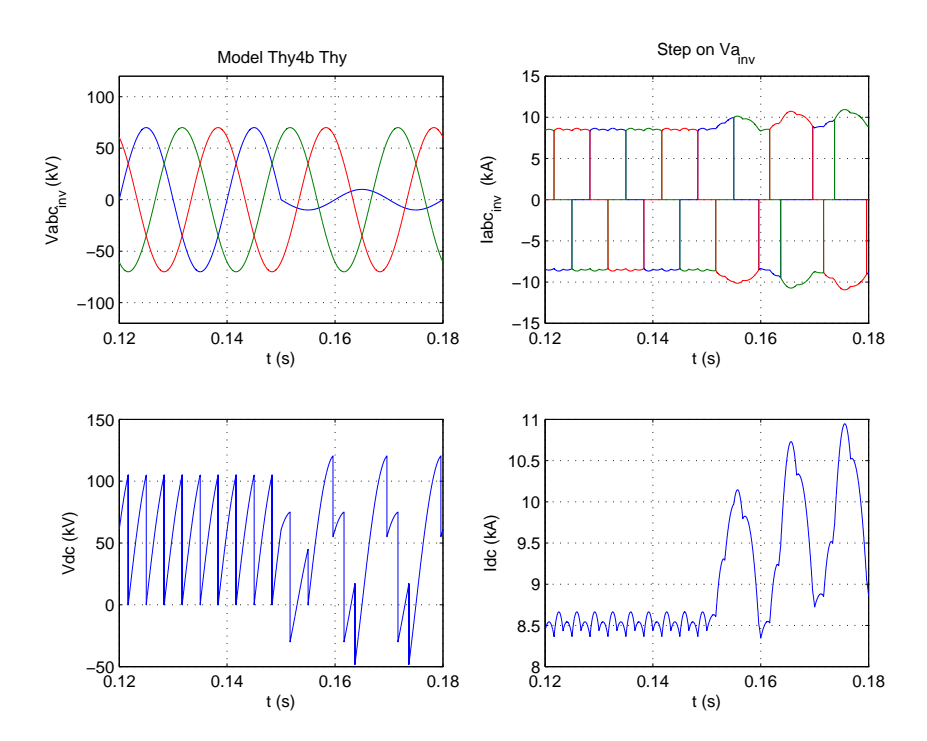


Figure 47: AC voltages, AC currents, DC voltage and DC current in the instantaneous inverter model without commutation inductance for step on voltage amplitude phase a ( $\alpha_{inv} = 150^{\circ}$ )

# 3.5.3 Instantaneous thyristor bridge with commutation inductance (Model Thy5)

Omitting the commutation inductance can cause large errors when the thyristor bridge is not working at normal operating points, for example during a grid voltage dip. Furthermore, if the inductance connected to the thyristor bridge is large, then omitting the commutation inductance may cause numerical instability, because the AC current through the inductor cannot change instantaneously while the output AC current of thyristor bridge is a square wave which changes instantaneously at the time of switch-on and switch-off. Therefore, the instantaneous thyristor bridge model with commutation inductance is developed. The new aspects of the model with commutation inductance are:

- the AC currents are trapezoidal, the increasing and decreasing slopes are determined by the AC line to line voltage and the commutation inductance;
- the switching function of each thyristor includes two additional states: switch-on, and switch-off;
- the switching function for current is not the same as for the voltage.

#### Implementation of Model Thy5 in Matlab/Simulink

The inputs and outputs of the instantaneous thyristor rectifier model with commutation inductance are the same for the model without commutation inductance.

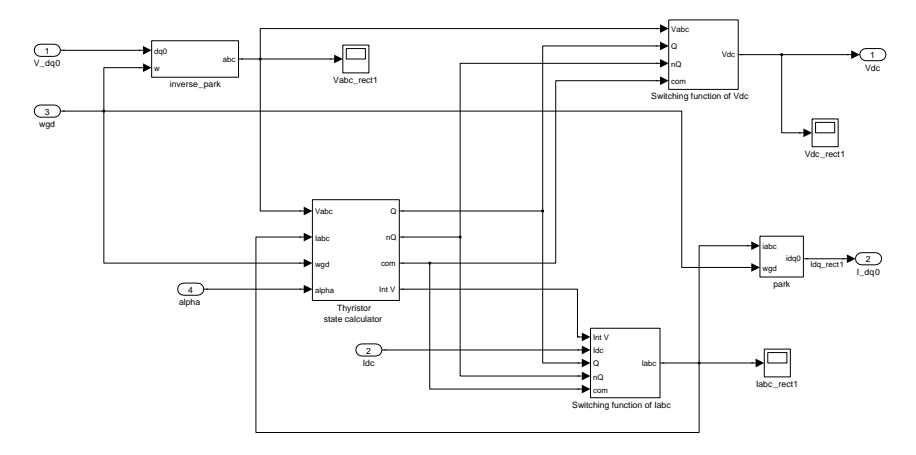


Figure 48: Instantaneous thyristor rectifier model with commutation inductance (Model Thy5)

The switch-off of a thyristor is not determined by the switch-on of the next thyristor but by the decrease of its own current to zero. Now each thyristor has four states: blocked, switch-on, conducting, and switch-off. This makes the model to calculate the state matrix of the thyristor converter complex.

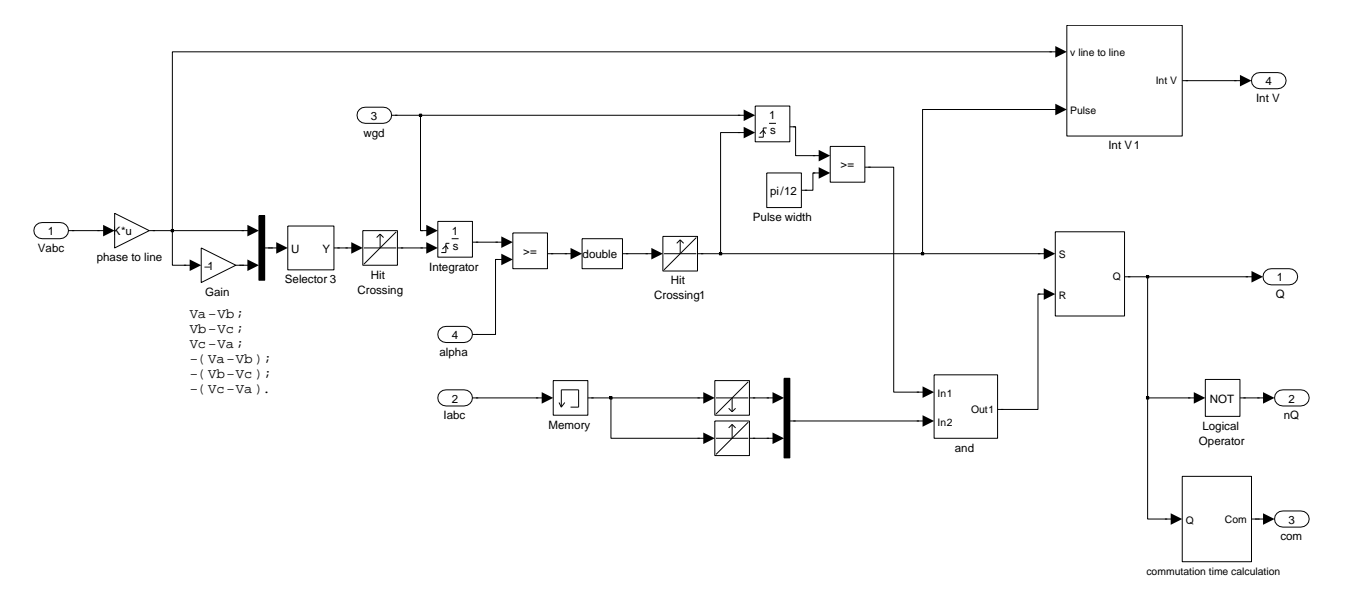


Figure 49: State calculation in the instantaneous rectifier model with commutation inductance (Model Thy5)

Figures 49 to 52 show the main model blocks of the instantaneous thyristor rectifier model with commutation inductance.

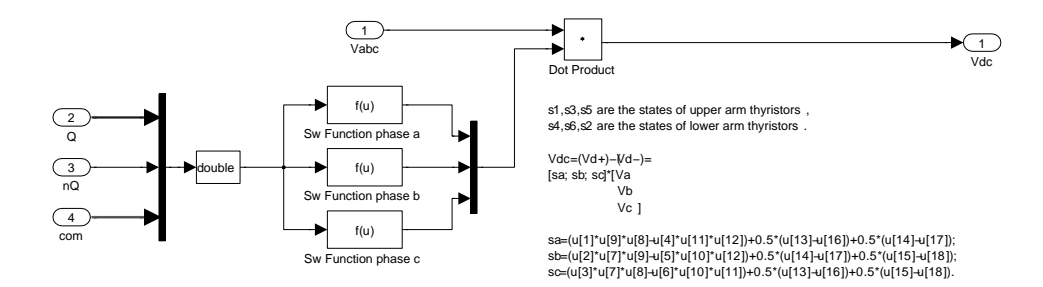


Figure 50: *DC voltage calculation of the instantaneous rectifier model with commutation inductance (Model Thy5)* 

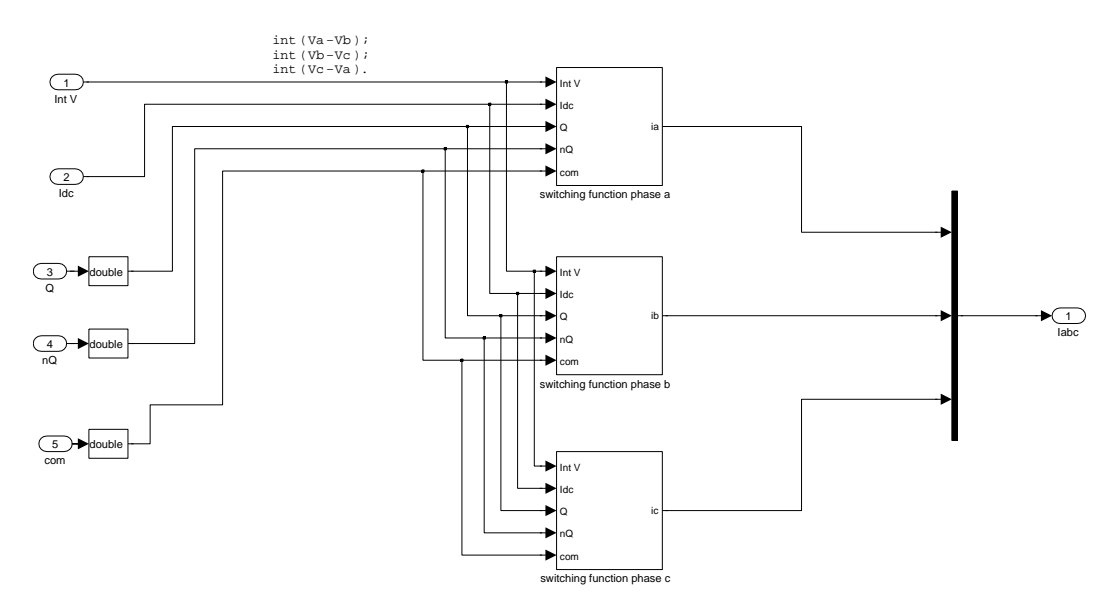


Figure 51: Three phase currents from switching functions in the instantaneous rectifier model with commutation inductance (Model Thy5)

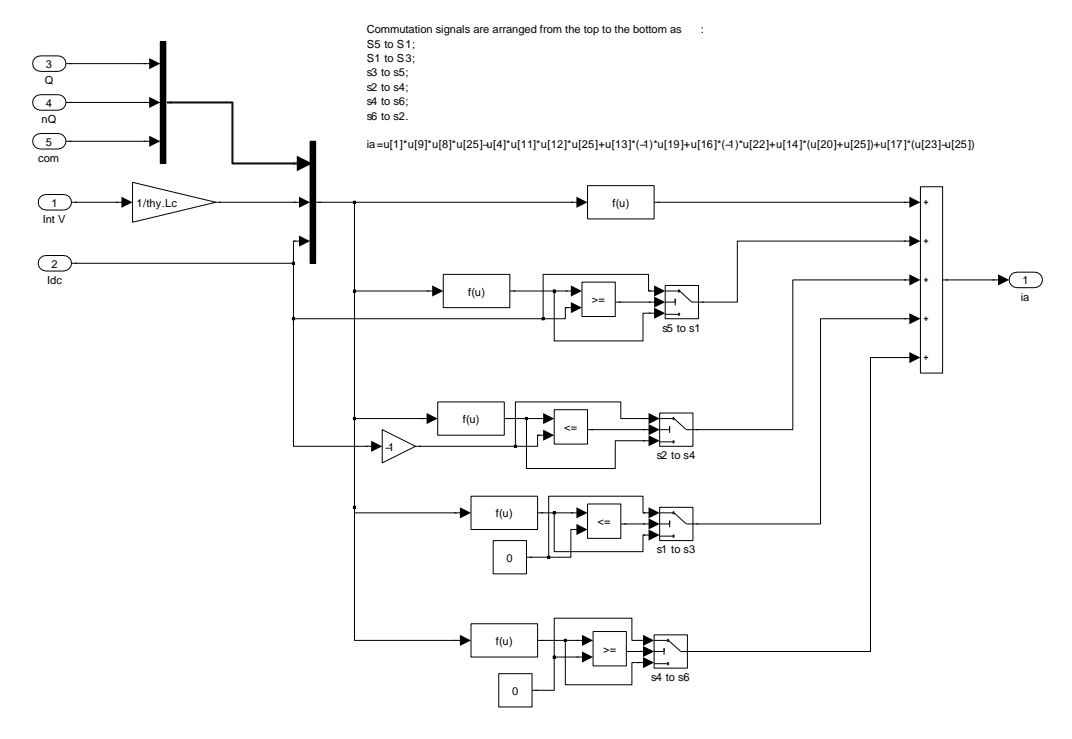


Figure 52: Switching function of phase a in the instantaneous rectifier model with commutation inductance (Model Thy5)

## Simulation example Model Thy5

The model of the instantaneous thyristor bridge with commutation inductance is tested in two simulations. First a voltage dip is applied to the AC voltage of rectifier phase a at 0.15 s, see figure 53. The AC voltages, AC currents, DC voltage and DC current are shown.

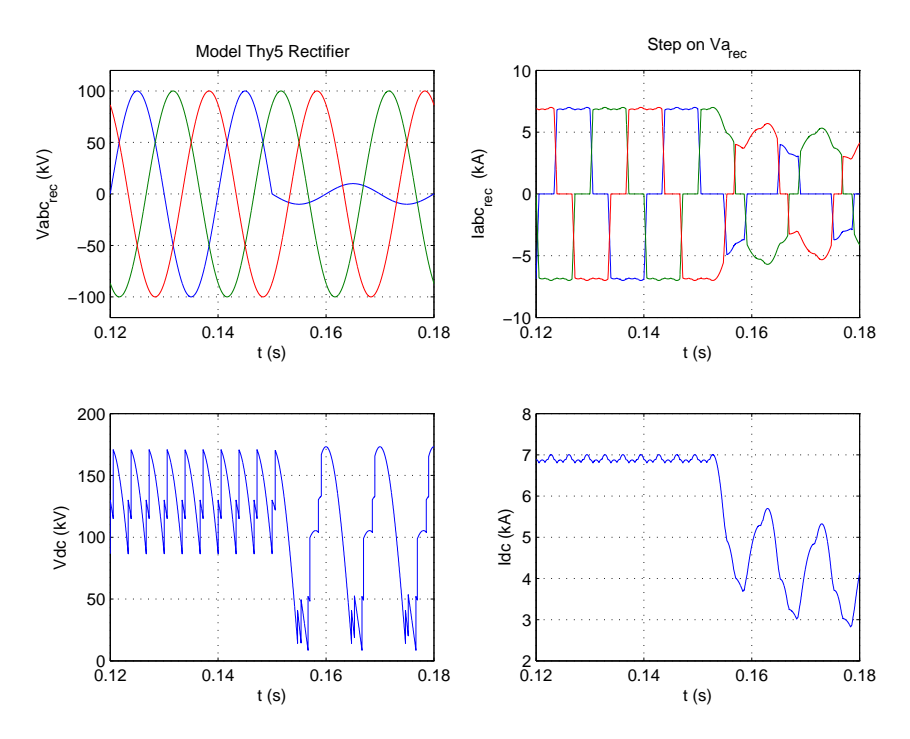


Figure 53: AC voltages, AC currents, DC voltage and DC current waveform in rectifier model with step on voltage amplitude phase a ( $\alpha=30^{\circ}$ )

In the second simulation, the same voltage dip is applied to the AC voltage of inverter phase a at  $0.15~\rm s$ :

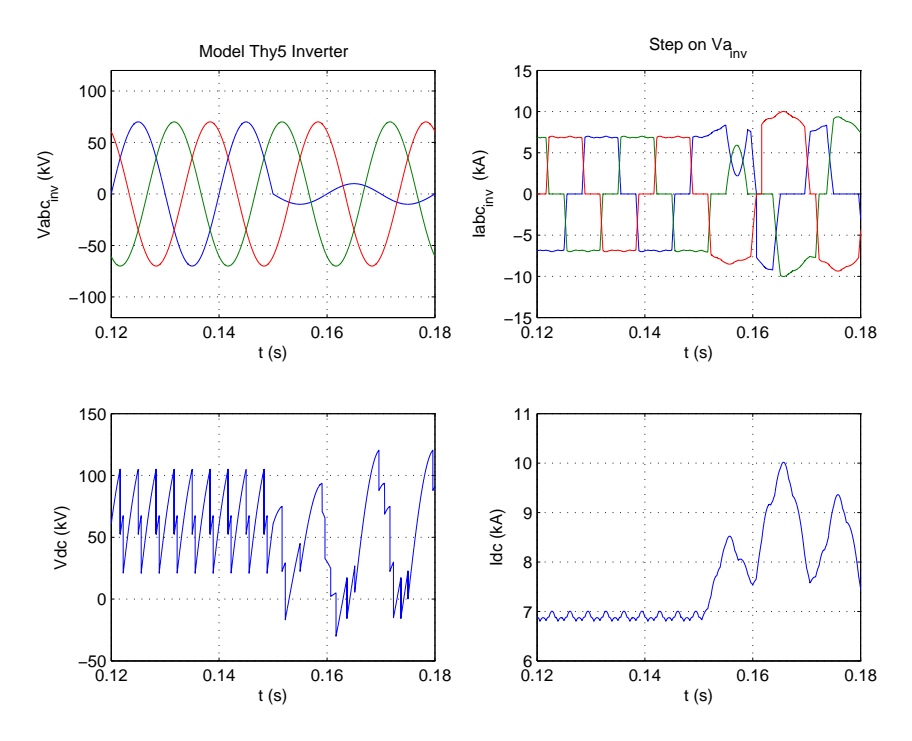


Figure 54: AC voltages, AC currents, DC voltage and DC current waveform in inverter model with step on voltage amplitude phase a ( $\alpha=150^{\circ}$ )

Details from the previous two simulations are shown in the next figures.

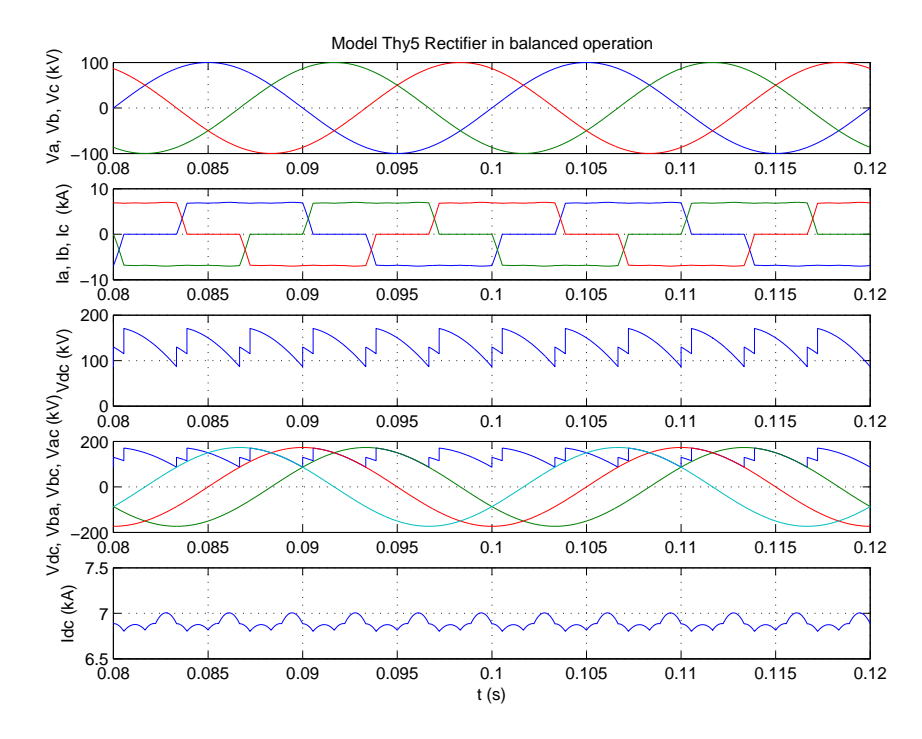


Figure 55: AC voltages, AC currents, DC voltage and DC current in the rectifier model in balanced operation ( $\alpha=30^{\circ}$ )

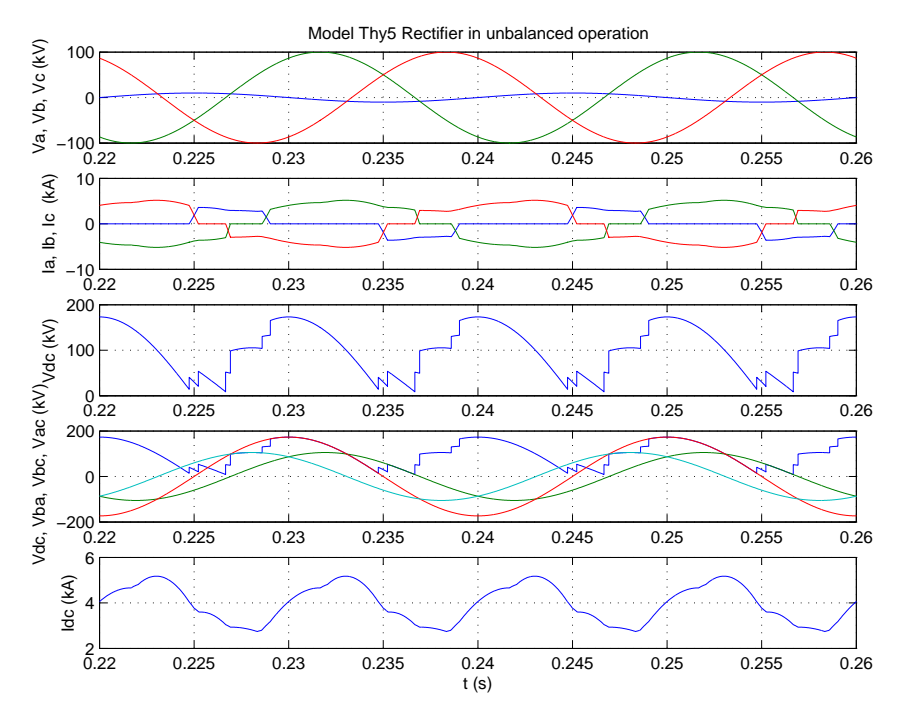


Figure 56: AC voltages, AC currents, DC voltage and DC current in the inverter model in unbalanced operation ( $\alpha=30^\circ$ )

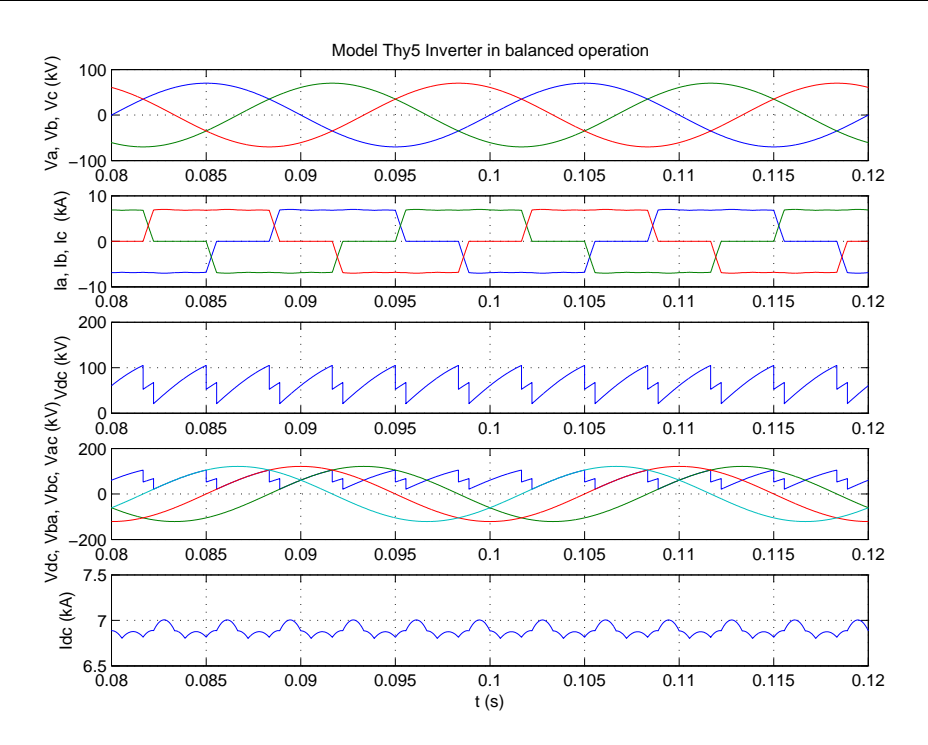


Figure 57: AC voltages, AC currents, DC voltage and DC current in the inverter model in balanced operation ( $\alpha=150^{\circ}$ )

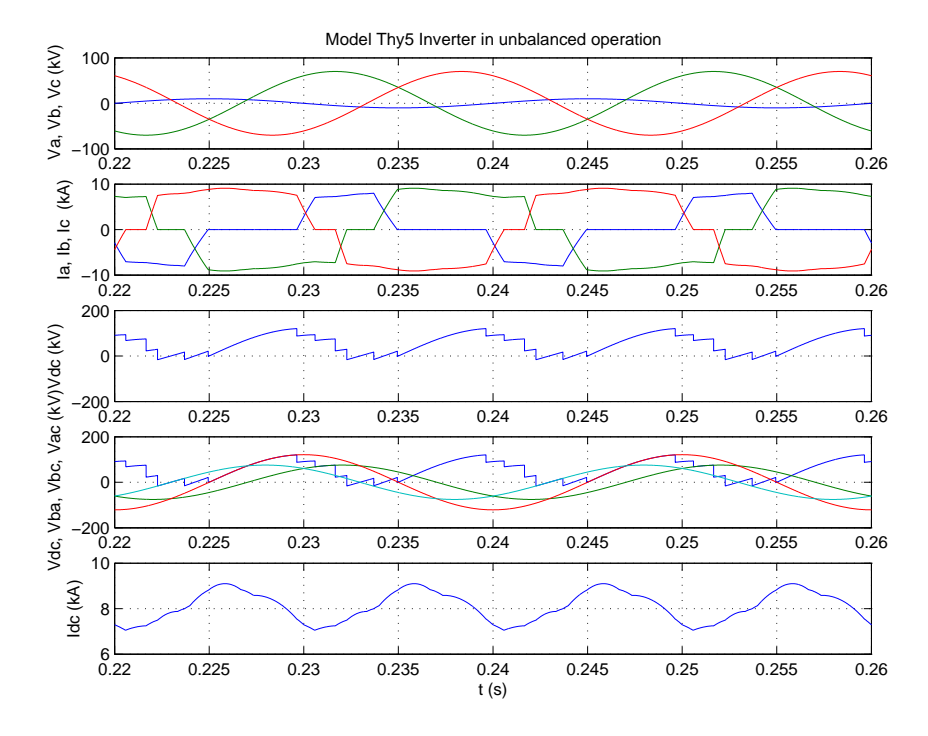


Figure 58: AC voltages, AC currents, DC voltage and DC current in the inverter model in unbalanced operation ( $\alpha=150^\circ$ )

# 3.6 Thyristor bridge models summary

The following models have been developed:

- Thy1 average quasi steady state model for commutation balanced conditions
- Thy2 average quasi steady state with commutation for unbalanced conditions, based on Fourier analysis
- Thy3 average quasi steady state with commutation for unbalanced partially symmetrical conditions
- Thy4a instantaneous, diode bridge without commutation for unbalanced conditions
- Thy4b instantaneous, thyristor bridge without commutation for unbalanced conditions
- Thy5 instantaneous, thyristor bridge with commutation for unbalanced conditions

The advantages of the average quasi steady-state Thyristor bridge models Thy1, Thy2 and Thy3 are:

- simple structure and fast calculation;
- the commutation inductance is considered.

#### Disadvantages are:

- Model Thy1 can only be applied to balanced conditions;
- Model Thy2 includes a time delay of half a cycle of the AC voltage;
- Model Thy3 can only be used if the conditions for which is was derived apply (two phases have equal RMS voltage and equal voltage phase angles).

The advantage of the instantaneous models Thy4a, Thy4b and Thy5 is:

suitable for both balanced and unbalanced three phase system.

#### Disadvantages are:

- the calculation speed is slow because instantaneous phase voltages are compared and  $\int \omega dt$  is compared to the firing angle  $\alpha$  (model Thy4b and Thy5);
- the calculation is even more complex and the simulation speed is very slow when the commutation inductance is included (model Thy5).

# 3.7 Verification of the thyristor bridge models

The five thyristor bridge models are verified by comparing the results to a simulation with the thyristor bridge model in the Power System Blockset of Simulink. The Blockset has been developed by Hydro Quebec and is used by a number of power system operators [29]. The thyristor bridge model in the Blockset is an instantaneous model. The five models developed in this project are compared to the model in Power System BlockSet in back-to-back configuration, see figure 59.

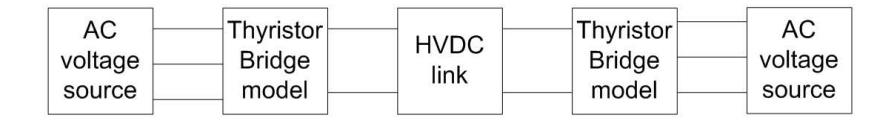


Figure 59: Back to back configuration for verification

Two sets of simulations are carried out. Simulation 1 is executed for all five models to compare the results under balanced conditions. Simulation 2 is executed for all models except model Thy1. It is used to compare the results under unbalanced conditions. The parameters in both simulations are the same:

Parameters		
Rectifier side AC voltages	1e5 V	
Rectifier firing angle	30°	
Inverter side AC voltages	0.7e5 V	
Inverter firing angle	120°	
AC inductance	0.01 H	
DC resistance	10 Ω	
DC inductance	0.1 H	

Events		
Simulation 1	Fire angle of rectifier changes from 30° to 45° at 1.0s.	
Simulation 2	Inverter side phase-a voltage decreases from 0.7e5 to 0.5e5 V at 1.0s.	

#### 3.7.1 Verifi cation for balanced conditions

The following figures compare the results of models Thy1, Thy2, Thy3, Thy4b, Thy5 and PSB for balanced conditions and a step in rectifier firing angle.

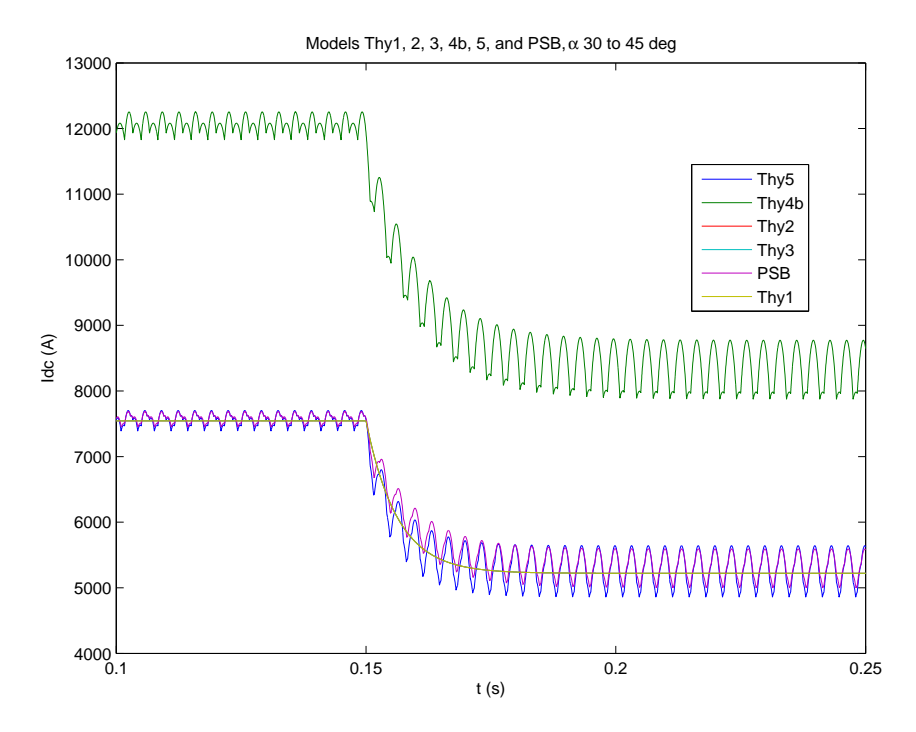


Figure 60: DC currents of models Thy1, Thy2, Thy3, Thy4b, Thy5 and PSB (step in rectifier firing angle)

Figure 60 shows the DC currents. Model Thy4b neglects the commutation inductance and this causes an error in the DC current, especially when the AC line inductance is large. Figure 61 zooms in on the currents during the transient, the DC currents of the quasi-steady models Thy1, Thy2 and Thy3 are average values and are equal. The small differences between the DC current of the PSB model and model Thy5 are caused by the assumption used in model Thy5 that the DC voltage outside the commutation periods is  $V_{dc} = v_i - v_j$ . The average DC currents of model Thy5 and PSB are almost the same, and equal to the DC currents of models Thy1, Thy2 and Thy3, so the active power transferred by the thyristor bridges of all the models

except model Thy4b is the same. This shows that models Thy1, Thy2, Thy3, and Thy5 are accurate enough for electromechanical simulations.

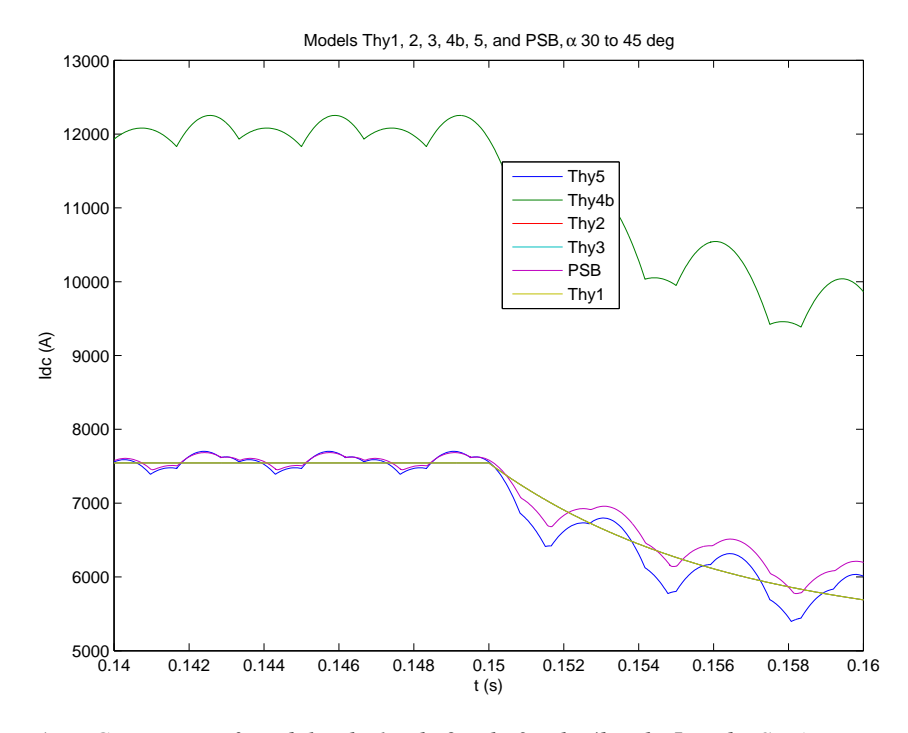


Figure 61: DC currents of models Thy1, Thy2, Thy3, Thy4b, Thy5 and PSB (step in rectifier firing angle, detail)

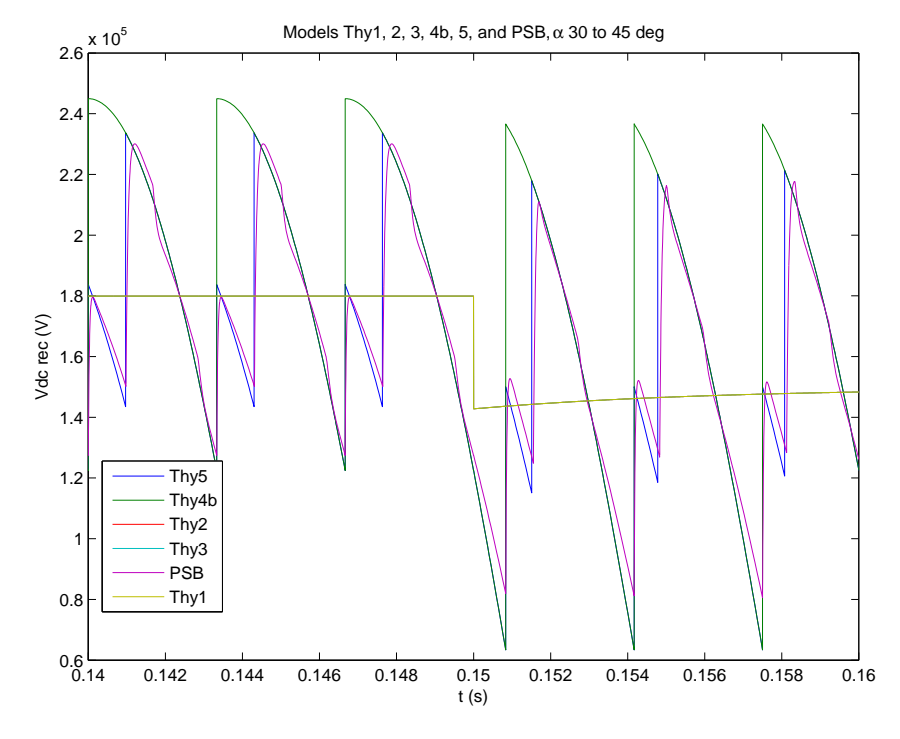


Figure 62: DC voltage at rectifier of models Thy1, Thy2, Thy3, Thy4b, Thy5 and PSB (step in rectifier firing angle)

Figure 62 shows the DC voltages. The DC voltages of quasi-steady models Thy1, Thy2, Thy3 are average values and are equal. The DC voltage of models Thy4b and Thy5 differs during the commutation interval. The differences between the DC voltage in the PSB and Thy5 model are small.

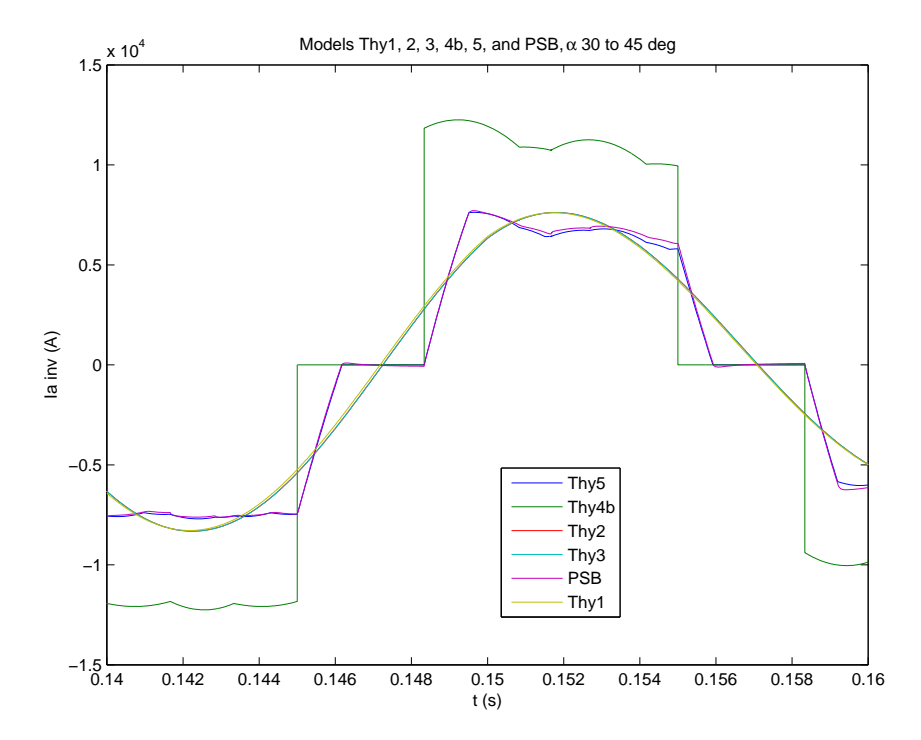


Figure 63: AC inverter currents of models Thy1, Thy2, Thy3, Thy4b, Thy5 and PSB (step in rectifier firing angle)

Figure 63 gives the AC current of phase A of the inverter during one period of the phase voltage at the moment of the step in rectifier firing angle. The RMS values of all models are practically equal, except for the model without commutation (Thy4b).

#### 3.7.2 Verifi cations for unbalanced conditions

In the second simulation, the results of model Thy2, Thy3, Thy4b and Thy5 are compared to the results of the PSB model for unbalanced conditions and a step in AC voltage at the inverter.

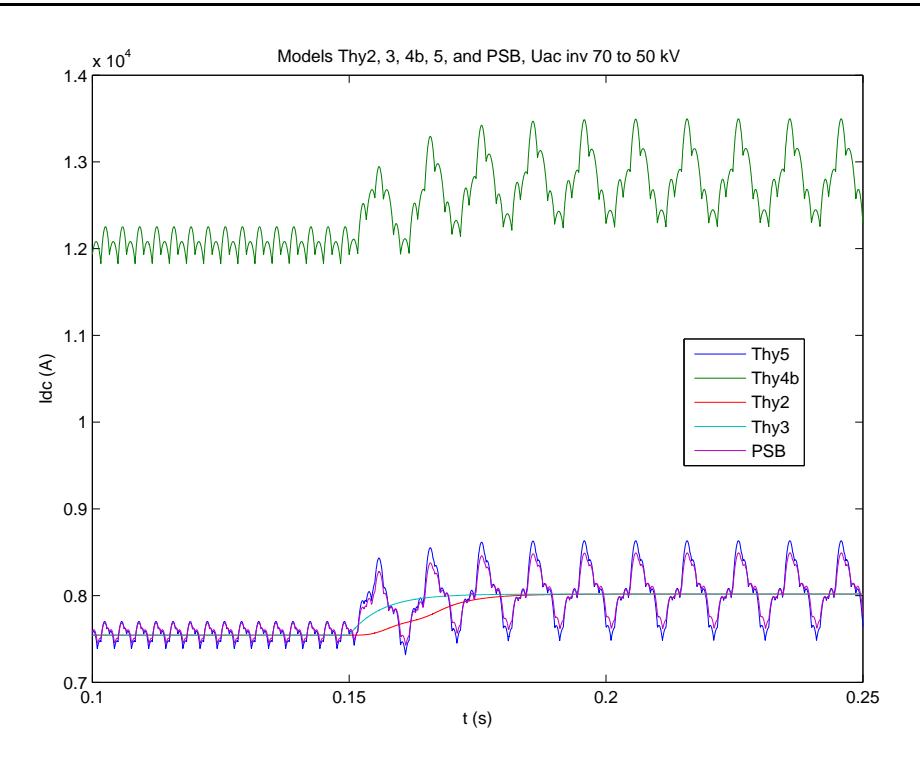


Figure 64: DC currents of models Thy2, Thy3, Thy4b, Thy5 and PSB during a single phase step in AC inverter voltage (simu 2)

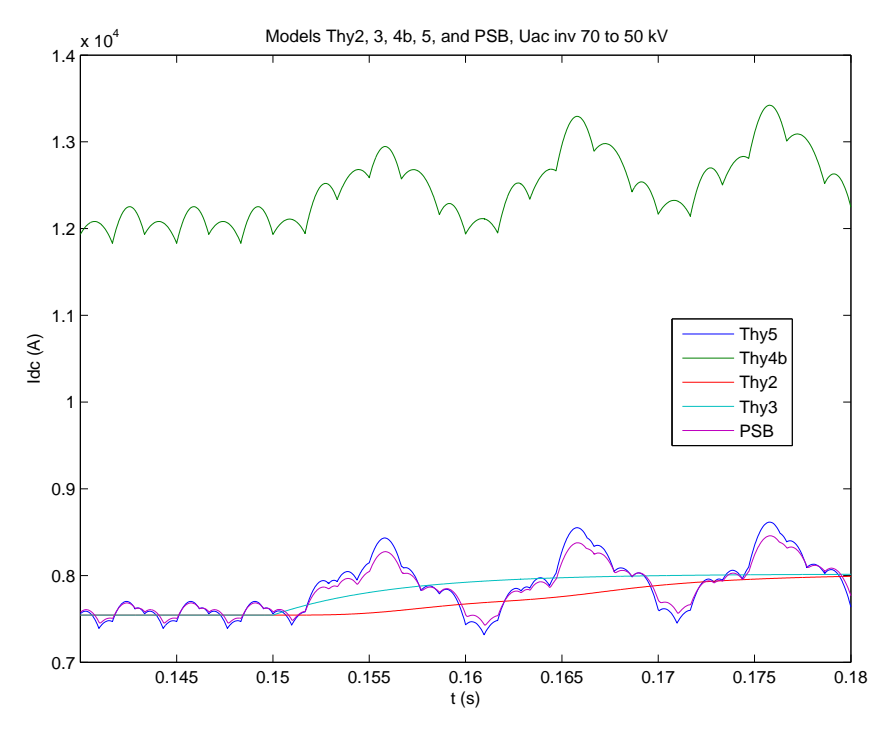


Figure 65: DC currents of models Thy2, Thy3, Thy4b, Thy5 and PSB during a single phase step in AC inverter voltage (simu 2)

As in the previous simulation, figure 64 shows that the DC current of model Thy4b has a

large error because the commutation inductance is omited. Due to the Fourier analysis, the DC current of model Thy2 lags model Thy3 around one cycle (0.1 second) until the steady state value is reached, figure 65. The DC current of model Thy5 differs only slightly when compared to the PSB result.

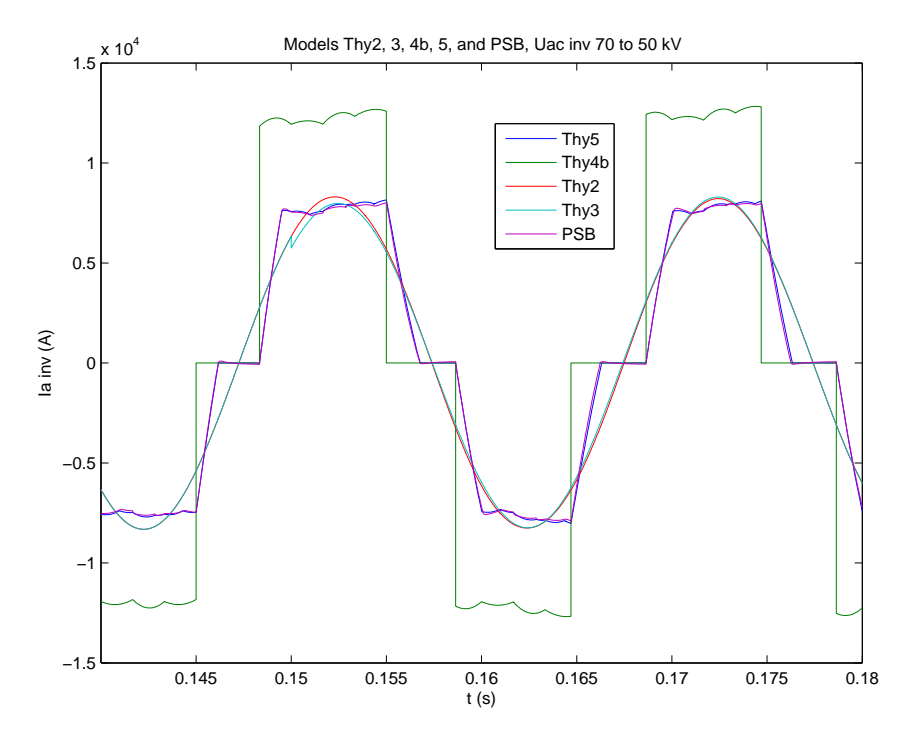


Figure 66: AC current of phase a in model Thy2, Thy3, Thy4b, Thy5 and PSB during a single phase step in AC inverter voltage (simu 2)

In figure 66, the two sinusoidal waveforms are the inverter phase currents of model Thy2 and Thy3, the two trapezoidal waveforms are those of model Thy5 and PSB. Model Thy 4b has a square waveform and the amplitude is higher. It is clear that the phase currents have nearly the same phase angles and RMS values, except for model Thy4, and that the instantaneous models contain high order harmonics.

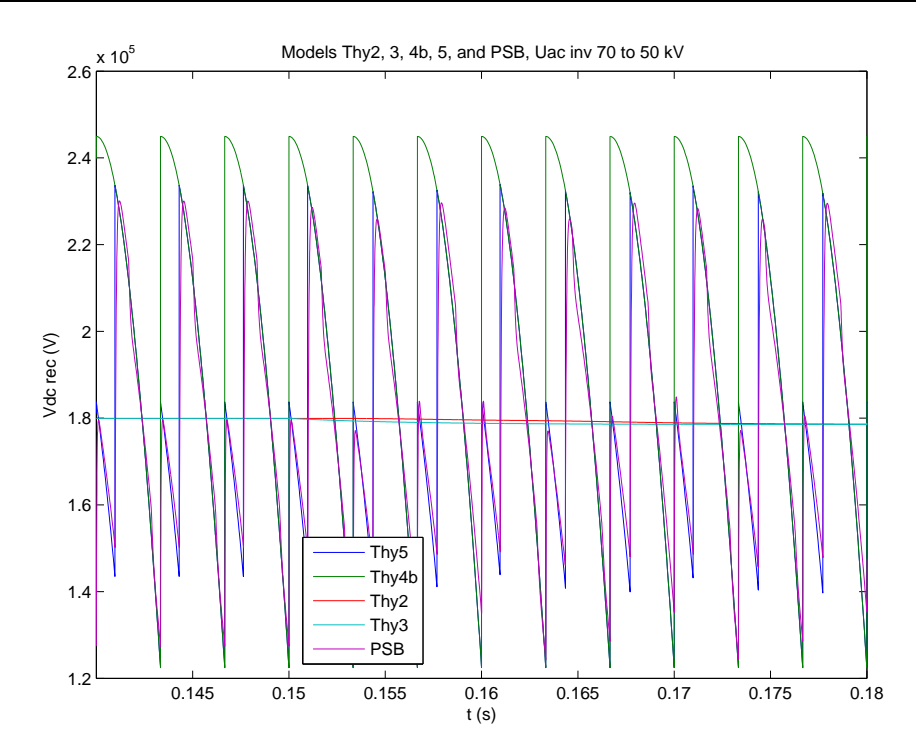


Figure 67: DC voltage in model Thy2, Thy3, Thy4b, Thy5 and PSB during a single phase step in AC inverter voltage (simu 2)

Figure 67 compares the DC voltages of model Thy2, Thy3, Thy4b, Thy5 and PSB under unbalanced situations. As in the balanced case the PSB DC voltage is on average higher.

The results shows that model Thy5 is accurate. Model Thy3 is accurate if the two assumptions of that model can be fulfilled. Model Thy2 is accurate in steady state, but has significant errors during transient state. The elapsed time for simulating three seconds for the models are compared in the next table:

Model name	Required simulation time
Model 1	1 second
Model 2	4 second
Model 3	3 second
Model 4	8 second
Model 5	40 second
PSB	220 second

All developed the models are faster than the thyristor bridge model in the Power System Block-Set. Model Thy5, the instantaneous model with commutation inductance is the slowest of the developed models, but still more than a factor 5 faster than the Power System Blockset model.

#### 3.8 Conclusion and recommendation

Five thyristor bridge models have been developed in Matlab/Simulink:

- (i) a symmetrical quasi-steady state model,
- (ii) an unsymmetrical quasi-steady state model using Fourier analysis,
- (iii) an unsymmetrical quasi-steady state model assuming partially symmetrical conditions,
- (iv) an instantaneous model without commutation inductance,

(v) an instantaneous model with commutation inductance.

The developed thyristor bridge models have been compared to the thyristor bridge model of the Simulink Power System Blockset:

- The symmetrical quasi-steady state model is accurate for both steady state and transient state under balanced situation.
- The unsymmetrical quasi-steady state model using Fourier analysis is accurate for steady state, but has significant errors during transient state because of the delay caused by the Fourier analysis method.
- The unsymmetrical quasi-steady state model assuming partially symmetrical conditions is accurate for both steady state and transient state, but only if the assumptions can be fulfilled.
- The instantaneous model without commutation inductance can have significant errors if the AC commutation inductance or DC current is very large.
- The instantaneous model with commutation inductance is accurate for both steady state and transient state, balanced and unbalanced situations but requires more simulation time.

All the five developed models are faster than Power System Blockset model. The instantaneous model with commutation inductance is the slowest of the five developed models because it has the most complex switching function.

#### Recommendations

- (i) Simplification of the switching functions of the instantaneous model with commutation inductance to improve simulation speed.
- (ii) Application of a phasor estimation in the unsymmetrical quasi-steady state models. Phasor estimation is widely used in power system protection. It estimates phasor values from two or more groups of instantaneous values. Thus the accuracy of unsymmetrical quasi-steady state model can be improved during transient states.

# 4 Models of wind farms with constant speed stall turbines (CSS)

This chapter describes the new system models based on the constant speed turbine. This starts with the layout and control characteristics of each system, followed by an overview of the implementation in Simulink and the demonstation of the model for normal operation (a wind gust from 5 to 25 m/s and back again).

# 4.1 Wind farm with a CSS-IG-dc electric system (# 1)

## 4.1.1 CSS-IG-dc layout and control

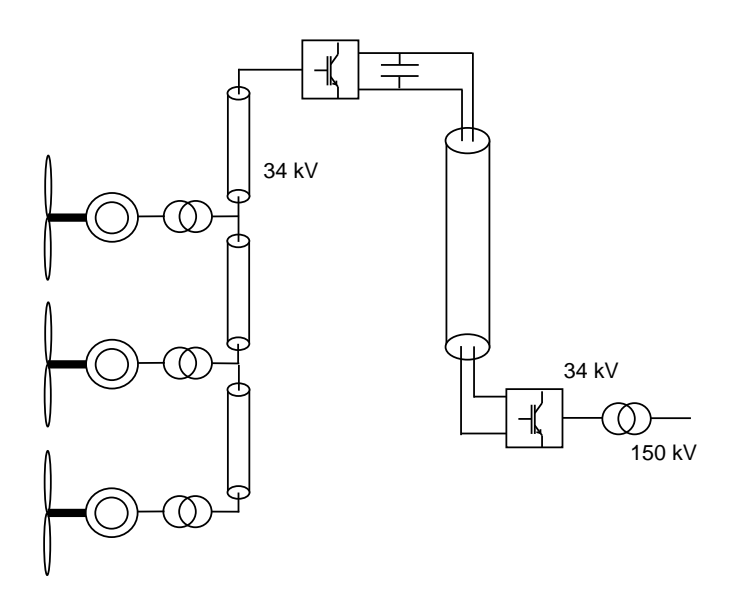


Figure 68: Constant speed stall WF with DC connection to shore (CSS-IG-dc)

The CSS-IG-dc system is a modification of the CSS-IG-ac system of Erao-2: the ac cable connecting the wind farm to the transformer in the substation on land is exchanged for a rectifier, a DC cable and an inverter. Figure 68 gives the layout of the CSS-IG-dc system used to demonstrate the model.

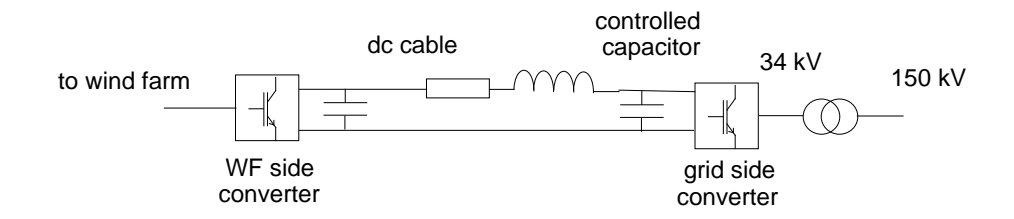


Figure 69: DC cable and converters of the connection to shore

For the DC voltage 39 kV was chosen, the converters operate between 34 kVac and 39 kVdc. The DC cable model is a CRLC-model, with a controlled capacitor at the DC side of the inverter (see figure 69). Since the cable parameter database did not include a suitable DC cable for this connection, the parameters of the 34 kV AC cable are used.

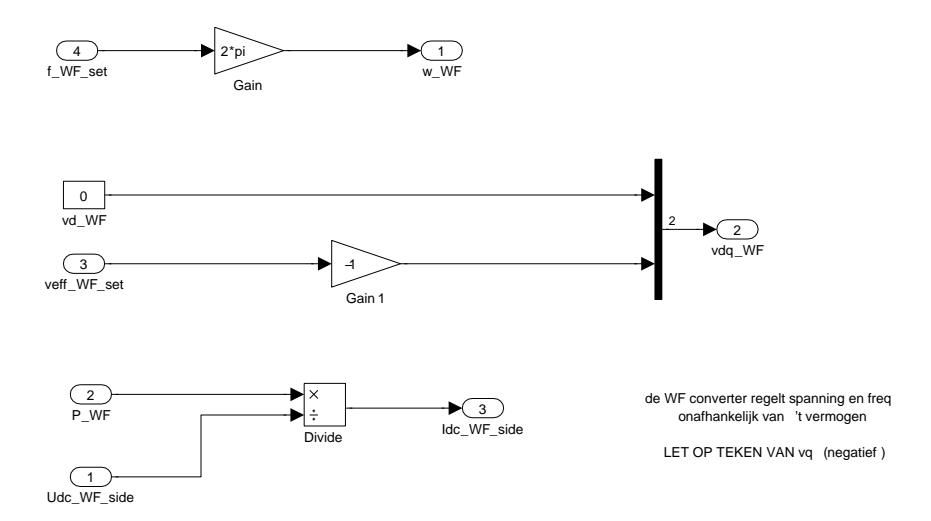


Figure 70: Control of the WF side converter of the CSS-IG-dc system

Figure 70 gives the control of the rectifier in the CSS-IG-dc system. The wind farm control strategy is simple. The frequency and the d- and q-voltage generated by the rectifier are constant (50 Hz, 0 and -34 kV). The turbines of the CSS-IG-dc system will run at constant speed. The turbine behaviour will be similar to an ac-connected wind farm, with the exception of the dynamic behaviour during grid faults. During a voltage dip, the system response is similar to the variable speed system response.

Figure 71 shows the implementation in Simulink. A description of most of the component models in the CSS-DC model can be found in the Erao-2 report [33, 34], only the DC cable model is new, see figure 72 and the converter and DC-link models have been updated.

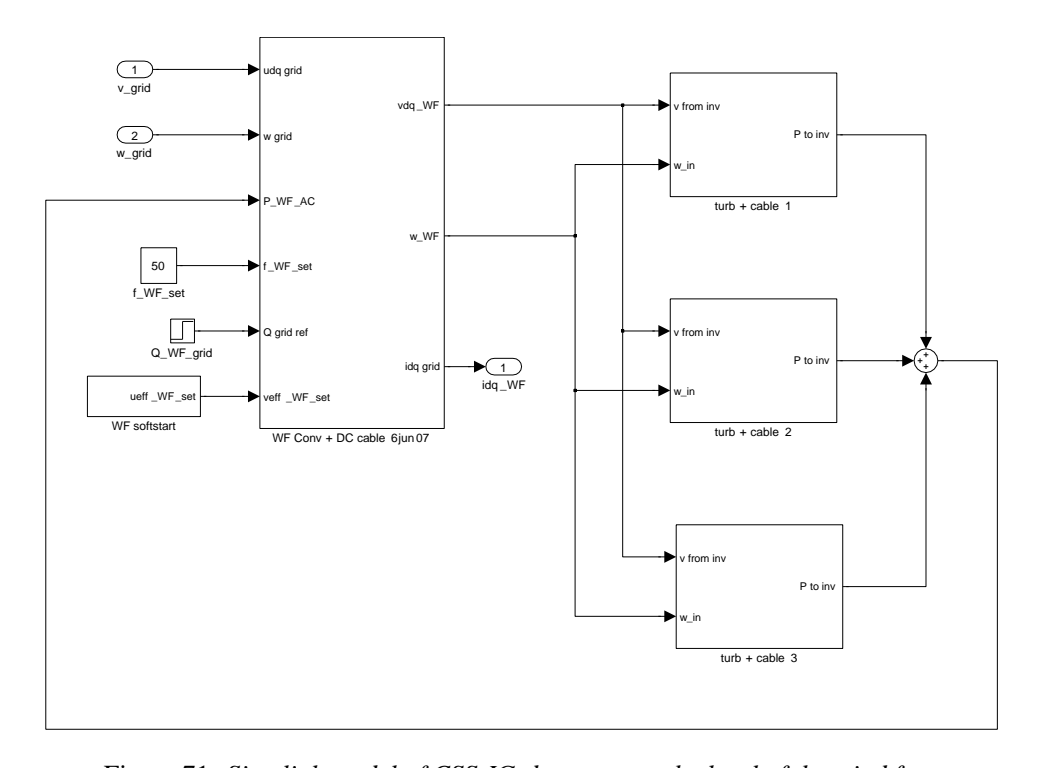


Figure 71: Simulink model of CSS-IG-dc system at the level of the wind farm

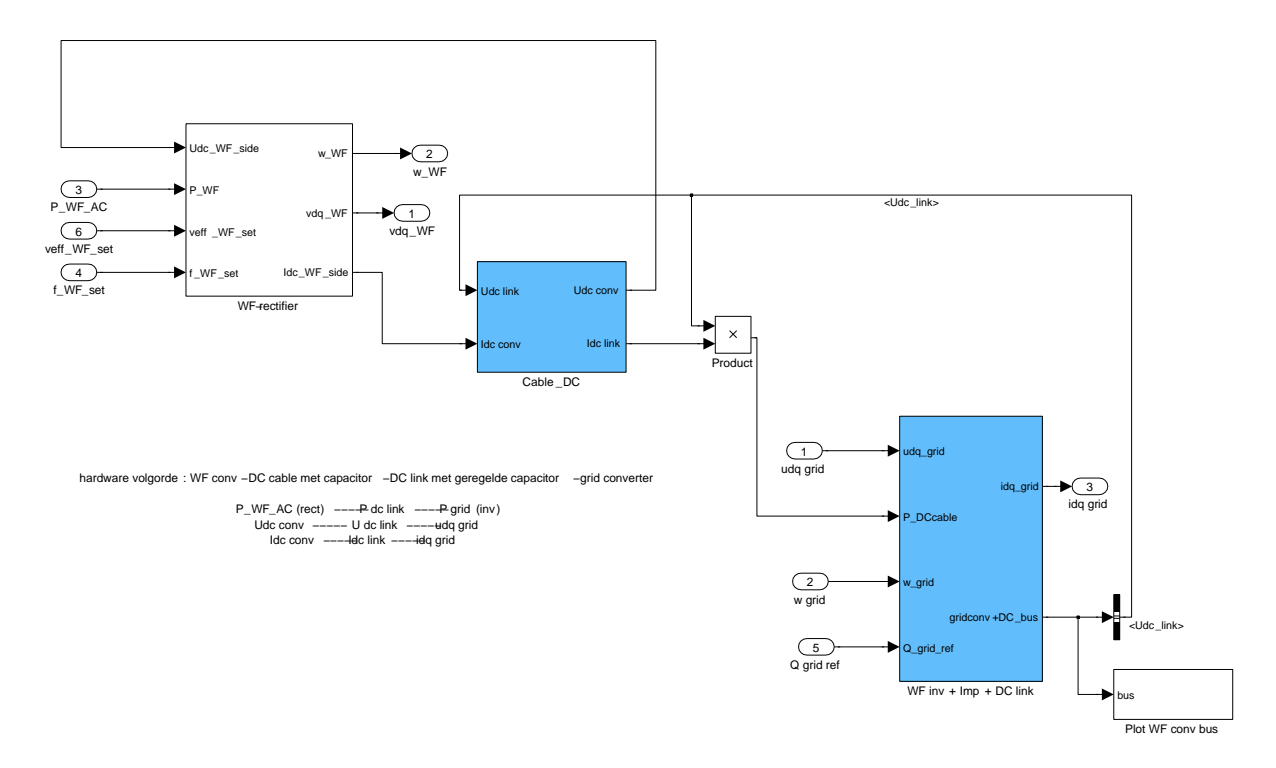


Figure 72: Simulink model of the CSS-IG-dc system at the converter and DC cable

## 4.1.2 CSS-IG-dc wind farm normal operation

Normal operation of the CSS-IG-dc system is demonstrated for a wind farm consisting of three 2.75 MW wind turbines and a DC cable connection to shore of 15 km length. The wind turbines in the farm are connected by 34 kV AC cables with a length of 0.66 km. Over a period of two minutes a wind gust from 5 m/s to 25 m/s and back passes the wind farm.

Figure 73 gives the response of the individual turbines. The gust reaches its maximum at each turbine at a different time. The frequency in the farm is 50 Hz, so there will only be small changes is turbine speed. The power, stator voltage, stator current and slip of each turbine are also shown in figure 73. The fast variations in the rotor effective wind speed and the aerodynamic power are caused by turbulence and rotational sampling.

The total wind farm active and reactive power at the grid side of the DC link are plotted in figure 74. The variation of the electric power is equivalent to that of a constant speed system, since the wind farm frequency is kept constant by the rectifier. The wind farm reactive power fluctuates around zero, since the inverter reactive power setpoint is zero. The inverter controller is used in all systems with inverters and is described in section 2.1. The inverter dq-voltages and currents in the substation and the DC link voltage are plotted in figure 74.

The wind farm model is connected to the standard grid model used in all simulations in this report. It consists of a frequency and voltage controlled synchronous generator (12 kV, 220 MVA), two consumer loads of 75 MW total, a 12-150kV transformer and cables. Figure 75 gives the response of the grid model to the changes in wind farm output. The wind power changes are no problem for the grid frequency and grid voltage control.

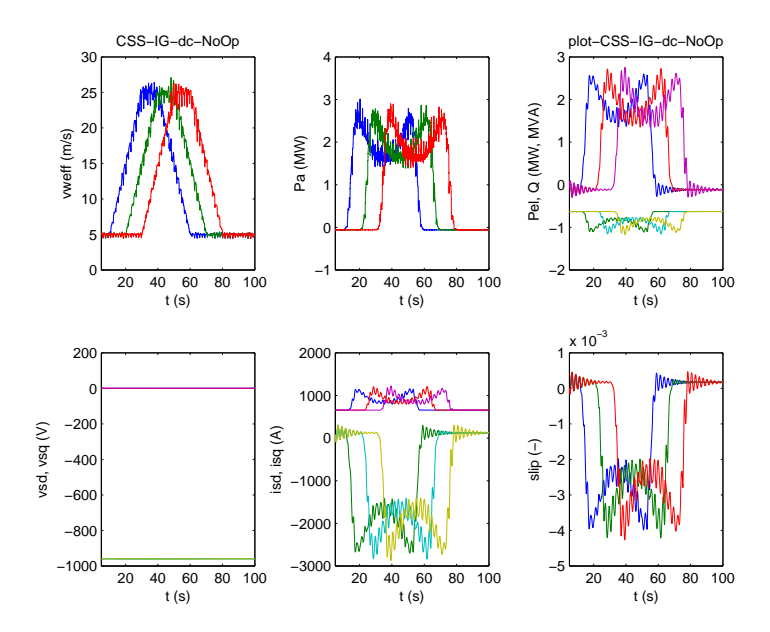


Figure 73: CSS-IG-dc wind farm, normal operation: rotor effective wind speed, aerodynamic power, electric and reactive power, stator d and q voltage, stator d and q current and slip per turbine

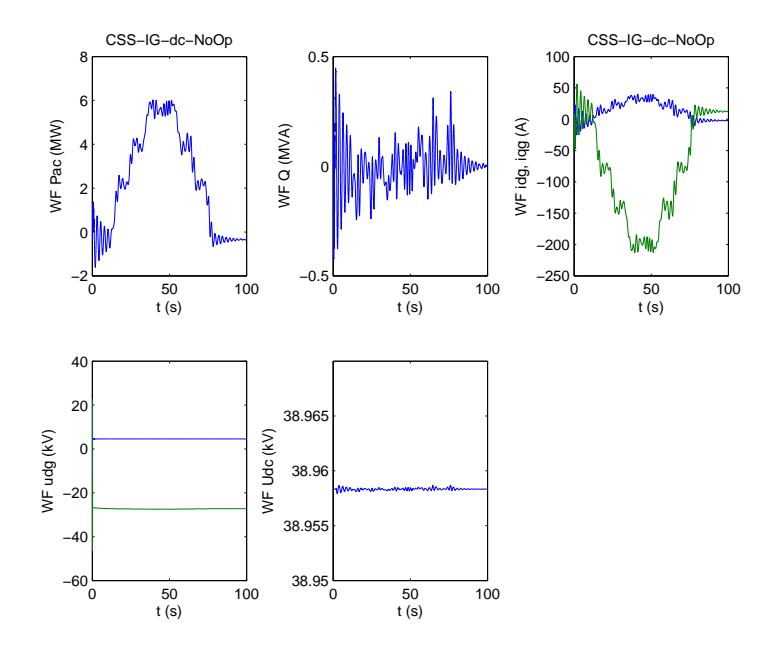


Figure 74: CSS-IG-dc wind farm, normal operation: active power, reactive power, inverter dq-currents, inverter dq-voltages, DC voltage and wind farm frequency

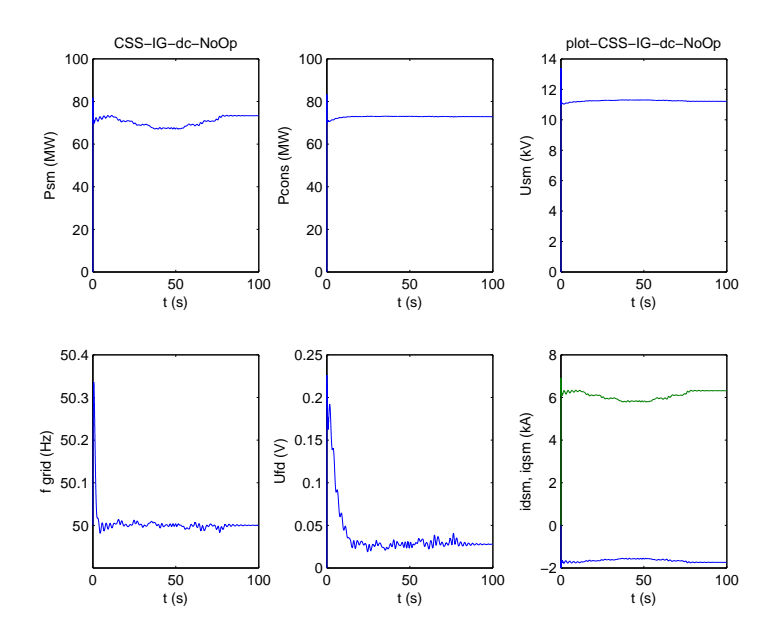


Figure 75: CSS-IG-dc model, normal operation: grid synchronous generator power, consumer load, synchronous machine voltage, grid frequency, exciter voltage and synchronous machine d and q currents

# 4.2 Wind farm with a CSS-CCIG-dc electric system (# 2)

# 4.2.1 CSS-CCIG-dc layout and control

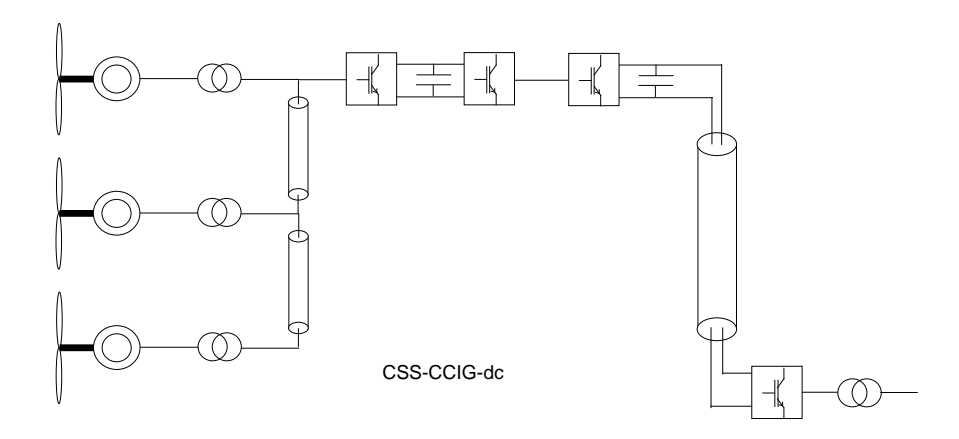


Figure 76: Cluster controlled WF (only one cluster shown) with DC connection to shore (CSS-CCIG-dc)

Figure 76 gives the layout of the electrical system of the second wind farm based on a Constant Speed Stall turbine. Cluster controlled turbines are connected to a DC-link to shore (acronym CSS-CCIG-dc). The stall controlled turbines with induction machines are operated in variable speed mode. The new aspect of this system is the connection of two converters in series (the cluster inverters and the wind farm rectifier) with an AC connection in between. This implies that there are multiple frequencies and multiple AC voltages to be controlled in the wind farm, viz. at the cluster rectifiers and at the wind farm rectifier. At wind farm rectifiers, the dq-voltage and the frequency setpoints are constant. At the cluster rectifier, the cluster frequency setpoint depends on the wind speed at the first turbine and the q-voltage is proportional to this frequency (see figure 5). The cluster control strategy was already demonstrated in the Erao-2 project [33]. Figure 77 shows the signal flow in the cluster converter with DC-link and the wind farm converter with DC-cable.

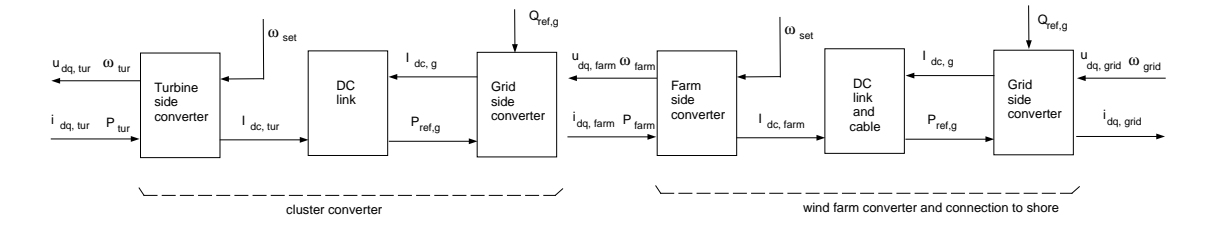


Figure 77: Converter signal flow in CSS-CIG-dc system

Figure 78 shows the Simulink model of the CSS-CCIG-dc wind farm on the level of a turbine cluster consisting of three turbines.

# 4 MODELS OF WIND FARMS WITH CONSTANT SPEED STALL TURBINES (CSS)

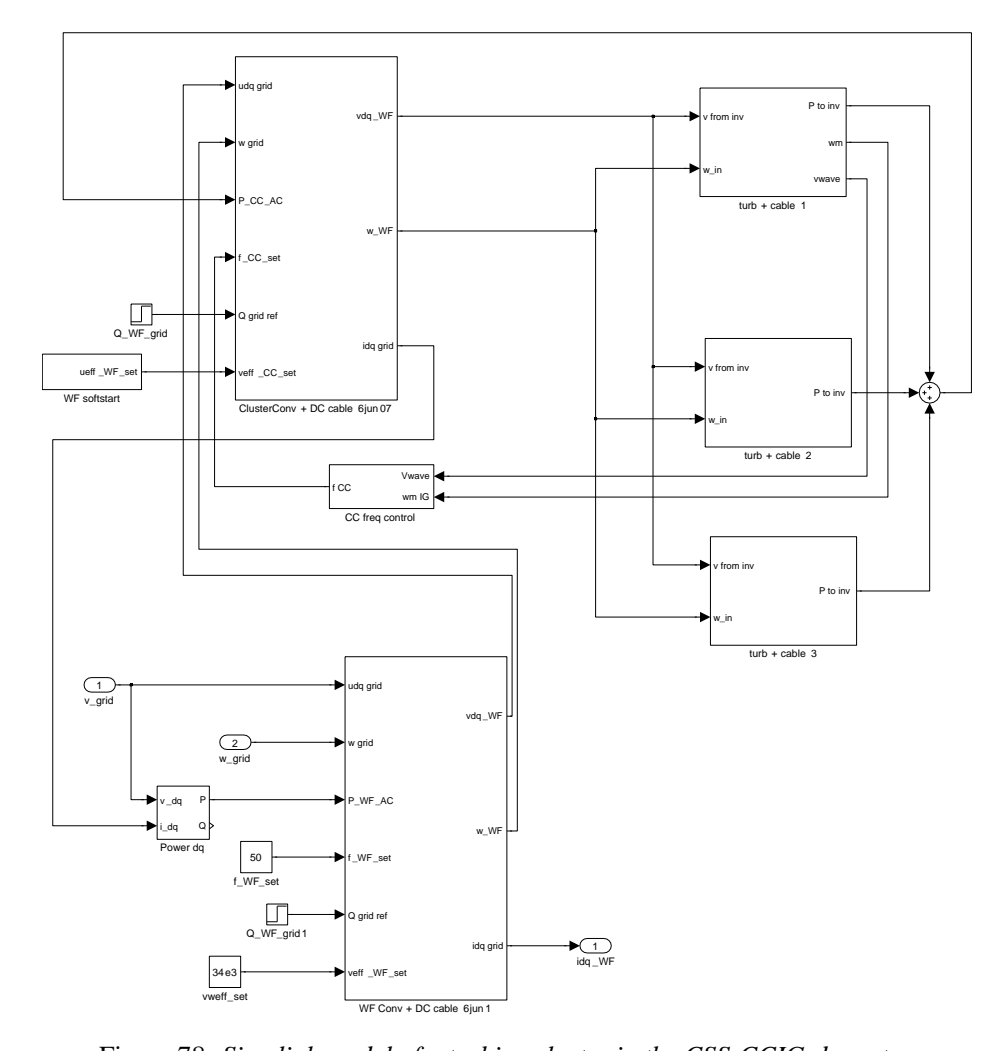


Figure 78: Simulink model of a turbine cluster in the CSS-CCIG-dc system

#### 4.2.2 CSS-CCIG-dc wind farm normal operation

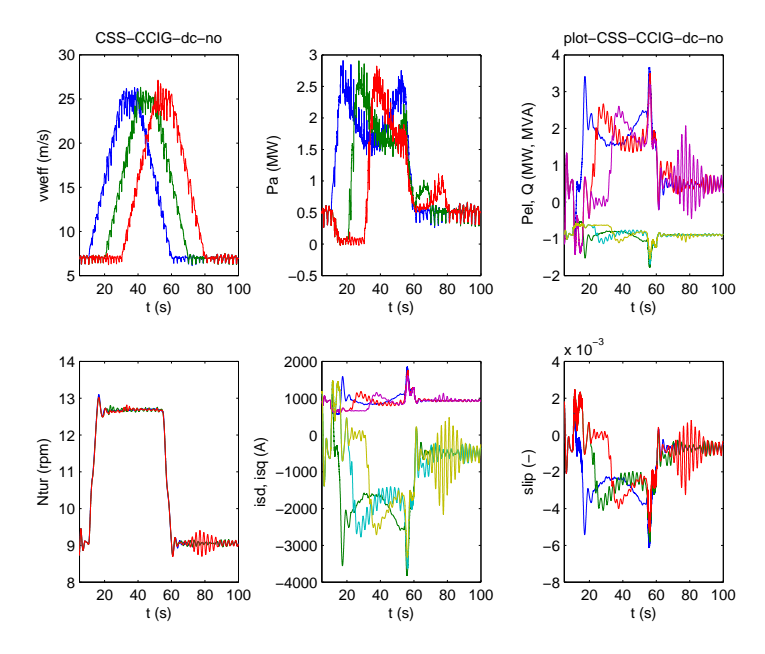


Figure 79: CSS-CCIG-dc wind farm, normal operation: wind speed, rotational speed, aerodynamic power, stator voltage, stator current and slip per turbine

Normal operation of the CSS-CCIG-dc system is demonstrated for a wind farm consisting of one cluster of three 2.75 MW wind turbines and a DC cable connection to shore of 15 km length. The wind turbines in the cluster are connected by 34 kV AC cables with a length of 0.66 km. A wind gust passes the wind farm, starting from 7 m/s to 25 m/s and back again. The turbine speeds increases with the wind speed at turbine 1, see figure 79, due to the increasing cluster frequency. The frequency is limited to 50 Hz to guarantee proper stall operation. This limits the turbine aerodynamic power more or less to the rated power. The voltage on the induction generators is constant (not shown in the figure). The variation in turbine power corresponds more to a constant speed system than to a variable system: the cluster speed control strategy does not reduce the power variations caused by turbulence and rotational sampling since the turbine speed is controlled and correlates to the wind speed at turbine 1. Turbine number 3 shows some severe oscillations at the end of the gust. This type of variable speed operation is not good in reducing the stress on the turbines.

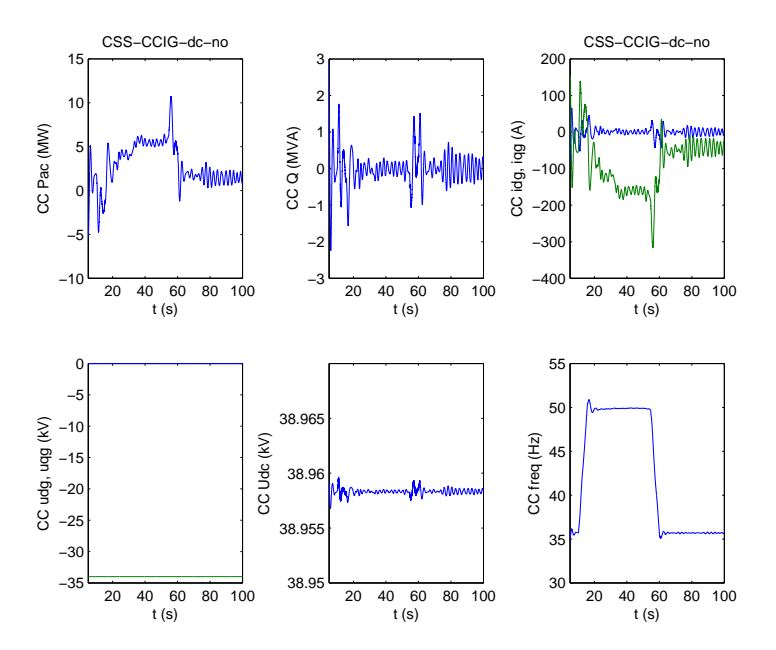


Figure 80: CSS-CCIG-dc wind farm, normal operation: cluster active power, reactive power, cluster inverter dq-currents, cluster inverter dq-voltages, DC voltage and cluster frequency

The cluster power in figure 80 corresponds to the oscillating power at the turbine level. The cluster reactive power at the grid side oscillates around zero, corresponding with the setpoint of the cluster inverter control. The plotted dq-currents  $i_{dg}, i_{qg}$  and voltages  $u_{dg}, u_{qg}$  in figure 80 are at the grid side of the cluster inverter. The DC voltage is controlled by the inverter and remains constant. The cluster frequency varies with the wind speed at turbine 1.

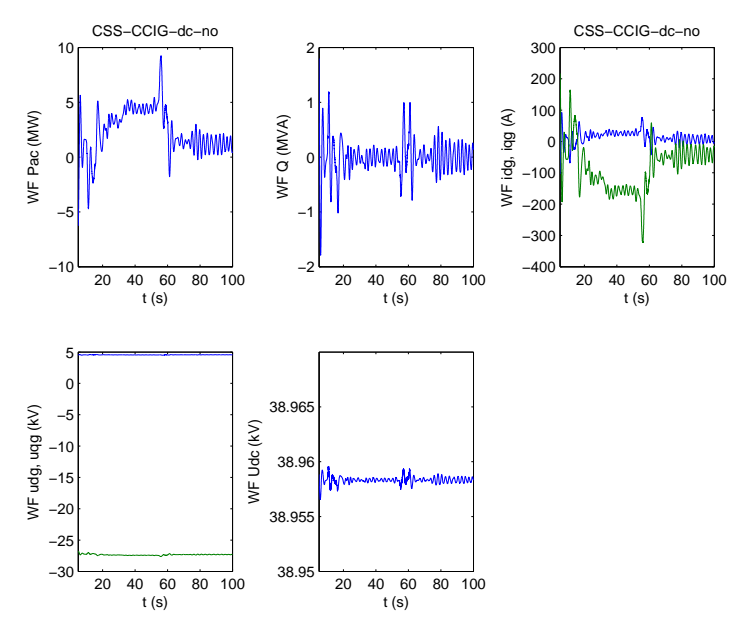


Figure 81: CSS-CCIG-dc wind farm, normal operation: wind farm active power, reactive power, WF inverter dq-currents, WF inverter dq-voltages, DC voltage

Figure 81 shows the same set of variables as in figure 80 but now for the wind farm converter, with the exception of the frequency at the wind farm rectifier, because it is constant (50 Hz). Since there is only one cluster connected, the wind farm power is almost the same as the cluster

power. The dq-currents  $i_{dg}, i_{qg}$  and voltages  $u_{dg}, u_{qg}$  differ from the cluster values due to the properties of the grid, consisting of a frequency and voltage controlled synchronous generator, two consumer loads of 75 MW total, transformers and cables.

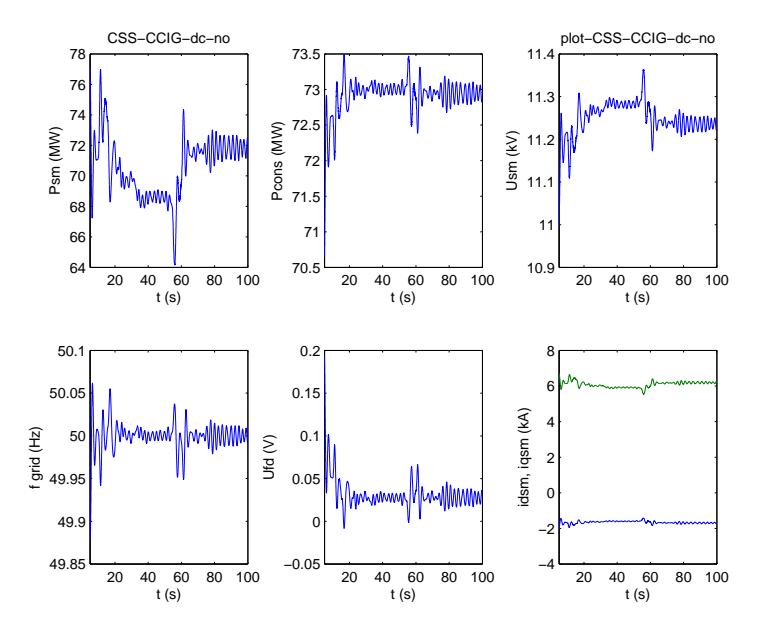


Figure 82: CSS-CCIG-dc model, normal operation: grid synchronous generator power, consumer load, synchronous machine voltage, grid frequency, exciter voltage and synchronous machine d and q currents

Figure 82 gives the response of the grid model to the changes in wind farm output. The wind power changes are no problem for frequency and voltage control.

- 5 Models of wind farms with variable speed pitch turbines (VSP)
- 5.1 Wind farm with a VSP-CCIG-ac electric system (# 3)

## 5.1.1 VSP-CCIG-ac layout and control

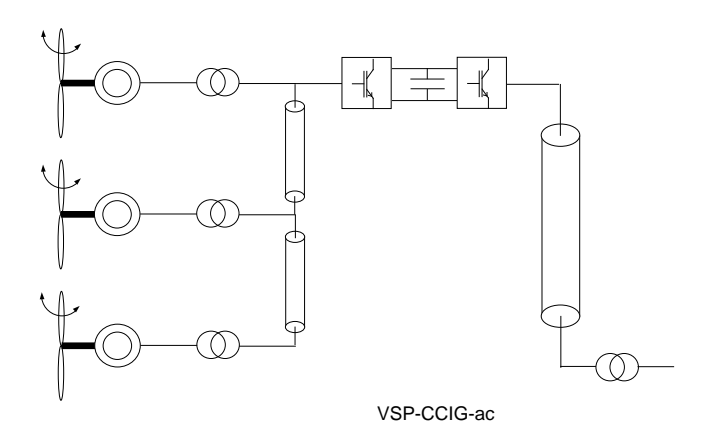


Figure 83: Cluster controlled VSP WF with AC connection to shore (VSP-CCIG-ac)

Figure 83 shows the layout of the VSP-CCIG-ac system, again with only one cluster. The VSP-CCIG-ac system is based on the variable speed pitch controlled turbine in cluster controlled mode of operation. The cluster control strategy is the same as for the CSS-CCIG-ac system (see figure 5). From figure 84 can be seen that limiting the cluster frequency to 50 Hz will limit the power to 3 MW at 15 m/s at constant pitch angle (no pitch control required). If the pitch control is modified, the speed limit can be increased. This would require a new design of the pitch controller, which is outside the scope of this project. For the demonstration of the overall behaviour of the VSP-CCIG-ac system this is not critical however.

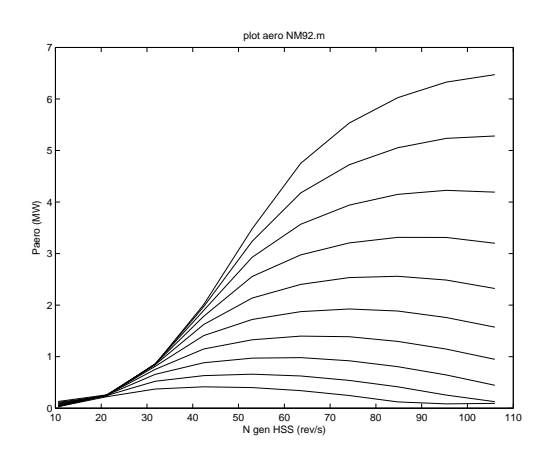


Figure 84: Aerodynamic power of the VSP turbine as function of the generator speed for windspeeds from 6 to 15 m/s and a pitch angle of 1 degree (default value)

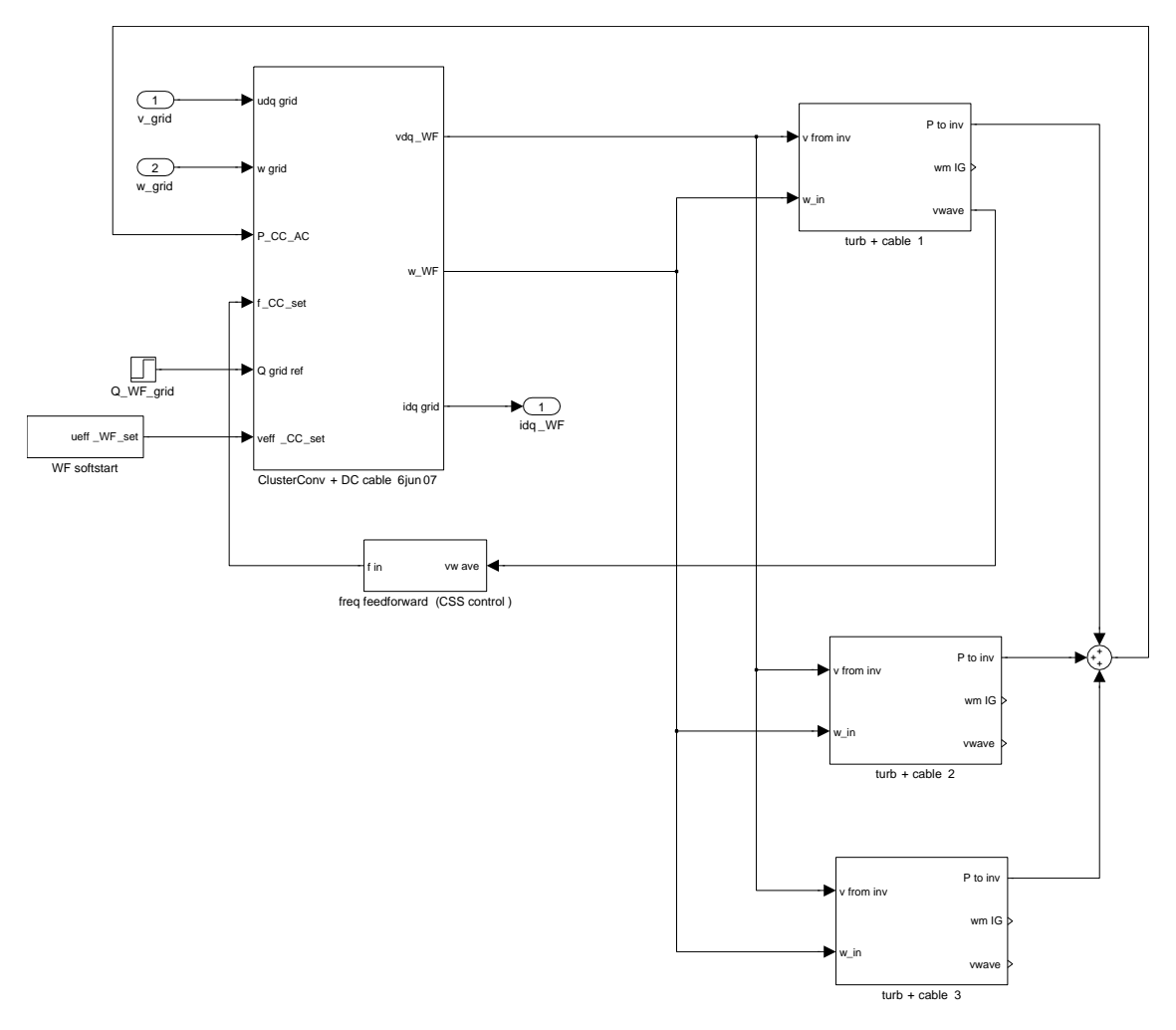


Figure 85: Simulink model of the VSP-CCIG-ac system (#3)

Figure 85 shows the Simulink model for VSP-CCIG-ac system at the level of a cluster of turbines.

#### 5.1.2 VSP-CCIG-ac wind farm normal operation

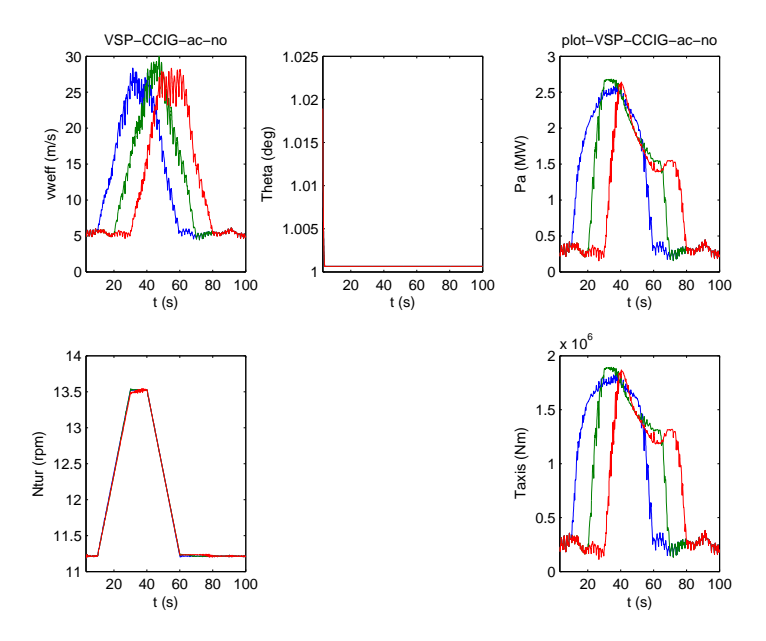


Figure 86: VSP-CCIG-ac wind farm, normal operation: wind speeds, pitch angles, aerodynamic powers, turbine rotational speeds and axial torques per turbine

Normal operation of the VSP-CCIG-ac system is demonstrated for a wind farm consisting of three 2.75 MW wind turbines and an AC connection of 15 km to shore. The wind turbines in the cluster are connected by 34 kV AC cables with a length of 0.66 km. Over a period of 100 s a wind gust passes the wind farm, starting from 5 m/s to 27 m/s and back again, see figure 86. The speed of the turbines in the cluster (Ntur) increases with the wind speed at turbine 1. The frequency is limited to 50 Hz to limit the turbine aerodynamic power to the rated power. The pitch angle during normal operation is 1 degree.

The variation in turbine power corresponds more to a constant speed system than to a variable system: the cluster speed control strategy does not reduce the power variations caused by turbulence and rotational sampling since the turbine speed is controlled and correlates to the wind speed at turbine 1.

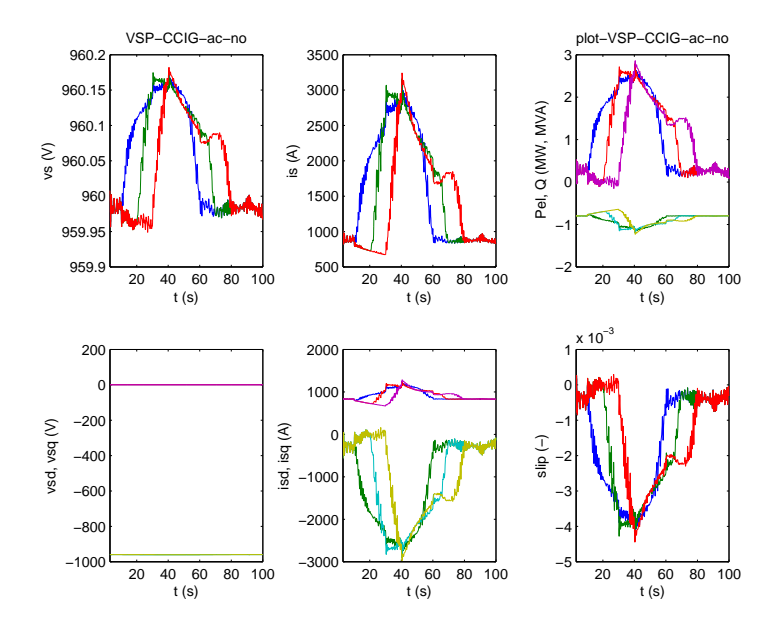


Figure 87: VSP-CCIG-ac wind farm, normal operation: stator voltages, stator currents, active and reactive powers, dq stator voltages, dq stator currents and slips per turbine

Figure 87 shows the voltages, currents, active and reactive powers and the slips of the three turbines in the cluster.

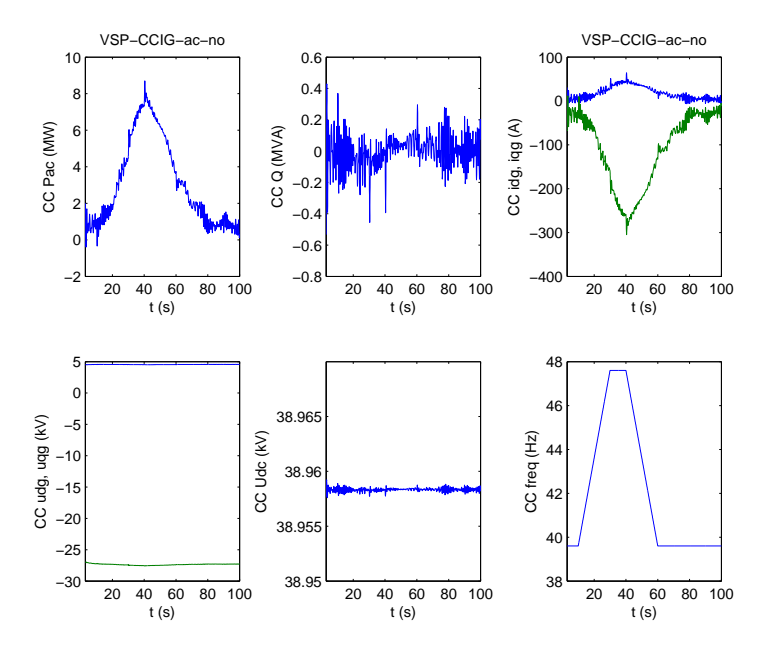


Figure 88: VSP-CCIG-ac wind farm, normal operation: cluster active and reactive power at the grid side, inverter dq-currents, inverter dq-voltages, DC voltage and cluster frequency

Figure 88 shows the operation of the cluster converter during the gust. The converter transfers the cluster power to the grid and the reactive power at the grid side is controlled to zero (on average). The grid side dq-currents and dq-voltages are plotted. The DC-link voltage is practically constant (controlled by the inverter). The cluster AC frequency increases relatively quickly due to the large increase in wind speed (5 to 27 m/s) and after a while decreases again.

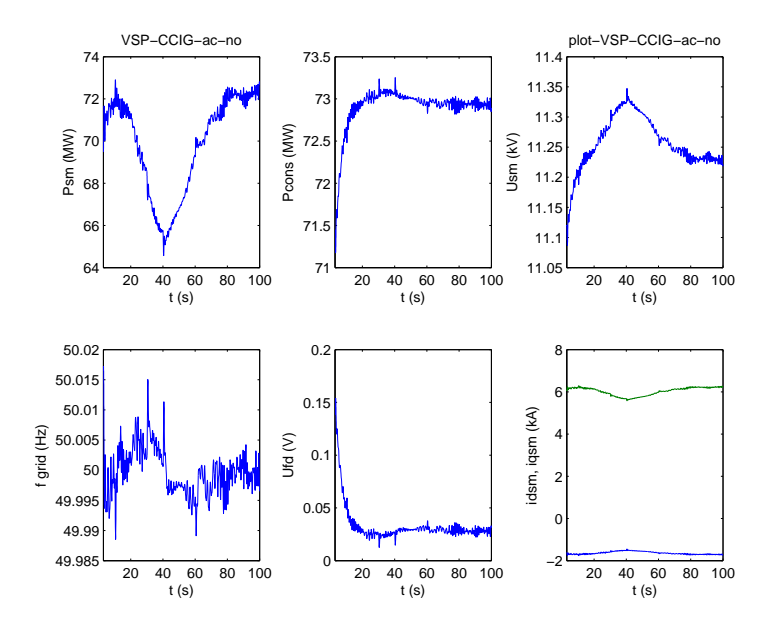


Figure 89: VSP-CCIG-ac wind farm, normal operation: grid synchronous generator power, consumer load, synchronous machine voltage, grid frequency, exciter voltage and synchronous machine d and q currents

The response of the grid to the changing wind farm output of the VSP-CCIG-ac wind farm can be seen in figure 89. The wind power changes are no problem for the grid frequency and voltage control.

# 5.2 Wind farm with a VSP-CCIG-dc electric system (# 4)

# 5.2.1 VSP-CCIG-dc layout and control

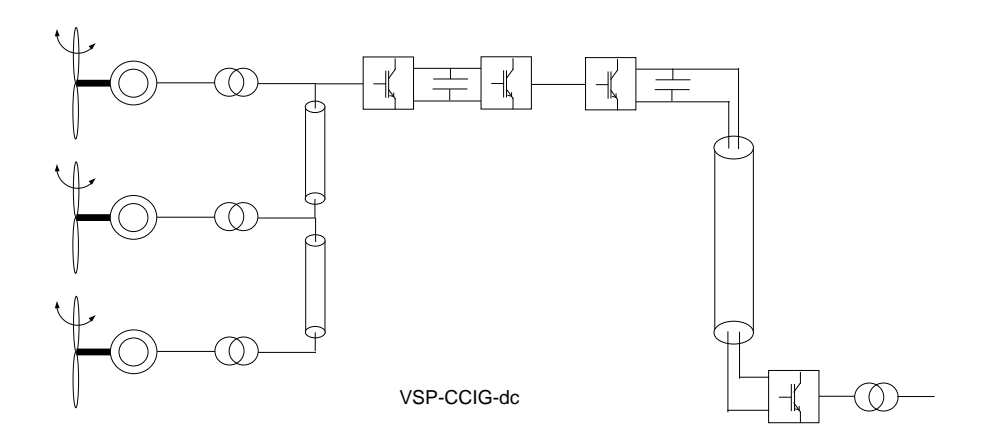


Figure 90: Cluster controlled variable speed turbine WF with DC connection to shore (VSP-CCIG-dc)

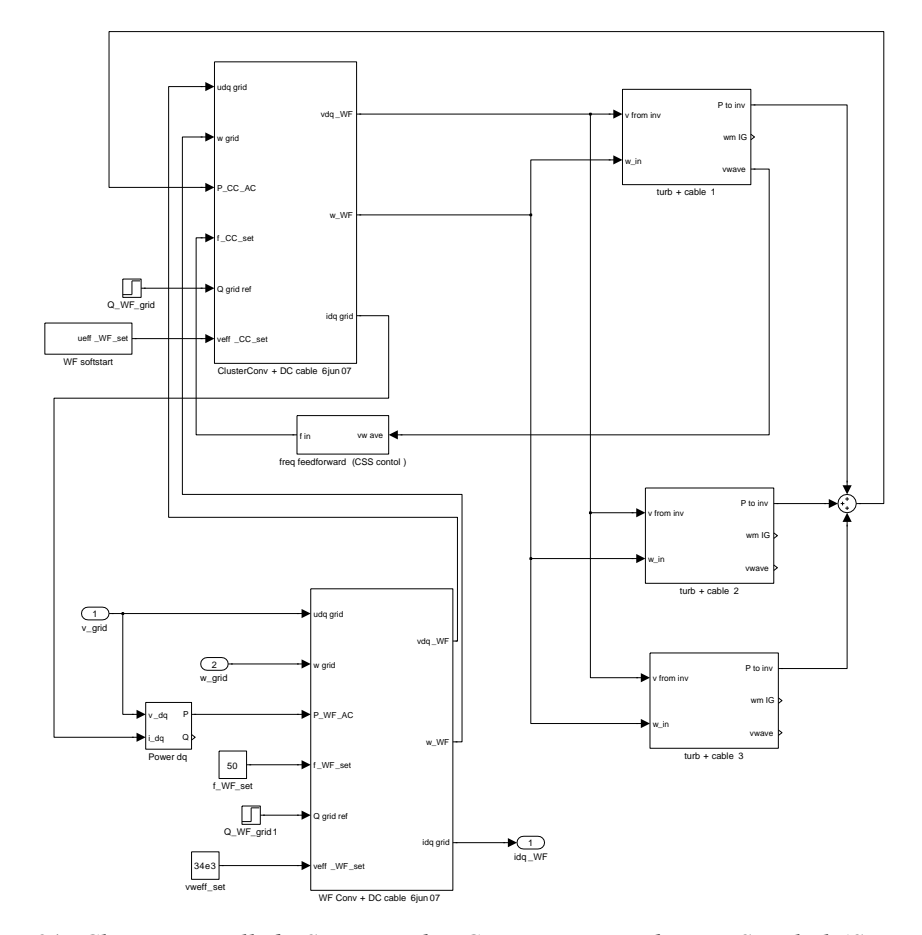


Figure 91: Cluster controlled VSP WF with DC connection to shore in Simulink (System # 4)

The main components of the cluster controlled variable speed wind farm with DC connection to shore (VSP-CCIG-dc) are shown in figure 90. The turbine cluster operation is similar to the VSP-CCIG-ac wind farm (system # 3), the rotational speed of the cluster is determined by the wind speed at turbine 1. Figure 91 shows the Simulink model of the VSP-CCIG-dc wind farm. The WF converter connects the windfarm to the grid transformer.

#### 5.2.2 VSP-CCIG-dc wind farm normal operation

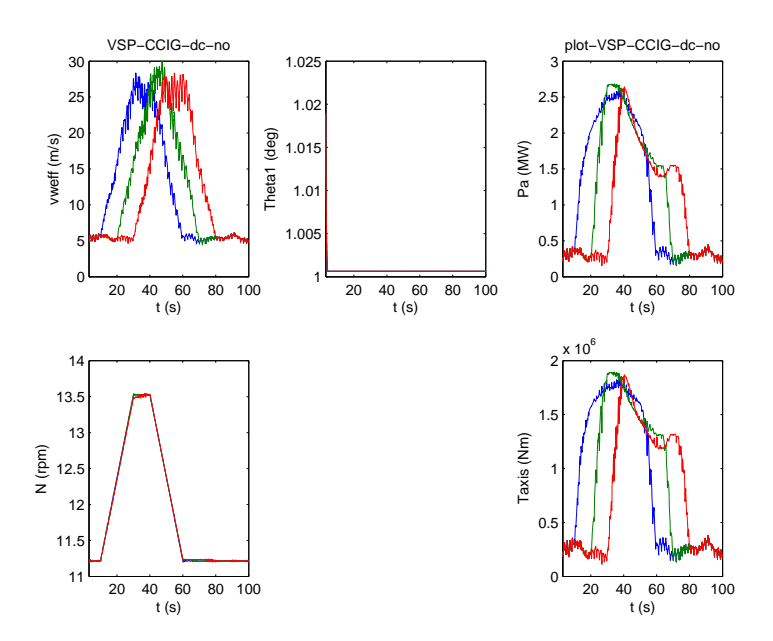


Figure 92: VSP-CCIG-dc wind farm, normal operation: wind speeds, pitch angles, aerodynamic powers, turbine rotational speeds and axial torques per turbine

The wind farm consists of a single cluster of three turbines. Since the wind farm rectifier of the VSP-CCIG-dc system creates a constant voltage and frequency, the dynamic behaviour under normal operating conditions is expected to be very simlar to system # 3 with AC connection. This is the case, as can be seen in figure 92, 93 and 94.

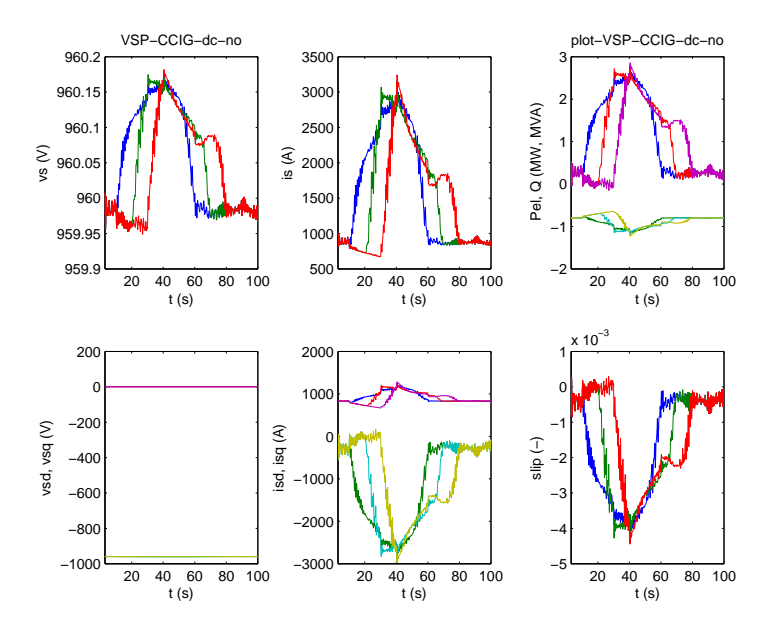


Figure 93: VSP-CCIG-ac wind farm, normal operation: stator voltages, stator currents, active and reactive powers, dq stator voltages, dq stator currents and slips per turbine

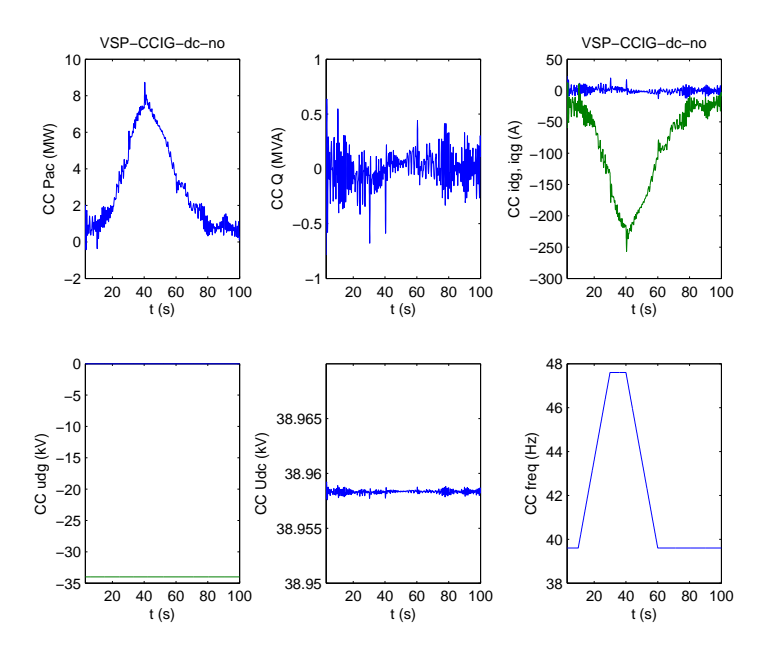


Figure 94: VSP-CCIG-dc wind farm, normal operation: cluster active power, reactive power, inverter dq-currents, inverter dq-voltages, DC voltage and cluster frequency

The cluster inverter, plotted in figure 94, operates at slightly different voltages and currents than in the system with AC connection to shore. At the wind farm inverter (figure 95) the behaviour is similar to that of the cluster inverter of system # 3. The grid response of systems # 3 and # 4 are practically the same (see figure 96).

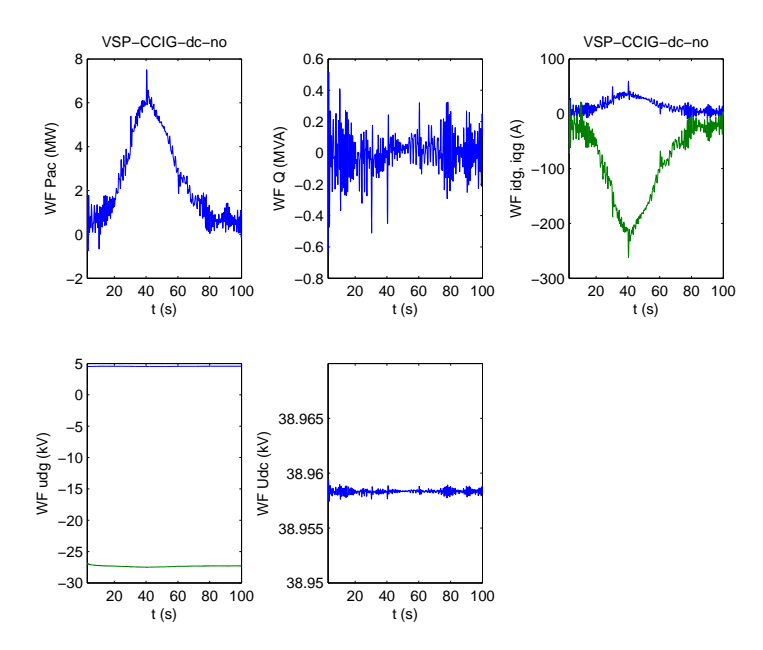


Figure 95: VSP-CCIG-dc wind farm, normal operation: WF active power and reactive power, WF inverter dq-currents and dq-voltages, DC voltage and frequency at the cluster inverter-WF rectifier connection

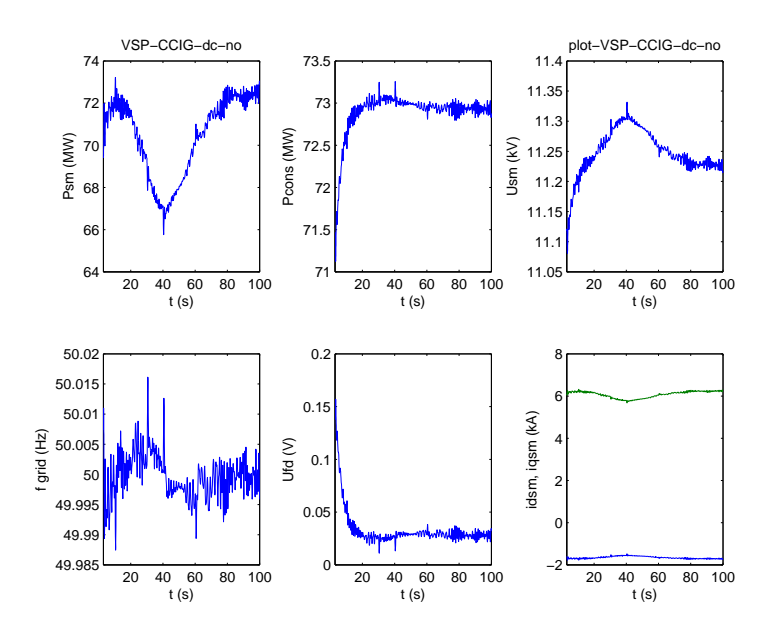


Figure 96: VSP-CCIG-dc wind farm, normal operation: grid synchronous generator power, consumer load, synchronous machine voltage, grid frequency, exciter voltage and synchronous machine d and q currents

## 5.3 Wind farm with a VSP-DFIG-dc electric system (# 5)

# 5.3.1 VSP-DFIG-dc layout and control

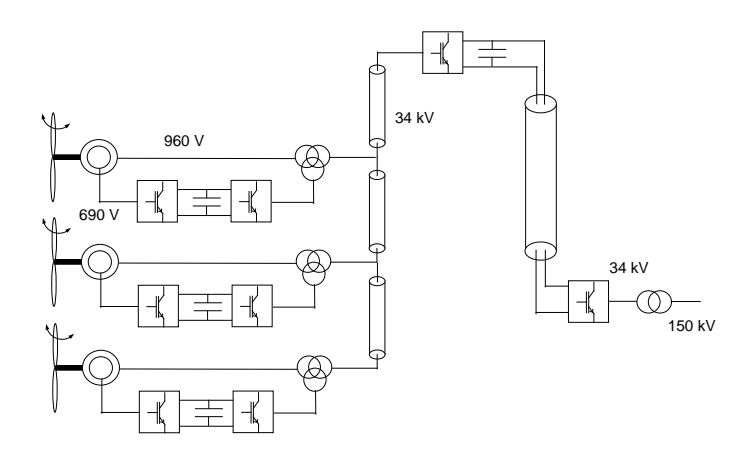


Figure 97: Variable speed pitch wind farm with DFIG and DC connection to shore

System number 5 is a variable speed pitch wind farm with DFIG and DC connection to shore (acronym VSP-DFIG-dc), see figure 97. The VSP-DFIG-ac system was already demonstrated in the Erao-2 project. During normal operation the VSP-DFIG-ac and the VSP-DFIG-dc systems are expected to have the similar dynamic response at the turbine level as well as at the wind farm level. The behavior will be different during grid faults, since the induction machine and the DFIG converter will not be subjected to the grid fault directly. This may eliminate the need for a fault ride through capability on each DFIG system individually.

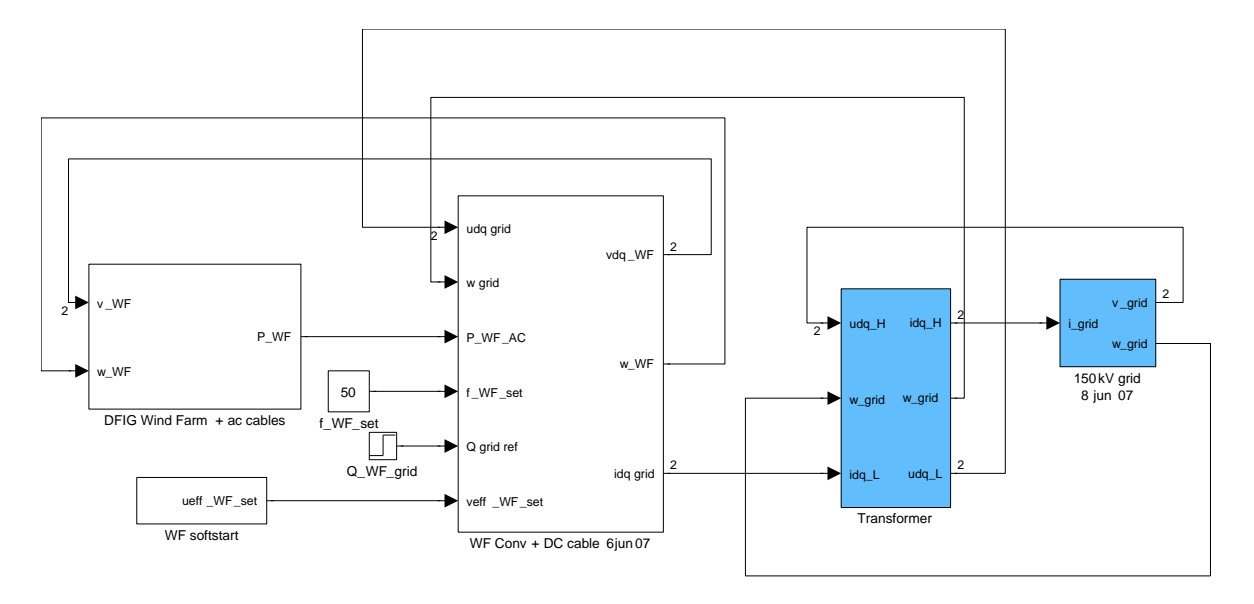


Figure 98: Simulink model of VSP-DFIG-dc system at the system level

Figure 98 shows the Simulink model of the VSP-DFIG-dc system at the level of the wind farm. The wind farm converter is located between the DFIG wind farm and the grid transformer and grid model. A simulation initialization procedure is used to connect the wind farm converter to the farm. The farm voltage is increased from zero to rated value in 1 sec. This eliminates the need to calculate a steady state condition before executing a simulation. Finding the steady

state for the VSP-DFIG-dc system sometimes was a problem. The DFIG wind farm consists of three DFIG turbines, including three winding transformers, connected to the wind farm converter by cables, see figure 99.

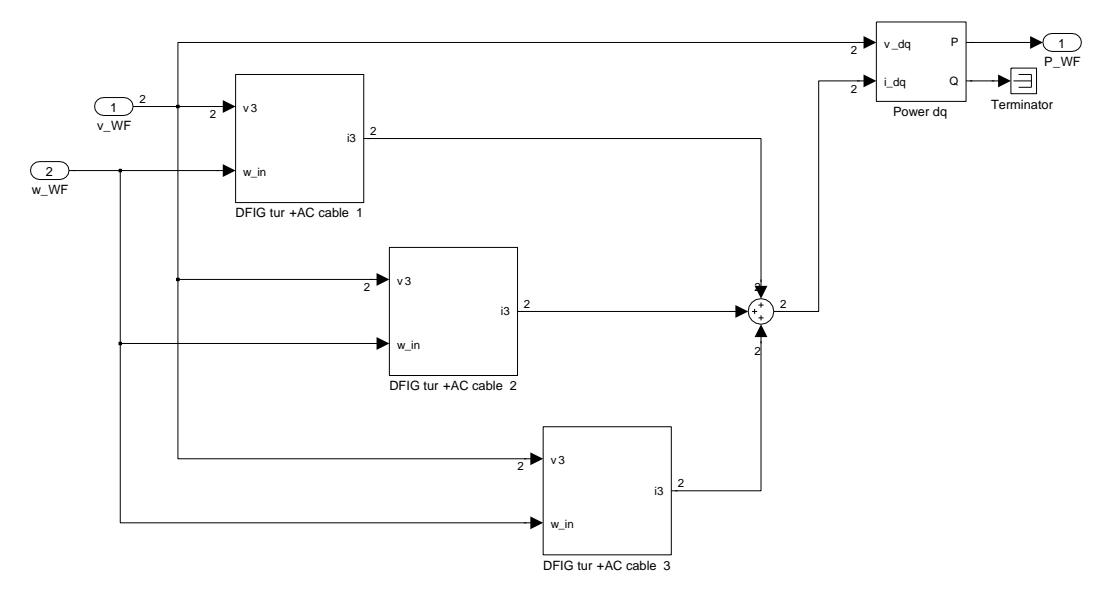


Figure 99: Simulink model of VSP-DFIG-dc system at the farm level

The wind farm converter and DC cable model in Simulink are shown in figure 100. The rectifier generates a constant frequency and (after the simulation initialization period has passed) a constant voltage. The wind farm inverter controls the DC link and cable voltage and the reactive power to the grid.

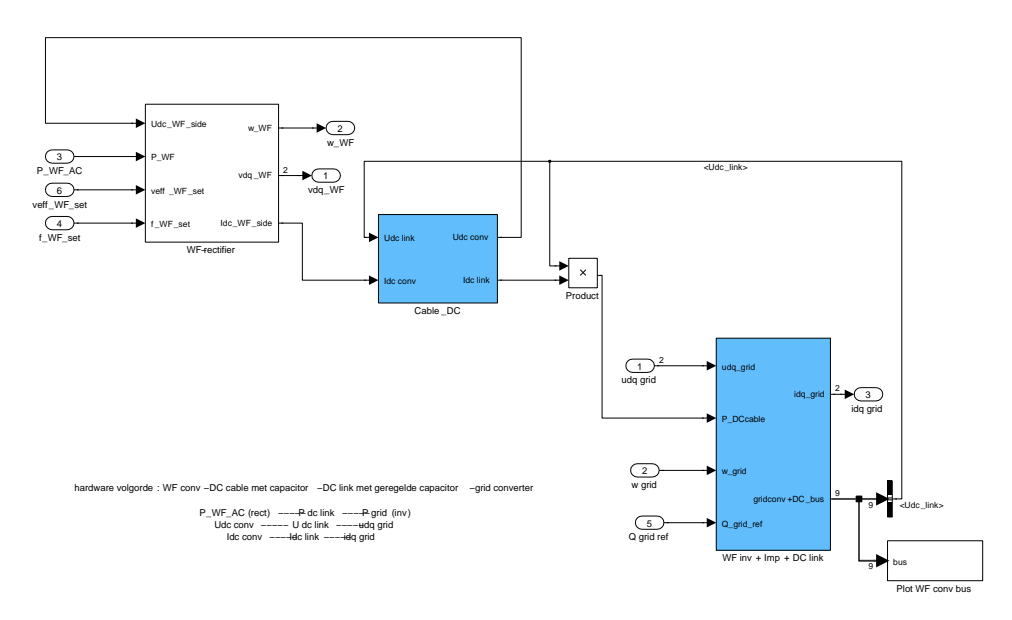


Figure 100: Simulink model of VSP-DFIG-dc system at the wind farm converter level

#### 5.3.2 VSP-DFIG-dc wind farm normal operation

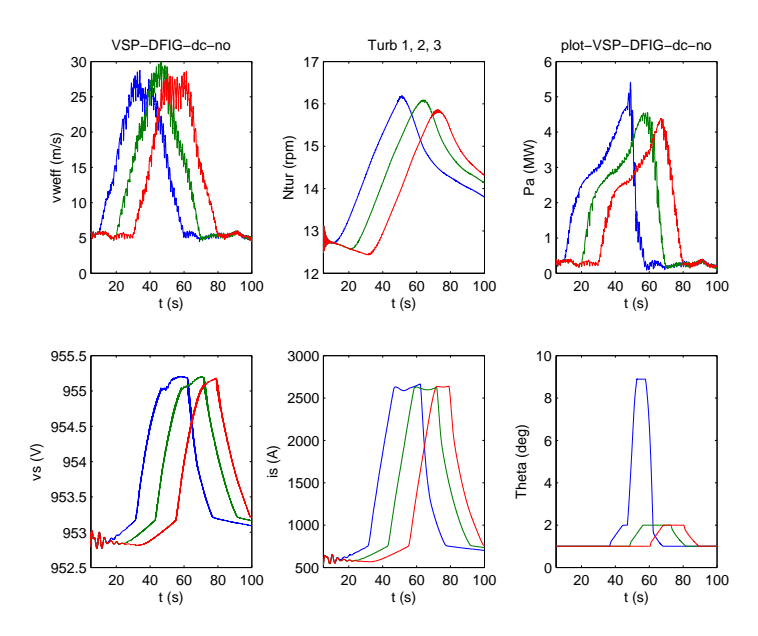


Figure 101: VSP-DFIG-dc system; Normal operation: wind speeds, rotational speeds, aero-dynamic powers, stator voltages, stator currents and pitch angles of the wind farm turbines

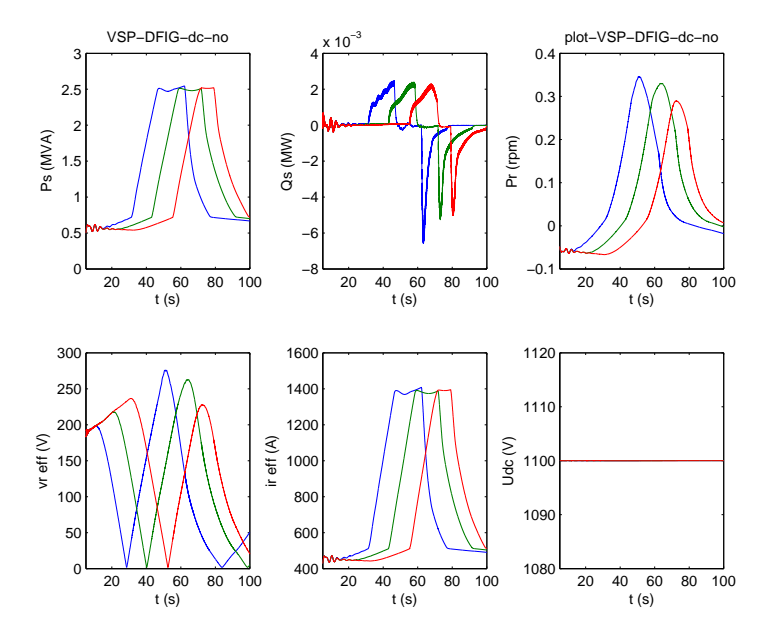


Figure 102: VSP-DFIG-dc system; Normal operation: turbine active, reactive and rotor powers, rotor voltages, rotor currents and DC voltages of the wind farm turbines

Figures 101 to 103 show the response of a VSP-DFIG-dc wind farm to the gust. Three turbines are simulated. The turbines are the same as in the VSP-DFIG-ac option of Erao-2. The first turbine reacts a bit differently to the gust than the other two: the pitch angle response is much larger. This is caused by the strongly non-linear behaviour of the pitch angle controller. There are also small differences in turbine speeds. The response to the gust in the electrical parameters for the three turbines is more or less the same, figure 102.

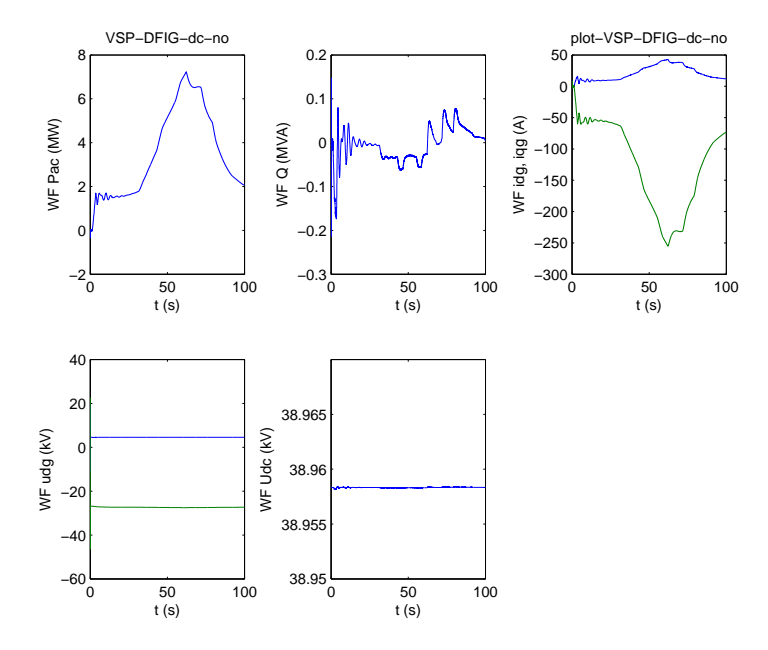


Figure 103: VSP-DFIG-dc system; Normal operation: wind farm AC power, reactive power, grid side currents and voltages, DC voltage

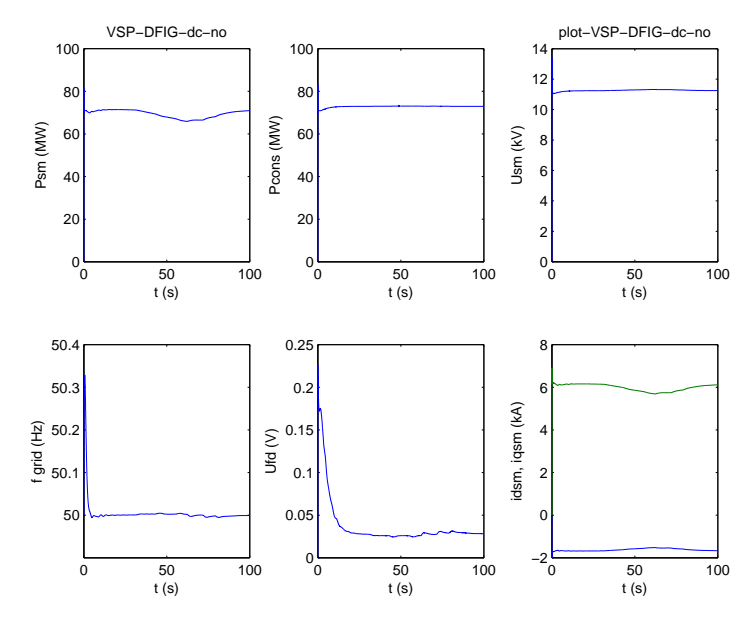


Figure 104: VSP-DFIG-dc system, normal operation: grid synchronous generator power, consumer load, synchronous machine voltage, grid frequency, exciter voltage and synchronous machine d and q currents

The responses of the whole wind farm (figure 103) and the grid (figure 104) do not show much variation, as could be expected for a variable speed system.

#### 5.4 Wind farm with a VSP-FCIG-ac electric system (# 6)

#### 5.4.1 VSP-FCIG-ac layout and control

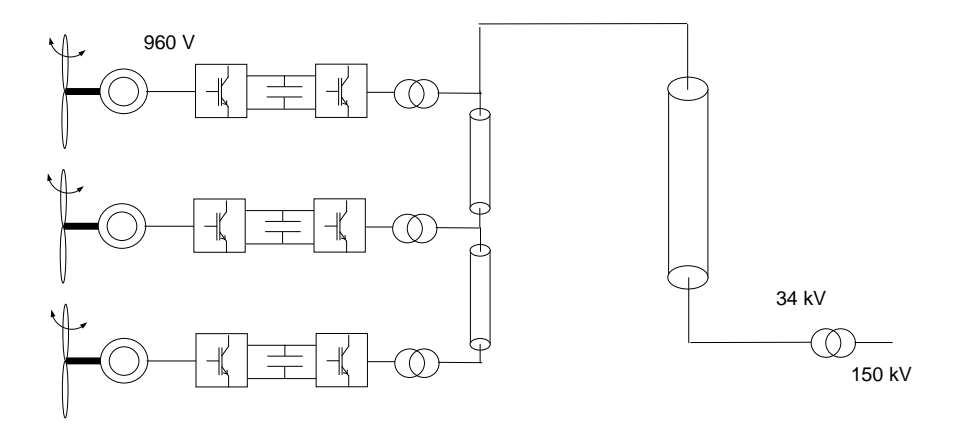


Figure 105: Variable speed pitch wind farm with FCIG and AC connection to shore

Figure 105 gives the lay-out of the variable speed pitch wind farm with full converter induction generator and AC connection to shore (VSP-FCIG-ac). The control of the machine side converter (rectifier) is different from the control of the rectifier in the previous system. In the VSP-DFIG system, the rectifier connects to the rotor of the induction machine and the rectifier control makes the electromagnetic torque and the reactive power of the stator. In the FCIG case, the rectifier connects to the stator of the induction machine and controls the electromagnetic torque and the stator voltage. The reactive power can not be controlled independently, since it is determined by the torque of the (squirel cage) induction machine, the rotational speed and the stator voltage. The FCIG rectifier controller which is used was developed in this project. The next section describes the criteria and characteristics of the rectifier controller and demonstrate its performance.

#### Control of the rectifier of the FCIG system

The rectifier control makes use of the space vector concept. Appendix D introduces the description of induction machine dynamic behavour by space vectors and discusses the control of an induction machine in field coordinates (a coordinate system linked to the space vector of the rotating magnetic field in the machine). Generally, the space vector machine model is described in a reference system fixed to the **stator** voltage or flux phasor which rotates with the electrical frequency  $\omega_s$  of the stator. For a grid connected induction machine this frequency is almost constant. In case of a FCIG, the stator frequency is variable and not a priory known: it is equal to the sum of the mechanical speed times the number of pole pairs and the frequency of the rotor current. An option could be to impress a chosen stator frequency by the rectifier. Then the problem is that the instantaneous electromagnetic torque is determined by the rotor speed, i.e. the slip and that a small change in slip will result in a large change in torque. At a slip of more than a few percent the pull out torque may be passed. Therefore it makes sence to choose a reference frame fixed to the rotor. The advantage of this choice is that the stator frequency need not be known, it will automatically result from the recifier controller action. The disadvantage of this choice is that the d- and q-variables will not be constant in steady state: they will have the slip frequency, since in steady state the flux in the machine rotates with  $\omega_s = (1-s)p\omega_m$  and the reference frame rotates with  $p\omega_m$ .  $\omega_s$  is the stator angular speed, s is the slip,  $\omega_m$  is the mechanical angular speed of the rotor and p is the number of pole pairs. Due to the choice of the reference frame, the slip frequency will occur in all dq-variables. Since the slip frequency is small, the effect on the calculation time needed for a simulation is not that

The choice of the reference frequency slightly modifies the standard voltage equations of the

#### 5 MODELS OF WIND FARMS WITH VARIABLE SPEED PITCH TURBINES (VSP)

induction machine [13]. In the standard reference frame fixed to the stator angular speed, the voltage equations of the induction machine are (generator convention, sign convention according to IEC Standard 34-10):

$$v_{ds} = -R_s i_{ds} - \omega_s \Psi_{qs} - \frac{d}{dt} \Psi_{ds}$$

$$v_{qs} = -R_s i_{qs} + \omega_s \Psi_{ds} - \frac{d}{dt} \Psi_{qs}$$

$$v_{dr} = -R_r i_{dr} - s\omega_s \Psi_{qr} - \frac{d}{dt} \Psi_{dr} = 0$$

$$v_{qr} = -R_r i_{qr} + s\omega_s \Psi_{dr} - \frac{d}{dt} \Psi_{qr} = 0$$

For a reference frame fixed to the rotor (rotational speed  $p\omega_m$ ), the voltage equations of the induction machine are:

$$v_{ds} = -R_s i_{ds} - p\omega_m \Psi_{qs} - \frac{d}{dt} \Psi_{ds}$$

$$v_{qs} = -R_s i_{qs} + p\omega_m \Psi_{ds} - \frac{d}{dt} \Psi_{qs}$$

$$v_{dr} = -R_r i_{dr} - \frac{d}{dt} \Psi_{dr} = 0$$

$$v_{qr} = -R_r i_{qr} - \frac{d}{dt} \Psi_{qr} = 0$$

The stator angular speed  $\omega_s$  and the slip s are not present in this set of voltage equations. The flux equations are unchanged:

$$\Psi_{ds} = L_s i_{ds} + L_m i_{ds} 
\Psi_{qs} = L_s i_{qs} + L_m i_{qs} 
\Psi_{dr} = L_m i_{ds} + L_r i_{ds} 
\Psi_{qr} = L_m i_{qs} + L_r i_{qs}$$

The electromagnetic torque equals:

$$T_{el} = -\Psi_{ds}i_{qs} + \Psi_{qs}i_{ds} = \hat{\Psi}_s\hat{i}_s\sin\theta$$

In field oriented control, the current component in the direction of the flux and perpendicular to it are controlled. The current component perpendicular to the flux determines the electromagnetic torque of the machine. The current component in the direction of the flux determines the magnitude of the flux and thus the voltage of the stator. The flux is direction is not constant, the flux vector rotates with respect to the reference frame, also in steady state. This complicates the controller a bit, since the control still works in a reference frame fixed to the flux. A coordinate transformation determines the current component in the direction of the flux and perpendicular to it. These instantaneous current components are compared to the current setpoints, see figure 106. The setpoint for the current perpendicular to the flux is generated from the actual torque and the torque setpoint from a master control loop on the speed. In the variable speed turbine the torque setpoint is determined by the desired torque-speed curve. The setpoint of the current in the direction of the flux is generated from the actual flux and the flux setpoint from a second master control loop on the voltage. The resulting controller output voltages are back-rotated to align with the rotor reference frame.

Before applying these voltages to the stator, a further adjustment is required. The stator voltage equations include cross-coupling terms, linking the voltage in one direction to the flux in the

other direction  $(-p\omega_m\Psi_{qs})$  and  $p\omega_m\Psi_{ds}$  and thus to the currents in the other direction . These cross-coupling terms are dominant: they are several magnitudes larger than the other two term in the stator voltage equation. The cross-coupling leads to bad controlability, but can easily be eliminated by subtracting the cross-coupling terms from the voltages fed to the stator of the induction machine. This completes the control of the machine side converter, see figure 106.

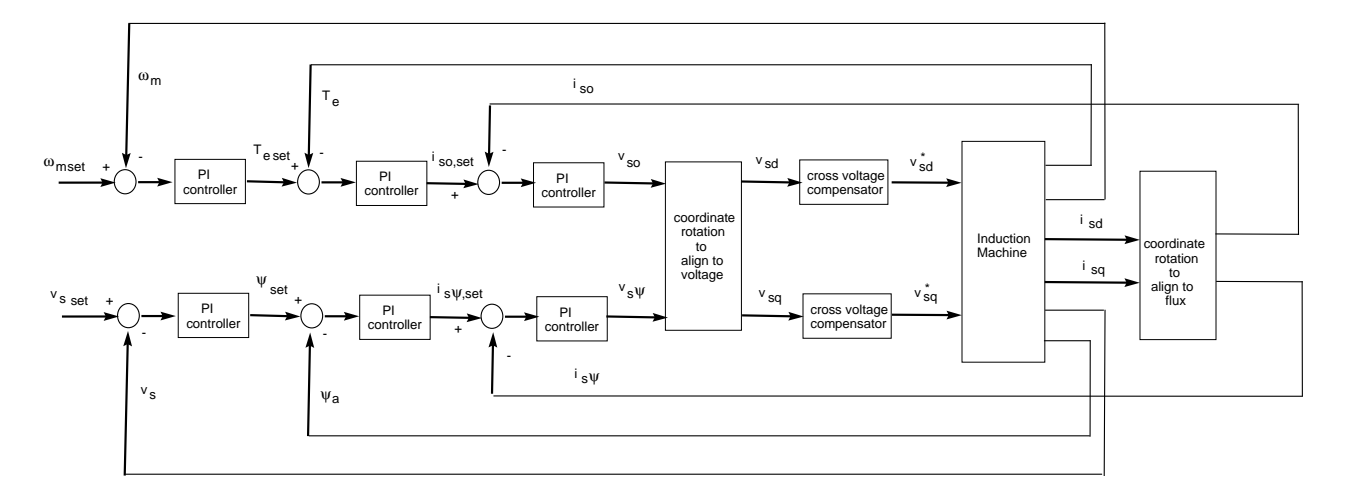


Figure 106: FCIG control diagram

Summarizing, the characteristic elements of the control of the machine side converter of the FCIG system are:

- a coordinate system is chosen which is fixed to the rotor. The advantage is that the electrical frequency of the stator is not an explicit variable in the voltage equations;
- field oriented control is used;
- a coordinate rotation is used to switch between the rotor fixed and the field coordinates;
- the chosen coordinate system will not result in constant space vector variables in steady state;
- two sets of master-slave control loops are used to control the speed and the stator voltage respectively;
- the cross-coupling in the voltage equation is compensated.

Figures 107 to 109 give the implementation of the VSP-FCIG-ac system in Simulink. The items mentioned in the previous paragraph can be identified as separate blocks in figure 109.

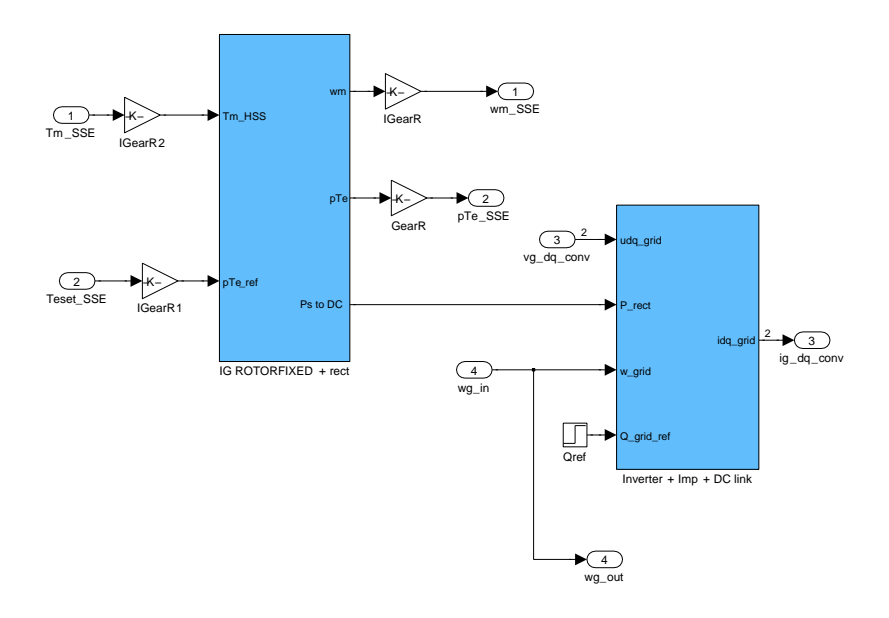


Figure 107: VSP-FCIG-ac Simulink model at the level of the DC link connecting rectifier and inverter

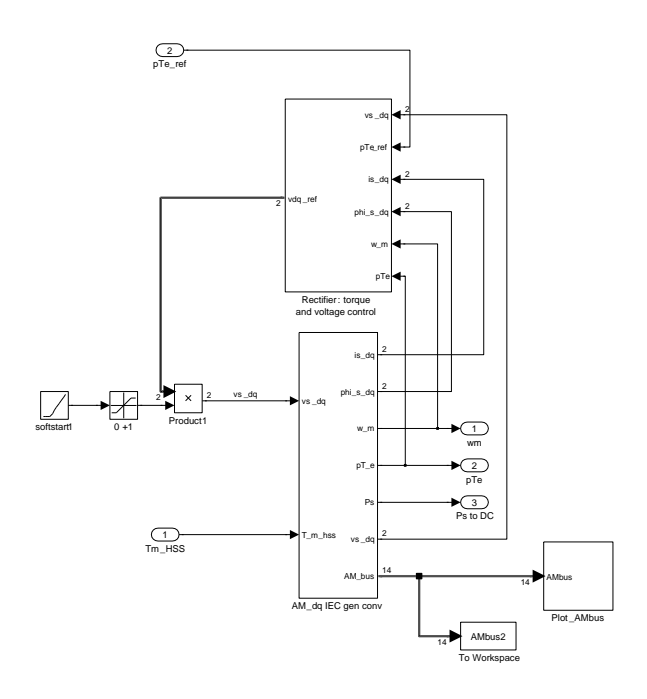


Figure 108: VSP-FCIG-ac Simulink model at the level of the rectifier and induction machine

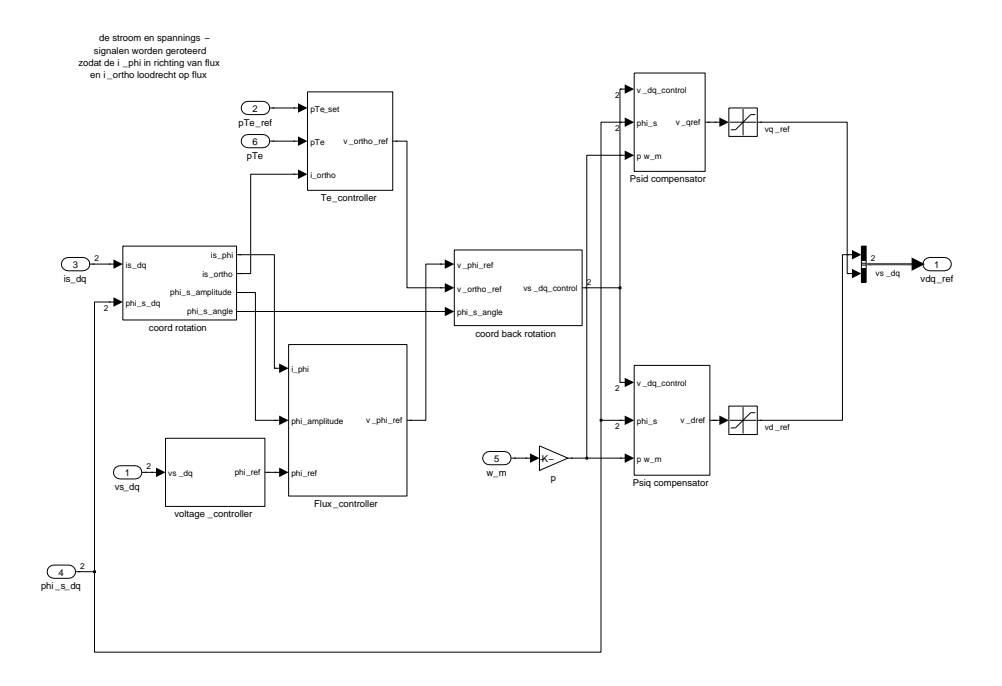


Figure 109: VSP-FCIG-ac Simulink model showing the rectifier controller

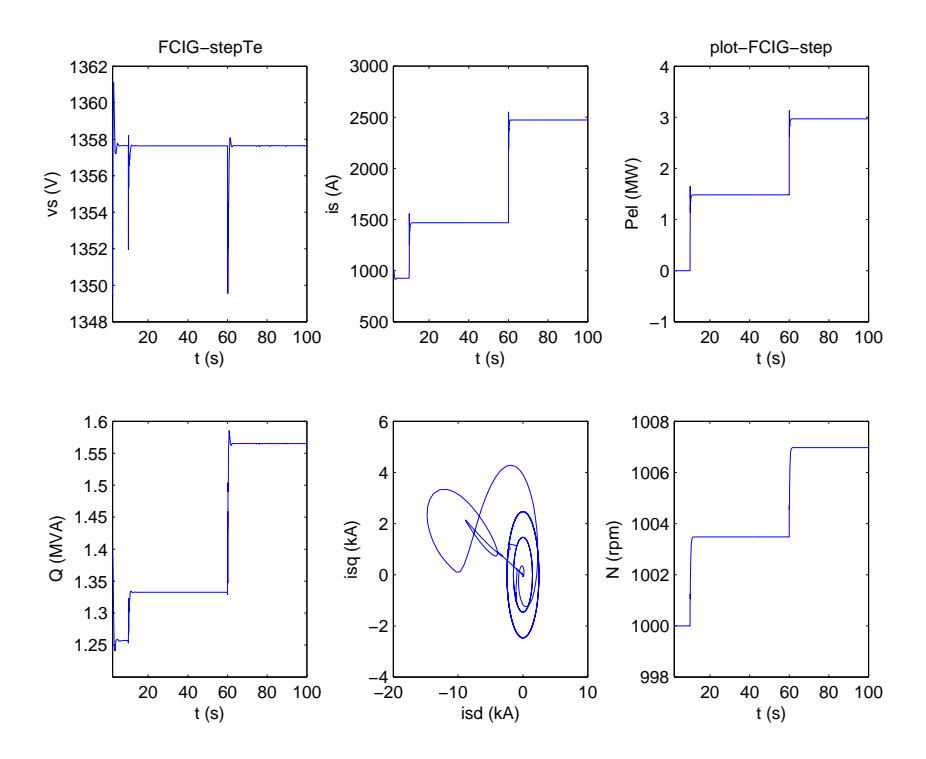


Figure 110: FCIG response to two steps in torque setpoint: stator voltage, stator current, power, reactive power, stator q-current versus stator d-current and rotor speed

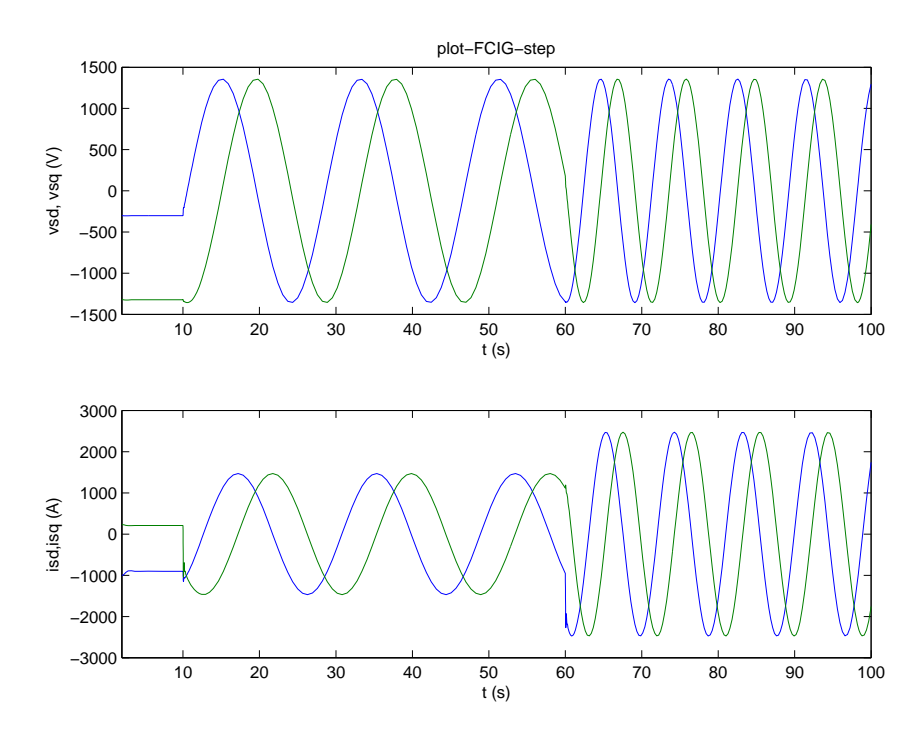


Figure 111: FCIG response to two steps in torque setpoint: voltage and current vector components

Figures 110 and 111 show the response of the rectifier control to a step in the torque setpoint. The input mechanical torque changes in the same way as the setpoint, to keep the speed practically constant. The electrical torque follows the torque setpoint almost instantly. Figure 111 shows the effect of the torque on the frequency of the dq-variables.

#### 5.4.2 VSP-FCIG-ac wind farm normal operation

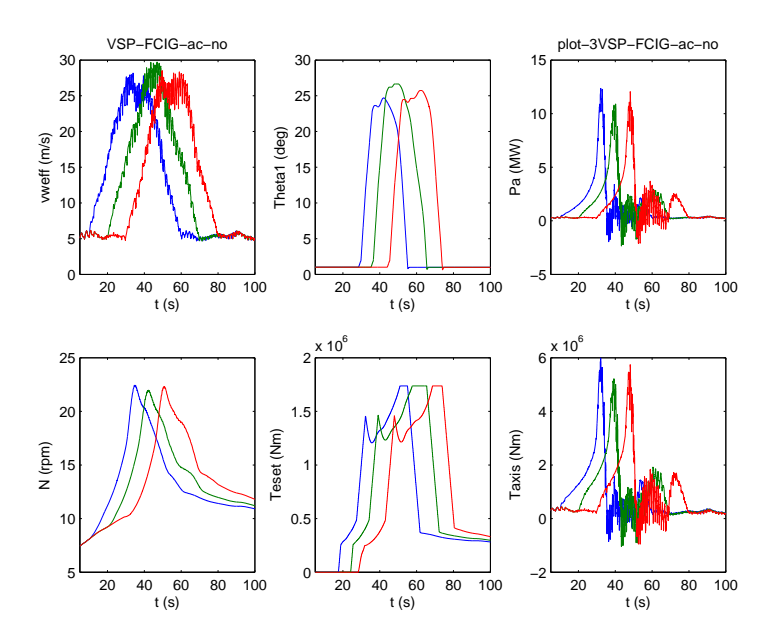


Figure 112: VSP-FCIG-ac normal operation: wind speeds, pitch angles, aerodynamic power, rotor speeds, electric torque setpoints and mechanical torque of the three turbines

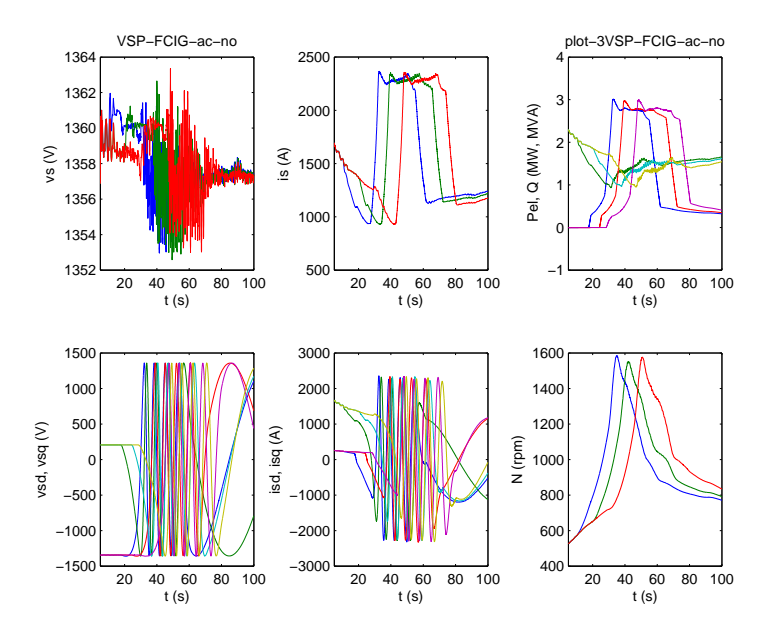


Figure 113: VSP-FCIG-ac normal operation: stator voltages, stator currents, active and reactive powers, stator dq-voltages, stator dq-currents and rotational speeds of the three turbines

Figure 112 demonstrates the VSP-FCIG-ac wind farm with three turbines for a wind speed increase from about 5 m/s to about 27 m/s and back again. The turbine speeds increase to 27 rpm and the pitch control reduces the aerodynamic power to prevent overspeeding. The torque setpoint is linked to the turbine speed. Figure 113 shows that the electric power control of the FCIG limits the power to the desired maximum and gives the reactive power needed by the induction machine which is supplied by the machine side converter. The rectifier keeps the

stator voltage almost constant. As described in the previous section, the stator dq-voltage and dq-current phasors rotate with respect to the rotor reference frame.

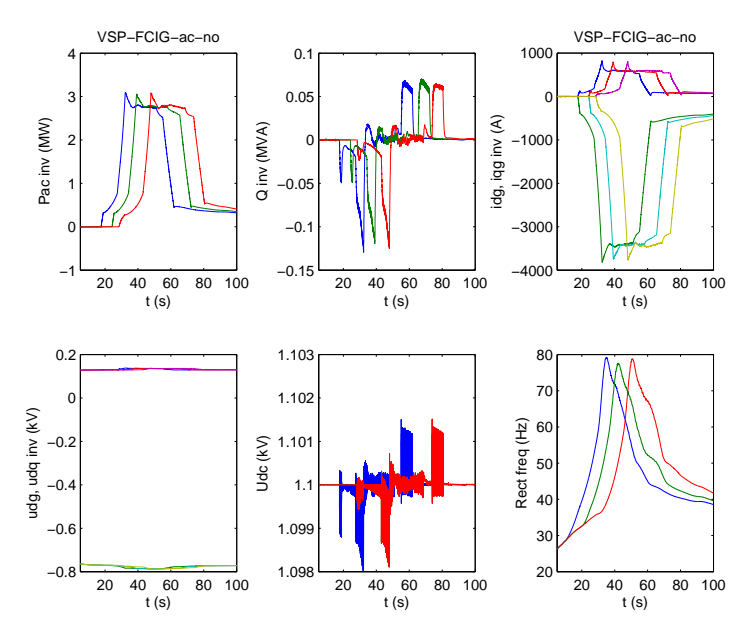


Figure 114: VSP-FCIG-ac normal operation: Inverter active and reactive power, inverter dq-currents, inverter dq-voltages, DC voltage and rectifier frequencies

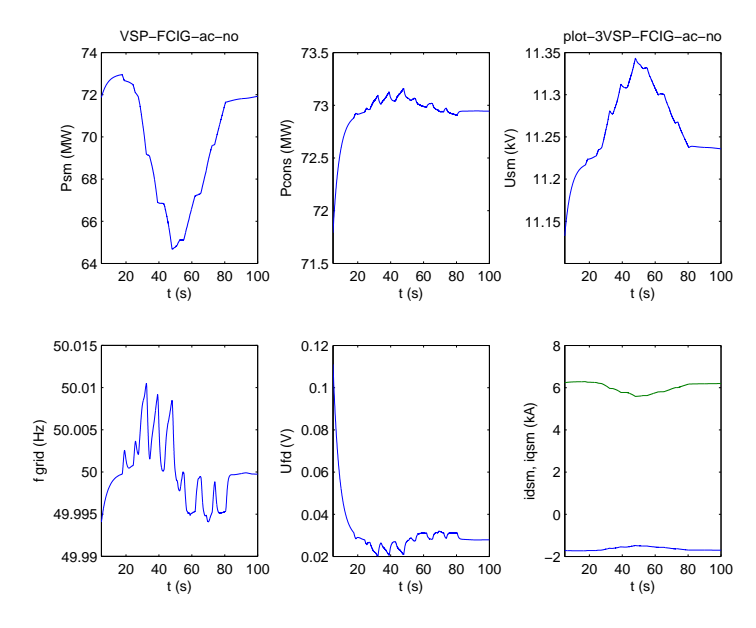


Figure 115: VSP-FCIG-ac wind farm, normal operation: grid synchronous generator power, consumer load, synchronous machine voltage, grid frequency, exciter voltage and synchronous machine d and q currents

As can be expected for a variable speed system the wind farm output power changes relatively slowly, without oscillations and the grid responds correspondingly (figure 115).

## 5.5 Wind farm with a VSP-FCSM-ac electric system (# 7)

## 5.5.1 VSP-FCSM-ac layout and control

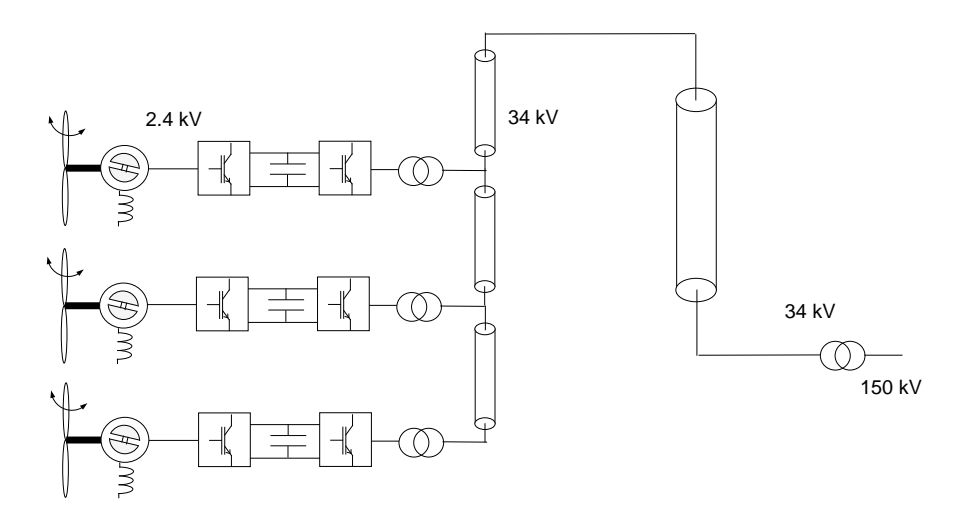


Figure 116: Variable speed pitch wind farm with full converter controlled synchronous generators and AC connection to shore

Figure 116 shows the layout of a variable speed pitch controlled wind farm with full converters, synchronous generators (VSP-FCSM) and AC connection to shore. The operation of the VSP-FCSM is simular to the system with full converters and permanent magnet generators developed in the Erao-2 project [33]. The difference is the controllable field current. Since the synchronous generator is connected to an IGBT converter, the field current control is not strictly required. Compared to the induction machine with full converter, described in the previous section, there are a number of differences. Due to the DC current in the rotor of the synchronous machine, the rotor flux rotates with the same speed as the rotor, in contrast to the flux of an induction machine, which rotates with the slip frequency with respect to the rotor. The control of the torque of the synchronous machine by the machine side converter is less complicated. A transformation between the rotor fixed reference frame and the reference frame fixed to the flux, is not required. The dq-reference system is fixed to the rotor with the d-axis aligned to the rotor field. The stator d-current is in the direction of the rotor field and the q-current is perpendicular to it.

The synchronous machine model to be used is the three winding representation, damper windings are not taken into account. Generator convention is adopted:

$$u_d = -R_s \cdot i_d - \omega_s \cdot \Psi_q - \frac{d\Psi_d}{dt}$$

$$u_q = -R_s \cdot i_q + \omega_s \cdot \Psi_d - \frac{d\Psi_q}{dt}$$

$$u_{fd} = R_{fd} \cdot i_{fd} + \frac{d\Psi_f}{dt}$$

with the electromagnetic fluxes:

$$\begin{array}{rcl} \Psi_d & = & L_d \cdot i_d + L_{md} \cdot i_{fd} \\ \Psi_q & = & L_q \cdot i_q \\ \Psi_f & = & L_{md} \cdot i_d + L_f \cdot i_{fd} \end{array}$$

The electromagnetic torque equals:

$$T_e = p \cdot (\Psi_q \cdot i_d - \Psi_d \cdot i_q)$$

If the stator current in the d-axis is controlled to zero, the torque can be controlled by the stator current in the q-axis. The field current can be used to adjust the internal voltage of the machine, it will not control the stator voltage, which is realised by the converter. Figure 117 gives the control diagram of a full converter controlled synchronous generator with an optional loop for the adjustment of the field current. The cross-coupling terms in the voltage equations of the stator of the synchronous machine are compensated.

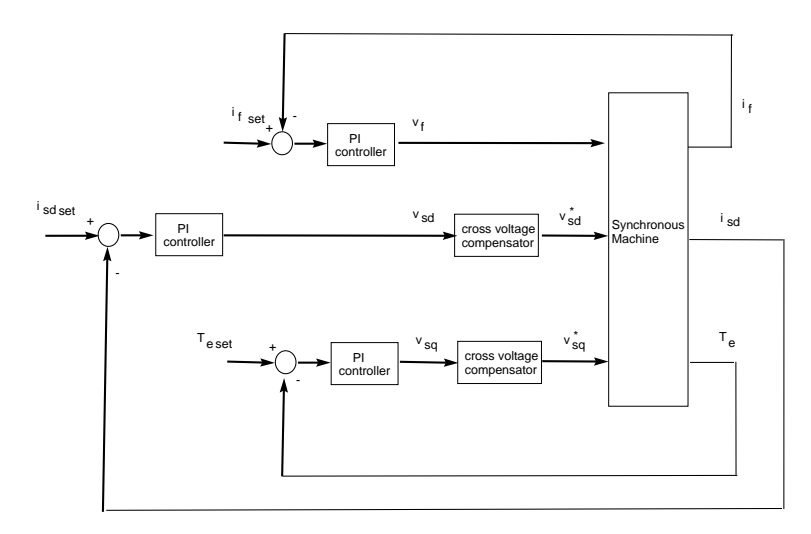


Figure 117: Control diagram of a full converter controlled synchronous generator

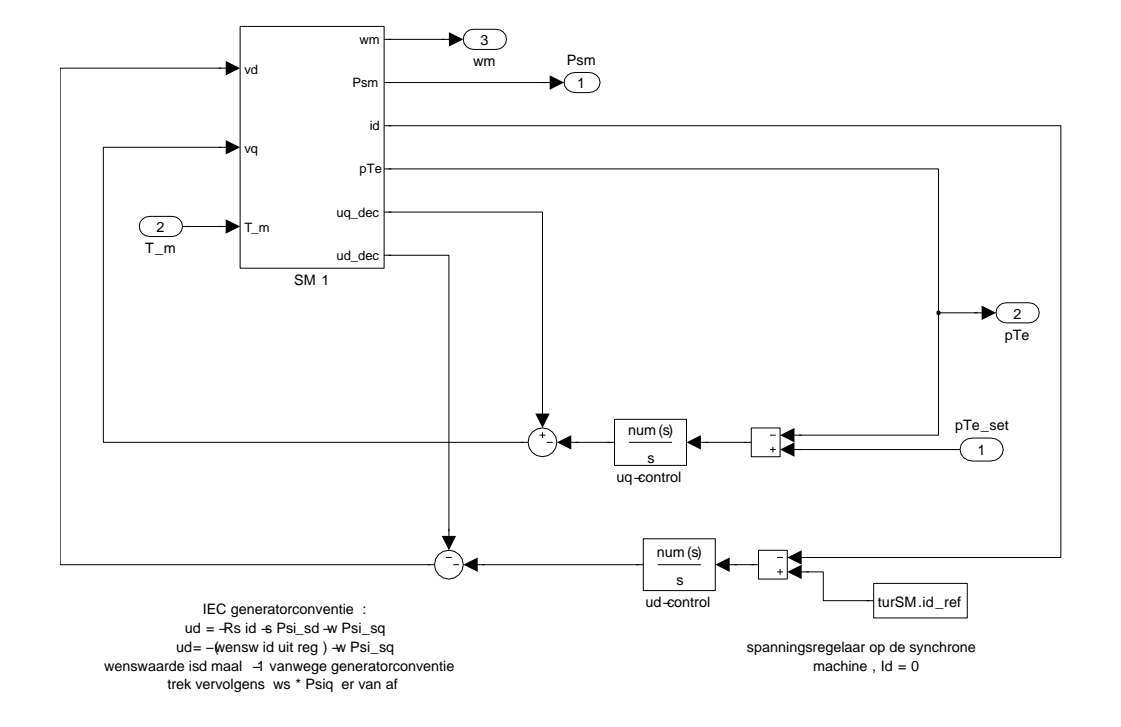


Figure 118: VSP-FCSM-ac Simulink model with synchronous generator and rectifier controllers

Figure 118 shows the implementation of the synchronous generator and rectifier controllers in Simulink.

# Choice of a suitable synchronous generator and determination of the machine parameters

For the demonstration of the VSP-FCSM-ac system, the parameters of a synchronous machine with a rated power of about 3 MW are required. A suitable machine was found in the Power Systems Blockset of Simulink. The machine's rated power is 3.25 MW and the parameter list is based on the standard data sheet for synchonous machines. This requires a conversion between data sheet parameters and the parameter set used in the we@sea synchronous machine model. Appendix F lists the conversion to model parameters.

#### 5.5.2 VSP-FCSM-ac wind farm normal operation

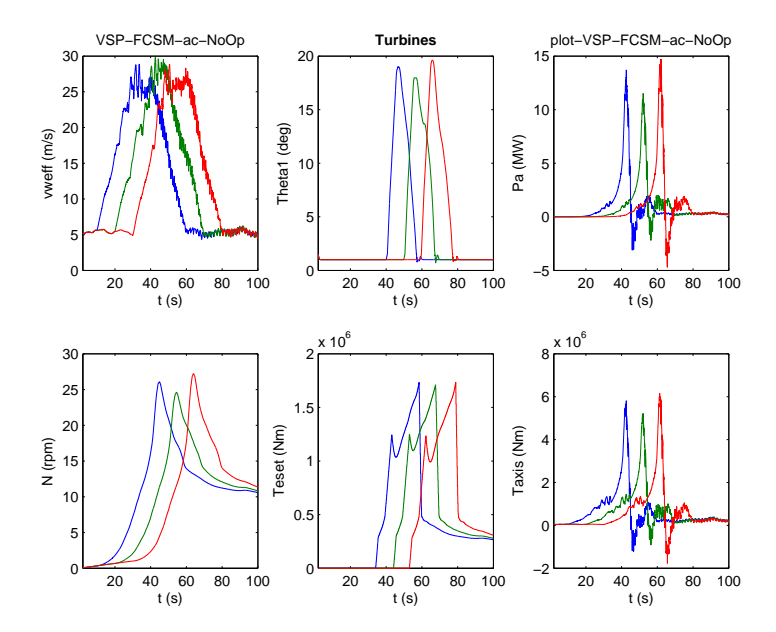


Figure 119: VSP-FCSM-ac normal operation: wind speeds, pitch angles, aerodynamic power, rotor speeds, electric torque setpoints and mechanical torque of the three turbines

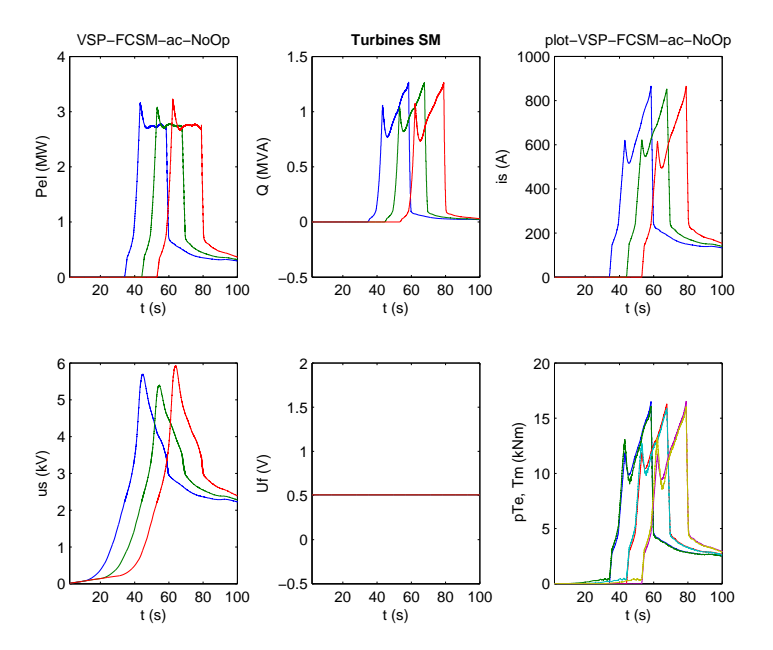


Figure 120: VSP-FCSM-ac wind farm, normal operation: power, reactive power, stator current, stator voltage, exciter voltage, electrical and mechanical torque per turbine

Figure 119 demonstrates the VSP-FCSM-ac model with 3 turbines. The response to the wind gust is similar to the response of the previous system (VSP-FCIG-ac). The pitch control prevents overspeeding. The rectifier controller limits the power to the rated power, with some overshoot during the steep increase in wind power and speed. The  $i_d$  setpoint is zero. The field voltage  $u_f$  is constant, resulting in a constant field current in steady state. The stator voltage increases with turbine speed (in steady state practically equal to the product of speed and flux). The stator current first follows the increase in electric power and the increase further at constant power and decreasing voltage. The reactive power more or less follows the current changes. Using the field control on the synchronous machine, the response can be optimized. The response of the inverters is shown in figure 121.

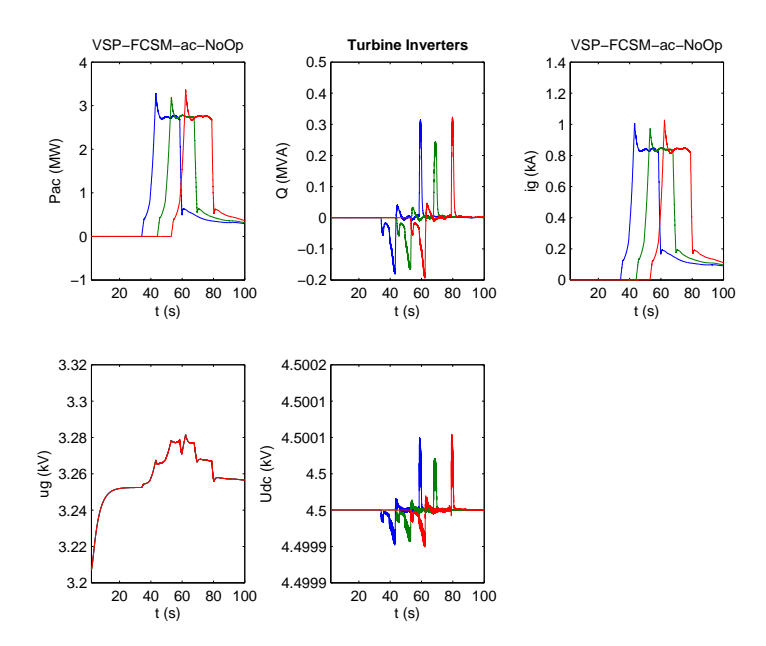


Figure 121: VSP-FCSM-ac wind farm, normal operation: power and reactive power, AC voltage, AC current and DC voltage

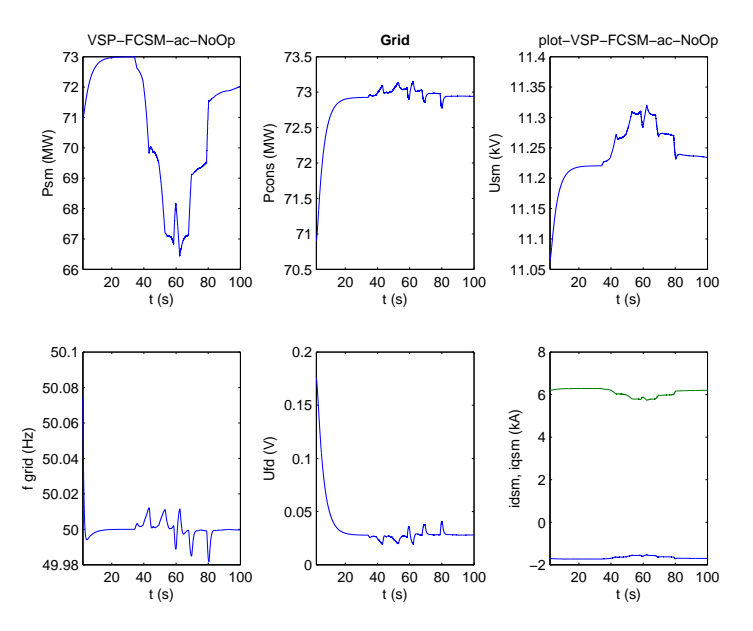


Figure 122: VSP-FCSM-ac wind farm, normal operation: grid synchronous generator power, consumer load, synchronous machine voltage, grid frequency, exciter voltage and synchronous machine d and q currents

The reaction of the grid to the changing output of the wind farm is shown in figure 122.

# 5.6 Wind farm with a VSP-FCSM-dc electric system (# 8)

# 5.6.1 VSP-FCSM-dc layout and control

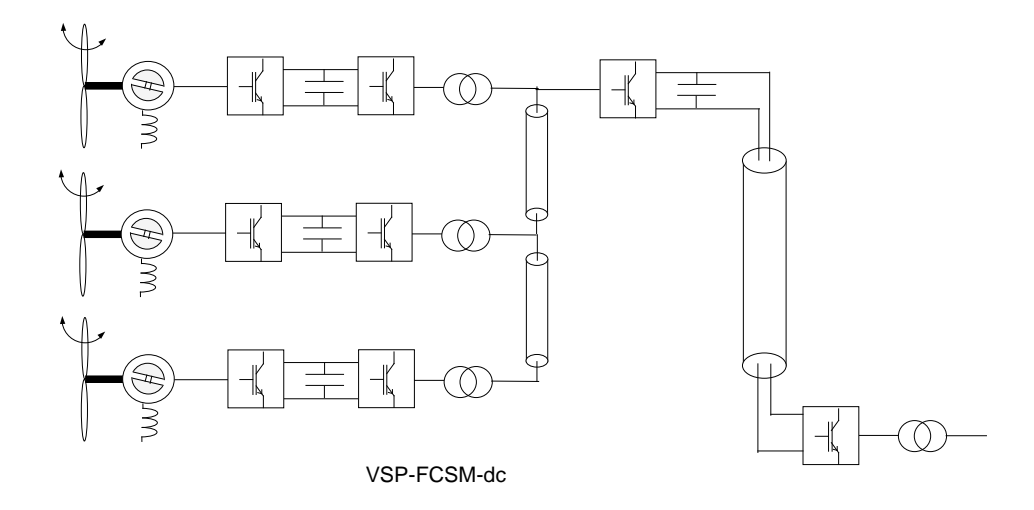


Figure 123: Variable speed pitch controlled WF with converter controlled synchronous generators and DC connection to shore (VSP-FCSM-dc)

The VSP-FCSM-dc wind farm main components and connection are shown in figure 123. The VSP-FCSM is operated in the same way as in the previous system with AC connection. Figure 124 shows the Simulink model of the wind farm converter.

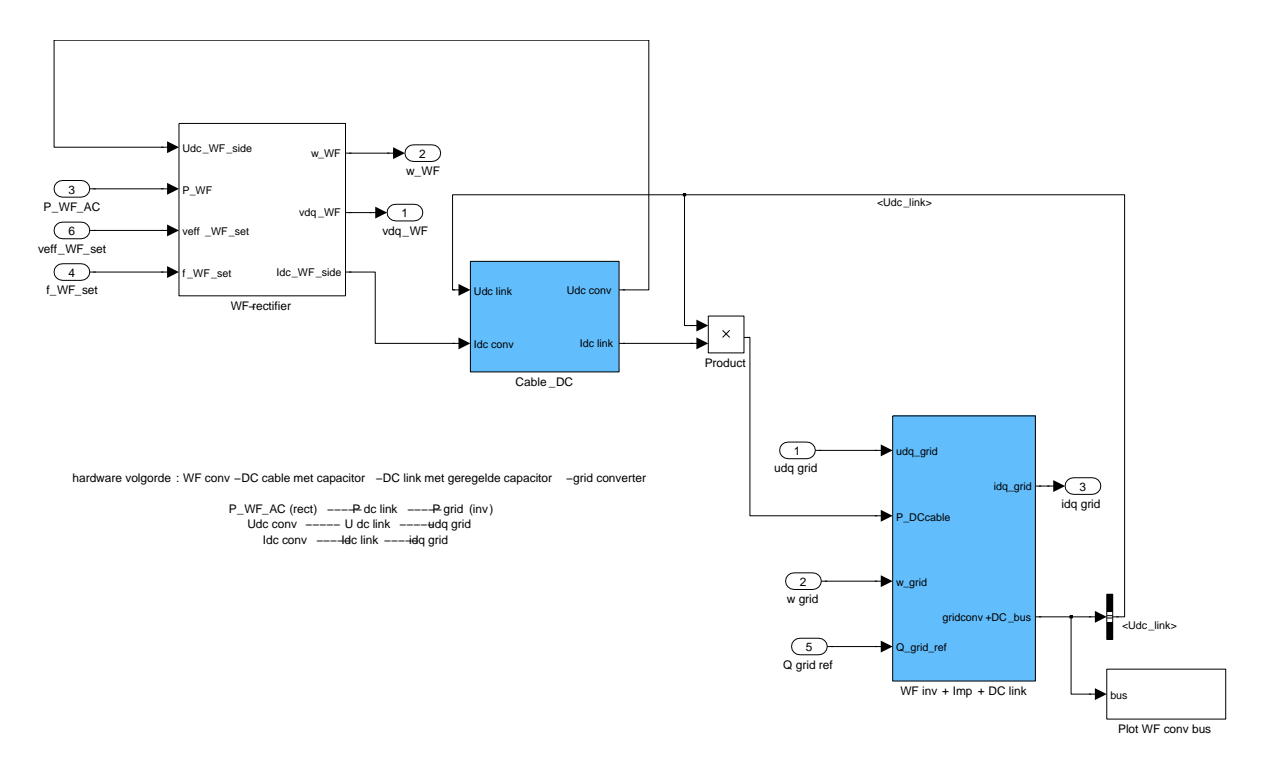


Figure 124: VSP-FCSM-dc Simulink model: wind farm converter

#### 5.6.2 VSP-FCSM-dc wind farm normal operation

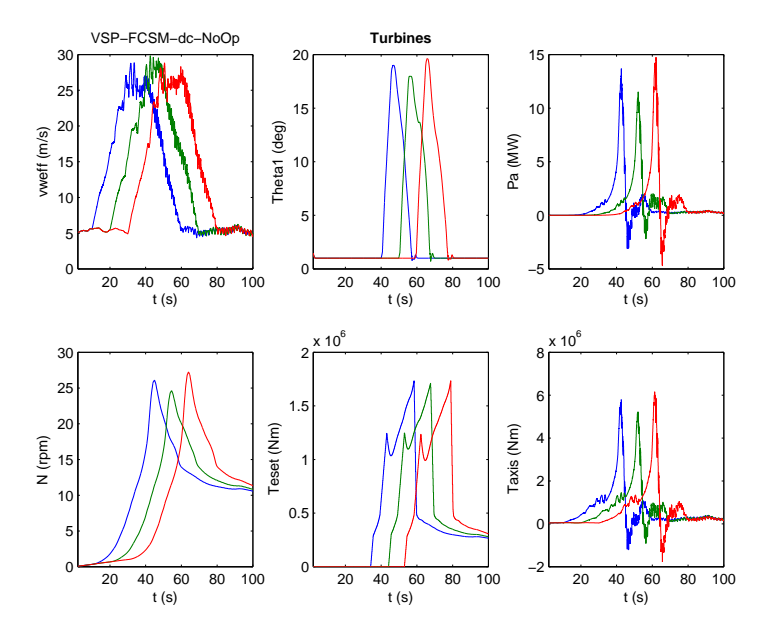


Figure 125: VSP-FCSM-dc normal operation: wind speeds, pitch angles, aerodynamic power, rotor speeds, electric torque setpoints and mechanical torque of the three turbines

The wind farm converter generates a constant voltage and frequency at the wind farm side. The response of the VSP-FCSM-dc wind farm will be similar to the response of the VSP-FCSM-ac system. This is shown in figure 125. The response of the turbine inverters (figure 127) and the grid (figure 129) is also similar to the VSP-FCSM-ac wind farm. The wind farm converter response is shown in figure 128.

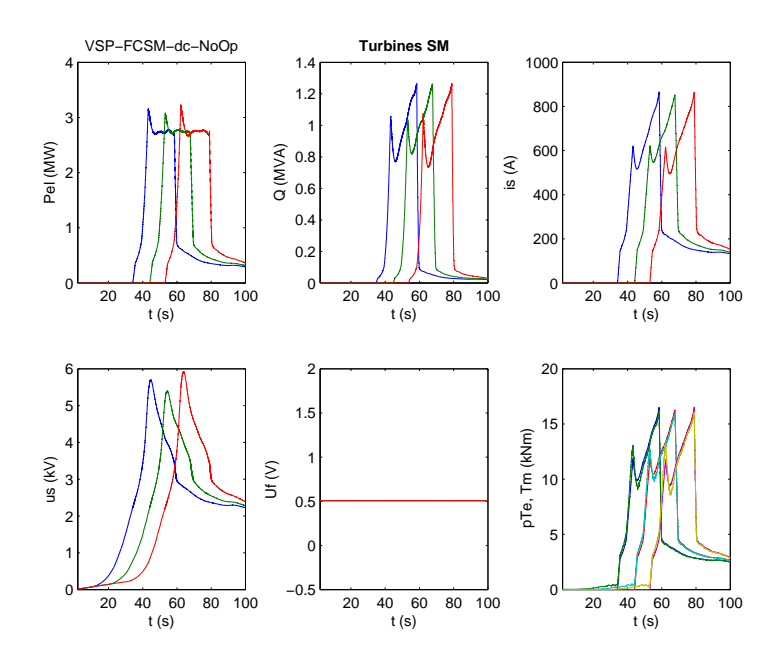


Figure 126: VSP-FCSM-dc normal operation: power, reactive power, stator current, stator voltage, exciter voltage, electrical and mechanical torque per turbine

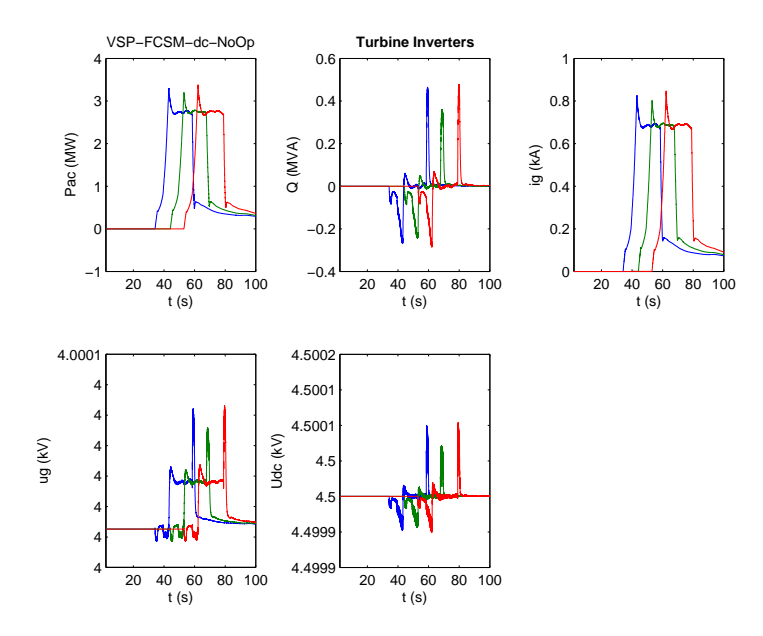


Figure 127: VSP-FCSM-dc wind farm, normal operation: power and reactive power, AC voltage, AC current and DC voltage

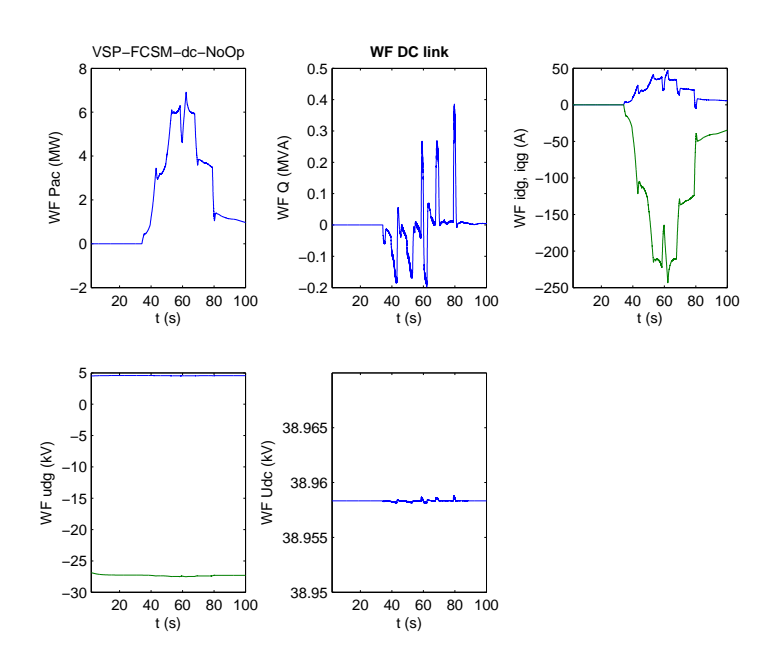


Figure 128: VSP-FCSM-dc wind farm, normal operation: Wind farm converter power, reactive power, dq-current, dq-voltage and DC voltage

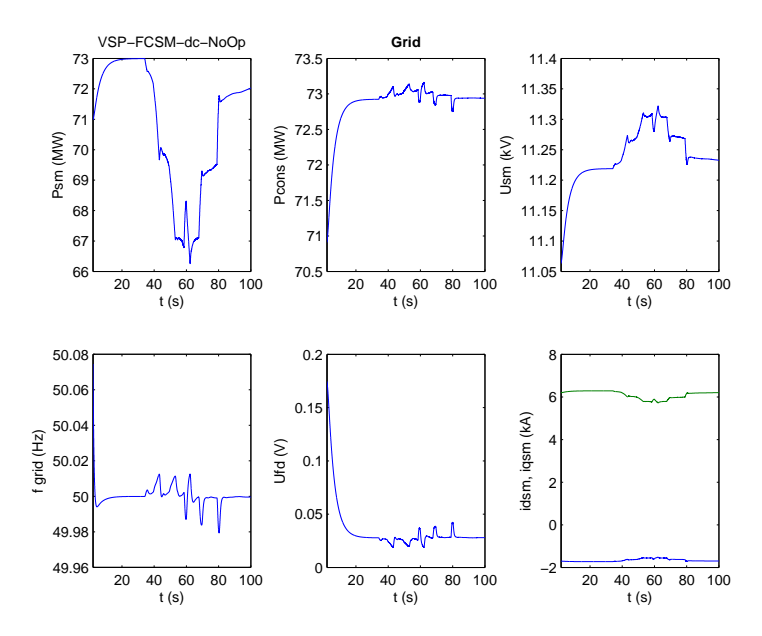


Figure 129: VSP-FCSM-dc wind farm, normal operation: grid synchronous generator power, consumer load, synchronous machine voltage, grid frequency, exciter voltage and synchronous machine d and q currents

## 6 Wind farm with a VSP-DFIG-thy electric system (# 9)

#### 6.1 Objective

The control the multiple DFIG systems connecting to a thyristor bridge is new and not well investigated. In literature, the DFIGs are considered to be connected to a strong power grid, which means that the voltage at the point of common coupling is practically constant when the power and reactive power of the DFIGs are varying. Traditionally, the thyristor bridge is used to connect two strong power grids. Connecting multiple wind turbine DFIG systems to a thyristor bridge will lead to problems with the traditional control of the DFIG. To use the traditional grid-flux oriented controller of the DFIG in a wind farm connected to a thyristor bridge requires:

- reactive power compensation to keep the voltage level of the wind farm constant;
- a control strategy for the thyristor bridge in coordination with the DFIG converters of the individual wind turbines.

During transient operation, imbalances of active power between wind turbines and thyristor bridge will cause voltage fluctuations. To prevent these fluctuations, a centralized controller, additional reactive power compensation system or an energy storage device can be used but this will increase the total cost of the wind farm and a potential economical advantage of this concept may be lost.

In this case study, effective controllers will be developed which can control the active power of each wind turbine independently without the necessity of a centralized controller or an additional reactive power compensation system.

The objective of this case study is to:

- model the DFIG-thy system in Matlab/Simulink;
- determine the steady state behavior of the DFIG-thy system;
- develop the control the DFIG-thy system, i.e. to:
  - control P and Q of each wind turbine independently;
  - control the whole system: DFIGs and thyristor bridge P and Q in coordination.

#### 6.2 DFIG-thy Steady State

#### 6.2.1 System layout

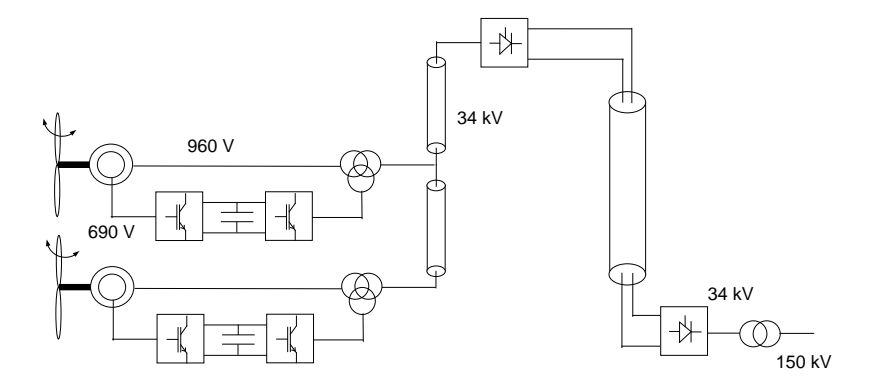


Figure 130: Variable speed pitch controlled WF with doubly fed induction generators and thyristor based DC connection to shore (VSP-DFIG-th)

The system investigated in this case study is shown in Figure 130. A group of DFIGs is connected in parallel and integrated with power grid through a HVDC thyristor bridge link.

#### 6.2.2 Steady State Calculation

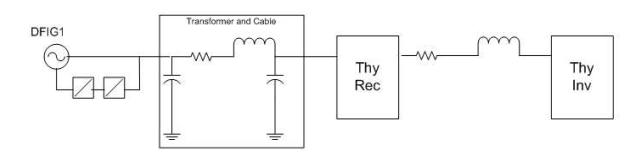


Figure 131: Topology of Steady State Calculation

In order to understand the behavior of the DFIG-Thyristor system and to design appropriate controllers for the wind farm, the steady state behaviour is calculated first. A simplified steady state model is used which includes the main electrical components and contains only one DFIG. The purpose is to calculate the rotor voltages in relation to changes of active power, rectifier AC voltage and mechanical speed. Two steady state calculations have been made:

- (i) The AC voltage at thyristor rectifier side  $V_{rec}$  and the active power through the thyristor rectifier  $P_{rec}$  are given, the firing angle  $\alpha_{rec}$  of the thyristor rectifier is calculated;
- (ii) The firing angle  $\alpha_{rec}$  of the thyristor rectifier is set to 14 degree and the active power through the thyristor rectifier  $P_{rec}$  is given, the thyristor rectifier AC voltage  $V_{rec}$  is calculated.

The procedure of the calculation is:

(i) The inverter firing angle  $\alpha_{inv}$  and the inverter AC voltage  $V_{inv}$  are constant.  $I_{dc}$  can be calculated when  $P_{rec}$  is known:

$$R_{dclink}I_{dc}^2 + V_{dcinv}I_{dc} = P_{dcrec} (56)$$

 $V_{dcrec}$  is calculated and the firing angle  $\alpha_{rec}$  or  $V_{rec}$  of the rectifier is calculated.

- (ii) The active power and reactive power flow to the rectifier is calculated, thus the AC current flow to the rectifier can be calculated. The AC current in the cable is the sum of the AC current of rectifier and shunt capacitor. Then the AC voltage across the cable can be calculated.
- (iii) In the same way as in the previous step, the stator voltages and stator currents of DFIG are calcultated and from the generator equations the rotor currents and rotor voltages are calcultated.

The results are given as 3D plots which have the active power  $P_{rec}$  and the per unit mechanical rotation speed  $\frac{\omega_m}{\omega_g}$  as coordinates. They are shown in figures 132 to 135. The model is listed in appendix F.7.

# Steady state Calculation 1:

Input variables:  $P_{rec}$ ,  $V_{rec}$ , Output variables:  $\alpha_{rec}$ , voltages and currents of DFIG

# 6 WIND FARM WITH A VSP-DFIG-THY ELECTRIC SYSTEM (# 9)

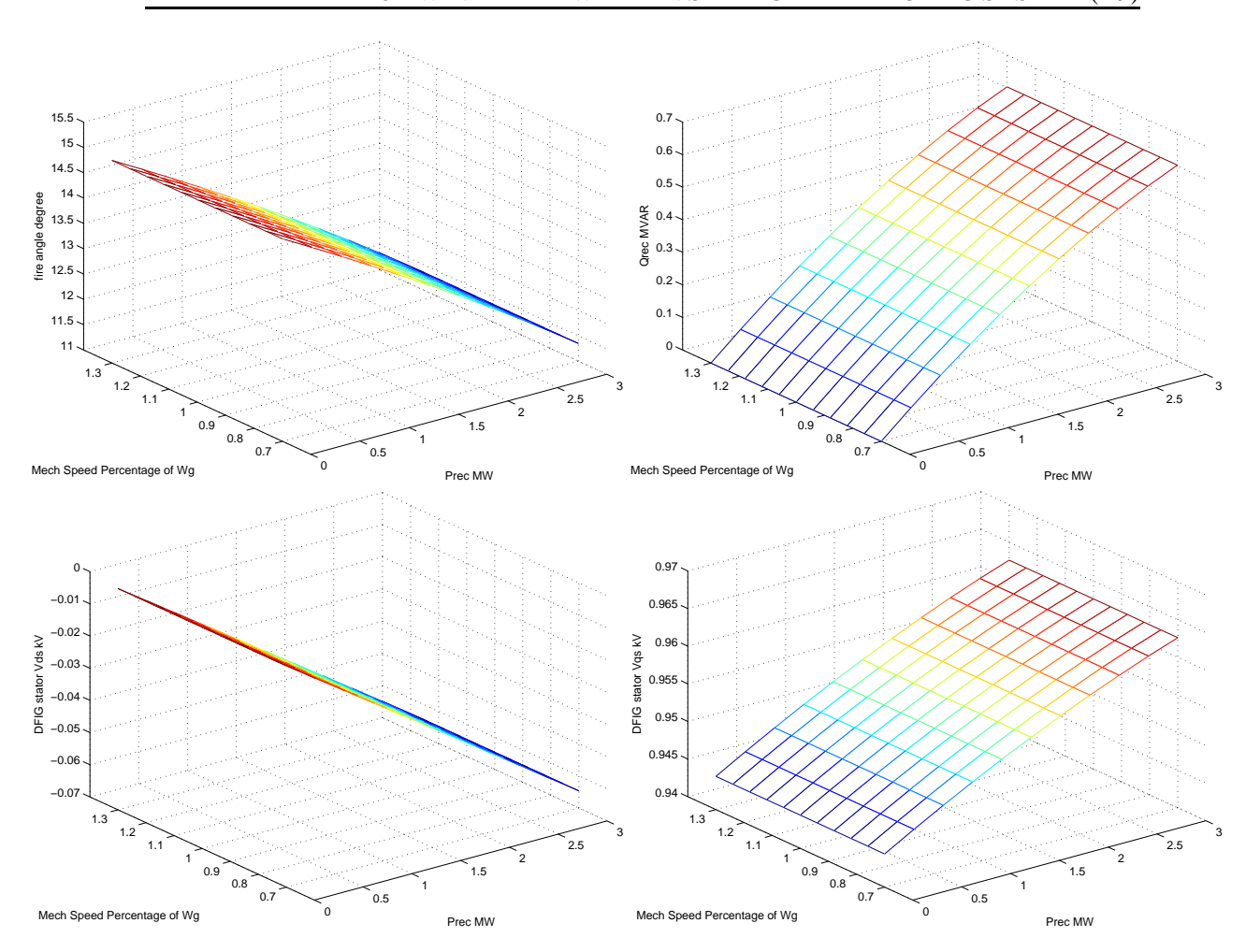


Figure 132: Steady state calculation 1: Rectifier firing angle, rectifier reactive power, stator d- and q-voltage as function of mechanical speed and rectifier power

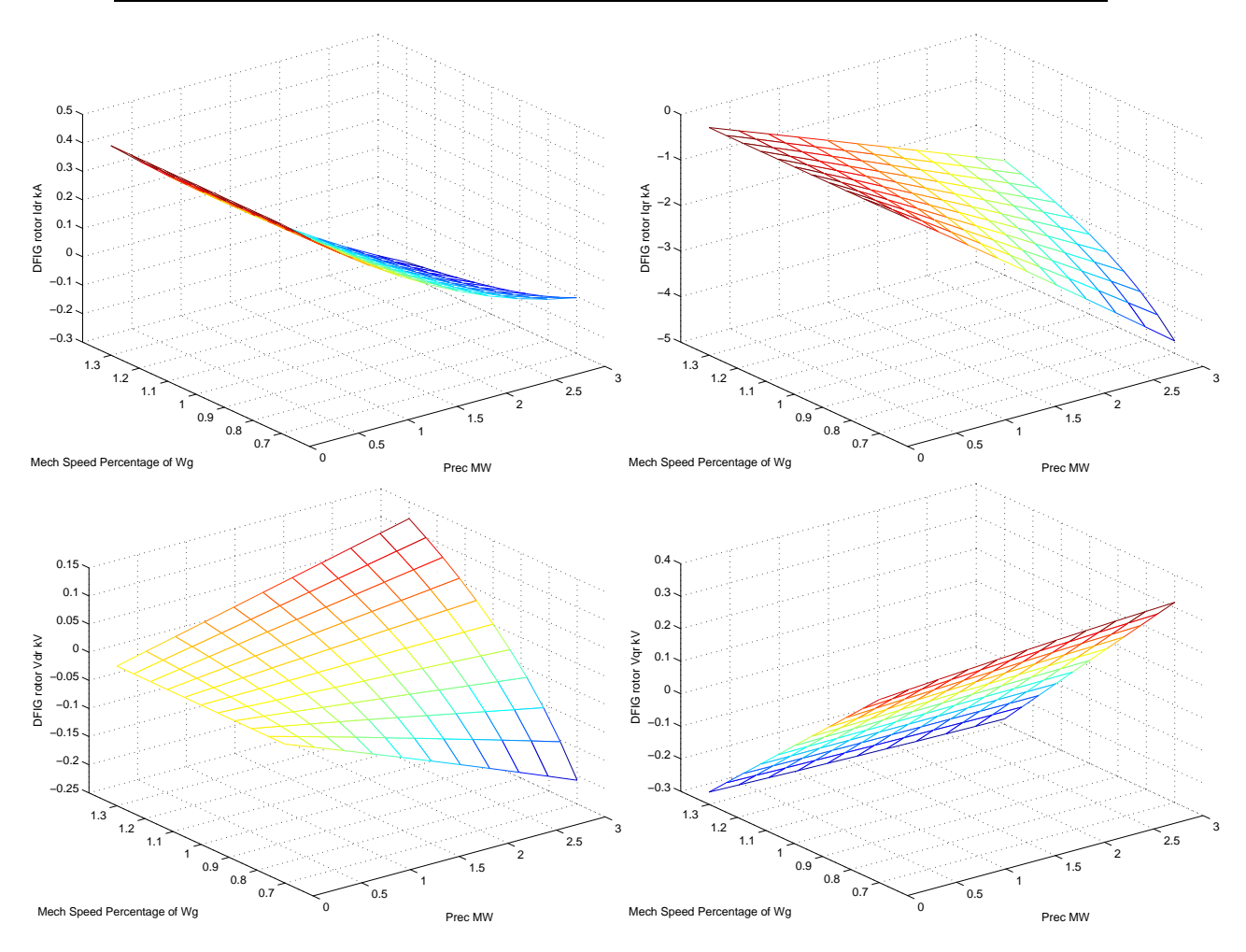


Figure 133: Steady state calculation 1: Rotor d- and q-current, rotor d- and q-voltage as function of mechanical speed and rectifier power

Steady state Calculation 2: Input variables:  $P_{rec}$ ,  $\alpha_{rec}$ , Output variables:  $V_{rec}$ , voltages and currents of DFIG

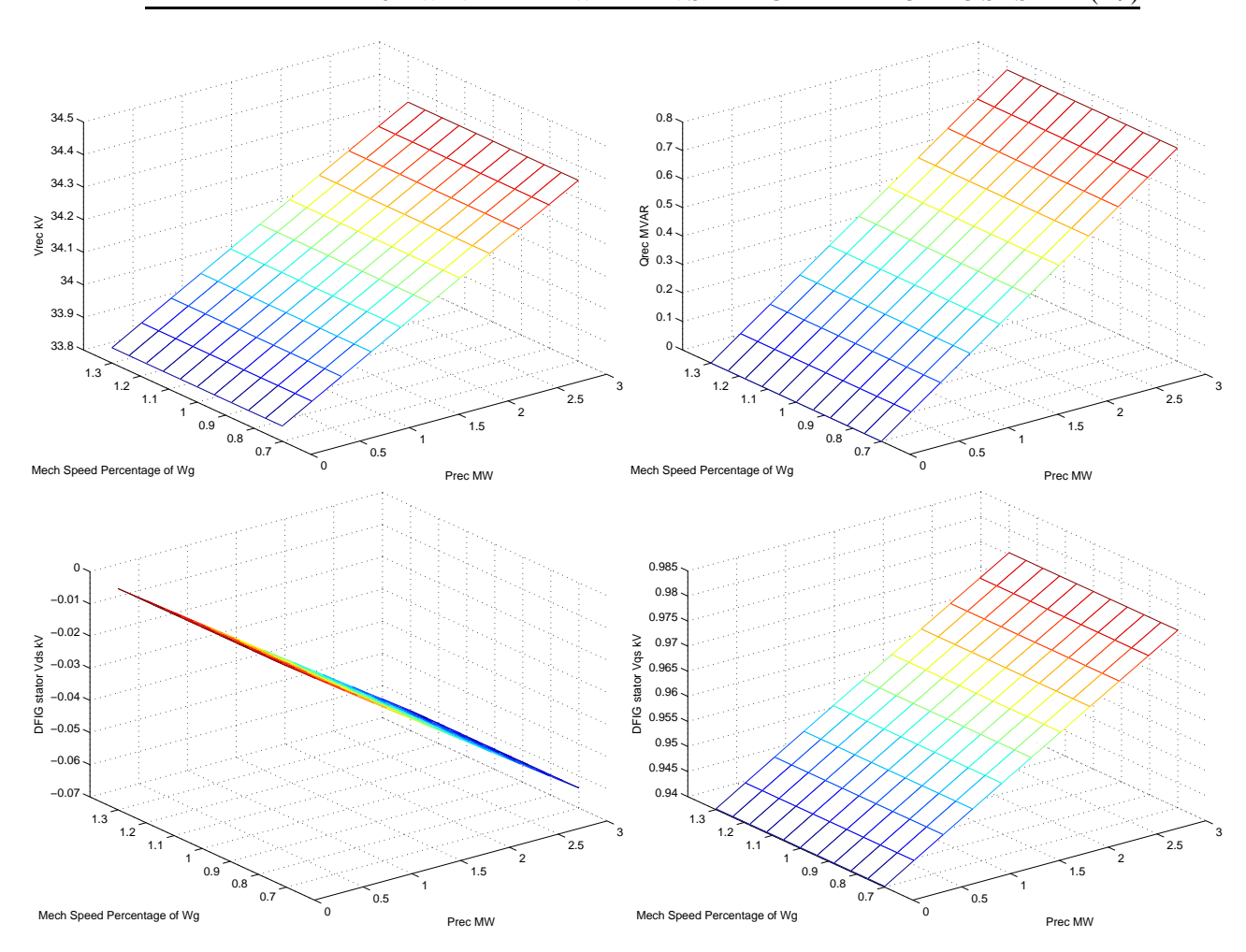


Figure 134: Steady state calculation 2: Rectifier firing angle, rectifier reactive power, stator d- and q-voltage as function of mechanical speed and rectifier power

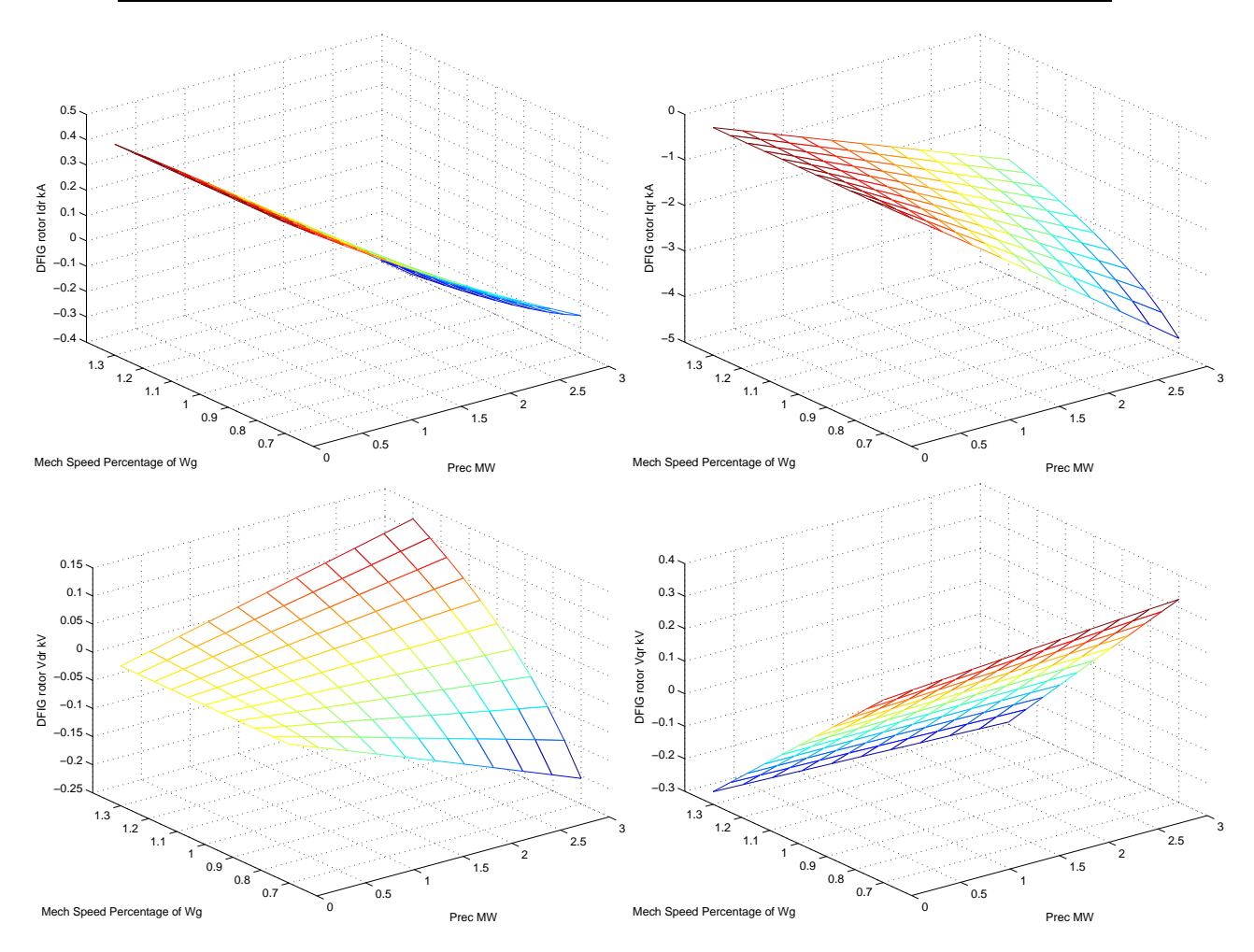


Figure 135: Steady state calculation 2: Rotor d- and q-current, rotor d- and q-voltage as function of mechanical speed and rectifier power

The result of calculation 1 and 2 shows that the change of  $V_{dr}$  and  $V_{qr}$  are smooth in relation to  $P_{rec}$  and  $w_m$ . When  $V_{rec}$  or  $\alpha_{rec}$  of is fixed, it is possible to use  $V_{dr}$  and  $V_{qr}$  to control the active power.

As discussed in section 6.1, maintaining AC voltage  $V_{rec}$  can be difficult during transient states. In steady state calculation 2, the firing angle of the rectifier is kept constant which gives the rectifier the characteristics of an (almost) constant impedance load. By varying the voltage magnitude in the wind farm, the total active power can be controlled.

# 6.3 Control of DFIG-thy

# 6.3.1 Traditional P, Q control in high voltage transmission power system

In order to effectively control active power P and reactive power Q, they have to be effectively decoupled in such a way that controlling one will not influence the other. In a high voltage power grid with high inductance, the reactive power flow is only related to magnitude differences of voltages and active power flow is only related to angle differences of voltages. This is based on the following equations:

$$\Delta V = |V_i| - |V_j| = \frac{PR + QX}{|V_i|} \approx \frac{QX}{|V_i|}$$
(57)

$$\delta_{vi} - \delta_{vj} = \frac{PX - QR}{|V_j|} \approx \frac{PX}{|V_j|} \tag{58}$$

From equations 57 and 58, we can see that only if X>>R, P and Q are decoupled. Decoupling is guaranteed in a high voltage transmission power grid, since the high voltage power grid is based on relatively high reactance over-head power transmission lines. In low or middle voltage distribution power grids which are constructed using cables, the reactance X is often of the same order of magnitude as the resistance R. Then P and Q both influence the voltages' magnitudes and phase angles. An offshore wind farm is also connected by cables and X is not much larger than R, so P and Q are coupled in the voltage magnitudes and phase angles. The traditional P, Q controller in high voltage transmission power system cannot be used to control the DFIG-thy system, we have to find a way to decouple P and Q.

#### 6.3.2 Traditional Grid-Flux Oriented Control of DFIG

Nearly all literature on DFIG control considers the situation where a DFIG is connected to a stiff power grid. When a DFIG is connected to a strong power grid, the voltage at point of common coupling will not be influenced by the active and reactive power of DFIG. From this fact, a grid-flux oriented controller is developed, which can control P and Q of DFIG independently [25, 18, 1, 28, 5]. The grid-flux oriented controller aligns the DFIG's stator flux along its d-axis by choosing a reference frame whith the q-axis in the direction of the grid voltage phasor. Because the grid voltage is stiff, the  $v_{ds}$  and  $v_{qs}$  will maintain almost constant when P and Q of DFIG varies, so  $v_{ds}$  remains practically zero. By choosing this reference frame, the stator fluxs  $\psi_{qs}$ =0 and  $\psi_{ds}=|\psi|$ .

The equations of the DFIG are:

$$v_{ds} = -R_s i_{ds} - \omega_s \psi_{qs} + \frac{d\psi_{ds}}{dt}$$
 (59)

$$v_{qs} = -R_s i_{qs} + \omega_s \psi_{ds} + \frac{d\psi_{qs}}{dt}$$
 (60)

$$v_{dr} = -R_r i_{dr} - s\omega_s \psi_{qr} + \frac{d\psi_{dr}}{dt}$$
 (61)

$$v_{qr} = -R_r i_{qr} + s\omega_s \psi_{dr} + \frac{d\psi_{qr}}{dt}$$
 (62)

$$T_e = p(\psi_{ds}I_{qs} - \psi_{qs}I_{ds}) \tag{63}$$

$$\psi_{ds} = -(L_s + L_m)i_{ds} - L_m i_{dr} \tag{64}$$

$$\psi_{qs} = -(L_s + L_m)i_{qs} - L_m i_{qr} \tag{65}$$

$$\psi_{dr} = -(L_s + L_m)i_{dr} - L_m i_{ds} \tag{66}$$

$$\psi_{qr} = -(L_s + L_m)i_{qr} - L_m i_{qs} \tag{67}$$

If the stator resistance  $R_s$  can be omitted, and we assume steady state, equations 59 and 60 can be simplified to:

$$v_{ds} = -\omega_s \psi_{qs} = 0 \tag{68}$$

$$v_{qs} = \omega_s \psi_{ds} = |v_s| \tag{69}$$

From these equations, the active and reactive power P and Q as function of the stator voltages and the rotor currents are:

$$P_{s} = v_{ds}i_{ds} + v_{qs}i_{qs} = v_{qs}\frac{L_{m}}{L_{s} + L_{m}}i_{qr}$$
(70)

$$Q_{s} = v_{qs}i_{ds} - v_{ds}i_{qs} = \frac{v_{qs}}{L_{s} + L_{m}}\psi_{ds} - \frac{v_{qs}L_{m}}{L_{s} + L_{m}}i_{dr}$$
(71)

Thus, P and Q are decoupled, and can be controlled independently by the rotor currents  $i_{qr}$  and  $i_{dr}$  respectively. The rotor currents are controlled by the rotor voltage  $v_{dr}$  and  $v_{qr}$  through PI controllers. But in the DFIG-thy case, the wind farm grid is weak when the rectifier is treated as a constant impedance load: the voltage will be variable and depending on the load. The P and Q of the DFIGs will strongly influence the  $v_{ds}$  and  $v_{qs}$  at the point of common coupling. As  $v_{ds}$  and  $v_{qs}$  fluctuate when P and Q of the DFIGs vary, it is not possible in practice to find a reference system whose  $v_{ds}$  remains zero under transient states. The AC voltage of the wind farm is difficult to control. The traditional dynamic reactive power controllers such as SVC or STATCOM may be not able to control the voltage magnitude of wind farm, because the mismatch of active power between wind farm and thyristor bridge under transient states will cause dynamic voltage fluctuations. An energy storage device may be required to maintain a constant voltage in the wind farm.

So the traditional way to decouple P and Q in high voltage transmission power system and the traditional grid-flux oriented controller of DFIG cannot be used in this case study. The traditional firing angle controller of the thyristor bridge could be used but needs an energy storage device to control the voltage in the wind farm. Including an energy storage device or a STATCOM is expensive and the objective of this study is to find a solution without a storage device.

Two new controllers will be developed in this case study: a terminal voltage controller and a stator-flux oriented controller. Both treat the thyristor bridge as a constant impedance load. They do not need an energy storage device in the wind farm and can control the active power transferred through the thyristor bridge. But they have some shortcomings:

- the terminal voltage controller has large power oscillations and the parameters of the PI controllers are sensitive:
- the stator-flux oriented controller is fast and does not have large oscillations, but it is not working properly at (almost) zero rectifier power.

The two controllers will be discussed in the following sections.

# 6.3.3 Terminal Voltage Control of DFIG-thy

In order to decouple P and Q, a method similar to the grid-flux oriented controller of DFIG is chosen. If  $v_{ds}=0$ , then P and Q are decoupled. In the DFIG-thy system,  $v_{ds}$  will not automatically be (almost) zero in the reference frame of the flux, due to the wind farm's fluctuating power. A possible solution is to use the rotor voltages  $v_{dr}$  and  $v_{qr}$  to control the terminal voltage  $v_{ds}$  and  $v_{qs}$  in this case.

#### Control of a single DFIG

First consider the control of a single DFIG. The rectifier can be seen as an impedance load if the firing angle is constant. It has a large resistance R and small reactance X, the ratio depends on the firing angle. If the firing angle is set to 14 degree, then  $R\approx 4X$ . Both P and Q are determined by the voltage magnitude:

$$P = \frac{R(v_{ds}^2 + v_{qs}^2)}{R^2 + X^2} \tag{72}$$

$$Q = \frac{X(v_{ds}^2 + v_{qs}^2)}{R^2 + X^2} \tag{73}$$

In the case of a single DFIG, if P is controlled then Q will be determined automatically. There is no need to add an explicit Q controller loop. The terminal voltage controller of single DFIG is shown in figure 136.

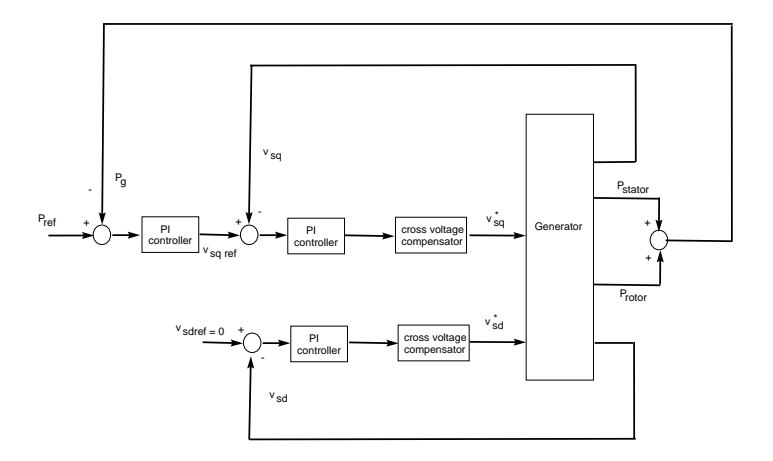


Figure 136: Terminal voltage controller of a single DFIG

#### Coordinated control of two or more DFIGs

In the case of controlling two or more DFIGs connected to the same thyristor rectifier, a change in P and Q of generator 1 will influence the terminal voltage of generator 2 which will again influence the P and Q of generator 2 and vice versa. This may cause large oscillations in the wind farm. Secondly, there may be a large amount of reactive power Q exchanged between the two generators. The reason is the setpoint for the d-component of the stator voltage,  $v_{ds}=0$  for all generators. The only possibility to change the active power flow between generator and thyristor bridge is to change  $v_{qs}$  at the generator. The voltage at the thyristor bridge is determined by the voltages at the two generators and the currents flowing to the bridge. This relation and the current resulting from it can create voltages at the two generators which are very different. A large reactive power exchange between the two DFIGs occurs, which is undesirable.

The solution is to add a Q controller to one of the DFIGs, which can change the reference value  $v_{dsref}$  by a small value. The other generator's reactive power Q will be determined by the wind farm rectifier reactive power demand. The Q control loop is shown in figure 137. Since the d-component of the stator voltage of one DFIG is no longer zero, the decoupling of P and Q is lost. P and Q are decoupled in the time scale by choosing different integration coefficient  $k_i$  of PI controller.

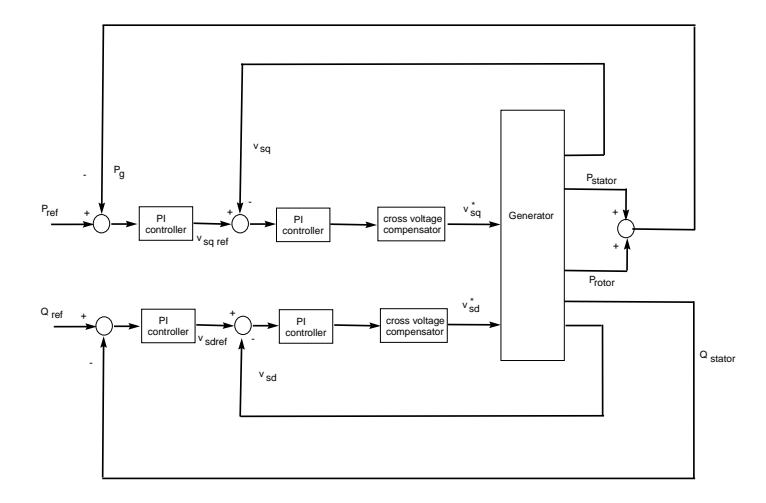


Figure 137: Terminal voltage contoller with Q loop

# **Dynamics of DFIG-thy Terminal Voltage Control**

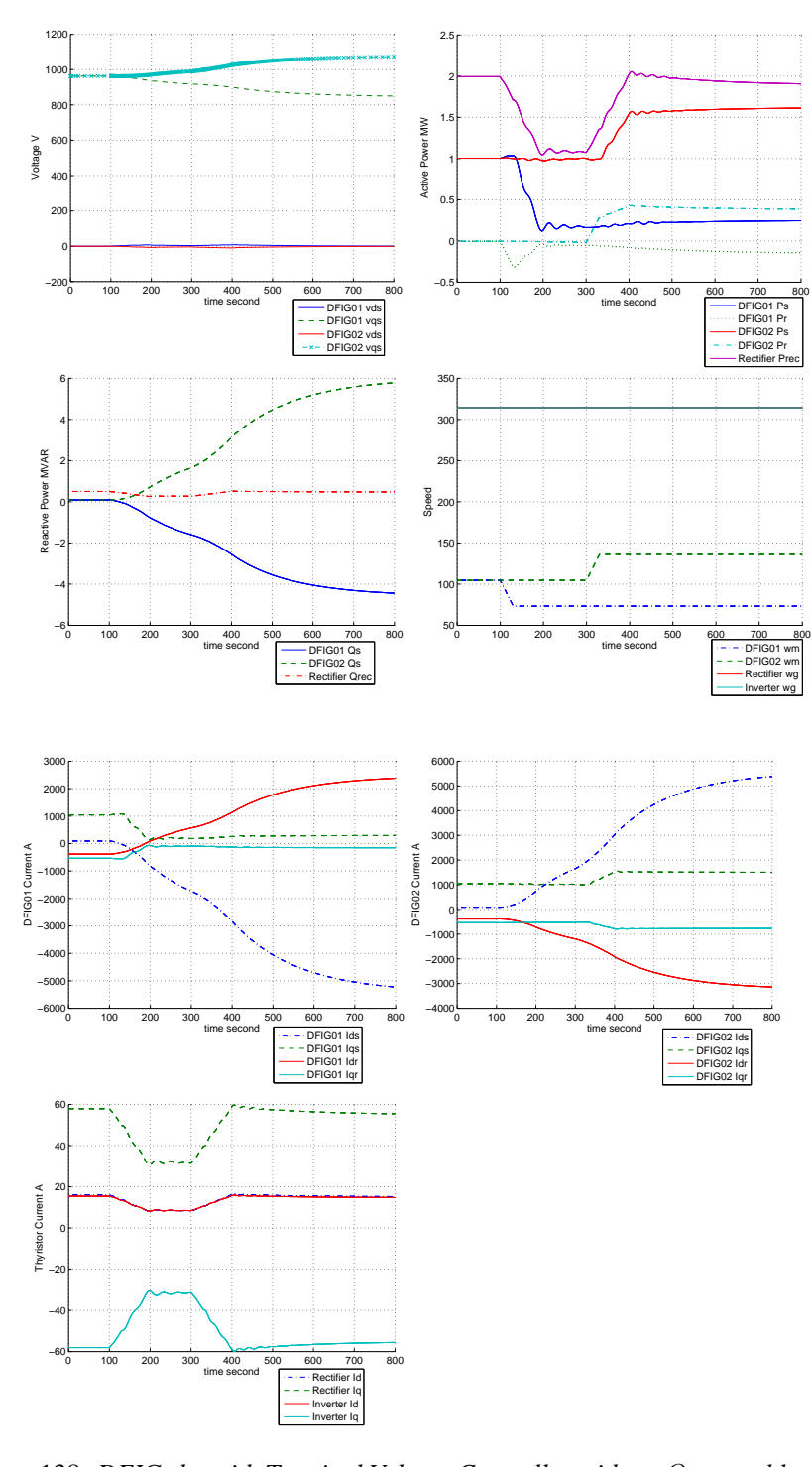


Figure 138: DFIG-thy with Terminal Voltage Controller without Q control loop

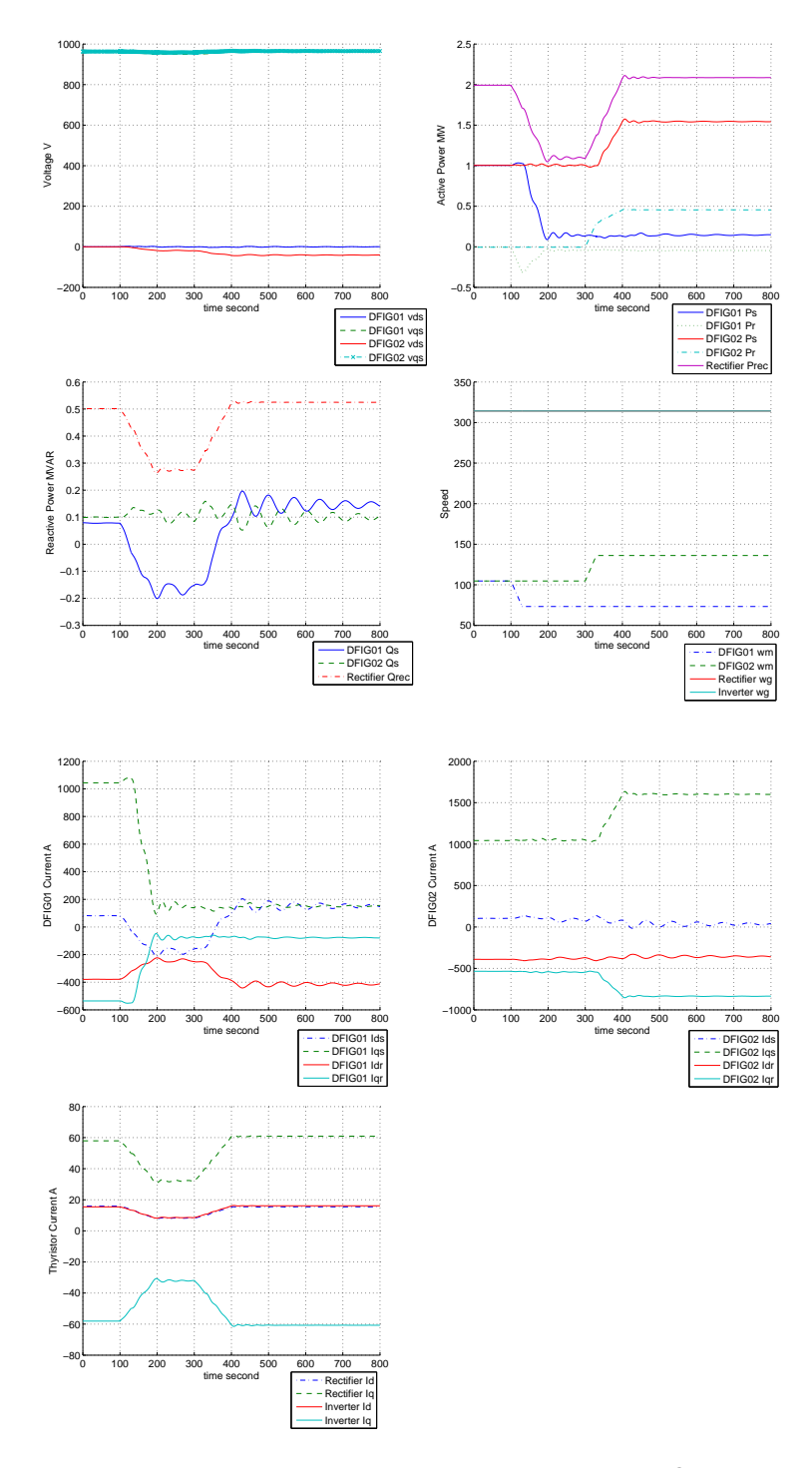


Figure 139: DFIG-thy with Terminal Voltage Controller with Q control loop

Figure 138 shows the effect of a decrease in speed of DFIG1 followed by an increase in speed of DFIG2. The setpoint of the power of DFIG1 is also decreased, while the setpoint of the power of DFIG2 is increased. The rectifier firing angle is constant. The changes in power have a large effect on the voltage magnitudes and the reactive power flowing between DFIG1 and DFIG2.

Figure 139 shows the effect of the same changes in setpoint as in figure 138 for the DFIG-Thy system with a reactive power controller on DFIG2. The setpoint changes cause reactive power changes at the thyristor rectifier, which are compensated by DFIG1. The DFIG voltage amplitudes are more or less constant now,  $v_{ds}$  of DFIG2 is no longer constant. The reactive power oscillations are not well damped.

Comparing figures 138 and 139, the explicit Q control loop avoids a large reactive power exchange between the two DFIGs. The terminal voltage controllers are sensitive, the PI controllers are difficult to tune.

# 6.3.4 Stator-Flux Oriented Control of DFIG-thy

# Control of a single DFIG

Pena [27] developed a flux controller for a single DFIG connected with an isolated load. This configuration is similar to our case of a DFIG connected to a thyristor bridge. The objective again is to make  $v_{ds}=0$ , but not directly by controlling the generator's terminal voltages, but by controlling the stator fluxes. Flux oriented control is considered superior to the terminal voltage controller, because the terminal voltages can be strongly polluted by the harmonics. From the stator voltage equation 59, under steady state, the stator voltage  $v_{ds}=0$  if  $\psi_{qs}$  can be controlled to zero. From stator flux equation 65,  $\psi_{qs}=0$  if we can control the rotor current:

$$i_{qr} = -\frac{(L_s + L_m)}{L_m} i_{qs} \tag{74}$$

This stator-oriented flux controller is fast and robust for a single DFIG, although it has some limitations:

- the flux level  $\psi_{ds}$  is set as constant, thus for a resistance dominated load, the load power is constant. Pena adds a variable load to balance the varying output power of the DFIG. This has to be modified for the DFIG-thy system;
- without modification the two DFIGs will exchange a large amount of reactive power again.

From stator equations 60 and 61 follows that the flux level determines the voltage level under steady state. The voltage level determines power P and reactive power Q according to equations 72 and 73. From torque equation 63, the reference of the flux level can be calculated by:

$$\psi_{ds}^* = \frac{T_e^*}{pi_{qs}} \tag{75}$$

when  $\psi_{qs}=0$  and p is the number of pole pairs of the generator. Same as for the terminal voltage controller, Q is determined when flux level  $\psi_{ds}$  is set. Figure 140 shows the controller for a single DFIG.

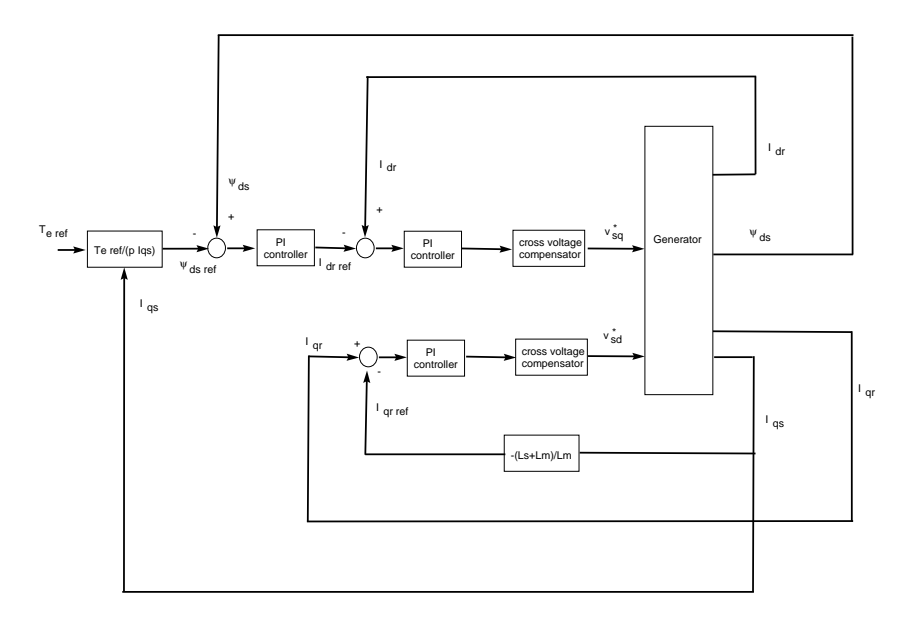


Figure 140: Stator-flux oriented controller of a single DFIG

### Coordinated control of two or more DFIGs

When controlling two or more generators, we have to avoid large reactive power exchange between close generators by adding a Q controller on one generator, allowing for a change in the stator flux  $\psi_{qs}$ . Since  $\psi_{qs}$  is no longer zero, the decoupling of P and Q is lost. P and Q are decoupled in the time scale by choosing different integration coefficient  $k_i$  of PI controller.

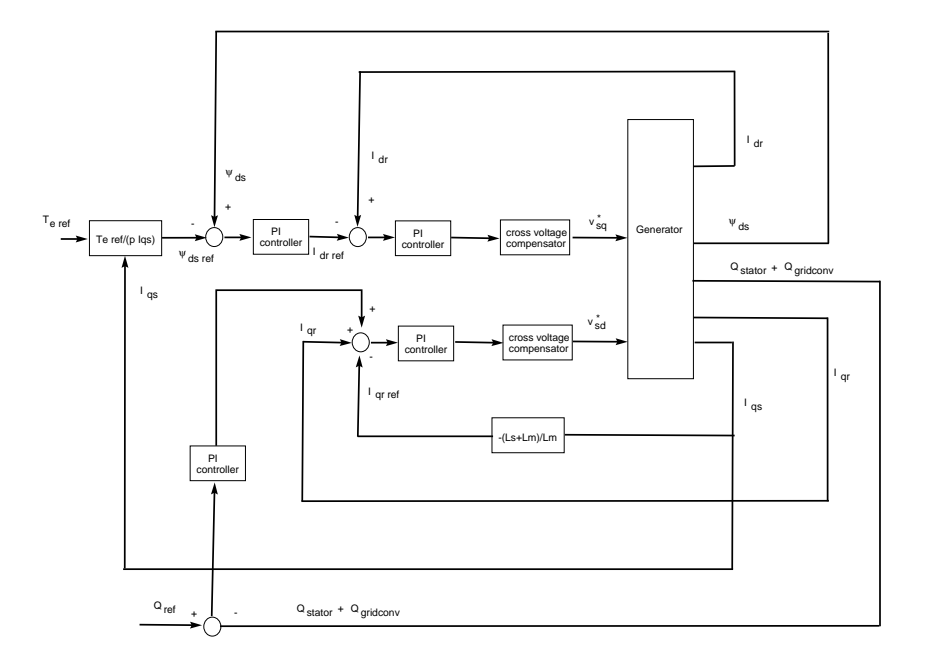


Figure 141: Stator-flux controller of DFIG with explicit Q control loop

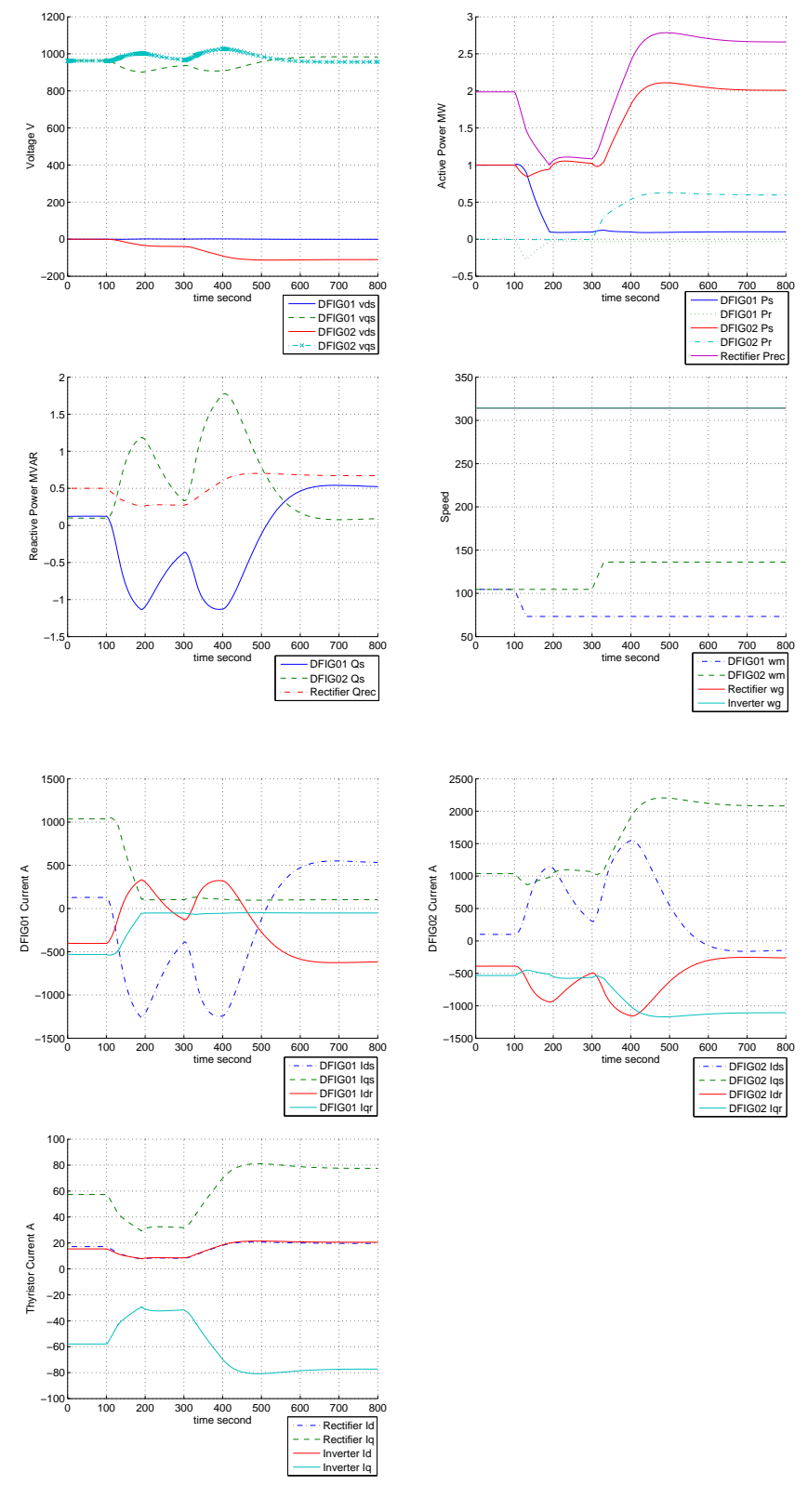


Figure 142: Stator-Flux oriented controller with explicit Q control loop

### **Dynamics of New Stator-Flux Oriented Controller**

Figure 142 shows that Q control loop on the second DFIG prevents the exchange of reactive power between the two DFIGs, though the reactive power control is slow. The controller still allows quite large exchanges of reative power between the two DFIGs. The simulation becomes unstable when the active power of both DFIGs' is ramped down to a small value. This has to be investigated.

#### Minimum extinction angle control of thyristor bridge

An AC voltage dip in the grid at inverter side can cause commutation failure in the inverter. In order to prevent the commutation failure, the extinction angle  $\gamma$  has to be kept beyond a minimum value,  $15^{\circ}$  for example.

$$\gamma = 180^{\circ} - (\alpha + \mu) \tag{76}$$

Where  $\alpha$  and  $\mu$  are the firing angle and the commutation angle of the inverter, respectively. A possible minimum extinction angle controller on the inverter side is shown in figure 143.

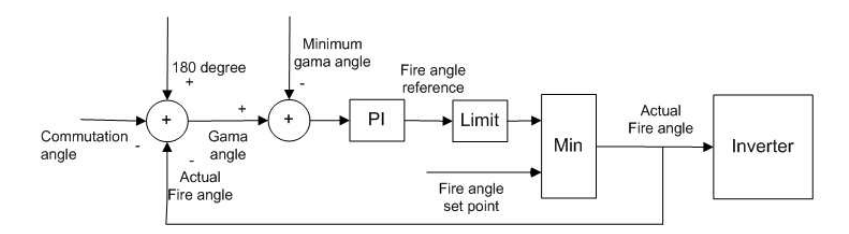


Figure 143: Minimum extinction angle controller of thyristor bridge

At normal operation point, the commutation angle is small and the extinction angle  $\gamma$  will be much larger than the minimum value of  $15^\circ$ . The output of the PI controller is the maximum value ( $165^\circ$  for example). The set point of the inverter firing angle is  $155^\circ$  in this case study and compared to the output of PI controller. The minimum value of the two is chosen as the fire angle of the inverter. Thus, at normal operation point, the actual fire angle is the inverter firing angle set point. During a voltage dip the commutation angle will increase and extinction angle will decrease. This will decreased the output of the PI controller which will keep the extinction angle above the minimum value of  $15^\circ$ .

- 6.4 Simulink Models of Terminal Voltage Control and Stator-Flux Oriented Control
- 6.4.1 DFIG-thy with terminal voltage control

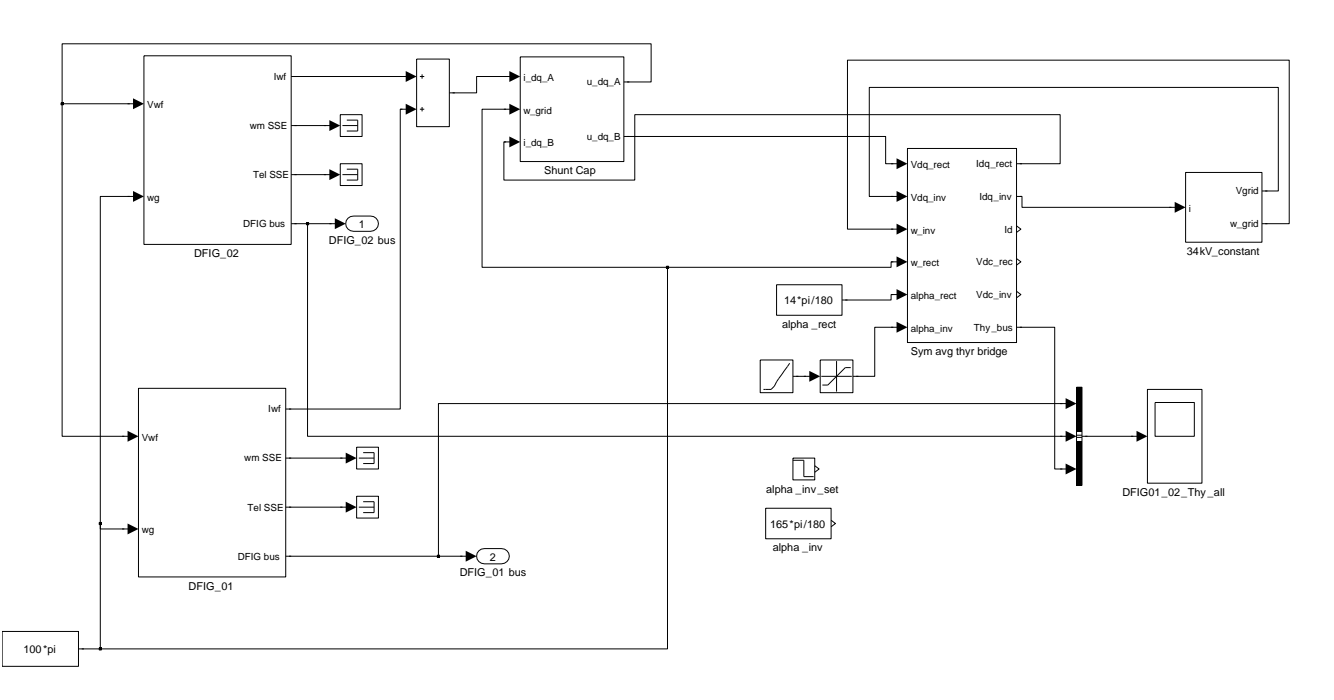


Figure 144: Main Simulink diagram of DFIG-thy with terminal voltage control

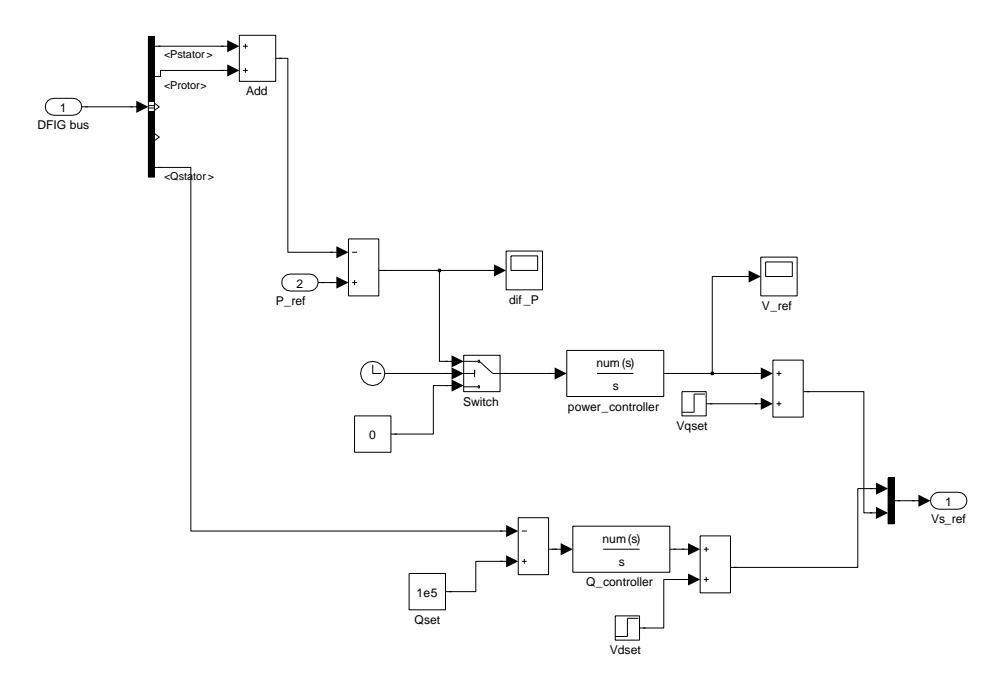


Figure 145: PQ master control loops of DFIG-thy with terminal voltage control

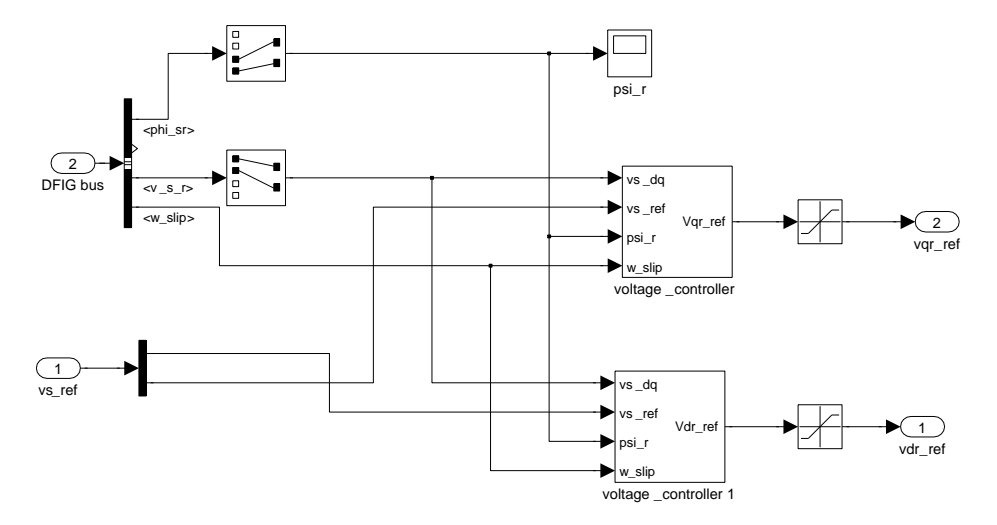


Figure 146: Top level of voltage controller in DFIG-thy with terminal voltage control

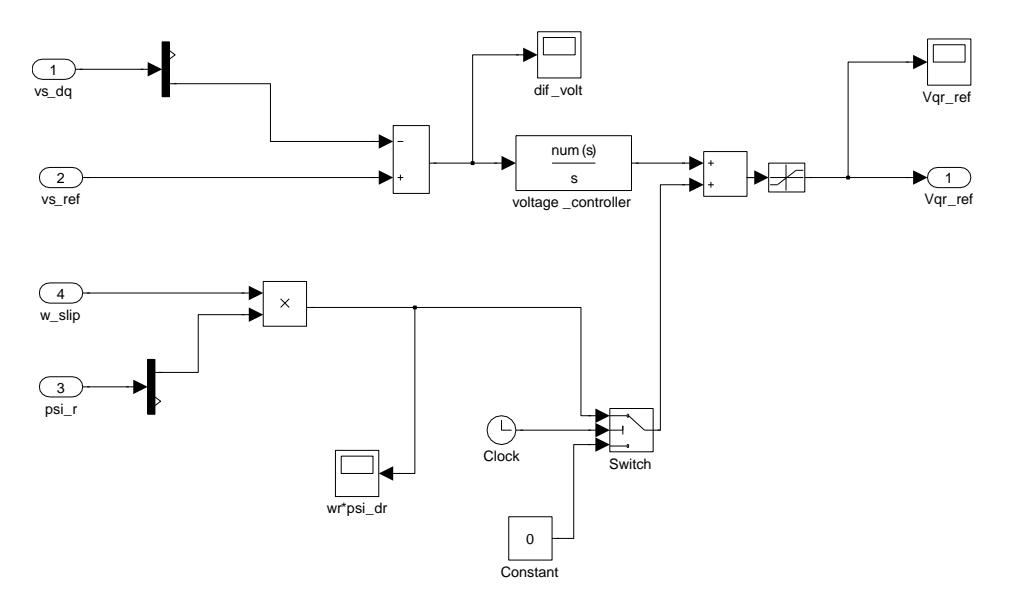


Figure 147: Voltage controller in DFIG-thy with terminal voltage control

# 6.4.2 DFIG-thy with Stator-Flux Oriented Control

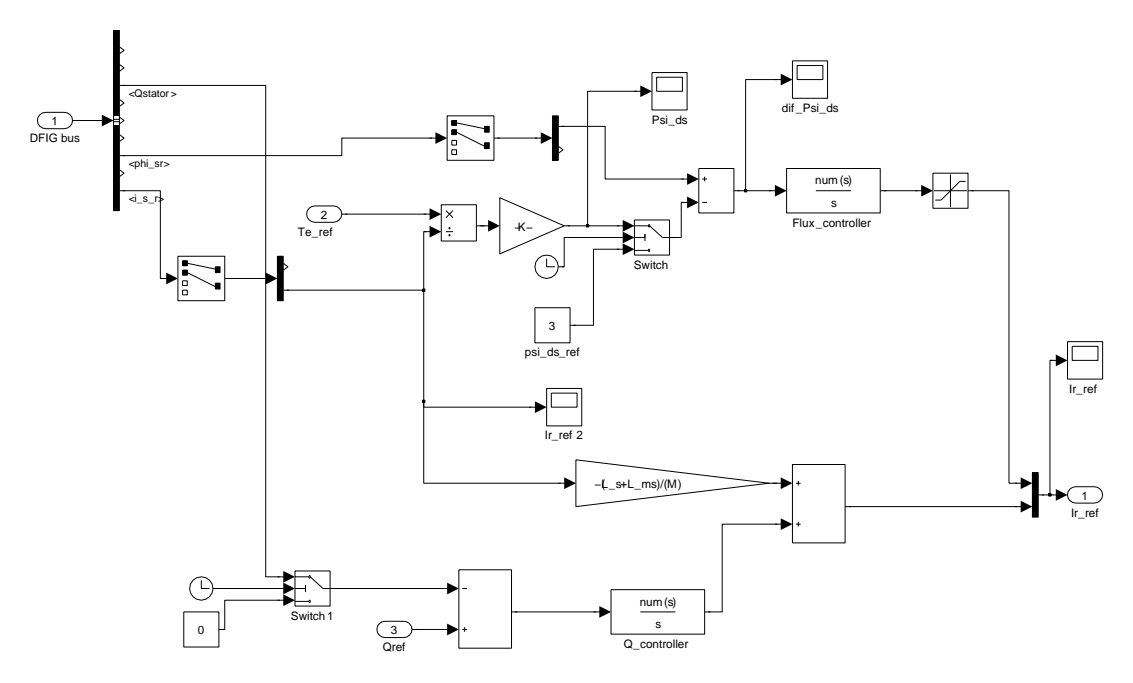


Figure 148: Top level of flux and Q controller in DFIG-thy with flux control

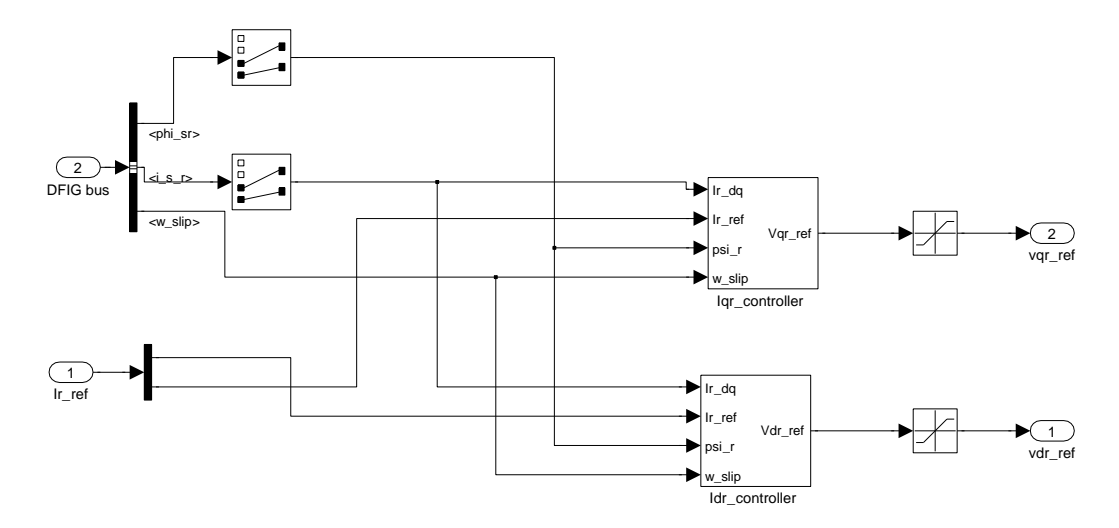


Figure 149: Current controller in DFIG-thy with flux control

# 6.5 VSP-DFIG-thy normal operation

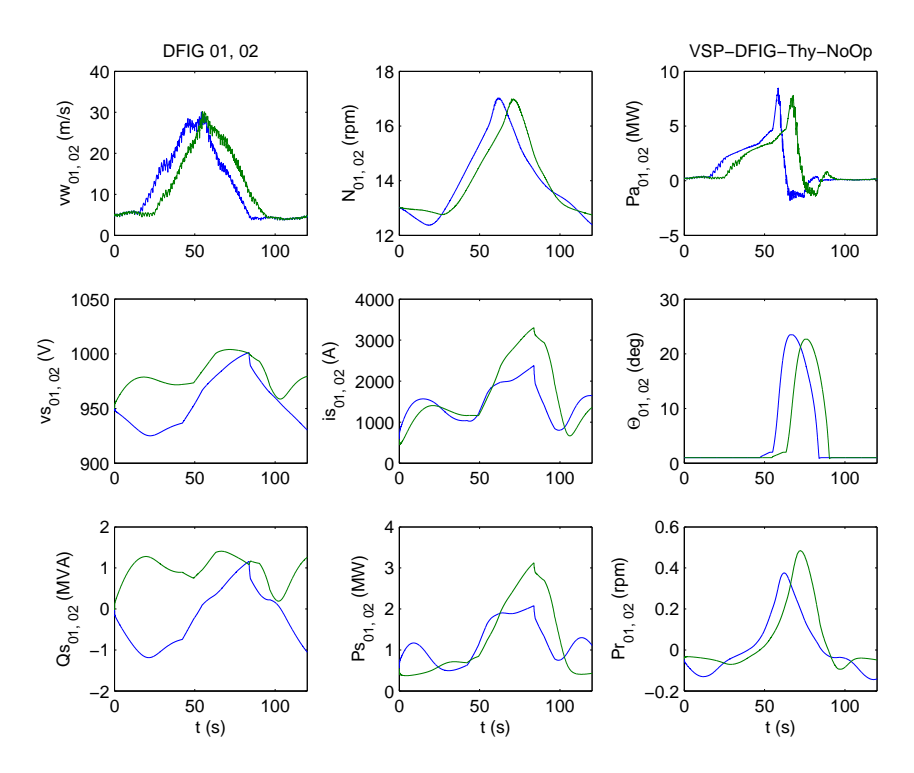


Figure 150: DFIG-thy with flux oriented control during normal operation: wind speed, rotational speed, aerodynamic power, stator voltage amplitude, stator current amplitude, pitch angle, stator reactive power, stator power and rotor power

Figure 150 shows the response of the VSP-DFIG-thy wind farm for a gust in wind speed from 7 to 25 m/s and back. The rotational seed of the turbines increases with power. When the wind speed decreases the aerodynamic power falls rapidly due to the large pitch angle that has been reached at that time. The stator and rotor electric power show less drastic changes. The reactive powers show some slow oscillations but remain within acceptable limits. The reactive power controller is installed on turbine 2.

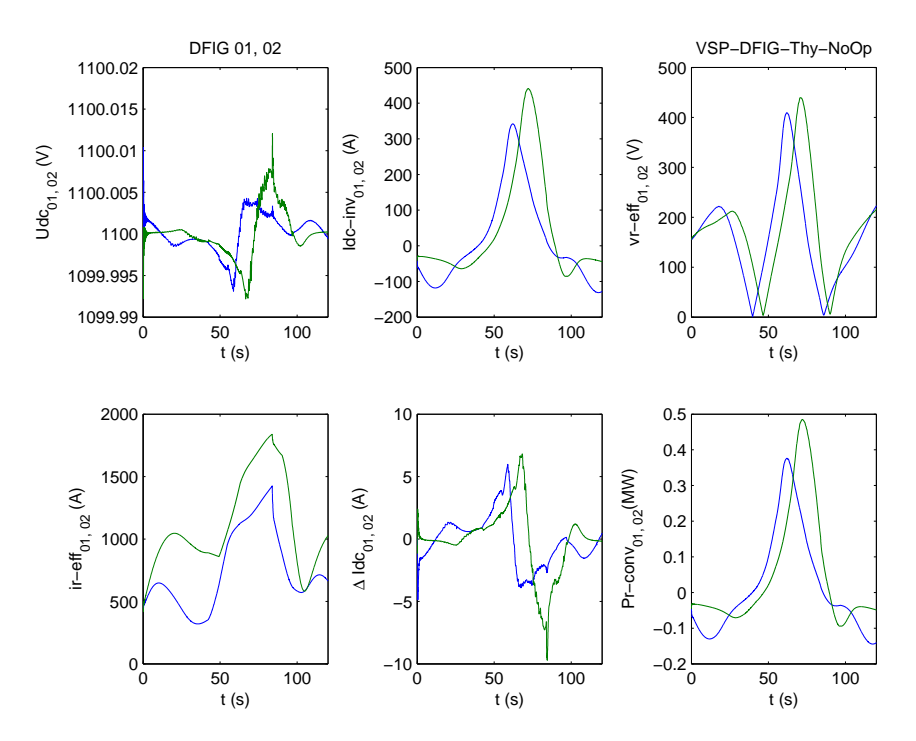


Figure 151: DFIG-thy with flux oriented control during normal operation: DC voltage, DC current, rotor voltage, rotor current, deviation from DC current setpoint and rotor converter power

Variables related to the DFIG converter are show in figure 151.

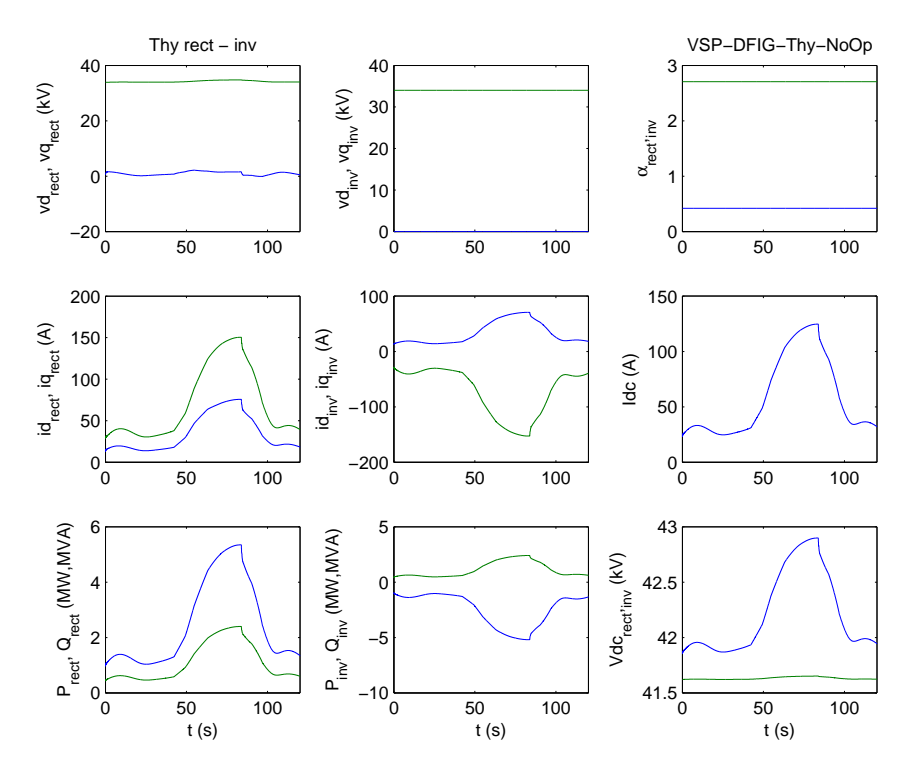


Figure 152: DFIG-thy with flux oriented control during normal operation: thyristor rectifier d and q voltage, inverter d and q voltage, rectifier and inverter firing angle, rectifier d and q current, inverter d and q current, thyristor DC current, rectifier power and reactive power, inverter power and reactive power, rectifier and inverter DC voltage

Figure 152 shows the response of the thyristor bridge.

### 6.6 Conclusions and future work

- (i) Using a thyristor bridge and DC cable to connect a wind farm to the power grid is similar to connecting the wind farm to a very weak AC power system.
- (ii) Connecting DFIGs to a very weak power grid or to a stand alone load is a new topic. Most literature on DFIG concentrates on how to control the DFIGs connecting to a strong power grid. The standard grid-flux oriented control is not appropriate for DFIGs connecting to a weak power grid or stand alone load. In this study, two controllers have been developed which can control DFIGs connected to a weak power grid or stand alone load: a terminal voltage controller and a stator-flux oriented controller. The controllers operate on the rotor voltages of the DFIGs, the firing angles of thyristor rectifier and inverter are kept constant. No energy storage device and no centralized controller are required.
- (iii) A problem for the control of a wind farm is that the resistance and the reactance at the point of common coupling are often of equal magnitude. Therefore, it is difficult to decouple P and Q like in a high voltage transmission power grid. This problem occurs especially if multiple DFIGs operate in paralel.
- (iv) When two or more nearby DFIGs are connected to a weak power grid or a stand alone load, Q control loops are required to prevent large reactive power circulation between nearby generators. The interactions between two nearby DFIGs in a weak power grid and how to decouple P and Q requires more research. For the moment, P and Q are decoupled in the frequency domain by choosing different integration constants  $k_i$  of the PI controllers, but this is not an optimal solution.

(v) The stator-flux oriented controller performs better than the terminal voltage controller. Oscillations are better damped by the stator-flux oriented controller. However, the results for the stator-flux oriented controller become unstable when both DFIGs are ramped down to low power. This may be caused by numerical instability or may have a physical background and needs further investigation.

#### **Recommendations for future work**

- How to control P and Q of two or more nearby DFIGs in a weak power grid, i.e. how to
  decouple P and Q in a power grid where resistance is not much smaller than reactance.
  This will require a multi-variable control appoach.
- Investigation of the unstable behaviour of the stator-flux oriented controller when all DFIGs are ramped down to low power.

# 7 Case studies

#### 7.1 Introduction

In addition to the behaviour of the nine wind farm systems during a wind gust to illustrate normal operation (see chapters 4, 5 and 6), the systems characteristics will be demonstrated for the following conditions (if applicable):

- flicker evalation during normal operation;
- response to a voltage dip;
- response to a frequency dip;

To limit the number of simulations, the systems will first be classified with respect to their expected dynamic response under these conditions. As already demonstrated in the previous chapter, some of the systems have practically identical dynamic behaviour.

Table 5: Classification of the electrical configurations developed in WaP with respect to dynamic behaviour in case studies

	System	ficker	voltage dip	freq. dip
1	CSS-IG-dc	С	V	V
2	CSS-CCIG-dc	CC	V	CC
3	VSP-CCIG-ac	CC	V	CC
4	VSP-CCIG-dc	CC	V	CC
5	VSP-DFIG-dc	V	V	V
6	VSP-FCIG-ac	V	V	V
7	VSP-FCSM-ac	V	V	V
8	VSP-FCSM-dc	V	V	V
9	VSP-DFIG-thy	V	V-thy	V

С	=	response typical for a constant speed system
V	=	response typical for a variable speed full converter system
CC	=	response typical for cluster controlled system
V-thy	=	response typical for variable speed system with thyristor converter

Most systems classify as variable speed system (V), due to the presence of converters in the system and the type of control of the rectifier connected to the turbines. The exceptions are:

- cluster controlled systems, which combine constant and variable speed characteristics;
- the system with a thyristor bridge converter system, which is a variable speed system but behaves differently during a voltage due to the limited controllability of the thyristors (grid commutated instead of self commutated).

Therefore, the following systems are chosen for the case study:

- (i) CSS-IG-dc system
- (ii) VSP-CCIG-ac system
- (iii) VSP-FCIG-ac system
- (iv) VSP-DFIG-thy system

# 7.2 Flicker evaluation

The currents and voltages calculated in the previous chapters 4, 5 and 6 for 100 s of normal operation have been used to calculate instantaneous flicker values for the CSS-IG-dc, VSP-CCIG-ac, VSP-FCIG-ac and VSP-DFIG-thy wind farm. This is a deviation from the standard procedure, but following the standard would require a substantial amount of computer time. On the other hand, using the wind gust applied in the previous chapter guarantees including the full range of wind speeds and is sufficient to compare the systems.

For the details of the flicker calculation model is referred to Chapter 5 of Volume 1 of the Erao-2 report [33]. The short circuit power for the flicker calculation is 50 times the rated power of the wind farm: 412.5 MVA. A grid angle of  $30^{\circ}$  has been chosen. The sample frequency in the wind farm calculations was 400 Hz. Flicker values have been binned during intervals of 6 s, resulting in 2400 values per binning period, except for the final interval.

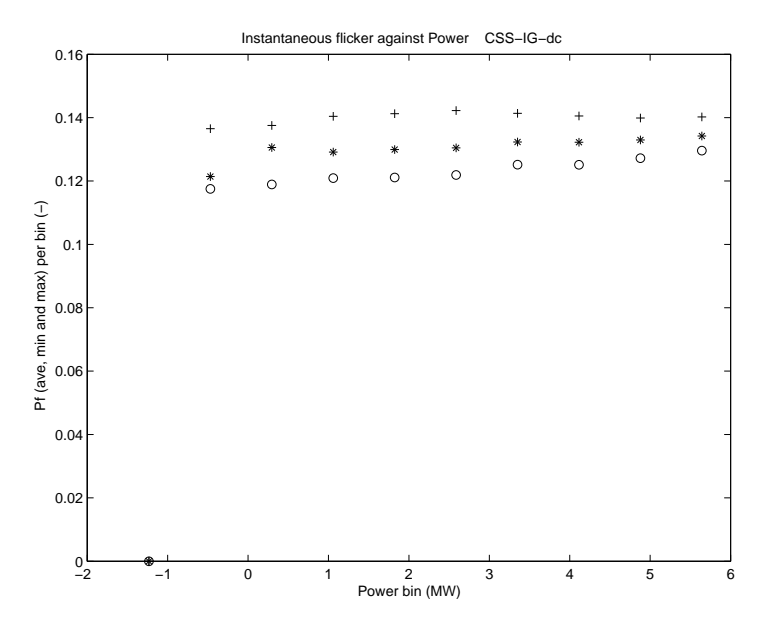


Figure 153: Instantaneous flicker level binned against the wind farm power calculated for the CSS-IG-dc wind farm

The average flicker level of the CSS-IG-dc wind farm is between 0.10 and 0.14, increasing with wind farm power. The flicker level for the constant speed system in [34] was 0.10-0.28, which were determined in a sligtly different way (only one turbine and a wind speed range of 5-15 m/s). The CSS-IG-dc wind farm level is lower than the constant speed turbine level, which can be caused by the averaging of the variations from the individual turbines.

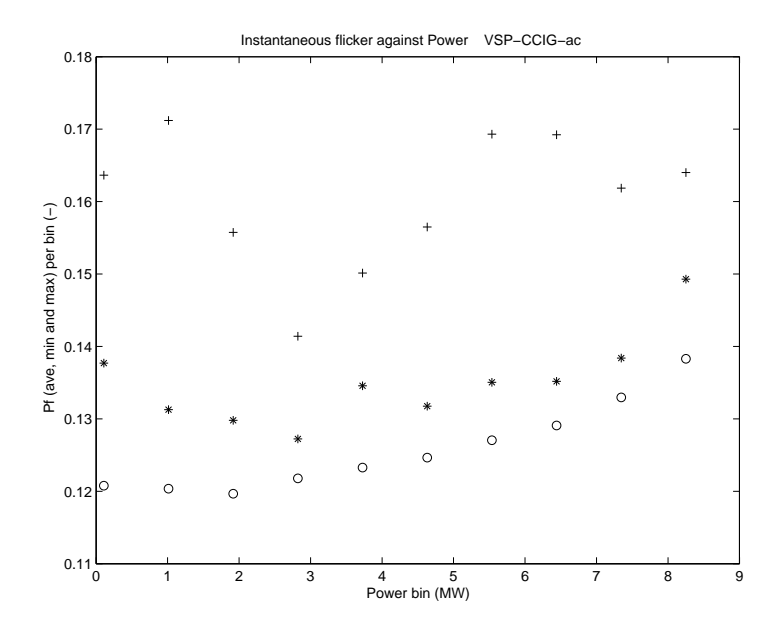


Figure 154: Instantaneous flicker level binned against the wind farm power calculated for the VSP-CCIG-ac wind farm

With regard to flicker, the VSP-CCIG-ac wind farm is expected to resemble the constant speed system. The average flicker level of the VSP-CCIG-ac wind farm is about 0.14, almost independent of the wind farm power.

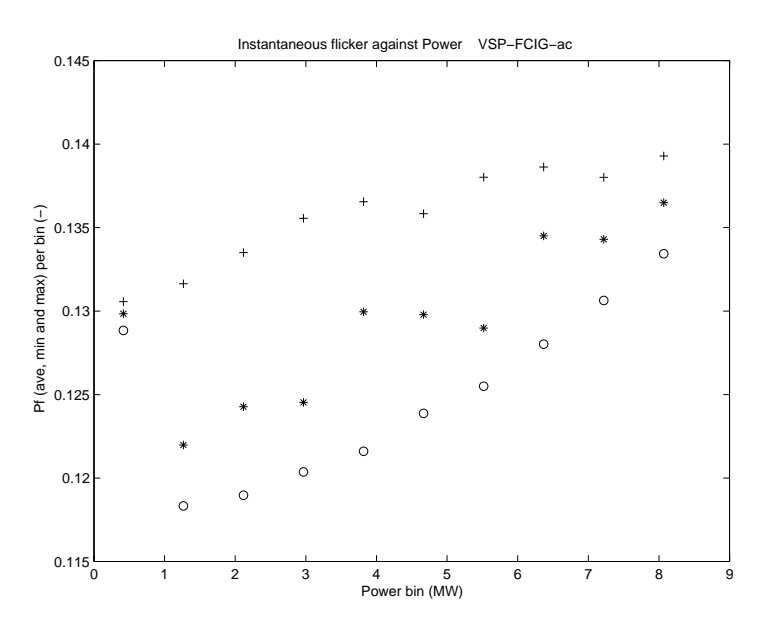


Figure 155: Instantaneous flicker level binned against the wind farm power calculated for the VSP-FCIG-ac wind farm

The average flicker level of the VSP-FCIG-ac wind farm is between 0.12 and 0.14, increasing with wind power. The level is comparable to the flicker levels of the variable speed turbine in [34] (0.10 to 0.18), which were determined in a sligtly different way (only one turbine and a wind speed range of 5-15 m/s).

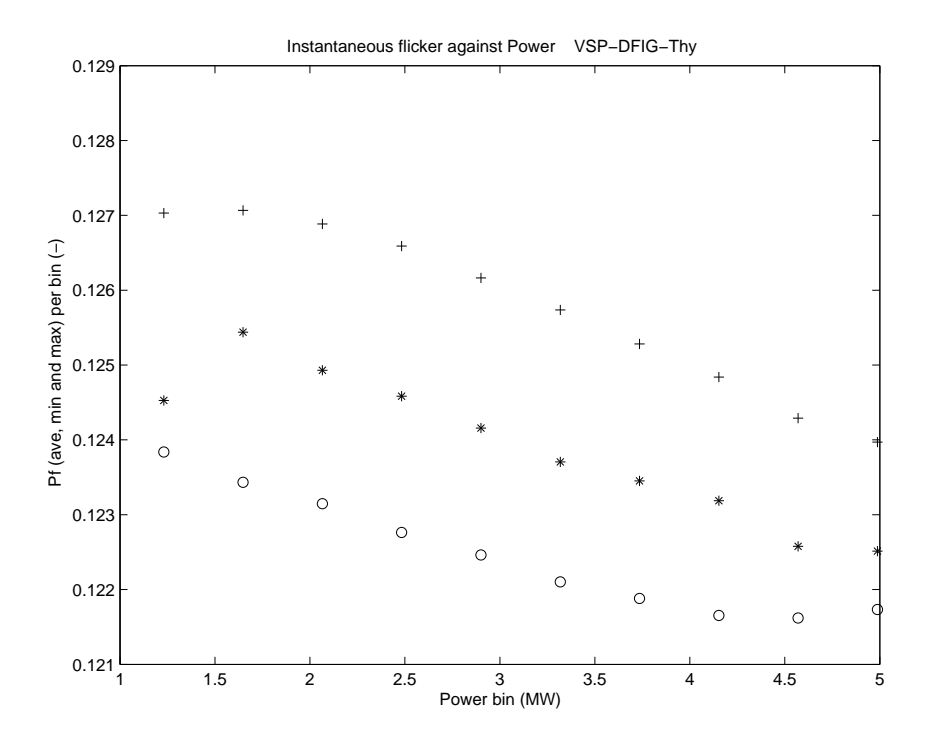


Figure 156: DFIG-thy with flux oriented control: binned instantaneous flicker levels

The average flicker level of the VSP-DFIG-thy turbine is 0.124 and not strongly dependent on the wind farm power. Compared to the previous systems, the DC inductance of the thyristor bridge acts as an additional energy buffer between the wind farm and the power grid.

# 7.3 Response to a balanced voltage dip

In this section the effect of voltage dips, resulting from a balanced short circuit, on the four wind farm concepts in this case study will be described. Three voltage dips will be investigated: a 30% dip during 10 seconds, a 50% dip during 0.5 seconds and an 85% dip during 0.2 seconds, the same dips as in the Erao-2 study [34]. The grid is modelled as an ideal voltage source.

### CSS-IG-dc wind farm voltage dip (system # 1)

Dip of 30%-10 seconds, starting at t=30s

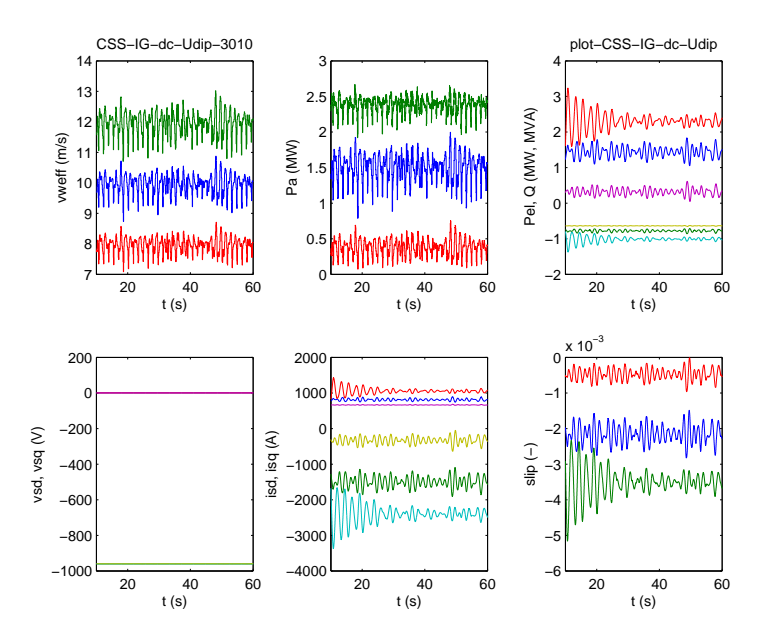


Figure 157: CSS-IG-dc wind farm, voltage dip 30%, 10 sec: rotor effective wind speed, aero-dynamic power, electric and reactive power, stator d and q voltage, stator d and q current and slip per turbine

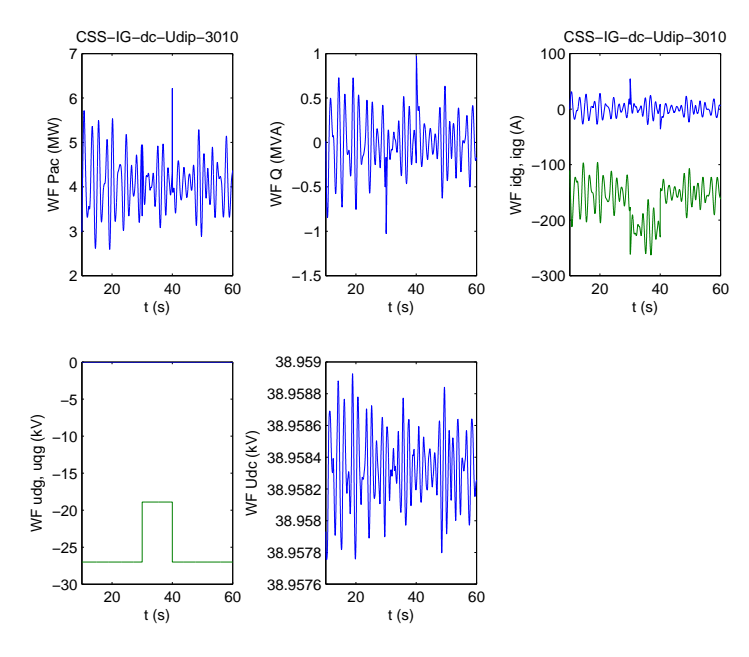


Figure 158: CSS-IG-dc wind farm, voltage dip 30%, 10 sec: active power, reactive power, inverter dq-currents, inverter dq-voltages, DC voltage and wind farm frequency

The only effect of the 30%, 10 sec voltage dip at the grid side terminals of the wind farm inverter of the CSS-IG-dc wind farm is the almost instantaneous increase of the inverter AC current. The DC voltage, controlled by the inverter, is not affected by the AC voltage dip. There is no significant effect on the wind turbine powers and the wind farm power to the grid.

#### Dip of 50%-0.5 seconds

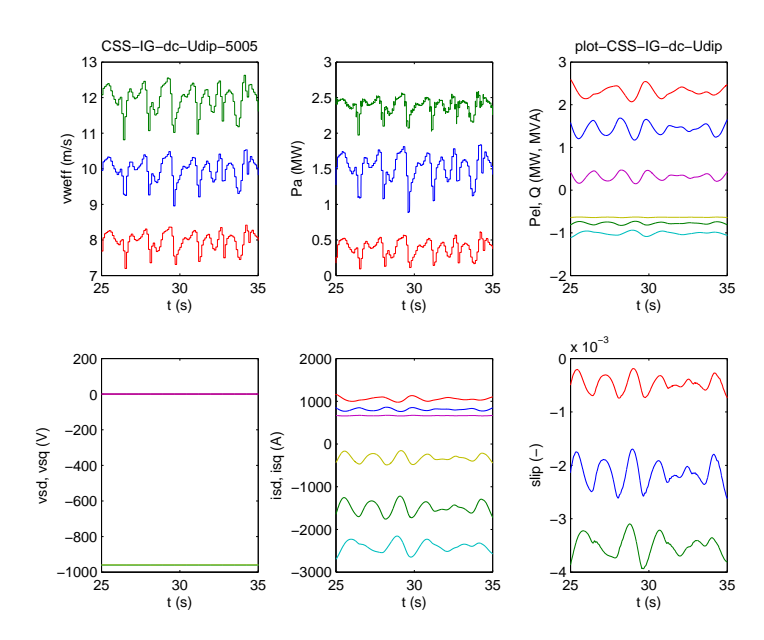


Figure 159: CSS-IG-dc wind farm, voltage dip 50%, 0.5 sec: rotor effective wind speed, aero-dynamic power, electric and reactive power, stator d and q voltage, stator d and q current and slip per turbine

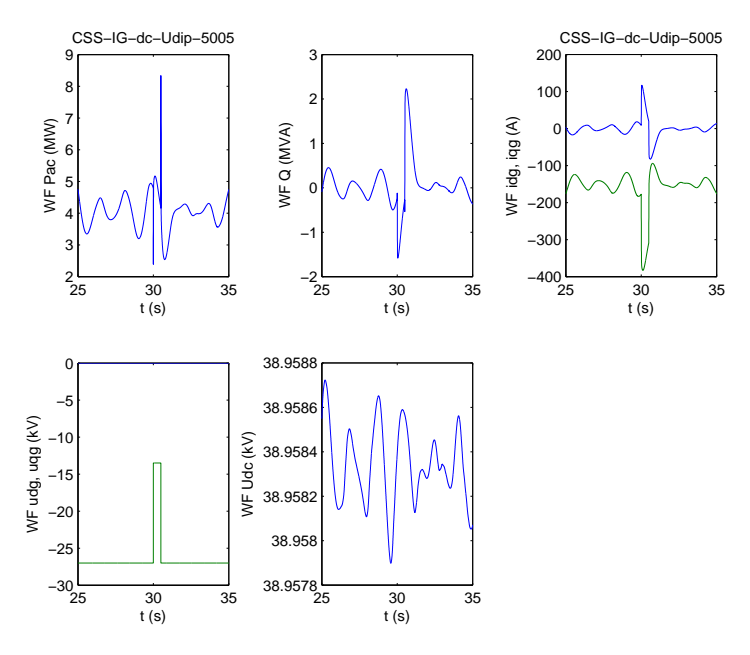


Figure 160: CSS-IG-dc wind farm, voltage dip 50%, 0.5 sec: active power, reactive power, inverter dq-currents, inverter dq-voltages, DC voltage and wind farm frequency

The 50%, 0.5 sec voltage dip at the grid side terminals of the CSS-IG-dc wind farm inverter (figure 159 and 160) has no effect on the turbines. The inverter current increases from 200 to 400 A and inverter power and reactive power peak. The DC voltage is not affected by the grid voltage drop.

# Dip of 85%-0.2 seconds

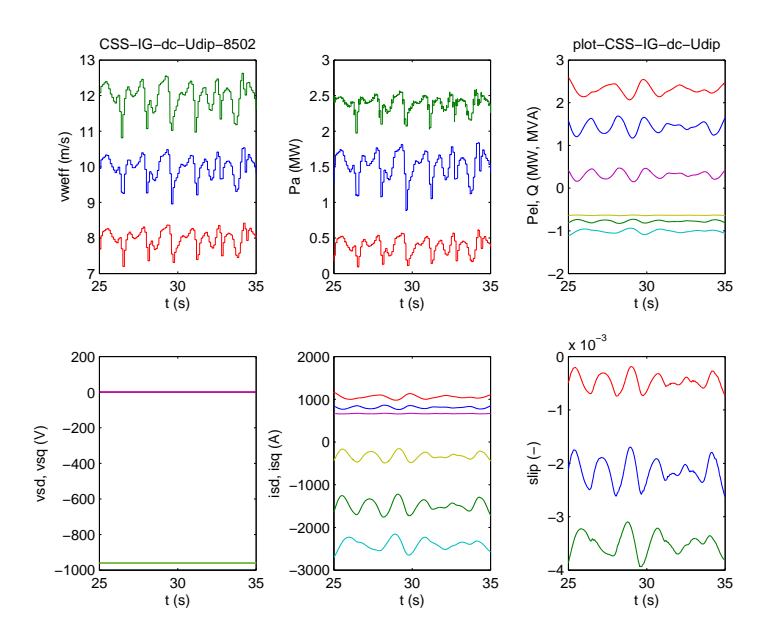


Figure 161: CSS-IG-dc wind farm, voltage dip 85%, 0.2 sec: rotor effective wind speed, aero-dynamic power, electric and reactive power, stator d and q voltage, stator d and q current and slip per turbine

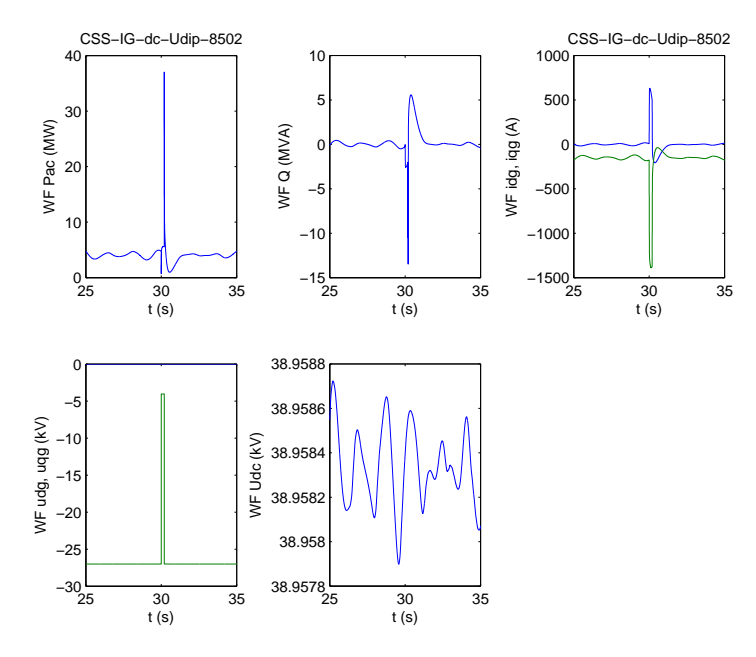


Figure 162: CSS-IG-dc wind farm, voltage dip 85%, 0.2 sec: active power, reactive power, inverter dq-currents, inverter dq-voltages, DC voltage and wind farm frequency

The 50%, 0.5 sec voltage dip at the grid side terminals of the CSS-IG-dc wind farm inverter (figure 161 and 162) has no effect on the turbines. The inverter current increases from 200 to about 1500 A and inverter power and reactive power peak. The DC voltage is not affected by the grid voltage drop. The DC link voltage control can be relaxed to limit the AC current peak. This will only have a significant effect if a relatively large deviation in DC voltage is

alowed. A deviation can be prevented by simultaneously reducing the power of the rectifier, which can cause turbine overspeed since the rectifier frequency is constant. Adapting the CSS-IG-dc control strategy in combination with finetuning of the CSS-IG-dc controls is expected to reduce the current peak problem to an acceptable level.

#### VSP-CCIG-ac wind farm voltage dip (system # 3)

Dip of 30%-10 seconds

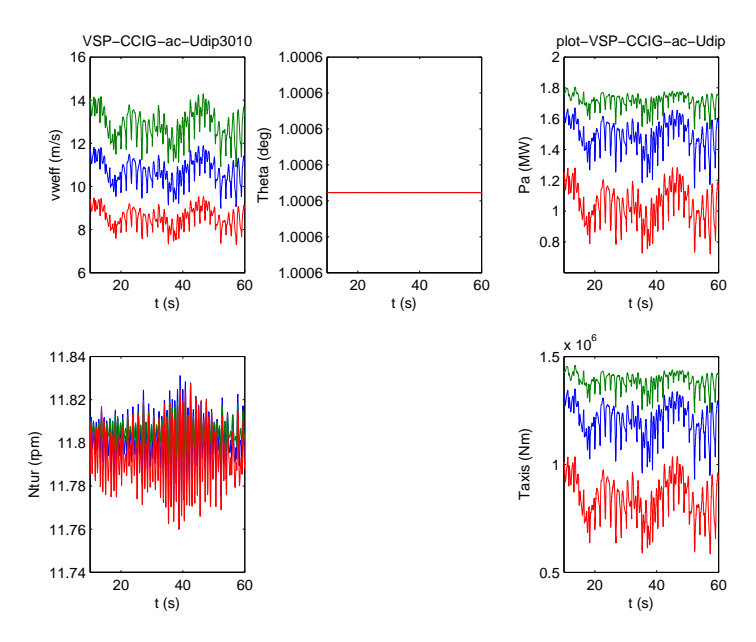


Figure 163: VSP-CCIG-ac wind farm, voltage dip 30%, 10 sec: wind speeds, pitch angles, aerodynamic powers, turbine rotational speeds and axial torques per turbine

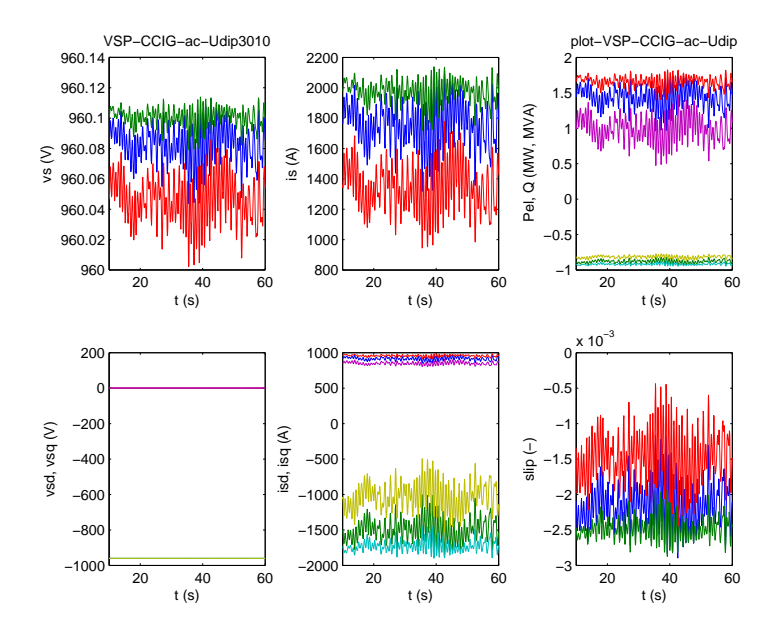


Figure 164: VSP-CCIG-ac wind farm, voltage dip 30%, 10 sec: stator voltages, stator currents, active and reactive powers, dq stator voltages, dq stator currents and slips per turbine

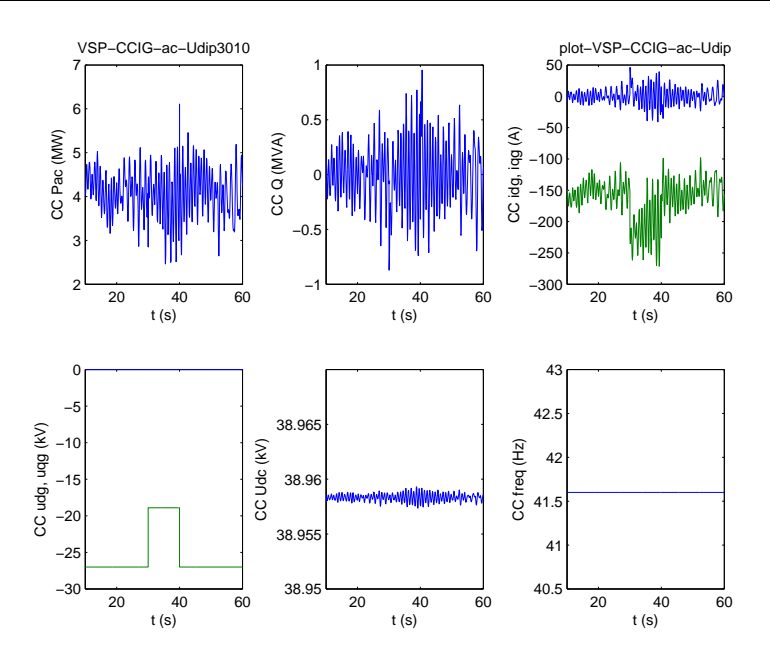


Figure 165: VSP-CCIG-ac wind farm, voltage dip 30%, 10 sec: cluster active and reactive power at the grid side, inverter dq-currents, inverter dq-voltages, DC voltage and cluster frequency

The turbines are not affected by a 30%, 10 sec voltage dip in the VSP-CCIG-ac wind farm (figures 163 and 164). The only variable that significantly responds to the dip is the inverter current (figure 164). For this dip the increase in current is relatively small.

### Dip of 50%-0.5 seconds

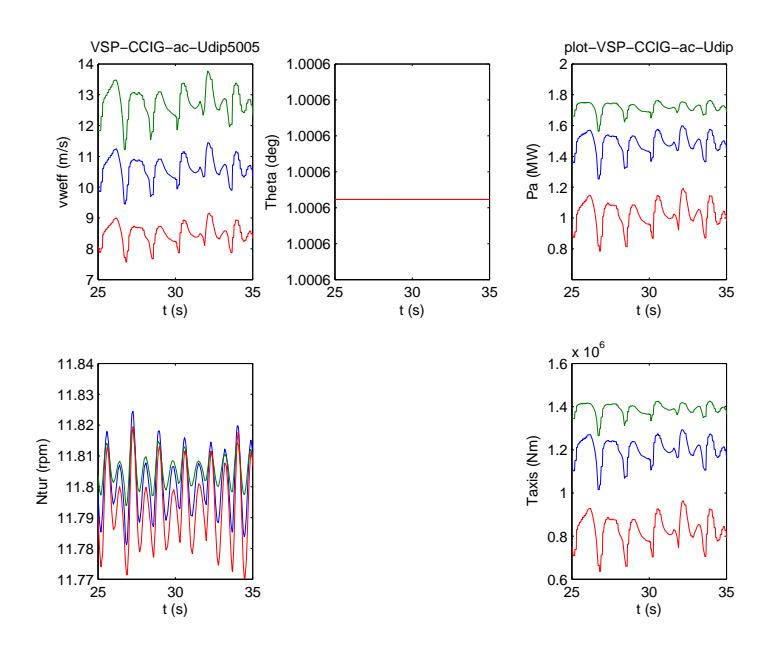


Figure 166: VSP-CCIG-ac wind farm, voltage dip 50%, 0.5 sec: wind speeds, pitch angles, aerodynamic powers, turbine rotational speeds and axial torques per turbine

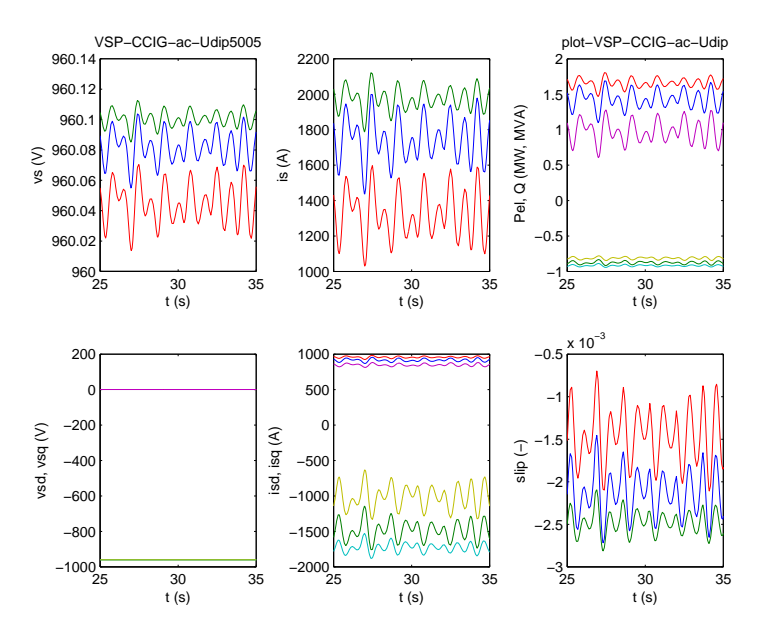


Figure 167: VSP-CCIG-ac wind farm, voltage dip 50%, 0.5 sec: stator voltages, stator currents, active and reactive powers, dq stator voltages, dq stator currents and slips per turbine

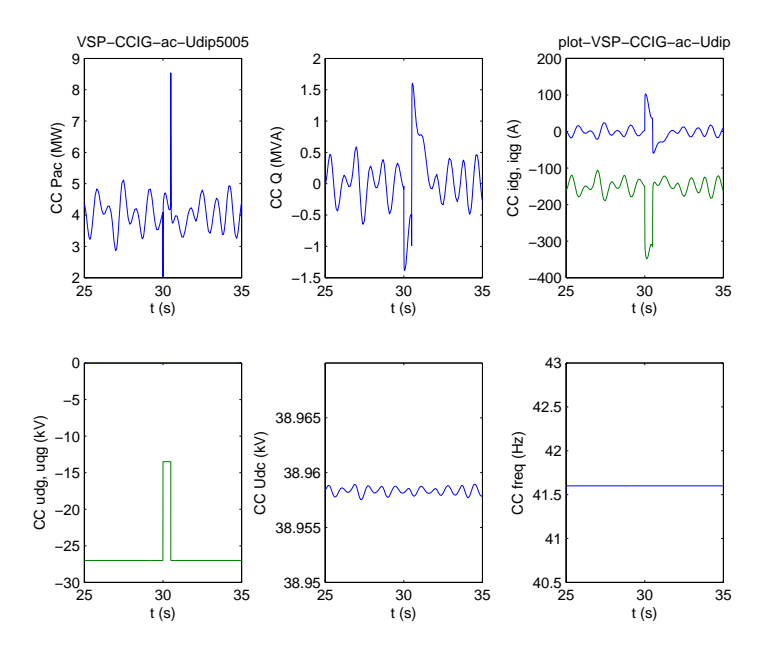


Figure 168: VSP-CCIG-ac wind farm, voltage dip 50%, 0.5 sec: cluster active and reactive power at the grid side, inverter dq-currents, inverter dq-voltages, DC voltage and cluster frequency

Peaks occur in the power, reactive power and current of the cluster inverter in the VSP-CCIG-ac wind farm for a 50%, 0.5 sec voltage dip (figure 168). Turbine and rectifier variables as well as the DC-link voltage are not affected.

# Dip of 85%-0.2 seconds

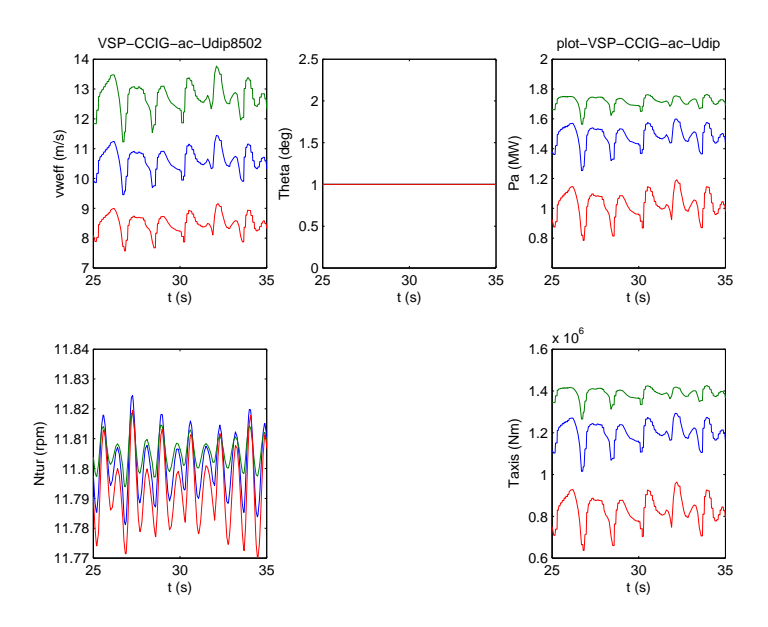


Figure 169: VSP-CCIG-ac wind farm, voltage dip 85%, 0.2 sec: wind speeds, pitch angles, aerodynamic powers, turbine rotational speeds and mechanical torques per turbine

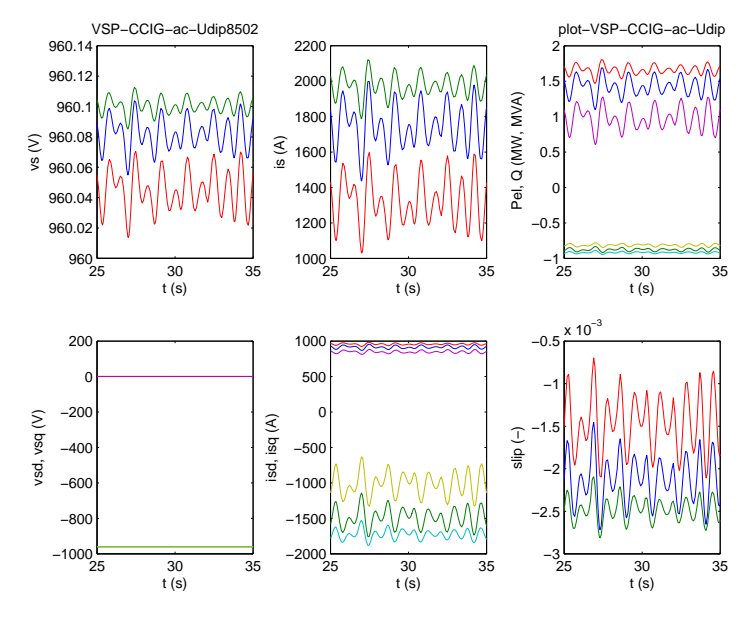


Figure 170: VSP-CCIG-ac wind farm, voltage dip 85%, 0.2 sec: stator voltages, stator currents, active and reactive powers, dq stator voltages, dq stator currents and slips per turbine

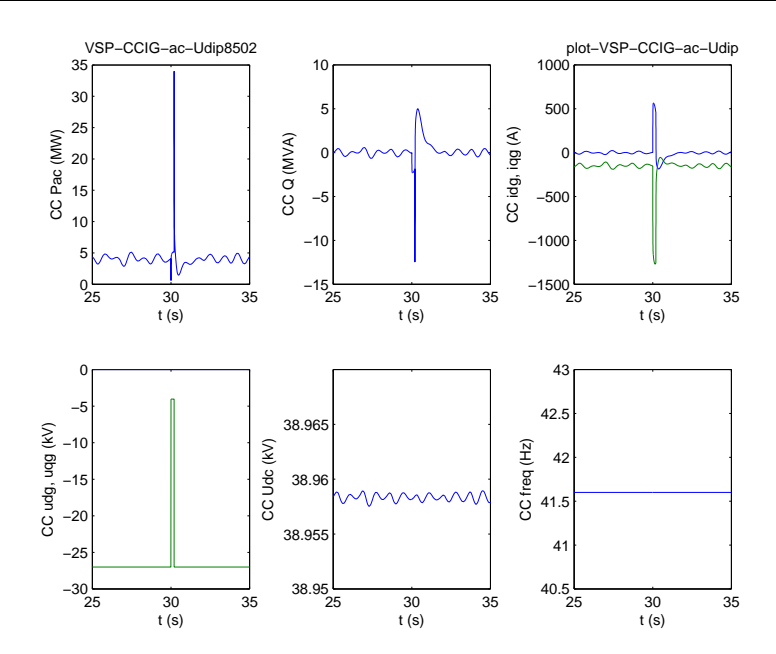


Figure 171: VSP-CCIG-ac wind farm, voltage dip 85%, 0.2 sec: cluster active and reactive power at the grid side, inverter dq-currents, inverter dq-voltages, DC voltage and cluster frequency

The VSP-CCIG-ac wind farm experiences the same problem for a 85%, 0.2 sec voltage dip as the CSS-IG-dc wind farm: a current peak of about 1500 A and peaks in the power and the reactive power of the wind farm inverter (figure 171). The solution is the same: relax the DC link voltage control and simultaneously reducing the power of the rectifier. Again, danger of turbine overspeding exists since the rectifier frequency is determined by the wind speed of turbine 1.

# VSP-FCIG-ac wind farm voltage dip (system #6)

# Dip of 30%-10 seconds

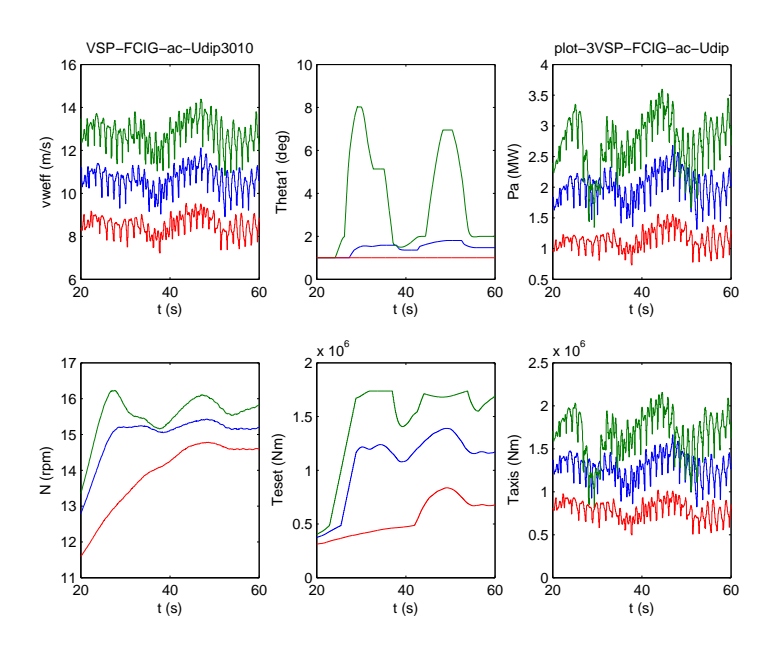


Figure 172: VSP-FCIG-ac wind farm, voltage dip 30%, 10 sec: wind speeds, pitch angles, aerodynamic powers, turbine rotational speeds, electromagnetic torque setpoints and mechanical torques per turbine

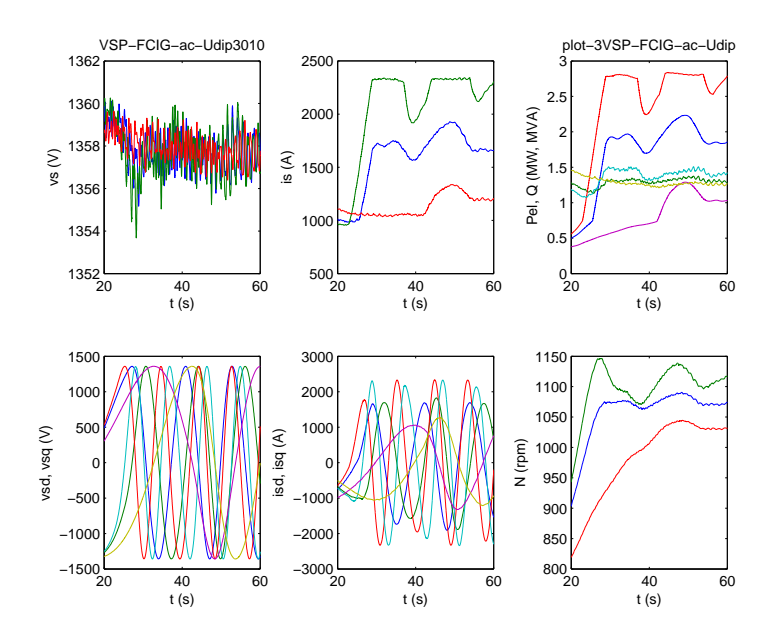


Figure 173: VSP-FCIG-ac wind farm, voltage dip 30%, 10 sec: stator voltages, stator currents, active and reactive powers, dq stator voltages, dq stator currents and turbine rotational speeds per turbine

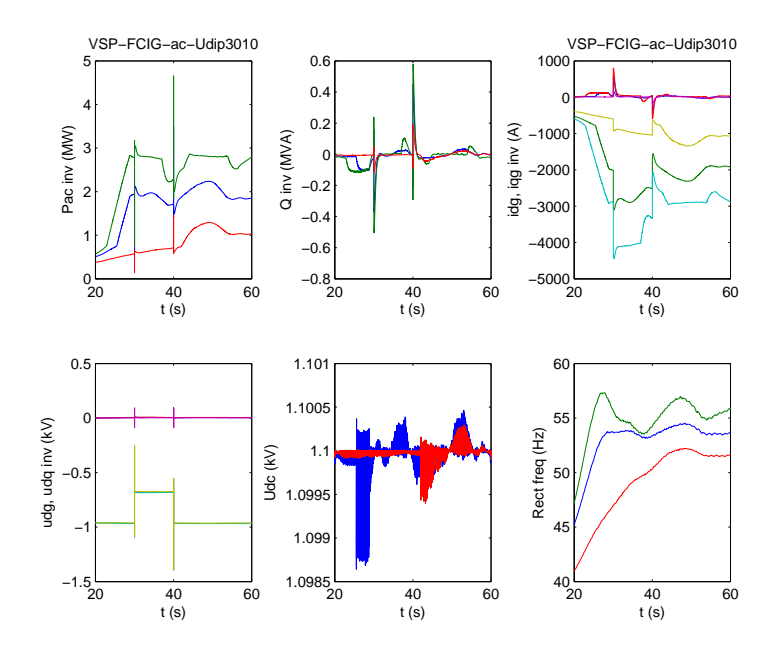


Figure 174: VSP-FCIG-ac wind farm, voltage dip 30%, 10 sec: inverter active and reactive powers, inverter dq-currents, inverter dq-voltages, DC voltages and rectifier frequencies per turbine

The effect of a 30%, 10 sec voltage dip on the wind turbines in the VSP-FCIG-ac wind farm is minimal. The variations in figures 172 and 172 are caused by turbine speed increases and pitch control. The dip does affect the inverter variables: peaks in power, reactive power and current. The DC voltage is not affected (see figures 174). The inverter currents in this case are much larger than in the previous cases due to the low voltage level of the DC converter voltage (1 kV). The converters are turbine converters, the converters shown in the previous cases are cluster and wind farm converters with a lager power rating and operating at about 35 kV.

# Dip of 50%-0.5 seconds

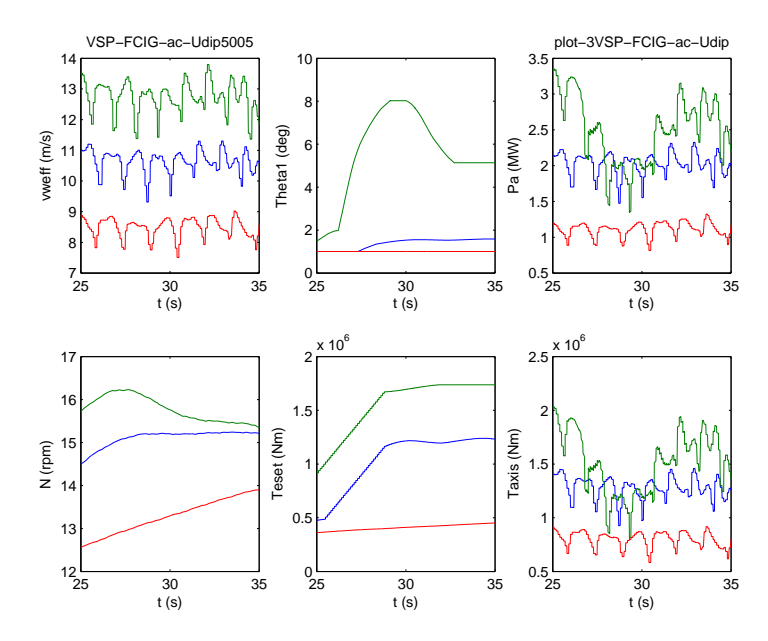


Figure 175: VSP-FCIG-ac wind farm, voltage dip 50%, 0.5 sec: wind speeds, pitch angles, aerodynamic powers, turbine rotational speeds, electromagnetic torque setpoints and mechanical torques per turbine

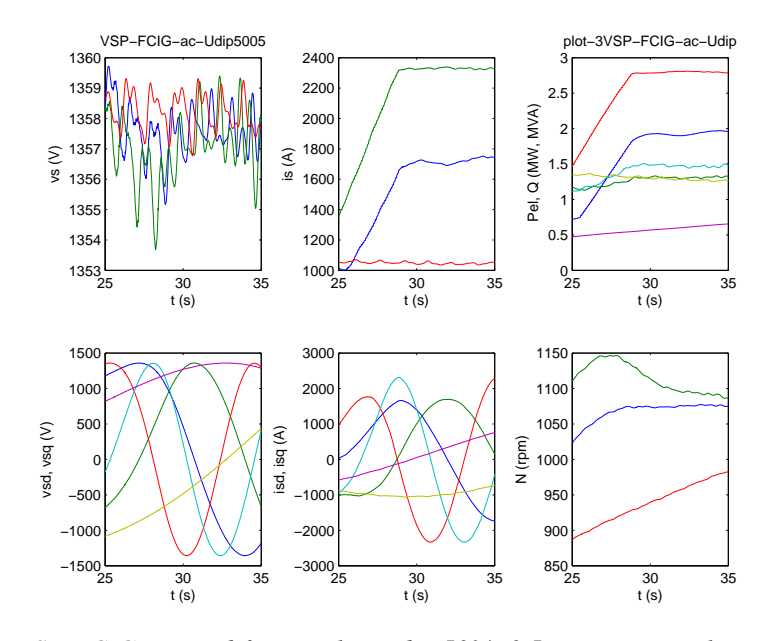


Figure 176: VSP-FCIG-ac wind farm, voltage dip 50%, 0.5 sec: stator voltages, stator currents, active and reactive powers, dq stator voltages, dq stator currents and turbine rotational speeds per turbine

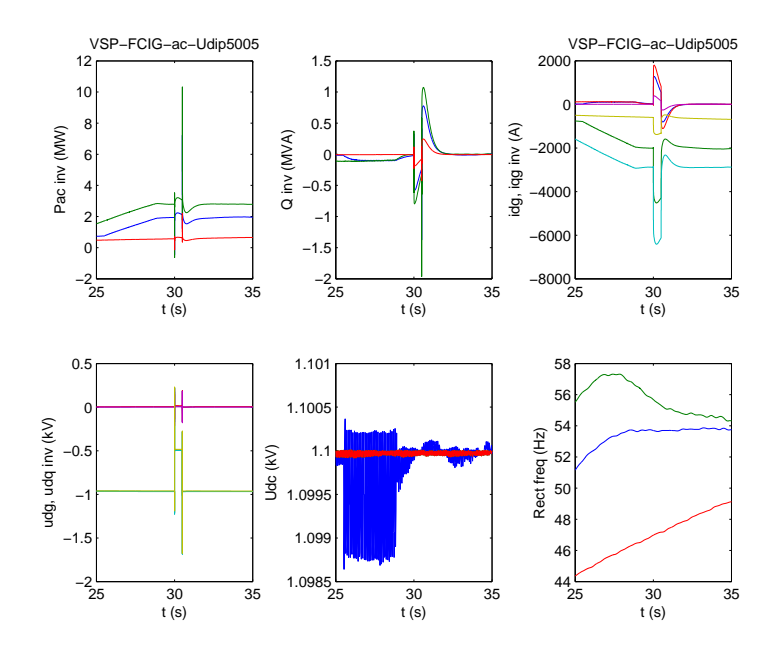


Figure 177: VSP-FCIG-ac wind farm, voltage dip 50%, 0.5 sec: inverter active and reactive powers, inverter dq-currents, inverter dq-voltages, DC voltages and rectifier frequencies per turbine

There is no effect of the 50%, 0.5 sec voltage dip on the wind turbines of the VSP-FCIG-ac wind farm (figure 175 and 176). Inverter powers, reactive powers and currents peak. The DC voltage is not affected (figure 177)

## Dip of 85%-0.2 seconds

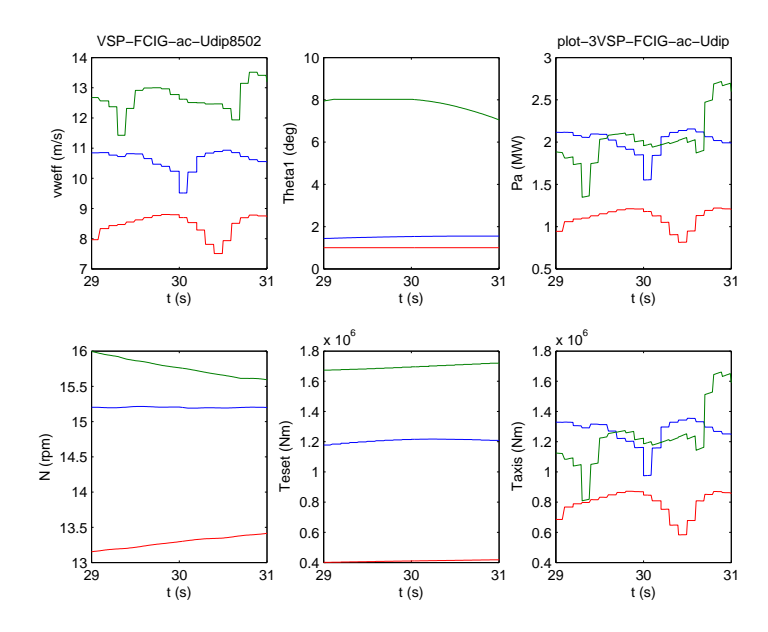


Figure 178: VSP-FCIG-ac wind farm, voltage dip 85%, 0.2 sec: wind speeds, pitch angles, aerodynamic powers, turbine rotational speeds, electromagnetic torque setpoints and mechanical torques per turbine

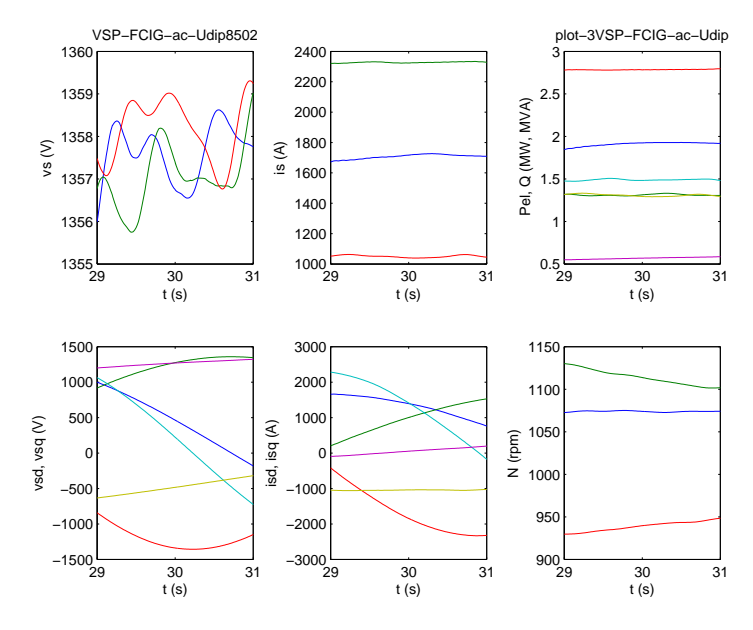


Figure 179: VSP-FCIG-ac wind farm, voltage dip 85%, 0.2 sec: stator voltages, stator currents, active and reactive powers, dq stator voltages, dq stator currents and turbine rotational speeds per turbine

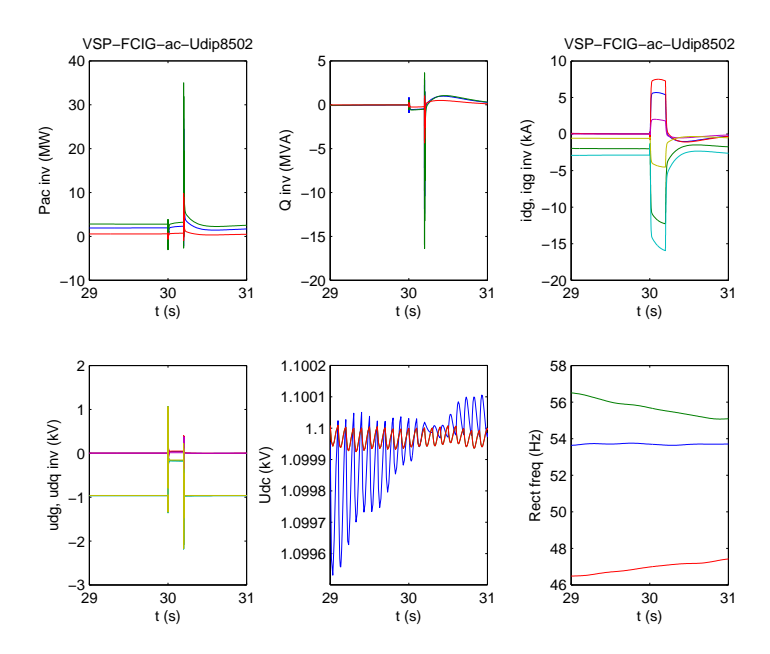


Figure 180: VSP-FCIG-ac wind farm, voltage dip 85%, 0.2 sec: inverter active and reactive powers, inverter dq-currents, inverter dq-voltages, DC voltages and rectifier frequencies per turbine

The result is similar to the 50% dip with higher peaks in currents and powers.

## VSP-DFIG-thy wind farm voltage dip (system # 9)

The VSP-DFIG-thy wind farm consists of two turbines, flux-oriented control and reactive power control on the second turbine.

Voltage dip of 30% - 10 seconds

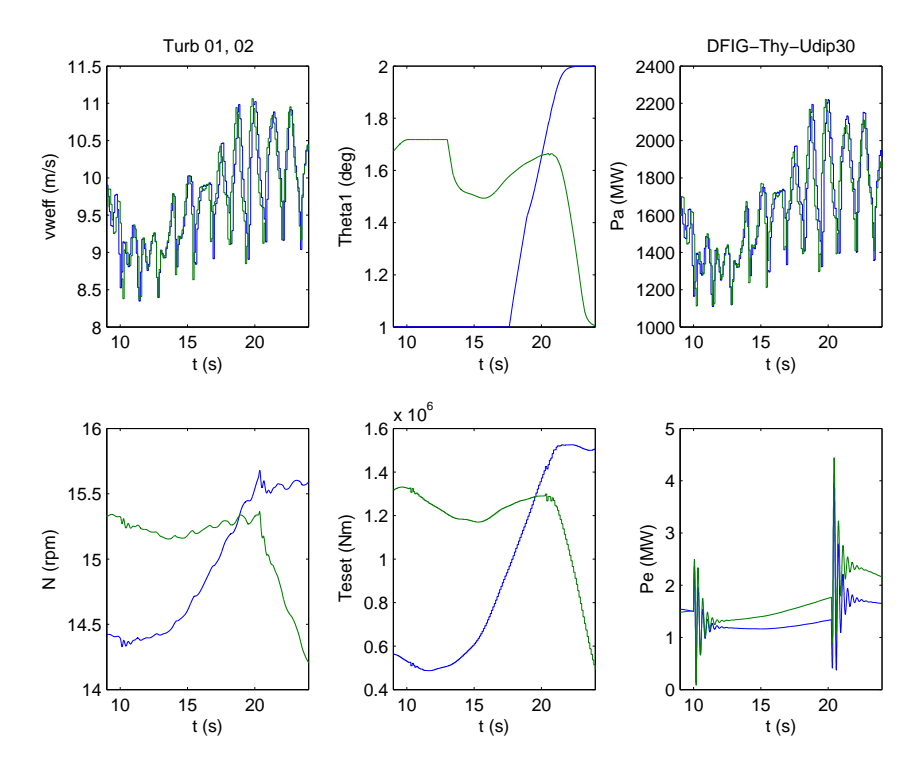


Figure 181: VSP-DFIG-thy voltage dip of 30% - 10 seconds: wind speeds, pitch angles, aero-dynamic powers, turbine rotational speeds, electromagnetic torque setpoints and electric powers per turbine

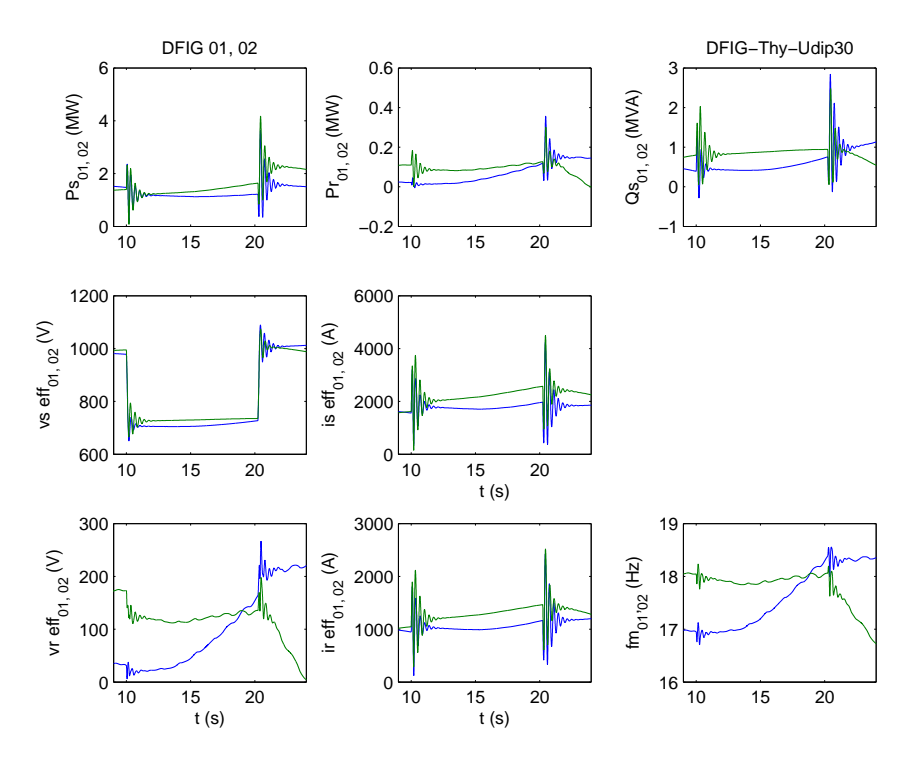


Figure 182: VSP-DFIG-thy voltage dip of 30% - 10 seconds: stator power, rotor power, stator reactive power, stator voltage, stator current, rotor voltage, rotor current and stator frequency

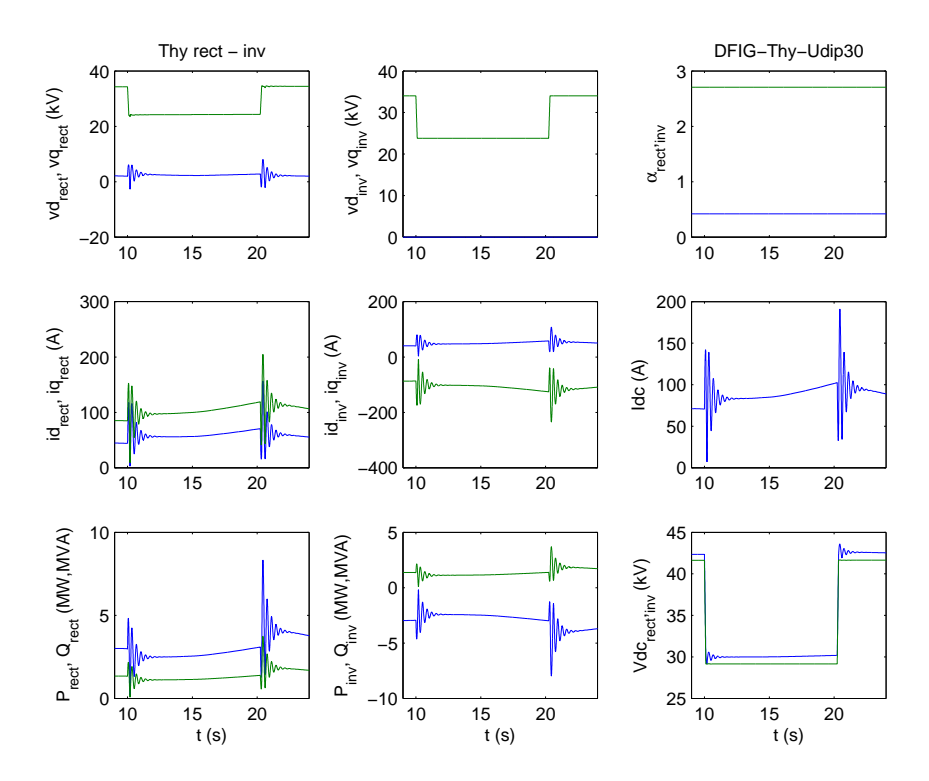


Figure 183: VSP-DFIG-thy voltage dip of 30% - 10 seconds: rectifier voltages, inverter voltages, firing angles, rectifier currents, inverter currents, DC current, rectifier active and reactive power, inverter active and reactive power, rectifier and inverter DC voltage of the thyristor bridge

The voltage dip of 30% during 10 seconds on the turbine variables causes oscillations in the voltages, currents active and reactive power of the VSP-DFIG-thy wind farm, see figures 181, 182 and 183. The step in inverter voltages results in a step in DC voltage and in rectifier AC voltage. The stator power decreases and the stator current increases due to the dip. The rotor currents effective value is intially 1000 A and peaks to about 2500 A.

### Voltage dip of 50% - 0.5 seconds

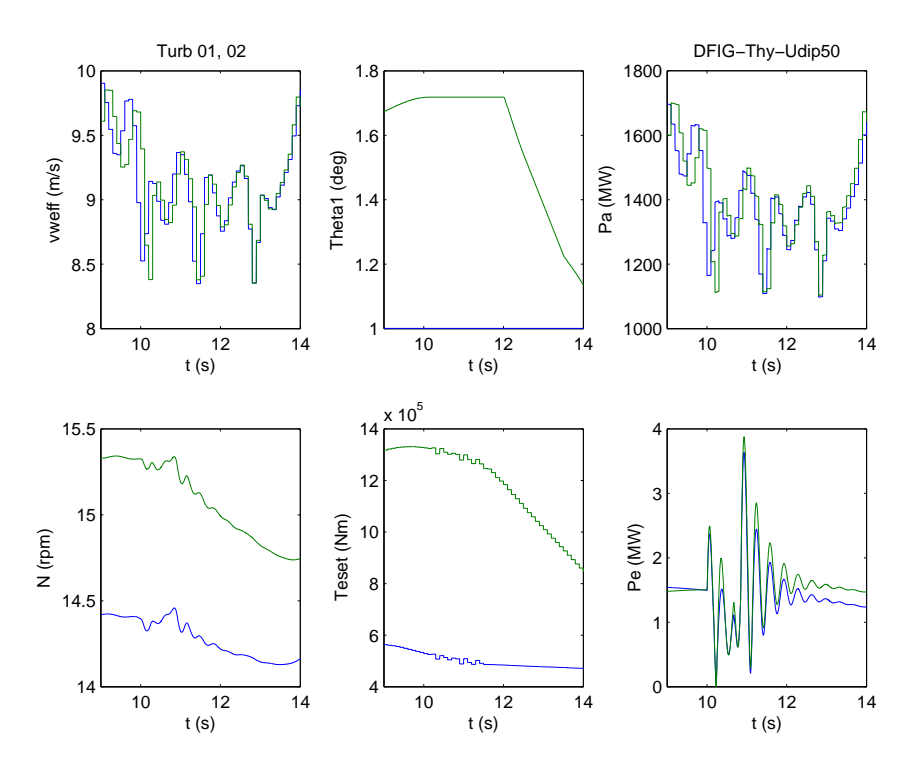


Figure 184: VSP-DFIG-thy voltage dip of 50% - 0.5 seconds: wind speeds, pitch angles, aerodynamic powers, turbine rotational speeds, electromagnetic torque setpoints and electric powers per turbine

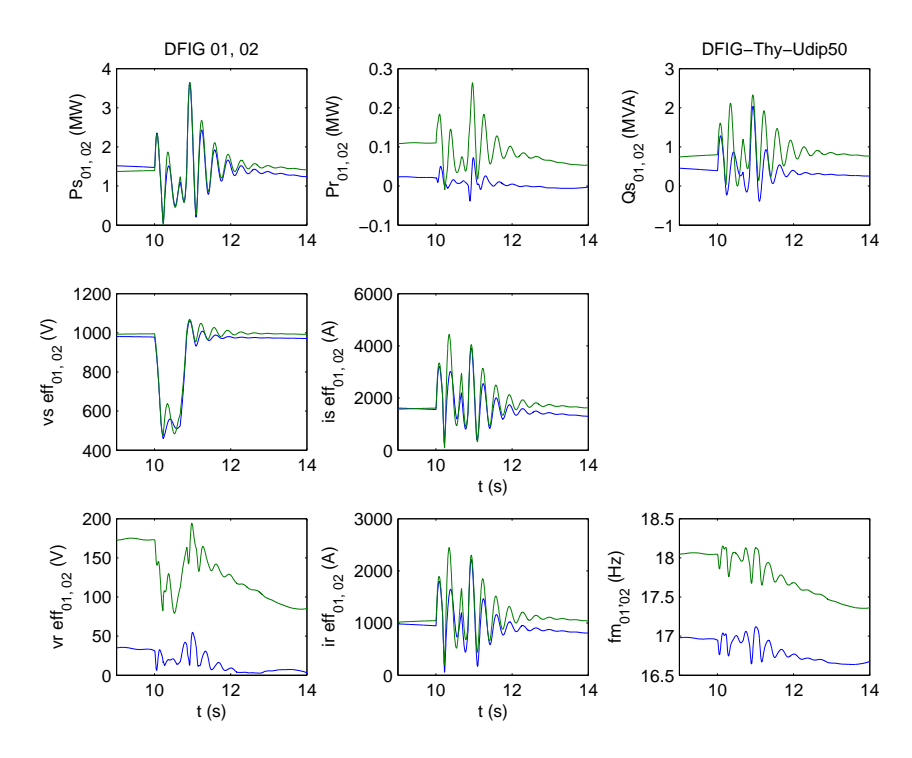


Figure 185: VSP-DFIG-thy voltage dip of 50% - 0.5 seconds: stator power, rotor power, stator reactive power, stator voltage, stator current, rotor voltage, rotor current and stator frequency

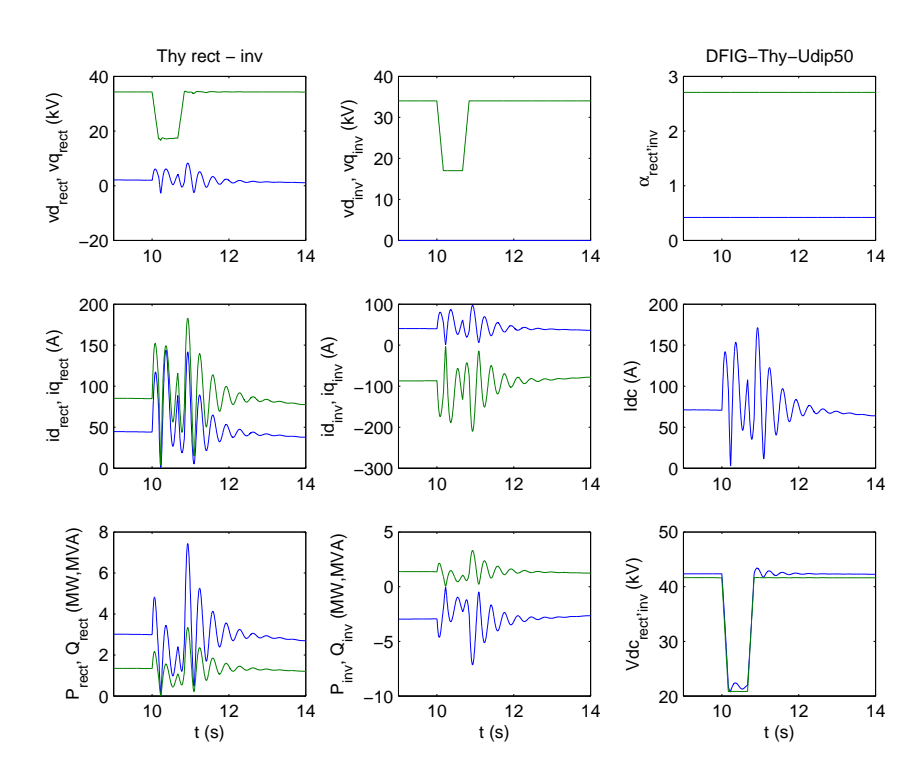


Figure 186: VSP-DFIG-thy voltage dip of 50% - 0.5 seconds: rectifier voltages, inverter voltages, firing angles, rectifier currents, inverter currents, DC current, rectifier active and reactive power, inverter active and reactive power, rectifier and inverter DC voltage of the thyristor bridge

Similar oscillations are found for the voltage dip of 50% during 0.5 seconds. The rotor currents effective value is intially 1000 A and peaks to about 2500 A, about the same as in the 30% dip. Voltage dip of 85% - 0.2 seconds

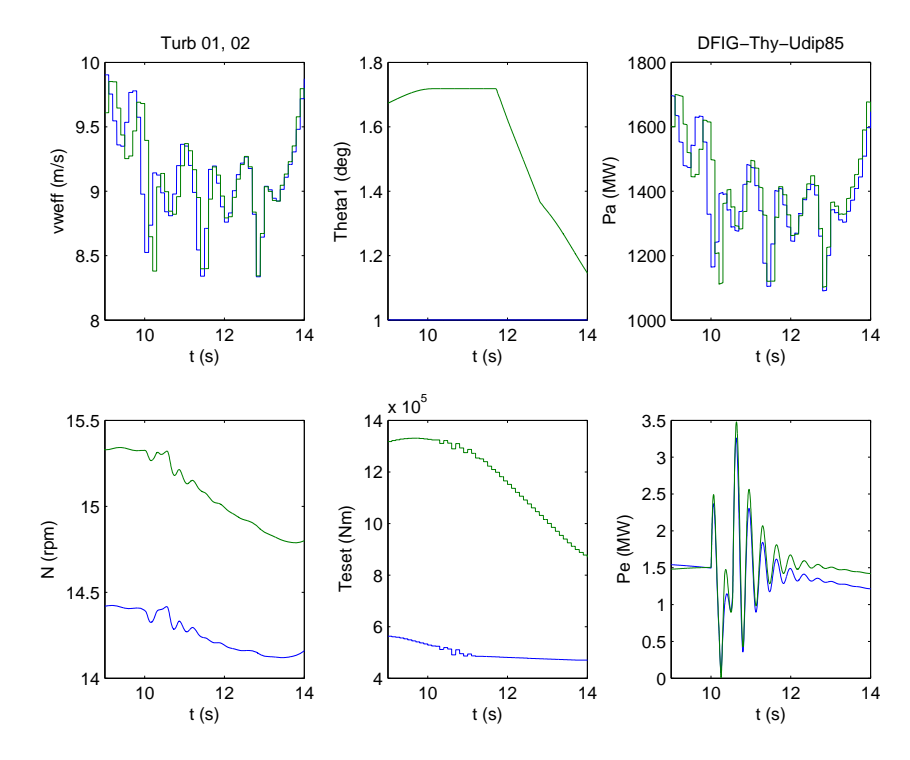


Figure 187: VSP-DFIG-thy voltage dip of 85% - 0.2 seconds: wind speeds, pitch angles, aerodynamic powers, turbine rotational speeds, electromagnetic torque setpoints and electric powers per turbine

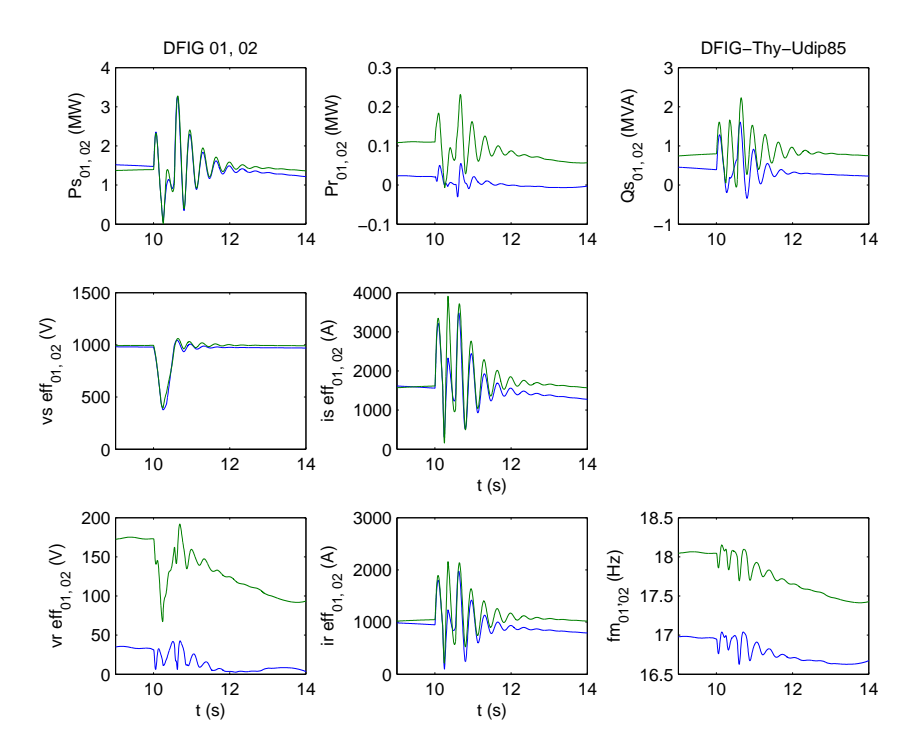


Figure 188: VSP-DFIG-thy voltage dip of 85% - 0.2 seconds: stator power, rotor power, stator reactive power, stator voltage, stator current, rotor voltage, rotor current and stator frequency

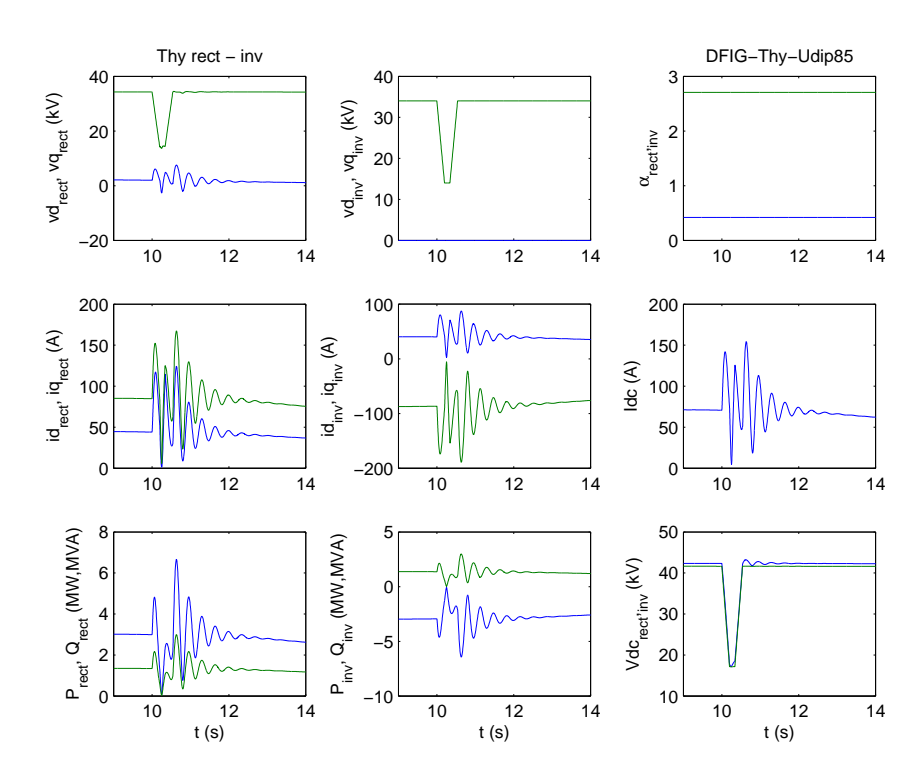


Figure 189: VSP-DFIG-thy voltage dip of 85% - 0.2 seconds: rectifier voltages, inverter voltages, firing angles, rectifier currents, inverter currents, DC current, rectifier active and reactive power, inverter active and reactive power, rectifier and inverter DC voltage of the thyristor bridge

The rotor currents effective value for the voltage dip of 85% during 0.2 seconds is intially 1000 A and peaks to about 2100 A.

From the above results, we can see that the wind farm can ride through all the voltage dips without transient over-current in the rotor. It is not necessarily to short circuit the rotor by a crowbar to protect the rotor converter. The reason is that during voltage dips, the flux controller will decrease the flux level to limit its output active power, thus the currents are automatically limited during voltage dips. This feature also helps to prevent commutation failure of the thyristor bridge inverter.

So, a crowbar is not necessary in this wind farm concept. If crowbar protection is used, the grid side rotor converter should be able to support all the reactive power required by the generator and thyristor bridge when the crowbar is working. The reason is that when the crowbar is working, the DFIG becomes a constant speed induction generator which draws reactive power from the stator for excitation, and the thyristor bridge also consumes reactive power. It is possible for the rotor grid converter to provide large amount of reactive power when the crowbar is working, because the active power required to be transferred from the rotor is zero during this time.

## 7.4 Response to a frequency dip

## CSS-IG-dc frequency dip (system # 1)

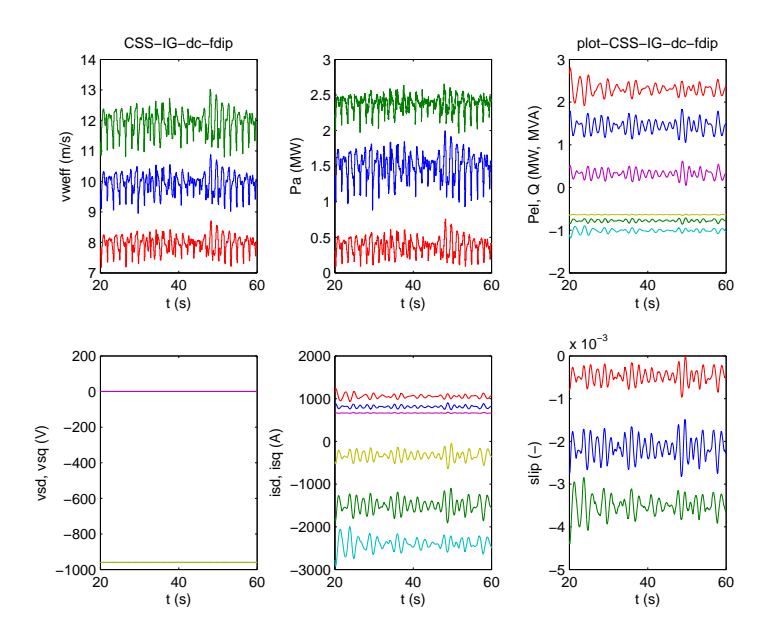


Figure 190: CSS-IG-dc wind farm, frequency dip 10%, 10 sec: rotor effective wind speed, aerodynamic power, electric and reactive power, stator d and q voltage, stator d and q current and slip per turbine

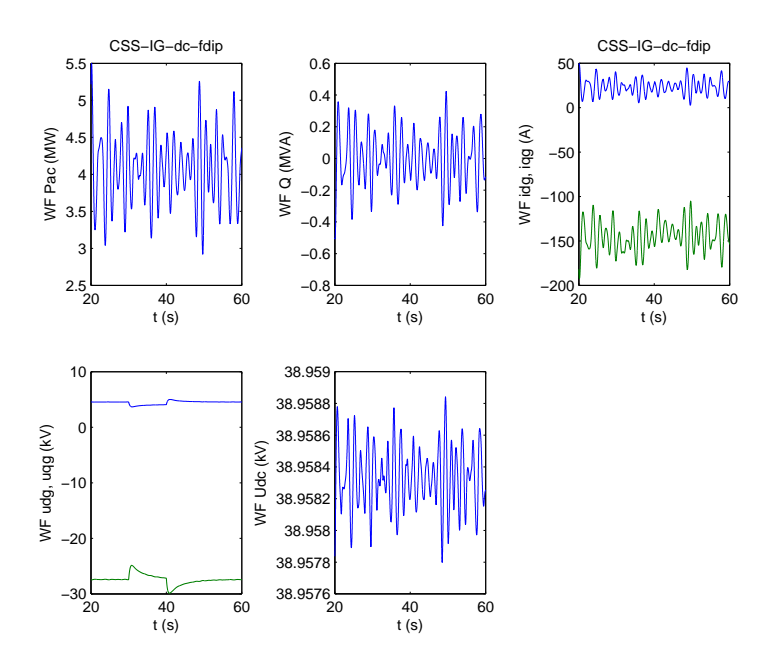


Figure 191: CSS-IG-dc wind farm, frequency dip 10%, 10 sec: active power, reactive power, inverter dq-currents, inverter dq-voltages, DC voltage and wind farm frequency

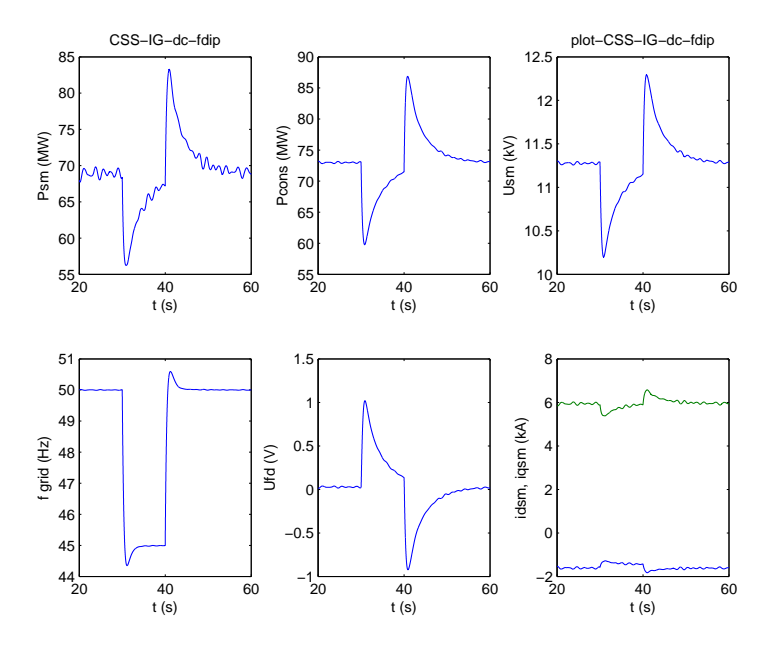


Figure 192: CSS-IG-dc model, frequency dip 10%, 10 sec: grid synchronous generator power, consumer load, synchronous machine voltage, grid frequency, exciter voltage and synchronous machine d and q currents

The wind turbines of the CSS-IG-dc wind farm are not affected by the frequency dip, see figure 190. The DC voltage is not affected either, the d and q grid voltage change dynamically (figure 191). This corresponds to response of the grid model: due to the frequency change there are also transients in synchronous machine excitation, terminal voltage and consumer load (figure 192).

## VSP-CCIG-ac frequency dip (system # 3)

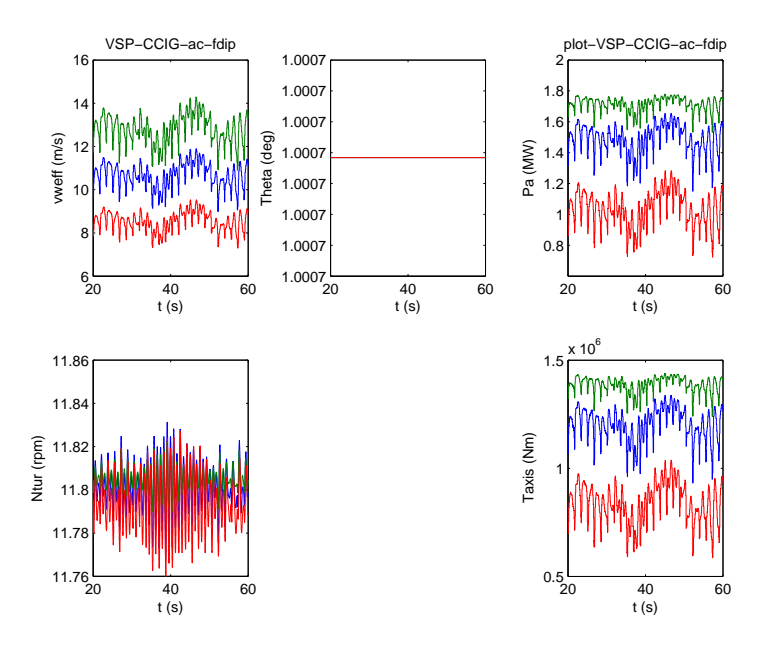


Figure 193: VSP-CCIG-ac wind farm, frequency dip 10%, 10 sec: wind speeds, pitch angles, aerodynamic powers, turbine rotational speeds and axial torques per turbine

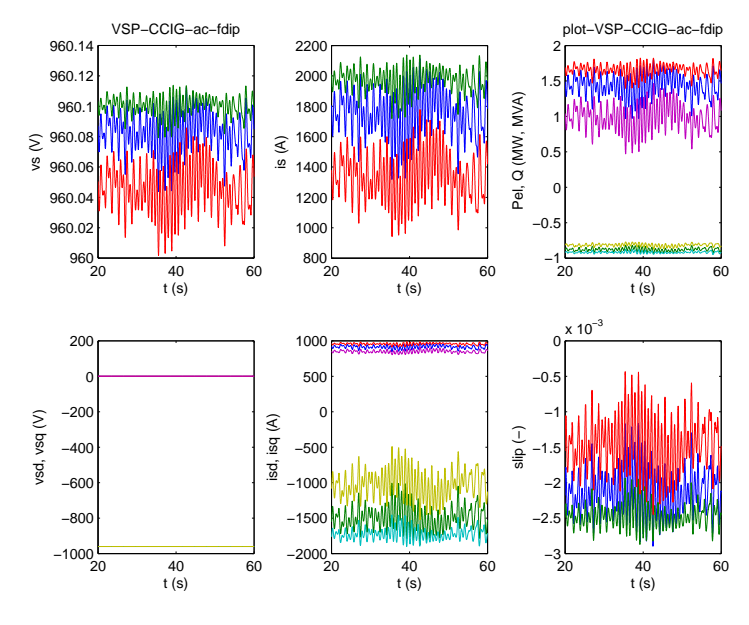


Figure 194: VSP-CCIG-ac wind farm, frequency dip 10%, 10 sec: stator voltages, stator currents, active and reactive powers, dq stator voltages, dq stator currents and slips per turbine

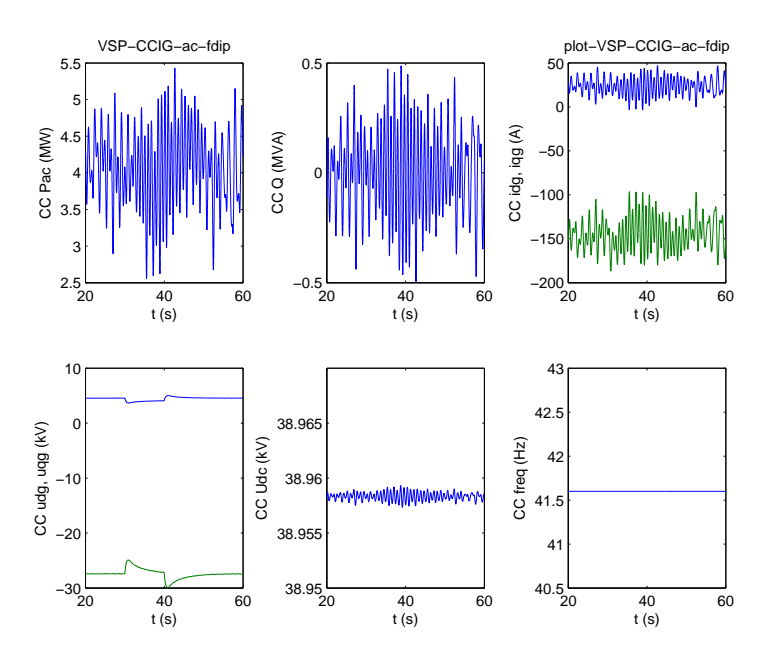


Figure 195: VSP-CCIG-ac wind farm, frequency dip 10%, 10 sec: cluster active and reactive power at the grid side, inverter dq-currents, inverter dq-voltages, DC voltage and cluster frequency

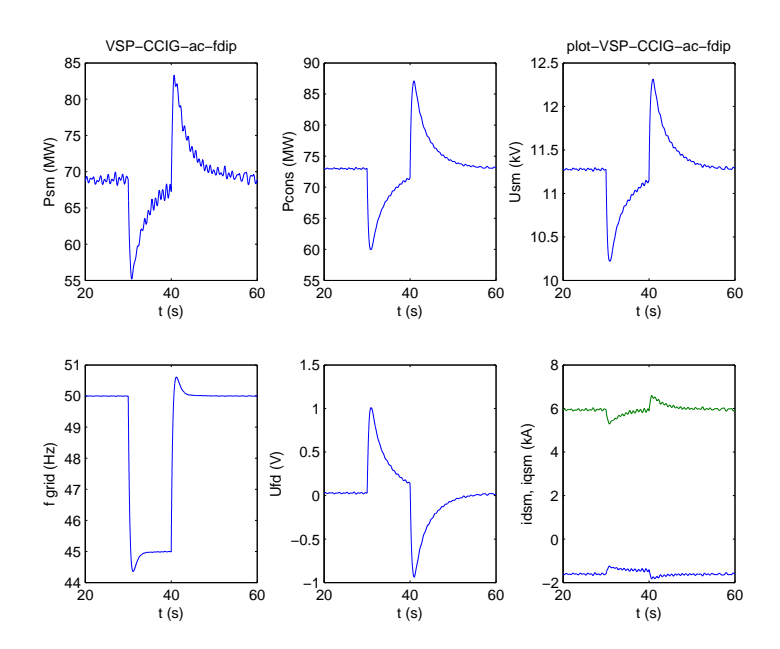


Figure 196: VSP-CCIG-ac wind farm, frequency dip 10%, 10 sec: grid response

The results for the VSP-CCIG-ac wind farm are similar to those for the CSS-IG-dc wind farm: the turbines are not affected by the frequency dip, only grid voltages and powers change during the dip.

# VSP-FCIG-ac frequency dip (system #6)

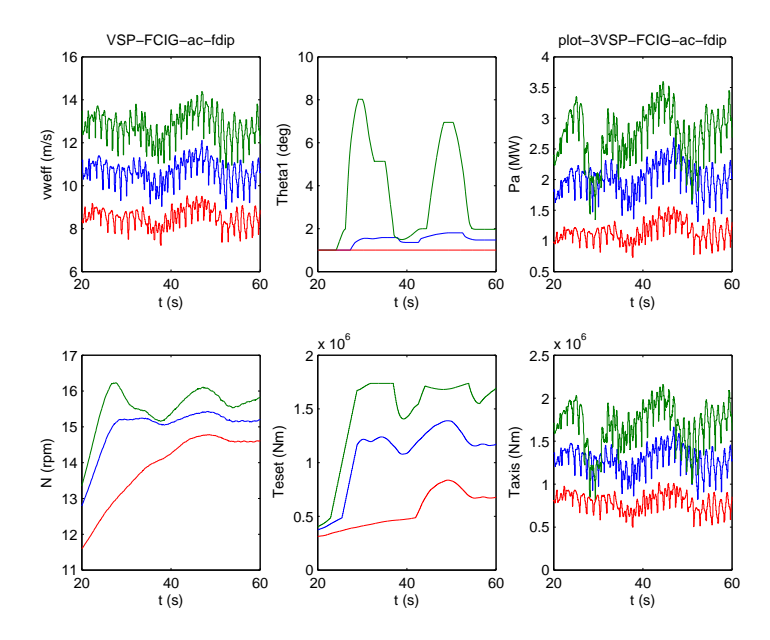


Figure 197: VSP-FCIG-ac wind farm, frequency dip 10%, 10 sec: wind speeds, pitch angles, aerodynamic powers, turbine rotational speeds, electromagnetic torque setpoints and mechanical torques per turbine

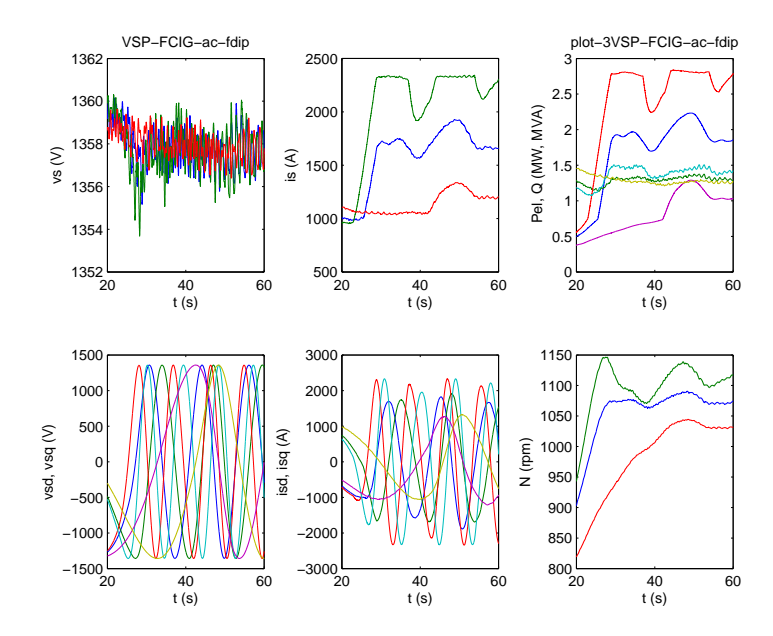


Figure 198: VSP-FCIG-ac wind farm, frequency dip 10%, 10 sec: stator voltages, stator currents, active and reactive powers, dq stator voltages, dq stator currents and turbine rotational speeds per turbine

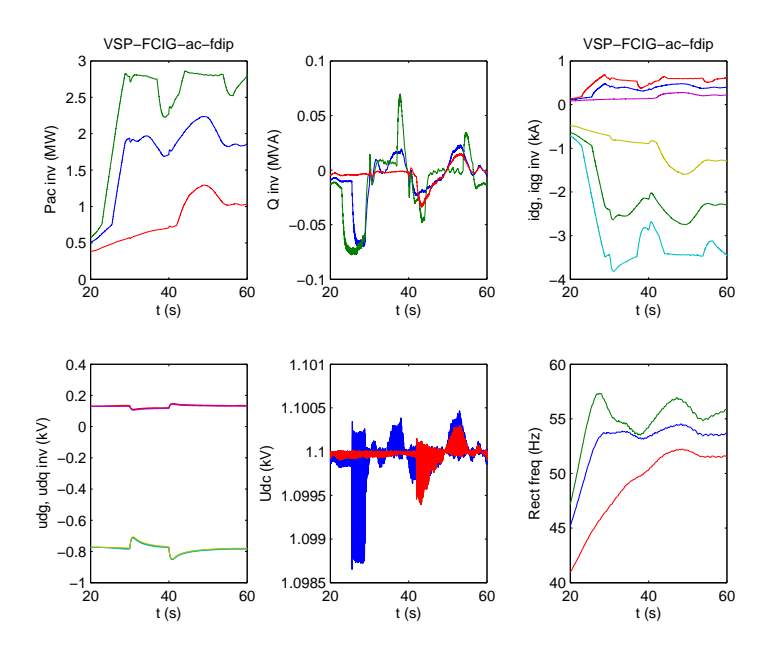


Figure 199: VSP-FCIG-ac wind farm, frequency dip 10%, 10 sec: inverter active and reactive powers, inverter dq-currents, inverter dq-voltages, DC voltages and rectifier frequencies per turbine

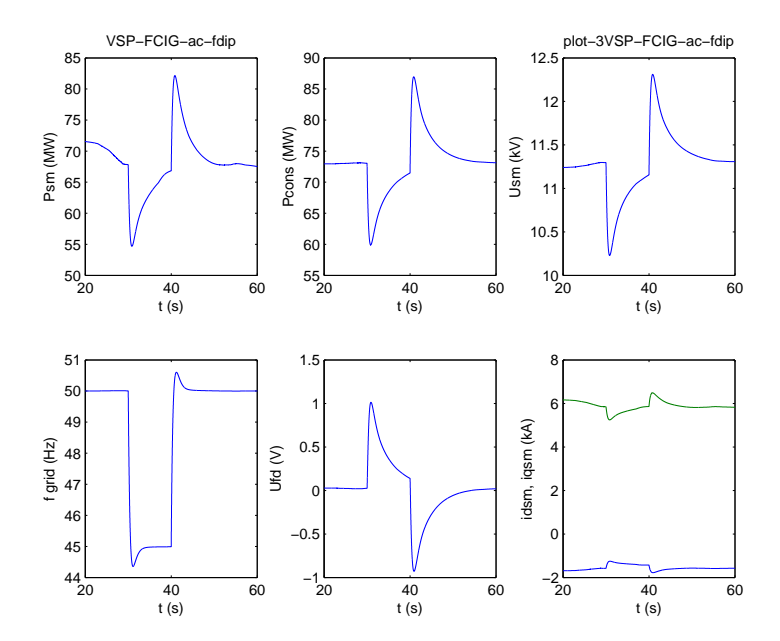


Figure 200: VSP-FCIG-ac wind farm, frequency dip 10%, 10 sec: grid response

The results for the VSP-FCIG-ac wind farm are similar to the two previous systems: the turbines are not affected by the frequency dip, only grid voltages and powers change.

#### Model Thy5 Inverter freq dip 50% Vb, Vc (kV) 100 0 ۷a, -100 <del>-</del> 0.05 0.1 0.15 0.2 0.25 (<u>k</u> 10 <u>ပ</u> 0 <u>6</u> <u>ø</u> -10 └─ 0.05 0.15 0.2 0.25 200 Vdc, Vba, Vbc, Vac (kV)<sub>Vdc</sub> (kV) 0.05 0.1 0.15 0.2 0.25 200 200 └─ 0.05 0.1 0.15 0.2 0.25 6 0.05 0.1 0.15 0.2 0.25 t (s)

## VSP-DFIG-thy frequency dip (system # 9)

Figure 201: VSP-DFIG-thy inverter response to a frequency dip of 50% and 0.1 sec

The response of the VSP-DFIG-thy to a frequency dip is determined by the inverter. Critical condition is the possibility of commutation failure. This can best be examined by the instantaneous model of the thyristor bridge (Model Thy5 in section 3.5.3), the averaged model may not represent the effect of changing instantaneous voltages correctly. Figure 201 demonstrates that a severe frequency dip of 50% is not a problem for the thyristor bridge rectifier. The commutation is not affected, the average DC voltage slightly decreases and the DC current is only slightly increased. The effect on the VSP-DFIG wind farm will be minimal.

### 7.5 Case study conclusions

- All nine new electrical wind farm configurations have at least one converter in the path from turbine to high voltage grid. Of these configurations, four have been chosen for evaluation in the case study: CSS-IG-dc, VSP-CCIG-dc, VSP-FCIG-ac and VSP-DFIGthy.
- The flicker levels of the wind farms in the case study are of equal magnitude.
- Three voltage dips have been simulated: 30%-10 sec, 50%-0.5 sec and 85%-0.2 sec. The 85%-0.2 sec dip caused high inverter current peaks in the systems with voltage source converter. The current control of the inverter may be improved to cope with these peaks and the control of the DC voltage may be relaxed. The turbine side was not affected by the dip due to the practically constant DC voltage.
- A frequency dip was not transmitted to the wind turbine side of wind farms with voltage source self commutating full converters in (CSS-IG-dc, VSP-CCIG-dc and VSP-FCIGac);

• The frequency dip did not result in inverter commutation failure for the wind farm with current source grid commutating full converter (VSP-DFIG-thy) and the frequency dip was not transmitted to the wind turbine side.

## 8 Control of the DFIG-ac system for an unbalanced short circuit

Low voltage ride through (LVRT) capability of DFIG has been studied extensively [25, 34, 2, 28, 17], but only for a symmetrical fault. Transient over-current in the rotor is identified as the most severe LVRT problem of the DFIG, because the rotor side voltage source converter (VSC) is very sensitive to thermal overload. The active crowbar protection is designed to short circuit the rotor under such circumstances, both to protect the rotor side VSC and to damp out the oscillations faster. In the high voltage grid, unsymmetrical faults happen more frequently than symmetrical faults.

For an unsymmetrical fault, the most severe problem is not the transient over-current in the rotor, but the large electric torque pulsation which potentially causes gearbox failure, and the large voltage ripple in the DC link of back to back VSC which may decrease the lifetime of the DC capacitance.

New definitions of the instantaneous active and reactive power [19, 3] can be used to analyse an unsymmetrical fault and to design and operate the grid connected VSC under unbalanced situations [35, 24]. Unlike the symmetrical operating condition, which is characterized by a constant instantaneous active power input from the rotor VSC, the rotor VSC of DFIG can send a pulsating instantaneous active power to the DC link during asymmetrical voltage dips. To improve the control of DFIG under unsymmetrical voltage dip, it is first necessary to study the dynamic behavior of DFIG for an unsymmetrical voltage dip.

#### 8.1 Introduction

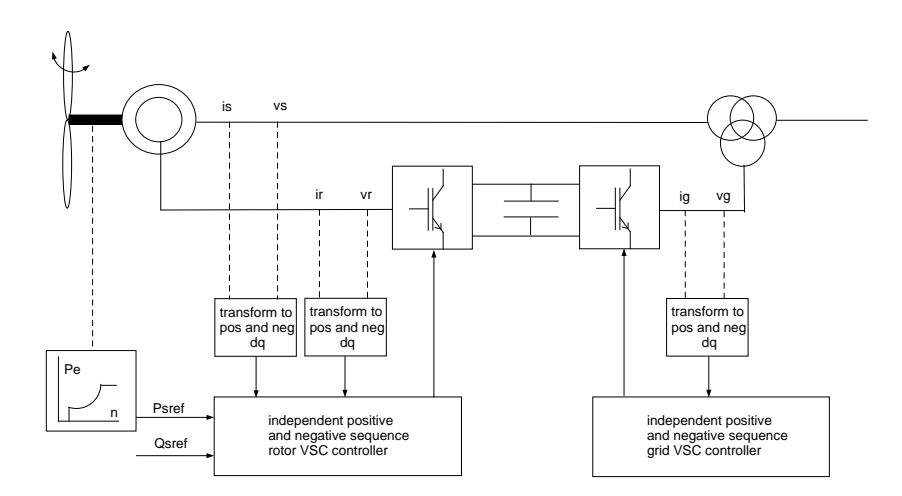


Figure 202: Simplified diagram of the proposed DFIG unbalanced fault control system

Figure 202 describes the proposed DFIG unbalanced fault control system. The controllers on the rotor VSC and the grid VSC control the stator currents and the grid converter currents, both positive and negative sequences components independently. According to symmetrical components theory [23], during an unbalanced voltage dip, the system can be decoupled into positive, negative and zero sequence components. Both the positive and negative sequence components are themselves balanced three phase systems, they can be transformed into a positive dq system and a negative dq system. Then the voltages and currents in the positive and negative dq system are DC values, which can easily be controlled by simple PI controllers.

The positive and negative sequence components have to be totally decoupled. Otherwise, when controlling the positive sequence, the negative sequence will be influenced, and vice versa. A coupling between positive and negative sequence will deteriorate the control performance.

In order to fully decouple positive and negative sequence, the following assumptions are made:

• the DFIG stator and rotor windings are assumed to be symmetrical;

• the grid three phase AC inductances and resistances are symmetrical.

The reference stator currents and grid converter currents are calculated according to the instantaneous reactive power theory [19, 3]. When applying it to a three phase three line power system, the theory is simple and easy to understand. It becomes complex for a three phase four line power system. In this paper, only the three phase three, line power system is studied, the zero sequence is omitted. This choice is justified by the following reasons:

- the windturbine transformer is often  $Y/\Delta$  connected;
- the neutral point of the stator winding of a DFIG is not grounded.

In the next sections, the simulation results of a DFIG under symmetrical and unsymmetrical voltage dips will be presented first and the instantaneous reactive power theory will be used to analyze the result.

### 8.1.1 Symmetrical and unsymmetrical voltage dip

Distinctive differences between the behavior of the DFIG under symmetrical and unsymmetrical voltage dips can be seen in Figure 203.

The figure shows that for a symmetrical voltage dip, the problem is the magnitude of the transient current in the rotor. This problem is generally solved by the so called crowbar protection system, which uses a thyristor controlled resistor bank to short circuit the rotor windings.

Figure 203 also shows that for an unsymmetrical voltage dip, the maximum rotor currents can be smaller, but have second order harmonic which causes a large DC voltage ripple in the DC link. The magnitude of the rotor transient currents for the unsymmetrical voltage dip depends on the starting moment of the dip, which determines the magnitude of the initial stator currents and thus determines the response of the stator currents. Depending on the magnitude of rotor transient currents, the unsymmetrical voltage dip may activate the crowbar protection system.

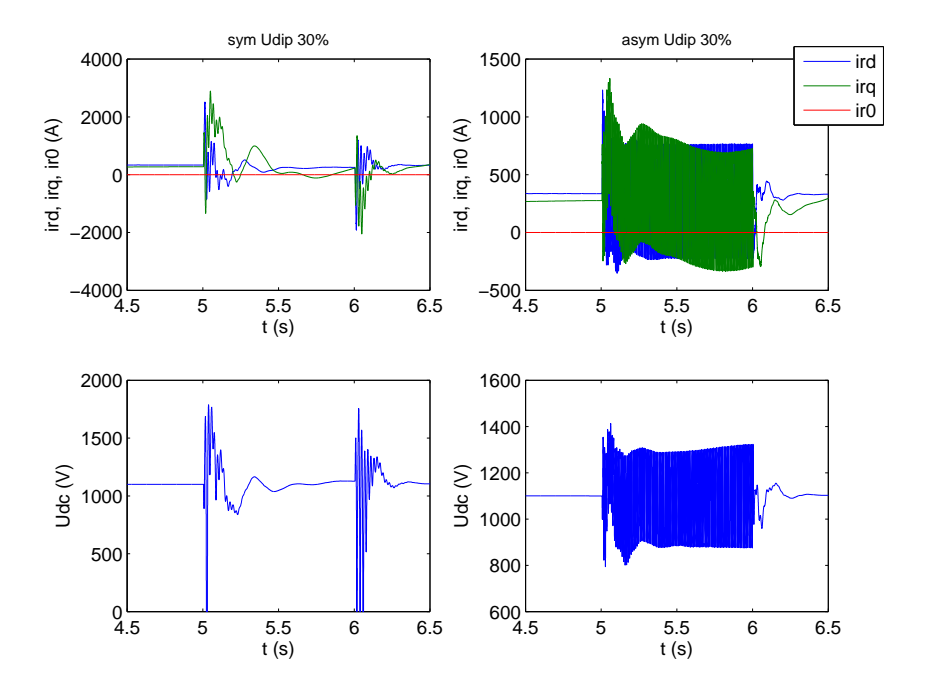


Figure 203: DFIG symmetrical (left) and unsymmetrical voltage dip (right): rotor currents and DC voltage

# 8.1.2 Instantaneous active and reactive power with positive and negative sequence components

According to the instantaneous reactive power theory [19], the instantaneous power p and q in the stationary  $\alpha\beta$ -reference frame are:

$$\begin{bmatrix} p \\ q \end{bmatrix} = \begin{bmatrix} v_{\alpha}i_{\alpha} + v_{\beta}i_{\beta} \\ v_{\beta}i_{\alpha} - v_{\alpha}i_{\beta} \end{bmatrix}$$
(77)

with

$$\begin{bmatrix} v_0 \\ v_{\alpha} \\ v_{\beta} \end{bmatrix} = \sqrt{\frac{2}{3}} \begin{bmatrix} \frac{1}{\sqrt{2}} & \frac{1}{\sqrt{2}} & \frac{1}{\sqrt{2}} \\ 1 & -\frac{1}{2} & -\frac{1}{2} \\ 0 & \frac{\sqrt{3}}{2} & -\frac{\sqrt{3}}{2} \end{bmatrix} \begin{bmatrix} v_a \\ v_b \\ v_c \end{bmatrix}$$
(78)

and

$$\begin{bmatrix} i_0 \\ i_{\alpha} \\ i_{\beta} \end{bmatrix} = \sqrt{\frac{2}{3}} \begin{bmatrix} \frac{1}{\sqrt{2}} & \frac{1}{\sqrt{2}} & \frac{1}{\sqrt{2}} \\ 1 & -\frac{1}{2} & -\frac{1}{2} \\ 0 & \frac{\sqrt{3}}{2} & -\frac{\sqrt{3}}{2} \end{bmatrix} \begin{bmatrix} i_a \\ i_b \\ i_c \end{bmatrix}$$
 (79)

Eq.77 is true for both balanced and unbalanced three phase three line system. The stationary  $\alpha\beta$ -reference frame can be decoupled into positive and negative sequence:

$$\begin{bmatrix} v_{\alpha}(t) \\ v_{\beta}(t) \end{bmatrix} = \begin{bmatrix} v_{\alpha}^{+}(t) + v_{\alpha}^{-}(t) \\ v_{\beta}^{+}(t) + v_{\beta}^{-}(t) \end{bmatrix}$$
(80)

Using Eq.77, Eq.80 and the Park transformation, the instantaneous active and reactive power of the positive and negative dq-sequences can be derived:

$$\begin{bmatrix} p \\ q \end{bmatrix} = \begin{bmatrix} \bar{p} + \tilde{p} \\ \bar{q} + \tilde{q} \end{bmatrix} = \begin{bmatrix} (v_d^+ i_d^+ + v_q^+ i_q^+ + v_d^- i_d^- + v_q^- i_q^-) \\ (v_q^+ i_d^+ - v_d^+ i_q^+ + v_q^- i_d^- - v_d^- i_q^-) \end{bmatrix}$$

$$+ \sin(2\theta) \begin{bmatrix} (v_d^+ i_q^- - v_q^+ i_d^- + v_q^- i_d^+ - v_d^- i_q^+) \\ (v_d^+ i_d^- + v_q^+ i_q^- + v_d^- i_d^+ + v_q^- i_q^+) \end{bmatrix}$$

$$+ \cos(2\theta) \begin{bmatrix} v_d^+ i_d^- + v_q^+ i_q^- + v_d^- i_d^+ + v_q^- i_q^+ \\ v_d^+ i_q^- - v_q^+ i_d^- + v_q^- i_d^+ - v_d^- i_q^+ \end{bmatrix}$$
(81)

The terms  $\sin(2\theta)$  and  $\cos(2\theta)$  in Eq.81 are the oscillation parts of the instantaneous power p and q. The oscillating parts of the instantaneous active power p are linked to the DC voltage ripple and an electric torque pulsation, as shown in the simulation results in figure 203.

In order to limit the DC voltage ripple and the torque pulsation for an unsymmetrical voltage dip, the terms of  $\sin(2\theta)$  and  $\cos(2\theta)$  of the instantaneous active power p in Eq.81 have to be controlled to zero. Rearranging Eq.81, four independent equations can be used to determine the four reference currents  $i_d^+, i_q^+, i_d^-, i_q^-$ , and the currents can be controlled by the voltages  $v_d^+, v_q^+, v_d^-, v_q^-$  imposed by the VSC. This can be realised by relatively simple PI controllers.

$$\begin{bmatrix} \bar{p} \\ \bar{q} \\ \tilde{p}_{\sin 2\theta} \\ \tilde{p}_{\cos 2\theta} \end{bmatrix} = \begin{bmatrix} P_{ref} \\ Q_{ref} \\ 0 \\ 0 \end{bmatrix} = \begin{bmatrix} v_d^+ i_d^+ + v_q^+ i_q^+ + v_d^- i_d^- + v_q^- i_q^- \\ v_q^+ i_d^+ - v_d^+ i_q^+ + v_q^- i_d^- - v_d^- i_q^- \\ v_d^+ i_q^- - v_q^+ i_d^- + v_q^- i_d^+ - v_d^- i_q^+ \\ v_d^+ i_d^- + v_q^+ i_q^- + v_d^- i_d^+ + v_q^- i_q^+ \end{bmatrix}$$
(82)

 $\tilde{p}_{\sin 2\theta}$  and  $\tilde{p}_{\cos 2\theta}$  are the two oscillation terms of instantaneous active power p. In order to reduce these to zero, the instantaneous voltage and current have to be separated into positive and negative sequence in real time.

# 8.2 Real time determination of positive and negative sequence components

The proposed control method requires fast and accurate determination of positive and negative sequence components. Two methods are often used [35].

The first method is based on the fact that the negative sequence component appears as second order harmonic in the synchronously rotating frame (positive dq variables), and the positive sequence component appears as second order harmonic in the negative synchronously rotating frame (negative dq variables). A low pass filter can be used to suppress the high frequency oscillations. Thus the positive and negative sequences are separated in real time. The method is shown in figure 204.

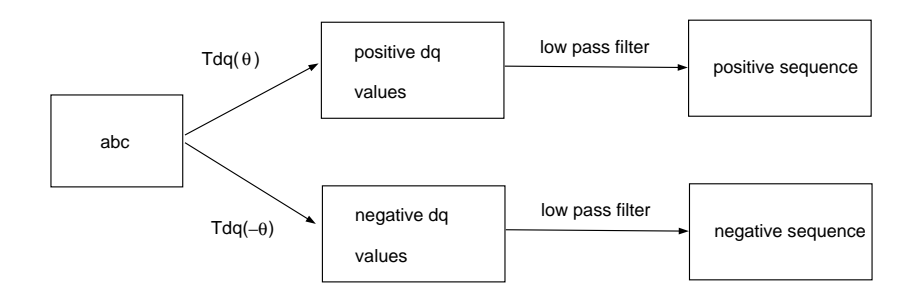


Figure 204: Positive and negative dq sequence components by low pass filters

The second method is called *signal delay cancellation* method. The abc system is first transformed to a stationary reference frame of  $\alpha\beta$ -coordinates using Clark's transformation. The result is delayed by T/4. The positive and negative sequence can be calculated by adding or subtracting the present real time signal with the delayed signal. It is explained mathematically in the following way.

The abc system can be transformed into stationary  $\alpha\beta$ -reference frame using Clark's transformation, and can be expressed in positive and negative sequence as:

$$\begin{bmatrix} v_{\alpha}(t) \\ v_{\beta}(t) \end{bmatrix} = \begin{bmatrix} v_{\alpha}^{+}(t) + v_{\alpha}^{-}(t) \\ v_{\beta}^{+}(t) + v_{\beta}^{-}(t) \end{bmatrix} = \begin{bmatrix} v^{+}\cos(\omega t + \phi^{+}) + v^{-}\cos(-\omega t + \phi^{-}) \\ v^{+}\sin(\omega t + \phi^{+}) + v^{-}\sin(-\omega t + \phi^{-}) \end{bmatrix}$$
(83)

Delay this signal for T/4:

$$\begin{bmatrix} v_{\alpha}(t - \frac{T}{4}) \\ v_{\beta}(t - \frac{T}{4}) \end{bmatrix} = \begin{bmatrix} v^{+}\sin(\omega t + \phi^{+}) - v^{-}\sin(\omega t + \phi^{-}) \\ -v^{+}\cos(\omega t + \phi^{+}) + v^{-}\cos(-\omega t + \phi^{-}) \end{bmatrix}$$
(84)

Comparing the equations of  $\alpha\beta(t)$  and  $\alpha\beta(t-T/4)$ , it is clear that the positive and negative sequence can be derived by adding or subtracting:

$$\begin{bmatrix} v_{\alpha}^{+}(t) \\ v_{\beta}^{+}(t) \\ v_{\alpha}^{-}(t) \\ v_{\beta}^{-}(t) \end{bmatrix} = \frac{1}{2} \begin{bmatrix} 1 & 0 & 0 & -1 \\ 0 & 1 & 1 & 0 \\ 1 & 0 & 0 & 1 \\ 0 & 1 & -1 & 0 \end{bmatrix} \cdot \begin{bmatrix} v_{\alpha}(t) \\ v_{\beta}(t) \\ v_{\alpha}(t - T/4) \\ v_{\beta}(t - T/4) \end{bmatrix}$$
(85)

The positive and negative sequence in  $\alpha\beta$ -coordinates can be further transformed into positive dq and negative dq sequence components using:

$$\begin{bmatrix} v_{d}^{+}(t) \\ v_{q}^{+}(t) \end{bmatrix} = \begin{bmatrix} \cos \theta & \sin \theta \\ -\sin \theta & \cos \theta \end{bmatrix} \cdot \begin{bmatrix} v_{\alpha}^{+}(t) \\ v_{\beta}^{+}(t) \end{bmatrix}$$
$$\begin{bmatrix} v_{d}^{-}(t) \\ v_{q}^{-}(t) \end{bmatrix} = \begin{bmatrix} \cos(-\theta) & \sin(-\theta) \\ -\sin(-\theta) & \cos(-\theta) \end{bmatrix} \cdot \begin{bmatrix} v_{\alpha}^{-}(t) \\ v_{\beta}^{-}(t) \end{bmatrix}$$
(86)

At the moment of the voltage dip and the voltage recovery, the "signal delay cancellation" method will have a large transients and also a time delay of T/4. The 'signal delay cancellation" method is summarized in the following graph:

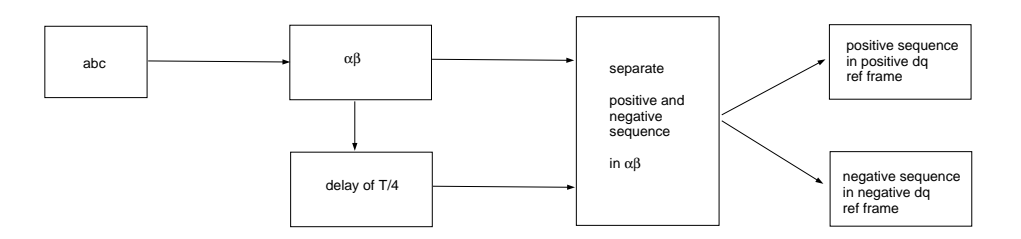


Figure 205: Positive and negative dq sequence components by signal delay cancellation

The unbalanced voltages in the positive dq reference frame applying the two separation methods are shown in the next figure:

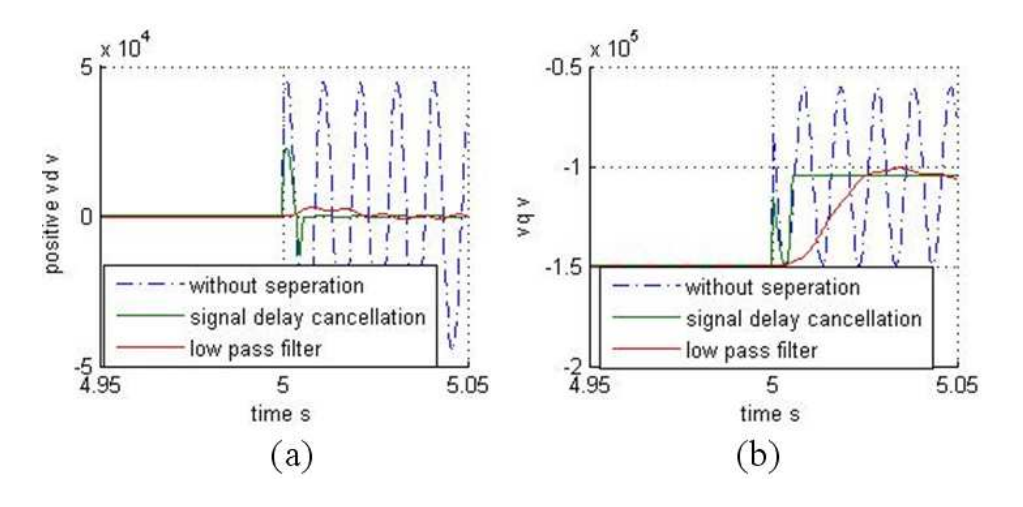


Figure 206: Unbalanced voltages in positive dq reference frame  $v_d$  and  $v_q$  without separation and using the two separation methods

Without separation, the unbalanced three phase voltage or current has second order harmonics in the positive dq reference frame. Both separation methods have a transient before their outputs reaches a steady state. The "signal delay cancellation" is faster than "low pass filter" method, but it has a larger transient at the start and end of the voltage dip.

## 8.3 Positive and negative sequence control of DFIG

#### 8.3.1 Positive and negative sequence control of the rotor VSC

Assuming the DFIG itself is symmetrical, the voltage equations of positive and negative dq sequence components in generator convention are:

$$\begin{bmatrix} v_{ds}^{\pm} \\ v_{qs}^{\pm} \\ v_{qr}^{\pm} \\ v_{qr}^{\pm} \end{bmatrix} = \begin{bmatrix} -R_s i_{ds}^{\pm} - (\pm \omega_s \psi_{qs}^{\pm}) + \frac{d\psi_{ds}^{\pm}}{dt} \\ -R_s i_{qs}^{\pm} + (\pm \omega_s \psi_{ds}^{\pm}) + \frac{d\psi_{qs}^{\pm}}{dt} \\ -R_r i_{dr}^{\pm} - (\pm \omega_s - \omega_r) \psi_{qr}^{\pm} + \frac{d\psi_{qr}^{\pm}}{dt} \\ -R_r i_{dr}^{\pm} + (\pm \omega_s - \omega_r) \psi_{dr}^{\pm} + \frac{d\psi_{qr}^{\pm}}{dt} \end{bmatrix}$$
(87)

In equation 87,  $\omega_s$  is the stator electrical angular velocity,  $\omega_r$  is the rotational speed of rotor times the number of pole pairs, i.e.  $p\omega_m$ .

The positive and negative sequence components are completely decoupled, as can be seen in equation 87, so the DFIG can be controlled in positive and negative dq sequence independently. The controller of the rotor VSC is based on equation 87, using the rotor voltages to control the stator currents. The setpoints of the stator currents are based on the active and reactive power as shown in figure 202. The controller is shown in figure 207.

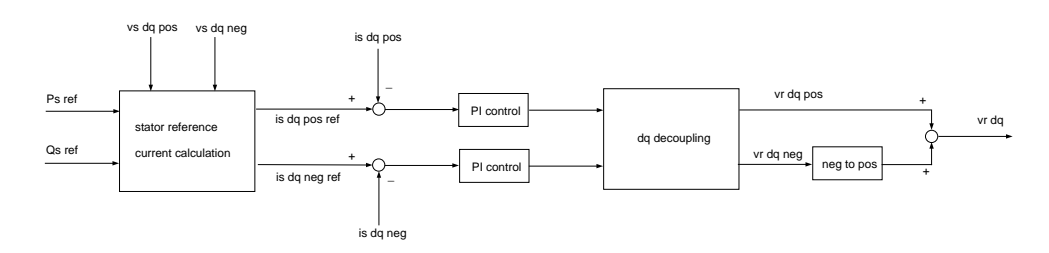


Figure 207: Separated positive and negative sequence component controller by the rotor VSC

The cross-coupling terms between d and q coordinates in the voltage equations are  $(\pm \omega_s - \omega_r)\psi_{qr}^\pm$  and  $(\pm \omega_s - \omega_r)\psi_{dr}^\pm$ . So the positive and negative sequence compensation is different. To decouple d and q axis, the cross-coupling terms are added to the outputs of PI controllers as in the conventional controllers for the balanced case.

#### 8.3.2 Positive and negative sequence control of the grid VSC

Assuming a symmetrical smoothing ac inductance and resistance at the grid VSC, the voltage equations of positive and negative dq sequence components in motor convention are:

$$\begin{bmatrix} v_{dc}^{\pm} \\ v_{qc}^{\pm} \end{bmatrix} = \begin{bmatrix} v_{dg}^{\pm} + R_c i_{dc}^{\pm} + (\pm \omega_s L_c i_{qc}^{\pm}) + L_c \frac{d i_{dc}^{\pm}}{dt} \\ v_{ag}^{\pm} + R_c i_{ac}^{\pm} - (\pm \omega_s L_c i_{dc}^{\pm}) + L_c \frac{d i_{ac}^{\pm}}{dt} \end{bmatrix}$$
(88)

Unlike the work presented in [35] and [24], for the DFIG the DC voltage ripple is caused by both the rotor VSC and the grid VSC. The instantaneous active power of the grid VSC has to be controlled together with the rotor VSC, in order to eliminate the DC voltage ripple. The reference currents of the grid VSC are calculated from the DC link voltage  $V_{dc}$ , the grid ac voltage, the rotor power and the reference reactive power  $Q_{ref}$ . The details of this controller can be seen in figure 208. In grid VSC controller, the cross-coupling terms between d and q coordinates are  $(\pm \omega_s L_c i_{qc}^{\pm})$  and  $(\pm \omega_s L_c i_{dc}^{\pm})$ . Same as in the rotor VSC controller, these are added to the outputs of the PI controllers (dq-decoupling).

#### 8 CONTROL OF THE DFIG-AC SYSTEM FOR AN UNBALANCED SHORT CIRCUIT

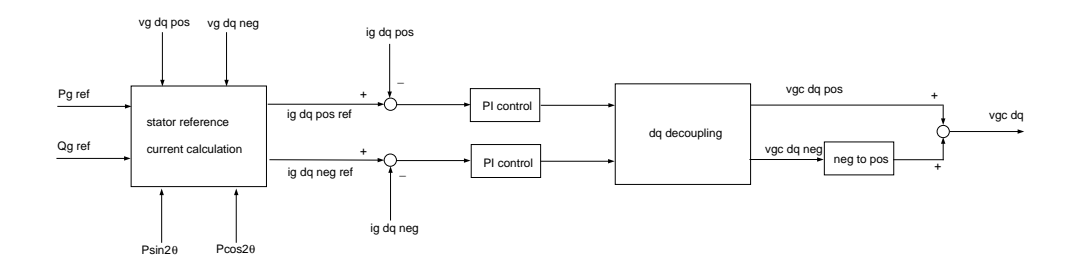


Figure 208: Separated positive and negative sequence component controller by the grid VSC

## 8.4 Modeling and simulation

# 8.4.1 Simulink model of the control of the DFIG system for an asymmetrical dip

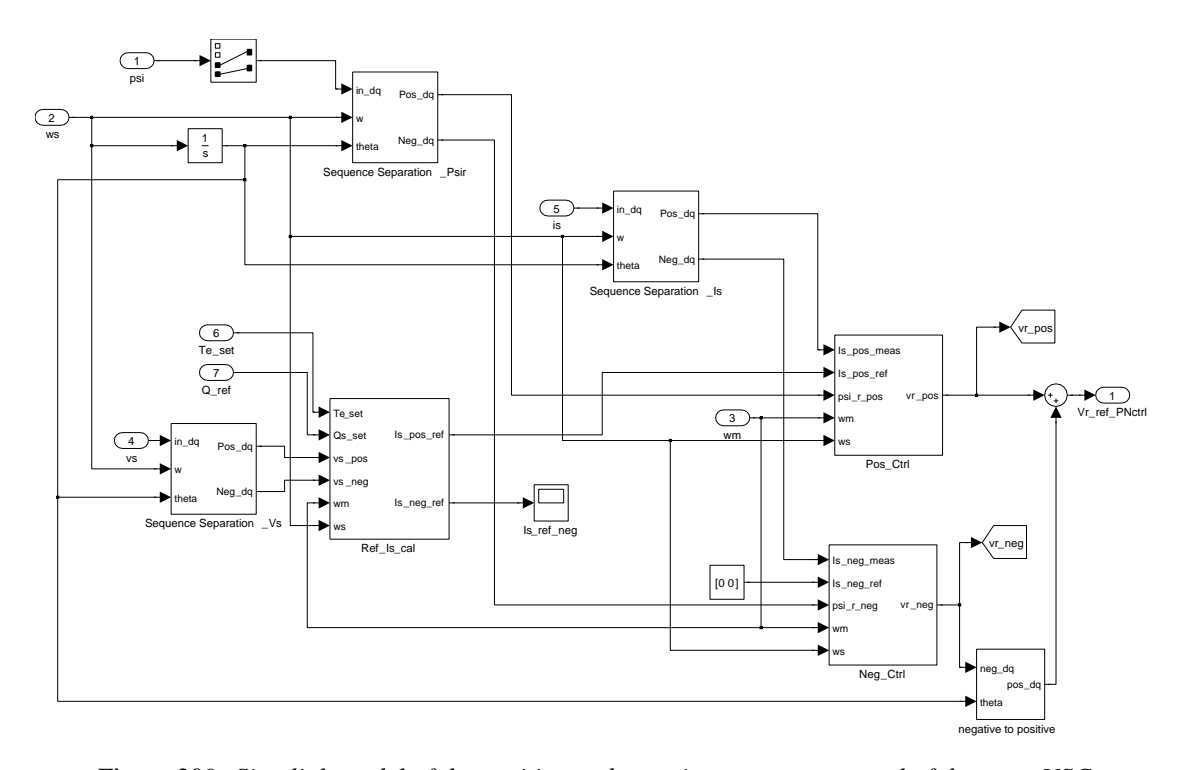


Figure 209: Simulink model of the positive and negative sequence control of the rotor VSC

Figure 209 shows the positive and negative sequence control of the rotor VSC in Simulink. The stator voltage and current and the rotor flux are separated into their positive and negative sequence dq components by sequence separation blocks. The reference positive sequence stator current is calculated from the reference torque and the reactive power setpoint. Two PI-controllers calculate the positive and negative dq rotor voltage. The negative dq rotor voltage is transformed to the positive reference frame and added to the positive dq rotor voltage, since the generator model reference frame is the positive sequence frame.

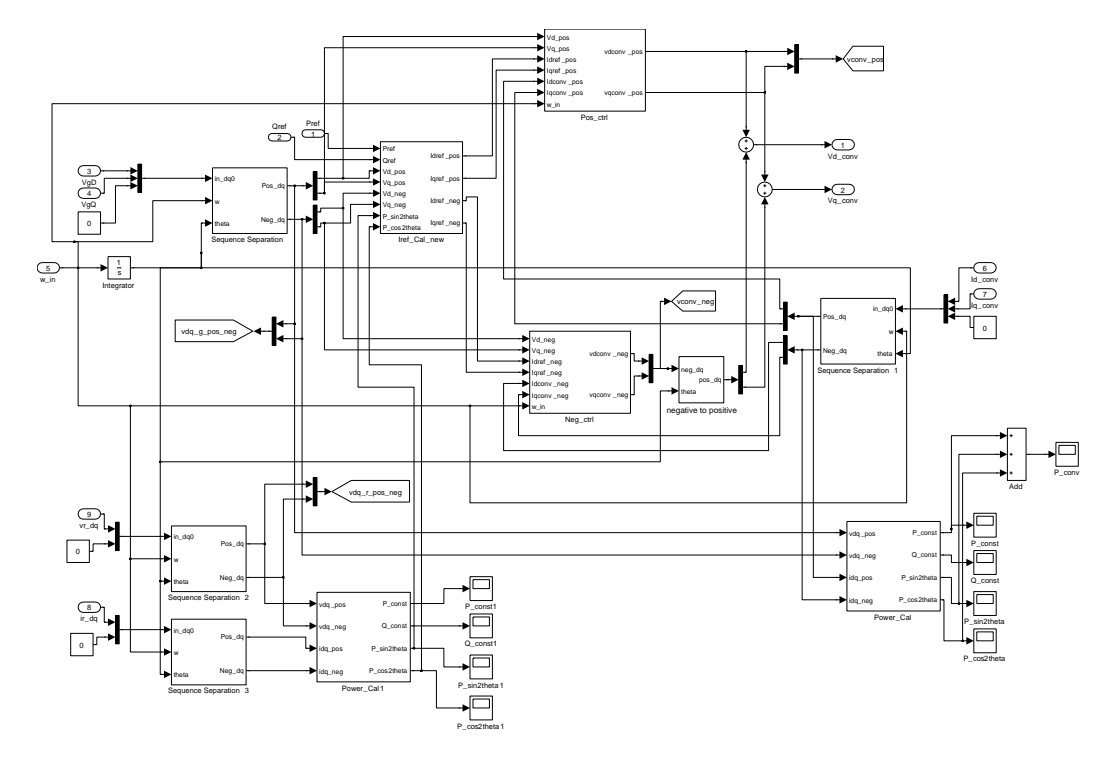


Figure 210: Simulink model of the positive and negative sequence control of the grid VSC

The control of grid VSC is similar to that of the rotor VSC, see figure 210. The main difference is that it has to be controlled together with the rotor VSC, in order to eliminate the effects on the DC voltage caused by rotor power oscillations.

In order to improve simulation speed in Simulink, the DC link is modified, based on the following equation:

$$v_{dc}(t) = \sqrt{\frac{2}{C} \left[ \int_{0}^{t} (p_{rec}(t) - p_{inv}(t))dt + v_{dc}(0)^{2} \right]}$$
 (89)

The next figure shows the modified DC link in Simulink:

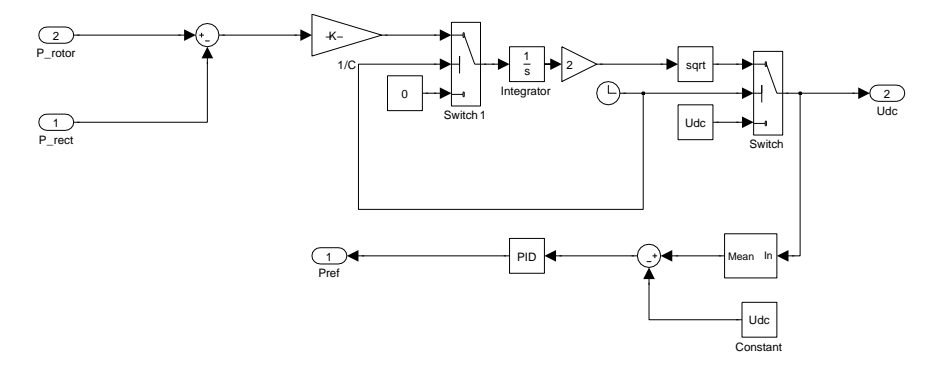


Figure 211: Modified DC link in Simulink

## 8.4.2 Rotor VSC asymmetrical control results

The simulation results of proposed asymmetrical rotor VSC control and the standard symmetrical control are compared in figure 212 for a single phase asymmetrical voltage dip of 70%. Only the positive and negative sequence control of the rotor converter is switched on, the grid converter is still operating as standard symmetrical controller. The control of the rotor VSC limits the electromagnetic torque pulsation to less than 20% of the symmetrical control value. The stator power oscillation is reduced, but the rotor power oscillation increases, as well as the ripple in the DC voltage. Since the stator power often dominates the total power of the generator, the total power oscillation is still reduced.

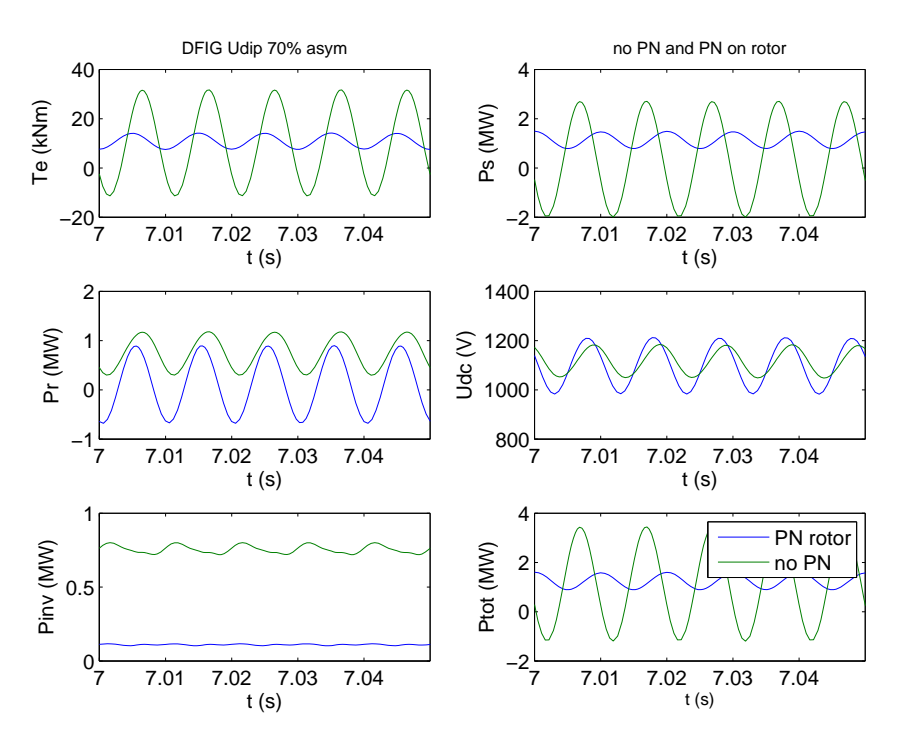


Figure 212: DFIG asymmetrical voltage dip with and without positive and negative sequence controller on the rotor: electromagnetic torque  $T_e$ , stator power  $P_s$ , rotor power  $P_r$ , DC voltage  $V_{dc}$ , inverter power  $P_{inv}$ , total DFIG power  $P_{tot}$ 

The DFIG rotor voltages in positive and negative sequence for the standard symmetrical controller and the asymmetrical controller are shown in Figure 213. During the asymmetrical voltage dip, the standard symmetrical controller also tries to counteract to the 100 Hz oscillation in the electric torque. It generates a negative sequence voltage, but the value deviates considerably from the value of the asymmetrical controller, as shown in Figure 213. The standard symmetrical controller can be tuned to be very fast to limit the torque pulsations during an unsymmetrical voltage dip, but this will decrease the stability margin.

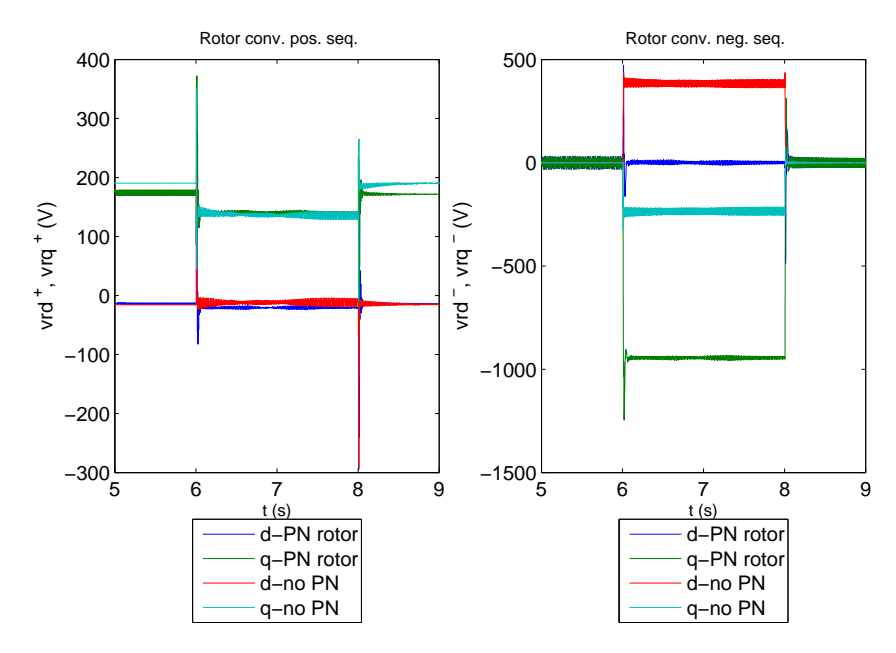


Figure 213: DFIG asymmetrical voltage dip with and without separated positive and negative sequence controller on the rotor: positive (left) and negative sequence dq rotor voltages (right).

## 8.5 Rotor and grid VSC asymmetrical control result

The simulation results of proposed asymmetrical rotor and grid VSC control and the standard symmetrical control are compared in figure 214. When the grid VSC controls positive and negative sequence separately and the rotor VSC asymmetrical controller is also switched on, the DC voltage ripple is limited to less than 10% of the value for symmetrical control. The instantaneous active power of the grid VSC is intentionally controlled to have a second order harmonic, in order to reduce effect of the rotor power oscillation on the DC link voltage.

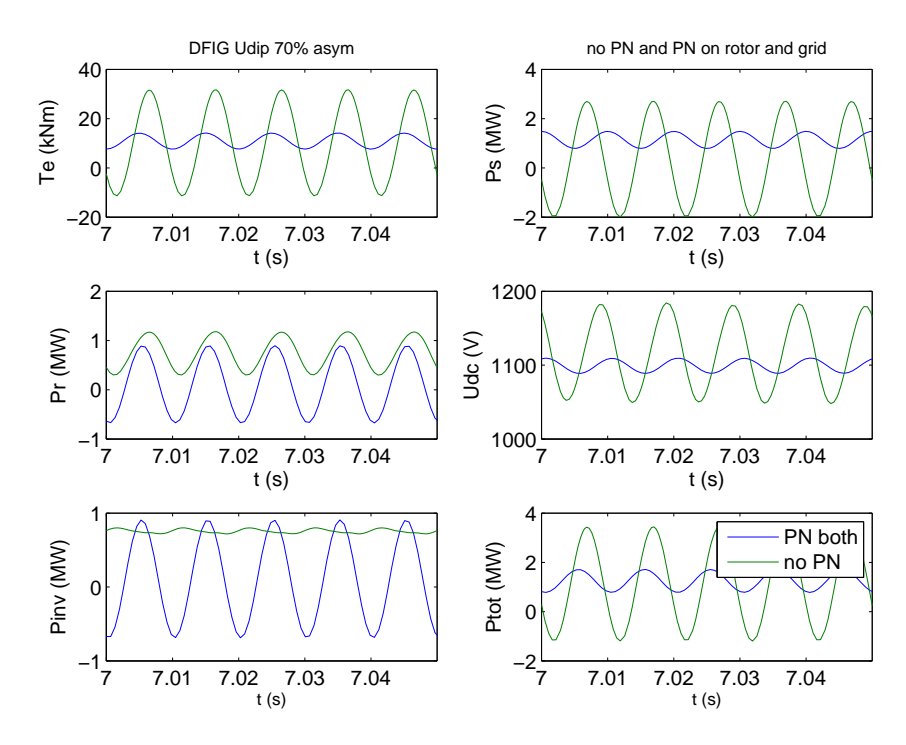


Figure 214: DFIG asymmetrical voltage dip with and without separated positive and negative sequence controller on rotor and grid converter: electromagnetic torque  $T_e$ , stator power  $P_s$ , rotor power  $P_r$ , DC voltage  $V_{dc}$ , inverter power  $P_{inv}$ , total DFIG power  $P_{tot}$ 

Figure 215 shows the positive and negative sequence dq voltages of the grid VSC for standard symmetrical control and proposed asymmetrical rotor and grid VSC control. The positive dq voltages are the same, the negative dq voltages are different.

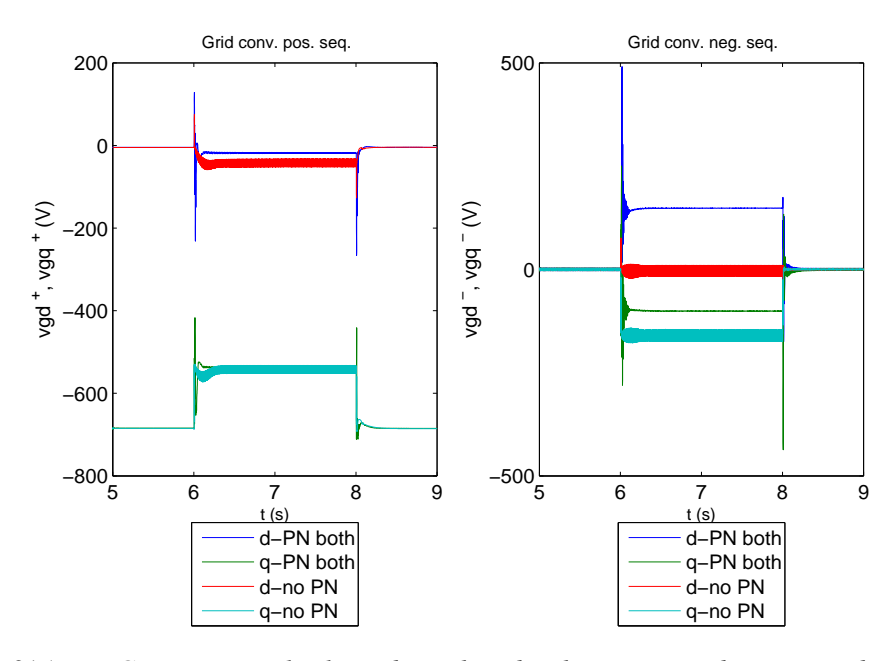


Figure 215: DFIG asymmetrical voltage dip with and without separated positive and negative sequence controller on rotor and grid converter: positive (left) and negative sequence dq rotor voltages (right).

## 8.6 Conclusions and recommendations

The LVRT capability of the DFIG for a symmetrical voltage dip is well described in literature, while the DFIG behavior during an unsymmetrical voltage dip is seldomly studied. Apart from the transient rotor current, which is caused by a voltage dip, the large electromagnetic torque pulsation and DC voltage ripple in the DC link are identified as the most severe problems of DFIG during a unsymmetrical voltage dip.

In this study, the DFIG is proposed to be controlled in positive and negative sequence independently. In order to implement the separated positive and negative sequence controllers of DFIG, two methods to separate positive and negative sequence in real time have been compared. The "signal delay cancellation" is faster than the "low pass filter" and is chosen. Equations for the instantaneous active and reactive power and the voltage equations of DFIG and grid VSC in positive dq and negative dq sequence have been derived. The DFIG system with the proposed positive and negative sequence controllers is modeled in Matlab/Simulink. The simulation results show that the positive and negative sequence controllers of rotor VSC and grid VSC effectively limit the electric torque pulsation, the pulsating power to the grid and DC voltage ripple.

The control objective focused on how to improve performance of DFIG itself under unsymmetrical voltage dip when it is connected to a strong power grid. A future research item will be how to use DFIG to improve grid performance when it is connected to a weak power grid, for instance to reduce grid voltage unbalance.

# 9 Aggregate wind farm models

The objective of this part of the WaP project is to make and demonstrate an aggregate wind farm model (AWFM) suitable for Power System calculations. An aggregate model represents the dynamic behaviour of a wind farm but does not include a full dynamic model for each turbine. Individual turbine wind farm models (ITWFM) are too complicated and simulation time consuming to be included in Power System models. Aggregate wind farm models can be used to investigate the effect of large scale wind power on global grid parameters, for instance the power balance (matching electric power production and demand within a grid control area) or the frequency control [29].

Point of departure for the preparation of an aggregate model is the individual turbine wind farm model. The most detailed ITWFM is used as a reference in evaluating simplified ITWFM and AWFM models. Depending on the application objective, the models may need to represent wind farm active and reactive power production, dynamically as well as steady state, within the time frame of interest.

The requirements for the aggregate wind farm model developed in WaP was determined by the we@sea project *Systeemintegratie en balanshandhaving bij grootschalige windenergie op zee*. The aggregate model will be used for a power balance study of the Dutch national grid. The requirements are:

- (i) scalability;
- (ii) incorporation of the effect of different WF locations in the North Sea on the wind farm power production;
- (iii) accurate representation of active power in the frequency range of 0-0.5 Hz. For other applications the frequency range or the number of represented parameters may be wider;
- (iv) accurate representation of turbine and wind farm control. This requirement is implicitly included in the previous frequency range requirement.

The following approach has been taken:

- (i) simplification of the existing individual turbine model;
- (ii) investigation of the effects of the wind farm size by increasing the number of turbines;
- (iii) comparing different methods of making an aggregate model;
- (iv) validation of methods by comparing outputs of the aggregate and the individual turbine model:
- (v) incorporation of the effect of the location and the layout of a farm.

First a constant speed stall wind farm aggregate model will be made, since this is expected to be relatively straightforward due to the absence of turbine control. In a future project, an aggragate variable speed wind farm will be developed.

## 9.1 Aggregate model for a CSS wind farm

#### Step 1: Simplification of the model of the CSS turbine.

Since the model is primarily used to investigate system balancing, reactive power and voltage fluctuations need not be taken into account. Grid voltage at the point of common coupling and grid frequency are assumed to be constant. This leads to a number of simplifications:

- the turbine cable and the transformer model are eliminated from the turbine model and the dynamic model of the induction generator is replaced by the torque-slip curve;
- the tower model (nodding and naying) is eliminated from the turbine model;

• the drive train model (two inertias and a shaft) is exchanged for a single inertia model.

Figures 216 to 218 compare the auto power spectral density (APSD) of the electric power Pe of the full and the reduced models. In the low frequency range, the rotational sampling of the wind is the main source of oscillation. For the modelled turbine, 1P equals 0.2134 Hz, so 3P is about 0.64 Hz. This frequency is present. The effect of deleting the dynamic models of cable, transformer, induction machine and tower is small for the frequency range 0-5 Hz, see figure 216 and 217. Exchanging the two inertia plus shaft model for a single inertia model does have a significant effect however, the power spectrum reduces to the spectrum of the rotationally sampled wind Pa, see figure 218 and figure 219.

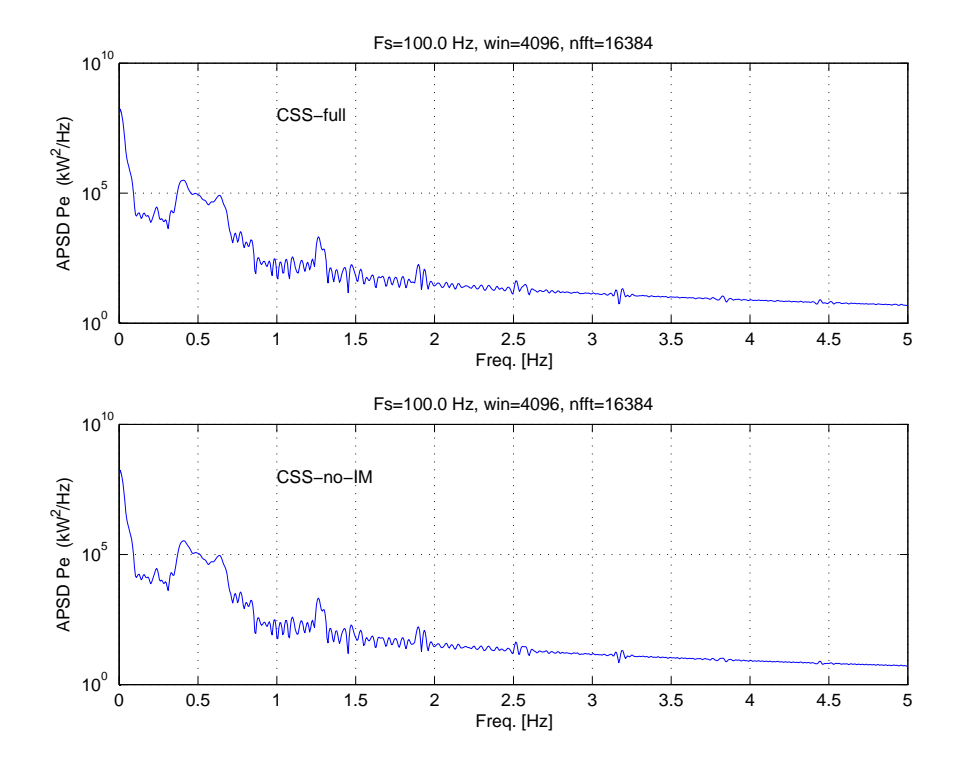


Figure 216: APSD of electric power for the full WT model and the WT model with torque-slip curve

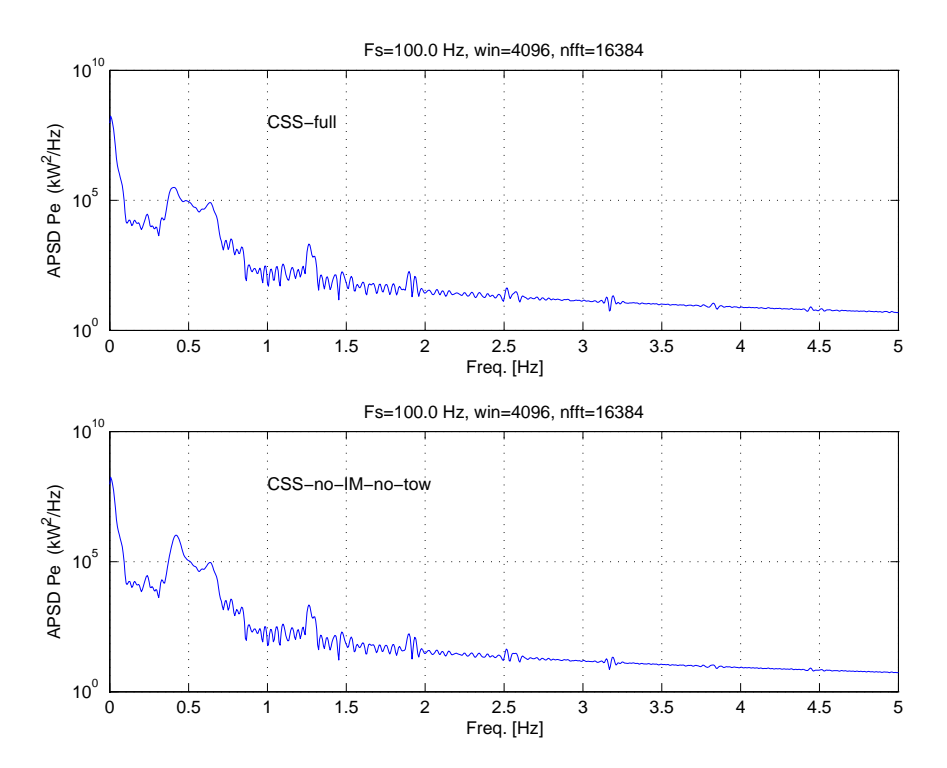


Figure 217: APSD of electric power for full WT model and model with torque-slip curve without tower model

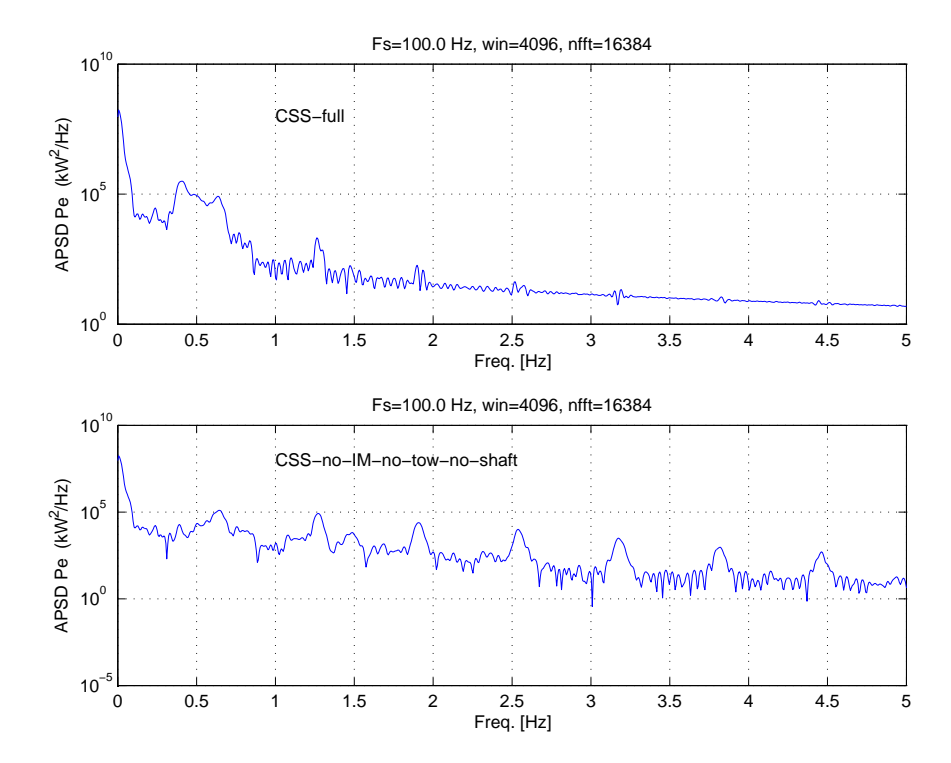


Figure 218: APSD of electric power for full WT model and model with torque-slip curve without tower and shaft model (a single inertia)

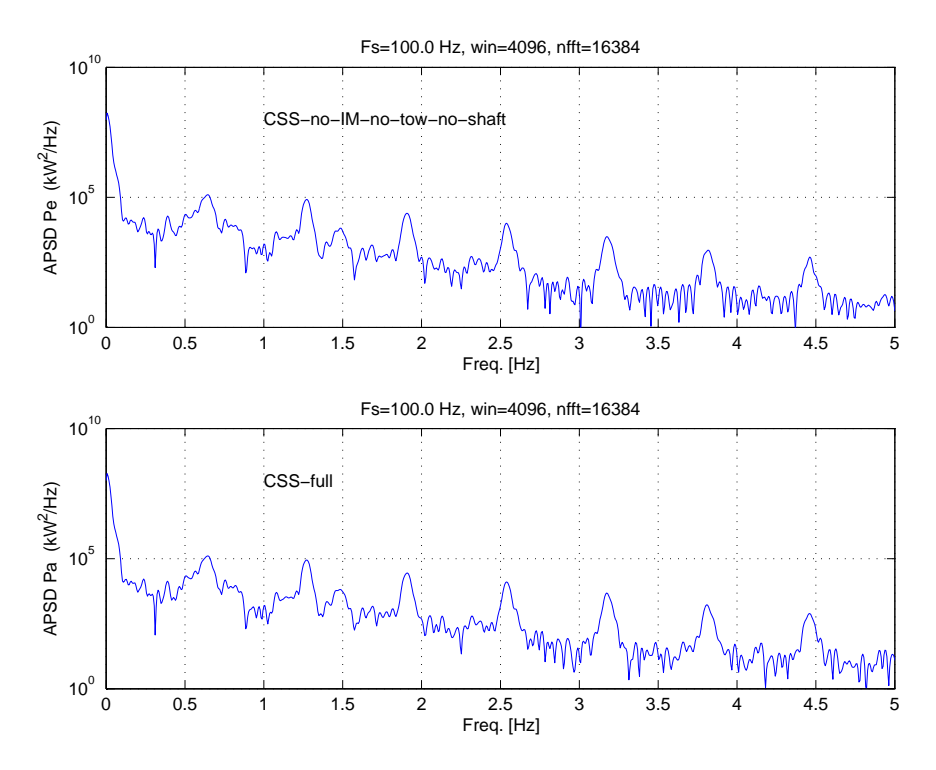


Figure 219: APSD of WT electric power and aerodynamic power for full model

### Step 2: Effect of increasing number of wind turbines

To determine the effect of multiple turbines on the variations in the power output of a farm, the wind inputs for the turbines in the model need to be different. This is realised by:

- different initial values of the azimuth angle;
- different average or quasi-steady values of the undisturbed wind speed.

Different initial values of the azimuth angle prevent rotor synchronisation (coincidence of the rotor effective wind 3P and 6P oscillations). A single normalised wind speed realisation can be used. The initial value of the azimuth and the average or quasi-steady state wind speed (read from file or generated by a Simulink block) determine the instantaneous wind speed at each turbine.

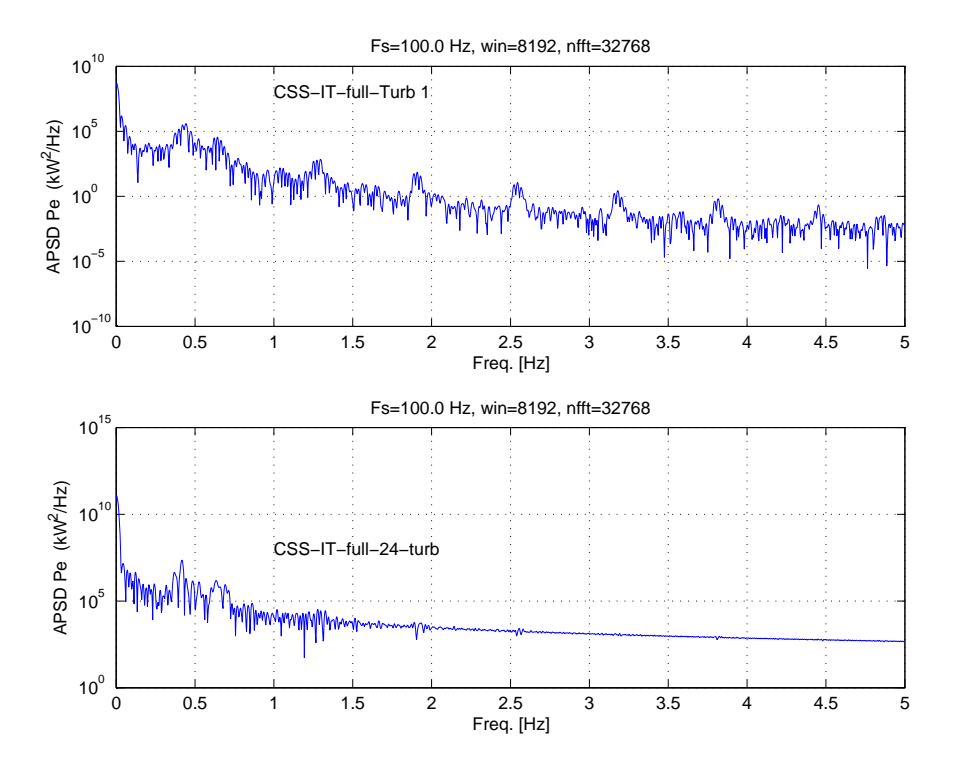


Figure 220: APSD of WT electric power for IT full model with 1 and 24 turbines

Figure 220 gives the APSDs for models with 1 and 24 individual turbines. Increasing the number of turbines has two effects: the average level (absolute, not relative) of the oscillations is increased and some peaks in the spectrum are reduced. The nP oscillations of different turbines average out, due to differences in instantaneous rotor position of different turbines. These results serve as a reference for the aggregate model to be developed.

#### **Step 3: Methods of aggregation**

The following methods of aggregation are proposed:

- Method 1 separate scaling of variations and quasi-steady state value of the output of a model of a single turbine to estimate the output of the farm;
- Method 2 filtering of variations of a single turbine or a wind signal to estimate the wind farm output variability, i.e. estimation of a transfer function;
- Method 3 wind farm model built from simplified turbine models (strictly speaking not an aggregate model);
- Method 4 time shifting and addition of variations of a single turbine and linear scaling of quasisteady state value;
- Method 5 pre-calculated scalable power series from a library (strictly speaking not an aggregate model);

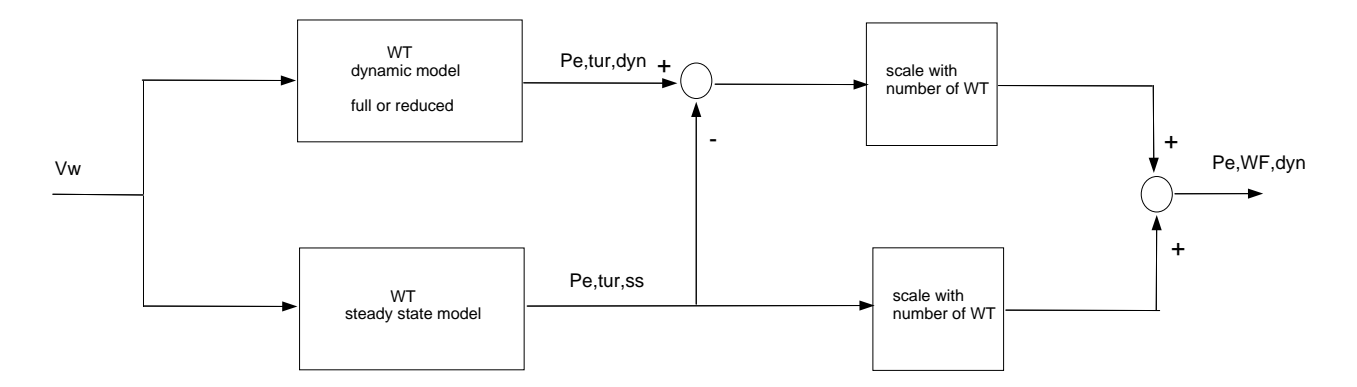


Figure 221: AWFM Method 1

Method 1 uses a dynamic model of the CSS turbine and a steady state model of the same turbine and separates the short term variability from the quasi-steady state trend in the electric power, see figure 221. The variability as well as the trend are scale with the number of turbines, but in a different way. The trend is either simply multiplied by the number of turbines or by (variable) factor based on the wind farm size and layout. If a factor is used, the wind speed deficit in the farm can be taken into account. The variability is either multiplied by the square root of the number of turbines, assuming uncoherent wind, or by a factor corrected for wakes in the farm (dependent on the wind farm layout). A separate model is available to estimate wake deficits and increasing turbulence for a given wind farm layout, see appendix A. The instantaneous quasi-steady state electric power is required to determine the variations in the electric power. This is less easy to estimate than the quasi-steady state aerodynamic power. Therefore the aerodynamic power is used to determine the variations.

#### Advantages of method 1:

- scaling is very simple if wind farm wakes and deficit are neglected;
- since only one turbine is simulated, simulation is fast;
- a further reduction in simulation time is possible using the reduced model of the previous section;

#### Disadvantages of *method 1*:

- only a single quasi-steady state or average wind input signal per wind farm is used since the aggregate wind farm model contains only a single turbine;
- in the model, the 0p, 3P, 6P etc. variations of different turbines are not real time cancelled, instead a reduction is achieved by a factor of about  $\sqrt{N}$  applied to the variations of a single turbine. This factor is somewhat arbitrary, it depends on the coherence between de power outputs of the different turbines. If rotor positions synchronize, coherence between the 3P etc. variations can be close to 1. In unsynchronized operation the coherence is practically zero. Since the unsynchronized operation is expected to prevail, a factor close to  $\sqrt{N}$  is justified.

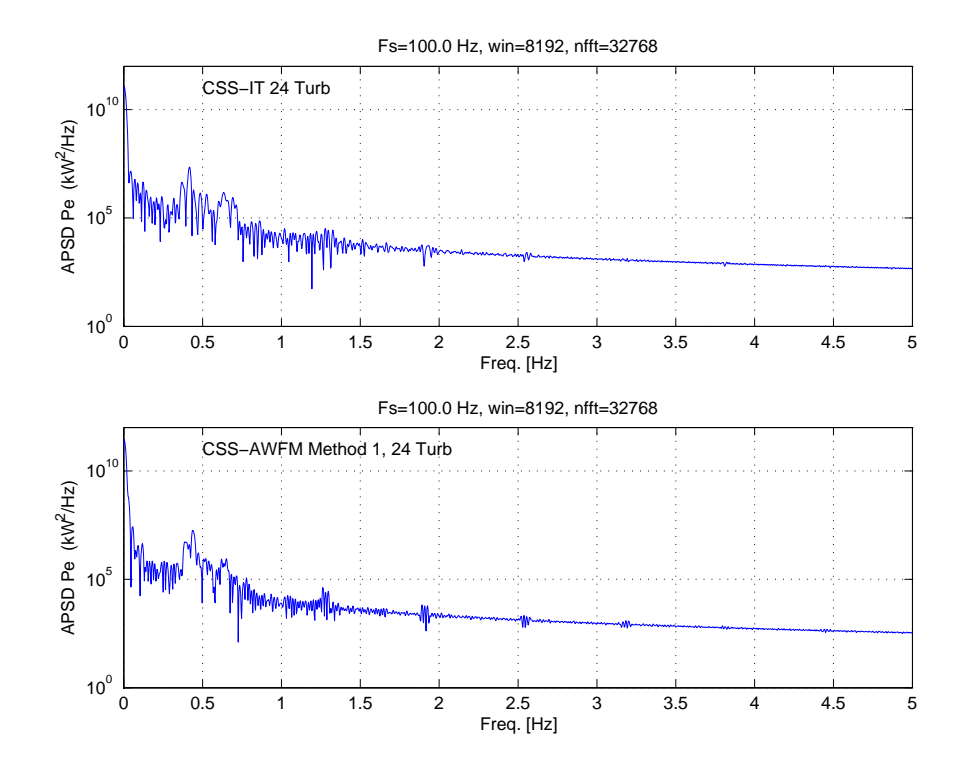


Figure 222: Comparing AWFM Method 1 to IT full model for 24 turbines

Figure 222 compares the result of *method 1* to the ITWF full model for a farm of 24 turbines. Neither the ITWF model nor the AWFM *method 1* model include wake effects. The result of the AWFM *method 1* is quite good. Peak reduction is similar to the full model and the average level is similar. *method 1*, applied to the constant speed stall wind farm, seems to meet the requirements.

Two options can be distinguished for *method 2* (filtering):

- the filter (transfer function) represents the farm behaviour from wind speed to power output;
- the filter only represents the effect of an increasing number of turbines in the farm;

#### Disadvantages of *method 2*:

- since the method is based on estimation of a transfer function, the model does not have a physical interpretation;
- the 0p, 3P, 6P etc. variations of different turbines are not real time cancelled;
- the filter parameters are difficult to determine, especially in relation to the size of the farm;
- the operating conditions most likely affect the filter parameters.

Since *method 1* already produced a satisfactory result, *method 2* will not be examined further. *Method 3*, using simplified IT models, will not be investigated for the same reason.

*Method 4*, shifting power output variations in time by means of a delay block), seems to be a promising option, since this closely resembles the actual process in a wind farm.

Advantages of method 4:

• altough a single turbine model is used, the OP, 3P, 6P etc. variations of different turbines are cancelled in real time.

However, this method incorporates a few serious disadvantages:

- scalability is problematic since it involves extending the number of delay blocks in the model;
- the memories of the delay blocks have to be filled before any meaningful output can generated, resulting in an increase in simulation time with the size of the wind farm;
- variations of different turbines are fully correlated since shifted over a fixed interval.

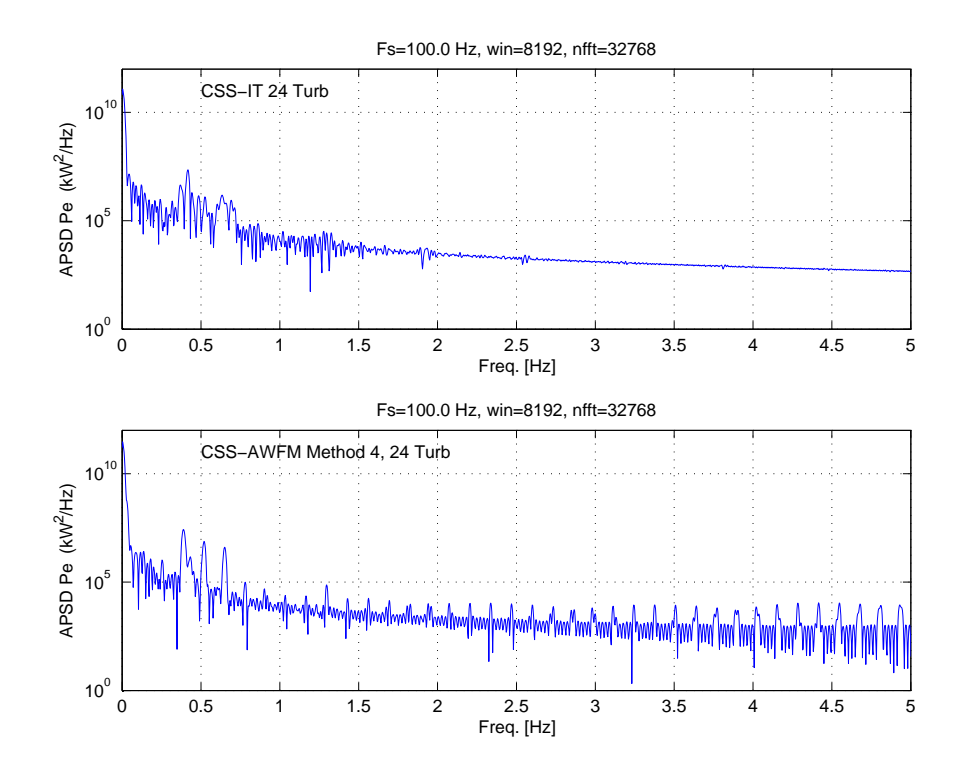
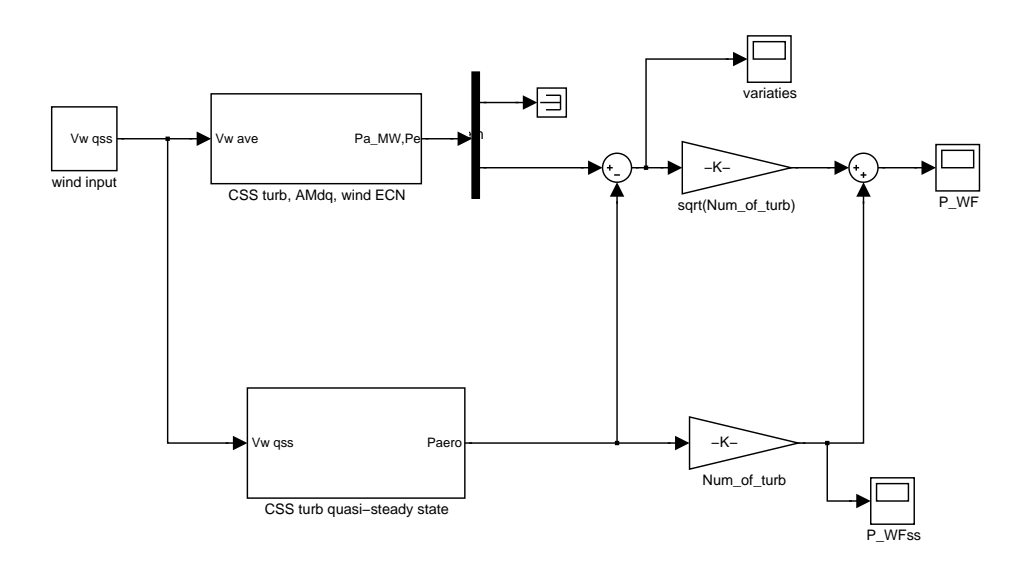


Figure 223: Comparing AWFM Method 4 to IT full model for 24 turbines

Figure 223 compares the results of  $method\ 4$  and the ITWF full model for a farm of 24 turbines. Neither the ITWF model nor the AWFM model compensate for wake effects. The result of the AWFM  $method\ 4$  is not as good as  $method\ 1$ . Peak reduction is a bit less than in the full model, this may be related to the choice of the time shift (7.7 s is relatively near to 5/(3P)=7.8101 s). The average level also is similar. For the constant speed stall wind farm  $method\ 1$  is preferred.

# 9.2 Implementation of CSS-AWFM in Simulink

## 9.2.1 Model layout



Aggregate WF model for CSS turbine based of full AM dq model (c) 2003,2005 Jan Pierik (ECN), Johan Morren (TUD), Tim van Engelen (ECN)

Figure 224: Simulink implementation of CSS-AWFM

Figure 224 shows the implementation of the *method 1* aggregate model in Simulink.

# 9.3 Aggregate model for a VSP wind farm

An AWFM model for a variable speed pitch (VSP) wind farm seems to be more complicated than for a CSS farm. The VSP turbine includes turbine specific controllers and can be equiped with different types of generators and different converters. Then there is a range of VSP systems: VSP-DIFG (Doubly Fed Induction Generator), VSP-FCIG (Full Converter Induction Generator), VSP-FCSPM (Full Converter Permanent Magnet Generator), VSP-CCIG (Cluster Controlled Induction Generator). These options differ in the type of electrical system, the turbine rotor and pitch control is similar. Since the control of the electrical system intends to smooth the electric power output and the eigenfrequencies of the electrical system and its control are expected to exceed 0.5 Hz (and probably also 5 Hz), the expectation is that the differences between systems below 5 Hz are small. The expectation is that the same method of aggregation can be applied to the VSP wind farm as has been demonstrated for the CSS wind farm. The demonstration is postponed to a future project.

#### 9.4 Conclusions and recommendations

An aggregate constant speed wind farm model has been developed and compared to a
wind farm model based on individual turbine models. Power variations in the range
of 0-5 Hz are represented accurately by the aggregate model. The implemented aggregate model only generates electric power variations. By modifying the detailed turbine

model, i.e. including the electrical system models, the aggregate model can generate other electrical variables as well.

- Although the overall dynamic behaviour of the AWFM and the ITWM model are similar (same frequency response), the instantaneous behaviour will be different, due to the use of only a single versus multiple turbine models. Since wind farm power production is stochastic by nature, this is not a problem.
- The aggregate constant speed wind farm model can be scaled easily.
- The aggregate constant speed wind farm model only requires a single wind speed time series as input. This time series represents the average wind speed in the farm.
- The effect of the wind farm location is taken into account by different wind speed inputs.
- The effect of different operating conditions of different turbines is taken into account by a factor that represents addition, i.e. averaging of variations.
- The effects of wakes on average power and power variability are not taken into account.
- In a future project an aggregate VSP wind farm will be developed.

## 10 Conclusions

- (i) Nine new electrical system models for offshore wind farms have been realised. Some of the wind farm electrical system models required new electrical component models and new control concepts. The nine new wind farm models have been demonstrated for normal operation.
- (ii) For the wind farm with Full Converter Induction Generator (FCIG) a new control concept was developed which does not require knowledge of or a setpoint for the stator angular frequency. This is realised by choosing a reference frame for the Park transformation that is fixed to the rotor. The stator frequency now implicitly results from the control of the instantaneous currents in the direction of and perpendicular to the induction machine flux. The controller is demonstrated in the VSP-FCIG-ac wind farm.
- (iii) Controlling the Doubly Fed Induction Generator wind farm with Thyristor bridge DC link to shore (DFIG-thy) required a new control concept due to dynamic interaction of the turbines connected to the thyristor bridge and the resulting variablility of the wind farm AC grid. Two control concepts have been investigated: terminal voltage control and stator flux oriented control. The stator flux oriented control provided the best damping but is unstable if all turbines ramp down to low power. The control of the DFIG-thy wind farm still needs further refinement. One aspect to be investigated further is the independent control of power and reactive power in a weak grid with equal resistance and reactance.
- (iv) For a representative selection of four wind farm electrical systems a case study to assess the dynamic behavior has been executed. The case study determined the flicker production, the response to a voltage dip and the response to a frequency dip of the four wind farm concepts.
- (v) Five thyristor bridge models, of average or instantaneous type and for symmetrical or asymmetrical conditions have been developed. These models can be used to represent the classical HVDC connection for the transport of wind power to shore. The symmetrical quasi-steady state model for averaged balanced conditions was used in the analysis of the VSP-DFIG-thy system in this report.

The developed thyristor bridge models have been compared to the thyristor bridge model of the Simulink Power System Blockset:

- The symmetrical quasi-steady state model is accurate for both steady state and transient state under balanced situation.
- The unsymmetrical quasi-steady state model using Fourier analysis is accurate for steady state, but has significant errors during transient state because of the delay caused by the Fourier method.
- The unsymmetrical quasi-steady state model assuming partially symmetrical conditions is accurate for both steady state and transient state, but only if the assumptions can be fulfilled.
- The instantaneous model without commutation inductance can have significant errors if the AC commutation inductance or DC current is very large.
- The instantaneous model with commutation inductance is accurate for both steady state and transient state, balanced and unbalanced situations but requires more simulation time.
- (vi) For the Doubly Fed Induction Generator with AC connection to shore (DFIG-ac) a model for the evaluation of asymmetrical voltage dips has been realised. The DFIG-ac system is extra sensitive to grid faults since it exposed via two routes: stator-rotor and converter-rotor. The model has been used to develop a new control strategy to limit oscillations in the DFIG-ac system during the asymmetrical voltage dip by controlling the positive and negative sequence component of the fault current independently. The rotor converter limits the electrical torque pulsation and the power to the grid while the grid converter limits the DC voltage ripple.

- (vii) An aggregate wind farm model (AWFM) for the constant speed stall wind farm has been developed. The model was verified by comparison to the wind farm model consisting of individual turbine models (ITWFM). Power variations in the range of 0-5 Hz are represented accurately by the aggregate model. The aggregate model only calculates electric power variations. By modifying the detailed turbine model from which the aggregate model is derived, i.e. including electrical subsystem models, the aggregate model can generate other electrical variables as well. In a future project an aggregate VSP wind farm will be developed.
- (viii) A new dynamic model for the VSP turbine has been made. The new model is based on Simulink, while the previous VSP model used Matlab. The model has been incorporated in the new wind farm models developed in this project.
- (ix) A simple model for the main parameters of the wind speed at different locations inside a wind farm has been implemented, based on the wind turbine wake model by G.C. Larsen. The wind speed deficit results have been compared to measurements and are comparable.

## Recommendations

- (i) The control of the DFIG-Thy system requires further improvement, especially with respect to the independent control of power and reactive power in a grid with equal resistance and reactance.
- (ii) An aggregate wind farm model for the variable speed pitch wind farm has to be developed.
- (iii) The wind farm dynamic model library now is fairly complete and has been tested. It still requires further verification by comparison to measurements, especially voltage dips. It is recommended to search for suitable measurements and turbine data and execute verification exercises.
- (iv) Keeping the previous recommendation in mind, the wind farm dynamic model library is now in a stage of development that it can be used in dynamic studies on large scale integration of wind power in the grid. It can be especially useful in developing control strategies for large offshore wind farms that support the grid during normal operation and during faults (e.g. steady state voltage support, stability improvement during faults, damping of angle oscillations, delta control and power curtailment, frequency droop control, limitation of short circuit contribution). Integrating an increasing amount of wind power in the electric power system will require the utilisation of the full potential of wind farms. Therefore, it is recommended to start the development, implementation and demonstration of wind farm control strategies, that statisfy existing and forseen grid code requirements, for different types of commercially interesting wind farm types and evaluate these strategies in a representative dynamic grid model, for instance the RTDS of TUD-EPS.

## References

- [1] Akhmatov, V. (2003): Analysis of dynamic behavior of electric power systems with large amount of wind power. Report ISBN 87-91184-18-5, Technical University of Denmark. PhD thesis.
- [2] Akhmatov, V. (2003): Analysis of Dynamic behaviour of Electric Power Systems with Large Amount of Wind Power. Report ISDN 87-91184-18-5, Denmark Technical University. PhD Thesis.
- [3] Akira, N. and T. Tanaka (1996): A new definition of instantaneous active-reactive current and power based on instantaneous space vectors on polar coordinates in three-phase circuits. IEEE Transactions on Power Delivery, pages Volume 11, Issue 3.
- [4] Chen, Z. and E. Spooner (1998): *Grid interface options for variable speed, permanent magnet generators*. IEE Proc.-Electr. Power Appl. Vol 145, No. 4.
- [5] Datta, R. and V.T. Ranganathan (????): Decoupled control of Active and Reactive Power for a Grid-connected Doubly-fed Wound Rotor Induction Machine without Position Sensors
- [6] Dekker, J. and J.T.G. Pierik (ed.) (1999): European Wind Turbine Standards II. Report ECN-C-99-073, ECN.
- [7] Deleroi, W. (1979): Collegedictaat Elektrische Machines II. T.U. Delft, Delft.
- [8] Dragt, J. (1985): Load fluctuations and response of rotor systems in turbulent wind fields . Report ECN-172, ECN .
- [9] (ed.), L.F. (1990): Wind Energy Conversion Systems . Prentice Hall Int., Hertfordshire.
- [10] (Editor), T.A. (2005): Wind Power in Power Systems. John Wiley & Sons, LTD.
- [11] van Engelen, T. (????): Comments in vwroteff.m.
- [12] van Engelen, T., E. van der Hooft and P. Schaak (2004): *Ontwerpgereedschappen voor de Regeling van Windturbines*. Report –, ECN. To be published.
- [13] H., K. (1980): Stromrichtergespeiste Drehfeldmachinen. Springer Verlag, Wien, New York. P. 197.
- [14] Hansen, L.H., L. Helle and F. Blaabjerg (2001): Conceptual survey of generators and power electronics for wind turbines . Report, Risø National Laboratory .
- [15] Hindmarsh, J. (1970): Electrical machines and their applications. Pergamon Press, Oxford.
- [16] Hoeijmakers, M. (1984): On the steady state performance of a synchronous machine with converter. Report ISBN-90-9000602-8, TU Eindhoven. Dissertation.
- [17] Holdsworthm, L., X. Wu, J. Ekanayake and N. Jenkins (2003): Comparison of fixed speed and doubly-fed induction wind turbines during power system disturbances. IEE Proc.-Gener. Transm. Distrib. Vol. 150, No. 3, pages 343 352.
- [18] Hopfensperger, B., D. Atkinson and R. Lakin (????): Stator-flux-oriented control of a doubly fed induction generator with and without position encoder.
- [19] Kim and H. Akagi (1997): *The instantaneous power theory based on mapping matrices in three-phase four-wire systems*. Proceedings of the Power Conversion Conference. Nagaoka.
- [20] Kirby, N.M., L. Xu, M. Luckett and W. Siepman (2002): *HVDC transmission for large offshore wind farms*. Power engineering Journal.
- [21] Larson, G.C. (1999): Fax describing the GCL wake model.

- [22] Lundberg, S. (2003): Configuration study of large wind parks. Report, Chalmers University of Technology. PhD thesis.
- [23] Lyon, W.V. (1954): Transient analysis of alternating current machinery. An application of the methods of symmetrical components. John Wiley & Sons, New York.
- [24] Marques, G. (1998): A comparison of active power filter control methods in unbalanced and non-sinusoidal conditions. 24th Annual Conference of the IEEE Industrial Electronics Society.
- [25] Morren, J., J. Pierik, S. de Haan and J. Bozelie (2005): *Grid interaction of offshore wind farms. Part 1. Models for dynamic simulation*. Wind Energy, 8 (3).
- [26] Newland, D. (1975): Random vibrations and spectral analysis. Longman, London.
- [27] Pena, R., J. Clare and G. Asher (????): A doubly fed induction generator using back-to-back PWM converters supplying an isolated load from a variable speed wind turbine
- [28] Petersson, A. (2005): Analysis, modeling and control of doubly-fed induction generators for wind turbines. Report, Chalmers University of Technology. PhD thesis.
- [29] Pierik, J., J. Montero Quiros, T. van Engelen, D. Winkelaar and R. Sancho Chaves (2003): Costa Rica Grid Feed-in Study: Effect of wind power on grid frequency. Report ECN-CX-03-080, ECN.
- [30] Pierik, J. and J. Morren (2007): Constant Speed Wind Farm Dynamic Model Validation; Alsvik measurements and simulations. Report ECN-E-07-007, ECN.
- [31] Pierik, J. and J. Morren (2007): Validation of dynamic models of wind farms (Erao-3): Executive summary, benchmark results and model improvements. Report ECN-E-07-006, ECN.
- [32] Pierik, J. and J. Morren (2007): Variable Speed Wind Turbine Dynamic Model Validation; JWT measurements and simulations. Report ECN-E-07-008, ECN.
- [33] Pierik, J., J. Morren, E. Wiggelinkhuizen, S. de Haan, T. van Engelen and J. Bozelie (2004): *Electrical and Control Aspects of Offshore Wind Turbines II (Erao-2). Volume 1: Dynamic models of wind farms*. Report ECN-C- -04-050, ECN. Available at the web site of ECN (www.ecn.nl, use search option).
- [34] Pierik, J., J. Morren, E. Wiggelinkhuizen, S. de Haan, T. van Engelen and J. Bozelie (2004): *Electrical and Control Aspects of Offshore Wind Turbines II (Erao-2). Volume 2: Offshore wind farm case studies*. Report ECN-C--04-051, ECN. Available at the web site of ECN (*www.ecn.nl*, use search option).
- [35] Saccomando and J. Svensson (2001): Transient operation of grid-connected voltage source converter under unbalanced voltage conditions. Industry Applications Conference, 36 IAS Annual Meeting.
- [36] Schepers, G. (2004): email on subroutine GCL(wakecon).
- [37] Winkelaar, D. (1996): Ontwikkeling en validatie van een stochastich windbelastingsmodel, Deel 1: Windmodellering . Report ECN-C-96-096, ECN .

# A A simple model for local wind conditions inside a wind farm

The development of dynamic models of wind farms has been started in a previous project: *Elektrische en Regeltechnische Aspecten van Offshore windparken 2: Erao-2* [33, 34] and continued in this we@sea project *Windfarm as Powerplant*. In Erao-2 wake effects have been neglected. Wakes will have an effect on the average power production but also on the turbulence and therefore on the dynamic response and flicker production. One of the objectives in *Windfarm as Powerplant* is the implementation of a simple model, suitable for dynamic evaluations, for the wind inside a farms. Wake modelling is already used for the prediction of fatigue of turbines in a wind farm [6]. For this project the GCL-model has been chosen, because it is simple, generates all required parameters and is well documented. A short description of the GCL-model will be given. First, the rotor effective wind model in the Erao-2 programme will be described.

### A.1 Turbine wind model: rotor effective wind

#### A.1.1 Stochastic wind model

In the Erao-2 wind turbine model, an equivalent single point wind speed realisation is used to describe the wind speed seen by a given turbine rotor. The method to generate this equivalent wind speed was developed for controller design [12]. The equivalent wind speed is called the *rotor effective wind speed* and can be described as a single point wind speed realisation that gives the same rotor torque as the actual distributed stochastic wind field acting on the turbine rotor. This single point wind speed is based on the statistical properties of the undisturbed wind and includes the statistical variation of the wind in the rotor plane and the effect of the blade rotation on the torque variations produces by the rotor, often called rotational sampling. It consists of three separate parts to represent the wind speed variations:

- variations due to wind shear,
- variations due to tower passage;
- variations due to turbulence in the rotor plane.

The first two are deterministic and linked to the azimuth angle. The determination of the stochastic part, the turbulence in the rotor plane, is described in the project *Koppeling SWIFT aan Handboek Ontwerpwindgegevens Windturbines versie 3* [37]. This section gives a overview of the turbulent wind calculation. The next section will focus on the calculation of the rotor effective wind.

The following description of the stochastic and rotor effective wind model are copied from the comments in the *vwroteff.m* routine developed by Tim van Engelen. To compile a more or less complete description of the calculation of the wind inside the farm, it is included here. Point of departure for the wind speed calculation is the Kaimal spectrum for the turbulence in a single point, described by the auto power spectral density function (APSD)  $S_{ii}$  [37]. The nomenclature of [37] is adopted:

$$\frac{f \cdot S_{ii}(f)}{\sigma_i^2} = \frac{4fL_i/V_{hub}}{(1 + 6fL_i/V_{hub})^{5/3}} \tag{90}$$

$$\sigma_i = 1.2I_{ave}(0.75V_{hub} + 0.16V_{ave}) \tag{91}$$

with:

frequency

index representing the wind speed component:

: 1=longitudinal, 2=transversal, 3=vertical

: single sided power density spectrum in a point of component i

stingle sided points
standard deviation of component i
integral length scale for the i component of the windspeed at hub height
10 minute average wind speed at hub height
annually average turbulence intensity
annually average wind speed at hub height

The integral length scale  $L_i$  is related to the turbulence length scale  $\Lambda_i$  according to table 6.

Table 6: Parameters of the Kaimal-model

i	$\sigma_i$	$L_i$
1	$\sigma_1$	$8.1~\Lambda_1$
2	$0.8 \sigma_1$	$2.7~\Lambda_1$
3	$0.5 \sigma_1$	$0.66 \Lambda_1$

The turbulence length scale  $\Lambda_1$  is defined as the wave length at which the dimensionless longitudinal spectral density  $fS_{11}(f)/\sigma_1^2$  equals 0.05.

$$\Lambda_1 = \begin{cases}
0.678z_{hub} & \text{for } z_{hub} < 30\text{m} \\
20.3\text{m} & \text{for } z_{hub} \ge 30\text{m}
\end{cases}$$
(92)

The corresponding spacial coherence function for the wind speed variations in two locations in the rotor plane is:

$$Coh_{11}(r,f) = e^{-8.8 \cdot \sqrt{(\frac{r \cdot f}{V_{\text{hub}}})^2 + (\frac{0.12 \cdot r}{L_1})^2}}$$
 (93)

r is the distance between two points in the plane perpendicular to the average wind direction. Compared to equation 91, [12] uses a different relation for the standard deviation of the longitudinal wind speed:

$$\sigma_u = \frac{I_{ht}(ht + a \cdot V_{hub})}{a + 1} \tag{94}$$

with:

turbulence intensity for the u component of the windspeed at height ht $I_{ht}$ 

parameter for the dependence of the turbulence on the average wind speed (=2 in [12])

#### A.1.2 Rotor effective wind

With the statistical properties of the wind in the rotor plane determined, the next step is the calculation of a single point wind speed, called the rotor effective wind, which will generate approximately the same instantaneous torque as the time and space dependent wind variations in the rotor plane. The method to meet this objective is derived in Appendix A of the ControlTool report [12] and is based on the mathematical description of the effect of rotational sampling on the power spectrum of the wind [8]. The Matlab routines vwroteff.m, vweffshr.m, *vwefftow.m* and *timegen.m* perform the calculations. The implementation of the rotor effective wind calculation is as follows, see [11]:

The calculation of the dynamic behaviour of the wind farm and the wind speed calculation is separated in time. First, the wind speed realisations are calculated and writen to a file. The wind farm model then reads the instantaneous wind speed from this file. This procedure offers two major advantages over a simultaneous calculation: (1) the wind speed calculation only has to be performed once, which makes the already time consuming wind farm calculation

faster and (2) indentical wind files can be used to investigate behaviour of different controller settings or wind farms.

Two index-variables are associated with the pre-calculated variation histories: time t and azimuth angle  $\psi$ . Tower stagnation and windshear depend by nature on  $\psi$ ; turbulence on time index t. The time-index-array timebase corresponds exactly to azimuth-index-array azimbase if the rotor speed is exactly constant, corresponding to  $f_{0v}$  (Hz). At varying rotor speed the azimuth angle differs from the product  $2\pi f_{0v}t$ . Since stagnation and wind shear only depend on azimuth angle and are calculated and stored separately, the procedure also works in case of variable rotor speed.

For wind turbulence, time-dependent wind speed variations are generated by inverse Fourier transform of the rotor effective wind spectrum. This wind spectrum incorporates:

- spectral energy density that corresponds to the rotor-average windspeed (the 0p-mode  $dVw_{m0}(t)$ );
- spectral contents corresponding to the rotational sampling of the turbulent wind field (the mBp-modes  $dVw_{mBp}(t)$ , p = the rotational frequency of the turbine).

The latter spectrum has peaks around the centre-frequencies  $mBf_{0v}$  with

m: integer multiplier; B: number of blades;  $f_{0v}$ : rotor frequency.

Turbulent wind speed variations are generated for the Op-mode in array  $vw_{eff,m0}$  and for the 1Bp- and 2Bp-modes in array  $vw_{eff,m036}$ . These arrays are full coherent.

#### Windshear and tower stagnation

For windshear and tower stagnation azimuth-dependent normalised wind speed variations are calculated in arrays  $nvw_{shr}$  and  $nvw_{tow}$ . Real-value wind variations are obtained by multiplication with the sum of the average wind speed at hub height  $U_{hubv}$  and the Op-mode variation  $dVw_{m0}(t = \psi/(2\pi * f_{0v}))$  in array  $vw_{eff,m0}$ .

Azimuth dependent tower stagnation is based on the 3D-potential theory for a semi-infinite dipole:

$$dVw(\psi, x, y, z) = \frac{(U_{hubv} + dVw_{m0}(t(\psi))) * d_{tow}^2}{8(x^2 + y^2)} \cdot (\frac{x^2 - y^2}{x^2 + y^2} \cdot \frac{1 - z}{r} - \frac{x^2/z}{r^3})$$
(95)

with:

azimuth angle;

x,y: longitudinal and lateral position relative to tower top; z: vertical position relative to tower top (z>0 is above tower top);  $dVw_{m0}(t(\psi))$ : rotor average wind speed variation by wind turbulence,

time-index relates to azimuth-index through through rotor speed;

: equivalent tower diameter for tower stagnation assessment;  $d_{tow}$ distance  $\sqrt{(x^2+y^2+z^2)}$  of point (x,y,z) to tower top.

The rotor average effect is calculated by considering the tower stagnation on 2/3 Rb depending on the azimuth, dividing by the number of blades B and summing the wind speed variations over the B blades.

The azimuth dependent wind shear is determined by an exponential shear profile according to IEC61400:

$$dVw(\psi) = U_{hubv} * ((z(\psi)/Z_{hub})^{\alpha_{shear}} - 1)$$
(96)

with:

height; : azimuth angle; : hub height;

: exponent acc. to IEC61400.

### Turbulence and rotational sampling

A realisation of the turbulent wind speed variation is obtained from the auto power spectrum S(f) and the coherence function  $\gamma(\hat{f}, d)$  by inverse Fourier transform:

$$dVw_{eff}(t) = \mathcal{F}^{-1}[S_{dVw_{eff}}(f,\gamma(f,d))] \tag{97}$$

with  $\mathcal{F}^{-1}$  the inverse Fourier transform and

t : time;
f : frequency;
d : distance over which coherence is being considered.

The rotor averaging effect is calculated by integrating the torque-production by turbulent wind speed variations over the rotating blades in the rotor disk, while the frequency-domain approach to rotational sampling is applied. This yields the following formulation for the APSD  $S_{dVw_{eff}}(f)$  of the rotor effective turbulent wind speed variations:

$$S_{dVw_{eff}}(f) = \sum_{i_n=1}^{N} \sum_{i_b=1}^{N} \frac{r(i_a) \cdot r(i_b)}{r_{sq}} \times$$

$$\times \sum_{m=-\infty}^{\infty} \left[ S(f - mBf_{0v}) \int_{0}^{2\pi} e^{-jmB\psi} \gamma(d(r(i_a), r(i_b), \psi), f - mBf_{0v}) d\psi \right]$$
(98)

with:

 $i_a, i_b$ counters for blade element numbers (between 1 and N);

counter for the B-multiple mode in het rotor effective wind spectrum;

azimuth angle for integration of the coherence over rotor disk;

 $f_{0v}$  : rotational frequency of the turbine rotor; r(ia), r(ib) : radii of the blade elements (distance to rotor centre);  $r_{sq}$  : squared sum blade element radii  $(\sum_{ix=1}^{N} r(ix)^2)$ .

The first part of this equation represents the integration over the rotor disc of the contribution of all blade elements, while the second part constructs the auto power spectral density resulting from sampling the coherent wind variations in the rotor plane with a multiple of the rotational frequency times the number of blades [8]. Only the contributions of the first two rotational sampling frequencies (m = 1, 2) are taken into account.

For the proof that the rotor effective wind spectrum of equation (98) is the stochastically correct representation of the single point wind speed for calculation of the aerodynamic torque of the turbine is referred to the appendix of [12].

The result is constrained by (but sufficient with respect to the objective):

- APSD wind speed and  $\gamma \leftrightarrow d$  dependency are non-varying over rotordisk;
- equal aerodynamic power extraction over rotor disk;
- rigid rotor behaviour in the frequency range of interest;
- constant rotor speed (variable speed would broaden and reduce the mB peaks in the spectrum, this is not taken into account).

### GCL wind farm wake model

In the EWTS-II project [6] six wind farm wake models have been described. The GCL model, developed by G.C. Larsen of Risoe National Laborotory in Denmark, generates all parameters

relevant for the Wind farm as Power plant project, i.e. wind speed depreciation, turbulence and coherence. The model is based on simple engineering formulas, is easily programmed and does not require much CPU time. It is suitable for the wind speed and turbulence estimation prior to the rotor effective wind speed calculation as input for the electrical evaluations in the Wind farm as Power plant project.

To have a more or less complete description of the wind modeling in the Wind farm as Power plant project, the GCL model description in [21] and [36] is reproduced here.

#### A.2.1 GCL model

The GCL-method determines the wake deficit, the wake turbulence intensity, the wake turbulence length scale and the wake coherence decay factor of a single wind turbine. Dependent on two boundary conditions, viz. the wake radius at the turbine and the wake radius at a location 9.5D behind the turbine, the equations for the wake conditions are:

$$R_n : \left(\frac{105}{2\pi}\right)^{0.2} c_l^{0.4} (c_{d,ax} Ax)^{0.333}$$
 (99)

$$R_{nb} : \max[1.08D, 1.08D + 21.7D * (I_a - 0.05)]$$
 (100)

$$R_{nb}$$
 :  $\max[1.08D, 1.08D + 21.7D * (I_a - 0.05)]$  (100)  
 $R_{w95}$  :  $0.5 * [R_{nb} + \min(H, R_{nb})]$  (101)

$$x_0 : 9.5D/(\frac{2R_{w95}}{D})^3 - 1)$$
 (102)

$$c_l : \sqrt{(\frac{D}{2})^5 \frac{2\pi}{105} (c_{d,ax} A x_0)^- 1.667}$$
 (103)

$$\Delta V : -\frac{V_a}{9} (c_{d,ax} A x^2)^{0.333} [r^{1.5} (3c_l^2 c_{d,ax} A x)^{-0.5} - (\frac{35}{2\pi})^{0.3} (3c_l^2)^{-0.2}]^2$$
 (104)

$$I_w : 0.29S^{-0.333}\sqrt{1-\sqrt{1-c_{d,ax}}}$$
 (105)

$$I_{wt} : \sqrt{I_a^2 + I_w^2}$$
 (106)

(107)

with:

 $R_n$ wake radius at location x

non-dimensional mixing length, depending on Prandtls mixing length l

thrust coefficient, also called axial force coefficient  $c_{d,ax}$ 

x-coordinate of position in wake for calc. of deficit:  $x = x_0 + dist$ x

with dist the distance to turbine that generates wake

 $R_{nb}$ boundary condition of wake radius at location x

rotor diameter of upstream turbine

ambient turbulence intensity at hub height, limited to 0.05-0.15 wake radius at 9.5D behind the turbine that generates wake

tower height of turbine that generates wake x-coordinate of the turbine generating the wake wake deficit: wind speed reduction in the wake

undisturbed wind speed at hub height

distance to hub centre

distance in rotor diameters to turbine that generates wake  $\frac{dist}{D}$ turbulence intensity increase due to tubine operation

total resulting turbulence intensity in wake

#### Turbulence length scale and coherence decay

The GCL model also takes into account the turbulence length scale and the coherence decay in the wake in the direction of the wind speed. The corresponding description in [6] Part 1, Sub A is reproduced here. The length scale and coherence are used to determine the rotor effective wind speed, see section A.1.

Point of departure of the GCL model is the standard Kaimal formulation of the turbulence spectrum S(f) of the wind speed as formulated in the Danish Code of Practice:

$$\frac{f \cdot S_u(f)}{\sigma_u^2} = \frac{f \cdot L_u/\overline{V}_a}{(1 + 1.5 \cdot f \cdot L_u/\overline{V}_a)^{5/3}}$$
(108)

with

variance of the longitudinal turbulence component frequency in Hz

If the Kaimal formulation in IEA 1400-1 is adopted, the length scales of formula 108 should be divided by a factor 4.

The coherence function is defined in [6] as the magnitude of the complex cross-spectral density of the longitudinal wind velocity components at to two spacially separated points, divided by the square root of the product of the respective autospectrum functions. The standard Davenport formulation is adopted:

$$Coh(s,f) = e^{-a^{u} \cdot \frac{f_{s}}{\overline{V}_{a}}}$$
(109)

with s the projection of the separation vector between the two spacial points on a plane perpendicular to the average wind direction. The wake wind field parameters are defined as follows

- The wake deficit is described in terms of the maximum wake deficit  $\Delta \overline{V}$  within the wake.
- The ambient turbulence intensity,  $I_a^u$ , is defined as the standard deviation of the horizontal turbulence component (as it is usually obtained from cup anemometer measurements) divided by the undisturbed mean wind speed  $\overline{V}_a$ . Both values refer to turbine hub height.
- The wake turbulence intensity,  $I^u_{wt}$ , is defined as the maximum standard deviation of the horizontal turbulence component within the wake divided by the undisturbed mean wind speed at turbine hub height.
- The ambient turbulence length scale,  $L_a^u$ , is defined as the (Kaimal) length scale of the u-turbulence component for frequency  $f_L$ , where half of the turbulence energy relates to frequencies heigher than  $f_L$ .  $L_a^u$  refers to the turbine hub height.
- The wake turbulence length scale,  $L_w^u$ , is defined in analogy with the ambient turbulence length.  $L_w^u$  refers to the position within the wake where the reduction in the length scale takes its maximum.
- The ambient transversal turbulence component,  $\sigma_a^v$ , refers to the turbine hub height.
- The wake transversal turbulence component,  $\sigma_w^v$ , refers to the position within the wake where the maximum value is obtained.
- The ambient coherence decay factor,  $a_a$ , relates to a Davenport coherence description. Both horizontal and vertical separation are accepted, and to facilitate the use of cup anemometers, the decay factor relates to the horizontal turbulence component.
- The wake coherence decay factor,  $a_w$ , relates to a Davenport coherence description. Both horizontal and vertical separation is accepted, and the decay factor relates to the horizontal turbulence component. Vertical and horizontal separation are again indicated by adding a "V" or a "H" to the table value.

The modified length scale depends on the rotor thrust coefficient, the spacing distance, the rotor diameter, and the undisturbed turbulence length scale. Assuming an approximate linear relationship between thrust coefficient and mean wind speed (for a stall controlled turbine), and referring to a Kaimal formulation of the turbulence spectrum, the length scale for the uturbulence component inside a wake,  $L_w^u$ , is determined from :

$$L_w^u = L_a^u \left( 1 - \min \left( \frac{12.2 \left( 1 - \frac{D}{L_a} \right)}{\overline{V}_a S_r^{0.6}}, 0.9 \right) \right)$$
 (110)

where  $L^u_a$  denotes the u-turbulence length scale in the undisturbed flow,  $\overline{V}_a$  is the undisturbed mean wind velocity at hub height, and the reduced spacing,  $S_r$ , between the turbines is defines as:

$$S_r = 2^{0.8} + (S - 2)^{0.8}$$
 for  $S \ge 2$  (111)

The undisturbed length scale and the resulting wake length scale refer to conditions at hub height.  $L_w^u$  is seen to be monotonous in  $\overline{V}_a$ ,  $L_a^u$ ,  $S_r$ , and D. The coherence is given a Davenport–formulation and is thus expressed as:

$$Coh(s, f) = \sqrt{\exp\left(-\frac{asf}{\overline{V}_a}\right)}$$
 (112)

where f is the frequency in [Hz], s is the separation in [m],  $\overline{V}_a$  is the (ambient) mean wind speed in [m/s]. The ambient (undisturbed) coherence decay factor,  $a_a$ , is determined by:

$$a_a = \begin{cases} 12 + \frac{11|z_2 - z_1|}{z_{average}} & \text{for vertical separation} \\ 12 + \frac{11\Delta y}{z_{average}} & \text{for lateral separation} \end{cases}$$
(113)

with the measuring heights denoted by  $z_1$ ,  $z_2$ , the average of these equal to  $z_{average}$ , and  $\Delta y$  being the lateral separation. The following expression for the wake coherence decay factor,  $a_w$ , is proposed

$$a_w = \begin{cases} (1 + K_w)a_a & \text{for } 2 \le S < 7.5\\ a_a & \text{for } 7.5 \le S \end{cases}$$
 (114)

where S denote the spacing expressed in rotor diameters and the wake correction factor,  $K_w$ , is given by

$$K_{w} = \begin{cases} \frac{7.5 - S}{5.5} & \text{for } \overline{V}_{a} < 6\\ \frac{7.5 - S}{5.5} (\frac{1}{3} \overline{V}_{a} - C_{s}) & \text{for } 6 \le \overline{V}_{a} \le 15\\ \frac{4(7.5 - S)}{5.5} & \text{for } 15 < \overline{V}_{a} \end{cases}$$
(115)

For vertical separation  $C_s \equiv 1$  and for horizontal separation  $C_s \equiv 2$ . For spacings less than 2 rotor diameters the value of the wake coherence decay factor is assumed to equal the value related to a 2 diameter spacing.

Transversal turbulence, i.e. in a direction perpendicular to the wind direction, is also considered. Expressions for turbulence intensity and length scales in v and w direction are given. The rotor effective wind in the Wind farm as Power plant project only considers the u component, however.

#### A.2.2 GCL model in Matlab

The GCL model was implemented in Matlab and the results have been compared to the results reported in [6]. Figure 225 shows that Matlab program gives the same wind speed deficits, except for two of the 30 measurements. This may be caused by typing errors in the manuscript and will not be investigated further.

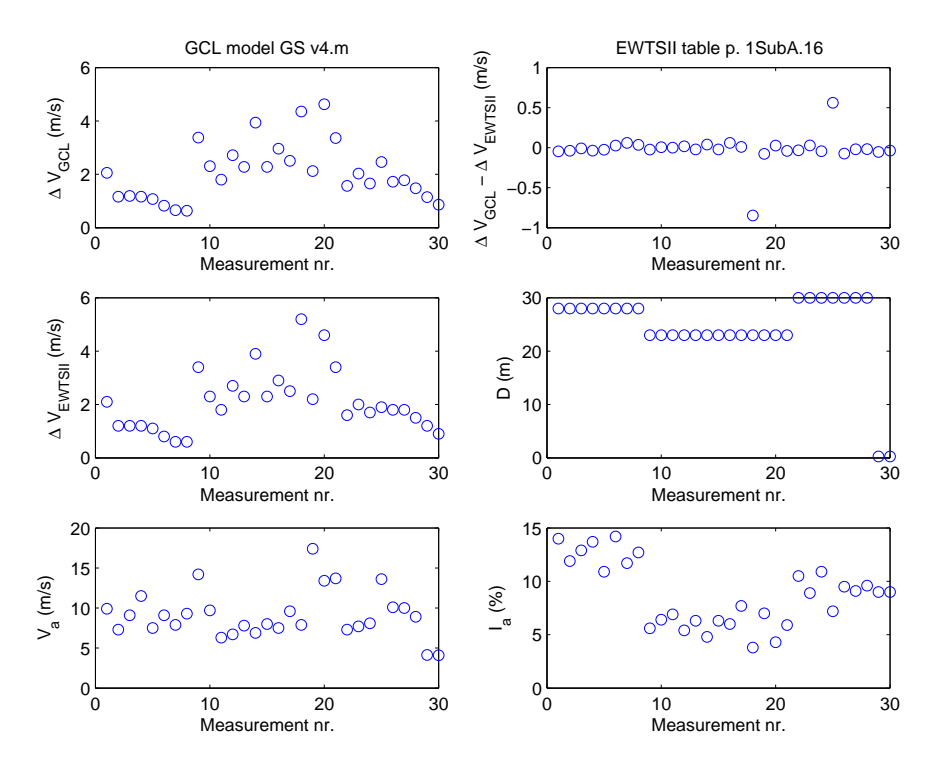


Figure 225: GCL-model results and comparison to EWTS-II measurements table

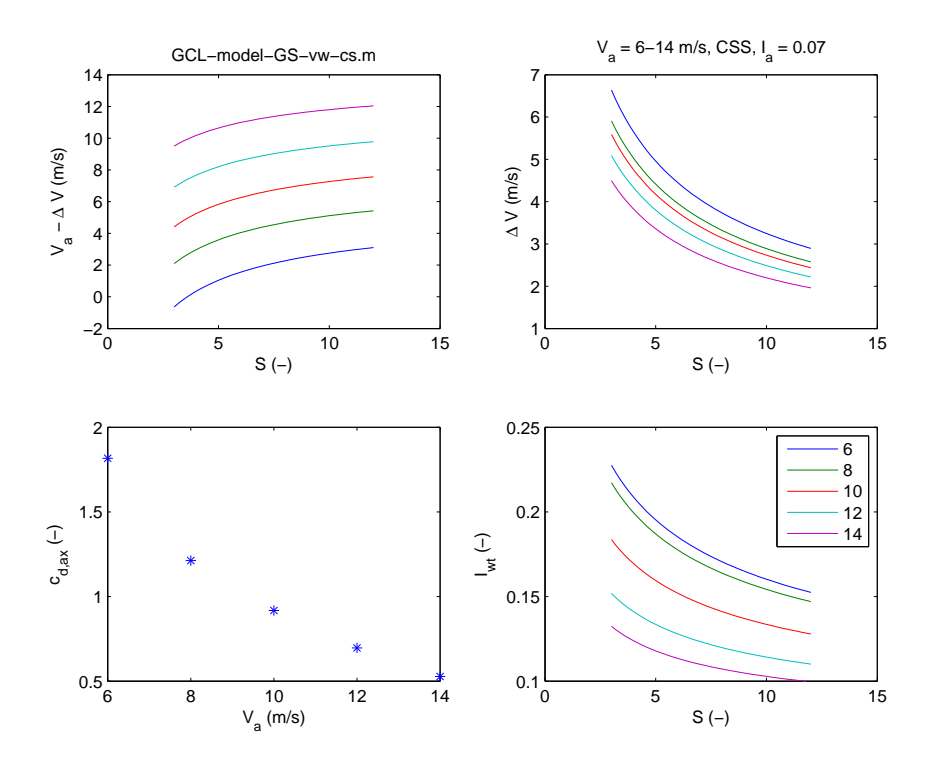


Figure 226: Wind speed deficit  $\Delta V$  and turbulence intensity  $I_{wt}$  against relative distance to wake generating turbine S for a constant speed turbine and five wind speeds

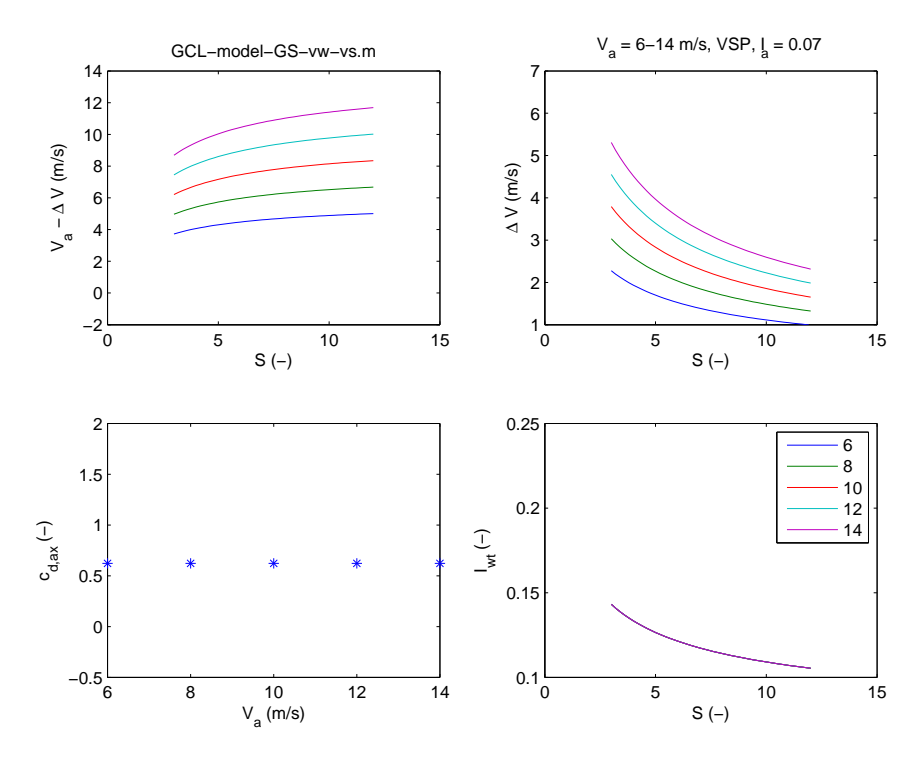


Figure 227: Wind speed deficit  $\Delta V$  and turbulence intensity  $I_{wt}$  against relative distance to wake generating turbine S for a variable speed turbine and five wind speeds

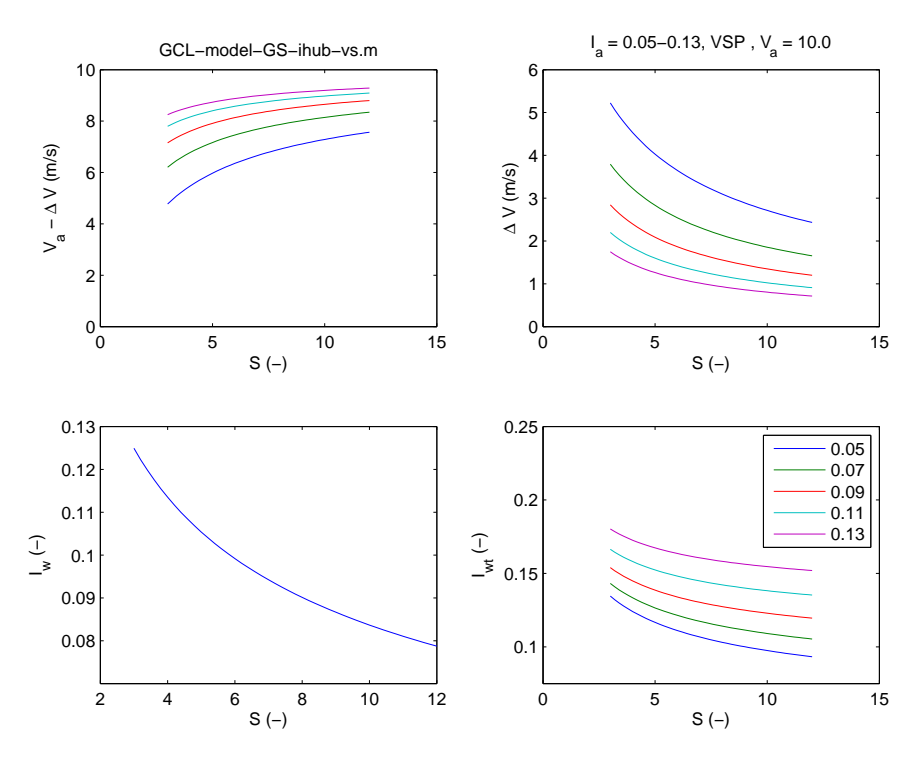


Figure 228: Wind speed deficit  $\Delta V$  and turbulence intensity  $I_{wt}$  against relative distance to wake generating turbine S for a variable speed turbine and five values of the undisturbed turbulence intensity

Figure 226 gives the wind speed deficits and turbulence intensities for a constant speed turbine as a function of the relative distance behind the wake creating turbine and the wind speed. Deficit and turbulence decrease with increasing distance and both also decrease with increasing wind speed. For increasing wind speed the axial thrust coefficient decreases and this effect is stronger than the effect of increasing wind speed on deficit and turbulence.

Figure 227 shows the results for a variable speed turbine. Now the axial thrust coefficient is constant. Deficit and turbulence decrease with increasing distance. The deficit increases with wind speed, while the turbulence intensity is wind speed independent.

Figure 228 plots the effect of ambient turbulense intensity on deficit and wake turbulence. Higher turbulence leads to lower deficit, while the turbulence increase caused by the turbine  $I_w$  is not affected by the ambient turbulence level.

### A.3 Conclusion

A simple model for the wind speed deficit and the turbulence increase inside a wind farm has been programmed, based on the GCL-model, developed by G.C. Larsen of Risoe National Laboratory. The model can be used to make the rotor effective wind speed calculation dependent on the position of the turbine in the wind farm, if a fixed wind direction is assumed. The model can also be used to make a better estimate of the wind farm power production. The latter is outside the scope of this project. The model implementation was verified by comparison to measurements and demonstrated for a constant and a variable speed turbine.

### Summary of parameters in random processes

Since frequent use is made of parameters and variables that describe random processes, the definitions used in the analysis of random variables are summarised. For a more complete overview is referred to [26].

- (1) The probability that a variable x(t) is in the range between x and x + dx equals p(x)dx. The function p(x) is called the probability density function.
- (2) The probability distribution function P(x) is defined by  $P(x) = \int_{-\infty}^{x} p(x) dx$ .
- (3) The joint probability p(x,y)dxdy is the probability that x(t) is in the range between x and x+dx and at the same time y(t) is in the range between y and y+dy. For a finite interval:  $\operatorname{Prob}(x_1 \leq x(t) \leq x_2)$  and  $\operatorname{Prob}(y_1 \leq y(t) \leq y_2)$  equals  $\int_{x_1}^{x_2} \int_{y_1}^{y_2} p(x,y) dx dy$ . If x and y are independent, p(x,y) = p(x)p(y). The units of p(x,y) are 1/units of xy.
- (4) The average or mean value is the statistical expectation E of a random variable and is defined by:  $E(x(t)) = \int_{-\infty}^{+\infty} xp(x)dx$ . The units of E(x) are the units of x.
- (5) The average value of the square of a random signal thus equals:  $E(x^2(t)) = \int_{-\infty}^{+\infty} x^2 p(x) dx$ .
- (6) The standard deviation  $\sigma$  and the variance  $\sigma^2$  follow from:  $\sigma^2 = E[(x E[x])^2] = E[x^2] (E[x])^2$ . The units of  $\sigma$  are the units of x.
- (7) For a function f(x,y) of two random variables x(t) and y(t), the average value of the function is defined through the joint probability p(x,y) of x and y:  $E[f(x,y)] = \int_{-\infty}^{+\infty} \int_{-\infty}^{+\infty} f(x,y) p(x,y) dx dy.$
- (8) The joint expectation of two stochastic variables thus is:  $E[x(t),y(t)]=\int_{-\infty}^{+\infty}\int_{-\infty}^{+\infty}xyp(x,y)dxdy$ .
- (9) The correlation coefficient or normalised covariance  $\rho_{xy}$  of two random variables x and y is defined by:  $\rho_{xy} = \frac{E[(x-m_x)(y-m_y)]}{\sigma_x\sigma_y}$  with  $m_x, m_y$  the mean values of x and y.
- (10) The auto-correlation function  $R_{xx}(\tau)$  is the average value of the product  $x(t)x(t+\tau)$ , i.e.  $E[x(t)x(t+\tau)] = \int_{-\infty}^{+\infty} \int_{-\infty}^{+\infty} x(t)x(t+\tau)p(x(t)x(t+\tau))dx(t)dx(t+\tau)$ . The units of  $R_{xx}$  are the units of  $x^2$ .
- (11) The correlation coefficient  $\rho_{xx}$  of  $x(t)x(t+\tau)$  and the autocorrelation function are related:  $\rho_{xx}(\tau) = \frac{R_{xx}(\tau) m_x^2}{\sigma_x^2}$ .
- (12) The cross-correlation function  $R_{xy}(\tau)$  is the average value of the product  $x(t)y(t+\tau)$ , i.e.  $E[x(t)y(t+\tau)]$ . For a stationairy process,  $R_{xy}(\tau) = R_{xy}(-\tau)$  but in general  $R_{xy}(\tau) \neq R_{yx}(\tau)$ .
- (13) Fourier transform in complex notation equals:  $X(\omega) = \frac{1}{2\pi} \int_{-\infty}^{\infty} x(t) \mathrm{e}^{-j\omega t} dt$  and  $x(t) = \int_{-\infty}^{\infty} X(\omega) \mathrm{e}^{j\omega t} d\omega$
- (14) The auto power spectral density function  $S_{xx}(\omega)$  is the Fourier transformation of the autocorrelation function  $R_{xx}(\tau)$ :  $S_{xx}(\omega) = \frac{1}{2\pi} \int_{-\infty}^{\infty} R_{xx}(\tau) \mathrm{e}^{-j\omega\tau} d\tau$ . This is the two-sided version. Inverse transformation thus yields:  $R_{xx}(t) = \int_{-\infty}^{\infty} S_{xx}(\omega) \mathrm{e}^{j\omega\tau} d\omega$ . The units of  $S_{xx}$  are units of  $x^2$  per unit of angular frequency.
- (15) Since  $R_{xx}(\tau=0)=\int_{-\infty}^{\infty}S_{xx}(\omega)d\omega$  and  $R_{xx}(\tau=0)=E[x^2]$ , the area under the auto power spectral density function equals the mean square value of x. Therefore, a more complete name of  $S_{xx}(\omega)$  is the mean square spectral density.
- (16) Similarly, the cross power spectral density function  $S_{xy}(\omega)$  is the Fourier transformation of the cross correlation function  $R_{xy}(\tau)$ :  $S_{xy}(\omega) = \frac{1}{2\pi} \int_{-\infty}^{\infty} R_{xy}(\tau) \mathrm{e}^{-j\omega\tau} d\tau$ .

Frequency response of linear passive systems:

- (17) For input x(t) the output y(t) can be calculated in the frequency domain:  $Y(\omega) = H(\omega)X(\omega)$ , with  $X(\omega) = \frac{1}{2\pi} \int_{-\infty}^{\infty} x(t) \mathrm{e}^{-j\omega t} dt = \mathcal{F}(x(t))$  and  $H(\omega)$  the transfer function of the process.
- (18) In the time domain, the same result is obtained by the convolution integral which is based on the superposition principle applied to a linear system:  $y(t) = \int_{-\infty}^{t} h(t-\tau)x(\tau)d\tau$ , with h(t) the response of the process at time t to an impulse input at time 0.
- (19) Process response in terms of spectral density:  $S_{yy}(\omega) = \sum_{r=1}^{N} \sum_{s=1}^{N} H_r^*(\omega) H_s(\omega) S_{x_r x_s}(\omega)$  with  $x_{1,\dots,N}$  the input signals and  $H_{1,\dots,N}(\omega)$  the transfer functions for a specific input.
- (20) For a single input:  $S_{yy}(\omega) = H^*(\omega)H(\omega)S_{xx}(\omega) = |H(\omega)|^2S_{xx}(\omega)$ .
- (21) For uncorrelated inputs:  $S_{yy}(\omega) = \sum_{r=1}^{N} |H_r(\omega)|^2 S_{x_r x_r}(\omega)$ .
- (22) Cross-correlation between output and an input for a system with multiple inputs. In case of two inputs:  $R_{x_1y}(\tau) = \int_{-\infty}^{\infty} h_1(\theta) R_{x_1x_1}(\tau-\theta) d\theta + \int_{-\infty}^{\infty} h_2(\theta) R_{x_1x_2}(\tau-\theta) d\theta$
- (23) By taking the Fourier transform, the cross-spectral desity results:  $S_{x_1y}(\omega) = H_1(\omega)S_{x_1x_1}(\omega) + H_2(\omega)S_{x_1x_2}(\omega)$ .
- (24) For uncorrelated inputs  $S_{x_1y}(\omega) = H_1(\omega)S_{x_1x_1}(\omega)$  and  $S_{yx_1}(\omega) = S_{x_1y}^*(\omega) = H_1^*(\omega)S_{x_1x_1}(\omega)$  since  $S_{x_1x_1}(\omega)$  is always a real quantity.
- (25) The coherence function for a single input-single output system is:  $\eta_{yx_1}^2(\omega) = \frac{H_1(\omega)S_{yx_1}(\omega)}{S_{yy}(\omega)}$ . Since  $H_1(\omega) = \frac{S_{x_1y}(\omega)}{S_{x_1x_1}(\omega)}$  this is equivalent to:  $\eta_{yx_1}^2(\omega) = \frac{S_{x_1y}(\omega)S_{yx_1}(\omega)}{S_{x_1x_1}(\omega)S_{yy}(\omega)}$ .
- (26) The complex spectra can be writen in terms of the real coherence  $\gamma$  and the phase  $\theta$ :  $\frac{S_{xy}(f)}{\sqrt{S_{xx}(f)S_{yy}(f)}} = \gamma_{xy} \mathrm{e}^{-j\theta_{xy}(f)}.$

## **Definitions and formulas wind turbulence**

The following definitions and formulas have been taken from Chapter 2 of [9], which gives an overview of wind structure and statistics.

Turbulence intensity is defined by:

$$I_u = \frac{\sigma_u}{U_{mean}} \tag{116}$$

The turbulence intensity is a function of the height z above the earth:

$$I_u(z) = \frac{1}{\ln(z/z_0)} \tag{117}$$

with  $z_0$  the roughness length of the terrain, typically in the range of  $10^{-5}-4$  m. The Prandtl logarithmic law describes the average wind speed as function of the height above the earth:

$$U_{mean}(z) = \frac{u_*}{k} \ln \frac{z}{z_0} \tag{118}$$

with k = 0.4 the Von Karman constant and  $u_*$  the friction velocity. A simple estimation of the average wind speed as function of the height is:

$$\frac{U_{mean}(z)}{U_{mean}(H)} = (\frac{z}{H})^{\alpha} \tag{119}$$

with  $\alpha$  the power law exponent, which depends on the roughness length of the terrain, typically 0.10 - 0.32:

$$z_0 = 15.25 e^{-\frac{1}{\alpha}} \tag{120}$$

Experimental observations indicate a Gaussian probability density function p(u) for the wind fluctuations:

$$p(u) = \frac{1}{\sigma_u \sqrt{2\pi}} e^{\frac{-u^2}{2\sigma_u}} \tag{121}$$

The longitudinal length scale  $L_u$  is the average size of the eddies (i.e. the circular or spiral flow areas) in the direction of the mean flow, defined by:

$$L_u = \int_0^\infty R(r)dr \tag{122}$$

with R(r) the cross correlation function. The longitudinal length scale is linked to the longitudinal time scale by:

$$L_u = U_{mean} T_x \tag{123}$$

and is a function of the height:

$$L_u = 25 \frac{z^{0.35}}{z_0^{0.063}} \tag{124}$$

The contribution of the eddies of different sizes to the total variance of the turbulence is provided by the spectral density function  $S_u(f)$  of the wind. A suitable approximation is the Von Karman spectrum:

$$\frac{nS(f)}{\sigma_u^2} = \frac{4\tilde{f}}{(1+70.8\tilde{f}^2)^{\frac{5}{6}}}$$
(125)

with  $\tilde{f} = fL_u/U_{mean}(z)$ .

# B Simulation initialization procedure

A simulation initialization procedure similar to the startup procedure of a wind turbine is used. From a computational point of view, it has the advantage that it is not necessary to calculate a steady state initial condition before running the actual simulation and it prevents starting with an initial condition that leads to instability. The calculation of the initial condition can be a problem for complex electrical models and for large wind farm models. In Simulink the initial condition is calculated by a simulation, using the final values of the states for subsequent simulations. Sometimes no steady state is reached due to excessive oscillations or instability. The simulation initialization procedure avoids these problems.

The simulation initialization procedure is demonstrated for the VSP-DFIG turbine. The procedure is simple:

- the initial vales of the magnetic fields in the generator are set to zero;
- all capacitance initial voltages are set to zero with the exception of the DC link voltage, which is set to 0.01 V;
- all inductance initial currents are set to zero;
- the turbine rotates at nominal speed;
- the DC link voltage setpoint is ramped up from 0.01 V to 1100 V in 1 second;
- the grid voltage that is applied to the IG and rotor converter is ramped up from zero to the rated value in 1 second.

Figures 229 to 232 show the main variables of the VSP-DFIG turbine with simulation initialization procedure and subsequent wind gust. Most electrical parameters reach their steady state without oscillation. Only the rotor speed and the rotor voltage are oscillating during the first seconds of the simulation.

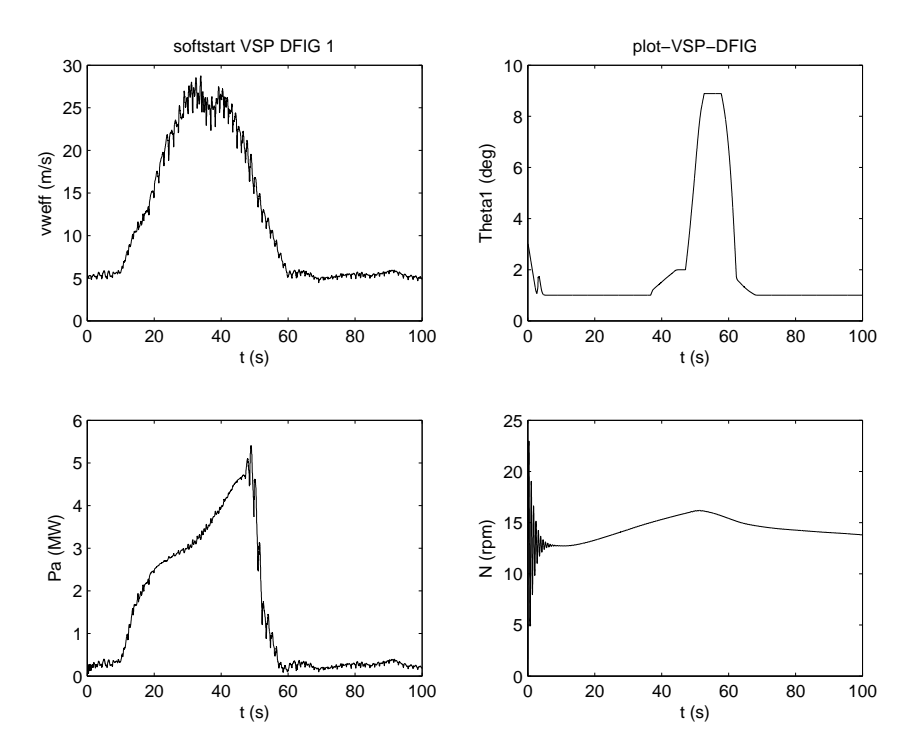


Figure 229: Simulation initialization procedure VSP DFIG

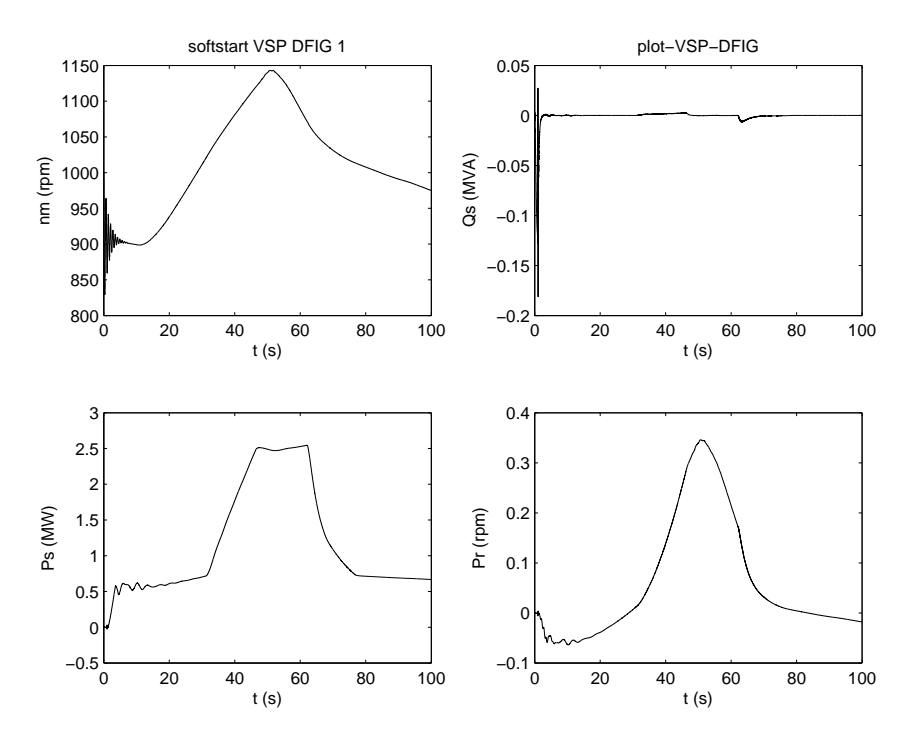


Figure 230: Simulation initialization procedure VSP DFIG

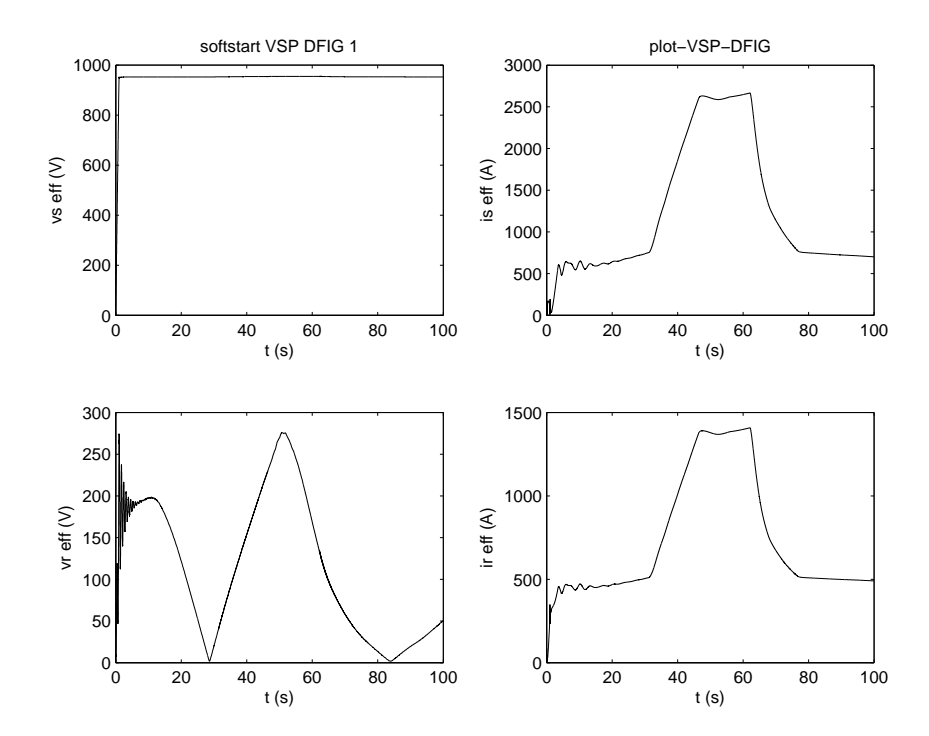


Figure 231: Simulation initialization procedure VSP DFIG

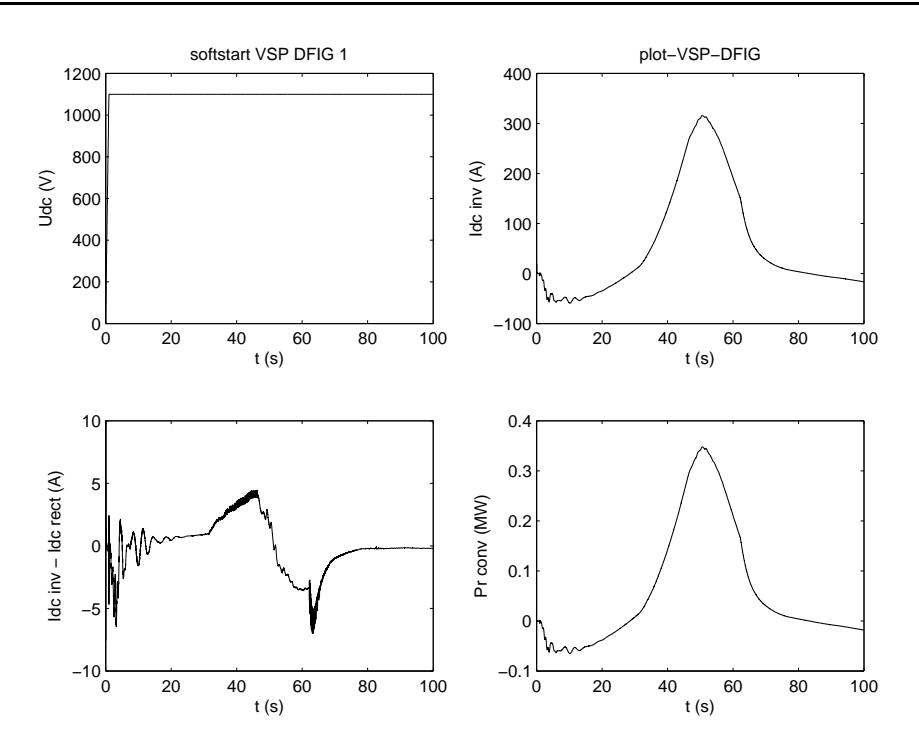


Figure 232: Simulation initialization procedure VSP DFIG

# C New Variable Speed Pitch turbine model

The Variable Speed Pitch (VSP) turbine model developed in the Erao-2 project uses the Matlab S-function option in Simulink. The model causes problems when used in the Simulink environment:

- it is less transparent and more difficult to modify then the standard Simulink based models;
- it requires more CPU time due to more the time consuming Matlab code;
- the pitch controller caused instability.

To solve these problems, a new VSP model has been made in standard Simulink. The model consists of five main components, see figure 233:

- the mechanical and aerodynamic part of the turbine model, including the pitch actuator, see figure 234;
- the pitch controller, figure 235;
- the generator master controller which determines the electric torque setpoint, see figure 236;
- the signal conditioning, consisting of four filters, see figure 237;
- a preprocessor to determine the generaor state and the allowed pitch speed, see figure 238.

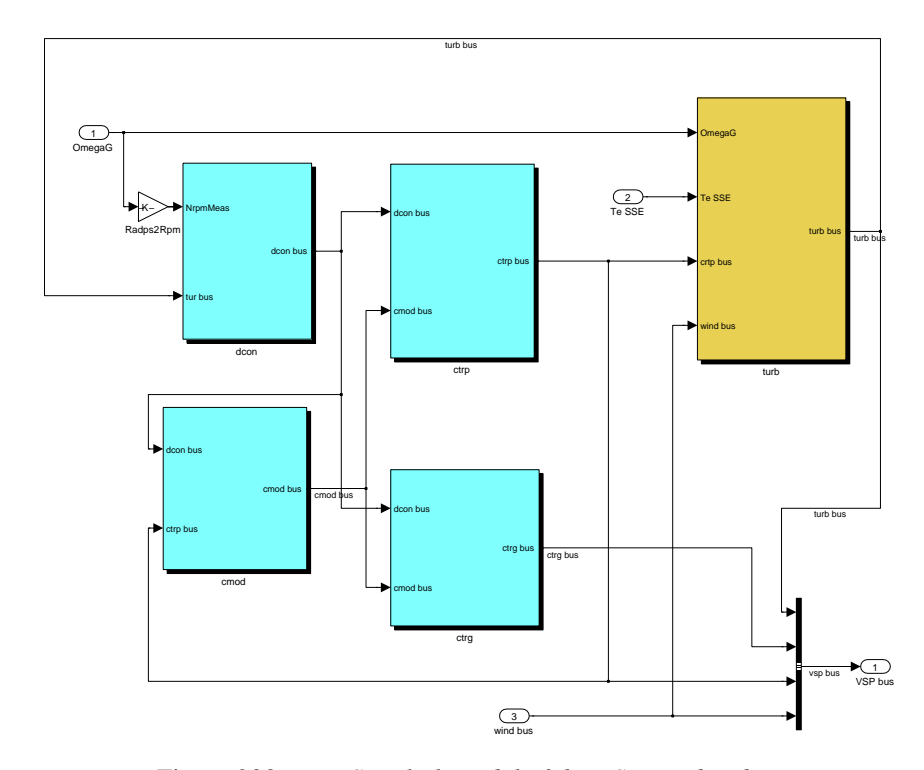


Figure 233: New Simulink model of the VSP wind turbine

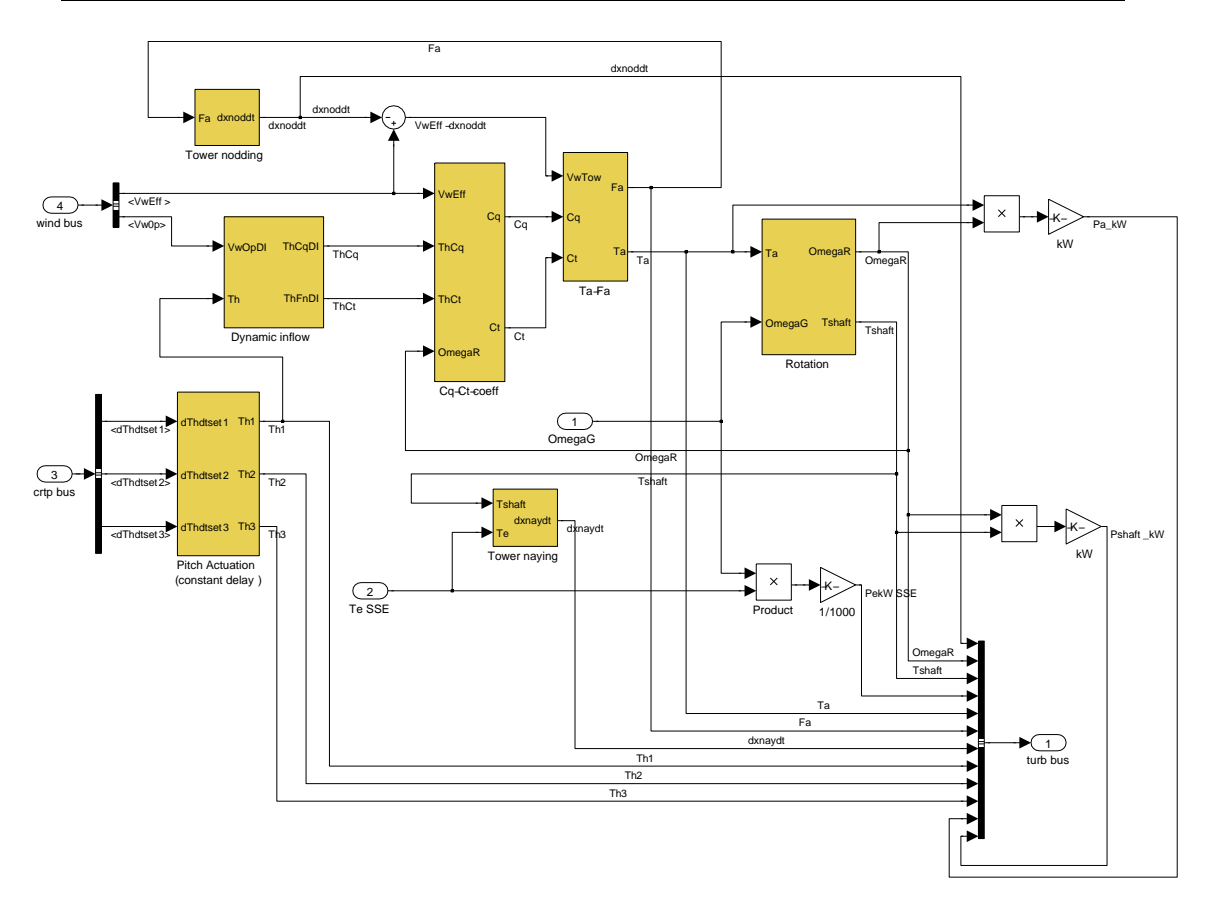


Figure 234: Mechanical and aerodynamic part of the new Simulink VSP turbine model

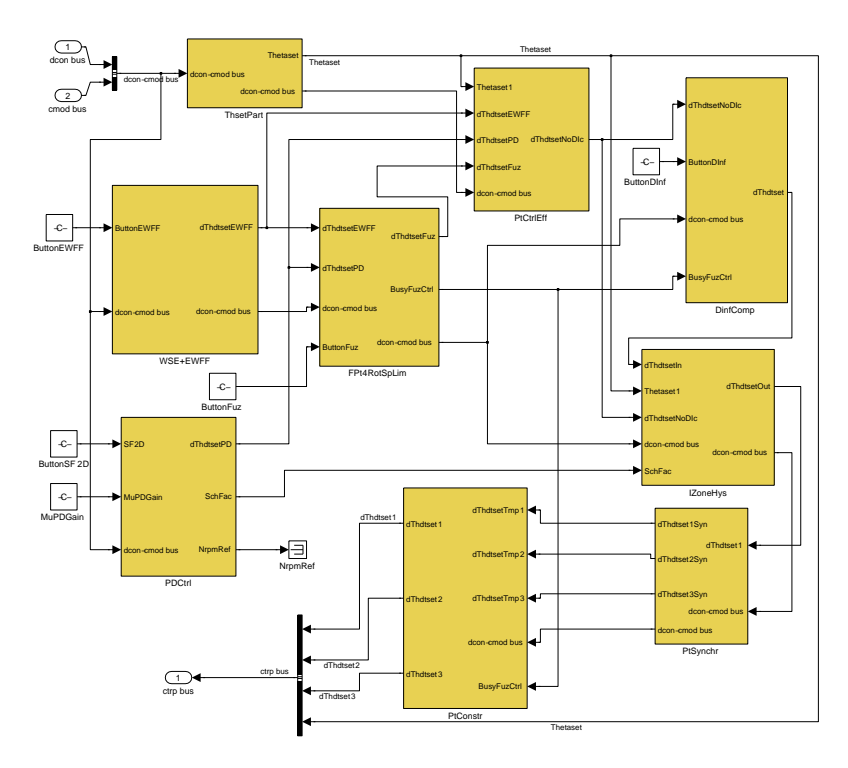


Figure 235: Pitch controller of the new Simulink VSP turbine model

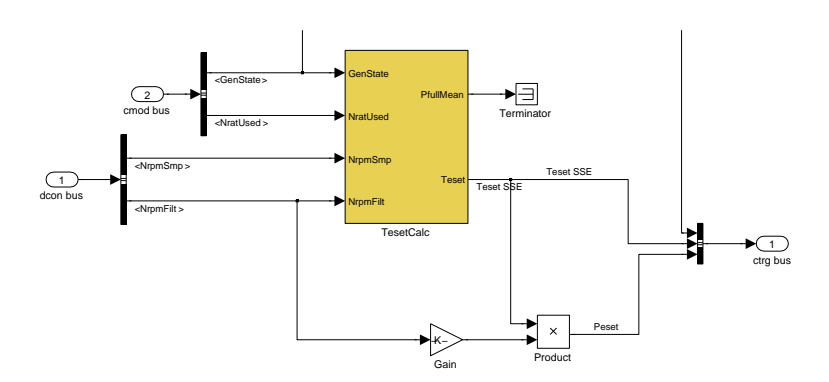


Figure 236: Generator master controller of the new Simulink VSP turbine model

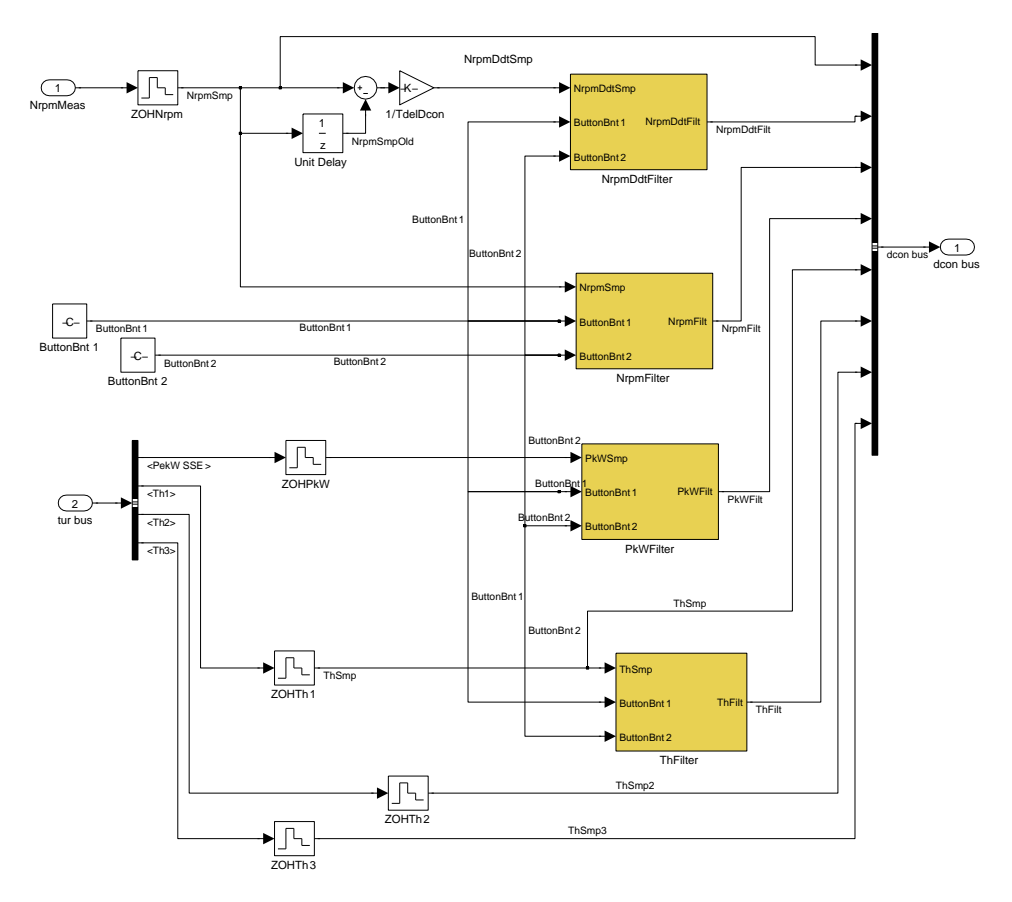


Figure 237: Signal conditioning of the new Simulink VSP turbine model

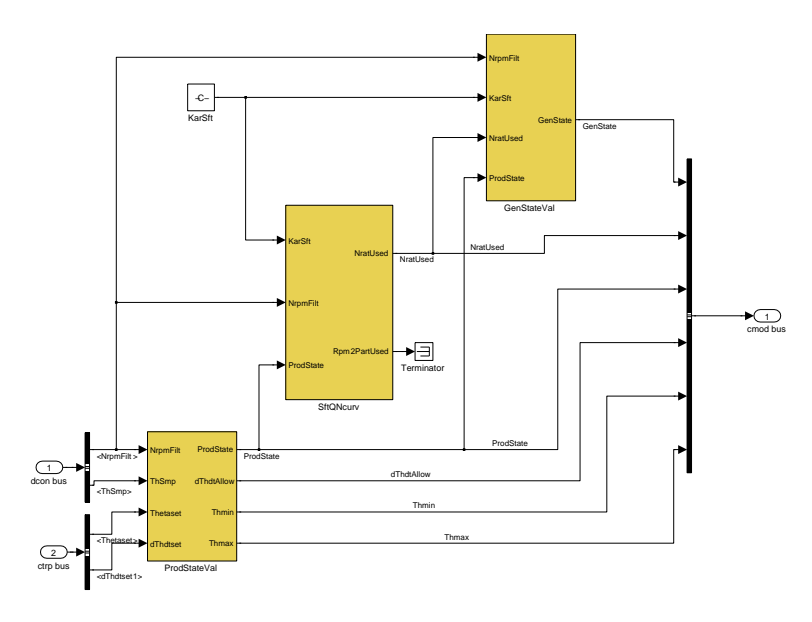


Figure 238: Preprocessor of the new Simulink VSP turbine model

## D Induction machine flux oriented control

#### **Induction machine operation**

Figure 239 illustrates the main features of the asynchronous or induction machine. The stator is a hollow steel cylinder with slots for the wires of a three phase winding system. The windings of phases A, B and C are displaced by  $120^{\circ}$ . The + and the · indicate the direction of the current: + into the plane of the paper and • out of the plane. The current in phase A produces a flux perpendicular to the winding, according to the cork-screw rule, as indicated by  $\Psi_{sa}$ . Generally, the induction machine is connected to a three phase AC grid with voltages lagging  $120^{\circ}$ . An alternating current in phase A will give an oscillating flux  $\Psi_{sa}$  and the same applies to phases B and C. Adding the vectors of the individual phase magnetic fields gives the total field  $\Psi_{ss}$  caused by stator currents, as indicated by the vector diagram in figure 239:

$$\Psi_{ss} = \Psi_{sa} + \Psi_{sb} + \Psi_{sc} \tag{126}$$

When the three phases carry alternating currents of angular velocity  $\omega_s$ , which are  $120^o$ out of phase, the oscillating fluxes produced in each phase add up to a rotating magnetic flux  $\Psi_{ss}$  of constant magnitude and constant angular speed  $\omega_s$  (see appendix E).

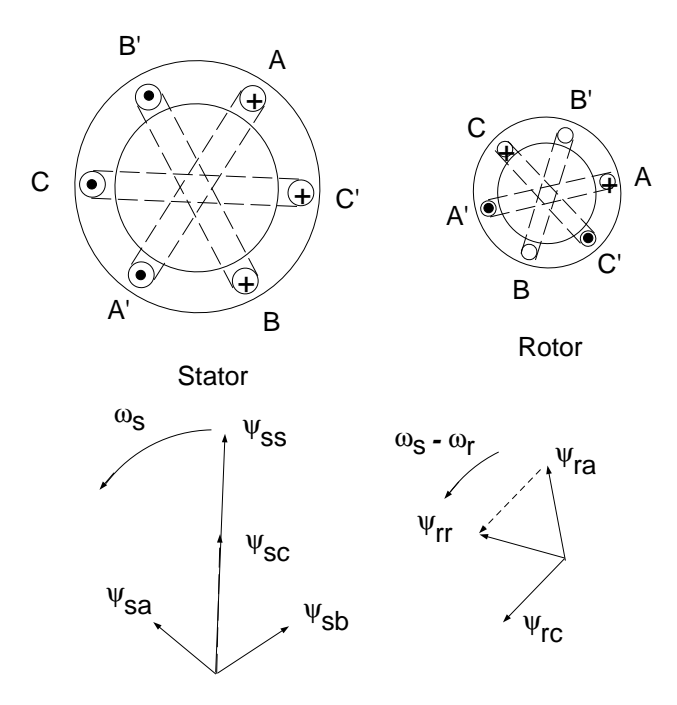


Figure 239: Induction machine with one pole pair

In most cases, the rotor of an induction machine consists of an iron cylinder with slots that carry copper bars, short circuited by rings at the two flat ends of the rotor. This construction is frequently referred to as a squirrel cage. For the generation of torque it is essential that two magnetic fields, one linked to the stator and one to the rotor, interact. Since there is no external current source connected to the rotor, a current must be produced in a different way, namely by electromagnetic induction. In steady state, the rotor speed and the speed of the rotating magnetic field must be different to produce a current in the rotor. Then the squirrel cage moves relative to the stator flux, the enclosed flux changes and a current is induced. The relative difference between the mechanical rotor speed  $\omega_r$  and the angular speed of the stator flux  $\omega_s$  is called the slip s:

$$s = \frac{\omega_s - \omega_s}{\omega_s}$$

The angular frequency of the induced voltages and currents in the rotor is  $(\omega_s - \omega_r)$ . When the stator field speed is higher than the mechanical rotor speed, the induced rotor flux, as seen from a fixed position on the rotor, rotates in the direction of the stator field rotation. The induction machine operates as motor. When the rotor mechanical speed is higher than the stator field speed, the induced rotor flux as seen from a fixed position on the rotor rotates backwards, in the opposite direction of the stator field rotation. The induction machine operates as generator. The number of pole pair in this discussion was assumed to be one, otherwise the mechanical speed of the rotor is a fraction of the stator field speed.

Figure 239 only shows the fluxes created by stator and rotor currents. The linked fluxes of the stator and rotor result from all currents:

$$\Psi_s = L_s i_s + L_m i_r$$

$$\Psi_r = L_m i_s + L_r i_r$$
(127)
(128)

$$\Psi_r = L_m i_s + L_r i_r \tag{128}$$

The linked stator and rotor fluxes, seen by an observer fixed to the stator, rotate at the same speed, as is the case for a synchronous machine. This is a requirement for a constant electromagnetic torque and power. The angle  $\delta$  between the linked stator flux and the linked rotor flux (in the synchronously rotating reference frame) is called the load angle and it is a measure for the electromagnetic torque:

$$T_{em} = -K\hat{\Psi}_s\hat{\Psi}_r\sin\delta\tag{129}$$

For the calculation of the torque any two flux space vectors and the angle between them can be chosen ([15], p. 18), for instance the flux only caused by the stator currents  $\Psi_{ss}$  and the flux only caused by the rotor currents  $\Psi_{rr}$  or the linked fluxes  $\Psi_s$  and  $\Psi_r$ . This is caused by the fact that only the perpendicular components of the two fluxes contribute to the torque (delta=90°) and the unidirectional components do not. This also implies that there is no unique load angle, but that it depends on the choice of the fluxes.

The equation often used to calculate the torque are:

$$\Psi_s = \Psi_{sq} + j\Psi_{sd} \tag{130}$$

$$i_s = i_{sq} + ji_{sd} (131)$$

$$\Psi_{s} = \Psi_{sq} + j\Psi_{sd}$$
(130)
 $i_{s} = i_{sq} + ji_{sd}$ 
(131)
 $T_{em} = \Psi_{q}i_{ds} + \Psi_{d}i_{qs}$ 
(132)

so only the current perpendicular to the flux contributes to the electromagnetic torque. This property of electrical machines is used in field oriented control by controlling the current components perpendicular to and in the direction of the flux independently. This requires a power electronic converter.

### Voltage source converter connected to an induction machine

By changing the direction of the voltage in a stator winding (or in a rotor winding in case of a doubly fed induction generator) the amplitude and the direction of the (rotating) current vector caused by the three phase winding in the machine can be changed. If the position of the linked flux seen by the windings is known, the torque and the amplitude of the flux can be controlled by injecting the current corresponding to a desired current vector position with respect to the flux position.

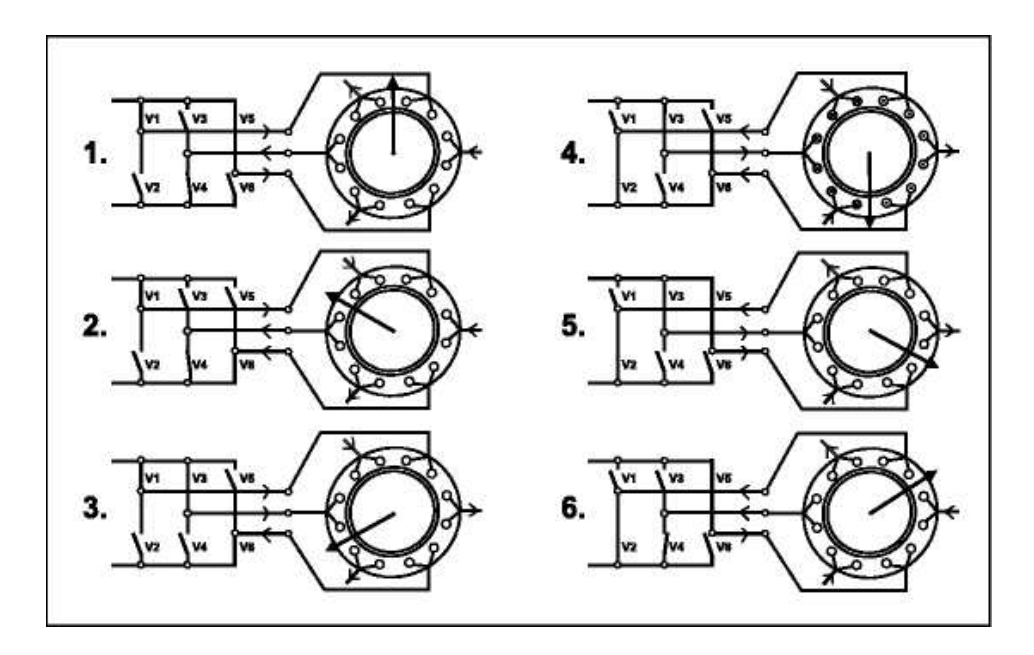


Figure 240: Rotating current vector generated by a voltage source converter (source ABB)

There are eight different switching positions in an AC-DC converter. In two cases, viz. when all the phases are connected to the same DC bus, either negative or positive, the voltages over the stator phases are zero. In the remaining six switching positions, there is a voltage over the windings, and this voltage creates currents in the windings and a current vector results. The figure 240 shows the direction of the current vector depending on the switching positions of the converter. Referring to eq. 132, the current vector components  $i_{sd}$  and  $i_{sq}$  are controlled to produce the correct torque and at the same time to have the correct flux, according to eq. 128.

# E Three phase AC systems, time and space vector

A three phase AC system consists of three conductors carrying AC voltages and currents and optionally a zero conductor. Only balances stationary conditions of the fundamental angular frequency  $\omega$  will be considered.

The three currents of the balanced case are displaced with respect to each other by an angle of  $120^{\circ}$ :

$$i_a(t) = \hat{i}\cos\omega t \tag{133}$$

$$i_b(t) = \hat{i}\cos(\omega t + \frac{2\pi}{3}) \tag{134}$$

$$i_c(t) = \hat{i}\cos(\omega t + \frac{4\pi}{3}) \tag{135}$$

Representation by **time vectors**, sometimes called phasors:

$$\vec{i}_a(t) = \hat{i}(\cos\omega t + j\sin\omega t) = \hat{i}e^{\omega t}$$
 (136)

$$\vec{i}_b(t) = \hat{i}(\cos(\omega t + \frac{2\pi}{3}) + j\sin(\omega t + \frac{2\pi}{3})) = \hat{i}e^{(\omega t + \frac{2\pi}{3})}$$
 (137)

$$\vec{i}_c(t) = \hat{i}(\cos(\omega t + \frac{4\pi}{3}) + j\sin(\omega t + \frac{4\pi}{3})) = \hat{i}e^{(\omega t + \frac{4\pi}{3})}$$
 (138)

Due to the symmetry, it is often sufficient to consider only one phase to calculate all relevant circuit quantities. The conditions for the other 2 phases are displaced in time by  $2\pi/3\omega$  and  $4\pi/3\omega$ . In electrical machines the effect of the individual phases has to be combined taking the spacial arrangement and interaction of the phases into account. This can be accomplished efficiently by applying space vectors.

The **space vector** of the current (sometimes called space phasor) is the vectorial additions of the currents in the three phase windings of the machine. The positive directions of these current vectors are 120 degrees rotated in space with respect to each other (see figure 239). In complex notation a rotation over 120 degrees is represented by  $e^{-j*2\pi/3}$ 

Then the space vector of the current is defined by:

$$\vec{i} = i_a + i_b * e^{-j\frac{2\pi}{3}} + i_c * e^{-j\frac{4\pi}{3}}$$
(139)

The power of this method is that if the phase currents  $i_a$ ,  $i_b$  and  $i_c$  are symmetrical, i.e. are sinusoidal, 120 degrees out of phase and have the same amplitude, then the space vector amplitude and rotational speed are constant:

$$\vec{i} = \hat{i}\cos\omega t + \hat{i}\cos(\omega t + \frac{2\pi}{3}) * e^{-j\frac{2\pi}{3}} + \hat{i}\cos(\omega t + \frac{4\pi}{3}) * e^{-j\frac{4\pi}{3}}$$
(140)

$$= \hat{i} \left[ \frac{1}{2} e^{j\omega t} + \frac{1}{2} e^{-j\omega t} + \left( \frac{1}{2} e^{j\omega t + \frac{2\pi}{3}} + \frac{1}{2} e^{-j\omega t - \frac{2\pi}{3}} \right) * e^{-j\frac{2\pi}{3}} \right]$$
(141)

$$+\left(\frac{1}{2}e^{j\omega t + \frac{4\pi}{3}} + \frac{1}{2}e^{-j\omega t - \frac{4\pi}{3}}\right) * e^{-j\frac{4\pi}{3}}] \tag{142}$$

$$= \hat{i} \left[ \frac{3}{2} e^{j\omega t} + \frac{1}{2} e^{-j\omega t} + \frac{1}{2} e^{-j\omega t - \frac{4\pi}{3}} + \frac{1}{2} e^{-j\omega t - \frac{8\pi}{3}} \right]$$
(143)

$$= \hat{i} \left[ \frac{3}{2} e^{j\omega t} \right] \tag{144}$$

$$= \frac{3}{2}[i_q(t) + j * i_d(t)] \tag{145}$$

This is conveniently represented in the complex plane. In a reference frame rotating with  $\omega t$ ,  $i_q$  and  $i_d$  are constants.

# F Synchronous machine parameters from manufacturers' data sheet

### F.1 Introduction

This section deals with the estimation of synchronous machine model parameters from the standard data supplied by manufacturers. If no measurement of machine parameters can be performed, this may be the only way of finding parameters for the dynamic calculations for a system with synchronous generator. The use of data sheets for the estimation of model parameters has two drawbacks however:

- The data sheet parameters represent the machine behavior at rated and therefore saturated conditions. In most cases the level of saturation is not specified.
- Some parameters needed for the models are not on the standard list of manufacturers' data and can not be calculated from the given parameters either. The division of the leakage inductance between circuits and the resistance of the damper circuits are often not specified. For these parameters a educated guess is made.

In section F.2 the parameters commonly supplied by manufacturers and of interest for the dynamic models are discussed. Equations which relate these parameters to the model parameters are given. In section F.4 an example of the estimation of the model parameters is given. Section F.5 compares the result to measured values.

# F.2 Models and model parameters

The voltage equations for the  $5^{th}$  order model of a synchronous machine with damper windings are:

$$u_{ds} = -r_a i_{ds} - \omega \psi_{qs} - \frac{d}{dt} \psi_{ds}$$

$$u_{qs} = -r_a i_{qs} + \omega \psi_{ds} - \frac{d}{dt} \psi_{qs}$$

$$u_f = r_f i_f + \frac{d}{dt} \psi_f$$

$$0 = r_{1d} i_{1d} + \frac{d}{dt} \psi_{1d}$$

$$0 = r_{1q} i_{1q} + \frac{d}{dt} \psi_{1q}$$

The fluxes are:

$$\begin{array}{rcl} \psi_{ds} & = & l_d i_{ds} + l_{afd} i_f + l_{a1d} i_{1d} \\ \psi_{qs} & = & l_q i_{qs} + l_{a1q} i_{1q} \\ \psi_f & = & l_{afd} i_{ds} + l_{ffd} i_f + l_{f1d} i_{1d} \\ \psi_{1d} & = & l_{a1d} i_{ds} + l_{f1d} i_f + l_{11d} i_{1d} \\ \psi_{1q} & = & l_{a1q} i_{qs} + l_{11q} i_{1q} \end{array}$$

The parameters that have to be determined for the  $5^{th}$  order synchronous machine model are:

Resistances	$r_a$	$r_f$	$r_{1d}$	$r_{1q}$					
Inductances	$l_d$	$l_{afd}$	$l_{a1d}$	$l_{f1d}$	$l_{ffd}$	$l_{11d}$	$l_q$	$l_{a1q}$	$l_{11q}$

The model of the synchronous machine in the we@sea toolbox has been reduced: the damper equations are left out.

# F.3 Data sheet parameters

Table 7 gives an example of a manufacturer supplied data sheet for a synchronous machine. The parameters normally given in these data sheets, and which are of interest for the electrical models are:

Time constants	$T'_d$	$T_d''$	$T'_{d0}$		
Resistances	$r_a$	$r_f$			
Reactances	$X_d$	$X'_d$	$X_d''$	$X_q$	$X_q''$

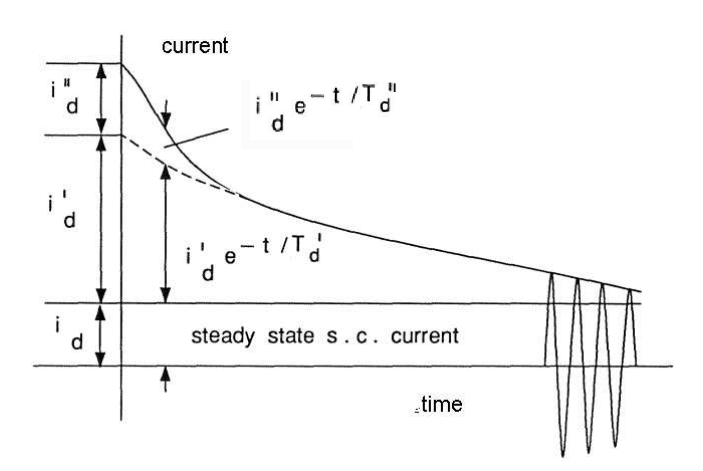


Figure 241: Experimental determination of the direct-axis short-circuit time constants from a short circuit at the machine terminals for no-load condition

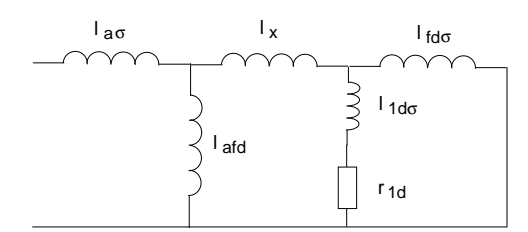


Figure 242: Equivalent circuit for the subtransient time constants of the direct-axis of the synchronous machine

Table 7: Manufacturer supplied data sheet for a synchronous machine

## FRAME HC234-244A1 WINDING 311

		T	50	0 Hz			60	Hz.	
Voltage		380	400	415	440	416	440	460	480
Ratings 125/130°C (50/60Hz)	kVA	37.5	37.5	37.5	37.5	43.8	45	47.5	47.5
	kW	30	30	30	30	35	36	38	38
Ratings 100/105°C (50/60Hz)	kVA	32.5	35	35	35	40	42.5	45	45
	kW	26	28	28	28	32	34	36	36
Voltage Regulation				土12%	(Standar	d) ±1%	(Special)	Ġ.	
Overload (Long Term) 1hr in a 12hr period		1		- 37	110% rat	ed kW lo	ad		
Overload (Short Term 10 secs) (%)	Series 3	275	275	275	275	275	275	275	275
	Series 4	230	230	230	230	230	230	230	230
Insulation System		1			Class H	througho	ut		
Short Circuit Current Capacity (%)			3	00 (Serie	s 3 Only	) 350 (Se	ries 3 On	ly)	
Waveform Distortion (THD)	No Load	1			< 1	1.5 %			
Radio Interference		Ť	BS	800. For	other sta	ındard ap	ply to fac	ctory	
Telephone Interference			THE	< 2%			TIF	< 50	
Unbalanced Magnetic Pull at FL	(kN/mm)	POSPOSION I			3	.93			
Heat Dissipation at FL	(W)	5253	4965	4803	4522	6080	7509	5880	5578
Cooling Air Requirement	(m³/sec)	1	0.	225				270	
	(cfm)	55450	- 4	77		05/36/11	57	2.4	
Inertia Constant (H)	seconds	0.14	0.14	0.14	0.14	0.12	0.11	0.11	0.11
Max Overspeed	(rev/min)				22	250			
DE Bearing	(ISO)					312-2RS			
NDE Bearing	(ISO)				Ball 63	309-2RS			
Stator Winding				12 ends	s reconne	ctable, 2	layer lap		
Weights Wound Stator Assy.	(kg)	ł				26			
Rotor Assy.	(kg)					36			
Complete Machine	(kg)					90			
% Efficiencies 125/130°C	FL	87.6	88.0	88.3	88.6	87.9	88.3	88.5	88.8
	3/4 FL	88.7	89.0	89.1	89.3	89.1	89.4	89.5	89.7
	1/2 FL	89.3	89.4	89.3	89.2	89.8	89.9	89.9	89.9
	1/4 FL	87.8	87.4	87.1	86.6	88.3	88.1	88.1	87.8
100/105°C	FL	88.2	88.4	88.6	88.8	88.4	88.6	88.8	89.0
	3/4 FL	88.9	89.2	89.2	89.4	89.4=	89.5	89.6	89.7
	1/2 FL	89.2	89.4	89.1	89.1	89.7	89.8	89.8	89.8
	1/4 FL	87.4	87.2	86.4	85.8	87.9	87.9	87.9	87.4
Reactances (FL)	$X_d$ (pu)	2.23	2.01	1.87	1.66	2.78	2.55	2.46	2.26
(1.2)	$X'_d$ (pu)	0.18	0.16	0.14	0.14	0.20	0.20	0.18	0.16
	$X_d^n(pu)$	0.12	0.11	0.10	0.09	0.14	0.14	0.13	0.11
	$X_q$ (pu)	1.02	0.93	0.86	0.77	1.29	1.17	1.13	1.04
	$X_q''$ (pu)	0.14	0.13	0.12	0.10	0.13	0.12	0.12	0.10
	$X_L$ (pu)	0.079	0.072	0.066	0.059	0.092	0.085	0.081	0.075
	$X_2$ (pu)	0.13	0.12	0.11	0.09	0.13	0.12	0.12	0.10
	$X_0$ (pu)	0.089	0.080	0.075	0.066	0.088	0.081	0.087	0.073
	4.0								
ime Constants	$T'_{\rm d}$ (sec)	0.025							
	$T_d^{\prime\prime} (\text{sec})$	0.006							
	$T'_{d0}$ (sec)	0.065							
	$T_a$ (sec)				0.0	005			
hort Circuit Ratio	$(1/x_d)$	0.448	0.497	0.533	0.602	0.360	0.393	0.406	0.442
excitation Amps	FL	1.49	1.49	1.49	1.49	1.42	1.44	1.50	1.50
	NL	0.43	0.46	0.49	0.54	0.39	0.40	0.43	0.46
tator Winding Resistance	(20°C)	300	100		0.17 Ω li				0.40
totor Winding Resistance	(20°C)	ľ.			0.5				

ECN-E-08-017 217

#### **Time constants**

The dynamic behaviour of a synchronous machine as seen at the terminals can be described by a transfer function with a number of time constants [16]. These can be divided in short-circuit and open-circuit time constants. The short-circuit time constants are determined from a short-circuit test (see figure 241). The envelope of the stator current after a short-circuit decays approximately following exponential curves determined by the subtransient and the transient time constants  $T_d''$  and  $T_d'$ , respectively  $T_q''$ . The initial condition determines whether the direct or quadrature-axis time constants are found.

The equivalent circuit for  $T_d''$  and  $T_q''$  are found by deleting the voltage sources and the resistances (except the damper resistance) from the equivalent circuits of the synchronous machine. Figure 242 gives the circuit for the direct-axis subtransient time constants, with:

$$\begin{array}{rcl} l_{a\sigma} & = & l_d - l_{afd} \\ l_x & = & l_{f1d} - l_{afd} \\ l_{fd\sigma} & = & l_{ffd} - (l_{afd} + l_x) \\ l_{1d\sigma} & = & l_{11d} - (l_{afd} + l_x) \end{array}$$

In the following equations the leakage inductance  $l_x$  is assumed to be zero. Therefore, all mutual inductances in the d-axis are equal. The equivalent circuit for  $T_d'$  is found by inserting the field resistance instead of the damper resistance. The subtransient time constants of the direct-axis is given by:

$$T_d'' = \frac{1}{r_{1d}} (l_{1d\sigma} + \frac{l_{fd\sigma} l_{a\sigma} l_{afd}}{l_{fd\sigma} l_d + l_{a\sigma} l_{afd}})$$

which can be approximated by:

$$T_d'' = \frac{1}{r_{1d}} (l_{1d\sigma} + \frac{l_{fd\sigma} l_{a\sigma}}{l_{fd\sigma} + l_{a\sigma}})$$

The transient time constant of the direct-axis is given by:

$$T'_{d} = \frac{1}{r_{f}} (l_{fd\sigma} + \frac{l_{a\sigma}l_{afd}}{l_{d}})$$

which can be approximated by:

$$T_d' = \frac{1}{r_f} (l_{fd\sigma} + l_{a\sigma})$$

The subtransient time constant of the quadrature-axis is given by:

$$T_q'' = \frac{1}{r_{1a}} (l_{1q\sigma} + \frac{l_{a\sigma}l_{a1q}}{l_a})$$

which can be approximated by:

$$T_q'' = \frac{1}{r_{1q}}(l_{1q\sigma} + l_{a\sigma})$$

218 ECN-E-08-017

The open-circuit time constants are defined for the condition in which the stator does not carry a current. There are two subtransient open-circuit time constants  $T''_{d0}$  and  $T''_{q0}$  sometimes specified on manufacturers' data sheets:

$$T_{d0}'' = \frac{1}{r_{1d}} \frac{l_{ffd} l_{11d} - l_{afd}^2}{l_{ffd}}$$

and:

$$T_{q0}^{"} = \frac{l_{11q}}{r_{1q}}$$

The direct-axis transient open-circuit time constant  $T'_{d0}$  is:

$$T'_{d0} = \frac{l_{ffd}}{r_f}$$

#### **Operational inductances**

The transient and subtransient inductances (sometimes refered to as operational inductances) are also measured at the terminals of the machine and represent different time scales. The subtransient inductances  $l''_d$  and  $l''_q$ , are defined by the change in stator flux divided by the change in stator current immediately following a sudden change in operating conditions:

$$l''_d = \frac{\Delta \psi_d}{\Delta i_d} (t = 0^+)$$
  
$$l''_q = \frac{\Delta \psi_q}{\Delta i_q} (t = 0^+)$$

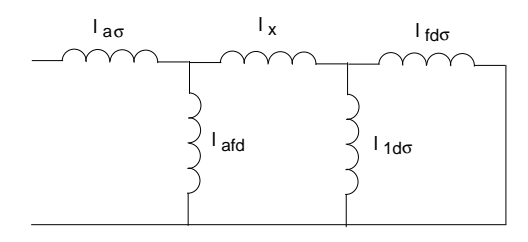


Figure 243: Equivalent circuit for the subtransient inductance of the direct-axis of the synchronous machine

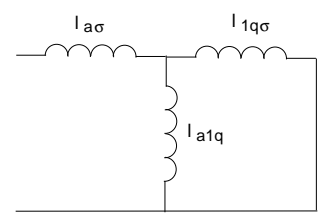


Figure 244: Equivalent circuit for the subtransient inductance of the quadrature-axis of the synchronous machine

ECN-E-08-017 219

After the damper winding current in the direct-axis has died out, the inductance seen from the stator is the transient inductance  $l'_d$ . The values of  $l''_d$  and  $l'_d$  are determined from the amplitude of the stator current after a three phase short circuit of the machine terminals starting from no-load conditions (see figure 241):

$$\begin{array}{rcl} l_d'' & = & \frac{l_{afd}i_f}{i_d + i_d' + i_d''} \\ l_d' & = & \frac{l_{afd}i_f}{i_d + i_d'} \end{array}$$

After the transient current has died out the synchronous inductance remains:

$$l_d = \frac{l_{afd}i_f}{i_d}$$

The equivalent circuits for  $l_d''$  and  $l_q''$  are found by deleting the resistances and the voltage sources from the equivalent circuits of the synchronous machine. Figures 243 and 244 give these circuits, representing a condition of constant flux, the flux is trapped in the machine since there is no dissipation. From the direct-axis equivalent circuit (figure 243) the following relationship can be found (assuming  $l_x = 0$ ):

$$l_d'' = l_{a\sigma} + \frac{l_{afd}l_{1d\sigma}l_{fd\sigma}}{l_{afd}l_{1d\sigma} + l_{afd}l_{fd\sigma} + l_{1d\sigma}l_{fd\sigma}}$$

which can be approximated by:

$$l_d'' = l_{a\sigma} + \frac{l_{1d\sigma}l_{fd\sigma}}{l_{1d\sigma} + l_{fd\sigma}}$$

Therefore  $l_d''$  is mainly determined by the leakage inductances. The transient inductance is:

$$l_d' = l_{a\sigma} + \frac{l_{afd}l_{fd\sigma}}{l_{afd} + l_{fd\sigma}}$$

which can be approximated by:

$$l'_d = l_{a\sigma} + l_{fd\sigma}$$

After the transient in the field current  $i'_f$  has died out as well, the inductance of the stator is the synchronous inductance:

$$l_d = l_{a\sigma} + l_{afd}$$

From the quadrature-axis equivalent circuit (figure 244) the following relationship can be found:

$$l_q'' = l_{a\sigma} + \frac{l_{a1q}l_{1q\sigma}}{l_{a1q} + l_{1q\sigma}}$$

which can be approximated by:

$$l_a'' = l_{a\sigma} + l_{1q\sigma}$$

After the damper winding current in the quadrature-axis has died out the stator current  $i_q$  is constant and the inductance of the stator for this direction is the synchronous inductance:

$$l_q = l_{a\sigma} + l_{a1q}$$

220 ECN-E-08-017

## F.4 Conversion example

In this section the parameters of the synchronous machine at 380 V and 50 Hz in table 7 are converted to the parameter set needed for a  $5^{th}$  order synchronous machine model. First an estimation is made of the leakage inductance of the stator:

$$l_{a\sigma} \approx \frac{l_d'' + l_q''}{4} = 0.065 \text{ [pu]}$$

For small machines a value of  $l_{a\sigma}$  between 0.04 and 0.08 pu is quite common [7]. Applying the equations of section F.3 (all in p.u.):

$$\begin{split} l_{afd} &= l_d - l_{a\sigma} = 2.165 \\ r_f &= \frac{l'_d}{T'_d} = 0.0229 \\ l_{fd\sigma} &= l'_d - l_{a\sigma} = 0.115 \\ l_{1d\sigma} &= -\frac{(l''_d - l_{a\sigma}) \cdot l_{fd\sigma}}{l''_d - l_{a\sigma} - l_{fd\sigma}} = 0.1054 \\ l_{ffd} &= l_{afd} + l_{fd\sigma} = 2.28 \\ l_{11d} &= l_{afd} + l_{1d\sigma} = 2.2704 \\ l_{a1q} &= l_q - l_{a\sigma} = 0.955 \\ l_{1q\sigma} &= l''_q - l_{a\sigma} = 0.075 \\ l_{11q} &= l_{afd} + l_{1q\sigma} = 1.03 \\ r_{1d} &= \frac{1}{T''_d} (l_{1d\sigma} + \frac{l_{fd\sigma}l_{a\sigma}}{l_{fd\sigma} + l_{a\sigma}}) = 0.0779 \\ r_{1q} &= \frac{l''_q}{T''_q} \end{split}$$

Since  $T_d''$  is not given take  $r_{1q} = r_{1d} = 0.0779$ .

## F.5 Comparison of estimated results with measured parameter values

In this section data sheet values and estimated results are compared to measured parameter values. The data sheet base values are:

$$\begin{array}{rcl} u_{base} & = & 220 \ [\mathrm{V}] \\ i_{base} & = & 57 \ [\mathrm{A}] \\ \omega_{base} & = & 100\pi \ [\mathrm{rad/s}] \\ r_{base} & = & 3.860 \ [\Omega] \\ l_{base} & = & 0.01229 \ [\mathrm{H}] \\ t_{base} & = & 0.00318 \ [\mathrm{s}] \end{array}$$

From  $r_{f,real}$  and  $r_{f}$  (transformed to stator) the stator winding - field winding turns ratio can be calculated:

$$C_f = \sqrt{\frac{r_f}{r_{f,real}}} = 0.39$$

ECN-E-08-017 221

From the measured unsaturated  $l_{afd}$  and the data sheet saturated  $l_{afd}$  the following is obtained:

$$C_f = \frac{l_{afd,datasheet}}{\sqrt{\frac{2}{3}}l_{afd,measured}} = 0.25$$

In the measured value the factor  $\sqrt{\frac{2}{3}}$  of the power invariant transformation is included. Due to the different saturation level, this difference can be expected.

Table 8: Measured and calculated parameter values for the machine of the data sheet

Parameter	measured	data sheet value	
$l_d$	0.03707 [H]	3.02 [pu]	2.23 [pu]
$l_q$	0.01759 [H]	1.43 [pu]	1.02 [pu]
$l_d^{\prime\prime}$	0.00188 [H]	0.15 [pu]	0.12 [pu]
$l_d^q$	0.00289 [H]	0.24 [pu]	0.14 [pu]
$r_a$	$0.188 [\Omega]$	_	$0.085[\Omega]$
$r_{f,real}$	$0.66-0.73 [\Omega]$		$0.58 [\Omega]$
$\tilde{T}'_{d0}$	0.71-0.78 [s]		0.065 [s]

Table 8 lists measured and data sheet values. The difference between measured and data sheet values is significant. The measured values of inductances are unsaturated, the data sheet values are given at rated conditions and will be saturated. The value of  $T_{d0}^{\prime}$  calculated from measurements of  $l_{ffd}$  and  $r_f$  is about ten times the data sheet value. A different saturation level can be part of the explanation, more likely the data sheet value of 0.065 s is not correct. Based on other data sheet parameters:

$$T'_{d0} = \frac{l_{ffd}}{100\pi \cdot r_f} = 0.317[\text{pu}]$$

## F.6 Conclusion

Parameters for the dynamic model of the synchronous machine have been estimated from the manufacturers' data sheet. The result will only be an approximation. The inductances specified by manufacturers are the saturated values. The saturation level is not specified and will not be the same for all parameters.

222 ECN-E-08-017

## F.7 Appendix A. Matlab file of Steady State Calculation DFIG-thy

```
steady_state_PrecVar_wmVar_VrecFix02.m
%Steady state calculation
%Vrec is constant,
%Prec changes from 0 to 3e6 in 100 steps,
%wm changes from 0.7wg to 1.3 wg in 100 steps
%calculate voltages, currents, fire angles, and draw three dimentional plots
clear all;
%grid parameters
wg=100*pi;
%Doubly fed induction generator
Pm=1.5e6;
p=1;
% Mutual inductance
Lms=4.55e-3;
Lmr=4*4.55e-3;
M=sqrt(Lms*Lmr);
% Leakage inductace
Ls=0.118e-3;
Lr=4*0.077e-3;
% Resistances
Rs=0.0012;
Rr=4*0.0013;
%Rs=0;
%Rr=0;
%wm = (1+s)*wg;
%two winding transformer, refered to the stator side of DFIG, the rotor
%voltage is assumed to be equal to the stator voltage
L_trafo=6.5508e-005;
R_trafo=0.0016;
C_trafo=0.1e-6;
U_HV_trafo=34e3;
U_MV_trafo=960;
U_LV_trafo=690;
%Cable
L_cable=1.9958e-4;
R_cable=0.1069;
C_cable=1e-006;
%Thyristor Bridge
gama=165*pi/180;
VLL_inv=34e3;
%DC link
R_dclink=10;
L_dclink=0.1;
%Thyristor AC commutation
L_commu=0.001;
%steady state calculation
%Thyristor Bridge
%Inverter omit the commutation effect
Vdc_inv=abs(3*sqrt(2)*VLL_inv/pi*cos(gama));
n=1;
k=11;
j=11;
delta_wm=0.6/(k-1);
delta_P=3e6/(j-1);
```

ECN-E-08-017 223

```
for m=1:k
               for n=1:j
               wm(m,n)=0.7*wg+(m-1)*delta_wm*wg;
               wr(m,n)=wg-p*wm(m,n);
               s(m,n)=(wg-p*wm(m,n))/wg;
              Pdc_rec(m,n) = (n-1)*delta_P;
               Idc(m,n)=findzero(R_dclink, Vdc_inv, -Pdc_rec(m,n),0);
              VLL rec=34e3;
              V_cable_B_rms=VLL_rec/sqrt(3);
              V_cable_B_phi=pi/2;
              V_cable_B=V_cable_B_rms*cos(V_cable_B_phi)+i*V_cable_B_rms*sin(V_cable_B_phi);
               %Rectifier
              Vdc_rec(m,n)=R_dclink*Idc(m,n)+Vdc_inv;
               cos_alpha(m,n)=pi/(3*sqrt(2))*Vdc_rec(m,n)/VLL_rec;
               if cos_alpha(m,n) >1
                      alpha(m,n)=0;
                      P_{rec(m,n)=0};
                      0 \operatorname{rec}(m,n) = 0;
                      else
                      alpha(m,n)=acos(pi/(3*sqrt(2))*Vdc_rec(m,n)/VLL_rec);
                      P_{rec(m,n)} = Vdc_{rec(m,n)} * Idc(m,n);
                      Q_{rec(m,n)=P_{rec(m,n)*tan(alpha(m,n))};
               I_{rec(m,n)=conj((P_{rec(m,n)+i*Q_{rec(m,n))/(3*V_{cable_B}));}
               %cable
               I_cable_B(m,n)=I_rec(m,n);
               I_cable_B_C(m,n)=i*wg*C_cable*V_cable_B;
               I_cable(m,n) = I_cable_B_C(m,n) + I_cable_B(m,n);
              V_{cable}(m,n) = V_{cable}(m,n) * (R_{cable} + i * wg * L_{cable});
               I_cable_A_C(m,n)=i*wg*C_cable*V_cable_A(m,n);
               %Two winding transformer of DFIG, the rotor voltage equals stator
               %voltage
              L_trafo_HV=(U_HV_trafo/U_MV_trafo)^2*L_trafo;
              R_trafo_HV=(U_HV_trafo/U_MV_trafo)^2*R_trafo;
              V_trafo_HV(m,n)=V_cable_A(m,n);
              I_{trafo_HV(m,n)=I_cable(m,n)+I_cable_A_C(m,n)};
               V\_trafo\_MV(\mathfrak{m},n) = (U\_MV\_trafo/U\_HV\_trafo) * (V\_trafo\_HV(\mathfrak{m},n) + I\_trafo\_HV(\mathfrak{m},n) * (R\_trafo\_HV + i * wg + i * 
               I_trafo_C(m,n)=i*wg*C_trafo*V_trafo_MV(m,n);
               I_trafo(m,n)=(U_HV_trafo/U_MV_trafo)*I_trafo_HV(m,n); refer the transformer's current to
               I_{trafo_MV(m,n)} = I_{trafo(m,n)} + I_{trafo_C(m,n)};
               %Doubly fed induction generator, referred to the stator side
               %stator calculation
               V_dfig_sta(m,n)=V_trafo_MV(m,n);
               I_dfig(m,n)=I_trafo_MV(m,n);
               %V_dfig_sta_phi(m,n)=atan2(imag(V_dfig_sta(m,n)),real(V_dfig_sta(m,n)));
              P_dfig(m,n)=real(3*V_dfig_sta(m,n)*conj(I_dfig(m,n))); %total active power
               %if s=(wg-p*wm)/wg, then stator power is approximately (1+s)*Ptotal, when stator resistance
               Ps(m,n)=(1+s(m,n))*P_dfig(m,n);
               Ps_real(m,n)=(1+s(m,n))*Pm;stator power is also (1+s)*Pmech
               %deltaP(m,n)=P_dfig(m,n)-P_rec(m,n);
               %Qs(m,n)=Q_dfig(m,n);%Qconv is zero
               %Vs(m,n)=V_dfig_sta(m,n);
               %phi_Vs(m,n)=V_dfig_sta_phi(m,n);
               SIs(m,n) = conj((Ps(m,n)+i*Qs(m,n))/(3*Vs(m,n)));
               %phi_Is(m,n)=atan2(imag(Is(m,n)),real(Is(m,n)));
               %Vds(m,n)=sqrt(3)*abs(Vs(m,n))*sin(phi_Vs(m,n));
               Vqs(m,n)=-sqrt(3)*abs(Vs(m,n))*cos(phi_Vs(m,n));
               ids(m,n) = sqrt(3) * abs(Is(m,n)) * sin(phi_Is(m,n));
               (m,n) = -\operatorname{sqrt}(3) \cdot \operatorname{abs}(\operatorname{Is}(m,n)) \cdot \operatorname{cos}(\operatorname{phi}_{\operatorname{Is}}(m,n));
```

224 ECN-E-08-017

```
Vds(m,n)=sqrt(3)*real(V_dfig_sta(m,n));
         Vqs(m,n)=sqrt(3)*imag(V_dfig_sta(m,n));
         Vdg = Vds(m,n);
         Vqg = Vqs(m,n);
         Pg = P_dfig(m,n);
         Qg = Q_dfig(m,n);
         wgg = wg;
         wgr = wr(m,n);
         Rgs = Rs;
         Rgr = Rr;
         Lgs = Ls;
         Lgr = Lr;
         Mg = M;
         yg = [0;0;0;0;0;0]
         yg = fzeroMulVar(Vdg,Vqg,Pg,Qg,wgg,wgr,Rgs,Rgr,Lgs,Lgr,Mg);
         Ids(m,n)=sqrt(3)*real(Is(m,n));
         \{Iqs(m,n)=sqrt(3)*imag(Is(m,n));
         Ids(m,n) = yg(1);
         Iqs(m,n) = yg(2);
         Idr(m,n) = yq(3);
         Iqr(m,n) = yg(4);
         Vdr(m,n) = yg(5);
         Vqr(m,n) = yq(6);
         %rotor calculation
         idr(m,n) = (Vqs(m,n) + Rs * Iqs(m,n) + wg * (Ls + M) * Ids(m,n)) / (-wg * M);
         (m,n)=(Vds(m,n)+Rs*Ids(m,n)-wg*(Ls+M)*Iqs(m,n))/(wg*M);
          \label{eq:Vdr} $$Vdr(m,n) = -Rr*Idr(m,n) + wr(m,n)*((Lr+M)*Iqr(m,n)+M*Iqs(m,n)); $$
          \label{eq:Vqr(m,n)=-Rr*Iqr(m,n)-wr(m,n)*((Lr+M)*Idr(m,n)+M*Ids(m,n)); } \\
         Ps(m,n)=Vds(m,n)*Ids(m,n)+Vqs(m,n)*Iqs(m,n); %check the stator power
         Qs(m,n)=Vqs(m,n)*Ids(m,n)-Vds(m,n)*Iqs(m,n);
         Pr(m,n)=Vdr(m,n)*Idr(m,n)+Vgr(m,n)*Igr(m,n); %check the rotor power
         %this rotor power excludes the resistance loss in the rotor, thus this Pr does not
         Qr(m,n)=Vqr(m,n)*Idr(m,n)-Vdr(m,n)*Iqr(m,n);
         Psids(m,n) = -(Ls+M)*Ids(m,n)-M*Idr(m,n);
         \texttt{Psiqs}(\texttt{m},\texttt{n}) = -(\texttt{Ls+M}) * \texttt{Iqs}(\texttt{m},\texttt{n}) - \texttt{M} * \texttt{Iqr}(\texttt{m},\texttt{n}) ;
         Psidr(m,n) = -(Lr+M)*Idr(m,n)-M*Ids(m,n);
         Psiqr(m,n) = -(Lr+M)*Iqr(m,n)-M*Iqs(m,n);
         n=n+1;
         end
         m=m+1;
end
%plot three dimentional graphs
x_val=1e-6*(Pdc_rec);
x_label='Prec MW';
y_val=wm/wg;
y_label='Mech Speed Percentage of Wg';
z_val_1=alpha*180/pi;
z_label_1='fire angle degree';
z_val_2=1e-6*Q_rec;
z_label_2='Qrec MVAR';
z_val_3=1e-3*Vds;
z_label_3='DFIG stator Vds kV';
z_val_4=1e-3*Vqs;
z_label_4='DFIG stator Vqs kV';
z_val_5=1e-3*Idr;
z_label_5='DFIG rotor Idr kA';
z_val_6=1e-3*Iqr;
z_label_6='DFIG rotor Iqr kA';
z_val_7=1e-3*Vdr;
```

ECN-E-08-017 225

```
z_label_7='DFIG rotor Vdr kV';
z_val_8=le-3*Vqr;
z_label_8='DFIG rotor Vqr kV';
z_val_9=le-6*Ps;
z_label_9='DFIG stator Ps MW';
z_val_10=le-6*Qs;
z_label_10='DFIG stator Qs MVar';
z_val_11=le-6*Pr;
z_label_11='DFIG rotor Pr MW';
z_val_12=le-6*Qr;
z_label_12='DFIG rotor Qr MVar';
plot_val;
%plot_val;
```

226 ECN-E-08-017

## G Conference contributions and journal paper of the WaP project

- Wind park and grid integration issues
   Y. Zhou, P. Bauer, J. A. Ferreira, J.T.G. Pierik
   IEEE Young Reseacher Symposium, 2006
- Park and Grid Integration Issues
   Y. Zhou, J.T.G. Pierik, P. Bauer, J. A. Ferreira
   Sixth International Workshop on Large-Scale Integration of Wind Power and Transmission Networks for Offshore Wind Farms, Delft, 26 to 28 October 2006
- New Thyristor Bridge models for Dynamic Simulation of Grid Integration of Offshore Wind Farms
   Y. Zhou, P. Bauer, J. A. Ferreira, J.T.G. Pierik
   PCIM 2006
- Aggregated models of offshore wind farm components Y. Zhou, P. Bauer, J. A. Ferreira, J.T.G. Pierik PESC 2006
- Control of DFIG under unsymmetrical voltage dip Y. Zhou, P. Bauer, J.A. Ferreira, J.T.G. Pierik PESC 2007
- Grid-connected and islanded operation of a hybrid power system Y. Zhou, J.A. Ferreira, P. Bauer IEEE PES Power Africa 2007

ECN-E-08-017 227

228 ECN-E-08-017

# Wind park and grid integration issues

Y. Zhou, P. Bauer, B. Ferreira, J.T.G. Pierik.

IEEE , Young Researcher Symp 2006

## Wind Park and Grid Integration Issues

\*Y. Zhou, \*P. Bauer, \*J. A. Ferreira, \*\*J. Pierik

Abstract-- The fast increasing wind power production leads to the requirements of detailed studies of integration problems. Integration problems arise from the characteristics of wind power and various technologies used in wind energy industry. In this paper, integration problems are analyzed as well as their origins and possible solutions. Simulation models of wind turbines are proposed and their influences to the simulation results are discussed.

#### Index Terms—Wind power, Integration problem, Simulation

#### I. INTRODUCTION

FROM the beginning of 1990s, the wind power develops so quickly that it now has significant shares of power production in many countries. In Europe, The wind generation reached approximately 33,600 MW until the end of year 2004. The old low voltage protection of wind turbines can cause significant loss of active power which is not permitted from the point of view of transmission system operators. As the requirements of utilizing more wind power are still increasing, the integration of large scale wind power with power grid has to be studied. Today, the large scale wind farms are required to be controllable both in active power and reactive power, and to have the low voltage ride through capabilities.

This project focuses on the integration of large offshore wind farm with power grid, which includes investigations of dynamic behaviors inside wind farm, interactions between wind farm and power grid and develop appropriate controls both for the individual wind turbines and wind farm as a whole part.

In this paper, the state of the art wind turbine technologies and integration methods are reviewed, the possible integration problems and solutions are investigated, and finally the simulation and modeling issues are discussed.

#### II. WIND ENERGY FACTS

In this section, the characteristics of wind power and the technologies used in wind energy industry are introduced.

#### A. The Wind

The kinetic energy of a moving body is proportional to its mass (or weight). The energy extractable from the wind is proportional to the cubic of the wind speed. The wind speed varies continuously as a function of time and height. From a power system perspective, the fluctuations of wind speed may affect the power quality of wind power productions. For example, the long term variations such as diurnal, weekly or seasonal cycles will affect the steady voltage and frequency of power system. While the short term variations such as turbulence may introduce serious flickers into power system. The impact of variations of wind speed on power quality depends very much on the turbine technology applied.

#### B. Wind Turbines

The various kinds of wind turbines can be found in literature [9], [12], [13] and [32]. They can be categorized by speed of generators:

- Fixed speed with gear box
- Variable speed with gear box
- Variable speed without gear box

Or categorized by the generator type:

- Induction generators
- Synchronous generators

Or categorized by whether converters are used or not:

- Directly connected with AC grid without converters
- Directly connected with AC grid using partially rated power converters on the rotor
- Full rated power converters on the stator

In [9], a survey of the world's top-10 wind turbine suppliers for the year 2002 is summarized. It lists the two largest wind turbines produced by each of the top-10 manufactures. It also presents a detailed overview of the market share of each wind turbine concept from 1998 to 2002. These studies provide very useful information on the trends of the installed wind turbines. The four dominating commercial wind turbines in modern wind energy industry are shown in Figure 1:

- Type A: Fixed speed squirrel cage induction generator
- Type B: Variable wound rotor resistance induction generator
- Type C: Doubly fed induction generator with partial scale back to back converters on the rotor
- Type D: Synchronous generator with full scale back to back converters on the stator

This work is part of the project PhD@Sea, which is substantially funded under the BSIK-program of the Dutch Government and supported by the consortium WE@Sea.

<sup>\*</sup> The authors are with Electrical Power Processing group of Delft University of technology, 2628 CD, Delft, the Netherlands. (e-mail: Yi.Zhou@tudelft.nl).

<sup>\*\*</sup> The author is with Energy Research Center of the Netherlands (ECN), Petten, the Netherlands. (Pierik@ecn.nl)

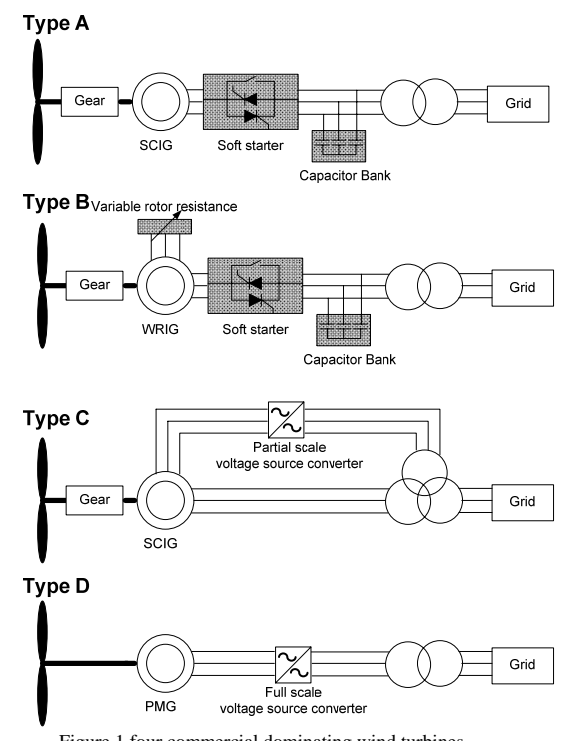


Figure 1 four commercial dominating wind turbines

#### C. Wind Farm Configurations and Integration Methods

Wind farm can be AC grid or DC grid. In [15], an evaluation program is developed to access the different configurations of wind park from the point of view of energy production cost. The "all AC" system is concluded as the best choice for moderate connection distance. But when considering the dynamic behavior, the "all AC" system is not feasible, especially for long transmission distance. Additionally, the cost of dynamic reactive power compensations has not been included in this work.

In [14], various layouts of wind parks are compared by energy production cost. And their influences to the power quality on the point of common connection are considered. It is concluded that for mid and long distance connection (longer than 20km), the total DC grid is the best choice.

In [16], several layouts of DC wind farm were investigated. The series connected DC wind turbines are the difficult to be controlled. DC voltage controller is required for each wind turbine. It is shown that use booster converter with DC transformer, the steady state operation of the series connected DC wind farm has good system response.

The integration methods can be AC connections, or HVDC voltage source converters, or HVDC thyristor bridges equipped with additional reactive power compensation system. The 180MW offshore wind farm Horns Rev was installed in 2002 in Denmark, and connected to the 150KV power grid with AC connection. But HVDC connections are more promising than AC connections for large scale wind farm in the aspect of electric power control.

In literatures [1], [2], [3], [9], [13], [15], [20], [22], and

[26], various integration methods are proposed and compared from different points of view: economic or dynamic behavior.

In [9] and [14], the AC connection is compared with HVDC connection, and draws the conclusion that HVDC is favorable than AC connection under the following conditions:

- Weak AC connection
- Distance > 100km
- Wind farm size > 350MW

The two HVDC systems: voltage source converter using IGBT switches and current source converter using Thyristor Bridges are compared in [1], [2], [9], [12], [14] and [26]. The CSC using Thyristor Bridge is cheap and robust but needs additional reactive power compensation. The VSC using IGBT switches can provide dynamic reactive power compensation, but much more expensive and sensitive to the faults. It is concluded that for weak AC connection, the VSC are more appropriate. And for strong AC connection, the CSC can be used [11, [9]].

#### III. INTEGRATION PROBLEMS AND SOLUTIONS

Integration of large scale wind farm with power grid raises several integration problems which are not encountered in the operation of the previous power system which is dominated by the traditional thermal power plant. These new integration problems arise from the characteristics of wind power and the various technologies adopted in the wind energy industry. This may require a step by step redesign of existing power system and operation approaches. In this section, the possible integration problems are analyzed and corresponding solutions are proposed.

Until now, most of the studies are concentrated on "transient voltage stability" <sup>[4], [17], [18], [19], [23], [32], [22], [24], [25], [26], <sup>[27], [28], [29], [30]</sup>, a small number are focused on "power quality" <sup>[5], [6], [34]</sup>. In [19], [32], and [35], the power quality problems are partly investigated.</sup>

The small signal stability and sub synchronous oscillation problems are seldom studied. Only a very few papers mentioned the sub synchronous oscillation [28], [32], [33]. In [32], it is considered not important, but in [28] and [33], the sub synchronous oscillations excited by wind power variations are recommended for future research.

#### A. Static Problems

The steady state problems are the overloading and static voltage/frequency deviations. It is caused by the variations of electric power due to the long term fluctuations of wind speed.

The possible solutions could be:

- Improve the wind speed forecast, use energy storage system, design coordinated central wind farm control and individual wind turbine control to make the output electric power of wind farm smooth and schedulable.
- Use reactive power compensation to control the reactive power and voltage.

In [9], two wind speed forecast model are discussed and compared. The short term wind predictions (hour-ahead) are very accurate but the long term (day-ahead) predictions still

have large errors.

In [31], the active and reactive power control of whole wind farm was discussed. It proposed to use a distribution function for the central control of active power and reactive power.

#### B. Power Quality

Two important power quality problems related with integration of wind power are flickers and harmonics.

Flicker is the 1-25 Hz voltage variations. This low speed voltage variation can be caused by short term fluctuations of wind speed, turbulence, tower shadow, wind shear effect and switching of the wind turbines. Flicker could be a very serious problem for the type A and B wind turbines, because the fluctuations of wind speed are directly reflected on the output electric power. For wind turbines type C and D, because the rotation speed is decoupled with power grid. The variable speed shafts become buffers which can absorb the fluctuations of wind speed. Noticing that the wind speed fluctuations are quite local phenomenon, the large geographical area will contribute a spatial smoothing effect on the output electric power of the large wind farm. The possible solutions could be:

- Reinforce the transmission system that is to decrease the transmission impedance.
- Implement anti flicker algorithm in the control systems of wind turbines C and D. [5]
- Design appropriate start-up and shut-down strategies of wind turbines to avoid large fluctuations of active power and reactive power. [32], [34]
- Use dynamic reactive power compensation to control the voltage on the point of common connection with power grid.

Harmonics are components with frequencies which are multiples of the supply frequency, i.e., 100 Hz, 150 Hz, 200 Hz, etc. Inter-harmonics are in a similar way defined as components having frequencies located between the harmonics of the supply frequency. Harmonics can be caused by the switching of the power converters, the saturation of transformers and unbalanced loads. The possible solutions could be:

- Passive filters can improve power factor, reduce highfrequency harmonics. Their performances depend on tuning the reactors according the unknown source impedance
- Active filters can inject the anti-phase PWM currents or voltages into the grid.
- Use PWM control techniques to eliminate specific dominating orders of harmonics.
- Reactive power compensation system STATCOM can also used to mitigate the specific orders of harmonics.

## C. Transient Stability

One challenge of integration of the large scale wind farm with power grid is the requirement of fault ride through capability (or low voltage ride through capability). It is normally related with the transient voltage stability of the wind generator during voltage dips.

For type A and B wind turbines, they are basically induction generators which require reactive power for magnetizing. The limited electric torque during voltage dips will lead to the accelerating of the generator and increase of the slip. From the torque-speed curve and reactive powerspeed curve, it is understood that when slip is larger than the critical value, the electric torque decreases, and the generator absorbs large amount of reactive power. This makes the voltage continues to drop and the generator shaft continues to accelerate. Without proper remediation, this will finally leads to voltage collapse and over speed of the generator. The type B wind turbine has variable rotor resistance which can increase the value of the critical slip. Thus the type B wind turbine has better LVTR capability than type A.

For type C DFIG wind turbine which is equipped with partial rated power VSC converters on the rotor, if the voltage dip is not severe, the rotor converters can control the DFIG to produce reactive power to the grid. But if the voltage dip is severe, then the rotor converter may face a transient over current and has to be blocked and the rotor is short circuited with resistances (active crowbar). Then the DFIG becomes a normal induction machine and requires substantial reactive power. This may cause voltage collapse and over speed of the generator.

The type D wind turbine with full scale back to back VSC converters on the stator has the best LVRT capability. The only possible problem due to the voltage dip is that the DC voltage may increase to a high level to trigger the protection of VSC converters. But with coordinated wind turbine speed control and rectifier's active power control, it is possible to limit the DC voltage level by temporarily decreasing the input mechanical power of wind turbine during severe voltage dips.

Some general solutions to improve the transient voltage stability of wind farms could be:

- Use dynamic reactive power compensations such as SVC, STATCOM or the grid side VSCs of type C and type D wind turbine to help the recovery of voltage
- Use active stall or blade pitch angle control to limit the input mechanical power, thus to avoid the over speed of generators
- Use HVDC link to decouple the wind farm from power grid
- Improve the control of DFIG converters to actively suppress the large oscillations excited by the severe voltage dip

#### D. Small Signal Stability

Small signal stability is the ability of the power system to maintain synchronism when subjected to small disturbances. The transient stability simulations in the time domain can not cover all the possible oscillation modes of the power system, thus the small signal analysis is necessary by calculating the Eigen values of the state matrix of the power system.

The small signal stability of wind turbine is seldom investigated at this moment.

Possible methods to improve small signal stability are:

 Implement supplementary controls of HVDC link, type C and D wind turbine, and SVC or STATCOM to increase the damping.<sup>[10]</sup>

#### E. Sub Synchronous Oscillation

Sub synchronous oscillations are the 0.2 Hz to 2 Hz low frequency mechanical oscillations of shafts which are excited by power oscillations of the grid. And without proper damp, it may continue for a long time or even increase the oscillation magnitude. The sub synchronous oscillation increases the fatigue of the shafts of generators and has to be avoided.

Only a very few papers mentioned this problem. <sup>[28], [[32], [33]</sup> In [32], it is considered not important. But in [28] and [33], the sub synchronous oscillations excited by wind power variations are recommended for future research.

#### IV. SIMULATION AND MODELLING ISSUES

Computer simulation is valuable in many aspects. It makes it possible to investigate the properties of prototype wind turbine and integration of wind farm without the necessary of full-scale test which is often expensive, time consuming or even impossible to be implemented.

The quality of the simulation depends on two facts: the quality of the model and the applied data. To achieve good simulation results, the simulation purpose has to be defined clearly. In reality, there is always a compromise between detail of the model, availability of the data and the acceptable simulation time.

In this section, the models of wind energy conversion system will be discussed in steps as shown in Figure 2 and the influences on the simulation results will be investigated.

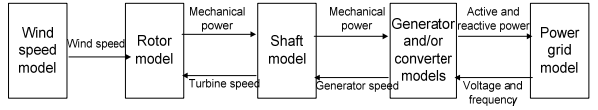


Figure 2 Model structure of wind turbine

#### A. Wind Speed

The wind speed should be made up of four components:

- The average value
- Ramp component representing a steady state increase of wind speed
- Wind gust component
- Wind turbulence

In [19], [34], the impacts of wind speed models are studied. The conclusions are:

- wind speed gust, speed ramp, and turbulence are important for flicker calculation of FSIG;
- Turbulence is not important for flicker calculation of DFIG and PMG but have large influences on shaft torque.

## B. Rotor and Pitch Servo

Two important phenomenons should be included in the rotor model:

 The unsteady inflow which influences the mechanical torque of wind turbines, thus influences the output

- electric power of type A and B wind turbines;
- The tower shadow effect (3p effect) which will influence the flicker level of type A and B wind turbines.

#### C. Shaft System

Due to the large inertia of low speed shaft of wind turbine, it is considered as "soft" which implies that the twist angle of it is large. It can be as large as 90 mechanical degrees at rated torque [11], thus the transient speed deviation between generator and wind turbine during disturbances will be large, and considerable elastic energy stored in the soft shaft will be dissipated out during grid disturbances. This has a large effect on the transient voltage stability of type A, B and C wind turbines.

So the shaft system should be modeled as two mass model for type A, B and C wind turbines. But for type D wind turbine which is totally decoupled from power grid by back to back VSCs, the lumped mass model can be used.

#### D. Generator

Perhaps the generator model receives most of the debates. Whether the third order or fifth order model should be used is still in argument. The difference between fifth order model and third order model is whether the transients of stator fluxes are included or not. The third order model omits the transients of the stator fluxes, thus the simulation speed is improved. Omitting the transients of stator fluxes introduces some errors:

 The fast damping DC offsets in the stator currents are omitted. These DC components will cause DC braking torque for the generator.

This error can be omitted due to the following reasons [10]

- Multi-phase faults are mostly sequentially developed which means the DC offsets in the fault currents are zero. This is validated by the records of oscillograms of actual short circuit currents.
- Ignoring this effect introduces a slight degree of conservation.

For type A wind turbine, the large transient stator currents using fifth order model are not interesting to us because this will not trigger any protections of the induction generator. But the DC breaking torque can be important because the speed of the induction generator is critical to the transient voltage stability. This is reported in [9] and [32]. But the influences of this error are still questionable because of the same reasons for omitting stator flux transients of synchronous generator as stated above.

For type C wind turbine, the large oscillation in the rotor will trigger the protection of rotor converter which will change the operation and behavior of type C wind turbine. So the fifth order model should be used in the type C wind turbine. If the number of type C wind turbines is large, then an approximate way may be used: The third order model is used, and the protection of the rotor converter is triggered by the degree of voltage dip.

For type D wind turbine, the generator is totally decoupled with power grid by the back to back converter, so the transients in the stator fluxes can be neglected

#### E. Converter

For all simulation purposes except the harmonic study, the converter can be modeled as controlled voltage source which means that the switches are ideal and voltage wave forms are perfect. Control of the converters can be found in [18], [32], [35].

The non ideal switches may introduce nonlinearities in the control function which will cause oscillations and errors. This phenomenon and the remediation are illustrated in [7] and [8].

#### F. Power Grid

To study the influences of large scale wind farm on the power system, the model of power grid should be implemented in some details with the data of transmission system operator, including the models of large power plants nearby, large consumption centers nearby, etc. Use one equivalent synchronous generator to represent the dynamic behaviors of power system is not accurate for some simulation purposes, for example, when investigating the sub synchronous oscillation of the synchronous generator due to the integration of wind farm.

#### G. Developed models

Matlab/Simulink is chosen as the dynamic simulation software. The electric models developed until now are all symmetrical models for balanced three phase system, they are:

- Wind speed model
- Rotor model
- Shaft model
- Generator models: type A, type C and type D.
- Power electronic converters' models
  - o Voltage source converter using IGBT switches
  - Current source converter using Thyristor Bridge
- Electric components' models
  - Transmission line and cable
  - Transformer
  - Shunt capacitor bank
- Simplified Grid model

The unsymmetrical electric models will be developed in the next step.

#### V. CONCLUSIONS

Due to the high penetration levels of wind power, the integration problems have to be investigated. These integration problems may be new comparing with the operation of traditional thermal power plant. Computer simulation is valuable to investigate the integration problems. The simulation models are always compromises between details of the model, availability of the data and the required simulation time.

#### VI. REFERENCES

#### Periodicals:

 Z. Chen, E. Spooner, "Grid interface options for variable speed, permanent magnet generators", *IEE Proc.-Electr. Power Appl.*, Vol 145, No. 4, July 1998.

- [2] N. M. Kirby, L. Xu, M. Luckett, W. Siepmaan, "HVDC transmission for large offshore wind farms", *Power engineering Journal*, June, 2002.
- [3] W. Lu and B. Ooi, "Optimal acquisition and aggregation of offshore wind power by multi terminal voltage source HVDC", IEEE transactions on power delivery, Vol. 18, No. 1, January, 2003.
- [4] F. D. Kanellos, N. D. Hatziargyriou, "the effects of variable-speed wind turbines on the operation of weak distribution networks", *IEEE* transactions on energy conversion, Vol. 17, No. 4, December, 2002.
- [5] T. Thiringer, T. Petru, C. Liljergren, "Power quality impact of a sea located hybrid wind park", *IEEE transactions on energy conversion*, Vol. 16. No. 2. June 2001.
- [6] A. Larsson, "Flicker emission of wind turbines caused by switching operations", *IEEE transactions on energy conversion*, Vol. 17, No. 1, March, 2002.
- [7] J. Svensson, "Grid connected voltage source converter control principle and wind energy applications", Technical report, No. 331, Chalmers University of Technology, Sweden, 1998.
- [8] M. Lindgren, "Modeling and control of voltage source converters connected to the grid", technical report No. 351, Chalmers University of technology, 1998.

#### Books:

- [9] "Wind power in power systems", John Wiley & Sons, ISBN: 0-470-85508-8, 2005.
- [10] P. Kundur, "Power system stability and control", McGraw-Hill, 1994.
- [11] S. Heier, "Wind energy conversion systems", John Wiley & Sons, 1998.

#### Technical Reports:

- [12] L. H. Hansen, L. Helle, F. Blaabjerg, "Conceptual survey of generators and power electronics for wind turbines", Technical report, Risø-R-1205(EN), Risø National Laboratory, Denmark, December, 2001.
- [13] M. R. Dubois, "Review of electromechanical conversion in wind turbines", Technical report, Report EPP00.R03, Electric Power Processing Group, Delft University of Technology, April, 2000.
- [14] S. Lundberg, "Configuration study of large wind parks", Technical report No. 474L, Chalmers University of Technology, Sweden, 2003.
- [15] J. T. G. Pierik, M. E. C. Damen, P. Bauer, S.W.H. de Haan, "Electrical and control aspects of offshore wind farms", Technical report of ECN&TUD, ECN-cx-01-083, June, 2001.
- [16] O. Martander, "DC grids for wind farms", Technical report No. 443L, Chalmers University of Technology, Sweden, 2002.
- [17] P. Sorensen, A. Hansen, L. Janosi, J. Bech, B. Bak-Jensen, "Simulation of interaction between wind farm and power system", Technical report, Riso-R-1281(EN), Risø National Laboratory, Denmark, December, 2001.
- [18] J. Perik, J. Morren, E.J. Wiggelinkhuizen, S.W.H de Haan, T.G. van Engelen, J. Bozelie, "dynamic models of wind farm", Technical report of ECN&TUD, ECN-C-04-050, Netherlands, 2004.
- [19] P. Sørensen, A. D. Hansen, P. Christensen, "Simulation and verification of transient events in large wind power installations", Technical report, Risø-R-1331(EN), Risø National Laboratory, Denmark, October, 2003.

### Papers from Conference Proceedings (Published):

- [20] P. Cartwright, L. Xu, C. Sasse, "Grid integration of large offshore wind farm using hybrid hvdc transmission", *Nordic wind power conference*, Chalmers university of technology, 01-02 March, 2004.
- [21] L. T. Hua, T. K. Saha, "Investigation of power loss and voltage stability limits for large wind farm connections to a sub transmission network", *IEEE Power Engineering Society General Meeting*, Denver, Colorado, USA, 6-10 June, 2004.
- [22] H. Binder, P. Lundserg, "Integration of wind power in the power system", IEEE 28<sup>th</sup> annual conference of the Industrial Electronic Society, Page: 3309-3316, Vol. 4, 2002.
- [23] F.W. Koch, I. Erlich, F. Shewarega, U. Bachmann, "Dynamic interaction of large offshore wind farms with the electric power system", *Power Tech conference*, Bologna, Italy, Page: 7, Vol. 3, June 23-26, 2003.
- [24] L. Holdsworth, N. Jenkins, G. Strbac, "Electric stability of large offshore wind farms", IEE 7<sup>th</sup> international conference on AC-DC power transmission, Page: 156-161, Vol. 1, November, 2001.
- [25] J. Wiik, J. O. Gjerde, T. Gjengedal, "Impacts from large scale integration of wind farm into weak power systems", *Proceedings of international* conference on Power System Technology, Pages: 49-54, Vol. 1, 2000.

- [26] Y. Noro, J. Arai, K. Takagi, "System study of direct current power transmission system connected to wind farm", *IEEE/PES Transmission* and Distribution Conference and Exhibition 2002, Pages: 944-949, Vol. 2, 2002.
- [27] L. Holdsworth, X.G. Wu, J.B. Ekanayake, "Comparison of fixed speed and doubly fed induction wind turbines during power system disturbances", *IEE Proceedings of Generation, Transmission and Distribution*, Pages: 343-352, Vol. 150, Issue. 3, May, 2003.
- [28] P. Pourbeik, R. J. Koessler, D. L. Dickmander, "Integration of large wind farms into utility grids (part2-performance issues)", *IEEE Power Engineering Society General Meeting*, Pages: 1522-1525, Vol. 3, 2003.
- [29] A. Kehrli, M. Ross, "Understanding grid integration issues at wind farms and solutions using voltage source converter FACTS technology", *IEEE Power Engineering Society General Meeting*, Pages: 1822-1828, Vol. 3, 2003.
- [30] F. W. Koch, I. Erlich, F. Shewarega, "Dynamic simulation of large wind farms integrated in a multi machine network", *IEEE Power Engineering Society General Meeting*, Pages:2159-2164, Vol. 4, 2003.
- [31] A.D. Hansen, P. Sorensen, F. Lov, F. blaabjerg, "Centralized control of wind farm with doubly-fed induction generators", *PCIM-2005 (Europe)*, Nuremberg, Germany, 07-09 June, 2005.

#### Dissertations:

- [32] V. Akhmatov, "Analysis of dynamic behavior of electric power systems with large amount of wind power", PhD thesis of Electrical power engineering, ISBN: 87-91184-18-5, Technical University of Denmark, April, 2003.
- [33] P. Rosas, "Dynamic influences of wind power on the power system", PhD Thesis of Electrical power engineering, ISBN: 87-91184-16-9, Technology University of Denmark, March, 2003.
- [34] A. Larsson, "Power quality of wind turbines", PhD thesis of Electrical power engineering, ISBN: 91-7197-970-0, Chalmers University of Technology, Sweden, 2000.
- [35] T. Petru, "Modeling of wind turbines for power system studies", PhD thesis of Electrical power engineering, ISBN: 91-7291-306-1, Chalmers University of Technology, Sweden, 2003.

#### VII. BIOGRAPHIES



Yi Zhou was born in China on Oct 7th, 1973. He received his Bs.C. degree in electrical engineering from Zhejiang University in 1995. After then, he worked in Anhui electric power company for 7 years, first as a power grid operator, then a power grid analyzer. In 2004, he received his M.Sc degree in electric power engineering from TU Delft. He is now working towards his PhD degree within electric power processing group of TUDelft. The title of his PhD project is "Wind Park and Grid Integration".



Paul Bauer received his Masters in Electrical Engineering at the Technical University of Kosice ('85) and Ph.D. from Delft University of Technology ('94). Since 1990 he is with the Delft University of Technology teaching Power Electronics, Electrical Drives and related subjects. Dr. Bauer published over 100 papers in his field, he holds an international patent and organized several tutorials. He is a reviewer of different IEEE proceedings and Journals and member of the International Steering

and Technical Committee of several conferences.



Jan Abraham Ferreira (F'05) was born in Pretoria, South Africa, in 1958. He received the B.Sc.Eng. (cum laude), M.Sc.Eng. (cum laude), and Ph.D. degrees in electrical engineering from the Rand Afrikaans University, Johannesburg, South Africa, in 1980, 1982, and 1988, respectively. In 1981, he was with the Institute of Power Electronics and Electric Drives, Technical University of Aachen, Aachen, Germany, and

worked in industry at ESD(Pty) Ltd from 1982 to 1985. From 1986 to 1997, he was on the Faculty of Engineering at Rand Afrikaans University, where he held the Carl and Emily Fuchs Chair of Power Electronics. Since 1998, he has been a Professor at the EWI Faculty of the Delft University of Technology, Delft, The Netherlands. Dr. Ferreira was Chairman of the South African Section of the IEEE, from 1993–1994. He is the Founding Chairman of the IEEE Joint IAS/PELS Benelux Chapter. He served as the Transactions Review Chairman of the IEEE IAS Power Electronic Devices and Components Committee and is an Associate Editor of the IEEE TRANSACTIONS ON POWER ELECTRONICS. He was a member of the IEEE PELS Adcom and is currently the Treasurer of the IEEE PELS. He served as Chairman of the CIGRE SC14 National Committee of the Netherlands and was a member of the Executive Committee of the EPE Society.

# Park and Grid Integration Issues

Y. Zhou, J.T.G. Pierik, P. Bauer, B. Ferreira.

Offshore Integration Workshop 2006, Delft.

# Wind Park and Grid Integration Issues

\*Y. Zhou, \*\*J. Pierik, \*P. Bauer, \*J. A. Ferreira,

Abstract— Due to the fast increase in wind power production there is a need for detailed studies of integration problems. Integration problems arise from the characteristics of wind power and various technologies used in wind energy industry. In this paper, integration problems are analyzed as well as their origins and possible solutions. A case study of doubly fed induction generators connected with HVDC thyristor bridge is investigated. New control strategies are proposed and simulation results are presented.

#### Index Terms—Wind power, Integration problem, Simulation

## I. NOMENCLATURE

DFIG - doubly fed induction generator

HVDC - high voltage direct current transmission

HVAC - high voltage alternate current transmission

LVRT - low voltage ride through

SCIG - squirrel cage induction generator

WRIG - wound rotor induction generator

PCC - point of common coupling

PMG - permanent magnet generator

## II. INTRODUCTION

FROM the beginning of 1990s, the wind power develops so quickly that it now has significant shares of power production in many countries. In Europe, wind generation reached approximately 33,600 MW by the end of year 2004. The old low voltage protection of wind turbines can cause significant loss of active power which is not permitted from the point of view of transmission system operators. As the requirements of utilizing more wind power are still increasing, the integration of large scale wind power with power grid has to be studied. Today, the large scale wind farms are required to be controllable both in active power and reactive power, and to have low voltage ride through capabilities.

This paper focuses on the integration of large offshore wind farm with power grid, which includes investigations of dynamic behaviors inside wind farm, interactions between wind farm and power grid and the development of appropriate

This work is part of the project PhD@Sea, which is substantially funded under the BSIK-program of the Dutch Government and supported by the consortium WE@Sea.

controls both for the individual wind turbines and wind farm.

In this paper, the state of the art wind turbine technologies and integration methods are reviewed, the possible integration problems and solutions are investigated, the simulation and modeling issues are discussed, and finally a wind farm composed of DFIGs connected with power grid through a HVDC thyristor bridge is studied.

#### III. WIND ENERGY FACTS

In this section, the characteristics of wind power and the technologies used in wind energy industry are introduced.

## A. The Wind

The kinetic energy of a moving body is proportional to its mass (or weight). The energy extractable from the wind is proportional to the cubic of the wind speed. The wind speed varies continuously as a function of time and height. From a power system perspective, the fluctuations of wind speed may affect the power quality of wind power production. For example, the long term variations such as diurnal, weekly or seasonal cycles will affect the steady voltage of power system. While the short term variations such as turbulence may introduce serious amount of flicker at the point of common coupling. The impact of variations of wind speed on power quality depends very much on the turbine technology applied.

## B. Wind Turbines

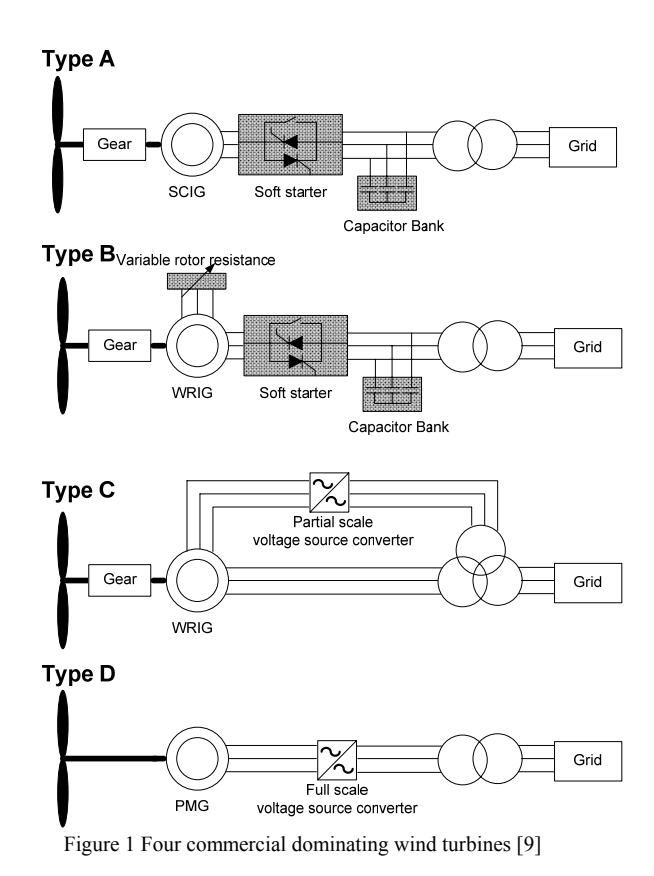
The various kinds of wind turbines can be found in literature [9], [12], [13] and [35].

In [9], a survey of the world's top-10 wind turbine suppliers for the year 2002 is summarized. It lists the two largest wind turbines produced by each of the top-10 manufactures. It also presents a detailed overview of the market share of each wind turbine concept from 1998 to 2002. These studies provide very useful information on the trends of the installed wind turbines. The four dominating commercial wind turbines in modern wind energy industry are shown in Figure 1:

- Type A: Fixed speed squirrel cage induction generator
- Type B: Variable wound rotor resistance induction generator
- Type C: Doubly fed induction generator with partial scale back to back converters on the rotor
- Type D: Synchronous generator with full scale back to back converters on the stator

<sup>\*</sup> The authors are with Electrical Power Processing group of Delft University of technology, 2628 CD, Delft, the Netherlands. (e-mail: Yi.Zhou@tudelft.nl).

<sup>\*\*</sup> The author is with Energy Research Center of the Netherlands (ECN), Petten, the Netherlands. (Pierik@ecn.nl)



C. Wind Farm Configurations and Integration Methods

Wind farm grids can be AC or DC. In [15], an evaluation program is developed to access the different electrical configurations of wind park from the point of view of energy production cost. The "all AC" system is concluded as the best choice for moderate connection distances. But when considering the dynamic behavior, the "all AC" system is not always feasible, especially for long transmission distance. Additionally, the cost of dynamic reactive power compensations has not been included in the comparison of different electrical configurations.

In [14], various layouts of wind parks are compared by energy production cost. And their influences to the power quality on the point of common connection are considered. It is concluded that for mid and long distance connection (longer than 20km), the total DC grid is the best choice.

In [16], several layouts of DC wind farm were investigated. The series connected DC wind turbines are the most difficult to be controlled. A DC voltage controller is required for each wind turbine. It is shown that use booster converter with DC transformer, the series connected DC wind farm has good system response at steady state.

The integration methods can be AC connections, or HVDC voltage source converters, or HVDC thyristor bridges equipped with additional reactive power compensation system. HVDC connections are more promising than AC connections for large scale wind farm with respect to electric power control.

In literatures [1], [2], [3], [9], [13], [15], [21], [23], and [27], various integration methods are proposed and compared

from different points of view: economic or dynamic behavior.

In [9] and [14], the AC connection is compared with HVDC connection, and draws the conclusion that HVDC is favorable than AC connection under the following conditions:

- Weak AC connection
- Distance > 100km
- Wind farm size > 350MW

The two HVDC systems: voltage source converter using IGBT switches and current source converter using Thyristor Bridges are compared in [1], [2], [9], [12], [14] and [27]. The CSC using the Thyristor Bridge is cheap and robust but needs additional reactive power compensation. The VSC using IGBT switches can provide dynamic reactive power compensation, but much more expensive and sensitive to the faults. It is concluded that for weak AC connection, the VSC is more appropriate. And for strong AC connection, the CSC can be used <sup>[1], [9]</sup>.

#### IV. INTEGRATION PROBLEMS AND SOLUTIONS

Integration of large scale wind farm with the power grid raises several integration problems which are not encountered in the operation of the a power system which is dominated by the traditional thermal power plant. These new integration problems arise from the characteristics of wind power and the various technologies adopted in the wind energy industry. This may require a step by step redesign of existing power system and operation. In this section, the possible integration problems are analyzed and corresponding solutions are proposed.

Until now, most of the studies are concentrated on "transient voltage stability" <sup>[4], [17], [18], [20], [24], [35], [23], [25], [26], [27], [28], [29], [30], [31], a small number are focused on "power quality" <sup>[5], [6], [37]</sup>. In [20], [35], and [38], the power quality problems are partly investigated.</sup>

The small signal stability and sub synchronous oscillation problems are seldom studied. Only a very few papers mentioned the sub synchronous oscillation <sup>[29], [35], [36]</sup>. In [35], it is considered not important, but in [29] and [36], the sub synchronous oscillations excited by wind power variations are recommended for future research.

#### A. Static Problems

The steady state problems are the overloading and static voltage/frequency deviations. It is caused by the variations of electric power due to the long term fluctuations of wind speed.

The possible solutions could be:

- Improve the wind speed forecast, use energy storage system, design coordinated central wind farm control and individual wind turbine control to make the output electric power of wind farm smooth and schedulable.
- Use reactive power compensation to control the reactive power and voltage.

In [9], two wind speed forecast models are discussed and compared. The short term wind predictions (one hour-ahead) are accurate but the long term (one day-ahead) predictions still have large errors.

In [32], the active and reactive power control of whole wind farm was discussed. It proposed to use a distribution function for the central control of active power and reactive power.

#### B. Power Quality

Two important power quality problems related to integration of wind power are flicker and harmonics.

Flicker is the 1-25 Hz voltage variations. This low speed voltage variation can be caused by short term fluctuations of wind speed, turbulence, tower shadow, wind shear effect and switching operations of the wind turbines. Flicker can be a very serious problem for the type A and B wind turbines, because the fluctuations of wind speed are directly reflected in the output electric power. For wind turbines type C and D, because the rotation speed is decoupled with power grid, the variable speed drive train is a buffer which can absorb the fluctuations of wind speed. Noticing that the wind speed fluctuations are quite local phenomenon, the geographical dispersion of wind turbines will contribute to a spatial smoothing effect on the output electric power of the large wind farm. The possible solutions could be:

- Reinforce the transmission system that is to decrease the transmission impedance.
- Implement an anti flicker algorithm in the control systems of wind turbines C and D. [5]
- Design appropriate start-up and shut-down strategies of wind turbines to avoid large fluctuations of active power and reactive power. [35], [37]
- Use dynamic reactive power compensation to control the voltage on the point of common connection with power grid.

Harmonics are components with frequencies which are multiples of the supply frequency, i.e., 100 Hz, 150 Hz, 200 Hz, etc. Inter-harmonics are in a similar way defined as components having frequencies located between the harmonics of the supply frequency. Harmonics can be caused by the switching of the power converters, the saturation of transformers and unbalanced loads. The possible solutions could be:

- Passive filters to improve power factor and reduce high-frequency harmonics. Their performances depend on tuning the reactors according the unknown source impedance.
- Active filters cto inject the anti-phase PWM currents or voltages into the grid.
- PWM control techniques to eliminate specific dominating orders of harmonics.
- Reactive power compensation systems (STATCOMs) to mitigate the specific orders of harmonics.

#### C. Transient Stability

One challenge of integration of the large scale wind farm with power grid is the requirement of fault ride through capability (or low voltage ride through capability). It is normally related to the transient voltage stability of the wind turbine generator during voltage dips. [19]

For type A and B wind turbines, they are basically induction generators which require reactive power for magnetizing. The limited electric torque during voltage dips will lead to the accelerating of the generator and increase of the slip. From the torque-speed curve and reactive power-speed curve, it is understood that when slip is larger than the critical value, the electric torque decreases, and the generator absorbs large amount of reactive power. The voltage continues to drop and the generator shaft continues to accelerate. Without proper remediation, this will finally leads to local voltage collapse and over speeding of the generator. The type B wind turbine has variable rotor resistance which can increase the value of the critical slip. Thus the type B wind turbine has better LVRT capability than type A.

For type C DFIG wind turbine which is equipped with a partial rated power VSC converter on the rotor, if the voltage dip is not severe, the rotor converters can control the DFIG to produce reactive power to the grid. But if the voltage dip is severe, then the rotor converter may face a transient over current and has to be blocked and the rotor is short circuited with resistances (active crowbar). Then the DFIG becomes a normal induction machine and requires substantial reactive power. This may cause voltage collapse and over speed of the generator. [33]

The type D wind turbine with full scale back to back VSC converters on the stator has the best LVRT capability. The only possible problem due to the voltage dip is that the DC voltage may increase to a high level to trigger the protection of VSC converters. But with coordinated wind turbine speed control and rectifier's active power control, it is possible to limit the DC voltage level by temporarily decreasing the input mechanical power of wind turbine during severe voltage dips.

Some general solutions to improve the transient voltage stability of wind farms could be:

- Use dynamic reactive power compensations such as SVC, STATCOM or the grid side VSCs of type C and type D wind turbine to help the recovery of voltage
- Use active stall or blade pitch angle control to limit the input mechanical power, thus avoiding the over speed of generators
- Use a HVDC link to decouple the wind farm from the power grid
- Improve the control of DFIG converters to actively suppress the large oscillations excited by the severe voltage dip

## D. Other Stability Problems

Small signal stability and sub synchronous oscillation are other stability problems which can increase due to integration of large scale wind power.

Only very few papers mentioned these problems. [29], [[35], [36]

## V. SIMULATION AND MODDELLING

Computer simulation is valuable in many aspects. It makes it possible to investigate the properties of prototype wind turbines and wind farms including the wind farm electrical

system without the necessary of full-scale test which is often expensive and time consuming.

The quality of the simulation results depends on two facts: the quality of the model and the applied turbine and wind farm parameters. To achieve good simulation results, the simulation purpose has to be defined clearly. In reality, there is always a compromise between detail of the model, availability of the parameters and the acceptable accuracy of the results.

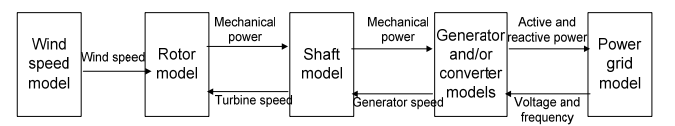


Figure 2 Model structure of wind turbine

#### A. Wind Speed

The wind speed should be made up of four components:

- The average value
- Ramp component representing a steady state increase of wind speed
- Wind gust component
- Wind turbulence

In [20], [37], the impacts of wind speed models are studied. The conclusions are:

- Wind speed gust, speed ramp, and turbulence are important for flicker calculation of FSIG;
- Turbulence is not important for flicker calculation of DFIG and PMG<sup>7</sup> but has large influences on the shaft torque.

#### B. Rotor and Pitch Servo

Two important phenomena should be included in the rotor model:

- Rotational sampling of the wind speed in the rotor plane influences the mechanical torque of wind turbines, thus influences the output electric power of type A and B wind turbines;
- The tower shadow effect (3p effect) which will influence the flicker level of type A and B wind turbines.

#### C. Drive train

The drive train of wind turbine is considered as "soft" because of the small shaft stiffness, this implies that the twist angle of shaft can be large during transient states.

The shaft system should be modeled as two mass model for type A, B and C wind turbines. But for type D wind turbine which is totally decoupled from power grid by back to back VSCs, the lumped mass model can be used for power grid study.

#### D. Generator

Perhaps the generator model receives most of the debates. Whether the third order or fifth order model should be used is still in argument. [34] The difference between fifth order model and third order model is whether the transients of stator fluxes are included or not. The third order model omits the transients of the stator fluxes, thus the simulation speed is improved. Omitting the transients of stator fluxes introduces some errors:

• The fast damping DC offsets in the stator currents are omitted. These DC components will cause a braking torque for the generator.

This error can be omitted due to the following reasons [10]

- Multi-phase faults are mostly sequentially developed which means the DC offsets in the fault currents are zero. This is validated by the records of oscillograms of actual short circuit currents.
- Ignoring this effect introduces a slight degree of conservation.

For type A wind turbine, the large transient stator currents using fifth order model normally will not trigger the over current protection because generator can accommodate large transient over current. But the DC breaking torque can be important because the speed of the induction generator is critical to the transient voltage stability. This is reported in [9] and [35]. But the influences of this error are still questionable because of the same reasons for omitting stator flux transients of synchronous generator as stated above.

For type C wind turbine, the large oscillation in the rotor will trigger the protection of rotor converter which will change the operation and behavior of type C wind turbine. So the fifth order model should be used in the type C wind turbine. If the number of type C wind turbines is large, then an approximate way may be used: The third order model is used, and the protection of the rotor converter is triggered by the degree of voltage dip.

For type D wind turbine, the generator is totally decoupled with power grid by the back to back converter, so the transients in the stator fluxes can be neglected

#### E. Converter

For all simulation purposes except the harmonic study, the voltage source converter can be modeled as controlled voltage source neglecting the switching of the current from one IGBT to the next. This means that the switches are ideal and voltage wave forms are perfect. Control of the converters can be found in [18], [35], [38].

The non ideal switches may introduce nonlinearities in the control function which will cause oscillations and errors. This phenomenon and the remediation are illustrated in [7] and [8].

#### F. Power Grid

To study the influences of large scale wind farm on the power system, the model of the power grid should be implemented in some details based on the data of transmission system operator, including the models of large power plants nearby, large consumption centers nearby, etc. Use of only one equivalent synchronous generator to represent the dynamic behaviors of power system is not accurate for some simulation purposes, for example, when investigating the sub synchronous oscillation of the synchronous generator due to the integration of wind farm.

#### G. Developed models

Matlab/Simulink is chosen as the dynamic simulation software, the electrical dynamic models are in dq coordinates which is intentionally chosen to improve the simulation speed.

[18]

The electric models developed until now are all symmetrical models for a balanced three phase system in dq coordinates. The dynamic models include:

- Wind speed model
- Rotor model
- Shaft model
- Generator models: type A, type C and type D.
- Power electronic converter models
  - Voltage source converter using IGBT switches
  - Current source converter using Thyristor Bridge
- Electric component models
  - o Transmission line and cable
  - Transformer
  - Shunt capacitor bank
- Simplified Grid model (a single synchronous generator with voltage and frequency control, consumers, transformers, cables and overhead lines)

The unsymmetrical electric models will be developed in the next step.

#### VI. CASE STUDY

From the economic points of view, DFIGs and HVDC thyristor bridge can be a candidate for large offshore wind farm connecting with power grid over long distance. However, control strategy of this concept is not straight forward.

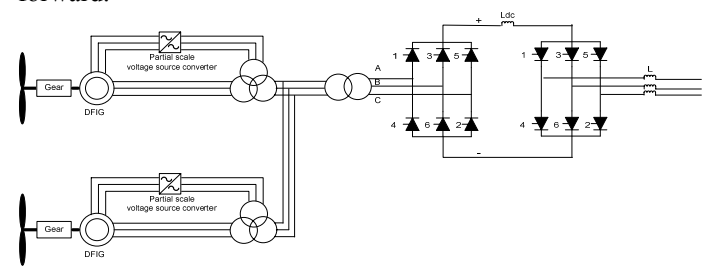


Figure 3 topology of case study

The traditional grid-flux oriented controller of DFIG is only appropriate for the situation when DFIG is connected with stiff power grid whose voltage at PCC is constant. To use this grid-flux oriented controller of DFIG in a wind farm connected with power grid through HVDC thyristor bridge requires:

- Additional reactive power compensation system to keep the voltage level of the wind farm constant.
- Centralized control to balance the transmitted power through thyristor bridge to the power of the wind turbines.

The solution is economically not favorable. Therefore a new control concept is developed which does not have the drawback of the traditional grid-flux oriented controller of DFIG. The new proposal is to treat the thyristor bridge as a constant impedance load by keeping the fire angle of thyristor bridge constant under normal operating conditions. The active power transmitted through thyristor bridge is controlled

through dynamically controlling the voltage level of wind farm. In this case, the DFIGs are considered to be connected with a very weak power grid. The traditional grid-flux oriented controller cannot work.

Two new controllers of DFIG were developed in this case study. One is terminal voltage controller and the other is stator-flux oriented controller. They both control the voltage level of the wind farm in order to control the active power transmitted through thyristor bridge. The terminal voltage controller uses the rotor voltages to control the terminal voltages of generator directly. The stator-flux oriented controller controls the stator fluxes, thus controls the terminal voltages indirectly. In order to prevent large reactive power circulating between nearby generators, an explicit reactive power controller is added.

At this stage, only two DFIGs are simulated in the wind farm. Simulation event is that one DFIG's active power and rotation speed ramps down while the other's P and wm ramps up after some time. Simulation results are shown in the following graphs.

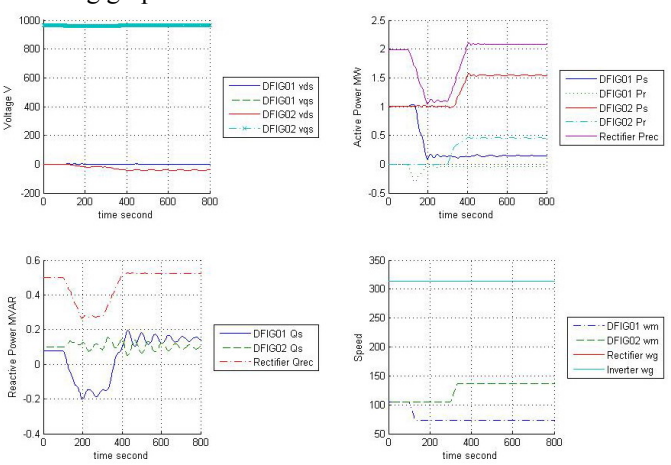


Figure 4 simulation results of terminal voltage controller

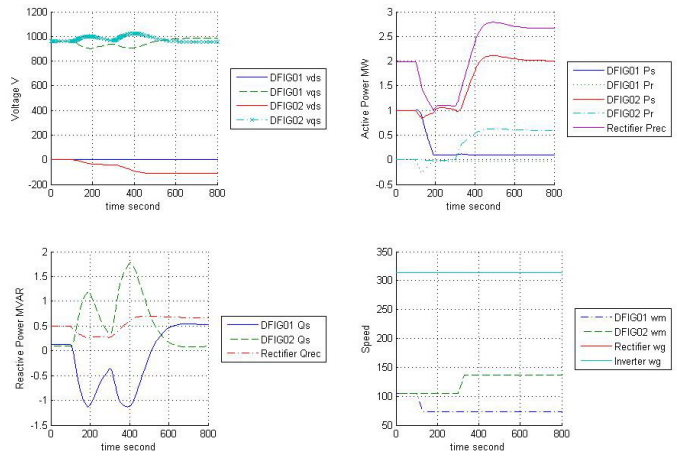


Figure 5 simulation results of stator-flux oriented controller

In Figure 4 and Figure 5, the upper right graph depicts the terminal voltages of DFIGs, the upper left graph depicts the active power of DFIGs and Thyristor Rectifier, the bottom right graph depicts the reactive power of DFIGs and Thyristor Rectifier, and the bottom right depicts the electrical frequencies of wind farm, power grid, and rotation speed of

#### DFIGs.

Results prove that the two new controllers can control the active power of each DFIG independently. However they both have some drawbacks.

The terminal voltage controller has oscillations which take time to damp out, and the stator-flux controller has a relatively slow reactive power control. These problems are caused by the coupling of active power and reactive power on each generator and between the two generators.

These control problems are caused by the fact that the wind farm's characteristic is such that resistance R is similar as the reactance X in this case study, thus both active power and reactive power will influence AC voltage vds and vqs. It is not possible to use AC voltage's phase angle difference and magnitude difference to decouple P and Q as in the high voltage transmission power system.

Because AC voltage of wind farm is intentionally controlled to be variable, the traditional grid-flux oriented control is also not appropriate for this case study.

Research is still ongoing to improve this multi-variable control system.

#### VII. CONCLUSIONS

Due to the high penetration levels of wind power, the integration problems have to be investigated. These integration problems may be new comparing with the operation of traditional thermal power plant. Computer simulation is valuable to investigate the integration problems. The simulation models are always a compromise between details of the model, availability of the parameters and the required accuracy of the results.

A case study of doubly fed induction generators with HVDC thyristor bridge is presented. Two new types of controllers have been developed. They do not require a centralized controller and additional reactive power compensation system, and can control active power of each generator independently. However, decoupling P and Q of multiple DFIGs when connected to a very weak AC grid is a new research topic, these two new controllers still have some drawbacks. Future works will concentrate on the improvements of this multi-variable control system.

#### VIII. REFERENCES

#### Periodicals:

- Z. Chen, E. Spooner, "Grid interface options for variable speed, permanent magnet generators", *IEE Proc.-Electr. Power Appl.*, Vol 145, No. 4, July 1998.
- [2] N. M. Kirby, L. Xu, M. Luckett, W. Siepmaan, "HVDC transmission for large offshore wind farms", *Power engineering Journal*, June, 2002.
- [3] W. Lu and B. Ooi, "Optimal acquisition and aggregation of offshore wind power by multi terminal voltage source HVDC", IEEE transactions on power delivery, Vol. 18, No. 1, January, 2003.
- [4] F. D. Kanellos, N. D. Hatziargyriou, "the effects of variable-speed wind turbines on the operation of weak distribution networks", *IEEE transactions on energy conversion*, Vol. 17, No. 4, December, 2002.
- [5] T. Thiringer, T. Petru, C. Liljergren, "Power quality impact of a sea located hybrid wind park", *IEEE transactions on energy conversion*, Vol. 16, No. 2, June 2001.

- [6] A. Larsson, "Flicker emission of wind turbines caused by switching operations", *IEEE transactions on energy conversion*, Vol. 17, No. 1, March, 2002.
- [7] J. Svensson, "Grid connected voltage source converter control principle and wind energy applications", Technical report, No. 331, Chalmers University of Technology, Sweden, 1998.
- [8] M. Lindgren, "Modeling and control of voltage source converters connected to the grid", technical report No. 351, Chalmers University of technology, 1998.

#### Books:

- [9] "Wind power in power systems", John Wiley & Sons, ISBN: 0-470-85508-8, 2005.
- [10] P. Kundur, "Power system stability and control", McGraw-Hill, 1994.
- [11] S. Heier, "Wind energy conversion systems", John Wiley & Sons, 1998.

## Technical Reports:

- [12] L. H. Hansen, L. Helle, F. Blaabjerg, "Conceptual survey of generators and power electronics for wind turbines", Technical report, Risø-R-1205(EN), Risø National Laboratory, Denmark, December, 2001.
- [13] M. R. Dubois, "Review of electromechanical conversion in wind turbines", Technical report, Report EPP00.R03, Electric Power Processing Group, Delft University of Technology, April, 2000.
- [14] S. Lundberg, "Configuration study of large wind parks", Technical report No. 474L, Chalmers University of Technology, Sweden, 2003.
- [15] J. T. G. Pierik, M. E. C. Damen, P. Bauer, S.W.H. de Haan, "Electrical and control aspects of offshore wind farms I (Erao I), Phase 1: Steady state electrical design, power performance and economic modeling", Technical report of ECN&TUD, ECN-cx-01-083, June, 2001.
- [16] O. Martander, "DC grids for wind farms", Technical report No. 443L, Chalmers University of Technology, Sweden, 2002.
- [17] P. Sorensen, A. Hansen, L. Janosi, J. Bech, B. Bak-Jensen, "Simulation of interaction between wind farm and power system", Technical report, Riso-R-1281(EN), Risø National Laboratory, Denmark, December, 2001.
- [18] J. Pierik, J. Morren, E.J. Wiggelinkhuizen, S.W.H de Haan, T.G. van Engelen, J. Bozelie, "Electrical and control aspects of offshore wind farms II (Erao II), Volume 1: dynamic models of wind farm", Technical report of ECN&TUD, ECN-C-04-050, Netherlands, 2004.
- [19] J. Pierik, J. Morren, E.J. Wiggelinkhuizen, S.W.H de Haan, T.G. van Engelen, J. Bozelie, "Electrical and control aspects of offshore wind farms II (Erao II), Volume 2: Offshore wind farm case studies", Technical report of ECN&TUD, ECN-C-04-051, Netherlands, 2004.
- [20] P. Sørensen, A. D. Hansen, P. Christensen, "Simulation and verification of transient events in large wind power installations", Technical report, Risø-R-1331(EN), Risø National Laboratory, Denmark, October, 2003.

## Papers from Conference Proceedings (Published):

- [21] P. Cartwright, L. Xu, C. Sasse, "Grid integration of large offshore wind farm using hybrid hvdc transmission", *Nordic wind power conference*, Chalmers university of technology, 01-02 March, 2004.
- [22] L. T. Hua, T. K. Saha, "Investigation of power loss and voltage stability limits for large wind farm connections to a sub transmission network", *IEEE Power Engineering Society General Meeting*, Denver, Colorado, USA, 6-10 June, 2004.
- [23] H. Binder, P. Lundserg, "Integration of wind power in the power system", *IEEE 28th annual conference of the Industrial Electronic Society*, Page: 3309-3316, Vol. 4, 2002.
- [24] F.W. Koch, I. Erlich, F. Shewarega, U. Bachmann, "Dynamic interaction of large offshore wind farms with the electric power system", *Power Tech conference*, Bologna, Italy, Page: 7, Vol. 3, June 23-26, 2003.
- [25] L. Holdsworth, N. Jenkins, G. Strbac, "Electric stability of large offshore wind farms", IEE 7<sup>th</sup> international conference on AC-DC power transmission, Page: 156-161, Vol. 1, November, 2001.
- [26] J. Wiik, J. O. Gjerde, T. Gjengedal, "Impacts from large scale integration of wind farm into weak power systems", *Proceedings of international* conference on Power System Technology, Pages: 49-54, Vol. 1, 2000.
- [27] Y. Noro, J. Arai, K. Takagi, "System study of direct current power transmission system connected to wind farm", *IEEE/PES Transmission* and Distribution Conference and Exhibition 2002, Pages: 944-949, Vol. 2, 2002.
- [28] L. Holdsworth, X.G. Wu, J.B. Ekanayake, "Comparison of fixed speed and doubly fed induction wind turbines during power system

- disturbances", IEE Proceedings of Generation, Transmission and Distribution, Pages: 343-352, Vol. 150, Issue. 3, May, 2003.
- [29] P. Pourbeik, R. J. Koessler, D. L. Dickmander, "Integration of large wind farms into utility grids (part2-performance issues)", *IEEE Power Engineering Society General Meeting*, Pages: 1522-1525, Vol. 3, 2003.
- [30] A. Kehrli, M. Ross, "Understanding grid integration issues at wind farms and solutions using voltage source converter FACTS technology", *IEEE Power Engineering Society General Meeting*, Pages: 1822-1828, Vol. 3, 2003.
- [31] F. W. Koch, I. Erlich, F. Shewarega, "Dynamic simulation of large wind farms integrated in a multi machine network", *IEEE Power Engineering Society General Meeting*, Pages:2159-2164, Vol. 4, 2003.
- [32] A.D. Hansen, P. Sorensen, F. Lov, F. blaabjerg, "Centralized control of wind farm with doubly-fed induction generators", *PCIM-2005 (Europe)*, Nuremberg, Germany, 07-09 June, 2005.
- [33] J. Morren, J. Pierik, S. W. H. de Haan, "ride through of wind turbines with doubly-fed induction generator during a voltage dip", *IEEE Trans. Energy Conversion*, Vol. 20, Issue 2, 2005.
- [34] J. Morren, S. W. H. de Haan, P. Bauer, J. Pierik, "Comparison of complete and reduced models of a wind turbine using Doubly-Fed Induction Generator", *IEE Proceedings—Generation, Transmission and Distribution*, Vol. 150, Issue 3, 2003.

#### Dissertations:

- [35] V. Akhmatov, "Analysis of dynamic behavior of electric power systems with large amount of wind power", PhD thesis of Electrical power engineering, ISBN: 87-91184-18-5, Technical University of Denmark, April, 2003.
- [36] P. Rosas, "Dynamic influences of wind power on the power system", PhD Thesis of Electrical power engineering, ISBN: 87-91184-16-9, Technology University of Denmark, March, 2003.
- [37] A. Larsson, "Power quality of wind turbines", PhD thesis of Electrical power engineering, ISBN: 91-7197-970-0, Chalmers University of Technology, Sweden, 2000.
- [38] T. Petru, "Modeling of wind turbines for power system studies", PhD thesis of Electrical power engineering, ISBN: 91-7291-306-1, Chalmers University of Technology, Sweden, 2003.

## IX. BIOGRAPHIES



Yi Zhou was born in China on Oct 7th , 1973. He received his Bs.C. degree in electrical engineering from Zhejiang University in 1995. After then, he worked in Anhui electric power company for 7 years, first as a power grid operator, then a power grid analyzer. In 2004, he received his M.Sc degree in electric power engineering from TU Delft. He is now working towards his PhD degree within electric power processing group of TUDelft. The title of his PhD project is "Wind Park and Grid Integration".



Jan Pierik was born in The Netherlands in 1954. He received his M.Sc. degree in Chemical Engineering from the Technical University Twente in 1978. Since 1980 he has been employed at the Energy Research Centre of the Netherlands ECN in Petten, presently as a Senior Research Scientist. His main technical interest is modelling and control of electrical systems for wind turbines and wind farms.



**Paul Bauer,** Delft University of Technology, received his Masters in Electrical Engineering at the Technical University of Kosice ('85) and Ph.D. from Delft University of Technology ('95). Since 1990 he is with the Delft University of Technology teaching Power Electronics, Electrical Drives and related subjects. Mr. Bauer published over 150 papers in his field, he holds an international patent and organized several tutorials.



Jan Abraham Ferreira (F'05) was born in Pretoria, South Africa, in 1958. He received the B.Sc.Eng. (cum laude), M.Sc.Eng. (cum laude), and Ph.D. degrees in electrical engineering from the Rand Afrikaans University, Johannesburg, South Africa, in 1980, 1982, and 1988, respectively. In 1981, he was with the Institute of Power Electronics and Electric Drives, Technical University of Aachen, Aachen, Germany, and worked in industry at ESD(Pty) Ltd

from 1982 to 1985. From 1986 to 1997, he was on the Faculty of Engineering at Rand Afrikaans University, where he held the Carl and Emily Fuchs Chair of Power Electronics. Since 1998, he has been a Professor at the EWI Faculty of the Delft University of Technology, Delft, The Netherlands. Dr. Ferreira was Chairman of the South African Section of the IEEE, from 1993–1994. He is the Founding Chairman of the IEEE Joint IAS/PELS Benelux Chapter. He served as the Transactions Review Chairman of the IEEE IAS Power Electronic Devices and Components Committee and is an Associate Editor of the IEEE TRANSACTIONS ON POWER ELECTRONICS. He was a member of the IEEE PELS Adcom and is currently the Treasurer of the IEEE PELS. He served as Chairman of the CIGRE SC14 National Committee of the Netherlands and was a member of the Executive Committee of the EPE Society.

# New thyristor bridge models for dynamic simulation

Y. Zhou, P. Bauer, B. Ferreira, J.T.G. Pierik.

PCIM 2006

# New Thyristor Bridge Models for Dynamic Simulation of Grid Integration of Offshore Wind Farms

Y. Zhou, P. Bauer, J. A. Ferreira, J. Pierik
Delft University of Technology, Mekelweg 4, 2628 CD Delft, The Netherlands
Energy Research Center of the Netherlands (ECN), Petten, The Netherlands
Yi.Zhou@TUDelft.nl, P.Bauer@TUDelft.nl, J.A.Ferreira@TUDelft.nl, Pierik@ecn.nl

Abstract: Today, large scale wind farm is required to be controllable both in active and reactive power, and to have the low voltage ride through capability when the grid faults happening. Therefore, the integration of large scale Wind Park with power grid is very important. Simulation is the most important tool for investigating the integration problems. Compromises between details of the models and simulation time have to be made. This leads to the requirement of developing fast and accurate models. In this paper, four thyristor bridge models for balanced and unbalanced three phase systems in dq0 coordinates are developed in Matlab/Simulink. Compared with models from Power System Block sets, the new models are proved to be time efficient and accurate.

Key words: thyristor bridge, model, Matlab/Simulink

#### 1. Introduction

The wind generation in Europe reached approximately 33,600 MW until the end of year 2004. The demands of connecting large scale wind parks to the power grid are continuously increasing. Nowadays, the large scale wind farms are required to be controllable both in active and reactive power, and to have the low voltage ride through capability when grid faults happening. The integration methods can be AC connections, or **HVDC** voltage converters, or HVDC thyristor bridges equipped with additional reactive power compensation system. The 180MW offshore wind farm Horns Rev was installed in 2002 in Denmark, and connected to the 150KV power grid with AC connection. But HVDC connections are more promising than AC connections for large scale wind farm in the aspect of electric power control. The voltage source converters using IGBT switches can provide dynamic reactive power compensation, but are much more expensive, and have large energy loss due to the high switching frequencies. The current source converters using thyristor bridges are cheap and robust, having low energy loss, but need additional reactive power compensations. The AC transmission system and those two HVDC systems are compared in [1], [2], [3], [4], and [6]. It is concluded that for weak AC transmission system, the Voltage Source Converters are more appropriate considering the overall system economics. For large wind farm (>350MW) integrated with strong AC transmission system, the thyristor bridges are more favorable than AC transmissions or HVDC VSC transmissions.

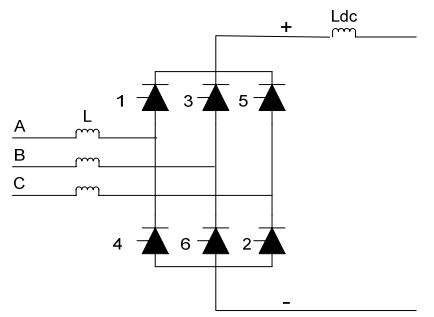


Figure 1. Schematic of thyristor bridge

As HVDC thyristor bridge can be a candidate for the integration of large wind farm, the thyristor bridge model are required.

Quasi-steady state models	Model 1	Symmetrical quasi- steady model
	Model 2	Unsymmetrical quasi- steady model using Fourier analysis
	Model 3	Unsymmetrical quasi- steady model using partial symmetric
Instantaneous model	Model 4	Instantaneous model without commutation effects
Instantaneous model	PSB	Power System BlockSets

Table 1. lists of the thyristor bridge models

In [5], simulations of the voltage source converter in the dq0 reference frame (Park's transformation) are proved to be much faster than the simulations in the abc reference frame. In this paper, one symmetrical and two unsymmetrical quasi-steady state thyristor bridge models in dq0 reference frame are developed for

the electromechanical simulations. In addition, an instantaneous model with commutation effects are also developed using the switching function concept.

The four thyristor bridge models developed in this paper are summarized in Table 1.

The developed models are verified and calibrated using Power System BlockSets. They are described in the next sections in detail.

## 2. Quasi-steady state thyristor bridge models in dq0 coordinates

In the quasi-steady state models, the converter are represented by equations relating average values of dc quantities and RMS values of ac fundamental components. It would accurately represent the HVDC thyristor bridges system performance in the electromechanical simulations.

The assumptions made for the quasi-steady state models are:

- The implementation of fire angle is instantaneous compared with slow a.c. system dynamics;
- The AC voltages and currents are assumed to be purely sinusoidal at fundamental frequency and all higher order harmonics are filtered out.
- The DC side voltage is considered to be smooth and it is the average value per 60 degrees;
- The DC side current is considered to be smooth due to the large smoothing DC inductance.

The inputs of the model are three phase voltages in dq0 coordinates  $v_d$ ,  $v_q$  and  $v_0$  and the DC current  $I_{dc}$ ; the outputs are three phase currents  $i_d$ ,  $i_q$ ,  $i_q$ ,  $i_0$  and DC voltage  $V_{dc}$ .

#### A. Model 1

Under balanced three phase system, the 0 components  $\nu_0$  and  $i_0$  are always zero. The RMS values and phase angles of voltage and current of phase-a can be calculated from  $\nu_d$ ,  $\nu_q$  and  $l_{dc}$  as:

$$\begin{split} V_{a} &= \frac{\sqrt{V_{d}^{2} + V_{q}^{2}}}{\sqrt{3}}, \phi_{va} = \frac{\pi}{2} + \arctan(\frac{V_{q}}{V_{d}}), \\ I_{a} &= k \frac{\sqrt{6}}{\pi} I_{dc}, \phi_{ia} = \phi_{va} - \phi_{vi}, \\ \phi_{vi} &\approx \alpha + \frac{\mu}{2}, \mu = \frac{2\omega L \cdot I_{dc}}{\sqrt{2} U_{LL} \sin \alpha} \end{split}$$

where  $\alpha$ ,  $\mu$  are fire angle and commutation angle respectively,  $k \approx 1$ .

The outputs  $V_{\text{dc}},\,i_{\text{d}}$  and  $i_{\text{q}}$  are  $^{[7],\,[8],\,\text{and}\,[10]}.$ 

$$V_{dc} = \frac{3\sqrt{2}}{\pi} \sqrt{3} V_a \cos \alpha - \frac{3}{\pi} \omega L I_{dc},$$
  

$$i_d = \sqrt{3} I_a \sin \phi_a, i_a = -\sqrt{3} I_a \cos \phi_a$$

Under balanced three phase system, voltages and currents in dq0 coordinates are time invariables, some numerical integration methods are very efficient for these calculations. But for an unbalanced three phase system, voltages and currents in the d, q, 0 coordinates are all time variables. After Park's transformation, the values in d and q coordinates are second order frequency components and the 0 values are the fundamental frequency components. More important, the RMS values and phase angles of phase voltages are six unknowns which cannot be calculated directly from those three independent equations.

#### B. Model 2 and 3

In the quasi-steady state models 2 and 3, two methods are used to solve the above mentioned problem, and lead to two different models:

- Model 2, quasi-steady state model using Fourier analysis for unbalanced three phase system
- Model 3, Quasi-steady state model using partial symmetric of the unbalanced three phase system

The first method is rather straightforward, but has shortcomings due to the Fourier analysis. The output DC voltage lags the change of input ac voltages with one cycle 0.02s.

The second method assumes that partial symmetric still exists under unbalanced three phase system. For example, when a single line to ground fault happens in phase a, the RMS values of b and c phase are equal. When double lines to ground fault or double line to line fault happen in phase b and phase c, the RMS values of b and c phase are still equal. The assumptions are:

- Two phase voltages' RMS values are always the same;
- The phase angles of phase voltages are displaced with each other in 120 degree.

The above two methods are used to calculate the RMS values and phase angles of AC voltages from the instantaneous  $v_d$ ,  $v_q$  and  $v_0$ .

The DC voltage and AC current equations for unbalanced three phase systems are much more complex [7]:

$$\begin{split} V_{dc} &= \frac{\sqrt{2}}{\pi} U_{ba} \left[ \cos(C_1 + \alpha - C_3 + \pi) - \cos(C_2 + \alpha - C_1 + \pi) \right] \\ &+ \frac{\sqrt{2}}{\pi} U_{ac} \left[ \cos(C_2 + \alpha - C_1) - \cos(C_3 + \alpha - C_1) \right] \\ &+ \frac{\sqrt{2}}{\pi} U_{bc} \left[ \cos(C_3 + \alpha - C_2) - \cos(C_1 + \alpha + \pi - C_2) \right] \\ &- \frac{I_{dc} (\omega L_1 + \omega L_2 + \omega L_3)}{\pi} \\ I_i &= \frac{4}{\pi} \frac{I_{dc}}{\sqrt{2}} \sin(\frac{T_i}{2}) \\ \phi_{Vi} &= \alpha + \frac{u_i}{2}, \phi_{fi} = \phi_V - \phi_{Vi}, \\ \mu_1 &= \arccos\left(\cos \alpha - \frac{\omega L_1 + \omega L_3}{\sqrt{2} V_{ac}} \cdot I_{dc}\right) - \alpha \\ \mu_2 &= \arccos\left(\cos \alpha - \frac{\omega L_2 + \omega L_1}{\sqrt{2} V_{ba}} \cdot I_{dc}\right) - \alpha \\ \mu_3 &= \arccos\left(\cos \alpha - \frac{\omega L_2 + \omega L_3}{\sqrt{2} V_{bc}} \cdot I_{dc}\right) - \alpha \end{split}$$

 $\alpha_i$ ,  $\mu_i$  are fire angles and commutation angles respectively.  $C_i$  are the initial angles of line to line voltages, and  $T_i$  are conduction periods of each phase which are explained as shown in Figure 2.

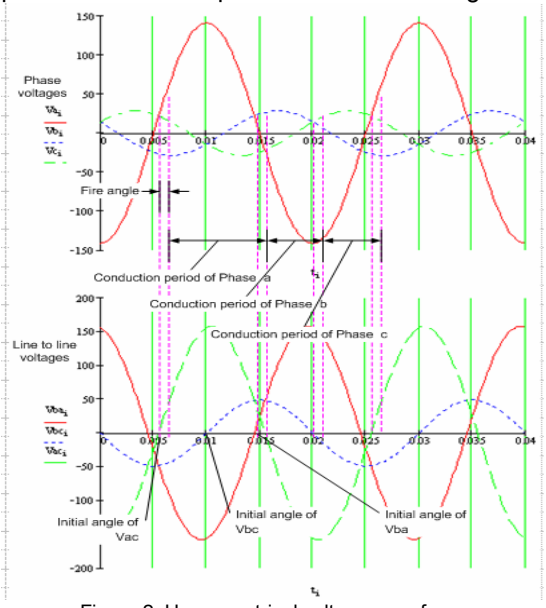


Figure 2. Unsymmetrical voltage waveforms

Both methods have their own limitations:

- The Fourier analysis cause phase shifts and value deviations on the output signals.
- The assumption that phase angles of phase voltages are displaced with each other in 120 degree maybe not true during the real unsymmetrical faults.

#### 3. Instantaneous thyristor bridge models

Due to the above mentioned limitations of quasistead state models for unbalanced three phase system, an instantaneous thyristor bridge model is developed. In order to calculate the instantaneous DC voltage and AC current, a state matrix SW of thyristor bridge is calculated with switching function<sup>[9]</sup>, and the instantaneous DC voltage and AC currents are calculated with SW.

The schematic of three-phase thyristor bridge is shown in Figure 1.

The thyristor is switched on by a pulse signal on the gate, but can not be switched off by gate signal. It is switched off only when the current flowing through approaches zero.

An instantaneous model of a three-phase diode bridge without commutation effects is realized in Simulink in [9]. There is no instantaneous thyristor bridge model in Matlab/Simulink.

Assuming the AC commutation inductances are small, this instantaneous thyristor bridge model does not considering the commutation effects. This means:

- At any time, only one thyristor in the upper group and one thyristor in the lower group are conducting;
- The DC voltage V<sub>dc</sub> always equals to the line to line voltages;
- The AC phase currents change instantaneously between DC current and 0.

The states of six thyristor are assigned as

	Conducting	Blocked
T1, T3, T5	1	0
T4, T6, T2	-1	0

The conducting sequence of the thyristor bridge in one cycle is

in one cycle	13			
Conducting	DC	i <sub>a</sub>	i <sub>b</sub>	i <sub>c</sub>
thyristor	voltage			
T1, T2	Va-Vc	I <sub>dc</sub>	0	-I <sub>dc</sub>
T3, T2	Vb-Vc	0	I <sub>dc</sub>	-I <sub>dc</sub>
T3, T4	Vb-Va	-I <sub>dc</sub>	I <sub>dc</sub>	0
T5, T4	Vc-Va	-I <sub>dc</sub>	0	I <sub>dc</sub>
T5, T6	Vc-Vb	0	-I <sub>dc</sub>	$I_{dc}$
T1 T6	Va-Vh	ldo	-lao	0

For model 4, the switching function, DC voltage  $V_{\text{dc}}$  and three phase AC currents can be calculated as

$$SW = \begin{bmatrix} T1 + T4 \\ T3 + T6 \\ T5 + T2 \end{bmatrix}, V_{dc} = SW \cdot \begin{bmatrix} V_a \\ V_b \\ V_c \end{bmatrix}, \begin{bmatrix} I_a \\ I_b \\ I_c \end{bmatrix} = SW \cdot I_{dc}$$

### 4. Implementation in Matlab/Simulink

All the four new models are implemented in Matlab/Simulink. The inputs are instantaneous three phase AC voltages  $v_d$ ,  $v_q$ ,  $v_0$ , DC currents

 $I_{\text{dc}}$  and fire angle  $\alpha$  ; the outputs are DC voltage  $V_{\text{dc}}$  and instantaneous three phase AC currents  $i_{\text{d}},\,i_{\text{o}},\,i_{\text{o}},\,i_{\text{o}}.$ 



Figure 3. General view of thyristor bridge model in Matlab/Simulink

In the quasi-steady state models, an interface is used to calculate the phasor values such as RMS voltages and phase angles from the input instantaneous values. The main differences between three quasi-steady state models are the implementations of this interface:

- Model 1, directly calculation for balanced three phase system;
- Model 2, Fourier analysis for unbalanced three phase system;
- Model 3, Use partial symmetric of unbalanced three phase system.

In the instantaneous model, firing pulses are used to trigger the thyristors which are represented by flip-flops, and the firing pulse of the next thyristor following the firing sequence is used to reset the flip-flops. Thus the thyristors' states and the switching function are calculated.

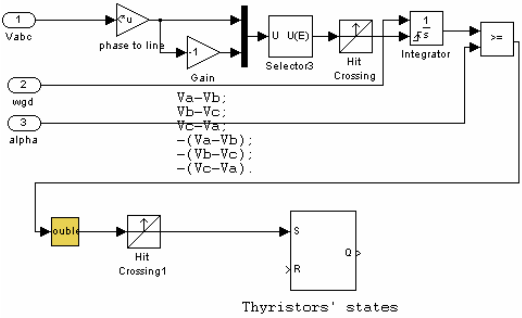


Figure 4. Firing pulses of thyristor bridge

## 5. Verify the thyristor bridge models in back to back configurations

All the four new models are compared with models from Power System BlockSets in back to back configurations as shown in Figure 5.

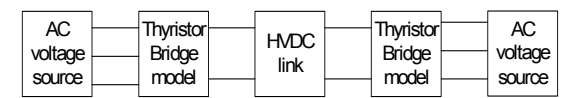


Figure 5. Back to back configuration of thyristor bridges The parameters and events of simulations are listed in Table 2. (For the symmetrical quasi steady state model: model 1, the inverter side AC voltages do not change.)

Table 2. Parameters and simulation events of verifications

Rectifier side	Va, Vb, Vc (Maximum amplitude)	1000V
	Fire angle of rectifier	increase from 30 degree to 45 degree at 2.0s
Inverter side	Va (Maximum amplitude)	drops from 500V to 200V at 1.0s
	Vb, Vc (Maximum amplitude)	500V
	Fire angle of inverter	150 degree
DC link	DC resistance	1Ω
	DC smoothing inductance	100mH

In Figure 6 and Figure 7, DC currents of model 1 and PSB are compared, the results prove that the symmetrical quasi-steady state model: model 1 is accurate.

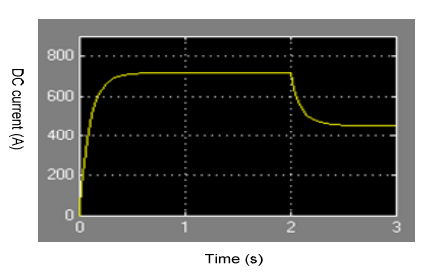


Figure 6. DC current of model 1

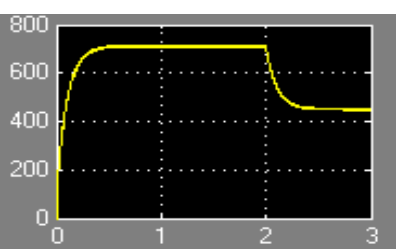


Figure 7. DC current of PSB

From Figure 9 to Figure 13, the Rectifiers' DC voltages, Inverters' DC voltages, and DC currents of Model 4 and PSB are compared. Model 4 is proved to be accurate when AC commutation inductances are small.

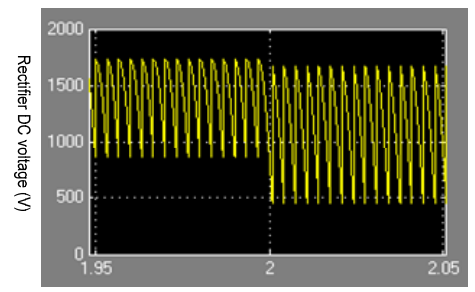


Figure 8. Rectifier's DC voltage of model 4

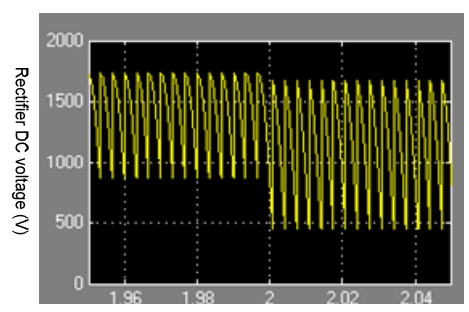


Figure 9. Rectifier's DC voltage of PSB

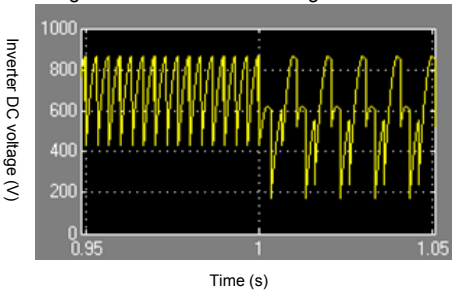


Figure 10. Inverter's DC voltage of model 4

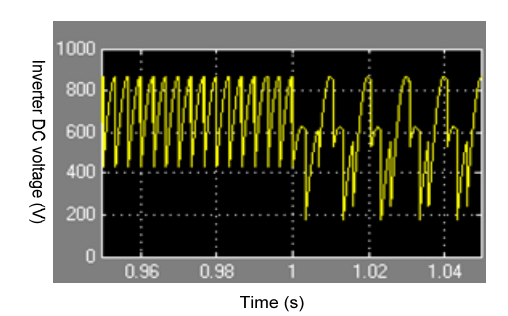


Figure 11. Inverter's DC voltage of PSB

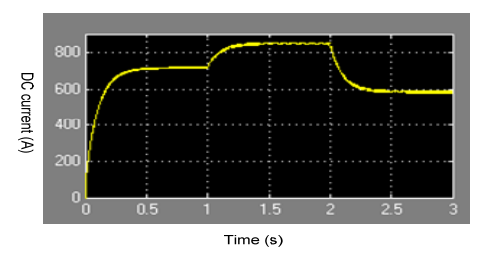


Figure 12. DC current of model 4

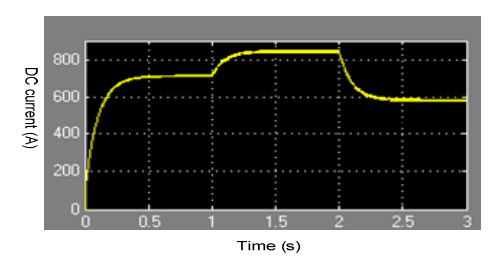


Figure 13. DC current of PSB

DC currents of two unbalanced quasi-steady state models: Model 2 and 3 are shown as in Figure 14 and Figure 15.

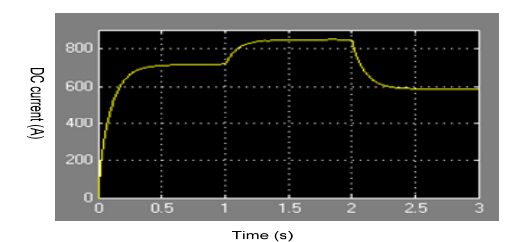


Figure 14. DC current of model 2

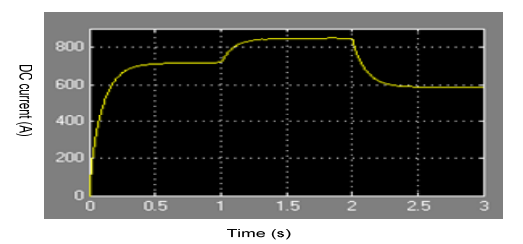


Figure 15. DC current of model 3

Comparing the DC currents of models 1, 2, 3, 4 and PSB, their DC currents have the same profile, except that for model 4 and PSB, the DC currents have larger ripples due to the ripples of instantaneous DC voltage.

The required simulation time for simulating 3s dynamics are recorded and compared in Table 3.

Table 3. Required simulation time for the models

Table 5. Nequired 3	rable 5. Required simulation time for the models			
Model type	Required simulation time			
PSB	236s			
Model 1	1s			
Model 2	4s			
Model 3	3s			
Model 4	8s			

## 6. Conclusions and future works

Three quasi-steady state thyristor bridge models for balanced or unbalanced three phase system

in dq0 reference system are presented in this paper which can be used for electromechanical simulations. An instantaneous model without commutation effects is also developed.

Compared with models from Power System BlockSets, all the quasi-steady thyristor bridge models are proved to be fast and accurate for balanced three phase system. For unbalanced three phase system, the two unsymmetrical quasi-steady state models have their own shortcomings: model 2 has a time lag due to the Fourier analysis, and model 3 can only be used when phase angles of three phase voltages are displaced with each other in 120 degree.

The instantaneous model without commutation effects is accurate if the AC commutation inductances are small.

Considering the possibility that error may exist if the AC commutation inductances are large, an instantaneous model with commutation effect is under developing.

#### **Acknowledgments**

This work is part of the project PhD@Sea, which is substantially funded under the BSIK-program of the Dutch Government and supported by the consortium WE@Sea.

#### References:

 Z. Chen, E. Spooner, "Grid interface options for variable speed, permanent magnet generators", IEE Proc.-Electr. Power Appl., Vol 145, No. 4, July 1998.

- L. H. Hansen, L. Helle, F. Blaabjerg, "Conceptual survey of generators and power electronics for wind turbines", Technical report, Risø National Laboratory, Denmark, December, 2001.
- S. Lundberg, "Configuration study of large wind parks", PhD thesis of Electrical power engineering, Chalmers University of Technology, Sweden, 2003.
- N. M. Kirby, L. Xu, M. Luckett, W. Siepmaan, "HVDC transmission for large offshore wind farms", *Power* engineering Journal, June, 2002.
- J. Morren, J.T.G. Pierik, S.W.H. de Haan, J. Bozelie, "Grid interaction of offshore wind farms. Part 1. Models for dynamic simulation", Wind Energy, 8 (3): JUL-SEP 2005
- "Wind Power in Power Systems", John Wiley & Sons, LTD, 2005.
- J. Arrillaga, N.R. Watson, "Computer modeling of electrical power systems", John Wiley & Sons, LTD, Second Edition.
- N.R.Waston, J. Arrillaga, "Power systems electromagnetic transients simulation", *The institution of electrical engineers*, London, United Kingdom, 2003.
- "A Simulation Platform to Model, Optimize and Design Wind Turbines", Institute of Energy Technology, Aalborg University, Denmark.
- N. Mohan, T. M. Undeland, W. P. Robbies, "Power electronics: converters, applications, and design", *John Wiley & Sons, LTD*, Second Edition.
- I. Nagy, D. Miklós, "An Intelligent Three Phase Thyristor Rectifier". Elektrotechnika. 1988., Nr. 8. Vol. 81. pp. 302-312. Budapest.
- Dudrik J., "New Methods in Teaching of Power Electronics Devices", I. Journal Of Electrical And Computer Engineering, Vol. 4, No. 2, Summer-Fall 2005

# Aggregated models of offshore wind farm components

Y. Zhou, P. Bauer, B. Ferreira, J.T.G. Pierik.

PESC 2006

# Aggregated models of offshore wind farm components for grid study

Y. Zhou, P. Bauer, J.A.Ferreira Delft University of Technology Electrical Power Processing 2628 CD, Delft, the netherlands Email: Y.Zhou@ewi.tudelft.nl,

P.Bauer@ewi.tudelft.nl, J.A.Ferreira@ewi.tudelft.nl

Abstract— The large offshore wind farms are planed to be connected with power grid at transmission level due to their large power capacity and possible long transmission distances. HVDC thyristor bridge as well as other integration methods requires systematical integration studies. In this paper, thyristor bridge models developed in Matlab/Simulink are fast and accurate enough for electromechanical and electromagnetic simulations.

#### III. INTRODUCTION

Wind power is the fastest growing power source through out the world in recent years. The offshore wind power draws special attention. The average wind speed offshore is higher than onshore which means larger power production, the turbulence and wind shear effect is lower offshore than onshore which implies higher power quality. These benefits initialize the plans of developing large offshore wind farms in many countries. Unlike the onshore wind turbines which are often dispersed in the distribution grid, the offshore wind turbines will be connected to the transmission grid as large wind farms. The connections between offshore wind farm and power grid can be high voltage alternating connection, high voltage direct current connection using thyristor bridge, or high voltage direct current connection using IGBT switches.

The demonstration offshore projects use HVAC connections at this moment, but HVDC links are superior for large power capacity and long transmission distances. The HVDC system can be current source converters using thyristor bridges or voltage source converters using IGBTs. Voltage source converters using IGBTs have better dynamic behaviors than thyristor bridges during voltage dips, but they are expensive and the power losses are higher. The three integration methods are compared in [1], [2], [3], [4] and [6]. A general conclusion is that HVAC can be used for small wind farm, 200MW for example, and short transmission distance, 100km for example. For large power capacities and long transmission distances, HVDC transmissions are more favorable. Considering the cost and efficiency, HVDC using thyristor bridges can be used for extremely large wind farm, 600 MW for example, which is connected with strong AC grid. HVDC using IGBTs can be integrated with relatively weak grid for its good low voltage J. Pierik
Energy Research Center
of the Netherlands
1755 ZG, Pattern, the Netherlands
Email: Pierik@ecn.nl

ride through capability.

The simulation is a valuable research method, because it makes it possible to investigate the integration problems without the necessary of full-scale test which is often expensive, time consuming and even impossible to be carried out. In [5], dynamic models using Park transformation are developed in Matlab/Simulink. The advantage of using Park transformati on is that voltages and currents under steady state in dq coordinates for balanced three phase system are dc values, very large simulation time steps can be used during steady state, and thus the simulation speed is greatly improved. The models include generator, transformer, transmission line and voltage source converter. As HVDC thyristor bridge can be a choice for integration of large offshore wind farm, thyristor bridge models are developed for grid studies in this paper.

Unlike the voltage source converters using IGBTs which can be modeled by switching functions, the thyristor bridge model is difficult to be modeled because of its uncontrollable switch-off characteristics.

Five models are developed. They are compromises between simulation purposes and simulation speed. For electromechanical simulation purpose, the quasi-steady state model is accurate enough, while for electromagnetic simulations purpose, the instantaneous model is required. All the models are compared with thyristor bridge model of Power System BlockSet in Matlab/Simulink in back to back configurations. They are summarized in table I.

TABLE I LISTS OF THYRISTOR MODELS

Quasi-steady state models	Model 1	Symmetrical quasi-steady model
	Model 2	Unsymmetrical quasi-steady model using Fourier analysis
	Model 3	Unsymmetrical quasi-steady model using partial symmetric
Instantaneous models	Model 4	Instantaneous model without commutation effects
	Model 5	Instantaneous model with commutation effects
Instantaneous models	PSB	Power System BlockSets

# IV. QUASI-STEADY STATE THYRISTOR BRIDGE MODELS IN DQ0 COORDINATES

In the quasi-steady state models, the converters are represented by equations relating average values of dc quantities and RMS values of ac fundamental components. It would accurately represent the HVDC thyristor bridges system performance in the electromechanical simulations.

The assumptions made for the quasi-steady state models are:

- The implementation of fire angle is instantaneous compared with slow a.c. system dynamics;
- The AC voltages and currents are assumed to be purely sinusoidal at fundamental frequency and all higher order harmonics are filtered out.
- The DC side voltage is considered to be smooth and it is the average value per 60 degrees;
- The DC side current is considered to be smooth due to the large smoothing DC inductance.

The inputs of the model are three phase voltages in dq0 coordinates  $v_d$ ,  $v_q$  and  $v_0$  and the DC current  $I_{dc}$ ; the outputs are three phase currents  $i_d$ ,  $i_q$ ,  $i_0$  and DC voltage  $V_{dc}$ .

#### A. Model 1

Under balanced three phase system, the 0 components  $v_0$  and  $i_0$  are always zero. The RMS values and phase angles of voltage and current of phase-a can be calculated from  $v_d$ ,  $v_q$  and  $I_{dc}$  as:

$$\begin{split} V_a &= \frac{\sqrt{V_d^2 + V_q^2}}{\sqrt{3}}, \phi_{va} = \frac{\pi}{2} + \arctan(\frac{V_q}{V_d}), \\ I_a &= k \frac{\sqrt{6}}{\pi} I_{dc}, \phi_{ia} = \phi_{va} - \phi_{vi}, \\ \phi_{vi} &\approx \alpha + \frac{\mu}{2}, \mu = \frac{2\omega L \cdot I_{dc}}{\sqrt{2} U_{LL} \sin \alpha} \end{split}$$

where  $\alpha$ ,  $\mu$  are fire angle and commutation angle respectively,  $k \approx 1$ .

The outputs  $V_{dc}$ ,  $i_d$  and  $i_q$  are  $^{[7],\,[8],\,and\,[10]}$ :

$$V_{dc} = \frac{3\sqrt{2}}{\pi} \sqrt{3} V_a \cos \alpha - \frac{3}{\pi} \omega L I_{dc},$$
  

$$i_d = \sqrt{3} I_a \sin \phi_a, i_a = -\sqrt{3} I_a \cos \phi_a$$

Under balanced three phase system, voltages and currents in dq0 coordinates are time invariables, some numerical integration methods are very efficient for these calculations. But for an unbalanced three phase system, voltages and currents in the d, q, 0 coordinates are all time variables. After Park's transformation, the values in d and q coordinates are second order frequency components and the 0 values are the fundamental frequency components. More important, the RMS values and phase angles of phase voltages are six unknowns which cannot be calculated directly from those three independent equations.

#### B. Model 2 and 3

In the quasi-steady state models 2 and 3, two methods are used to calculate the phasor values from instantaneous values, and lead to two different models:

- Model 2, quasi-steady state model using Fourier analysis for unbalanced three phase system.
- Model 3, Quasi-steady state model using partial symmetric of the unbalanced three phase system.

The first method is rather straightforward, but has shortcomings due to the Fourier analysis. The output DC voltage lags the change of input ac voltages with one cycle 0.02s.

The second method assumes that partial symmetric still exists under unbalanced three phase system. For example, when a single line to ground fault happens in phase a, the RMS values of b and c phase are equal. When double lines to ground fault or double line to line fault happen in phase b and phase c, the RMS values of b and c phase are still equal. The assumptions are:

- Two phase voltages' RMS values are always the same;
- The phase angles of phase voltages are displaced with each other in 120 degree.
- The above two methods are used to calculate the RMS values and phase angles of AC voltages from the instantaneous v<sub>d</sub>, v<sub>q</sub> and v<sub>0</sub>.

The DC voltage and AC current equations for unbalanced three phase systems are much more complex [7]:

$$\begin{split} V_{dc} &= \frac{\sqrt{2}}{\pi} U_{ba} \left[ \cos(C_1 + \alpha - C_3 + \pi) - \cos(C_2 + \alpha - C_1 + \pi) \right] \\ &+ \frac{\sqrt{2}}{\pi} U_{ac} \left[ \cos(C_2 + \alpha - C_1) - \cos(C_3 + \alpha - C_1) \right] \\ &+ \frac{\sqrt{2}}{\pi} U_{bc} \left[ \cos(C_3 + \alpha - C_2) - \cos(C_1 + \alpha + \pi - C_2) \right] \\ &- \frac{I_{dc} (\omega L_1 + \omega L_2 + \omega L_3)}{\pi} \\ I_i &= \frac{4}{\pi} \frac{I_{dc}}{\sqrt{2}} \sin(\frac{T_i}{2}) \\ \phi_{Vi} &= \alpha + \frac{u_i}{2}, \phi_{Ii} = \phi_V - \phi_{Vi}, \\ \mu_1 &= \arccos \left( \cos \alpha - \frac{\omega L_1 + \omega L_3}{\sqrt{2} V_{ac}} \cdot I_{dc} \right) - \alpha \\ \mu_2 &= \arccos \left( \cos \alpha - \frac{\omega L_2 + \omega L_1}{\sqrt{2} V_{ba}} \cdot I_{dc} \right) - \alpha \\ \mu_3 &= \arccos \left( \cos \alpha - \frac{\omega L_2 + \omega L_3}{\sqrt{2} V_{bc}} \cdot I_{dc} \right) - \alpha \end{split}$$

 $\alpha_i$ ,  $\mu_i$  are fire angles and commutation angles respectively.  $C_i$  are the initial angles of line to line voltages, and  $T_i$  are conduction periods of each phase as shown in figure 1.

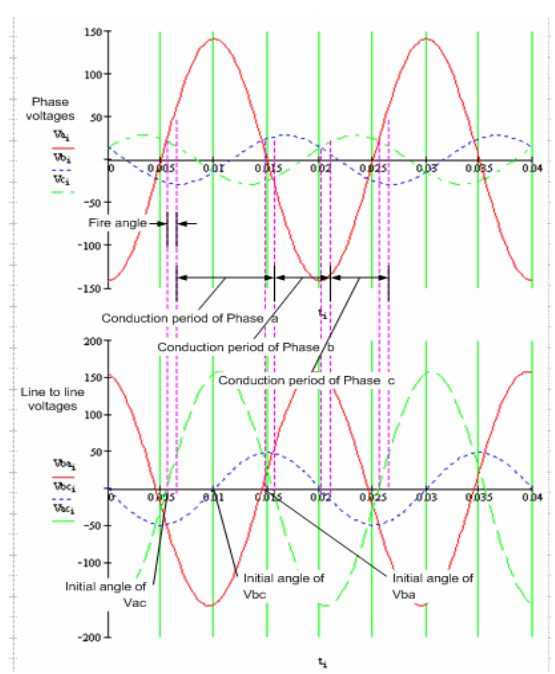


Figure 1: A sample of unsymmetrical voltages

Both methods have their own limitations:

- The Fourier analysis cause phase shifts and value deviations on the output signals.
- The assumption that the phase angles of each phase voltage are displaced with each other in 120 degree may not be true during the real unsymmetrical faults.

#### V. INSTANTANEOUS THYRISTOR BRIDGE MODELS

Due to the above mentioned limitations of quasi-stead state models for unbalanced three phase system, two instantaneous thyristor bridge models are developed. In order to calculate the instantaneous DC voltage and AC current, a state matrix SW of thyristor bridge is calculated with switching function, and the instantaneous DC voltage and AC currents are calculated by the state matrix.

The schematic of three-phase thyristor bridge is shown in Figure 2.

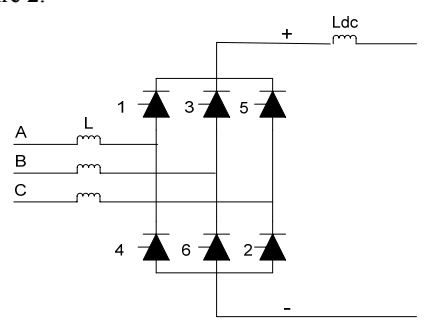


Figure 2: Schematic of thyristor bridge

The thyristor is switched on by a pulse signal on the gate, but can not be switched off by gate signal. It is switched off only when the current flowing through approaches zero.

An instantaneous model of a three-phase diode bridge without commutation effects is realized in Simulink in [9]. There is no instantaneous thyristor bridge model in Matlab/Simulink.

#### A. Model 4

Considering the commutation effect in thyristor bridge model will need many more integrators to calculate the instantaneous phase currents during commutation period. The large number of integrators decreases the simulation speed distinctively.

Considering the simulation speed, the first instantaneous model does not include the commutation effects of AC inductances. The thyristor is switched off actively as a GTO. This means:

- At any time, only one thyristor in the upper group and one thyristor in the lower group are conducting;
- The DC voltage V<sub>dc</sub> always equals to the line to line voltages;
- The AC phase currents change instantaneously between DC current and 0.

The states of six thyristor are assigned as table II.

TABLE II THYRISTOR STATES

	Conducting	Blocked
T1, T3, T5	1	0
T4, T6, T2	-1	0

The conducting sequence of the thyristor bridge in one cycle is listed in table III.

TABLE III
THYRISTOR BRIDGE CONDUCTION SEQUENCE

Conducting thyristor	DC voltage	ia	ib	ic
T1, T2	Va-Vc	Idc	0	-Idc
T3, T2	Vb-Vc	0	Idc	-Idc
T3, T4	Vb-Va	-Idc	Idc	0
T5, T4	Vc-Va	-Idc	0	Idc
T5, T6	Vc-Vb	0	-Idc	Idc
T1, T6	Va-Vb	Idc	-Idc	0

For model 4, the switching function, DC voltage  $V_{\text{dc}}$  and three phase AC currents can be calculated as

$$SW = \begin{bmatrix} T1 + T4 \\ T3 + T6 \\ T5 + T2 \end{bmatrix}, V_{dc} = SW \cdot \begin{bmatrix} V_a \\ V_b \\ V_c \end{bmatrix}, \begin{bmatrix} I_a \\ I_b \\ I_c \end{bmatrix} = SW \cdot I_{dc}$$

#### B. Model 5

Neglecting the commutation effect will lead to large errors when the ac inductances are large. More importantly, the commutation failure cannot be observed in the simulation during voltage dips.

Model 5 considers the commutation effects of the AC line inductances. For simplify reasons, the following

assumptions are made:

• During commutation periods, the DC current is constant  $(\frac{dI_{dc}}{dt} \approx 0)$ .

Based on this assumption, the DC voltage and AC phase currents can be calculated:

- The DC voltage during the commutation periods is  $V_{dc} = \frac{1}{2}(v_i + v_j)$ ,  $v_i$  and  $v_j$  are the phase voltages of commutating phases.
- To avoid the algebraic loops in Simulink, the DC voltage during other periods is  $V_{dc} = v_i v_j$ ,  $v_i$  and  $v_j$  are the phase voltages of the conducting phases.
- AC currents during commutation periods are  $i(t) = i(t_0) + \frac{1}{2L} \int_{t_0}^{t} (v_i v_j) dt$ .
- Ac currents at other periods are  $i(t) = I_{dc}$

The switching functions are much more complex compared with switching function of model 4, and they are not the same for DC voltage and phase currents. Generally, it can be represented by the following matrix.

$$SW = \begin{bmatrix} s_{a} & s_{ab} & s_{ac} \\ s_{ba} & s_{b} & s_{bc} \\ s_{ca} & s_{cb} & s_{c} \end{bmatrix}$$

DC voltage and phase currents can be calculated by

$$V_{dc} = SW_{v} \cdot \begin{bmatrix} V_{a} \\ V_{b} \\ V_{c} \end{bmatrix}, \begin{bmatrix} I_{a} \\ I_{b} \\ I_{c} \end{bmatrix} = SW_{i} \cdot \begin{bmatrix} I_{dc} + \frac{1}{2L} \int (v_{i} - v_{j}) dt \\ I_{dc} + \frac{1}{2L} \int (v_{i} - v_{j}) dt \\ I_{dc} + \frac{1}{2L} \int (v_{i} - v_{j}) dt \end{bmatrix}$$

#### VI. IMPLEMENTATION IN MATLAB/SIMULINK

All the five new models are implemented in Matlab/Simulink. The inputs are instantaneous three phase AC voltages  $v_d,\,v_q,\,v_0,\,DC$  currents  $I_{dc}$  and fire angle  $\alpha$ ; the outputs are DC voltage  $V_{dc}$  and instantaneous three phase AC currents  $i_d,\,i_q,\,i_0.$ 



Figure 3: General view of thyristor bridge model in Matlab/Simulink

In the quasi-steady state models, an interface is used to calculate the phasor values such as RMS voltages and phase angles from the input instantaneous values. The main differences between three quasi-steady state models are the implementations of this interface:

• Model 1, directly calculation for balanced three phase

- system;
- Model 2, Fourier analysis for unbalanced three phase system;
- Model 3, Use partial symmetric of unbalanced three phase system.

In the two instantaneous models, firing pulses are used to trigger the thyristors which are represented by flip-flops.

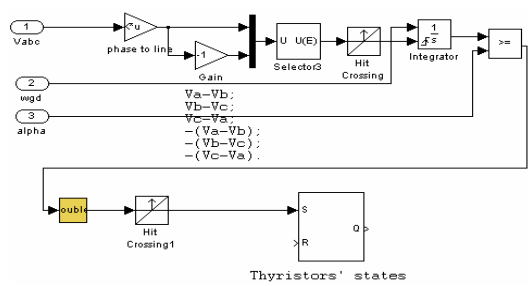


Figure 4: Firing pulses of thyristor bridge

The difference between the two instantaneous models is the reset signals of flip-flops. In model 4 it is the firing pulse of the next thyristor following the firing sequence and in the second model the reset signal is the thyristor's own currents. Thus the commutation effects are implemented in model 5.

To avoid that the zero current resets the flip-flops at the beginning of conduction period, a pulse width of 15 degree is used to block the currents at the beginning of conduction.

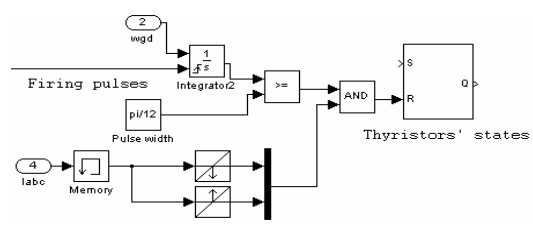


Figure 5: thyristor currents as reset signals

In order to get a converged solution in Matlab/Simulink, the thyristor currents are values from one simulation step

TABLE IV
SIMULATION PARAMETERS AND SIMULATION EVENTS

Parameters			
Rectifier side AC voltages		1e5 (v)	
Rectifier fire angle		30 (degree)	
Inverter side AC voltages		0.7e5 (v)	
Inverter fire angle		120 (degree)	
AC inductance		0.01 (H)	
DC resistance		10 (Ω)	
DC inductance		0.1 (H)	
Events			
Simulation 1	Fire angle of rectifier changes from 30 degree to 45 degree at 1.0s.		
Simulation 2	Inverter side phase-a voltage decreases from 0.7e5 to 0.5e5 volts at 1.0s.		

earlier. This introduces one simulation step error in the

switching functions at the end of each commutation period, and thus the DC voltage and AC phase currents all have errors. As the simulation steps are small around the end of commutation period, these errors can be assumed small.

#### VII. VERIFY THE THYRISTOR BRIDGE MODELS IN BACK TO BACK CONFIGURATIONS

All the five new models are compared with models from Power System BlockSets in back to back configurations as shown in Figure 6.

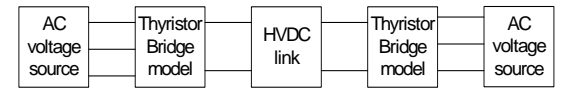


Figure 6: Back to back configuration of thyristor bridges

Two sets of simulations are carried out.

First set "simulation 1" is applied to all five models to compare the results under symmetrical situations.

The second set "simulation 2" is applied to the four models except model 1. It is used to compare the results under unsymmetrical situations.

They have the same parameters but different events.

The following graphs compare the results of five models and model from PSB in "Simulation 1".

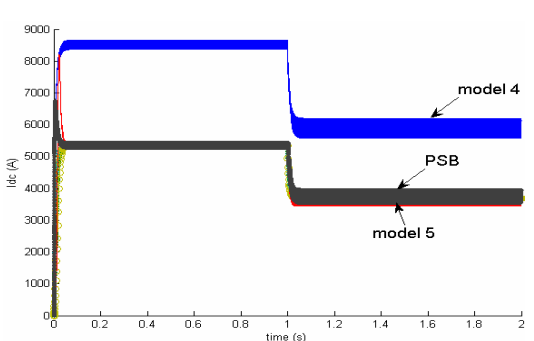


Figure 7: DC currents of all models of "simulation 1"

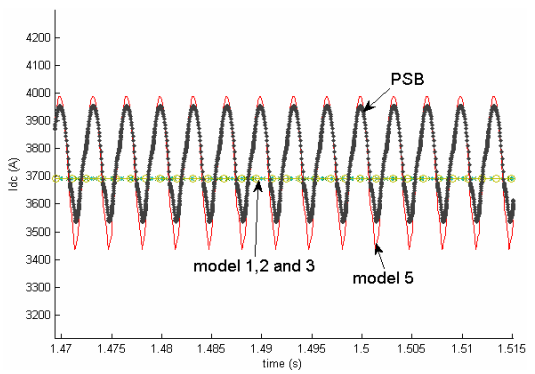


Figure 8: DC currents of Models 1,2,3,5 and PSB of "simulation 1"

As shown in Figure 7, neglecting the commutation effects will cause large errors in the DC current when the AC line inductances are large.

In Figure 8, the DC currents of quasi-steady models 1, 2, 3 are exactly the same.

The small differences between the DC currents of PSB and model 5 are caused by the assumption used in model 5 which assumes the DC voltage outside the commutation periods is  $V_{dc} = v_i - v_j$ . However, the average DC currents of model 5 and PSB are almost the same, and they equal to the DC currents of models 1, 2 and 3, so the active power transferred by the thyristor bridges of all the models except model 4 are the same. This proves that models 1, 2, 3, and 5 are accurate enough for electromechanical simulations.

In the second simulation, the results of model 2, 3, 4 and 5 are compared with PSB as shown in Figure 9.

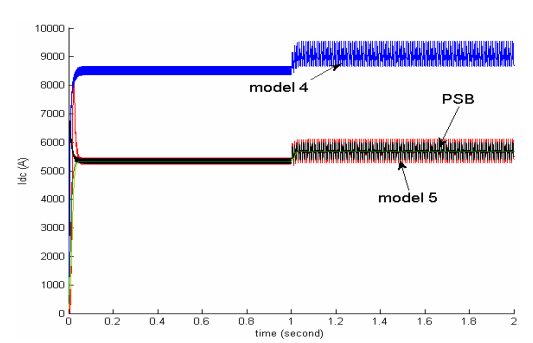
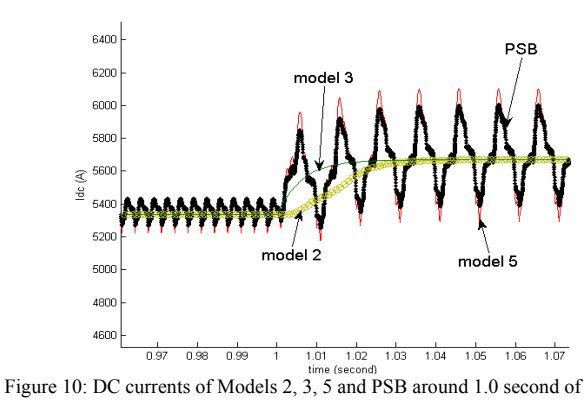


Figure 9: DC currents of models 2, 3, 4, 5 and PSB of "simulation 2"



"simulation 2"

Same as the previous simulation, Figure 9 shows that the DC current of model 4 has very large errors because it omits the commutation effects.

Due to the Fourier analysis, the DC current of model 2 lags model 3 around one cycle (0.2 second) until they reached the same steady state value.

The DC current of model 5 has only small difference compared with PSB.

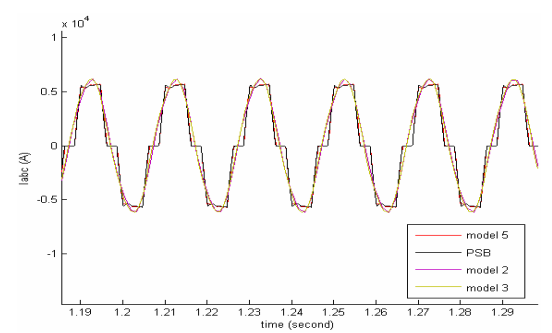


Figure 11: Inverters' AC phase-a currents of model 2, 3, 5 and PSB

In Figure 11, the two sinusoidal waveforms are the inverters' phase-a currents of model 2 and 3; two trapezoidal waveforms are those of model 5 and PSB.

It is clear that the phase currents have nearly the same phase angles and RMS values except that the instantaneous models have trapezoidal wave shapes which contain high order harmonics.

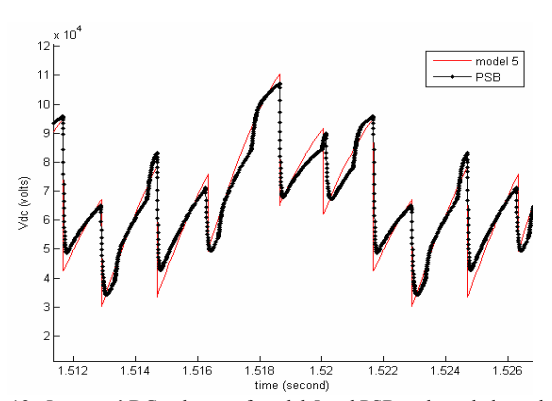


Figure 12: Inverters' DC voltages of model 5 and PSB under unbalanced three phase system

Figure 12 compares the DC voltages of model 5 and PSB under unbalanced situations.

The above results prove that model 5 is accurate. Model 3 is accurate if the two assumptions of that model can be fulfilled. Model 2 is accurate during steady state, but has significant errors during transient state.

The required time for simulating specific time period of dynamics of all models are recorded and compared. Results are shown in table V.

TABLE V
THYRISTOR BRIDGE CONDUCTION SEQUENCE

Model name	Required simulation time
Model 1	1 second
Model 2	4 second
Model 3	3 second
Model 4	8 second
Model 5	40 second
PSB	220 second

#### VIII. CASE STUDY

Comparing different types of wind turbines, the doubly fed induction generator is studied in this case. The topology is shown in the following graph.

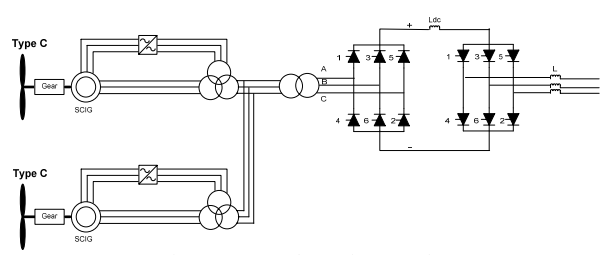


Figure 13: Topology of case study

The reasons to use doubly fed induction generators with thyristor bridge in this case study are its superior reactive power control capability comparing with fixed speed induction generator and its lower investment cost comparing with permanent magnet generator.

As the thyristor bridge absorbs reactive power, the conventional unit power control of doubly fed induction generator has to be modified. A voltage droop controller is implemented to control the voltage of ac wind farm. The frequency of ac wind farm is set to be 50 Hz because the doubly fed induction generator at present is designed to work best at this stator frequency.

At steady state, the controllers of thyristor bridge are implemented as:

- The inverter controller is a minimum extinction angle control, which sets up the dc voltage level, and absorbs the minimum reactive power from grid.
- The rectifier controller determines the power transmitted through the HVDC link by controlling the fire angle α. The power reference of the controller is the sum of the active power reference of all the doubly fed induction generators.

During grid voltage dip, the grid ac voltage is reduced, which affects the operation of thyristor bridge in the following ways:

- The inverter dc voltage will decrease, and the dc current will increase.
- If the voltage dip is serious, then a commutation failure may happen.

If commutation failure happens, the inverter is short circuited and no power can be transmitted through HVDC link. The inverter's extinction angle is then advanced to avoid the commutation failure and the rectifier's fire angle is increased to limit the dc current.

#### IX. CONCLUSIONS

Three quasi-steady state thyristor bridge models for balanced or unbalanced three phase system are presented in this paper which can be used for electromechanical simulations. Two instantaneous models with and without commutation effects are also developed.

Compared with model from Power System BlockSets, all the quasi-steady thyristor bridge models are proved to be fast and accurate for balanced three phase system. For unbalanced three phase system, the two unsymmetrical quasi-steady state models have their own shortcomings: model 2 has a time lag due to the Fourier analysis, and model 3 can only be used when phase angles of three phase voltages are displaced with each other in 120 degree. The instantaneous model without commutation effects has large errors if the ac inductances are large. The Instantaneous model with commutation effects is accurate and more time efficient than Power System BlockSets. It can be used for either balanced or unbalanced three phase case studies, either electromechanical or electromagnetic simulations.

#### ACKNOWLEDGMENTS

This work is part of the project PhD@Sea, which is substantially funded under the BSIK-program of the Dutch Government and supported by the consortium WE@Sea.

#### REFERENCES:

- Z. Chen, E. Spooner, "Grid interface options for variable speed, permanent magnet generators", IEE Proc.-Electr. Power Appl., Vol 145, No. 4, July 1998.
- [2] L. H. Hansen, L. Helle, F. Blaabjerg, "Conceptual survey of generators and power electronics for wind turbines", Technical report, Risø National Laboratory, Denmark, December, 2001.
- [3] S. Lundberg, "Configuration study of large wind parks", PhD thesis of Electrical power engineering, Chalmers University of Technology, Sweden, 2003.
- [4] N. M. Kirby, L. Xu, M. Luckett, W. Siepmaan, "HVDC transmission for large offshore wind farms", Power engineering Journal, June, 2002
- [5] J. Morren, J.T.G. Pierik, S.W.H. de Haan, J. Bozelie, "Grid interaction of offshore wind farms. Part 1. Models for dynamic simulation", Wind Energy, 8 (3): JUL-SEP 2005.
- [6] "Wind Power in Power Systems", John Wiley & Sons, LTD, 2005.
- [7] J. Arrillaga, N.R. Watson, "Computer modeling of electrical power systems", John Wiley & Sons, LTD, Second Edition.
- [8] N.R.Waston, J. Arrillaga, "Power systems electromagnetic transients simulation", The institution of electrical engineers, London, United Kingdom, 2003.
- [9] "A Simulation Platform to Model, Optimize and Design Wind Turbines", Institute of Energy Technology, Aalborg University, Denmark.
- [10] N. Mohan, T. M. Undeland, W. P. Robbies, "Power electronics: converters, applications, and design", John Wiley & Sons, LTD, Second Edition.

# Control of DFIG under unsymmetrical voltage dip

Y. Zhou, P. Bauer, B. Ferreira, J.T.G. Pierik.

PESC 2007

# Control of DFIG under unsymmetrical voltage dip

Y. Zhou, P. Bauer, J. A. Ferreira Delft University of Technology Mekelweg 4, 2628CD, Delft, the Netherlands

Abstract- Today, doubly fed induction generator (DFIG) gains the dominant market power in the wind energy industry. It provides the benefits of variable speed operation cost-effectively, and can control its active and reactive power independently. Crowbar protection is often adopted to protect the rotor side voltage source converter (VSC) from transient over current during grid voltage dip. But under unsymmetrical voltage dip, the severe problems are not the transient over current, but the electric torque pulsation and DC voltage ripple in the back to back VSCs. This paper develops dynamic models in Matlab/Simulink, investigates the behavior of DFIG during an unsymmetrical voltage dip, and proposes new controllers in separated positive and negative sequence. Methods to separate positive and negative sequence components in real time are also developed, and their responses to unsymmetrical voltage dip are compared. Simulation results prove that the separated positive and negative sequence controller limit the torque pulsation and DC voltage ripple effectively.

#### I. INTRODUCTION

The wind generation in Europe reached approximately 33,600 MW until the end of 2004. The demands of connecting large scale wind parks to the power grid are increasing. Nowadays, the large scale wind farms are required to be controllable both in active and reactive power, and to have the low voltage ride through capability when grid faults happen. Because of its ability to provide variable speed operation and independent active and reactive power control in a costeffective way, the doubly fed induction generator (DFIG) has the largest world market share of wind turbine concepts since the year 2002 [1]. Many researches have studied the low voltage ride through (LVRT) capability of DFIG [3] [4] [5] [6] [7], most of them are focused on the behaviors and protections of DFIG under symmetrical fault. Transient over current in the rotor is identified as the most severe LVRT problem of the DFIG, because the rotor side voltage source converter (VSC) is very sensitive to thermal overload. The active crowbar protection is designed to short circuit the rotor under such circumstance, both to protect the rotor side VSC and to damp out the oscillations faster. In reality, unsymmetrical fault happens much more frequently than symmetrical fault. Under unsymmetrical fault, the most severe problem is not the transient over current in the rotor, but the large electric torque pulsation which causes tear and wear of the gearbox, and large voltage ripple in the DC link of back to back VSC which may decrease the lifetime of the DC capacitance. Literatures [8] and [9] give new definitions of instantaneous active and reactive power. These definitions can be used to design and operate the grid connected VSC under unbalanced situations [10] [11]. Unlike the normal grid connected VSC which has a

## J. Pierik Energy Research Center of Netherlands

Westerduingweg 3, 1755 ZG, Pattern, the Netherlands

constant instantaneous active power input from the rectifier side in the above literatures, the rotor side VSC of DFIG can also send pulsating instantaneous active power to the DC link. Thus it is necessary to study the behavior of DFIG under unsymmetrical voltage dip, and design proper controllers to improve the behaviors of DFIG under unsymmetrical voltage dip.

#### II. DFIG SYSTEM DESCRIPTION

#### A. System description

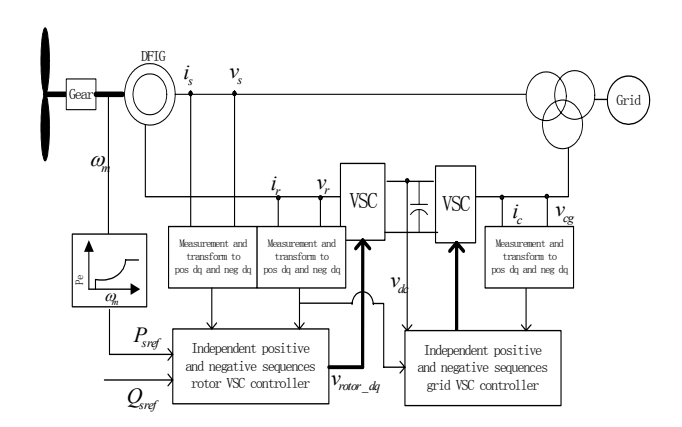


Figure 1 simplified diagram of DFIG system with proposed controllers

Figure 1 describes the DFIG system and the proposed controllers. The controllers of rotor VSC and grid VSC control stator currents and grid converter currents, both in independent positive and negative sequences. According to symmetrical components theory [2], during unbalanced voltage dip, the system can be decoupled into positive, negative and zero sequence. Positive and negative sequences are balanced three phase systems, they can be transferred to positive dq and negative dq system. Their voltages and currents are DC values and can be easily controlled by simple PI controller.

The positive and negative sequence has to be totally decoupled. Otherwise, when controlling the positive sequence, the negative sequence will be influenced, and vice versa. The coupling between positive and negative sequence will deteriorate the control performance.

In order to fully decouple positive and negative sequence, the following assumptions are made:

 DFIG's stator and rotor windings are assumed to be in symmetrical.  Grid VSC's three phase ac inductances and resistances are in symmetrical.

The reference stator currents and grid converter currents are calculated according to instantaneous reactive power theory. The instantaneous reactive power theory is given in [8] and [9]. When applying it on a three phase three line power system, the theory is simple and easy to understand. It becomes complex for three phase four line power system. In this paper, only three phase three line power system is studied, the zero sequence is omitted. This choice is justified by the following reasons:

- The transformer is often  $Y/\Delta$  connected.
- The neutral point of stator winding of DFIG is not grounded.

In the next sections, the simulation results of DFIG under symmetrical and unsymmetrical voltage dips will be presented first, then the instantaneous reactive power theory will be used to analyze this result.

#### B. Symmetrical and unsymmetrical voltage dip

Distinctive differences between the behaviors of DFIG under symmetrical and unsymmetrical voltage dips can be identified as Figure 2.

Figure 2 (a) shows that under symmetrical voltage dip, the most severe problem is the transient over current in the rotor. This over current problem is generally protected by the so called "crowbar protection", which use thyristor controlled resistor bank to short circuit the rotor windings.

Figure 2 (a) shows that under unsymmetrical voltage dip, the maximum rotor currents are smaller, but have second order harmonics, and cause large DC voltage ripples in the DC link. A noticeable point is that the magnitude of rotor transient currents under unsymmetrical voltage dip also depends on the starting moment of the dip. The starting moment of the voltage dip determines the initial conditions of the stator currents, and thus determines the natural response of the stator currents. The natural response of stator currents has a large influence on the transient rotor currents.

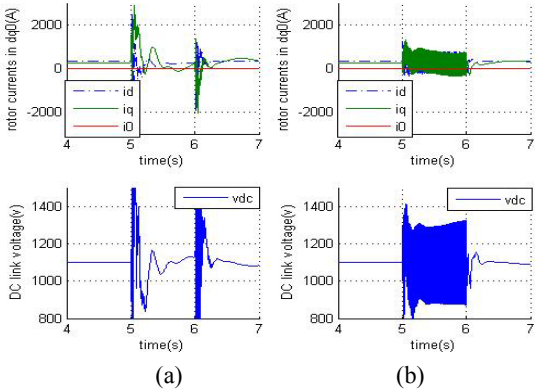


Figure 2simulation results of DFIG under (a) symmetrical and (b) unsymmetrical voltage dips. Graphs from top to bottom are rotor currents and DC voltage, respectively.

C. Applying Instantaneous reactive power theory on separated positive dq and negative dq sequence

According to instantaneous reactive power theory [8], the instantaneous power p and q in stationary  $\alpha\beta$  reference frame are

$$\begin{bmatrix} p \\ q \end{bmatrix} = \begin{bmatrix} v_a i_a + v_\beta i_\beta \\ v_\beta i_a - v_a i_\beta \end{bmatrix} \tag{1}$$

Eq. (1) is true for both balanced and unbalanced three phase three line system. The stationary  $\alpha\beta$  reference frame can be decoupled into positive and negative sequence as Eq.(2).

$$\begin{bmatrix} v_{\alpha}(t) \\ v_{\beta}(t) \end{bmatrix} = \begin{bmatrix} v_{\alpha}^{+}(t) + v_{\alpha}^{-}(t) \\ v_{\beta}^{+}(t) + v_{\beta}^{-}(t) \end{bmatrix}$$
 (2)

Using Eq. (1), Eq.(2) and Park's transformation, the instantaneous active and reactive power of positive and negative dq sequences can be derived as Eq. (3).

$$\begin{bmatrix} p \\ q \end{bmatrix} = \begin{bmatrix} \overline{p} + \widetilde{p} \\ \overline{q} + \widetilde{q} \end{bmatrix} = \begin{bmatrix} (v_{d}^{\dagger} i_{d}^{\dagger} + v_{q}^{\dagger} i_{q}^{\dagger} + v_{d}^{\dagger} i_{d}^{\dagger} + v_{q}^{\dagger} i_{q}^{\dagger}) \\ (v_{q}^{\dagger} i_{d}^{\dagger} - v_{d}^{\dagger} i_{q}^{\dagger} + v_{q}^{\dagger} i_{d}^{\dagger} - v_{d}^{\dagger} i_{q}^{\dagger}) \end{bmatrix}$$

$$+ \sin(2\theta) \begin{bmatrix} (v_{d}^{\dagger} i_{q}^{\dagger} - v_{q}^{\dagger} i_{d}^{\dagger} + v_{q}^{\dagger} i_{d}^{\dagger} - v_{d}^{\dagger} i_{q}^{\dagger}) \\ (v_{d}^{\dagger} i_{d}^{\dagger} + v_{q}^{\dagger} i_{q}^{\dagger} + v_{d}^{\dagger} i_{d}^{\dagger} + v_{q}^{\dagger} i_{q}^{\dagger}) \end{bmatrix}$$

$$+ \cos(2\theta) \begin{bmatrix} v_{d}^{\dagger} i_{d}^{\dagger} - v_{q}^{\dagger} i_{q}^{\dagger} + v_{d}^{\dagger} i_{d}^{\dagger} + v_{q}^{\dagger} i_{q}^{\dagger} \\ v_{d}^{\dagger} i_{q}^{\dagger} - v_{q}^{\dagger} i_{d}^{\dagger} + v_{q}^{\dagger} i_{d}^{\dagger} - v_{d}^{\dagger} i_{q}^{\dagger} \end{bmatrix}$$
(3)

The terms of  $sin(2\theta)$  and  $cos(2\theta)$  in Eq. (3) are the oscillation parts of instantaneous power p and q. The oscillation parts of instantaneous active power p will cause DC voltage ripple and electric torque pulsation, such as shown in simulation results of DFIG in Figure 2.

In order to limit the DC voltage ripple or torque pulsation under unsymmetrical voltage dip, the terms of  $\sin(2\theta)$  and  $\cos(2\theta)$  of instantaneous active power p in Eq. (3) has to be controlled to zero. Rearranging Eq. (3), four independent equations can be used to determine the four reference currents  $i_d^+$ ,  $i_q^+$ ,  $i_d^-$ ,  $i_q^-$ , and the currents can be controlled by voltages of VSC  $v_d^+$ ,  $v_q^+$ ,  $v_d^-$ ,  $v_q^-$  with simple PI controllers.

$$\begin{bmatrix} \overline{p} \\ \overline{q} \\ \widetilde{p}_{\sin 2\theta} \\ \widetilde{p}_{\cos 2\theta} \end{bmatrix} = \begin{bmatrix} P_{ref} \\ Q_{ref} \\ 0 \\ 0 \end{bmatrix} = \begin{bmatrix} v_d^+ i_d^+ + v_q^+ i_q^+ + v_d^- i_d^- + v_q^- i_q^- \\ v_q^+ i_d^+ - v_d^+ i_q^+ + v_q^- i_d^- - v_d^- i_q^- \\ v_d^+ i_q^- - v_q^+ i_d^- + v_q^- i_d^+ - v_d^- i_q^+ \\ v_d^+ i_d^- + v_q^+ i_q^- + v_d^- i_d^+ + v_q^- i_q^+ \end{bmatrix}$$
(4)

 $\tilde{p}_{\sin 2\theta}$  and  $\tilde{p}_{\cos 2\theta}$  are the two oscillation terms of instantaneous active power p. In order to control them to zero, instantaneous voltage and current has to be separated to positive and negative sequence in real time.

## III. REAL TIME SEPARATION OF POSITIVE AND NEGATIVE SEQUENCES

The proposed control method requires fast and accurate separation of positive and negative sequences. Two methods are often used [10].

The first method is based on the fact that the negative sequence component appears as second order harmonic in the synchronous rotating frame - positive dq, and the positive sequence component appears as second order harmonic in the negative synchronous rotating frame - negative dq. The low pass filter can be used to bypass the DC values and suppress the high frequency oscillations. Thus the positive and negative sequences are separated in real time. The description of this method is shown in Figure 3.

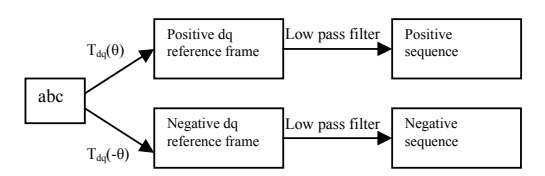


Figure 3 Separate positive and negative sequences by low pass filters

The second method is the so called "signal delay cancellation" method. The abc system is first transformed into stationary reference frame  $\alpha\beta$  coordinates using Clark's transformation, then it is delayed for T/4. The positive and negative sequence can be calculated by adding or subtracting the present real time signal with the delayed signal. It is explained mathematically in the following way.

The abc system can be transformed into stationary  $\alpha\beta$  reference frame using Clark's transformation, and can be expressed in positive and negative sequence as:

$$\begin{bmatrix} v_{\alpha}(t) \\ v_{\beta}(t) \end{bmatrix} = \begin{bmatrix} v_{\alpha}^{+}(t) + v_{\alpha}^{-}(t) \\ v_{\beta}^{+}(t) + v_{\beta}^{-}(t) \end{bmatrix} = \begin{bmatrix} v^{+}\cos(\omega t + \phi^{+}) + v^{-}\cos(-\omega t + \phi^{-}) \\ v^{+}\sin(\omega t + \phi^{+}) + v^{-}\sin(-\omega t + \phi^{-}) \end{bmatrix}$$
 (5)

Delay this signal for T/4:

$$\begin{bmatrix} v_{\alpha}(t-\frac{T}{4}) \\ v_{\beta}(t-\frac{T}{4}) \end{bmatrix} = \begin{bmatrix} v^{+}\sin(\omega t + \phi^{+}) - v^{-}\sin(\omega t + \phi^{-}) \\ -v^{+}\cos(\omega t + \phi^{+}) + v^{-}\cos(-\omega t + \phi^{-}) \end{bmatrix}$$
 (6)

Comparing the above equations of  $\alpha\beta(t)$  Eq.(5) and  $\alpha\beta(t-T/4)$  Eq.(6), it is clear that the positive and negative sequence can be derived by adding or subtracting them.

$$\begin{bmatrix} v_{\alpha}^{+}(t) \\ v_{\beta}^{+}(t) \\ v_{\alpha}^{-}(t) \\ v_{\beta}^{-}(t) \end{bmatrix} = \frac{1}{2} \begin{bmatrix} 1 & 0 & 0 & -1 \\ 0 & 1 & 1 & 0 \\ 1 & 0 & 0 & 1 \\ 0 & 1 & -1 & 0 \end{bmatrix} \cdot \begin{bmatrix} v_{\alpha}(t) \\ v_{\beta}(t) \\ v_{\alpha}(t - T/4) \\ v_{\beta}(t - T/4) \end{bmatrix}$$
(7)

The positive and negative sequence in  $\alpha\beta$  coordinates can be further transformed into positive dq and negative dq sequences using Eq.(8).

$$\begin{bmatrix} v_{d}^{+}(t) \\ v_{q}^{+}(t) \end{bmatrix} = \begin{bmatrix} \cos \theta & \sin \theta \\ -\sin \theta & \cos \theta \end{bmatrix} \cdot \begin{bmatrix} v_{\alpha}^{+}(t) \\ v_{\beta}^{+}(t) \end{bmatrix}$$

$$\begin{bmatrix} v_{d}^{-}(t) \\ v_{q}^{-}(t) \end{bmatrix} = \begin{bmatrix} \cos(-\theta) & \sin(-\theta) \\ -\sin(-\theta) & \cos(-\theta) \end{bmatrix} \cdot \begin{bmatrix} v_{\alpha}^{-}(t) \\ v_{\beta}^{-}(t) \end{bmatrix}$$
(8)

At the moment of voltage dip and/or recovering, the "signal delay cancellation" method will have large transients and also a time delay of T/4. This method is summarized as following graph.

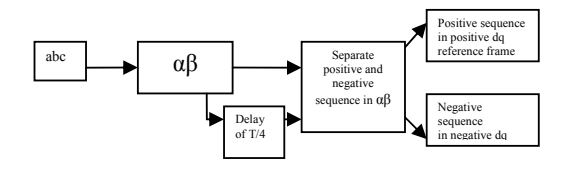


Figure 4 Separate positive and negative sequences by "signal delay cancellation" method

The unbalanced voltages in the positive dq reference frame with and without applying those two separation methods are shown in Figure 5.

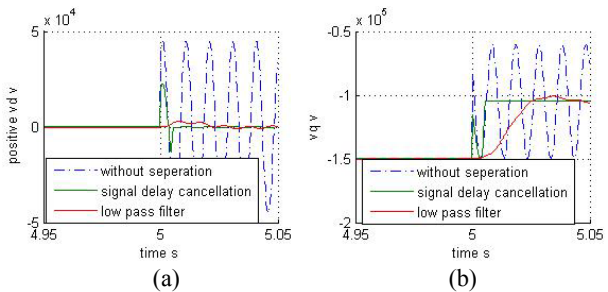


Figure 5 unbalanced voltages in positive dq reference frame with and without using the two separation methods (a) vd (b) vq

Without the two separation methods, the unbalanced three phase voltage or current has second order harmonics in the positive dq reference frame. Both separation methods have time delays before their outputs can reach to steady states. The "signal delay cancellation" is much faster than "low pass filter" method, but it has larger transients at the start and end period of voltage dip.

## IV. SEPARATED POSITIVE AND NEGATIVE SEQUENCE CONTROLLERS OF DFIG

### D. Control of rotor VSC

Assuming the DFIG itself is in symmetric, the voltage equations of positive and negative dq sequence in generator convention are

$$\begin{bmatrix} v_{ds}^{\pm} \\ v_{ds}^{\pm} \\ v_{qr}^{\pm} \end{bmatrix} = \begin{bmatrix} -R_{s}i_{ds}^{\pm} - (\pm\omega_{s}\psi_{qs}^{\pm}) + \frac{d\psi_{ds}^{\pm}}{dt} \\ -R_{s}i_{qs}^{\pm} + (\pm\omega_{s}\psi_{ds}^{\pm}) + \frac{d\psi_{qs}^{\pm}}{dt} \\ -R_{r}i_{dr}^{\pm} - (\pm\omega_{s} - \omega_{r})\psi_{qr}^{\pm} + \frac{d\psi_{dr}^{\pm}}{dt} \\ -R_{r}i_{dr}^{\pm} + (\pm\omega_{s} - \omega_{r})\psi_{dr}^{\pm} + \frac{d\psi_{qr}^{\pm}}{dt} \end{bmatrix}$$

$$(9)$$

In Eq.(9),  $\omega_s$  is the stator electrical angular velocity, and  $\omega_r$  is the rotational speed of rotor times the number of pole pairs  $\omega_m$ ·p.

The positive and negative sequences are completely decoupled as shown in Eq.(9), thus the DFIG can be controlled in positive and negative dq sequence independently. The controller of rotor VSC is designed from Eq.(9), which uses rotor voltages to control stator currents, and uses stator currents to control active and reactive power as shown in Figure 1. The controller is shown in Figure 6.

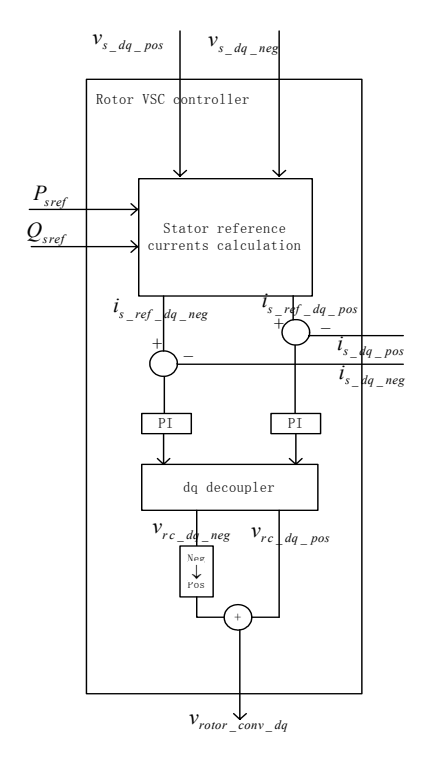


Figure 6 Separated positive and negative sequence controller of rotor VSC

In rotor VSC controller, the cross-coupling terms between d and q coordinates are  $(\pm \omega_s - \omega_r) \psi_{qr}^{\ \pm}$  and  $(\pm \omega_s - \omega_r) \psi_{dr}^{\ \pm}$ . They are different in positive and negative sequence. In order to completely decouple d and q axis, these cross-coupling terms are feed forwarded and added with the outputs of PI controllers.

#### E. Control of grid VSC

Assuming the smoothing ac inductance and resistance of grid VSC is balanced, the voltage equations of positive and negative dq sequence are

$$\begin{bmatrix} v_{dc}^{\pm} \\ v_{qc}^{\pm} \end{bmatrix} = \begin{bmatrix} v_{dg}^{\pm} + R_{c}i_{dc}^{\pm} + (\pm\omega_{s}L_{c}i_{qc}^{\pm}) + L_{c}\frac{di_{dc}^{\pm}}{dt} \\ v_{qg}^{\pm} + R_{c}i_{qc}^{\pm} - (\pm\omega_{s}L_{c}i_{dc}^{\pm}) + L_{c}\frac{di_{qc}^{\pm}}{dt} \end{bmatrix}$$
(10)

Unlike the works presented in [10] and [11], in this paper the DC voltage ripples are caused by both the rotor VSC and grid

VSC. The instantaneous active power of grid VSC has to be controlled in coordination with the rotor VSC, in order to eliminate the DC voltage ripple.

The reference currents of grid VSC are calculated from dc link voltage vdc, grid ac voltage, rotor power, and reference reactive power  $Q_{\text{ref}}$ . The details of this controller can be seen in Figure 7.

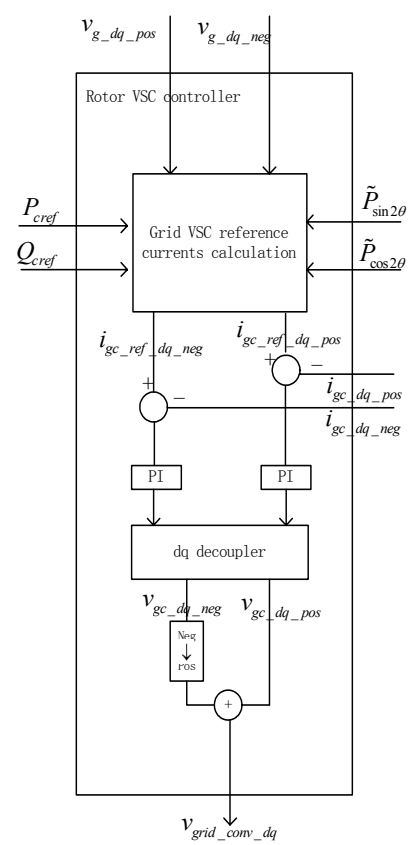


Figure 7 Separated positive and negative sequence controller of grid VSC

In grid VSC controller, the cross-coupling terms between d and q coordinates are  $(\pm \omega_s L_c i_{qc}^{\ \pm})$  and  $(\pm \omega_s L_c i_{dc}^{\ \pm})$ . Same as in the rotor VSC controller, they are feed forwarded and added with outputs of PI controllers.

#### V. MODELING AND SIMULATION

#### A. Modeling DFIG system

The complete DFIG system with controllers is modeled in Matlab/Simulink [3]. These models are developed in the synchronous rotating reference frame in order to improve the simulation speed, because the balanced three phase voltage and current in the synchronous rotating reference frame are DC values at steady state. The simulink model of DFIG system is shown in following graph.

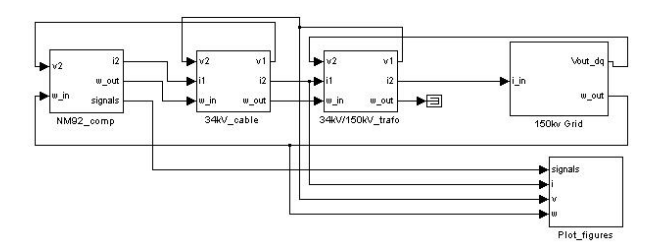


Figure 8 Simulink model of DFIG system

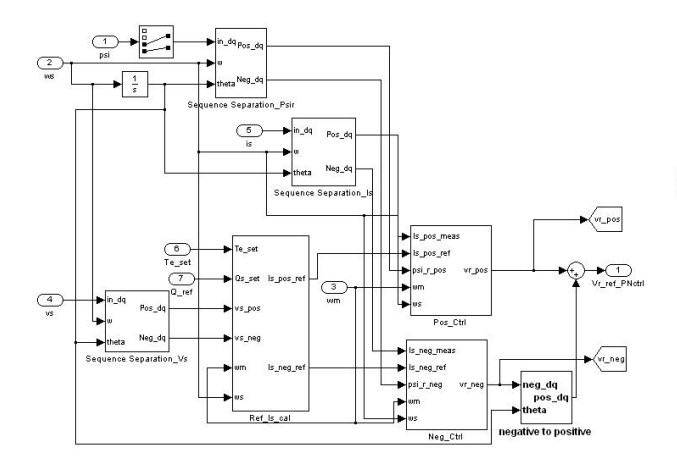


Figure 9 Simulink models of "separated positive and negative sequence controller" of rotor VSC

As shown in Figure 9, the stator voltages and currents are separated by "sequence separation" block, then fed into the "ref\_Ir\_cal" block with reference active and reactive power to calculate the reference stator currents. The stator currents are controlled through "pos\_ctrl" and "neg\_ctrl" blocks separately. Finally the required rotor voltages are calculated, which are assumed they can be perfectly produced by the rotor VSC.

The topology of the controller of grid VSC is quite similar as that of the rotor VSC. The main difference is that it has to be controlled in coordination with rotor VSC, in order to eliminate the effects caused by rotor power oscillations.

In order to improve simulation speed in Matlab/Simulink, the DC link is modified, based on the following equation.

$$v_{dc}(t) = \sqrt{\frac{2}{C}} \left[ \int_{0}^{L} (p_{rec}(t) - p_{inv}(t)) dt + v_{dc}(0)^{2} \right]$$
 (11)

#### B. Separated positive and negative controller of rotor VSC

The effects of proposed controller on rotor VSC can be seen in Figure 10.

The separated positive and negative controller of rotor VSC drastically limits the torque pulsation to less than 20% of the original value. The stator power oscillation is limited, but the rotor power oscillation increases a little bit. As the stator power

often dominates the total power of the generator, the total power oscillation is still limited a lot.

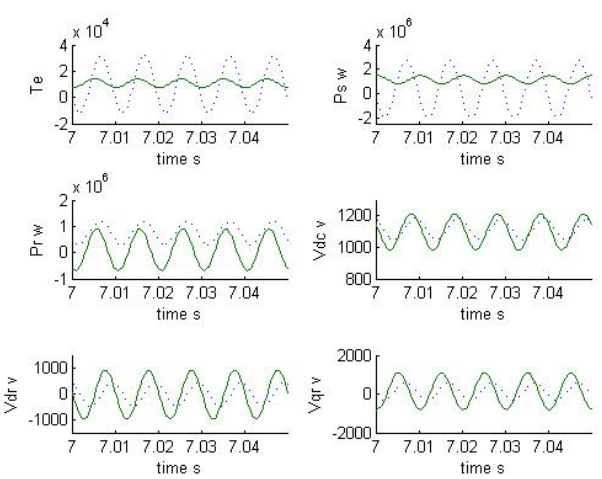


Figure 10 Compare the results of DFIG under unsymmetrical voltage dip with and without "separated positive and negative sequence controller". Dotted line – normal controller, solid line – "separated positive and negative sequence controller". Graphs from left to right and from top to bottom are electric torque Te, stator power Ps, rotor power Pr, DC voltage Vdc, rotor voltage Vdr, and rotor voltage Vqr, respectively.

The rotor reference voltages in positive and negative sequences from normal controller and new controller are shown in Figure 11.

During the unsymmetrical voltage dip, the normal controller also tries to counteract to the 100Hz oscillation in the electric torque Te. It outputs a certain degree of negative sequence voltage, but its output reference voltage is not correct comparing with the new controller as shown in Figure 11.

The normal controller can be tuned very fast to limit the torque pulsations during unsymmetrical voltage dip, but the stability margin will decrease.

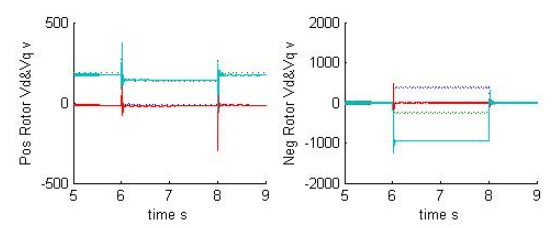


Figure 11 rotor voltages of positive dq and negative dq sequences. Dotted line – normal controller, solid line – "separated positive and negative sequence controller". Left graph is rotor voltage of positive sequence, and right graph is voltages of negative sequence.

## C. Separated positive and negative controller of grid VSC

The effects of proposed controller on grid VSC can be seen in the following graph.

When the grid VSC is controlled separately in positive and negative sequence, and controlled in coordination with the rotor VSC, the DC voltage ripple is drastically limited to less

than 10% of the original value. The instantaneous active power of grid VSC is intended to be controlled to have second order harmonic, in order to compensate the rotor power oscillation.

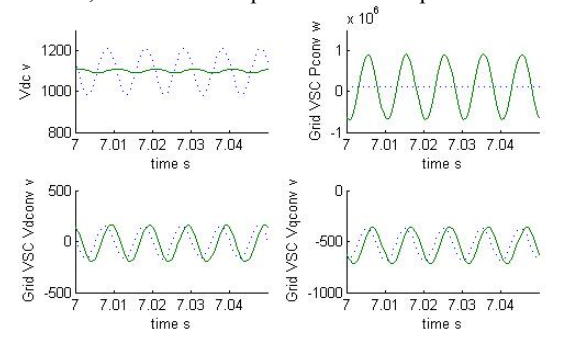


Figure 12 Compare the results of DC link of back to back VSCs under unsymmetrical voltage dip with and without "separated positive and negative sequence" controller. Dotted line – normal controller, solid line – "separated positive and negative sequence controller". Graphs from left to right and from top to bottom are DC voltage Vdc, grid VSC active power, rotor voltage Vdr, and rotor voltage Vqr, respectively.

Same as previously discussion of rotor VSC controller, the normal controller of grid VSC can be tuned very fast to counteract to the DC link voltage ripple, but its stability margin will decrease.

Figure 13 shows the positive dq and negative dq sequence voltages of grid VSC controlled by normal controller and new controller. The positive dq voltages are the same, but negative dq voltages are different.

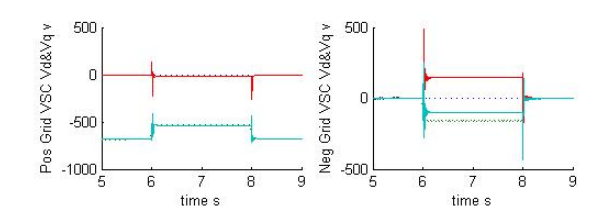


Figure 13grid VSC voltages of positive dq and negative dq sequences. Dotted line – normal controller, solid line – "separated positive and negative sequence controller". Left graph is grid VSC voltage of positive sequence, and right graph is voltages of negative sequence.

#### VI. CONCLUSIONS AND RECOMMENDATIONS

The LVRT capability of DFIG under symmetrical voltage dip has been thoroughly investigated in many researches, while DFIG's behavior under unsymmetrical voltage dip is seldom studied. Instead of the large transient rotor current which is caused by the symmetrical voltage dip, the large electric torque pulsation and DC voltage ripple in back to back VSCs are identified as the most severe problems of DFIG under unsymmetrical voltage dip. In this paper, the DFIG is proposed to be controlled in positive and negative sequence independently. In order to implement the separated positive and negative sequence controllers of DFIG, two methods to separate positive and negative sequence in real time are

compared. The "signal delay cancellation" is much faster than the "low pass filter", and is chosen in this study. Equations of instantaneous active p and reactive power q, and voltage equations of DFIG and grid VSC in positive dq and negative dq sequence are derived. The complete DFIG system with proposed controller is modeled in Matlab/Simulink. The simulation results prove that the independent positive and negative sequence controllers of rotor VSC and grid VSC effectively limit the electric torque pulsation and DC voltage ripple.

In this paper, the control objective is focused on how to improve performance of DFIG itself under unsymmetrical voltage dip when it is connected to a strong power grid. In future, the control objective will be focused on how to use DFIG to improve grid performance when it is connected with a weak power grid, such as to limit the grid voltage unbalance and etc.

#### ACKNOWLEDGMENT

This work is part of the project PhD@Sea, which is substantially funded under the BSIK-program of the Dutch Government and supported by the consortium WE@Sea.

#### REFERENCES

- "Wind power in power systems", John Wiley & Sons, ISBN: 0-470-85508-8, 2005.
- [2] W. V. Lyon, "Transient analysis of alternating current machinery. An application of the methods of symmetrical components", New York Willy, 1954.
- [3] J. Morren, J.T.G. Pierik, S.W.H. de Haan, J. Bozelie, "Grid interaction of offshore wind farms. Part 1. Models for dynamic simulation", Wind Energy, 8 (3): JUL-SEP 2005.
- [4] J. Pierik, J. Morren, E.J. Wiggelinkhuizen, S.W.H de Haan, T.G. van Engelen, J. Bozelie, "Electrical and control aspects of offshore wind farms II (Erao II), Volume 2: Offshore wind farm case studies", Technical report of ECN&TUD, ECN-C-04-051, Netherlands, 2004.
- [5] Akhmatov, "Analysis of dynamic behavior of electric power systems with large amount of wind power", PhD thesis of Electrical power engineering, ISBN: 87-91184-18-5, Technical University of Denmark, April, 2003.
- [6] Petersson, "Analysis, modeling and control of doubly-fed induction generators for wind turbines", PhD thesis, Electric Power Engineering, Chalmers University of Technology, 2005, Sweden.
- [7] L. Holdsworth, X.G. Wu, J.B. Ekanayake, "Comparison of fixed speed and doubly fed induction wind turbines during power system disturbances", IEE Proceedings of Generation, Transmission and Distribution, Pages: 343-352, Vol. 150, Issue. 3, May, 2003.
- [8] Kim,, H. Akagi, "The instantaneous power theory based on mapping matrices in three-phase four-wire systems", Proceedings of the Power Conversion Conference, 1997, Nagaoka.
- [9] N. Akira, T. Tanaka, "A new definition of instantaneous active-reactive current and power based on instantaneous space vectors on polar coordinates in three-phase circuits", IEEE Transactions on Power Delivery, Volume 11, Issue 3, July 1996.
- [10] Saccomando, J. Svensson, "Transient operation of grid-connected voltage source converter under unbalanced voltage conditions", Industry Applications Conference, 2001, 36 IAS Annual Meeting.
- [11] G.D.Marques,"A comparison of active power filter control methods in unbalanced and non-sinusoidal conditions", Proceedings of the 24th Annual Conference of the IEEE Industrial Electronics Society, 1998.
- [12] Y. Zhou, P. Bauer, J. Pierik, J. A. Ferreira, "New thyristor bridge models for dynamic simulation of grid integration of offshore wind farms", PCIM 2006, Nuremberg, Germany.

# Grid connected and islanded operation of a hybrid power system

Y. Zhou, P. Bauer, B. Ferreira.

PowerAfrica 2007

## Grid-connected and islanded operation of a hybrid power system

Y. Zhou, J. A. Ferreira, P. Bauer

Department of Electrical Power Engineering, Delft University of Technology Mekelweg 4, 2628CD, Delft, the Netherlands Phone: +31-15-27-85744, Fax: +31-15-27-82968

Email: y.zhou@ewi.tudelft.nl, j.a.ferreira@ewi.tudelft.nl, p.bauer@ewi.tudelft.nl

Abstract - Rural area often has only one transmission line in connection with main power grid. The safety of critical load cannot be insured. Instead of adding a second transmission line, distributed generation can be installed. In this paper, a hybrid power system is analyzed. It is composed of solar power, wind farm of doubly fed induction generators (DFIG), pumped storage station, residential load and industry load. Both grid connected operation and islanded operation of this hybrid power system are analyzed. A control strategy is proposed to stabilize this power system under islanded condition without the necessary of central master controller. The water tower with back to back voltage source converter (VSC) is operated as a pumped storage station under islanded situation, which controls the frequency and voltage of the islanded power system. Wind farm, solar power, and load contribute to frequency and voltage control of the hybrid power system.

#### I. INTRODUCTION

Distributed generation (DG) is an economic choice for remote areas. Using distributed generators as the main power source has some obvious advantages. Firstly the power loss on the long transmission line is reduced, secondly the reliability of the area is increased without the necessary to build a second transmission line for backup. Among the distributed generation sources, renewable energy source develops fast. Its development is driven by the government policy to reduce the greenhouse gas emissions and conserve fossil fuels.

In this paper, a hybrid power system for rural area is analyzed. It has a solar power system, a small wind farm composed of several DFIGs, a water tower operated as small pumped storage station, residential and industry load, and a long transmission line connected with main power grid. Because of the length and limited capacity of the line, the transmission line's impedance between the hybrid power system and power grid is large. In this weak power grid with low X/R ratio, voltage fluctuation may cause coupling effect between active and reactive power. More importantly, the distribution line can be out of service without notice. In this digest, firstly the configuration and parameters of this hybrid power system is given, secondly the issues of concern of safely operation of the system are discussed, and then the possible operation strategies and control methods are proposed, both under grid connected situation and islanding situation, and finally the simulation results in Matlab/Simulink are presented.

# II. CONFIGURATION AND PARAMETERS OF THE HYBRID POWER SYSTEM

#### A. Topology of hybrid power system

The hybrid power system includes a solar power system, a small wind farm composed of DFIGs, a water tower, residential and industry loads. It is connected with main power grid through a long and unreliable transmission line. The topology of this system is shown in Figure 1.

Wind farm and solar power are the main power source, their active and reactive power can be controlled independently by VSCs. They can participate in frequency and voltage controls of the power grid.

The water tower is integrated with the local grid through back to back VSCs. It can be operated either in motor mode or in generator mode. It is thus an energy storage device and can work as a small pumped storage station to balance generation and load. In the autonomous power system of [10] and [11], diesel generator or battery is required to start up the wind turbine. In this paper, the wind turbine can be started by the pumped storage station under islanded condition.

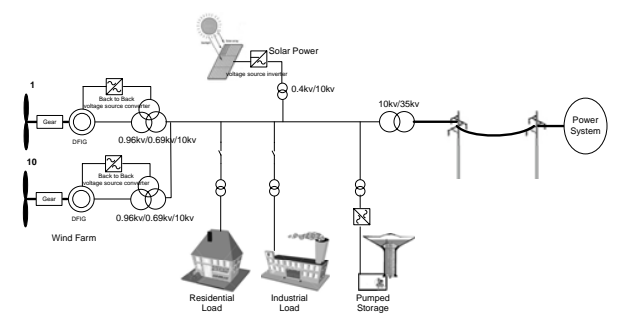


Figure 1 Topology of the hybrid power system

#### B. Typical parameters of the power system

Typical parameters of DFIG wind farm, transmission line, transformer and etc are taken from [7], [12] and [13].

In Table I, the transformer parameters are referred to the 10kV side. The DFIG's inertia is calculated by approximate equation in [13].

	Туре	R(Ω)	L (H)	C (µF)
DFIG generator	Stator	0.0033	0.0047	
	Rotor	0.0143	0.0185	
DFIG transformer	0.96/0.69/10kV	0.4889	0.0118	
Overhead line	35kV	0.17 Ω/km	0.0012 H/km	
Cable line	10kV	0.14 Ω/km	0.00024 H/km	0.42 μF/km
Transformer	10/35kV	0.664	0.208	
DFIG inertia J	Wind turbine	2949 kg/m2		
	Generator	240 kg/m2		

Table I Case study parameters

#### C. Typical grid connected operation of the power system

Typical data of power from wind, solar, and consumed load is recorded from [10] and [11]. The site under consideration in [11] is a small village in remote area of India. Here the load and wind power are scaled up to emulate a large town which has heavy industry. The pumped storage station is only working in motor mode for grid connected operation, providing water for drinking or irrigation and keeping water reservoir at a certain level. The power exchange with power grid is then calculated. At point A, the power drawn from grid is at maximum. At point B, the power sent to grid is at maximum. If the hybrid power system is disconnected from the power grid when absorbing large amount of power from the grid, then low frequency control is required. If it is disconnected from power grid when sending large amount of active power, then high frequency control is required. In section V, cases of point A and B will be studied.

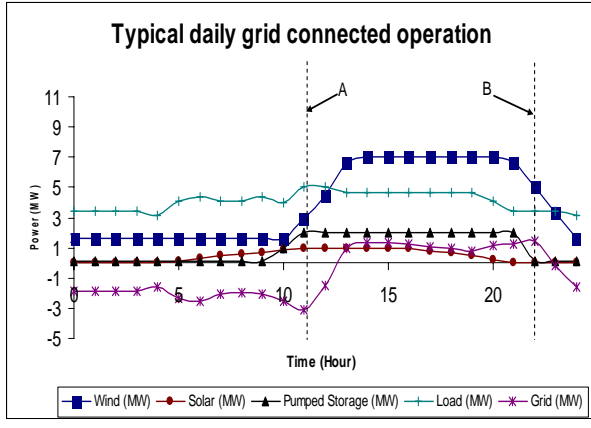


Figure 2 Typical daily operation of the hybrid power system

#### D. Simple design of pumped storage station

The duration time of islanded operation is taken as 24 hours. Under islanded situation, when load is higher than

generation such as point A shown in Figure 2, load shedding is used to limit the imbalance between generation and load. However, there are some critical loads which have to be maintained all time, for example, the load of high furnace of steel factory.

The renewable energy sources are working at their maximum power production before grid disconnection. They are not possible to increase their active power for a long time. For example, the kinetic energy in the shaft of variable speed wind turbine can only be used for short term primary frequency support. Normally, it can only last for several tens of seconds. Furthermore, when the kinetic energy of variable speed wind turbine is used for primary frequency control, the rotation speed will deviate from its optimum speed. The power captured from the wind will decrease. Thus from the point of view of long term, it is not good to use kinetic energy of variable speed wind turbine for islanded operation.

Thus the pumped storage station has to provide considerable energy to maintain critical load during islanded situation.

To simplify the design, the critical load is assumed to be 0.5 MW. The renewable sources can provide half of the total required energy. The volume of water tower has to be designed to provide the other half of required energy. The efficiency of pumped storage station is taken as 90%.

The required electrical energy to provide active power of 0.5MW for 12 hours is 6MWh. It is 2.16\*10<sup>10</sup> Joules. Taking into account of the efficiency, the required potential energy of water is then 2.4\*10<sup>10</sup> Joules. The potential energy of water is both related with the height of water head and the volume of water reservoir. The results are listed as in the following table. The water tower can be placed on a hill to increase water head and decrease the required volume of water reservoir. The water reservoir is assumed to be in cylindrical shape, and its height is taken as 10m.

Design number Water head (m) volume (liter) Radius (m) 20 1.22E+08 62 50 4 90E+07 39 2 3 100 2.45E+07 28 4 150 1.63E+07 23 200 1.22E+07 5 20 250 9.80E+6 18 6

Table 2 required volume and height of pumped storage

An existing design of water Tower with a capacity of  $1.2*10^7$  liters is found through internet. Its water head is 52 meter. If this water tower is placed on a hill of 150 meter, then it can provide enough energy for the islanded operation of this hybrid power system.

# III. PROBLEM IDENFICATION OF THE HYBRID POWER SYSTEM

Although this hybrid power system has many advantages such as reduced power loss and high reliability, it has to face challenges of some new control problems. The control problems include how to detect system separation fast and accurately, how to control several DFIGs and VSCs in parallel operation in a very weak power grid, how to control DFIGs and VSCs in islanded power system to stabilize frequency and voltage without the necessary of centralized controller, how the controllers of DG units can be transferred through grid connected operation to islanding operation and vice versa seamlessly in order to protect the critical load, and what are the influences of different load characteristics. In the following sections, these questions will be discussed in more detail, and then a proper control strategy will be proposed.

#### A. System separation detection

If the controllers of DG units under grid connected and islanded operation are quite different, then signals are required to determine the states of the power system and switch the controller between grid connected mode and islanded mode. Literature often suggests that the status of the circuit breaker is not a reliable signal for indication of system separation. The phase angle difference between local power grid and main power system is adopted as the indication of system separation [3], [5]. However, this method requires a central supervision system and continuous communication between central supervision system and DG units.

If controllers of DG units do not have any difference between grid connected and islanded operation, then it is not necessary to detect the states of the power system. In [6], a local control method is designed for VSC without the requirement of central supervision system.

#### B. Grid connected operation

It is often a challenge to control the voltage profile in distributed grid due to the low X/R ratio. The voltage profile is not mainly influenced by the reactive power as the case in high voltage transmission power grid. The active power flow is found to be critical in controlling the voltage profile in distribution power grid [7]. Thus the maximum active power that can be transmitted from or to the power grid through the distribution line is limited, in order to keep the voltage level of the hybrid power system in the allowable range.

In grid connected operation, DG units work in current controlled mode, assuming the grid voltage is more or less constant. However, in a very weak power grid, the terminal voltages of the generator and VSC will fluctuate. The fluctuation of voltage can cause coupling effect between active and reactive power. Phase locked loop is thus necessary to measure the accurate phase angle. With accurate phase angle

of the voltage, active and reactive power can be efficiently decoupled.

#### C. Islanded operation

In islanded operation, without a constant voltage source, the current control mode of DG unit of grid-connected operation is not appropriate. Without a reference voltage source, the DG units have to control the voltage and frequency in the power grid by themselves. This is not an easy control task, especially when several generators and VSCs are operated in parallel. The islanding operation of VSCs can be found in literatures [3], [4], [6], and [7]. The control method of single DFIG for stand-alone operation is found in literatures [1]and [2], but this method is not appropriate for controlling multiple DFIGs in one islanded system.

#### D. Influences of different kinds of load

The characteristics of load can have significant influences on the designation of the controller.

The load can be either static load or inertia load. The static load is resistive load whose consumed active power is related with its voltage level. The inertia load is the motor load whose active power is related with its rotating speed. If the islanded system is composed totally of static load, it will be difficult to operate several DG units in parallel. The reason is that both active and reactive power will influence the voltage level. Thus it is not possible to determine the active power imbalance from the frequency deviation, and reactive power imbalance from the voltage deviation.

In [8], it is stated that without enough inertia load, the system is difficult to be stabilized after being disconnected from main power grid.

## E. Transfer between grid connected operation and islanded operation

In order to protect the critical load, the transfer between grid connected operation and islanded operation must be smooth.

If the controllers of DG units in grid connected operation and islanded operation are quite different, then a master central controller and communications between all DG units are required to determine the change of DG units' controller mode. This will increase the cost and decrease the reliability of the system, and has to be avoided if it is possible.

## IV. PROPSED CONTROL STRAGETY OF THE HYBRID POWER SYSTEM

In order to solve those problems discussed in section III, the following control strategy is proposed.

This control strategy is explained in the following figure.

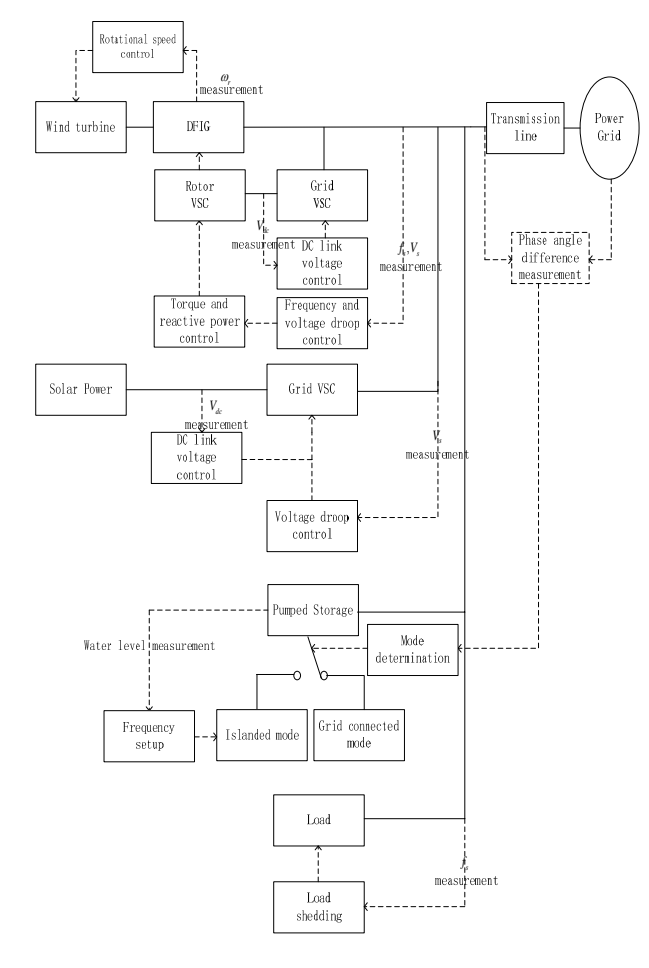


Figure 3 control strategy of the hybrid power system

In Figure 3, the dotted lines are the measurements and control loops, and the solid lines are the electrical connections.

## A. Principles of grid connected operation

The principles for grid connected operation are:

- DFIG wind farm operates under maximum power production mode;
- Solar power system operates under maximum power production mode;
- Pumped storage operates under motor mode, provides water for drinking or irrigation and keep water reservoir at a certain level. Grid side converter controls the DC voltage, generator side converter controls motor power;
- Residential and industrial loads work under maximum;
- The distribution line is in service, transmits power from or to the power grid depending on the balance between power production and consumption in this system;

- Frequency is controlled by the main power grid, while wind farm and solar power can participate in the primary frequency control by using frequency droop control;
- Pumped storage, wind farm and solar power system all participate in the voltage control of the local power grid.

#### B. Principles of islanded operation

The principles for islanding operation are:

- Pumped storage station works as a virtual power grid which determines the voltage and frequency of the hybrid power system. Grid side converter controls the AC voltage, generator side converter controls DC voltage;
- DFIG wind farm and solar power system participate in the frequency and voltage control;
- Load shedding is adopted to limit the frequency dip;
- Critical loads must be protected.

# C. Transfer between grid connected operation and islanded operation

Voltage angle difference between local power system and main power grid is measured. If the angle difference increases to an abnormal value which cannot happen under grid connected operation, then it is determined that the local power system is disconnected from the main power grid. This method is very fast, and can be done in less than one cycle.

A synchronization procedure is required to connect local power system with main power grid. Before synchronization, voltage magnitudes and phase angles of islanded system at point of common coupling (PCC) and grid are measured. The islanded power system at PCC can be controlled by the inverter VSC of pumped storage station. When the magnitude and angle differences between islanded system and main grid approach zero, the synchronization begins, and the hybrid power system is connected with power grid again.

In this control strategy, only one DG unit – the pumped storage station is required to change its control mode. Under grid connected status, the pump storage station is in standard current control mode, while under islanded status, it changes to voltage control mode, and set voltage and frequency of the hybrid power system. This, however, means that the pumped storage station will balance the active power of the hybrid power system. As the volume of the water tower is limited, the total energy that can be used for active power balancing is also limited. Load and DG units can be controlled to help active and reactive power balancing, but they need clear indexes to distinguish between active power imbalance and reactive power imbalance.

As being discussed in section III. D, unlike the main power grid which is composed of synchronous generators, the frequency of the local power system may not change if the

system is dominated by static load. Then it is not possible to control the load or other DG units for active power and reactive power balancing.

The pumped storage station can change its output - ac voltage's frequency based on its own water level. If the water level is beyond the maximum, its inverter will increase the output ac voltage's frequency. If the water level is less than the minimum, it will decrease the frequency. Then other DG units and load can be controlled by the frequency deviation. When DG units or load take part in the active power balancing, the requirement on the pumped storage station is alleviated.

#### V. SIMULATION

The hybrid power system is modeled in Matlab/Simulink. Dynamic models are developed in the synchronous rotating reference frame in order to improve the simulation speed, because the balanced three phase voltage and current in the synchronous rotating reference frame are DC values at steady state.[15]. Some important control tasks of this hybrid power system are simulated. Simulation results are shown in the following graphs.

#### A. Transfer between grid connected and islanded operation

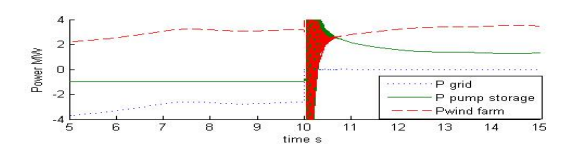


Figure 4 Steady state active power production of the hybrid power system. Dotted line – power flow to the grid, solid line – power production of pumped storage station, and dashed line – power production of wind farm.

During the grid connected period, the pumped storage station works in motor mode, which consumes active power. The imbalance between generation and load in the power system is transmitted to the power grid through the transmission line.

At the 10<sup>th</sup> second, the transmission line is tripped off. The power flow to the grid immediately drops to zero. Oscillations start in the islanded hybrid power system. After several tens of mille-seconds, the pumped storage station detects the system has been disconnected from the main power grid by measurement of phase angle difference. It then changes from current control mode to voltage control mode. It will work as virtual power grid to balance generation and load.

#### B. Low frequency control

When wind speed is low and load is high, the islanded power system may experience generation shortage which has to be balanced by the pumped storage station. As DG units like wind farm and solar power system cannot increase their output power for long time, load shedding is required. The islanded power system's frequency can be controlled by the pumped storage station to enable load shedding.

In Figure 2, at point A, the power absorbed by the hybrid power system is at maximum. Islanded operation at point A is simulated, and results are shown in Figure 5.

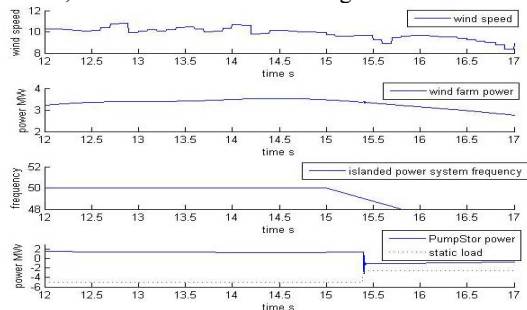


Figure 5 Low frequency control for islanded operation at point A of Figure 2. Graphs from top to bottom are wind speed, power production of wind farm, frequency of islanded power system, power production of pumped storage station and load.

When the islanded system's frequency drops to a low value, the load shedding will begin. After the load shedding, the imbalance between generation and load is limited. Power production of the pumped storage station decreases.

#### C. High frequency control

When wind speed is high and load is low, the islanded power system may have too much generation which has to be absorbed by the pumped storage station. DG units such as wind farm can take part in the high frequency control, by limiting their power production. The islanded power system's frequency can be controlled by the pumped storage station to enable power limitation of DG units.

When the islanded system's frequency increases to a high value, the DFIGs start to limit their active power output by frequency droop control loop in their rotor VSC controller. The imbalance between generation and load is limited, and power absorption of the pumped storage station decreases.

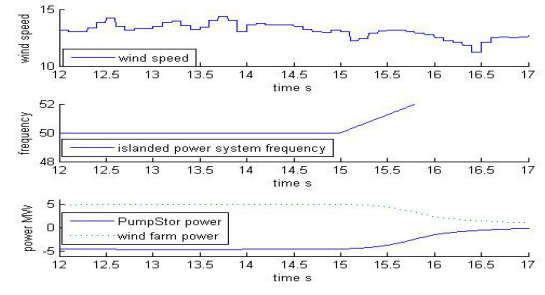


Figure 6 High frequency control for islanded operation at point B of Figure 2. Graphs from top to bottom are wind speed, frequency of islanded power system, power production of pumped storage station and wind farm.

In Figure 2, at point B, the hybrid power system sent maximum power to the power grid. Islanded operation at point B is simulated, and results are shown in Figure 6.

#### D. Voltage control

All the DG units should contribute to the voltage control by controlling their reactive power output. Otherwise, the pumped storage station will experience too much reactive power flow. Though the reactive power will not affect the stored energy in the water tower, too much reactive power output will increase the ac currents, and can cause over current problems of the VSC.

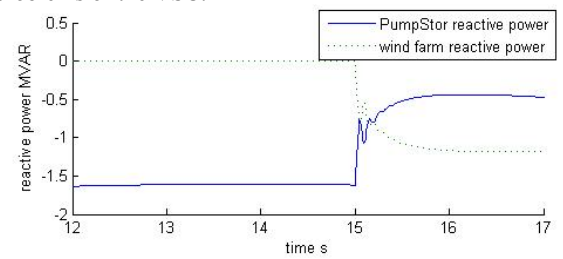


Figure 7 Reactive power production of wind farm and pumped storage station. Solid line – pumped storage station, dotted line – wind farm

Originally, the wind farm controls its reactive power to zero. The ac cables produce large amount of reactive power which has to be absorbed by the pumped storage station.

At 15<sup>th</sup> second, the wind farm begins its reactive power control through voltage-droop controller. The reactive power which has to be absorbed by the pumped storage station is limited.

#### VI. CONCLUSIONS AND RECOMMENDATIONS

A hybrid power system for rural area is analyzed. Control strategy is proposed for grid connected and islanded operation. The proposed control strategy functions well even the load is purely static. In this hybrid power system, the water tower with back to back VSCs is worked as pumped storage station. It changes from current control mode to voltage control mode when the hybrid power system is disconnected from the main power grid. It controls the ac voltage and frequency of the power system under islanded operation. DG units contribute to the high frequency control and voltage control. Load shedding is adopted for low frequency control. Simulation results prove that this hybrid power system works fine under grid connected and islanded operation at steady states, though large oscillations appear when the hybrid power system transfers from grid connected operation to islanded operation.

In this paper, it is assumed that the pumped storage station can change from motor mode to generator mode instantaneously. But in reality, several tens of seconds are required for the mode change. The time scale of this mode change is in accordance with the primary frequency control capability of variable speed wind turbine. Thus the kinetic energy of variable speed wind turbine may be used to provide primary frequency during this period.

In future, the transfer between grid connected and islanded operation will be analyzed in more detail, effects of delayed mode change of pumped storage station will be studied, the possibility to control DFIG as synchronous generator in the islanded power system to decouple active power and reactive power will be investigated.

#### ACKNOWLEDGMENT

This work is part of the project PhD@Sea, which is substantially funded under the BSIK-program of the Dutch Government and supported by the consortium WE@Sea.

#### REFERENCES

- R. S. Pena, R. J. Asher, G. M. Clare, "Vector controlled induction machines for stand-alone wind energy applications", Industry Applications Conference, Vol. 3, pp 1409-1415, 2000.
- [2] G. Iwanski, W. Koczara, "Island operation of the variable speed induction generator", Power Electronics and Motion Conference, Vol. 2, pp 896-901, 2004.
- [3] R. Teodorescu, F. Blaabjerg, "Flexible control of small wind turbines with grid failure detection operating in stand-alone and grid-connected mode", IEEE Transactions on Power Electronics, Vol. 19, Issue 5, pp 1323-1332, 2004.
- [4] R. Tirumala, N. Mohan, C. Henze, "Seamless transfer of grid-connected PWM inverters between utility-interactive and stand-alone modes", Applied Power Electronics Conference and Exposition, Vol.2, pp 1081-1086, 2002.
- [5] S. Agematsu, S. Imai, R. Tsukui, H. Watanabe, T. Nakamura, and T. Matsushima, "Islanding protection system with active and reactive power balancing control for Tokyo metropolitan power system and actual operational experiences", 7th International Conference on Developments in Power Systems Protection, pp 351-354, 2001.
- [6] S. Barsali, M. Ceraolo, P. Pelacchi, D. Poli,, "Control techniques of dispersed generators to improve the continuity of electricity supply", IEEE Power Engineering Society Winter Meeting, Vol. 2, pp 789-794, 2002
- [7] J. Morren, "Grid support by power electronic converters of distributed generator units", PhD thesis, Electric Power Engineering, Delft University of Technology, 2006, Netherlands.
- [8] P. Sorensen, A. D. Hansen, F. Iov, F. Blaabjerg, "Initial results of local grid control using wind farms with grid support", Technical report, Risø-R-1529, Risø National Laboratory, September, 2005, Denmark,.
- [9] "Wind power in power systems", John Wiley & Sons, ISBN: 0-470-85508-8, 2005.
- [10] R. Chedid, S. Rahman, "Unit sizing and control of hybrid wind-sloar power systems", IEEE Transactions on Energy Conversion, Vol. 12, No. 1, March, 1997.
- [11] P. K. Katti, M. K. Khedkar, "Integrated Operation of Decentralised Resources for Rural Area Power Supply Applications", 2005 IEEE/PES Transmission and Distribution Conference & Exhibition: Asia and Pacific Dalian, China, 2005.
- [12] "Power system steady state analyze", Chinese Hydro and Electrical Publication, June, 1991.
- "Wind energy the facts, volume 1- technology", www.ewea.org.
- [14] C.M. Yam, M. H. Harque, "Dynamic decoupled compensator for UPFC control", International conference on power system technology, Vol. 3, pp 1482-1487, 2002.
- [15] J. Morren, J.T.G. Pierik, S.W.H. de Haan, J. Bozelie, "Grid interaction of offshore wind farms. Part 1. Models for dynamic simulation", Wind Energy, 8 (3): JUL-SEP 2005.

## H Executive summary of the Erao-2 project

In The Netherlands offshore wind power is on the brink of implementation. Plans exist for two offshore wind farms of about 100 MW, located 12 and 25 km from the coast of the province of North Holland. In 2003 an investigation has been started to quantify the effect of 6000 MW offshore wind power on the high voltage grid. Only the steady state behaviour has been considered, resulting in suggestions for grid reinforcement. This investigation needs to be complemented by a study on the dynamic interaction of wind power and the electrical grid.

#### Objective of Erao-2

To investigate dynamic interaction of wind farms and the electrical grid, dynamic models of wind farms are needed. These models will be of great help in the evaluation of the behaviour of wind power during normal grid operation as well as during grid faults and in the design of controllers that enable wind farms to support the grid. Dynamic models of wind farms, including the relevant electrical components and sections of the grid, are not available however. The objective of the Erao-2 project is (1) to develop these models, (2) to demonstrate their use by evaluating wind farms with different types of electrical systems and (3) to design and demonstrate controllers that can cope with grid code requirements.

#### Part 1: Model development

The wind farm models are based on models of electrical components and controllers developed in this project and already existing models of wind, rotor, tower, mechanical drive train and pitch controller. The modelled electrical components and controllers are:

- induction generator
- · doubly-fed induction generator
- · permanent magnet generator
- IGBT converter and converter controller
- · transformer
- cable
- synchronous generator
- · consumer load
- · wind farm controller for grid frequency support
- converter controller for grid voltage support

A simple grid model and a model of the flicker meter has also been developed.

An important aspect of dynamic models of electrical systems is computational speed. Electrical transients have very small time constants, resulting in small time steps and long computation time. In Erao-2 special attention has been paid to computational speed. An important increase in speed can be realised by the use of the dq0-transformation, which has been applied to all models of electrical components in the Erao-2 component library.

Volume 1 of this report gives a mathematical derivation of the electrical component models, followed by the implementation of the models in Simulink, a computer program suitable for dynamic simulation. Turbines are modelled by connecting the electrical component models to the models of the rotor, tower, mechanical drive train and pitch controller. In the second step, individual turbine models are connected by cable models to produce the wind farm model.

#### Results and conclusions from model development

Dynamic models of wind farms based on individual turbine models are large and complicated. The number of state variables is high and some of the time constants are small, leading to a relatively long simulation time. The level of detail is high however, which makes these models suitable for the evaluation of wind farm dynamics and wind farm-grid interaction as well as for the design of controllers.

ECN-E-08-017 273

The application of the dq0-transformation significantly reduces the simulation time during normal operation of the wind farm, when transients from electrical switching operation have died out.

#### Part 2: Model demonstration

The second part of the Erao-2 project demonstrates the use of the developed wind farm models. In a number of case studies, four types of wind farms have been compared. The wind farm types use different turbines and different control methods, viz.:

- Constant Speed Stall turbine with directly coupled Induction Generator (CSS-IG, reference case);
- Constant Speed Stall turbine with Cluster Controlled induction generator operating in variable speed mode (CSS-CC);
- Variable Speed Pitch turbine with Doubly Fed Induction Generator (VSP-DFIG);
- Variable Speed Pitch turbine with Permanent Magnet generator and full converter (VSP-PM).

The layout of a proposed offshore wind farm, the Near Shore Wind farm (NSW), has been taken as reference. The Near Shore Wind Farm is planned in the North Sea near the town of Egmond in The Netherlands. One string of 12 turbines has been modelled with each of the four types of turbines. A simplified grid model has been included to enable simulation of wind farm-grid interaction.

For each type of wind farm, three cases have been evaluated:

- normal operation including flicker production;
- response to a grid frequency dip;
- response to a grid voltage dip.

For the wind farms which are able to support grid voltage or grid frequency, a converter controller or a wind farm controller suitable for this purpose has been developed and demonstrated. Volume 2 of this report describes the case study results.

#### Results and conclusions from case studies

Normal operation of the wind farms has been simulated by the response to a wind gust. The simulations demonstrated proper operation of the generator and converter models, the converter controllers and proper overall behaviour of the wind farm.

A limited flicker evaluation has been executed. Instantaneous flicker values have been determined over the complete range of operating conditions for the four types of wind farms. Flicker values of a single turbine have been compared to the values of a string of twelve turbines under the same operating conditions and fictitious grid parameters. The constant speed stall wind farm generates the highest flicker, the flicker production of the wind farms with partial and full converter is lower.

Wind farm response to grid frequency and grid voltage dips

The response of a wind farm to a grid frequency dip (5 Hz, 10 sec) strongly depends on the presence of a converter. A full converter, in the case of the CSS-CC and VSP-PM wind farms decouples the turbines from the disturbance. But also the system with a partial converter (VSP-DFIG) is hardly affected by the frequency dip due to the effective adjustment of the rotor currents by the rotor converter. The constant speed system on the other hand has serious problems with a frequency dip and the corresponding voltage dip: depending on the depth and the conditions at the start of the dip, current, power and reactive power peaks may exceed rated values and may lead to a wind farm shut down.

The farm with constant speed stall turbines and directly connected induction generators (CSS-IG) can stay connected during the voltage dips that have been applied (30%-10 sec, 50%-0.5 sec and 85%-0.2 sec). High currents are flowing during the voltage drop. Due to the high thermal capacity of the induction machine these currents will be no problem. The currents may trigger protective devices in the grid. The high amount of reactive power that is required

274 ECN-E-08-017

by the wind farm during a voltage disturbances can be more problematic. When the dip lasts too long this may lead to voltage collapse.

The Cluster Controlled wind farm (CSS-CC) can handle voltage dips if a resistor is placed in parallel to the dc-link capacitor and the surplus of energy during the voltage dip is dissipated.

Wind farms using doubly-fed induction machines (VSP-DFIG) are the most problematic concept when voltage dips are considered. Large currents will flow in the rotor circuits and in the converters. Due to the limited thermal capacity of the power electronic devices in the converters, these currents may destroy the converters. A possible solution is to limit the high currents in the rotor by providing a by-pass over a set of resistors connected to the rotor windings. With these resistors it is possible to survive grid faults without disconnecting the turbine from the grid. One of the case studies demonstrates this solution. Manufacturers of DFIG systems are working on this solution and are making progress in meeting the voltage ride-through requirement.

In the variable speed pitch wind farm with permanent magnet generators (VSP-PM), all the essential parameters can be controlled. Therefore good voltage dip ride-through can be achieved. The power supplied by the generator is reduced by the controllers during the dip. This is required because otherwise the current in the converters or the dc-link voltage becomes too high. To avoid overspeeding the pitch controller is activated.

Wind farms assisting grid frequency or grid voltage

The constant speed stall controlled wind farm (CSS-IG) can not assist in grid frequency control. The cluster controlled wind farm in the Erao-2 study is based on a stall controlled turbine (CSS-CC). It can not control aerodynamic power directly and therefore it can not assist in grid frequency support either.

Both variable speed pitch wind farms (VSP-DFIG and VSP-PM) can be controlled to support grid frequency, which has been demonstrated by simulations. The controller consists of two parts: delta-control to realise a power margin and frequency feed-back to act on a frequency deviation. Since frequency control capability for wind farms implies maintaining a power margin, this feature may not be cost-efficient.

Only systems with converters are suitable for grid voltage control. Different voltage and reactive power control strategies have been investigated for the VSP-DFIG wind farm. It has been shown that it is possible to control the power factor and that the wind farm can follow reactive power setpoints. Two voltage control options have been investigated. In the first option each turbine controls the voltage at its own terminal, in the second option the voltage at the grid connection point is controlled. Droop control has been implemented on each turbine. With this type of control, the wind farm behaviour during voltage deviations is similar to conventional power plant behaviour. The results depend on the X/R ratio of the grid: low X/R ratios require large amounts of reactive power to control the voltage and the wind farm converters are limited in current and thus in reactive power. Nonetheless, the simulations demonstrate the feasibility of voltage control for wind farms with doubly-fed induction generators.

There is no large difference between voltage control by wind farms with doubly-fed induction generators and voltage control by the other wind farms with IGBT converters: CSS-CC and VSP-PM. This has been demonstrated by simulations with a cluster of CSS-CC turbines and a string of VSP-PM turbines. The results are similar to those of the VSP-DFIG wind farm.

#### Economic evaluation

The load flow program and the database with electrical and economic parameters developed in the Erao-1 project has been used in an economic evaluation of the four wind farm electrical systems. For a wind regime representative of the North Sea, the power production including the electrical losses, has been determined for the layout of the Near Shore Wind farm. This results in the contribution of the electrical system to the Levelised Production Costs (LPC). The VSP-DFIG farm performs best: 1.42 Eurocent/kWh. The CSS-IG farm is of the same magnitude: 1.62 Eurocent/kWh, while the other two farms have relatively expensive electrical systems: 2.60 Eurocent/kWh (VSP-PM) and 4.57 Eurocent/kWh (CSS-CC). The high price for the Cluster Controlled system is caused by the expensive converters.

#### Recommendations

With the completion of the wind farm models based on individual turbines, verification of models should now have a high priority. The Erao-3 project has been started with model validation as one of the objectives.

ECN-E-08-017 275

For the incorporation of dynamic models of wind farms in models of national grids, the complexity of the wind farm models has to be reduced. Aggregated wind farm models, in which all turbines are represented by a single equivalent model are more suitable for this purpose. However, aggregated models loose the wide range of applicability of the wind farm models based on individual turbine models. It is recommended to develop aggregated wind farm models, tailored to application in power system models. The wind farm models developed in Erao-2 can serve as reference in the development of these aggregated models.

Systems with DC cables to shore have not been included in the Erao-2 case studies. The Erao-2 component library includes all models necessary to investigate DC connections, with the exception of the thyristor converter. This converter however, is a less likely option for the connection of offshore wind farms than the IGBT converter, due to its limited controllability and large footprint. DC connections are currently more expensive than AC, but may offer a number of advantages. It is recommended to include these systems in a future study and for comparison purpose also develop a thyristor converter model.

276 ECN-E-08-017